

---

<sup>2</sup> **Consolidation and longevity studies of the CMS  
3 Resistive Plate Chamber system in view of the  
4 High-Luminosity LHC Upgrade**

---

<sup>5</sup>



Alexis Fagot

Thesis to obtain the degree of  
Doctor of Philosophy in Physics  
Academic year 2018-2019





<sup>7</sup>

<sup>8</sup> Promotors: Dr. Michael Tytgat  
Prof. Dr. Dirk Ryckbosch

<sup>9</sup>  
<sup>10</sup> Ghent University  
<sup>11</sup> Faculty of Sciences  
<sup>12</sup> Department of Physics and Astronomy  
<sup>13</sup> Proeftuinstraat 86, B-9000 Ghent, Belgium  
<sup>14</sup> Tel.: +32 9 264.65.28  
<sup>15</sup> Fax.: +32 9 264.66.97

<sup>16</sup>



Alexis Fagot

Thesis to obtain the degree of  
Doctor of Philosophy in Physics  
Academic year 2018-2019





17

## Acknowledgements

18

19

*XX/XX/2018*

*Alexis Fagot*



# Table of Contents

21	<b>Acknowledgements</b>	i
22	<b>Nederlandse samenvatting</b>	vii
23	<b>English summary</b>	ix
24	<b>1 Introduction</b>	1-1
25	<b>2 Investigating the TeV scale</b>	2-1
26	2.1 The Standard Model of Particle Physics . . . . .	2-1
27	2.1.1 A history of particle physics . . . . .	2-2
28	2.1.2 Construction and validation of the Standard Model . . . . .	2-14
29	2.1.3 Investigating the TeV scale . . . . .	2-15
30	2.2 The Large Hadron Collider & the Compact Muon Solenoid . . . . .	2-20
31	2.2.1 LHC, the most powerful particle accelerator . . . . .	2-20
32	2.2.2 Timeline of operation . . . . .	2-23
33	2.2.3 High Luminosity LHC . . . . .	2-25
34	2.2.4 The Compact Muon Solenoid experiment . . . . .	2-25
35	2.2.4.1 The silicon tracker . . . . .	2-27
36	2.2.4.2 The calorimeters . . . . .	2-27
37	2.2.4.3 The muon system . . . . .	2-28
38	2.2.5 Description of the muon system . . . . .	2-29
39	2.2.5.1 The Drift Tubes . . . . .	2-30
40	2.2.5.2 The Cathode Strip Chambers . . . . .	2-31
41	2.2.5.3 The Resistive Plate Chambers . . . . .	2-32
42	<b>3 Physics of Resistive plate chambers</b>	3-1
43	3.1 Principle . . . . .	3-2
44	3.2 Rate capability and time resolution of Resistive Plate Chambers . . . . .	3-3
45	3.2.1 Operation modes . . . . .	3-3
46	3.2.2 Standard gas mixture for RPCs operated in collider experiments . . . . .	3-6
47	3.2.3 Detector designs and performance . . . . .	3-9
48	3.2.3.1 Double-gap RPC . . . . .	3-11
49	3.2.3.2 Multigap RPC (MRPC) . . . . .	3-13
50	3.2.3.3 Charge distribution and performance limitations . . . . .	3-15
51	3.3 Signal formation . . . . .	3-17
52	3.3.1 Energy loss at intermediate energies . . . . .	3-18
53	3.3.2 Primary ionization . . . . .	3-21
54	3.3.3 Development and propagation of avalanches . . . . .	3-24
55	3.3.4 Drift and diffusion of the electron cloud . . . . .	3-28
56	3.3.5 Space charge effect & streamers . . . . .	3-29

---

57	3.4 Effect of atmospherical conditions . . . . .	3-32
58	<b>4 Muon Phase-2 Upgrade</b>	<b>4-1</b>
59	4.1 Motivations for HL-LHC and the upgrade of CMS . . . . .	4-1
60	4.2 Necessity for improved electronics . . . . .	4-5
61	4.3 New detectors and increased acceptance . . . . .	4-7
62	4.3.1 Gas electron multipliers . . . . .	4-8
63	4.3.2 Improved forward resistive plate chambers . . . . .	4-11
64	4.4 Impact on Level-1 Trigger and physics performance . . . . .	4-14
65	4.5 Ecofriendly gas studies . . . . .	4-16
66	<b>5 Longevity studies and Consolidation of the present CMS RPC system</b>	<b>5-1</b>
67	5.1 Testing detectors under extreme conditions . . . . .	5-2
68	5.1.1 The Gamma Irradiation Facility . . . . .	5-4
69	5.1.2 The new Gamma Irradiation Facility . . . . .	5-5
70	5.2 Preliminary studies at GIF . . . . .	5-7
71	5.2.1 RPC test setup . . . . .	5-7
72	5.2.2 Geometrical acceptance of the setup layout to cosmic muons . . . . .	5-9
73	5.2.2.1 Geometrical acceptance simulation setup . . . . .	5-10
74	5.2.2.2 Results and limitations . . . . .	5-12
75	5.2.3 Photon flux at GIF . . . . .	5-14
76	5.2.4 Results and discussions . . . . .	5-17
77	5.3 Longevity tests at GIF++ . . . . .	5-20
78	5.3.1 Selection and characterization of CMS RPCs for longevity at GIF++ . . . . .	5-20
79	5.3.2 RPC test setup . . . . .	5-22
80	5.3.3 GIF++ data flow . . . . .	5-24
81	5.3.4 Measurements performed during beam periods . . . . .	5-26
82	5.3.4.1 Efficiency scans . . . . .	5-26
83	5.3.4.2 Rate scans . . . . .	5-27
84	5.3.4.3 Offline analysis and Data Quality Monitoring . . . . .	5-27
85	5.3.5 Measurements performed during irradiation periods . . . . .	5-29
86	5.3.5.1 Longevity scans . . . . .	5-30
87	5.3.5.2 Daily rate monitoring scans . . . . .	5-33
88	5.3.5.3 Weekly noise monitoring scans . . . . .	5-35
89	5.3.5.4 Weekly source scans . . . . .	5-36
90	5.3.5.5 Weekly current scans . . . . .	5-36
91	5.3.6 Extraction and monitoring of the resistivity . . . . .	5-36
92	5.3.7 Results and discussions . . . . .	5-40
93	<b>6 Improved RPC investigation and preliminary electronics studies</b>	<b>6-1</b>
94	6.1 FEE candidates for the production of iRPCs . . . . .	6-1
95	6.1.1 CMS RPCROC: the RPC upgrade baseline . . . . .	6-2
96	6.1.2 INFN Front-End Board: a robust back-up solution . . . . .	6-4
97	6.2 Preliminary electronics tests at CERN . . . . .	6-5
98	6.2.1 INFN preamplifiers as upgrade candidates . . . . .	6-5
99	6.2.2 INFN preamplifiers mounted onto CMS Front-End Board . . . . .	6-9
100	6.2.3 HARDROC 2 based RPC read-out . . . . .	6-20
101	6.2.4 Outlooks and current FEE certification status . . . . .	6-25
102	<b>7 Conclusions and outlooks</b>	<b>7-1</b>

---

<b>A A data acquisition software for CAEN VME TDCs</b>	<b>A-1</b>
A.1 GIF++ DAQ file tree . . . . .	A-1
A.2 Usage of the DAQ . . . . .	A-2
A.3 Description of the readout setup . . . . .	A-3
A.4 Data read-out . . . . .	A-3
A.4.1 V1190A TDCs . . . . .	A-4
A.4.2 DataReader . . . . .	A-7
A.4.3 Data quality flag . . . . .	A-10
A.5 Communications . . . . .	A-12
A.5.1 V1718 USB Bridge . . . . .	A-13
A.5.2 Configuration file . . . . .	A-14
A.5.3 WebDCS/DAQ intercommunication . . . . .	A-17
A.5.4 Example of inter-process communication cycle . . . . .	A-17
A.6 Software export . . . . .	A-18
<b>B Details on the offline analysis package</b>	<b>B-1</b>
B.1 GIF++ Offline Analysis file tree . . . . .	B-1
B.2 Usage of the Offline Analysis . . . . .	B-2
B.2.1 Output of the offline tool . . . . .	B-3
B.2.1.1 ROOT file . . . . .	B-3
B.2.1.2 CSV files . . . . .	B-5
B.3 Analysis inputs and information handling . . . . .	B-6
B.3.1 Dimensions file and IniFile parser . . . . .	B-7
B.3.2 TDC to RPC link file and Mapping . . . . .	B-8
B.4 Description of GIF++ setup within the Offline Analysis tool . . . . .	B-9
B.4.1 RPC objects . . . . .	B-9
B.4.2 Trolley objects . . . . .	B-10
B.4.3 Infrastructure object . . . . .	B-10
B.5 Handeling of data . . . . .	B-12
B.5.1 RPC hits . . . . .	B-13
B.5.2 Clusters of hits . . . . .	B-14
B.6 DAQ data Analysis . . . . .	B-15
B.6.1 Determination of the run type . . . . .	B-16
B.6.2 Beam time window calculation for efficiency runs . . . . .	B-17
B.6.3 Data loop and histogram filling . . . . .	B-18
B.6.4 Results calculation . . . . .	B-21
B.6.4.1 Rate normalisation . . . . .	B-21
B.6.4.2 Rate and activity . . . . .	B-23
B.6.4.3 Correction of muon performance parameters . . . . .	B-25
B.6.4.4 Strip masking tool . . . . .	B-27
B.6.4.5 Output CSV files filling . . . . .	B-29
B.7 Current information extraction . . . . .	B-31



144

## Nederlandse samenvatting –Dutch Summary–

145



## English summary



# List of Figures

147

148	2.1	Solar spectrum with spectral lines as it visually appeared to Fraunhofer. . . . .	2-2
149	2.2	Through the gold foil experiment, Rutherford could show that most of the mass of atoms was contained in a positively charged nucleus and could then propose a more accurate atomic model than that of Thomson. . . . .	2-3
150			
151			
152	2.3	(a): The orbits in which the electron may travel according to the Bohr model of the hydrogen atom. An electron jumps between orbits and is accompanied by an emitted or absorbed amount of electromagnetic energy ( $h\nu$ ).The orbits radius increases as $n^2$ . (b): Elliptical orbits with the same energy and quantized angular momentum $l = 0, 1, \dots, n - 1$ in the case $n = 5$ . (c): Illustration of quantum mechanical orbital angular momentum. The cones and plane represent possible orientations of the angular momentum vector for $l = 2$ and $m = -2, -1, 0, 1, 2$ . . . . .	2-5
153			
154			
155			
156			
157			
158			
159	2.4	(a): The spectral lines of mercury vapor lamp anomalous Zeeman effect without magnetic field (A) and with magnetic field (B - transverse Zeeman effect & C - longitudinal Zeeman effect). (b): Stern–Gerlach experiment: Silver atoms traveling through an inhomogeneous magnetic field and being deflected up or down depending on their spin. . . . .	2-6
160			
161			
162			
163			
164	2.5	(a): decay of a $\mu$ -meson in an emulsion. (b): track of a $\pi$ -meson in an emulsion signed by Lattes, Powell, and Occhialini. . . . .	2-8
165			
166	2.6	(a): Meson octet. (b): Baryon octet. (c): Baryon decuplet. . . . .	2-9
167	2.7	Discovery of the $J/\Psi$ by both (a) SPEAR (SLAC [74]) and (b) AGS (BNL [75]). In Figure (a), the cross section versus energy is showed for (a) multi hadron final states, (b) $e^+e^-$ final states, and (c) $\mu^+\mu^-$ , $\pi^+\pi^-$ and $K^+K^-$ final states. . . . .	2-10
168			
169			
170	2.8	(a): the color field of QCD only allows for "white" <i>baryons</i> , particles composed of quarks, to exist. Examples are given for mesons, composed of a quark and its anti-quark, and hadrons, composed of three differently colored quarks or anti-quarks. Other exotic baryons have been predicted and observed, such as tetraquarks and pentaquarks. (b): a crossed analysis performed thanks to the data collected by various experiments at different energies have showed that the coupling constant evolves as predicted by the mechanism of asymptotic freedom [87]. . . . .	2-11
171			
172			
173			
174			
175			
176			
177	2.9	Energy spectrum of beta particles emitted by a source of $^{210}Bi$ . . . . .	2-12
178	2.10	As explained through (a), the Wu experiment consisted in measuring the preferred direction of emission of beta rays of a Cobalt source placed in a stable magnetic field aligned, in one case, and anti-aligned, in the other case, with the nuclear spin. The result in (b) showed a violation of parity. . . . .	2-13
179			
180			
181			

182	2.11	The elementary particles of the Standard Model are shown along with their properties. Their interactions with the strong, weak and electromagnetic forces have been made explicit using color squares. In the left column, the scalar Higgs boson is depicted. The center is focused on the matter particles, the fermions, and the right column on the force carriers, the gauge bosons. The role of the Higgs boson in electroweak symmetry breaking is highlighted, and the corresponding way properties of the various particles differ in the (high-energy) symmetric phase (top) and the (low-energy) broken-symmetry phase (bottom) are shown. . . . .	2-15
190	2.12	(a): Total proton-proton cross-section as a function of the collisions center-of-mass energy $\sqrt{s}$ [116] with cosmic-ray data from Akeno Observatory and Fly's Eye Collaboration. (b): Total proton-(anti)proton and interaction channel cross-sections in the TeV scale. . . . .	2-16
194	2.13	Rotation curve (points) of the galaxy M33 compared with best fitting model (line). The short-dashed line represents the rotation profile that would be expected from the observation of the stellar disc alone [128]. . . . .	2-17
197	2.14	Cosmic Microwave Background as measured by the space observatory Planck which mean temperature is $T_\gamma = (2.7255 \pm 0.0006)$ K with anisotropies of the order of a few $\mu$ K. . . . .	2-18
200	2.15	CERN accelerator complex. . . . .	2-20
201	2.16	Pictures of the different accelerators. From top to bottom: first the LINAC 2 and the $Pb$ source of LINAC 3. Then the Booster and the LEIR. Finally, the PS, the SPS and the LHC. . . . .	2-21
204	2.17	(a): schematics of the LHC cryodipoles. 1: Superconducting Coils, 2: Beam pipe, 3: Heat exchanger Pipe, 4: Helium-II Vessel, 5: Superconducting Bus-bar, 6: Iron Yoke, 7: Non-Magnetic Collars, 8: Vacuum Vessel, 9: Radiation Screen, 10: Thermal Shield, 11: Auxiliary Bus-bar Tube, 12: Instrumentation Feed Throughs, 13: Protection Diode, 14: Quadrupole Bus-bars, 15: Spool Piece Bus-bars. (b): magnetic field and resulting motion force applied on the beam particles. . . . .	2-22
210	2.18	The LHC quadrupoles (a) showed together with the magnetic fields and resulting focussing force applied on the beam by two consecutive quadrupoles (b). . . . .	2-23
212	2.19	Distribution of the four-lepton invariant mass for the $ZZ \rightarrow 4l$ analysis as presented by both (a) ATLAS [112] and (b) CMS [113] in 2012. . . . .	2-23
214	2.20	Detailed timeline projection of LHC and HL-LHC operation until 2039 showing the evolution of the instantaneous and integrated luminosity as designed (a) and in the ultimate case where the instantaneous luminosity is increased to $7.5 \times 10^{34} \text{cm}^{-2} \text{s}^{-1}$ thanks to a new increase of instantaneous luminosity during Run 5 (b) [175-177]. . . . .	2-24
218	2.21	Picture of the CMS barrel. The red outer layer is the muon system hosted into the red iron return yokes. The calorimeters are the blue cylinder inside in magnet solenoid and the tracker is the inner yellow cylinder built around the beam pipe. . . . .	2-26
221	2.22	View of the CMS apparatus and of its different components. . . . .	2-26
222	2.23	Slice showing CMS sub-detectors and how particles interact with them. . . . .	2-27
223	2.24	The CMS tracker. . . . .	2-27
224	2.25	(a): The electromagnetic calorimeter. (b): The lead tungstate crystals composing the ECAL. . . . .	2-28
226	2.26	The CMS hadron calorimeter barrel. . . . .	2-28
227	2.27	A quadrant of the muon system, showing DTs (yellow), RPCs (blue), and CSCs (green). . . . .	2-29

229	2.28 (a): Barrel wheel with its detector rings and return yokes. (b): CSC endcap disk with the two CSC stations. The outer station is made of 10 deg detectors while the inner station is made of 20 deg detectors. (c): RPC endcap disk. The inner station is not equipped, leaving the inner CSC station visible. . . . .	2-29
233	2.29 (a): Cross section of a DT module showing the two superlayers measuring the $\phi$ coordinate, perpendicular to the cross section plane, and the superlayer measuring the $\eta$ coordinate, placed in between the two others with a honeycomb plate and parallel to the cross section plane. The DT detector is sandwiched in between 2 RPCs whose readout strips are perpendicular to the cross section plane, measuring the $\phi$ coordinate. (b): A DT cell is shown together with its electric field. The path of a muon through a superlayer is shown. . . . .	2-30
240	2.30 (a): Cathode strips and anode wire layout of a CSC panel. (b): Avalanche development and charge collection by anode wires and induction on cathode strips inside of a CSC panel. . . . .	2-31
243	2.31 Muon track reconstruction through the six panels of a CMS CSC using the information of anode wire groups and cathode strip charge distribution combined with comparator bits to decide on which half strip the muon is more likely to have passed. . . . .	2-31
246	2.32 Double-gap layout of CMS RPCs. Muons passing through the gas volumes will create electron-ions pairs by ionising the gas. This ionisation will immediately translate into a developing avalanche. . . . .	2-32
249	2.33 View of the positions of DT and RPC detectors in barrel Wheel W+2. . . . .	2-33
250	2.34 View of the positions of RPC detectors in endcap Disk +2. The first ring corresponding to RE+2/1 is not equiped with RPC detectors. . . . .	2-34
252	3.1 Different phases of the avalanche development in the RPC gas volume subjected to a constant electric field $E_0$ . a) An avalanche is initiated by the primary ionisation caused by the passage of a charged particle through the gas volume. b) Due to its growing size, the avalanche starts to locally influence the electric field. c) The electrons, lighter than the cations reach the anode first. d) The ions reach the cathode. While the charges have not recombined, the electric field in the small region around the avalanche stays affected and locally blinds the detector. . . . .	3-2
259	3.2 Movement of the charge carriers in an RPC. (a): Voltage across an RPC whose electrodes have a relative permittivity of 5 at the moment the tension is applied. (b): After the charge carriers moved, the electrodes are charged and there is no voltage drop over the electrodes anymore. The full potential is applied over the gas gap only. (c): The streamer discharge initiated by a charged particle transports electrons and cations towards the anode and cathode respectively. . . . .	3-4
265	3.3 Typical oscilloscope pulses in streamer mode (a) and avalanche mode (b). In the case of streamer mode, the very small avalanche signal is visible. . . . .	3-5
267	3.4 Rate capability comparison for the streamer and avalanche mode of operation. An order of magnitude in rate capability for a maximal efficiency drop of 10% is gained by using the avalanche mode over the streamer mode. . . . .	3-5
270	3.5 Comparison of the charge distribution of signals induced by cosmic muons in an RPC operated with a gas mixture of argon, butane and bromotrifluoromethane ( $CF_3Br$ ). The $Ar/C_4H_{10}$ is kept constant at 60/40 in volume while the total amount of $CF_3Br$ in the mixture is varied: 0% (a), 4% (b) and 8% (c) [184]. . . . .	3-6

274      3.6 Comparison of the efficiency and streamer probability, defined as the fraction of 275 events with an induced charge 10 times larger than that of the average avalanche, 276 with and without irradiation by a 24 GBq $^{137}Cs$ source of an RPC successively 277 operated with a 90/10 mixture $C_2H_2F_4/i-C_4H_{10}$ (a) and a 70/5/10/15 mixture of 278 $Ar/i-C_4H_{10}/CO_2/C_2H_2F_4$ (b) [185]. . . . .	3-7
279      3.7 Comparison of the fast charge ratio with and without irradiation by a 24 GBq $^{137}Cs$ 280 source of an RPC successively operated with a 90/10 mixture $C_2H_2F_4/i-C_4H_{10}$ (a) 281 and a 70/5/10/15 mixture of $Ar/i-C_4H_{10}/CO_2/C_2H_2F_4$ (b). The results are pro- 282 vided for both single-gap and double-gap operation [185]. . . . .	3-7
283      3.8 Efficiency (circles and stars with 30 mV and 100 mV thresholds respectively) and 284 streamer probability (opened circles) as function of the operating voltage of a 2 mm 285 single-gap HPL RPC flushed with a gas mixture containing (a) 5%, (b) 2%, (c) 1% 286 and (d) no $SF_6$ [187]. . . . .	3-8
287      3.9 Comparison of the rate capability of 8 mm and 2 mm wide RPCs. The lines are 288 linear fits on the data [204]. . . . .	3-9
289      3.10 Distributions of the induced charge of fast signals on 2 mm (a) and 8 mm (b) RPCs 290 exposed to a radiation rate of 100 Hz/cm <sup>2</sup> . Average induced charge of fast signals 291 as a function of the high voltage applied on 2 mm and 8 mm RPCs (c). In the case 292 of the 2 mm RPC, a saturation of the pre-amplifier was observed. The average of the 293 distribution is underestimated, and the median is shown together with the average to 294 account for this bias [204]. . . . .	3-10
295      3.11 Time distributions of the leading, trailing, and average of both leading and trailing 296 edges for 2 mm (top row) and 8 mm (bottom row) RPCs exposed to a 100 Hz/cm <sup>2</sup> 297 radiation rate. The data were collected with RPCs operated at the voltage corre- 298 sponding to the knee of the efficiency distribution, defined as the point where 95% 299 of the maximum efficiency is obtained [204]. . . . .	3-11
300      3.12 Possible double-gap RPC layouts: a) "standard" 1D double-gap RPC, as used in 301 the CMS experiment, where the anodes are facing each other and a 1D read-out 302 plane is sandwiched in between them, b) double read-out double-gap RPC as used in 303 ATLAS experiment, where the cathodes are facing each other and 2 read-out planes 304 are used on the outer surfaces. This last layout can offer the possibility to use a 2D 305 reconstruction by using orthogonal read-out planes. . . . .	3-11
306      3.13 Comparison of performance of CMS double and single-gap RPCs using cosmic 307 muons [205]. (a): Comparison of efficiency curves. (b): Voltage distribution at 308 95% of maximum efficiency. (c): Distribution of the voltage difference between the 309 point at 90% and 10% efficiency $\Delta_{10\%}^{90\%}$ . . . . .	3-12
310      3.14 Representation of different RPC layouts (wide gap (a), double-gap (b) and multigap 311 (c)), of the corresponding sensitive volume in gray, and of the associated avalanche 312 size [190]. . . . .	3-13
313      3.15 Time distributions of the leading, trailing, and average of both leading and trailing 314 edges for multigap RPCs consisting in two 4 mm (a) and four 2 mm (b) exposed to 315 a 100 Hz/cm <sup>2</sup> radiation rate. The data were collected with RPCs operated at the 316 voltage corresponding to the knee of the efficiency distribution, defined as the point 317 where 95% of the maximum efficiency is obtained [190]. . . . .	3-14
318      3.16 Presentation of a study for an ALICE MRPC cell prototype using 250 $\mu m$ gas gaps, 319 620 $\mu m$ outer glass electrodes, and 550 $\mu m$ inner floating electrodes (a), and of its 320 time resolution performance as a function of the applied high voltage for different ra- 321 diation levels corresponding to different filter settings of the 740 GBq $^{137}Cs$ source 322 at the former CERN Gif facility (b) [206]. . . . .	3-14

323	3.17 Comparison of the detector performance of ALICE ToF MRPC [212] at fixed applied voltage (in blue) and at fixed effective voltage (in red). The effective voltage is kept fixed by increasing the applied voltage accordingly to the current drawn by the detector.	3-15
324		
325		
326	3.18 Ratio between total induced charge and drifting charge have been simulated for single-gap, double-gap and multigap layouts [213]. The total induced charge for a double-gap RPC is a factor 2 higher than for a multigap. . . . .	3-15
327		
328		
329	3.19 Charge spectra have been simulated for single-gap, double-gap and multigap layouts [213]. It appears that while single-gaps show a decreasing spectrum, double and multigap layouts exhibit a spectrum whose maximum is significantly above zero. The shift of maximum value in the spectrum increases along with the number of gaps.	3-16
330		
331		
332	3.20 The maximal efficiency theoretical is simulated for single-gap, double-gap and multi-gap layouts [213] at a constant gap thickness of 2 mm and using an effective Townsend coefficient of $9 \text{ mm}^{-1}$ . . . . .	3-16
333		
334		
335		
336	3.21 Mass stopping power as a function of $\beta\gamma = p/Mc$ for positive muons in copper [115]. The total stopping power is indicated with a solid line and local components with dashed lines. The vertical bands are used to indicate boundaries between different approximations used at different energy range. . . . .	3-17
337		
338		
339		
340	3.22 Mean excitation energies normalized to the atomic number as adopted by the ICRU [115, 216, 217]. . . . .	3-18
341		
342		
343	3.23 Mean mass stopping power for liquid hydrogen, as used in bubble chambers, gaseous helium, carbon, aluminum, iron, tin, and lead without the inclusion of radiative effect at higher $\beta\gamma$ necessary for pions and muons in denser materials [115]. . . . .	3-19
344		
345	3.24 Mean mass stopping power at minimum ionization as a function of the atomic number [115]. . . . .	3-19
346		
347	3.25 Example of straggling function (solid) $f(\Delta)$ of particles passing through 1.2 cm of Argon gas with a $\beta\gamma$ of 3.6. The original Landau distribution is shown with a dashed line [219]. . . . .	3-20
348		
349		
350	3.26 Evolution of straggling functions $f(\Delta)$ of particles passing through a volume of Argon gas with a $\beta\gamma$ of 3.6 with increasing thickness $x$ [219]. . . . .	3-20
351		
352	3.27 Photoabsorption cross section as computed by HEED for nobles gases with different electron shell numbers [215]. . . . .	3-21
353		
354	3.28 Photoabsorption cross section as computed by HEED for typical RPC gas mixtures [215]. The RPC mixture with $CO_2$ corresponds to the mixture used by CALICE SD-HCAL [221] while the other one was foreseen for the experiment ATLAS [222] but has been changed since then. Both mixtures being largely composed of $C_2H_2F_4$ , the curves are nearly identical. . . . .	3-22
355		
356		
357		
358		
359	3.29 Distributions of number of electrons (left) and energy loss (right) for a 5 GeV/c muon passing through 1.2 mm of Helium (a), Argon (b) or a typical RPC gas mixture (c) [215]. . . . .	3-23
360		
361		
362	3.30 (a): Mean cluster density for muons through different gas volumes [215]. (b): Distribution of the number of electrons per cluster for a 5 GeV/c muon traveling through a mixture of 96.7% $C_2H_2F_4$ , 3% i- $C_4H_{10}$ and 0.3% $SF_6$ [215, 222]. . . . .	3-24
363		
364		
365	3.31 Townsend and attachment coefficient for a typical 96.7/3/0.3 mixture of $C_2H_2F_4$ /i- $C_4H_{10}$ / $SF_6$ , at a temperature $T = 296.15 \text{ K}$ and a pressure $P = 1013 \text{ hPa}$ [215, 222]. . . . .	3-24
366		
367		
368	3.32 Comparison of the distribution law of Furry and the Poisson law for $\bar{n} = 5$ [227]. . . . .	3-25
369		
370	3.33 Single-electron avalanche size distribution in a proportional counter filled with methanol at different $E/p$ values. (a) 70, (b) 76.5, (c) 105, (d) 186.5, (e) 426V/cm torr [229]. The straight lines correspond to an exponential fit. . . . .	3-26
371		

372      3.34	(a): Comparison of avalanche size distributions for different values of Townsend 373      and attachment coefficients. The effective Townsend coefficient is the same for both 374      distributions. (b): Fluctuation in avalanche sizes for avalanches started by a single 375      electron with $\alpha = 13 \text{ mm}^{-1}$ and $\eta = 3.5 \text{ mm}^{-1}$ [222]. . . . .	3-27
376      3.35	(a): Electrons mean drift velocity $v_D$ in pure $C_2H_2F_4$ and typical RPC gas mix- 377      tures. (b): Transverse diffusion coefficient in pure $C_2H_2F_4$ and a typical RPC gas 378      mixture. (c): Longitudinal diffusion coefficient in pure $C_2H_2F_4$ and a typical RPC 379      gas mixture. All results are given for a pressure $P = 760 \text{ Torr}$ and a temperature 380 $T = 296.15 \text{ K}$ [215]. . . . .	3-28
381      3.36	Comparison of the free charge carriers in the gas after a time $t = 7.90 \text{ ns}$ in the case 382      where no diffusion is taken into account to simulate the avalanche (a) and in the case 383      where the diffusion is implemented (b) [215]. . . . .	3-29
384      3.37	Schematic representation of an avalanche and of the electric field deformation it 385      causes due to the local concentration of charge carriers [197]. . . . .	3-30
386      3.38	Evolution of the charge induced by an avalanche started by a single electron in a 387      1.2 mm thick RPC with an applied electric field of 54 kV/cm in the case space 388      charge is not taken into account (a) and in the case it is implemented into the sim- 389      ulation (b). The total induced charge is correlated to the size of the avalanche [215]. . .	3-30
390      3.39	Distributions of charge carriers within the gas volume of a 1.2 mm thick RPC and 391      the corresponding deformation of the electric field at different time steps with an 392      applied electric field of 55.5 kV/cm [215]. . . . .	3-31
393      3.40	Representation of the weighting field in the volume of an RPC and the resulting 394      induced current in the strip placed at 1 V and its neighbour connected to the ground. 395      The induced current corresponds, as can be understood from Formula 3.22 [197]. . .	3-32
396      3.41	Schematics of CMS RPC FEE logic. . . . .	3-32
397      3.42	Equivalence in between the charge of the induced signal in input of the CMS FEE 398      and the signal strength on the output of the pre-amplifier. . . . .	3-33
399      3.43	Typical efficiency sigmoid of a CMS RPC detector. The black dots correspond to 400      the data, the blue line to the sigmoid fit and the open cross to the knee and working 401      point extracted from the fit. . . . .	3-33
402      3.44	Effect of the temperature variation on the rate (a) and the efficiency (b) of an RPC [232].	3-34
403      3.45	Effect of the pressure variation on the rate (a) and the efficiency (b) of an RPC [233].	3-35
404      4.1	The measured transit time of an HSCP in CMS is compared to the transit time of a 405      particle traveling at near the speed of light [177]. . . . .	4-2
406      4.2	Slice of the CMS detector showing examples of passage of SM particles and R- 407      hadrons. On the one hand, lepton-like HSCPs will appear to behave like slow and 408      heavy muons. On the other hand, R-hadrons are likely to convert into other kind of 409      charged or neutral R-hadrons due to interactions inside the detector volume. . . . .	4-2
410      4.3	Distribution of the energy-loss $dE/dx$ as described by Bethe-Bloch formula through 411      the estimator $I_h$ with increasing particle momentum for tracks in the 13 TeV data. 412      The estimator depends on the charge deposition of the particles per unit length in 413      the silicon detectors of CMS which is related to their energy loss as explained in a 414      publication by the CMS Collaboration [241]. The simulated HSCPs are singly or 415      multiply charged particles with masses of 400 and 1000 GeV. . . . .	4-3
416      4.4	Distribution of the average number of interactions per crossing (pileup) for pp- 417      collisions in 2011 (red), 2012 (blue), 2015 (purple), 2016 (orange), 2017 (light blue), 418      and 2018 (navy blue). The overall mean values and the minimum bias cross sections 419      are also shown [249]. . . . .	4-4

420	4.5	Absorbed dose in the CMS Cavern after an integrated luminosity of $3000 \text{ fb}^{-1}$ . Using the interaction point as reference, R is the transverse distance from the beamline and Z is the distance along the beamline [177]. . . . .	4-4
421			
422	4.6	Extrapolated fraction of failing channels of the present DT MiC1 electronics as a function of the integrated luminosity for different scenarios until LS4 [177]. . . . .	4-5
423			
424	4.7	The event loss fractions as a function of the instantaneous luminosity is compared for CFEBs (Phase-1) and DCFEBs (Phase-2) at different CSC locations. HL-LHC luminosity is marked with the dashed brown line [177]. . . . .	4-5
425			
426	4.8	Comparison of the simulated time residuals in between reconstructed and true muon times without (blue) and with (red) the upgraded RPC link system [177]. . . . .	4-6
427			
428	4.9	(a): Time delay with respect to a particle traveling at the speed of light measured at consecutive RPC stations for particles originating at different bunch crossings and traveling at different velocities [177]. (b): In blue is showed the standard Level-1 muon trigger efficiency as a function of $\beta$ and in blue is showed the RPC-HSCP trigger efficiency after upgrade of the RPC Link System [177]. . . . .	4-6
429			
430	4.10	A quadrant of the muon system, showing DTs (yellow), RPCs (blue), and CSCs (green). The locations of new forward muon detectors for Phase-2 are contained within the dashed box and indicated in red for GEM stations (ME0, GE1/1, and GE2/1) and dark blue for improved RPC (iRPC) stations (RE3/1 and RE4/1). . . . .	4-7
431			
432	4.11	RMS of the multiple scattering displacement as a function of muon $p_T$ for the proposed forward muon stations. All of the electromagnetic processes such as bremsstrahlung and magnetic field effect are included in the simulation. . . . .	4-8
433			
434	4.12	Schematics of a GEM. On top is the cathode and on the bottom, the anode on which a 2D read-out is installed. Finally, the GEM foil separates the gas volume into the drift region, in between the cathode and the foil, and the induction region, in between the foil and the anode. A negative voltage is applied on the cathode. The anode is connected to the ground. . . . .	4-8
435			
436	4.13	Top: Picture of a CMS GEM foil provided by a scanning electron microscope. Bottom: Representation of the electric field in a GEM hole and of the amplification electrons and ions undergo due to the very intense electric field. . . . .	4-9
437			
438	4.14	The gas volume of CMS triple-GEMs is divided into four areas. Primary electrons are created in the <i>Drift</i> area and amplified by three GEM-foils while drifting through <i>Transfer</i> areas. Reaching the <i>Induction</i> area, the avalanche induces current in the read-out. The typical dimensions and potentials are provided. . . . .	4-9
439			
440	4.15	Simulated (a) efficiency and (b) rate of the standalone Level-1 muon trigger using tracks reconstructed in CSCs and all GEM stations compared with Phase-1 values in the case where only CSCs are used or CSCs+GE1/1. The zones of inefficiency of the CSC subsystem are compensated by the addition of GEMs during Phase-2 and the trigger rates is kept from increasing due to the high luminosity [177]. . . . .	4-10
441			
442	4.16	(a): Simulated resolution of the muon direction measurement $\Delta\phi$ with Phase-2 conditions. In the second endcap station, the resolution is compared in the case of CSCs (ME2/1) alone and CSCs+GEMs (GE2/1+ME2/1) while a similar resolution measurement is given in the case of the first station (GE1/1+ME1/1) [177]. (b): The addition of GEM detectors on stations 1 and 2 (ME0 is considered to contribute to station 1) as redundant system to CSCs allows improving the muon momentum improvement through a more accurate measurement of the local bending angles $\phi_1$ and $\phi_2$ [177]. . . . .	4-11
443			
444			
445			
446			
447			
448			
449			
450			
451			
452			
453			
454			
455			
456			
457			
458			
459			
460			
461			
462			
463			
464			
465			
466			

467	4.17 Simulation of the impact of RPC hit inclusion onto the local trigger primitive efficiency in station 3 (a) and station 4 (b) [177]. The contribution of iRPC starts above $ \eta  = 1.8$ . . . . .	4-11
468		
469		
470	4.18 Expected hit rate due to neutrons, photons, electrons and positrons at HL-HLC instantaneous luminosity of $5 \times 10^{34} \text{ cm}^{-2}\text{s}^{-1}$ in RE3/1 and RE4/1 chambers [255, 256]. The sensitivities of iRPCs used in the simulation for each particle are reported and differ from one endcap disk to another as the energies of the considered particles varies with the increasing distance from the interaction point. . . . .	4-12
471		
472		
473		
474		
475	4.19 Measured average charge per avalanche as a function of the effective electric field for different gas gap thickness in double-gap RPCs using HPL electrodes [177]. . . . .	4-13
476		
477	4.20 Level-1 Trigger data flow during Phase-2 operations [177]. . . . .	4-14
478		
479	4.21 Efficiency of the L1 trigger in the endcap region after Phase-2 upgrade in the case CSC/GEM/RPC hits are requested in at least two stations out of four (a) and in all four stations (b) [177]. . . . .	4-15
480		
481	4.22 Comparison of L1 trigger performances for prompt muons with and without the addition of GEMs in the region $2.1 <  \eta  < 2.4$ at Phase-2 conditions [177]. GEMs would allow a reduction of the trigger accept rate by an order of magnitude (a) while increasing the trigger efficiency (b). . . . .	4-15
482		
483		
484		
485	4.23 The angular resolution on reconstructed muon tracks in the GEM overlap region $2.0 <  \eta  < 2.15$ is compared for Phase-2 conditions in the case CSC are alone (a) and in the case the GEMs' data, including ME0, is combined to which of CSCs (b) [177].	4-16
486		
487		
488	4.24 Resolution of the LCT ambiguous events thanks to the combination of CSC and iRPC readout data. Using CSCs only, two pairs of hits are possible [177]. . . . .	4-16
489		
490	4.25 Evolution of the efficiency, working voltage, and voltage at 50% of maximum efficiency for CMS Barrel (a) and Endcap (b) RPCs obtained through yearly voltage scans since 2011. The working voltage of each RPC is updated after each voltage scan to ensure optimal operation [261]. . . . .	4-17
491		
492		
493		
494	4.26 Efficiency (a) [203] and cluster size (b) of a standard double-gap RPC operated with $\text{CO}_2$ mixtures for different ratios of $SF_6$ . . . . .	4-18
495		
496	4.27 Efficiency of a CMS double-gap RPC operated with 30% of $HFO$ , 4.5% of $iC_4H_{10}$ , 1% of $SF_6$ and 64.5% of $\text{CO}_2$ [203]. . . . .	4-18
497		
498	4.28 The efficiency (solid lines) and streamer probability (dashed lines) of $HFO/\text{CO}_2$ (a) and $CF_3I/\text{CO}_2$ (b) based gas mixtures as a function of the effective high-voltage are compared with the present CMS RPC gas mixture represented in black [177, 203]. The detector used for the study is a single-gap RPC with similar properties than CMS RPCs. The streamer probability is defined as the proportion of events with a deposited charge greater than 20 pC. . . . .	4-19
499		
500		
501		
502		
503		
504	4.29 Efficiency (open symbols) and cluster size (full symbols) of an iRPC as a function of the effective voltage for the standard CMS gas mixture and an environmental-friendly gas mixture [177]. . . . .	4-20
505		
506		
507	5.1 Mean RPC Barrel (left column) and Endcap (right column) rate (top row) and current (bottom row) as a function of the instantaneous luminosity as measured in 2017 $p-p$ collision data. . . . .	5-2
508		
509		
510	5.2 Linear extrapolation of the hit rate (a) and of the integrated charge (b) per region (Barrel, Endcap) respectively to HL-LHC instantaneous luminosity ( $5 \times 10^{34} \text{ cm}^{-2} \text{ s}^{-1}$ ) and HL-LHC integrated luminosity ( $3000 \text{ fb}^{-1}$ ). . . . .	5-3
511		
512		

513	5.3 CMS RPC mean integrated charge in the Barrel region (a) and the Endcap region (b). The integrated charge per year is shown in blue. The red curve shows the evolution of the accumulated integrated charge through time. The blank period in 2013 and 2014 corresponds to LS1. . . . .	5-4
514		
515		
516		
517	5.4 Layout of the test beam zone of GIF at CERN. . . . .	5-4
518		
519	5.5 $^{137}\text{Cs}$ decays by $\beta^-$ emission to the ground state of $^{137}\text{Ba}$ (BR = 5.64%) and via the 662 keV isomeric level of $^{137}\text{Ba}$ (BR = 94.36%) whose half-life is 2.55min. . . . .	5-5
520		
521	5.6 Floor plan of the GIF++ facility. When the facility downstream of the GIF++ takes electron beam, a beam pipe is installed along the beam line (z-axis). The irradiator can be displaced laterally (its center moves from $x = 0.65$ m to 2.15 m), to increase the distance to the beam pipe. . . . .	5-6
522		
523		
524	5.7 Simulated unattenuated current of photons in the xz plane (a) and yz plane (b) through the source at $x = 0.65$ m and $y = 0$ m [267]. With angular correction filters, the current of 662 keV photons is made uniform in xy planes. . . . .	5-6
525		
526		
527	5.8 Description of the RPC setup. Dimensions are given in mm. A tent containing RPCs is placed at 1720 mm from the source container. The source is situated in the center of the container. RE-4-2-BARC-161 chamber is 160 mm inside the tent. This way, the distance between the source and the chambers plan is 2060 mm. Figure (a) provides a side view of the setup in the xz plane while Figure (b) shows a top view in the yz plane. . . . .	5-7
528		
529		
530		
531		
532		
533	5.9 (a) Shaping of the signals from the RPC strips by the FEE. The output LVDS signals are then read-out by a TDC module connected to a computer or converted into NIM and sent to scalers. (b) Trigger logic implementation with the RPC and photomulti- plier signals. . . . .	5-8
534		
535		
536		
537	5.10 RE-4-2-BARC-161 chamber is inside the tent as described in Figure 5.8. In the top right, the two scintillators used as trigger can be seen. . . . .	5-8
538		
539	5.11 Hit distributions over all three partitions of RE-4-2-BARC-161 chamber is showed. Top, middle and bottom figures respectively correspond to partitions A, B, and C. . . . .	5-9
540		
541	5.12 Comparison of the efficiency of chamber RE-4-2-BARC-161 with and without irradiation. Results are derived from data taken on half-partition B2 only. . . . .	5-10
542		
543	5.13 Representation of the layout used for the simulations of the test setup. (a) Global view of the simulated setup. (b) Zoomed view on the experimental setup. . . . .	5-11
544		
545	5.14 Geometrical acceptance distribution as provided by the Monte Carlo simulation. . . . .	5-12
546		
547	5.15 Comparison of the hit distribution recorded in the detector and of the normalised geometrical acceptance distribution. . . . .	5-13
548		
549	5.16 Effect of the variation of telescope inclination on the normalised geometrical accep- tance distribution. . . . .	5-13
550		
551	5.17 Correction of the efficiency without source. The efficiency after correction gets much closer to the Reference measurement performed before the study in GIF by reaching a plateau of $(93.52 \pm 2.64)\%$ . . . . .	5-13
552		
553	5.18 Hit distributions over read-out partition B of RE-4-2-BARC-161 chamber to- gether with skew distribution fits corresponding to forward and backward coming muons. . . . .	5-14
554		
555		
556	5.19 (a) Linear approximation fit performed on the data extracted from table 5.3. (b) Comparison of Equation 5.4 with the simulated flux using $a$ and $b$ given in fig- ure 5.19a in Equation 5.2 and the reference $D_0 = 50$ cm and the associated flux for each absorption factor $F_0^{ABS}$ from table 5.2. . . . .	5-16
557		
558		
559		

560	5.20 Efficiency (a) and cluster size (b) of chamber RE-4-2-BARC-161 measured at 561      GIF with Source OFF (red) and Source ON using different absorber settings: ABS 562      5 (green), ABS 2 (blue) and ABS 1 (yellow). The results are compared to the Refer- 563      ence values obtained with cosmics. . . . .	5-17
564	5.21 Rates in chamber RE-4-2-BARC-161 measured at GIF with Source OFF (red) and 565      Source ON using different absorber settings: ABS 5 (green), ABS 2 (blue) and ABS 566      1 (yellow). On Figure (b), the rates of Figure (a) were normalized to the measured 567      efficiency, and constant fits are performed on Source ON data showing the gamma 568      rate in the chamber. . . . .	5-18
569	5.22 Evolution of the voltages at half maximum and at 95% of the maximum efficiency 570      (Figure 5.22a), and of the maximum efficiency (Figure 5.22b) as a function of the 571      rate in chamber RE-4-2-BARC-161. The data is extracted from the fits in Fig- 572      ures 5.20a and 5.21b. . . . .	5-19
573	5.23 Presentation of a double-gap endcap RPC with its three RPC gaps. Due to the par- 574      titioning of the read-out strips into three rolls, the TOP layer of gap is divided into 575      two gaps: TOP NARROW (TN) and TOP WIDE (TW). The BOTTOM (B) only 576      consists in one gap. . . . .	5-19
577	5.24 Current density (a) and charge deposition per gamma avalanche (a), defined as the 578      current density normalized to the measured rate taken from Figure 5.21a as a func- 579      tion of the effective high voltage in chamber RE-4-2-BARC-161 measured at GIF 580      with Source ON using different absorber settings: ABS 5 (green), ABS 2 (blue) and 581      ABS 1 (yellow). . . . .	5-20
582	5.25 Characterization of CMS RPC detectors foreseen to be used at GIF++ for longevity 583      studies of the present system. Using cosmic muons, efficiency (a) and cluster size (b) 584      were measured as well as noise rate (c) and current density (d). For each detector, 585      the working voltage, defined as in Formula 3.25, was extracted from sigmoid fits 586      performed in Figure (a) and the values of efficiency, cluster size, noise rate and 587      current density at this voltage are reported using open crosses. . . . .	5-21
588	5.26 CMS RPC setup inside the GIF++ bunker during test beam (a) and ageing peri- 589      ods (b). The space in between the RPCs and the source is usually used by other 590      detectors while the space in between T1 and the upstream wall is not filled. Due to 591      the presence of the beam pipe, the trolley is moved away from the beam line during 592      irradiation periods and placed further away from the source for less intense irradia- 593      tion. The position of the trolley can vary due to the use of the space by other setups 594      and is then not exact. Nonetheless, the position of the chambers in the trolley is fixed 595      and given in Figure (c). . . . .	5-23
596	5.27 Visualisation of the main data flows in the CMS RPC setup at the GIF++. The yellow 597      flow lines correspond to the DIP flow used for source, environmental and gas 598      information. The red flow lines are for the CAEN flow through which the WebDCS 599      communicates the voltages to be applied on the detectors using pressure and tem- 600      perature information and retrieves the monitored voltages and currents. Finally, the 601      blue flow lines correspond to the DAQ flow through which the RPC data is collected 602      from the TDCs by the computer. . . . .	5-25
603	5.28 DIP monitoring history accessed through the GIF++ WebDCS interface. . . . .	5-26
604	5.29 Example of DQM page available on CMS RPC WebDCS at the GIF++: the his- 605      togram of the rate measured in one of the tracking chambers, namely GT1_20_20-BKL_JUL16_4, 606      is selected and displayed above the page. . . . .	5-28

607	5.30 Example of DQM ROOT Browser page available on CMS RPC WebDCS at the 608           GIF++: the strip activity profile, defined as the rate profile normalized to the mean 609           rate, in one of the tracking chambers, namely GT1_20_20-BKL_JUL16_4. Available 610           ROOT files and histograms can be browsed thanks to the left panel showing the 611           directory and files structures. . . . .	5-29
612	5.31 Longevity data for chamber RE2-2-NPD-BARC-9 in GIF++. For each month 613           since July 2017, the integrated charge (in blue) as well as the time efficiency of 614           irradiation (in gray) is reported. . . . .	5-29
615	5.32 Example of a longevity scan monitoring page available on CMS RPC WebDCS at 616           the GIF++: the current and effective voltage, as well as environmental parameters, 617           are monitored for the bottom gap of chamber RE2-2-NPD-BARC-9. The decrease 618           of current is related to a decrease of the voltage due to the daily rate scan procedure 619           or to periods during which the source was turned OFF. . . . .	5-31
620	5.33 Example of a longevity scan summary page available on CMS RPC WebDCS at the 621           GIF++: the integrated charge is computed for the bottom gap of chamber RE2-2-NPD-BARC-9. . . . .	5-31
622	5.34 Example of current monitoring summary and of corresponding integrated charge of 623           chamber RE2-2-NPD-BARC-09. . . . .	5-32
624	5.35 Example of daily scan procedure of chamber RE2-2-NPD-BARC-09 with high- 625           lighted runs on the CMS RPC WebDCS at the GIF++. . . . .	5-34
626	5.36 Example of rate (Figure 5.36a) and current (Figure 5.36b) monitoring of chamber 627           RE2-2-NPD-BARC-09 with increasing integrated charge. . . . .	5-35
628	5.37 Example of strip activity of chamber RE2-2-NPD-BARC-09 monitored over time. . . . .	5-35
629	5.38 Chamber RE2-2-NPD-BARC-09. . . . .	5-37
630	5.39 Chamber RE2-2-NPD-BARC-09. . . . .	5-38
631	5.40 Chamber RE2-2-NPD-BARC-09. . . . .	5-39
632	5.41 Chamber RE2-2-NPD-BARC-09. . . . .	5-39
633	5.42 Total integrated charge in the irradiated RPCs, RE2-2-NPD-BARC-9 and RE4-2-CERN-165, 634           in April 2019. The irradiation of the RE2 chamber started in June 2016 while the 635           RE4 chamber couldn't be irradiated before November 2016. . . . .	5-40
636	6.1 PETIROC 2A block diagram. . . . .	6-2
637	6.2 View of the RPCROC Front-End Electronics in which the PETIROC 2A ASIC is 638           visible as well as the FPGA on which the TDC is hosted. . . . .	6-3
639	6.3 The PETIROC time jitter as a function of the input signal amplitude, measured with 640           and without internal clocks. . . . .	6-3
641	6.4 View of the coaxial design (Figure 6.4a) and of the return design (Figure 6.4b) of 642           read-out panels used in the iRPC prototypes. Only half PCBs with 48 strips are 643           showed. . . . .	6-4
644	6.5 Experimental setup used to test the INFN preamplifier with respect to the CMS FEEs. . . . .	6-5
645	6.6 The four channels of INFN preamplifiers are mounted directly on a CMS RPC and 646           connected to the four outermost read-out strips of the detector. . . . .	6-6
647	6.7 Experimental setup used to test the INFN preamplifier with respect to the CMS FEEs. . . . .	6-7
648	6.8 The block diagrams corresponding to the signal treatment for both INFN preampli- 649           fier (Figure 6.8a) and CMS FEEs (Figure 6.8b) are shown. The digitized signals are 650           then counted in coincidence with the trigger signals provided by PMTs (Figure 6.8c). . . . .	6-8
651	6.9 Efficiency (Figure 6.9a) and noise rate per unit area (Figure 6.9b) of the CMS RE2-2 652           detector tested with the standard CMS FEBs (black) and with the INFN preamplifier 653           at different thresholds (red and blue). An extra HV scan was performed with better 654           conditions to measure the noise with a threshold of 3 fC on the INFN preamplifiers. . . . .	6-9

655	6.10 Figure reffig:Setup-INFN-904:A: Shielded Front-End Board on which the INFN 656 preamplifiers are to be mounted. Figure reffig:Setup-INFN-904:B: Three INFN 657 preamplifiers connected onto the test FEB. Figure reffig:Setup-INFN-904:C: Exper- 658 imental setup used to test the INFN preamplifier single mounted on a FEB similar to 659 the CMS FEB. . . . .	6-10
660	6.11 Similarly to Figure 6.8c, the signals are counted in coincidence with the trigger 661 signals provided by PMTs. To estimate the cluster size, the channels are counted by 662 groups of three, two but also alone. . . . .	6-11
663	6.12 Efficiency (Figure 6.12a), cluster size (Figure 6.12b) and noise rate per unit area 664 (Figure 6.12c) of the CMS RE2-2 detector tested with the standard CMS FEBs 665 (black and red) and with the INFN preamplifier mounted onto the CMS FEB at 666 different thresholds (blue, pink, green and purple). . . . .	6-12
667	6.13 The glass RPC developped by Ghent uses a double-gap design (Figure 6.13a). The 668 electrodes are made of four pieces of float glass glued into a single plate (Fig- 669 ure 6.13b). Indeed a gluing technique has been investigated as most new low re- 670 sistivity materials foreseen for RPCs of the new generation are not available in large 671 areas. . . . .	6-13
672	6.14 Figure 6.14a: A gap used to concieve the gRPC tested at CERN. Figure 6.14b: 673 Both gaps with their read-out panel are placed into a faraday made out of copper. 674 Figure 6.14c: The faraday cage containing the double-gap gRPC is finally placed 675 into its aluminium case. . . . .	6-14
676	6.15 Experimental setup used to test the INFN preamplifier mounted on the CMS like 677 FEB with the glass RPC build by Ghent. . . . .	6-15
678	6.16 Efficiency (Figure 6.16a), cluster size (Figure 6.16b) and noise rate per unit area 679 (Figure 6.16c) of the Ghent gRPC detector tested with the standard CMS FEBs (red) 680 and with the INFN preamplifier mounted onto the CMS FEB at different thresholds 681 (blue, pink, green and purple). . . . .	6-16
682	6.17 Figure 6.17a: Time difference between the first and last hit composing a cluster in 683 the gRPC. The maximum time difference is set to 300 ns. Figure 6.17b: Variation of 684 the reconstructed average cluster size as a function of the time constraint used in the 685 algorithm. . . . .	6-17
686	6.18 Evolution of the cluster size distribution with increasing voltage for the gRPC tested 687 with the INFN preamplifiers using a threshold of 5 fC. . . . .	6-18
688	6.19 Map of the cluster size distribution as a function of the cluster position with increas- 689 ing voltage for the gRPC tested with the INFN preamplifiers using a threshold of 690 5 fC. . . . .	6-18
691	6.20 Noise profile measured in the glass RPC built by Ghent tested with the standard 692 CMS FEB (Figure 6.20a) and the INFN preamplifiers mounted on a CMS-like FEB 693 (Figure 6.20b). . . . .	6-19
694	6.21 The arrival time of the hits recorded in the gRPC tested with the CMS FEB (Fig- 695 ure 6.21a) and with the INFN preamplifiers (Figure 6.21b), and recorded in the CMS 696 RE2 RPC tested with the INFN preamplifiers (Figure 6.21c). . . . .	6-20
697	6.22 Experimental setups used to test the HARDROC2 electronics with a CMS RE4-3 698 gap (Figure 6.22a) and a gRPC gap built in Ghent (Figure 6.22b). . . . .	6-21
699	6.23 HARDROC2 control chip with its "Mezzanine" used to collect the data from the 700 different HARDROC ASICs and communicate with the computer. On top of the 701 picture, the trigger is brought by a coaxial cable. The connection with the computer 702 is assured by both the USB cables. . . . .	6-21

703	6.24 Efficiency (Figure 6.24a), cluster size (Figure 6.24b) and noise rate per unit area (Figure 6.24c) of the CMS RE4-3 detector tested in single gap mode with the standard CMS FEBs (black) and with the HARDROC 2 readout panel at different thresholds (red, blue and pink). . . . .	6-22
707	6.25 Measured muon (Figure 6.25a) and noise (Figure 6.25a) profiles in the read-out pads of the HARDROC 2 over a CMS RE4-3 gap. The inner structure of the gap and the presence of the spacers in the volume is visible. . . . .	6-23
710	6.26 Efficiency (Figure 6.24a), cluster size (Figure 6.24b) and noise rate per unit area (Figure 6.24c) of the UGent gRPC tested in double-gap mode with the standard CMS FEBs (black) and in single-gap with the HARDROC 2 readout panel at a threshold of 143 fC (red). . . . .	6-24
714	6.27 Measured muon (Figure 6.27a) and noise (Figure 6.27a) profiles in the read-out pads of the HARDROC 2 over a gRPC gap built by Ghent. . . . .	6-25
716	A.1 (A.1a) View of the front panel of a V1190A TDC module [268]. (A.1b) View of the front panel of a V1718 Bridge module [269]. (A.1c) View of the front panel of a 6U 6021 VME crate [286]. . . . .	A-3
719	A.2 Module V1190A <i>Trigger Matching Mode</i> timing diagram [268]. . . . .	A-4
720	A.3 Structure of the ROOT output file generated by the DAQ. The 5 branches ( <code>EventNumber</code> , <code>number_of_hits</code> , <code>Quality_flag</code> , <code>TDC_channel</code> and <code>TDC_TimeStamp</code> ) are visible on the left panel of the ROOT browser. On the right panel is visible the histogram corresponding to the variable <code>nHits</code> . In this specific example, there were approximately 50k events recorded to measure the gamma irradiation rate on the detectors. Each event is stored as a single entry in the <code>TTree</code> . . . . .	A-10
726	A.4 The effect of the quality flag is explained by presenting the content of <code>TBranch number_of_hits</code> of a data file without <code>Quality_flag</code> in Figure A.4a and the content of the same <code>TBranch</code> for data corresponding to a <code>Quality_flag</code> where all TDCs were labelled as <code>GOOD</code> in Figure A.4b taken with similar conditions. It can be noted that the number of entries in Figure A.4b is slightly lower than in Figure A.4a due to the excluded events. . . . .	A-12
732	A.5 Using the same data as previously showed in Figure A.4, the effect of the quality flag is explained by presenting the reconstructed hit multiplicity of a data file without <code>Quality_flag</code> in Figure A.5a and the reconstructed content of the same RPC partition for data corresponding to a <code>Quality_flag</code> where all TDCs were labelled as <code>GOOD</code> in Figure A.5b taken with similar conditions. The artificial high content of bin 0 is completely suppressed. . . . .	A-12
738	A.6 WebDCS DAQ scan page. On this page, shifters need to choose the type of scan (Rate, Efficiency or Noise Reference scan), the gamma source configuration at the moment of data taking, the beam configuration, and the trigger mode. These information will be stored in the DAQ ROOT output. Are also given the minimal measurement time and waiting time after ramping up of the detectors is over before starting the data acquisition. Then, the list of HV points to scan and the number of triggers for each run of the scan are given in the table underneath. . . . .	A-14

- 745        B.1 Example of expected hit time distributions in the cases of efficiency (Figure B.1a)  
746                  and noise/gamma rate per unit area (Figure B.1b) measurements as extracted from  
747                  the raw ROOT files. The unit along the x-axis corresponds to ns. The fact that  
748                  "the" muon peak is not well defined in Figure B.1a is due to the contribution of all  
749                  the RPCs being tested at the same time that don't necessarily have the same signal  
750                  arrival time. Each individual peak can have an offset with the ones of other detectors.  
751                  The inconsistancy in the first 100 ns of both time distributions is an artefact of the  
752                  TDCs and are systematically rejected during the analysis. . . . . B-16  
753        B.2 The effect of the quality flag is explained by presenting the reconstructed hit multi-  
754                  plicity of a data file without `Quality_flag`. The artificial high content of bin 0 is the  
755                  effect of corrupted data. . . . . B-21  
756        B.3 Display of the masking tool page on the webDCS. The window on the left allows the  
757                  shifter to edit `ChannelsMapping.csv`. To mask a channel, it only is needed to set the  
758                  3rd field corresponding to the strip to mask to 0. It is not necessary for older mapping  
759                  file formats to add a 1 for each strip that is not masked as the code is versatile and  
760                  the default behaviour is to consider missing mask fields as active strips. The effect  
761                  of the mask is directly visible for noisy channels as the corresponding bin turns red.  
762                  The global effect of masking strips will be an update of the rate value showed on the  
763                  histogram that will take into consideration the rejected channels. . . . . B-28

# List of Tables

764

765	3.1	Properties of the most used electrode materials for RPCs. . . . .	3-3
766	4.1	Details of the greenhouse fluorinated gases used in CMS and of their GWP [177]. . .	4-17
767	5.1	Attenuation of single filters on each filter plane of the GIF++ Cesium source. . . . .	5-6
768	5.2	Total photon flux ( $E\gamma \leq 662$ keV) with statistical error predicted considering a $^{137}\text{Cs}$ activity of 740 GBq at different values of the distance $D$ to the source along the x-axis of irradiation field [264]. . . . .	5-14
770	5.3	Correction factor $c$ is computed with Formula 5.3 taking as reference $D_0 = 50$ cm and the associated flux $F_0^{ABS}$ for each absorption factor available in table 5.2. . . . .	5-15
771	5.4	The data at $D_0$ in 1997 is taken from [264]. Using Formula 5.4, the flux at $D$ , including an error of 1 cm, can be estimated in 1997. Then, taking into account the attenuation of the source activity, the flux at $D$ can be estimated at the time of the tests in GIF in 2014. Assuming a sensitivity of the RPC to gammas, $s = (2 \pm 0.2) \times 10^{-3}$ [271], an estimation of the hit rate per unit area is obtained. . . . .	5-16
772	5.5	Summary of the characterization measurement performed in Ghent on CMS RPC detectors foreseen to be used at GIF++ for longevity studies of the present system. For each detector, the working voltage, defined as in Formula 3.25, was extracted from sigmoid fits performed in Figure 5.25a. The values of efficiency, cluster size, noise rate and current density at this voltage are reported. . . . .	5-22
783	6.1	Results of the sigmoid fit (Formula 3.24) performed on the data presented in Figure 6.9a. The working point and its corresponding efficiency are computed using Formulas 3.24 and 3.25. . . . .	6-9
784	6.2	Results of the sigmoid fit (Formula 3.24) performed on the data presented in Figure 6.12a. The working point and its corresponding efficiency are computed using Formulas 3.24 and 3.25. . . . .	6-12
785	6.3	Results of the sigmoid fit (Formula 3.24) performed on the data presented in Figure 6.16a. The working point and its corresponding efficiency are computed using Formulas 3.24 and 3.25. . . . .	6-16
786	6.4	Results of the sigmoid fit (Formula 3.24) performed on the data presented in Figure 6.24a. The working point and its corresponding efficiency are computed using Formulas 3.24 and 3.25. . . . .	6-22
787	6.5	Results of the sigmoid fit (Formula 3.24) performed on the data presented in Figure 6.26a. The working point and its corresponding efficiency are computed using Formulas 3.24 and 3.25. . . . .	6-24
798	A.1	Inter-process communication cycles in between the webDCS and the DAQ through file string signals. . . . .	A-18
799			



# List of Acronyms

## List of Acronyms

802	<b>ABS</b>	Absorption factor
803	<b>AFL</b>	Almost Full Level
804	<b>ALCTS</b>	Anode local charged track boards
805	<b>BARC</b>	Bhabha Atomic Research Centre
806	<b>BCS</b>	Bardeen–Cooper–Schrieffer
807	<b>BJT</b>	Bipolar Junction Transistor
808	<b>BLT</b>	Block Transfer
809	<b>BMTF</b>	Barrel Muon Track Finder
810	<b>BNL</b>	Brookhaven National Laboratory
811	<b>BSM</b>	Physics beyond the Standard Model
812	<b>BR</b>	Branching Ratio
813	<b>CAEN</b>	Costruzioni Apparecchiature Elettroniche Nucleari S.p.A.
814	<b>CERN</b>	European Organization for Nuclear Research
815	<b>CFD</b>	Constant Fraction Discriminator
816	<b>CFEBs</b>	cathode front-end boards
817	<b>CKM</b>	Cabibbo–Kobayashi–Maskawa
818	<b>CMB</b>	Cosmic Microwave Background
819	<b>CMS</b>	Compact Muon Solenoid
820	<b>CSC</b>	Cathode Strip Chamber
821	<b>CuOF</b>	copper-to-optical-fiber translators
822	<b>DAQ</b>	Data Acquisition
823	<b>DCS</b>	Detector Control Software
824	<b>DIP</b>	Data Interchange Protocol
825	<b>DMBs</b>	Data acquisition mother boards
826	<b>DQM</b>	Data Quality Monitoring
827	<b>DT</b>	Drift Tube
828	<b>EDM</b>	electric dipole moment
829	<b>ECAL</b>	electromagnetic calorimeter
830	<b>EMTF</b>	Endcap Muon Track Finder
831	<b>FCC</b>	Future Circular Collider
832	<b>FEB</b>	Front-End Board
833	<b>FEE</b>	Front-End Electronics
834	<b>FWHM</b>	full-width-at-half-maximum
835	<b>GEANT</b>	GEometry ANd Tracking - a series of software toolkit platforms developed by CERN
836	<b>GEB</b>	GEM Electronics board
838	<b>GEM</b>	Gas Electron Multiplier
839	<b>GIF</b>	Gamma Irradiation Facility

840	GIF++	new Gamma Irradiation Facility
841	gRPCs	glass RPCs
842	GWP	Global Warming Potential
843	HARDROC	HAdronic RPC Digital Read-Out Chip
844	HCAL	hadron calorimeter
845	HEP	High-Energy Physics
846	HJT	Hetero Junction bipolar Transistor
847	HL-LHC	High Luminosity LHC
848	HPL	High-Pressure Laminate
849	HSCPs	Heavy Stable Charged Particles
850	HV	High Voltage
851	ICRU	International Commission on Radiation Units & Measurements
852	ILC	International Linear Collider
853	IPNL	Institut de Physique Nucléaire de Lyon
854	iRPC	improved RPC
855	IRQ	Interrupt Request
856	ISR	Intersecting Storage Rings
857	LEIR	Low Energy Ion Ring
858	LEP	Large Electron-Positron
859	LHC	Large Hadron Collider
860	LS1	First Long Shutdown
861	LS2	Second Long Shutdown
862	LS3	Third Long Shutdown
863	LSP	lightest supersymmetric particle
864	LV	Low Voltage
865	LVDS	Low-Voltage Differential Signaling
866	MC	Monte Carlo
867	MCNP	Monte Carlo N-Particle
868	MiC	Minicrate electronics
869	MiC1	first version of Minicrate electronics
870	mip's	minimum ionizing particles
871	MRPC	Multigap RPC
872	MSSM	Minimal Supersymmetric Standard Model
873	mSUGRA	minimal SUper GRAvity
874	NIM	Nuclear Instrumentation Module logic signals
875	OH	Optohybrid Board
876	OMTF	Overlap Muon Track Finder
877	OTMBs	Optical TMBs
878	PAI	Photo-Absorption Ionisation
879	PAIR	Photo-Absorption Ionisation with Relaxation
880	PMT	PhotoMultiplier Tube
881	PS	Proton Synchrotron
882	PU	pile-up
883	QCD	Quantum Chromodynamics
884	QED	Quantum Electrodynamics
885	RADMON	Radiation Monitoring
886	RMS	Root Mean Square
887	ROOT	a framework for data processing born at CERN
888	RPC	Resistive Plate Chamber

889	SC	Synchrocyclotron
890	SDHCAL	Semi-Digital HCAL
891	SiPM	Silicon Photomultiplier
892	SLAC	Stanford Linear Accelerator Center
893	SM	Standard Model
894	SPS	Super Proton Synchrotron
895	SUSY	supersymmetry
896	TDC	Time-to-Digital Converter
897	TDR	Technical Design Report
898	TMBs	Trigger mother boards
899	ToF	Time-of-flight
900	ToT	Time-over-Threshold
901	TPG	trigger primitives
902	webDCS	Web Detector Control System
903	WIMPs	Weakly Interacting Massive Particles
904	YETS	Year End Technical Stop



# 1

905

906

## Introduction

907 Grasping an understanding of the world in which they are leaving in has always been part of human  
908 life. Beyond the metaphysical questioning of our origins and purpose, curiosity has brought mankind  
909 to question its surroundings. Following the philosophy of the ancient Greeks and Indians came  
910 the development of the sciences as the systematic experimentation aimed at testing hypothesis and  
911 reproducing results obtained by fellow natural philosophers. With the industrial revolution and the  
912 organisation of science, it became possible to go always further in the understanding of the universe  
913 and of the matter in particular. Investigation on the constituent of matter proved to require more  
914 and more powerful machines in order to break apart the bricks of the world into ever smaller pieces,  
915 study their behaviour and extract new knowledge to help the development of humanity. So far, the  
916 largest and most powerful machine that was built to study the particles composing matter and test  
917 the models thought by physicists to explain their behaviour is the Large Hadron Collider (LHC),  
918 a circular particle accelerator used to collide protons and heavy ions. After only a few years of  
919 investigations conducted thanks to the LHC, several discoveries, predicted by the existing models,  
920 have been made. In the future, in order to boost the discovery potential on the LHC and be able to  
921 test hypotheses lying beyond the already acknowledged models, the instantaneous luminosity, i.e.  
922 the rate of particle interactions, will be slightly increased into a so-called High Luminosity phase to  
923 boost its discovery potential.

924 As the Large Hadron Collider will see its instantaneous luminosity be increased, the detectors  
925 on the different experimental sites will have to suffer an increased background irradiation due to the  
926 byproducts of the interaction of the beams with the infrastructure. This will cause for the detectors  
927 a stress which implications need to be understood throughout the High Luminosity LHC (HL-LHC)  
928 phase of operations. In the case of the Compact Muon Solenoid (CMS) experiment, it is important  
929 to understand if the detectors that will be subjected to the higher levels of radiation will be able to  
930 sustain higher detection rates while displaying the same performance they have so far been operated  
931 at and if this level of performance of the detectors will stay stable for a period longer than ten years.  
932 More specifically, the detectors placed very close to the beam line will be the most subjected to the  
933 change of luminosity. In CMS, the endcap detectors will then be particularly affected by the stronger

background radiation. The endcap detectors compose a part of the muon system of CMS and among them, the Resistive Plate Chamber (RPC) plays a key role in providing the experiment a reliable trigger on potentially interesting data. This PhD work takes place into this very specific context of muon detector consolidation and certification for the HL-LHC period in order to provide the CMS experiment with robust new detectors and confirm that the present system will survive through the next 20 years.

CMS experiment main focus revolves around testing the Standard Model (SM) of particle physics using a multipurpose detector design to detect the interaction products of the protons and ions colliding along the LHC. Looking at the successive evolution of the theoretical models that gave birth to the SM, the need for very intense particle beams in high energy physics experiment becomes clear in that the higher the center-of-mass energy for each interaction, the greater the probe on very small cross-section processes predicted by the theory, justifying the successive increase in beam energy and intensity at LHC.

The implications for LHC experiments and in particular for the CMS detector explain the need for longevity and rate capability studies conducted on the Resistive Plate Chambers which are an important part of its Muon System as it is needed to certify the quality of operation of the trigger detectors throughout the lifetime of HL-LHC.

RPCs are gaseous detectors which physics principles are non trivial and are still being investigated. Nevertheless, key processes driving the electron multiplication in the gas volume, rate capability and ageing have been successfully identified and will define the parameters that will have to be taken into consideration while producing the detectors extending the pseudo-rapidity coverage of RPCs toward the beam line as well as the ones to be monitored during the on-going longevity and rate capability certification campaign.

On the one hand, the present RPC sub-system consists in two different RPC productions. Indeed, most of the RPC detectors were produced in view of the start of LHC activities in 2010. These detectors were build in between 2007 and 2008 to equip the barrel and the three disks of each endcaps of the CMS apparatus. But during the First Long Shutdown (LS1) of LHC in between end of 2012 and 2015, a fourth disk of endcap was added in order to reinforce the redundancy of the endcap trigger. Hence, new RPC detectors using the same technology were built in between 2012 and 2013. These two sets of detector productions only differ in the properties of the High-Pressure Laminate (HPL) used for their electrodes that could lead to a different ageing rate. This is why spare detectors of both production periods have been tested over the past years to certify their good operation through HL-LHC.

On the other hand, producing detectors to equip a highly irradiated region such as the extension of CMS RPC endcaps requires to substantially improve the ageing properties of the chosen technology by reducing the charge deposition per ionizing particle. This can be achieved both by modifying the design of the detector volume or by improving the signal to noise ratio of the Front-End Electronics (FEE) used to process the charge collected by the read-out strips making them more sensitive to weaker signals. Two FEE technologies were selected and tested in order to equip the improved RPC (iRPC) that will extend the coverage of the CMS endcaps.

Thanks to the study presented in this document, preliminary conclusions will be brought on the production of iRPCs and on the longevity of the present RPC system, providing with a better understand of the future performance of the RPC sub-system within the CMS experiment.

# 2

977

978

## Investigating the TeV scale

979 Throughout history, physics experiment became more and more powerful in order to investigate finer  
980 details of nature to help understanding the building blocks of matter and the fundamental interactions  
981 that bind them in the microscopic world. Nowadays, the Standard Model of particle physics is the  
982 most accurate theory designed to explain the behaviour of particles and is able to make very precise  
983 predictions that are constantly verified. Nevertheless, some hints of new physics are visible as bricks  
984 are still missing to obtain a global description of the Universe.

985 To highlight the limits of the SM and test the different alternative theories, evermore powerful  
986 machines are needed. It is in this context that the Large Hadron Collider has been thought and built  
987 to accelerate and collide particles at energies exceeding anything that had been done before. Higher  
988 collision energies and high pile-up imply the use of enormous detectors to measure the properties of  
989 the interaction products. The Compact Muon Solenoid is a multipurpose experiment that have been  
990 designed to study the proton-proton collisions of the LHC and give answers on various high-energy  
991 physics scenarios such as different supersymmetry (SUSY) extensions to the Standard Model or  
992 Extra Dimensions models.

993 This Chapter will be the occasion to go through the history of the Standard Model of Particle  
994 Physics to understand the research conducted today in High-Energy Physics (HEP) facilities. From  
995 the discovery of the atom and of its inner structure to the development of the theories governing  
996 the fundamental interactions, all the elements leading to the construction SM will be discussed.  
997 Furthermore, highlights on the Physics beyond the Standard Model (BSM) will be given to replace  
998 the document in the context of today's research. Finally, a full description of the LHC and of the  
999 CMS detector will be provided.

### 1000 **2.1 The Standard Model of Particle Physics**

1001 In the early 21<sup>st</sup> century it is now widely accepted that matter is made of elementary blocks referred  
1002 to as *elementary particles*. The physics theory that classifies and describes the best the behaviour and  
1003 interaction of such elementary particles is the so-called Standard Model. The SM formalizes three of

1004 the four fundamental interactions (electromagnetic, weak and strong interactions). Its development  
 1005 happened since the 1960s thanks to a strong collaboration between theoretical and experimental  
 1006 physicists.

### 1007 2.1.1 A history of particle physics

1008 The idea that nature is composed of elementary bricks, called *atomism*, is not contemporary as it  
 1009 was already discussed by Indian or Greek philosophers during antiquity. In Greece, atomism has  
 1010 been rejected by *Aristotelianism* as the existence of *atoms* would imply the existence of a void that  
 1011 would violate the physical principles of Aristotle philosophy. Aristotelianism has been considered  
 1012 as a reference in the european area until the 15<sup>th</sup> century. With the *Rinascimento*, antic text and  
 1013 history started to be more deeply studied. The re-discovery of Platon's philosophy allowed opening  
 1014 the door to alternative theories and give a new approach to natural sciences where experimentation  
 1015 would become central. A new era of knowledge was starting. By the beginning of the 17<sup>th</sup> century,  
 1016 atomism was re-discovered by philosophers. The very first attempt at estimating the number of  
 1017 *particles* in a volume was provided by Magnenus in 1646 by calculating that the number of *particles*  
 1018 in a stick of incense [1]. He found a value of the order of  $10^{18}$  simply by considering the time  
 1019 necessary to smell it everywhere in a large church after the stick was lit on. It is now known that this  
 1020 number only falls short only by 1 order of magnitude.

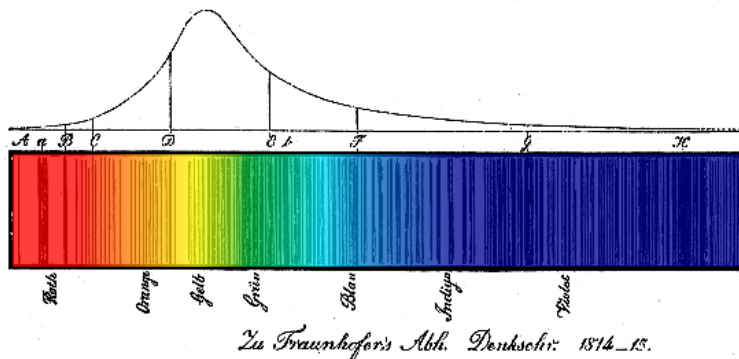


Figure 2.1: Solar spectrum with spectral lines as it visually appeared to Fraunhofer.

1021 An alternative philosophy to atomism popularized by Descartes was *corpuscularianism*. Built on  
 1022 ever divisible corpuscles, contrary to atoms, its principles were mainly used by alchemists like New-  
 1023 ton who would later develop a corpuscular theory of light. Boyle combined together ideas of both  
 1024 atomism or corpuscularianism leading to mechanical philosophy. The 18<sup>th</sup> century has seen the  
 1025 development of engineering providing philosophical thought experiments with repeatable demon-  
 1026 stration and a new point of view to explain the composition of matter. Lavoisier greatly contributed  
 1027 to chemistry and atomism by publishing in 1789 a list of 33 chemical elements corresponding to  
 1028 what are now called *atoms* [2]. In the early 19<sup>th</sup> century Dalton summarized the knowledge on  
 1029 composition of matter [3]. In his atomic model, the atoms are ball-like constituents of the chemical  
 1030 elements. All atoms of a given element are identical, in size, mass, and other properties while the  
 1031 atoms of different elements differ. He also considered that atoms cannot be divided into smaller  
 1032 particles, created nor destroyed and that they combine into chemical compounds. The essence of  
 1033 chemical reaction was then the combination, separation or rearrangement of atoms. Soon after,

1034 Fraunhofer invented the spectrometer and discovered the spectral lines in the sunlight spectrum, as  
 1035 showed in Figure 2.1 [4]. These were later linked to the absorption by chemical elements present in  
 1036 the solar atmosphere by Kirchhoff and Bunsen. The rise of atomic physics, chemistry and mathe-  
 1037 matical formalism unraveled the different atomic elements and ultimately, the 20<sup>th</sup> century saw the  
 1038 very first sub-atomic particles.

1039 **Discovery of the inner structure of the atom**

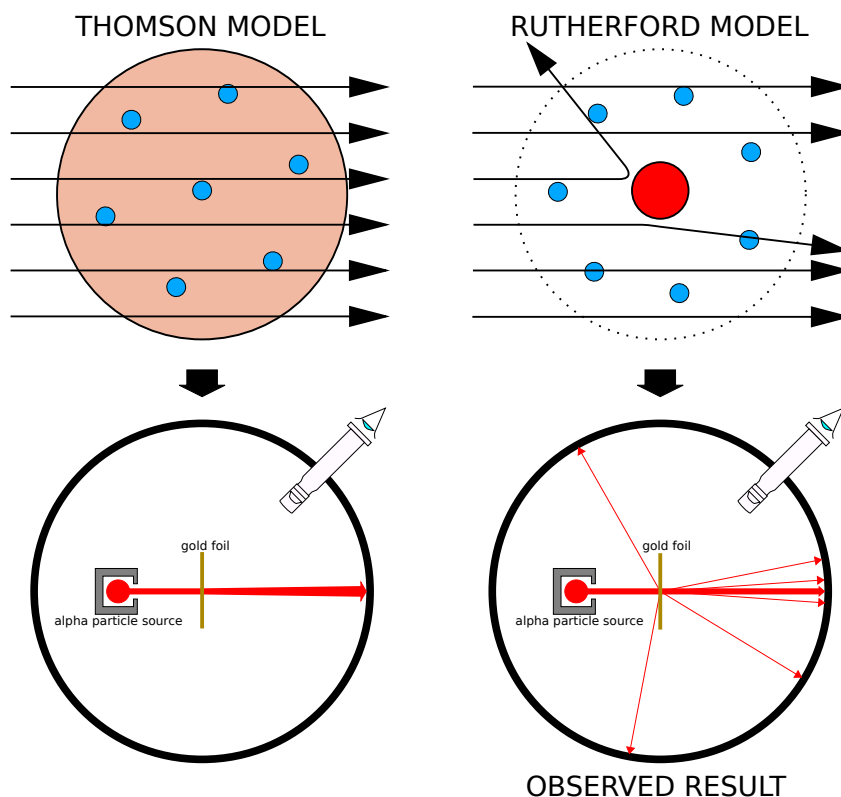


Figure 2.2: Through the gold foil experiment, Rutherford could show that most of the mass of atoms was contained in a positively charged nucleus and could then propose a more accurate atomic model than that of Thomson.

1040 The negatively charged *electron* was the first to be discovered in 1897 by Thomson after three  
 1041 decades of research on cathode rays [5]. He proved that the electrification observed in an elec-  
 1042 troscope, as reported by Perrin [6], was due to the rays themselves. Hence, they had to be composed  
 1043 of electrically charged particles. In 1900, Becquerel showed the *beta rays* emitted by radium had the  
 1044 same charge over mass ratio as was measured by Thomson for cathode rays, pointing to electrons as  
 1045 a constituent of atoms [7]. This discovery leads to Thomson's plum pudding atomic model in which  
 1046 electrons are embed into a uniform positively charged atom [8]. In 1907, Rutherford and Royds  
 1047 showed that *alpha* particles were helium ions [9]. Indeed, once captured in a tube and subjected to  
 1048 an electric spark causing an electron avalanche, they could combine with two electrons to form a  
 1049  ${}^4\text{He}$ .

This discovery was directly followed by the constraint of the atom structure in between 1908 and 1913 through the Geiger–Marsden gold foil experiments in which the deflection angle of alpha particles fired at a very thin gold foil was measured [10–13]. It highlighted that atoms were mainly empty with nearly all their mass contained into a tiny positively charged *nucleus*. With these two observations, Rutherford could formulate the Rutherford planetary model of the atom in 1911 [14], shown together with the Thomson plum pudding model in Figure 2.2. The link between atomic number and number of positive and negative charges contained into the atoms would fast be understood. Hence, the different kinds of element transmutations appeared to be purely nuclear processes making clear that the electromagnetic nature of chemical transformations could not possibly change nuclei. A new branch in physics appeared to exclusively study nuclei: *nuclear physics*. By studying alpha emission and the product of their interaction with nitrogen gas, Rutherford reported in 1919 the very first nuclear reaction [15]. It leads to the discovery that the hydrogen nucleus was composed of a single positively charged particle that was later baptised *proton* [16]. This idea came from 1815 Prout's hypothesis proposing that all atoms are composed of "*protyle*" (i.e. hydrogen atoms) [17, 18]. By using scintillation detectors, Rutherford could highlight typical hydrogen nuclei signature and understand that the impact of alpha particles with nitrogen would knock out a hydrogen nucleus and produce an oxygen 17, as showed in Formula 2.1 and would then postulate that protons are building bricks of all elements.



With this assumption and the discovery of *isotopes* together with Aston, elements with identical atomic number but different masses, Rutherford proposed that all elements' nuclei but hydrogen are composed of both charged particles, protons, and of chargeless particles, which he called *neutrons* [16, 19]. These neutral particles helped maintaining nuclei as one, as charged protons were likely to electrostatically repulse each other. He then introduced the idea of a new force, a *nuclear* force. The first idea concerning neutrons was a bond state of protons and electrons as it was known that the beta decay, emitting electrons, was taking place in the nucleus. However, it was then shown that electrons being confined into the nucleus would hardly be possible due to Heisenberg's uncertainty principle. Finally, in 1932, following the discovery of a new neutral radiation, Chadwick could discover the neutron as an uncharged particle with a mass similar to that of the proton which would solve the nucleus puzzle [20–24].

### 1079 Development of the Quantum Electrodynamics

Historically, the development of the quantum theory revolved around the question of emission and absorption of discrete amount of energy through light. Einstein used the initial intuition of Planck about the black-body radiation to develop in 1905 a model to explain the photoelectric effect in which light was described by discrete *quanta* now called *photons* [25, 26]. For this model, Einstein introduced the concept of wave-particle duality as classical theory was not able to describe the phenomenon. With the new understanding of atoms and of their structure, classical theories also proved unable to explain atoms' stability. Indeed, using classical mechanics, electrons orbiting around a nucleus should radiate an energy proportional to their angular momentum and hence, loose energy through time and the spectrum of energy emission should then be continuous. However, it was known since the 19<sup>th</sup> century and the discovery of spectral lines that the emission spectrum of material was discrete [4].

In 1913, quantum physics was introduced into the atomic model by Bohr to overcome the electron's energy loss due to orbiting radiation emission [27]. Using the correspondence principle stating that for large enough numbers the quantum calculations should give the same results than the classical theory, he proposed the very first quantum model of the hydrogen atom explaining the line spectrum by introducing the *principal quantum number*  $n$  describing the electron shell. The same year, Moseley confirmed Bohr's model through the Moseley's law [28]. Debye and then Sommerfeld extended it by introducing the quantization of the angular momentum [29]. The quantization the z-component of the angular momentum led to the *second and third quantum numbers*, or *azimuthal* and *magnetic quantum number*,  $l$  and  $m$ . The second defines the orbital angular momentum of the electrons on their shells and hence, the shape of the orbital, while the third the available orbital on the subshell for each electron as shown in Figure 2.3.

Nevertheless, although the model was not only limited to spherical orbitals anymore, making the atom more realistic, the Zeeman effect couldn't be completely explained by just using  $n$ ,  $l$  and  $m$  [30–33] nor could the result of the Stern-Gerlach experiment [34]. Both experiments are shown in Figure 2.4. A solution was brought after Pauli in 1925 proposed together with his exclusion principle the idea of a new quantum degree of freedom in order to resolve the apparent problem [35, 36]. This degree of freedom was interpreted as an intrinsic angular momentum vector associated to the particle itself, not to the orbital [37], and associated to a new quantum number  $s$ , the *spin* projection quantum number explaining the lift of degeneracy to an even number of energy levels [38]. The new quantum number helped in theorizing the neutron as a neutral particle rather than a bond state of a proton and an electron confined in the nucleus itself.

The introduction of the *spin* happened one year after another attempt of improvement of the theory was made by De Broglie in his Ph.D. thesis [39]. The original formulation of the quantum theory only considered photons as energy quanta behaving as both *waves* and *particles*. De Broglie proposed that *all* matter are described by waves and that their momentum is proportional to the oscil-

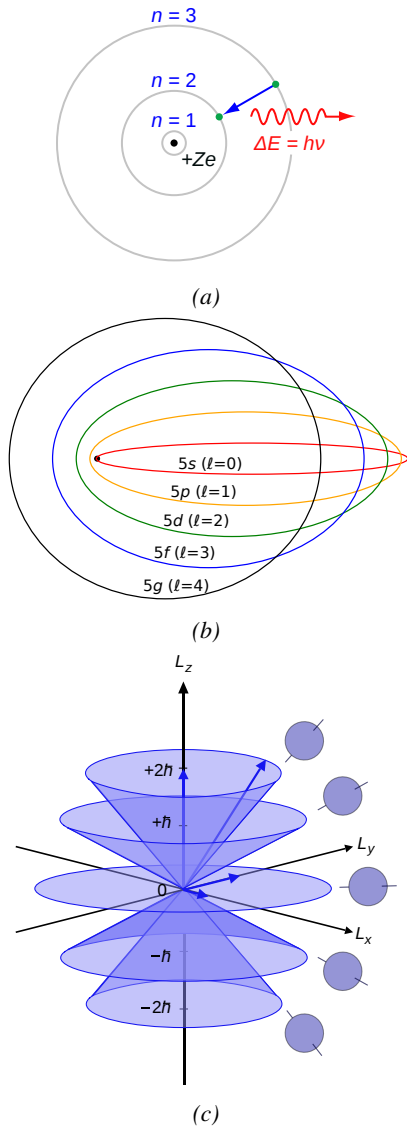


Figure 2.3: (a): The orbits in which the electron may travel according to the Bohr model of the hydrogen atom. An electron jumps between orbits and is accompanied by an emitted or absorbed amount of electromagnetic energy ( $h\nu$ ). The orbits radius increases as  $n^2$ . (b): Elliptical orbits with the same energy and quantized angular momentum  $l = 0, 1, \dots, n - 1$  in the case  $n = 5$ . (c): Illustration of quantum mechanical orbital angular momentum. The cones and plane represent possible orientations of the angular momentum vector for  $l = 2$  and  $m = -2, -1, 0, 1, 2$ .

1137 lation of quantized electromagnetic field oscillators. This interpretation was able to reproduce the  
 1138 previous version of the quantum energy levels by showing that the quantum condition involves an  
 1139 integer multiple of  $2\pi$ , as shown by Formula 2.2.

$$(2.2) \quad p = \hbar k \Leftrightarrow \int pdx = \hbar \int kdx = 2\pi\hbar n$$

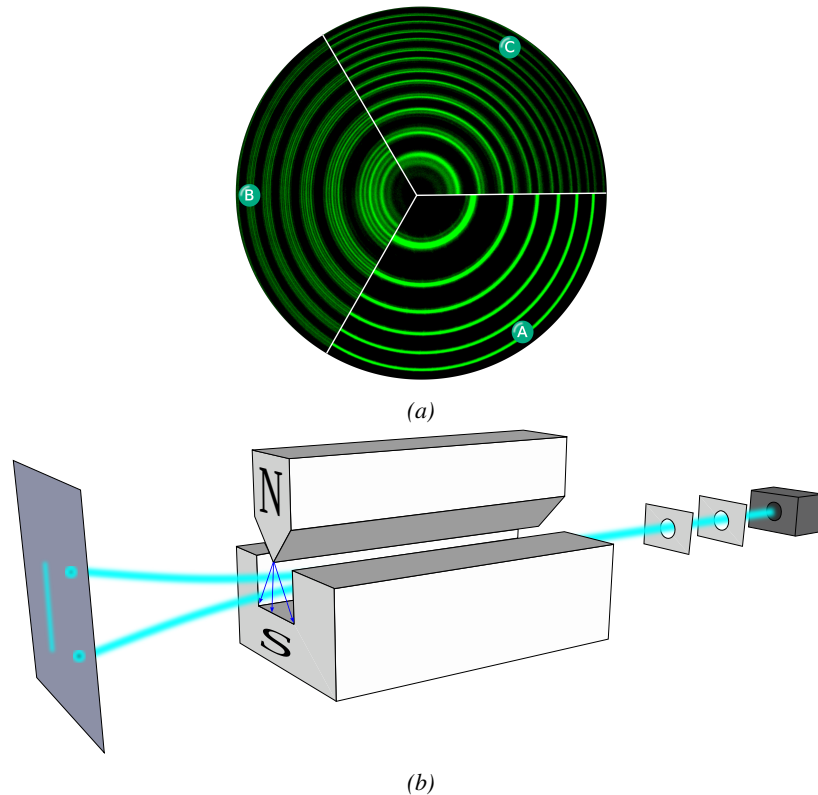


Figure 2.4: (a): The spectral lines of mercury vapor lamp anomalous Zeeman effect without magnetic field (A) and with magnetic field (B - transverse Zeeman effect & C - longitudinal Zeeman effect). (b): Stern-Gerlach experiment: Silver atoms traveling through an inhomogeneous magnetic field and being deflected up or down depending on their spin.

1140 Although the intuition of De Broglie about the wave-particle duality of all matter was a step in the  
 1141 right direction, his interpretation was semiclassical and it is in 1926 that the first full quantum wave  
 1142 equation would be introduced by Schrödinger to describe electron-like particles, reproducing the  
 1143 previous semiclassical formulation without inconsistencies [40]. This complex equation describes  
 1144 the evolution of the wave function  $\Psi$  of the quantum system, defined by its position vector  $\mathbf{r}$  and time  
 1145  $t$  as an energy conservation law, in which the hamiltonian of the system  $\hat{H}$  is explicit, by solving the  
 1146 Equation 2.3.

$$(2.3) \quad i\hbar \frac{\partial}{\partial t} |\Psi(\mathbf{r}, t)\rangle = \hat{H} |\Psi(\mathbf{r}, t)\rangle$$

1147 The spin was then included into Schrödinger equation by Pauli to take into account the interaction  
 1148 with an external magnetic field, as shown in Equation 2.4 in which the Hamiltonian operator is a  $2 \times 2$   
 1149 matrix operator due to the Pauli matrices [38].  $\mathbf{A}$  is the vector potential and  $\phi$  is the scalar electric  
 1150 potential.

$$(2.4) \quad i\hbar \frac{\partial}{\partial t} |\Psi\rangle = \left[ \frac{1}{2m} (\sigma \cdot (\mathbf{p} - q\mathbf{A})^2 + q\phi) \right] |\Psi\rangle$$

1151 Later in 1927, Dirac went further in his paper about emission and absorption of radiation by  
 1152 proposing a second quantization not only of the physical process at play but also of the electromagnetic  
 1153 field [41]. His equation provided the ingredients to the first formulation of *Quantum Electrodynamics (QED)*  
 1154 and the description of photon emission by electrons dropping into a lower energy state  
 1155 in which the final number of particles is different than the initial one. Nevertheless, in order to properly  
 1156 treat electromagnetism, the incorporation of the special relativity developed by Einstein was  
 1157 necessary. Derived in 1928, the Dirac equation, shown as Equation 2.5, similarly to Schrödinger  
 1158 equation, is a single-particle equation but it incorporates special relativity in addition to quantum  
 1159 mechanics rules [42].

$$(2.5) \quad i\hbar\gamma^\mu \partial_\mu \psi - mc\psi = 0$$

1160 It features the  $4 \times 4$  gamma matrices  $\gamma^\mu$  built using  $2 \times 2$  Pauli matrices and the unitary matrix,  
 1161 the 4-gradient  $\partial_\mu$ , the rest mass  $m$  of any half integer spin massive particle described by the wave  
 1162 function  $\psi(x, t)$ , also called a Dirac spinor and the speed of light  $c$ . In addition to perfectly reproduce  
 1163 the results obtained with quantum mechanics so far, it also provided *negative-energy solutions* that  
 1164 would later be interpreted as a new form of matter, *antimatter* [43, 44]. In the non-relativistic limit,  
 1165 the Dirac equation gives a theoretical justification to the Pauli equation that was phenomenologically  
 1166 constructed to account for the spin.

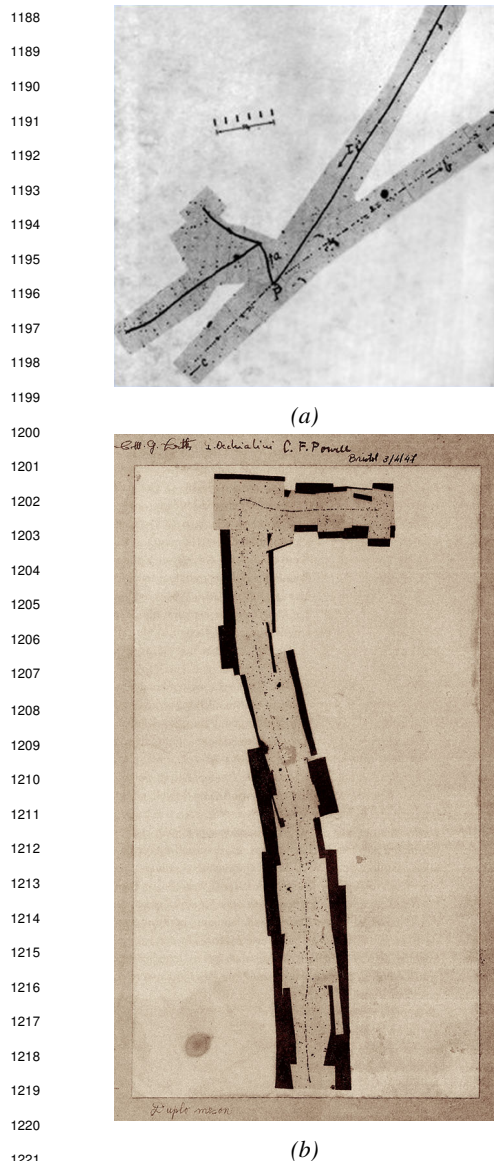
1167 The successes of the QED were soon followed with theoretical problems as computations of any  
 1168 physical process involving photons and charged particles were shown to be only reliable at the first  
 1169 order of the *perturbation theory* [45]. At higher order of the theory, divergent contributions were  
 1170 appearing giving nonsensical results. Only two effects were contributing to these infinities.

- 1171 • The self-energy of the electron (or positron), the energy that the particle has due to its own  
 1172 interaction with its environment.
- 1173 • The vacuum polarization, virtual electron–positron pairs produced by a background electro-  
 1174 magnetic field in the vacuum which is not an "empty" space. These virtual pairs affect the  
 1175 charge and current distributions generated by the original electromagnetic field.

1176 Solving this apparent problem was done by carefully defining the concepts of each observable,  
 1177 for example mass or charge, as these quantities are understood within the context of a non-interacting  
 1178 field equation. From the experimental point of view, they are abstractions as what is measured is  
 1179 "renormalized observables" shifted from their "bare" value by the interaction taking place in the  
 1180 measuring process. The infinities needed to be connected to corrections of mass and charge as those  
 1181 are fixed to finite values by experiment. This was the intuition of Bethe in 1947 who successfully  
 1182 computed the effect of such *renormalization* in the non-relativistic case [46]. Full covariant formula-  
 1183 tions of QED including renormalization were achieved by 1949 by Tomonaga, Schwinger, Feynman,

1184 and Dyson [47]. With the resolution of infinities, QED had mostly reached its final form, being still  
 1185 today the most accurate physical theory, and would serve as a model to build all other quantum field  
 1186 theories.

1187 **Development of the quark model and Quantum Chromodynamics**



1222 *Figure 2.5: (a): decay of a  $\mu$ -meson in an emul-  
 1223 sion. (b): track of a  $\pi$ -meson in an emulsion  
 1224 signed by Lattes, Powell, and Occhialini.  
 1225 ultimately identified in University of California's cyclotron in 1950 through the observation of its  
 1226 decay into 2 photons [55].*

1227 Also discovered in 1947 but in cloud chamber photographs, the  $K$  meson has also been an impor-

To explain the nuclear force that holds *nucleons* (protons and neutrons) together, Yukawa proposed in 1934 the existence of a force carrier called *meson* due to its predicted mass in the range in between the electron and nucleon masses [48]. Discovered in 1936 by Anderson and Neddermeyer [49, 50], and confirmed using bubble chambers in 1937 by Street and Stevenson [51], a first meson candidate was observed in the decay products of cosmic rays. Assuming it had the same electric charge as electrons and protons, this particle was observed to have a curvature due to magnetic field that was sharper than protons but smoother than electrons resulting in a mass in between the two. But its properties were not compatible with Yukawa's theory, which was emphasized by the discovery of a new candidate in 1947, again in cosmic ray products using photographic emulsions [52–54]. The detections of the mu-meson and of the pi-meson in emulsions are showed in Figure 2.5.

This new candidate, although it had a similar mass than the already believed *meson*, would rather decay into it. For distinction, the first candidate would then be renamed "*mu meson*" when the second would be the "*pi meson*". The *mu meson* was behaving like a heavy electron and didn't participate in the strong interaction whereas the pion was believed to be the carrier of the nuclear interaction. This led to classify the *mu* in a new category of particles that shared similar properties called *leptons* under the name of *muon* together with the electron. The *pi meson* was finally found to be a triplet of particles: a positively charged, a negatively charged, and a neutral *pi meson*. The neutral *pi meson* has been more difficult to identify as it wouldn't leave tracks on emulsions nor on bubble chambers and needed to be studied via its decay products. It was

tant step towards the establishment of the Standard Model [56]. A triplet of particles, two charged and a neutral, with a mass roughly half that of a proton, were reported. These particles were baptised *K meson* in contrast to the "light" *pi* and *mu* "L-mesons". The particularity of the *K* is their very slow decays with a typical lifetime of the order of  $10^{-10}$ s much longer than the  $10^{-23}$ s of *pi*-proton reactions. The concept of *strangeness*, a new quantum number was then introduced thanks to an idea of Pais as an attempt to explain this phenomenon as *strange* particles appeared as the pair production of a strange and anti-strange particle [57].

With the development of synchrotrons, the particle *zoo* grew to several dozens during the 1950s as higher energies were reachable through acceleration. In 1961, a first classification system, called *Eightfold Way*, was proposed by Gell-Mann [58]. It found its roots in the Gell-Mann–Nishijima formula, which relates the electric charge  $Q$ , the third component of the isospin  $I_3$ , the *baryon* number  $B$  and the strangeness  $S$ , as showed in Formula 2.6 [59–61].

$$(2.6) \quad Q = I_3 + \frac{1}{2}(B + S)$$

The isospin is a quantum number introduced in 1932 to explain symmetries of the newly discovered neutron using representation theory of SU(2) [62]. The baryon number, was introduced by Nishijima as a quantum number for baryons, i.e. particles of the same family as nucleons [59]. The mesons were classified in an octet and baryons of spin  $\pm \frac{1}{2}$  and  $\pm \frac{3}{2}$  were respectively classified into an octet and a decuplet, as shown in Figure 2.6. To complete the baryon decuplet, Gell-Mann predicted the existence of baryon  $\Omega^-$  which would later be discovered in 1964 [63].

Gell-Mann, and independently Zweig, then proposed a full theoretical model in which *hadrons* (strongly interacting particles, i.e. mesons and baryons) were not elementary particles anymore [64–66]. They were rather composed of three flavors of particles called *quarks* and their anti-particles. The three flavors were called *up*, *down* and *strange*. *Up* and *down* were used to explain the nucleons and non-strange mesons, while *strange* came into the composition of hadrons showing strangeness. *Up* and *down* flavors were discovered in 1968 thanks to the deep inelastic scattering experiments conducted at the Stanford Linear Accelerator Center (SLAC) [67, 68], and *strange* could only be indirectly validated even though it provided a robust explanation to *kaon* (*K*) and *pion* ( $\pi$ ).

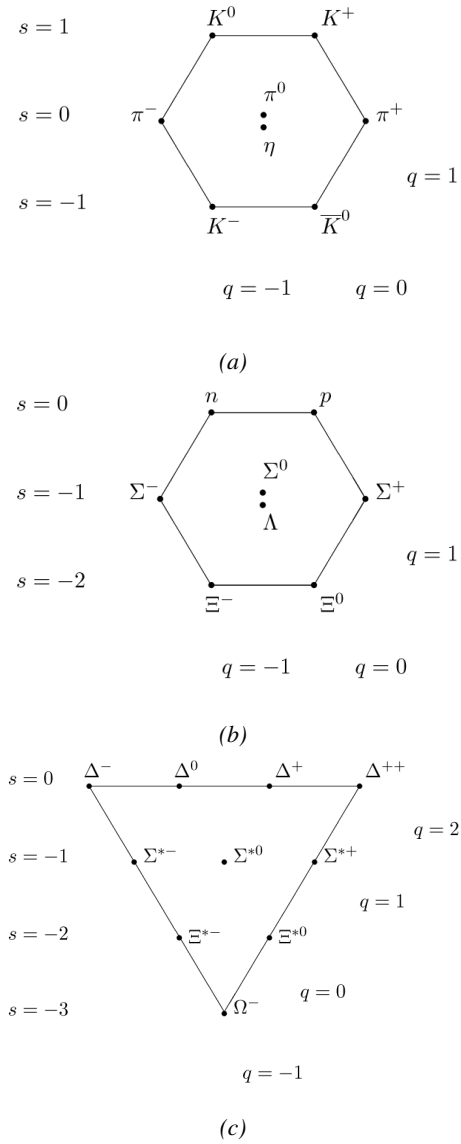
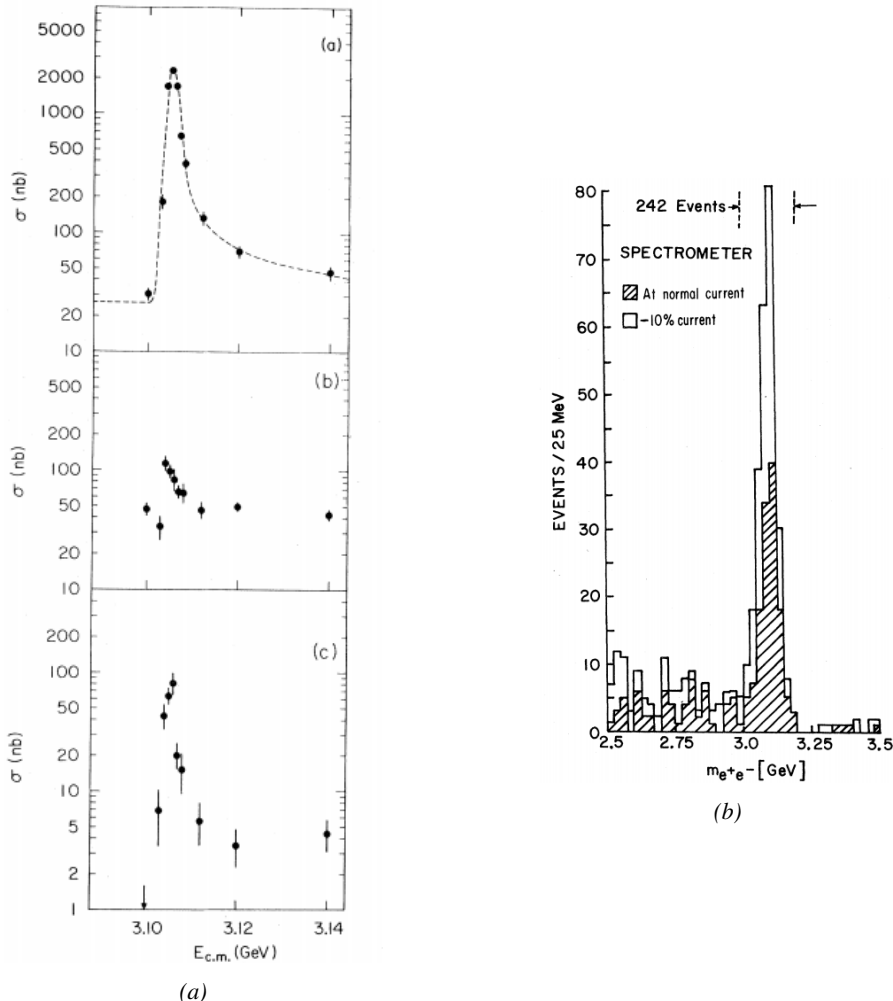


Figure 2.6: (a): Meson octet. (b): Baryon octet. (c): Baryon decuplet.

However, in the decade following the Gell-Mann-Zweig quark model proposition, several improvement to the model were brought. First by Glashow and Bjorken the same year that predicted the existence of a fourth quark flavor, the *charm*, that would equalize the then known number of quarks and leptons [69, 70]. Finally in 1973 by Kobayashi and Maskawa that increased the number of quarks to six to explain the experimental observation of CP violation [71, 72]. These two quarks were referred to as *top* and *bottom* for the first time in 1975 [73]. It's only after these additions to the quark model that finally the *charm* was discovered in 1974 at both SLAC and Brookhaven National Laboratory (BNL) [74, 75]. A meson in which the *charm* is bonded with an *anti-charm*, called  $J/\psi$  and presented in Figure 2.7, helped convince the physics community of the validity of the model. The *bottom* was discovered soon after in 1977 in Fermilab [76] and indicated the existence of the *top* that resisted to discovery until Fermilab's experiments CDF and D $\emptyset$  in 1995 due its very large mass and the energy needed to produce it [77, 78].



*Figure 2.7: Discovery of the  $J/\Psi$  by both (a) SPEAR (SLAC [74]) and (b) AGS (BNL [75]). In Figure (a), the cross section versus energy is showed for (a) multi hadron final states, (b)  $e^+e^-$  final states, and (c)  $\mu^+\mu^-$ ,  $\pi^+\pi^-$  and  $K^+K^-$  final states.*

As remarked by Struminsky, due to mesons such as  $\Omega^-$  or  $\Delta^{++}$ , the first SU(3) model already should have possessed an additional quantum number [79]. Indeed, these mesons are composed of three identical quarks, respectively three *strange* and *up* quarks, with parallel spins, which should be forbidden by the exclusion principle. Independently, Greenberg, and Han and Nambu proposed an additional SU(3) degree of freedom for the quarks [80, 81]. It was later referred to as *color charge gauge*, that could interact through *gluons*, the gauge boson octet corresponding to this degree of freedom. The color field is presented in Figure 2.8a. Nevertheless, as observing free quarks to prove their existence proved to be impossible, two visions of the quarks were argued. On one side, Gell-Mann proposed to see quarks as mathematical construct instead of real particles, as they are always confined, implying that quantum field theory would not describe entirely the strong interaction. He promoted the S-matrix approach to treat the strong interaction. Opposed to this vision, Feynman on the contrary argued that quarks are real particles, that he would call *partons*, that should be described as all other particles by a distribution of position and momentum [82]. The implications of quarks as point-like particles were verified at SLAC and helped abandon the S-matrix to the benefit of QFT [83]. The concept of *color* was then added to the quark model in 1973 by Fritzsch and Leutwyler together with Gell-Mann to propose a description of the strong interaction through the theory of Quantum Chromodynamics (QCD) [84]. The discovery the same year of asymptotic freedom within the QCD by Gross, Politzer, and Wilczek, allowed for very precise predictions thanks to perturbation theory [85, 86]. The evolution of the gauge constant of QCD with respect to the energy as described by asymptotic freedom is showed in Figure 2.8b.

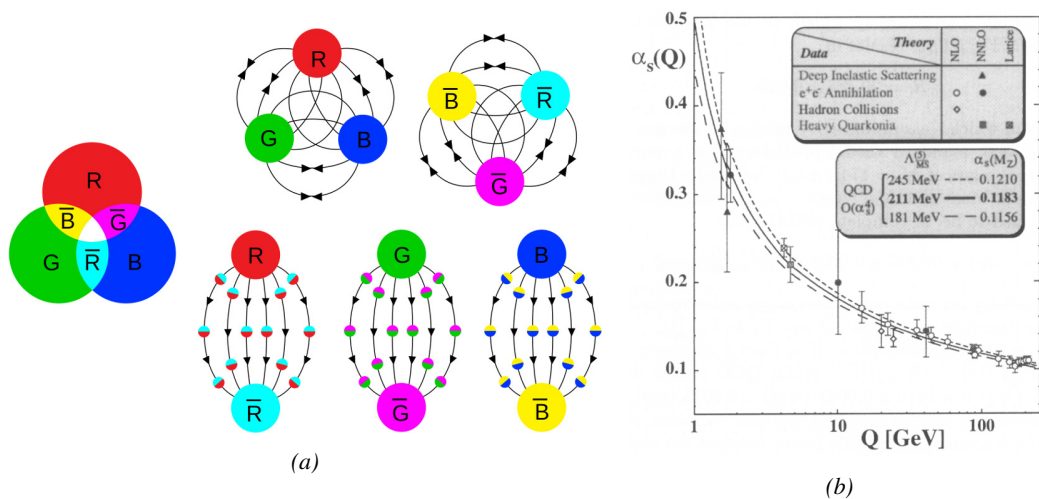
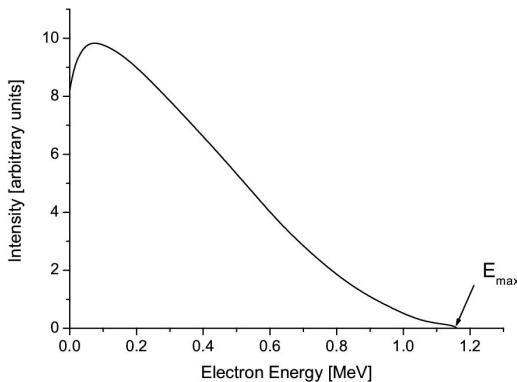


Figure 2.8: (a): the color field of QCD only allows for "white" baryons, particles composed of quarks, to exist. Examples are given for mesons, composed of a quark and its anti-quark, and hadrons, composed of three differently colored quarks or anti-quarks. Other exotic baryons have been predicted and observed, such as tetraquarks and pentaquarks. (b): a crossed analysis performed thanks to the data collected by various experiments at different energies have showed that the coupling constant evolves as predicted by the mechanism of asymptotic freedom [87].

1303 **The Weak interaction, spontaneous symmetry breaking, the Higgs mechanism and the Elec-**  
 1304 **troweak unification**

1305 The weak interaction is the process that causes radioactive decays. Thanks to the neutron discov-  
 1306 ery [23], Fermi could explain in 1934 beta radiations through the beta decay process in which the  
 1307 neutron decays into a proton by emitting an electron [88]. Though the missing energy observed dur-  
 1308 ing this process triggered a huge debate about the apparent non-conservation of energy, momentum  
 1309 and spin of the process, Fermi, as Pauli before him [89], proposed that the missing energy was due to  
 1310 a neutral not yet discovered particle that was then baptised *neutrino*. The impossibility to detect such  
 1311 a particle left some members of the scientific community sceptical, but hints of energy conservation  
 1312 and of the existence of the neutrino were provided by measuring the energy spectrum of electrons  
 1313 emitted through beta decay, as there was a strict limit on their energy, as showed in Figure 2.9.



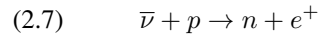
1324 *Figure 2.9: Energy spectrum of beta particles emitted by a source*  
 1325 *of  $^{210}\text{Bi}$ .*

1326 constraint the beta decay theory of Fermi and extend it to the case of the muon, Konopinski and  
 1327 Mahmoud proposed in 1953 that the muon decay would eject a particle similar to the neutrino [91].  
 1328 They predicted the existence of a muon neutrino that would be different to the one involved in the  
 1329 beta decay, related to the electron. With this, the idea of *lepton number* arised. The *muon neutrino*  
 1330 was successfully detected in 1962 by Lederman, Schwartz, and Steinberger [92].

1332 The theory could not be valid though as the probability of interaction, called *cross-section*, would  
 1333 have been increasing without limitation with the square of the energy. Fermi had proposed a two  
 1334 vector current coupling but Lee and Yang noted that an axial current could appear and would violate  
 1335 parity [93]. Gamov and Teller had already tried to account for such parity violation by describ-  
 1336 ing Fermi's interaction through allowed (parity-violating) and superallowed (parity-conserving) de-  
 1337 cays [94]. The Wu experiment in 1956 confirmed the parity violation [95], as showed by Figure 2.10.  
 1338 But the success of QED as a quantum field theory sparked the development of similar theory to de-  
 1339 scribe the weak interaction.

1340 As previously discussed, the great success of QED was built on an underlying symmetry, inter-  
 1341 preted as a gauge invariance so that the effect of the force is the same in all space-time coordinates,  
 1342 and of the possibility to renormalize it in order to resolve infinities. In 1967, Weinberg found a  
 1343 way to unite both the electromagnetic and weak interaction into a gauge theory involving four gauge  
 1344 bosons, three of which are massive and carry out the weak interaction and the last is a massless bo-

It's only 30 years later in 1953 that it was discovered by the team of Cowan and Reines using the principle of inverse beta decay described through Formula 2.7 [90].



The experiment consisted in placing water tanks sandwiched in between liquid scintillators near a nuclear reactor with an estimated neutrino flux of  $5 \times 10^{13} \text{ cm}^{-2} \text{ s}^{-1}$ . However, in order to explain the absence of some reactions in the experiment of Cowan and Reines and

son carrying the electromagnetic interaction [96]. Among the three massive bosons, two are charged and one is neutral, similarly to the previously theorized *pi meson* vector of the Yukawa model [48] and all have a mass much greater than nucleons and thus a very short life time implying a finite very short range, contrary to the contact interaction originally proposed by Fermi.

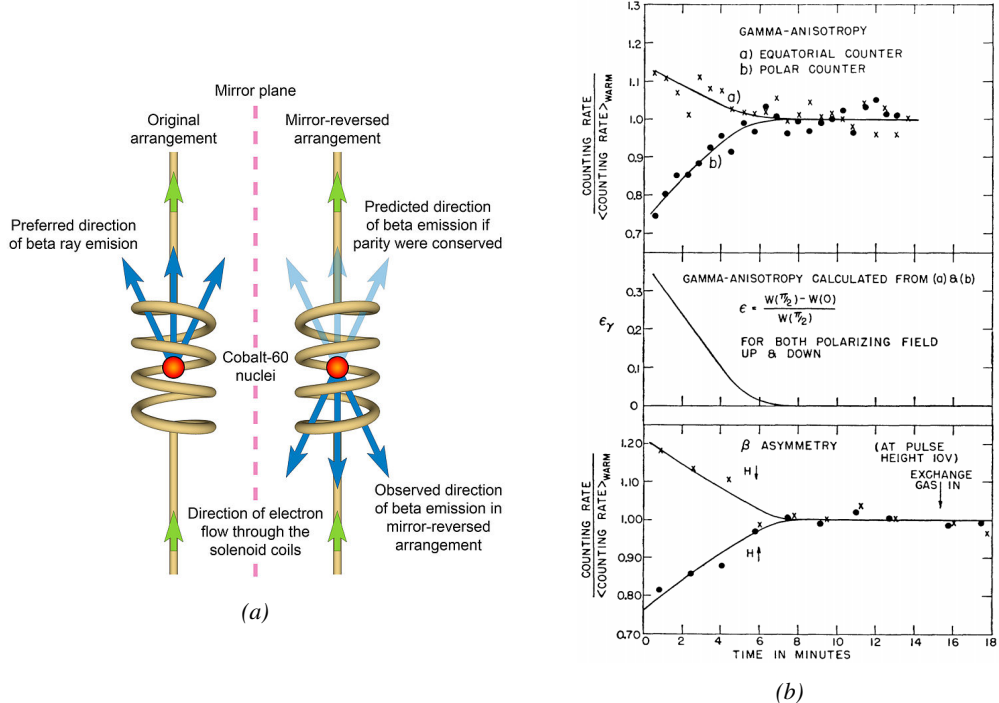


Figure 2.10: As explained through (a), the Wu experiment consisted in measuring the preferred direction of emission of beta rays of a Cobalt source placed in a stable magnetic field aligned, in one case, and anti-aligned, in the other case, with the nuclear spin. The result in (b) showed a violation of parity.

Breakthroughs in other fields of physics contributed in giving theoretical support and interpretation to the unified electroweak theory. The stepping stone was the use of spontaneous symmetry breaking that was inspired to Nambu at the beginning of the 1960s [97, 98] following the development of the Bardeen–Cooper–Schrieffer (BCS) superconductivity mechanism in 1957 [99]. Cooper had shown that BCS pairs, pairs of electrons bound together at low temperature, can have lower energy than the Fermi Energy and are responsible for superconductivity. This led to the discovery of Goldstone-Nambu bosons [100, 101] as a result of the spontaneous breaking of the chiral symmetry in a theory describing nucleons and mesons developed by Nambu and Jona-Lasinio in 1961, and now understood as a low-energy approximation of QCD. Similarly to the mechanism of energy gap appearance in superconductivity, the nucleon mass is suggested to be the result of a self-energy of a fermion field and is studied through a four-fermion interaction in which, as a consequence of the symmetry, bound states of nucleon-antinucleon pairs appear and can be regarded as virtual pions. Though the symmetry is maintained in the equations, the ground state is not preserved. Goldstone showed that the bound states correspond to spinless bosons with zero mass [101].

Although the model in itself didn't revolutionize particle physics, spontaneous symmetry breaking was generalized to quantum field theories. As all fundamental interactions are described using

gauge theories based on underlying symmetries, processes such as the chiral symmetry breaking were introduced soon after the publication of Nambu and Jona-Lasinio. In 1962, Anderson, discussed the implications of spontaneous symmetry breaking in particles physics [102]. He did so by following the idea of Schwinger who suggested that zero-mass vector bosons were not necessarily required to describe the conservation of baryons, contrary to the bosons emerging from chiral symmetry breaking [103]. A model was finally independently built in 1964 by Brout and Englert [104], Higgs [105], and Guralnik, Hagen, and Kibble [106], who discovered that combining an additional field into a gauge theory in order to break the symmetry, the resulting gauge bosons acquire a nonzero mass. Moreover, Higgs stated that this implied the existence of at least one new massive, i.e. self-interacting, scalar boson corresponding to this additional field, that is now known as *Higgs boson*. The Higgs mechanism today specifically refers to the process through which the gauge bosons of the weak interaction acquire mass. In 1967, Weinberg could point to the Higgs mechanism to integrate a Higgs field into a new version of the electroweak theory in which the spontaneous symmetry breaking mechanism of the Higgs field would explicitly explain the masses of the weak interaction gauge bosons and the zero-mass of photons [96].

### 2.1.2 Construction and validation of the Standard Model

The Standard Model of particle physics was built in the middle of the 1970s after the experimental confirmation of the existence of quarks [107]. It is based on the assembly of the models previously introduced and describing the fundamental interactions and their gauge bosons, except for gravitation, as well as the way elementary "matter" particles interact with the fields associated with these force carriers. In this sense, the development of QED and the unification of the electroweak interaction, of the Yukawa interaction and of QCD, and of the Higg mechanism made it possible to explain most of the contemporary physics.

In the SM, "matter" particles, are described by twelve fermion fields of spin  $\frac{1}{2}$  obeying the Fermi-Dirac statistics, i.e. subjected to the Pauli exclusion principle. To each fermion is associated its corresponding anti-particle. The fermions are classified according to the way they interact and thus according to the charges they carry. Six of them are classified as quarks ( $u, d, c, s, t$ , and  $b$ ) and are subjected to all interactions and the six others as leptons ( $e^-, \mu^-, \tau^-, \nu_e, \nu_\mu$ , and  $\nu_\tau$ ). Leptons are not subjected to the strong interaction and among them, the three neutrinos only interact weakly as they are neutral particles, which explains why they are so difficult to detect. The gauge boson fields are the gluons  $g$  for the strong interaction, the photon  $\gamma$  for the electromagnetic interaction and the weak bosons  $W^+, W^-,$  and  $Z^0$  for the weak interaction. Finally, the Higgs field  $H^0$  is responsible, through the spontaneous symmetry breaking, of the mixing of the massless electroweak boson fields  $W_1, W_2, W_3,$  and  $B$  leading to the observable states  $\gamma, W^+, W^-,$  and  $Z^0$  that can gain mass while interacting with the Higgs field. This picture of the SM is summarized through Figure 2.11 where the antifermions are not shown.

When the model was first finalized, the existence of the weak gauge bosons, of the charm, of the third quark generation composed of top and bottom quarks to explain the observed CP violation was not proven but the predictions were measured with good precision in the years following [74–78]. The weak bosons  $W$  and  $Z$  were discovered during the next decade in 1983 [108–111]. The very last predicted elementary particle of the model that was not observed yet proved to be very difficult to observe. The Higgs boson needed the start of the LHC to finally be observed in 2012 [112, 113]. A few years more of tests were necessary to measure its properties to confirm the observation of a scalar boson compatible with the predicted Higgs boson  $H^0$  [114].

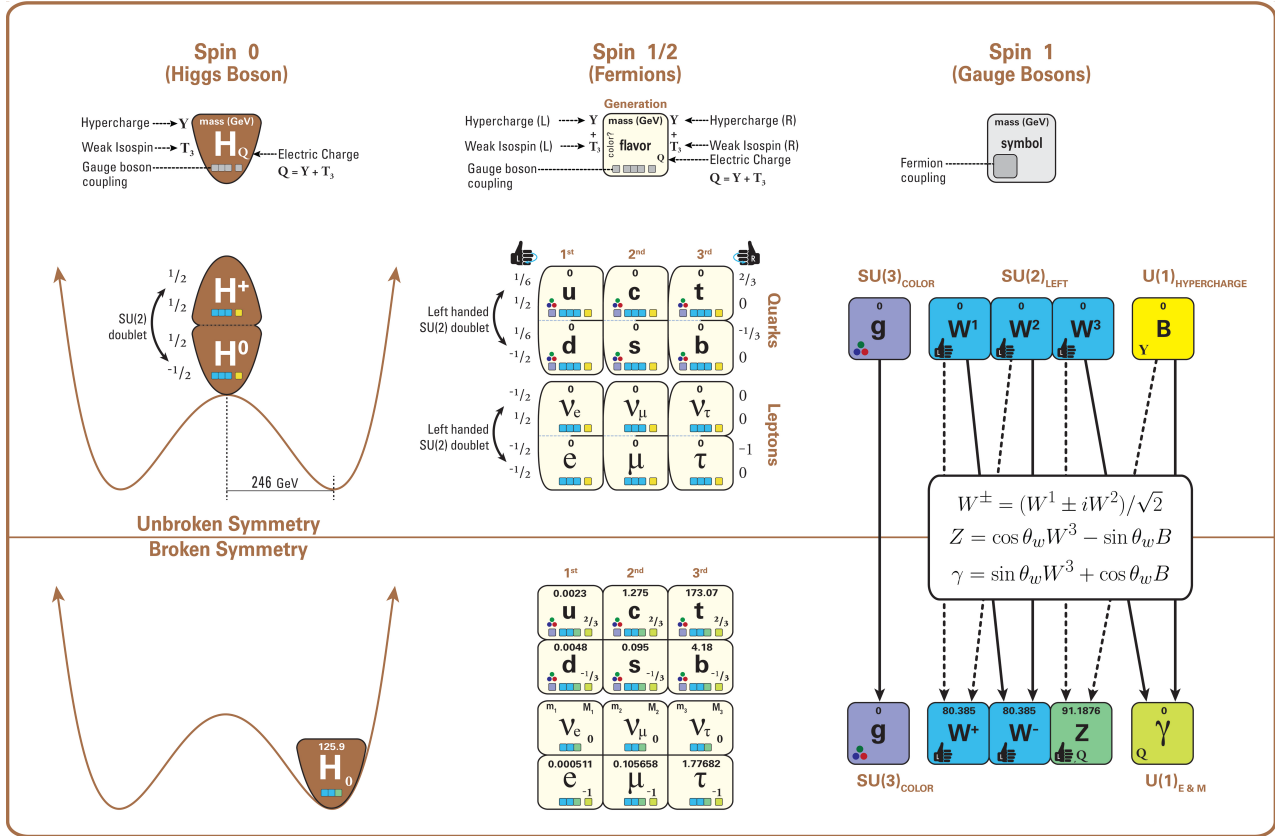


Figure 2.11: The elementary particles of the Standard Model are shown along with their properties. Their interactions with the strong, weak and electromagnetic forces have been made explicit using color squares. In the left column, the scalar Higgs boson is depicted. The center is focused on the matter particles, the fermions, and the right column on the force carriers, the gauge bosons. The role of the Higgs boson in electroweak symmetry breaking is highlighted, and the corresponding way properties of the various particles differ in the (high-energy) symmetric phase (top) and the (low-energy) broken-symmetry phase (bottom) are shown.

### 1409 2.1.3 Investigating the TeV scale

1410 In High-Energy Physics, the number of experimental events depends on the total interaction cross-  
 1411 section of the colliding particles and of the *instantaneous luminosity* [115]. The luminosity is a  
 1412 quantity providing an information on the interaction rate normalised to the interaction cross-section.  
 1413 The relationship between number of events  $N$ , cross-section and instantaneous luminosity  $\mathcal{L}$  is given  
 1414 in Formula 2.8.

$$(2.8) \quad \mathcal{L} = \frac{1}{\sigma} \frac{dN}{dt} \Leftrightarrow N = \sigma \int \mathcal{L} dt = \sigma \mathcal{L}_{int}$$

1415 The integral of the luminosity over time is referred to as the *integrated luminosity*  $\mathcal{L}_{int}$ . In fact,  
 1416 the instantaneous luminosity can be deduced from the beam parameters. New colliders now use  
 1417 bunched beams. The instantaneous luminosity then depends on the bunch crossing frequency  $f_{BX}$ ,  
 1418 on the number of particles contained in each bunch  $n$ , and on the RMS transverse beam sizes in the

horizontal,  $\sigma_x^*$ , and vertical directions,  $\sigma_y^*$ , at the level of the interaction point. The beam sizes can be assumed to be identical, leading to the relation of Formula 2.9.

$$(2.9) \quad \mathcal{L} = f_{BX} \frac{n^2}{\sigma^*}$$

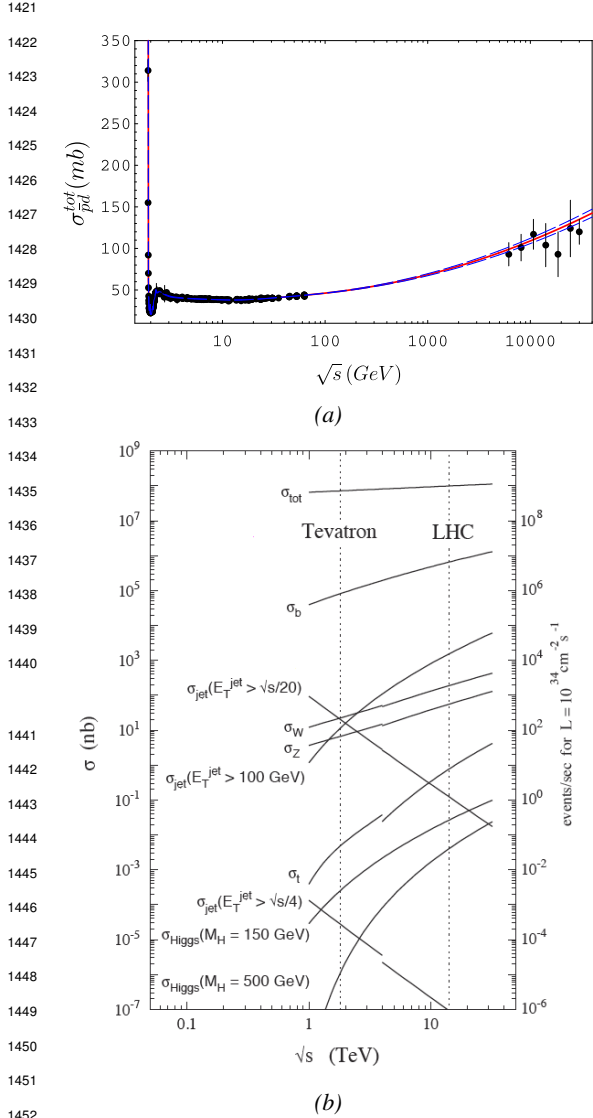


Figure 2.12: (a): Total proton-proton cross-section as a function of the collisions center-of-mass energy  $\sqrt{s}$  [116] with cosmic-ray data from Akeno Observatory and Fly's Eye Collaboration. (b): Total proton-(anti)proton and interaction channel cross-sections in the TeV scale.

radial velocity of visible objects in galaxies was increasing with increasing distance to the center of

This expression doesn't depend on time anymore and leads to a simple estimation of the integrated luminosity and hence, knowing the cross-section of each available physics channel, to the expected number of events in each channel. The total interaction cross section is the sum of all the different output channels allowed by the interaction process. In the case of highly relativistic protons, the proton-proton (pp) total cross-section increases with the center-of-mass energy of interactions, as can be seen from Figure 2.12.

Enhancing rare processes that allow to finely test the Standard Model is then achieved through an increase in both energy and luminosity. At the energy range that were scanned thanks to high-energy colliders, the SM has so far been a well tested theory. Nevertheless, several hints of physics going beyond its scope have been observed.

**Dark matter and gravity:** The discrepancy of velocity dispersion of stars in galaxies with respect to the visible mass they contain is known since the end of the 19<sup>th</sup> century where Kelvin proposed that this problem could be solved if a great majority of the stars would be dark bodies, idea strongly criticized by Pointcaré [117]. Throughout the 20<sup>th</sup> century, physicists like Kapteyn [118] or Zwicky [119, 120], showed the first hints of a *dark matter* by studying star velocities and galactic clusters, followed by robust measurements of galaxy rotation curves by Babcock which suggested that the mass-to-luminosity ratio was different from what would be expected from watching the visible light [121]. Later in the 1970s, Rubin and Ford from direct light observations [122] and Rogstad and Shostak from radio measurements [123] showed that the ra-

the galaxy. An example of galaxy rotation curve is provided in Figure 2.13. Finally observation of lensing effect by galaxy clusters, temperature distribution of hot gas in galaxies and clusters, and the anisotropies in the Cosmic Microwave Background (CMB), showed in Figure 2.14, kept on pointing to a *dark matter* [124]. From all the data accumulated, the visible matter would only account to no more than 5% of the total content on the visible universe [125]. Alternative theories have tried to investigate modified versions of the General Relativity as this theory is only well tested at the scale of the solar system but is not sufficiently tested on wider ranges or even theories in which gravitation is not a fundamental force but rather an emergent one [126, 127]. But so far, such theories have difficulties to reproduce all the experimental observations as easily as through dark matter.

A possible theory to offer dark matter candidates would be *super-symmetry* (SUSY) which proposes a relationship in between bosons and fermions in the frame of the Minimal Supersymmetric Standard Model (MSSM). In this model, each elementary particle, through a spontaneous space-time symmetry breaking mechanism would have a *super partner* from the other family of particles, pairing bosons and fermions together. The model was first introduced as a way to solve the *Hierarchy Problem* [129]. The discrepancy between the strength of the weak force and gravity translates into a light Higgs boson compared to the *Planck Mass*. In the SM, the Higgs mass is left to be a measured parameter rather than a calculated one even though the model requires a mass in between 100 and 1000 GeV/c<sup>2</sup> to stay unitary. Nevertheless, quantum corrections to the Higgs mass coming from its interactions with virtual particles should make the scalar boson much heavier than what measured [130]. Through the MSSM, the stability of fermion masses would provide stability to the Higgs boson mass via the introduction of a fermionic super partner.

On top of providing a solution to the Hierarchy Problem, the model comes with heavy dark matter candidates in the TeV scale [131]. Indeed, in the case *R-parity* is not violated, the lightest supersymmetric particle (LSP) cannot decay and could then explain the dark matter. The LSP in the model is neutral and can only interact through the weak and gravitational interactions. Typical candidates are the *neutralino*, the *sneutrino* or the *gravitino*.

Finally, gravity is not explained through the SM, and huge difficulties are encountered when trying to include it. The strength of gravitational interaction is expected to be negligible at the scale of elementary particles, nevertheless, adding gravitation in the perspective of developing a "theory of everything" leads to divergent integrals that could not be fixed through renormalization. Extensions to the MSSM, and in particular minimal SUper GRAvity (mSUGRA), include general relativity as mediator of the symmetry breaking. mSUGRA gives access to the hidden sector in which the MSSM only interacts gravitationally and suppresses the infinities arising from attempts to include gravity into the SM thanks to possible renormalization [132].

Signatures for the MSSM would come from the super partners of quarks and gluons that can

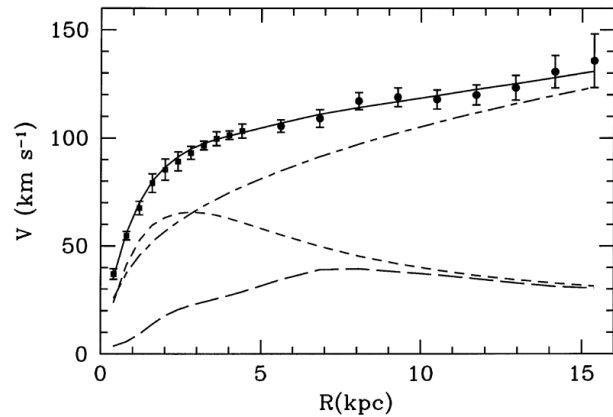


Figure 2.13: Rotation curve (points) of the galaxy M33 compared with best fitting model (line). The short-dashed line represents the rotation profile that would be expected from the observation of the stellar disc alone [128].

1507 decay into an LSP that could then be identified as missing energy as it escapes the detectors undetected.  
 1508 But even in the case MSSM predictions are not to be seen, the other models treating dark  
 1509 matter also propose Weakly Interacting Massive Particles (WIMPs) that could be observed in simi-  
 1510 lar ways than LSPs [133]. Moreover alternative models exist to provide solutions to the Hierarchy  
 1511 Problem. The most investigated models are extra dimensions such as Arkani-Hamed Dimopoulos  
 1512 Dvali [134, 135], Kaluza–Klein [136, 137] or Randall-Sundrum models [138, 139] that usually also  
 1513 include gravitation. Finally, alternative models also exist for the production of dark matter candi-  
 1514 dates. Models with a hidden valley that would unravel the existence of a new group of light particles  
 1515 through the extension of the SM with a new confining gauge group [140].  
 1516

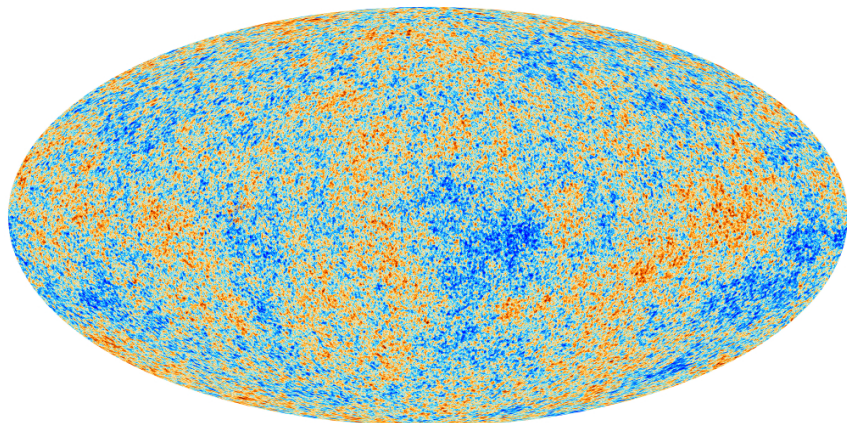


Figure 2.14: Cosmic Microwave Background as measured by the space observatory Planck which mean tem-  
perature is  $T_\gamma = (2.7255 \pm 0.0006)\text{K}$  with anisotropies of the order of a few  $\mu\text{K}$ .

1517 **Baryon asymmetry:** Another intriguing fact is that the universe is dominated by matter. However,  
 1518 the SM predicted that matter and antimatter should have been created in equal amounts. For an inter-  
 1519 action to produce matter and antimatter at different rates within the SM, three necessary conditions  
 1520 were highlighted by Sakharov[141]. First of all, there must be a violation of the baryon number  $B$ .  
 1521 Then, there must be a C-symmetry and CP-symmetry violation. The C-symmetry violation must  
 1522 happen to make sure that the processes creating more baryons than antibaryons are not compensated  
 1523 by processes creating more anti-baryons and similarly, the CP-symmetry violation makes sure that  
 1524 there are not equal numbers of left-handed baryons and right-handed anti-baryons produced. Fi-  
 1525 nally, the interactions must happen out of thermal equilibrium to make sure that CPT-symmetry does  
 1526 not balance the processes increasing the baryon number with processes doing otherwise [142]. An  
 1527 out-of-equilibrium interaction implies a new unstable heavy particle.

1528 The favoured model to explain this imbalance is the *baryogenesis* that requires electroweak sym-  
 1529 metry breaking to be first order phase transition to fall within the scope of SM [143, 144]. This  
 1530 means that the symmetry breaking process must involve the absorption or release of a fixed latent  
 1531 heat. Through the baryogenesis, the phase transition breaks P-symmetry spontaneously and allows  
 1532 for CP-symmetry violation. In turn, the CP violation makes the amplitude of interactions involving  
 1533 quarks different than the ones involving anti-quarks leading to the greater creation rate of baryons  
 1534 with respect to anti-baryons. The key to this baryon net creation would be found into the *sphaleron*.  
 1535 A sphaleron is a particle-like saddle point of the energy functional that appears at the top of the

transition barrier and that could be created if a sufficiently large amount of energy is brought as the tunneling effect through the barrier is largely suppressed for electroweak interactions. The existence of the sphaleron would allow violation of the conservation of  $B$  but also of the leptonic number  $L$  while conserving  $B - L$ . The detection at  $p - p$ -colliders of such a transition is foreseen to be made through processes with high-multiplicity final states such as  $u + u \rightarrow e^+ \mu^+ \tau^+ t\bar{t} b\bar{c} c\bar{s} d\bar{d} + X$  [145]. To be probed, the sphaleron transition requires an energy  $E_{sph} \approx 9$  TeV. Nevertheless, if such transition cannot be observed, other BSM models such as the WIMP baryogenesis could be then observed thanks to the detection of displaced vertices, featuring the decay of a WIMP leading to violation of  $B$  [146].

Another possibility to explain the apparent asymmetry would be the existence of an electric dipole moment (EDM) in any fundamental particle that would permit matter and antimatter particles to decay at different rates [147]. Indeed, the presence of an EDM violates in itself both  $P$  and  $T$  symmetries. Experiments are able to probe for the EDM of various fundamental particles such as the electron [147], the charm and strange quarks [148] or even a heavy neutrino EDM [149].

1550

**Neutrino mass and sterile neutrino scenario:** The SM considers neutrinos to be massless. But it was showed in the late 1960s by the Homestake experiment that the flux of solar neutrinos (i.e.  $\nu_e$ ) measured didn't match the predicted values [150]. The mechanism of neutrino oscillations as a solution to the discrepancy was proposed by Pontecorvo [151] and confirmed in the early 2000s by the Sudbury Neutrino Observatory [152]. This oscillation implies that neutrinos that can be observed are a superposition of massive neutrino states. The research on neutrino oscillation is already quite advanced with experiments looking at atmospheric, reactor or beam neutrinos in order to determine the elements of the mixing matrix (Pontecorvo–Maki–Nakagawa–Sakata matrix [153]) similar to the Cabibbo–Kobayashi–Maskawa (CKM) matrix describing the mixing of quarks [72]. Nevertheless, no answer to the origin of neutrino mass is yet provided.

Explaining the light non-zero mass of the neutrinos  $\nu_l$  ( $l = e, \mu, \tau$ ) of the order of the eV can be done through the Seesaw mechanism [154, 155]. This model features heavy Majorana counterparts  $N_l$  ( $l = e, \mu, \tau$ ) to the  $\nu_l$ . The masses of the light and heavy neutrinos are linked through a  $2 \times 2$  mass matrix  $A$  with eigenvalues  $\lambda_{\pm}$  expressed as in Equation 2.10.

$$(2.10) \quad \begin{aligned} A &= \begin{pmatrix} 0 & M \\ M & B \end{pmatrix} \\ \lambda_{\pm} &= \frac{B \pm \sqrt{B^2 + 4M^2}}{2} \end{aligned}$$

The Majorana mass term  $B$  is assumed to be comparable to the Grand Unified Theory scale ( $10^{16}$  GeV) while the Dirac mass term  $M$  is of the order of electroweak scale (246 GeV). In these conditions, the eigenvalue  $\lambda_+$  is almost  $B$  while  $\lambda_-$  is close to the ratio  $-M^2/B$  compatible with very light neutrinos with masses of the order of 1 eV. Studying the left-right symmetric model seeking for the parity violation in weak interactions leads to the incorporation of three additional gauge bosons  $W_R$  and  $Z'$  as a result of the spontaneous symmetry breaking. The processes that are predicted by the model and can be probed at colliders are processes such as  $pp \rightarrow W_R \rightarrow l + N_l + X$  and  $pp \rightarrow Z' \rightarrow N_l + N_l + X$  where the heavy neutrinos decay as  $N_l \rightarrow l + j_1 + j_2$ ,  $j_i$  being jets [156]. Other version of seesaw mechanisms exist to account for the neutrino mass that can also be explained thanks to supersymmetric models [157].

## 1575 2.2 The Large Hadron Collider & the Compact Muon Solenoid

1576 Throughout its history, CERN has played a leading role in high-energy physics. Large regional facil-  
 1577 ities such as CERN were planned after the second world war in an attempt to increase international  
 1578 scientific collaboration and to allow scientists to share the forever increasing costs of experimental  
 1579 facilities. Indeed, it is necessary to use always more powerful tools to improve the fine understanding  
 1580 of our Universe. The construction of the first CERN accelerators at the end of the 50s, the Synchro-  
 1581 cyclotron (SC) and the Proton Synchrotron (PS), was directly followed by the first observation of  
 1582 antinuclei in 1965 [158]. The very first proton-proton collider showing hints of protons not being  
 1583 elementary particles was the Intersecting Storage Rings (ISR). From this experience, the Super Pro-  
 1584 ton Synchrotron (SPS) was built in the 70s to investigate the structure of protons, the preference  
 1585 for matter over antimatter, the state of matter in the early universe or exotic particles, and led to  
 1586 the discovery in 1983 of the W and Z bosons [108–111]. These newly discovered particles and the  
 1587 electroweak interaction were then studied in detail by the Large Electron-Positron (LEP) collider  
 1588 that proved that there only are three generations of elementary particles in 1989 [159]. The LEP was  
 1589 then dismantled in 2000 to allow for the LHC to be constructed in the existing tunnel.

### 1590 2.2.1 LHC, the most powerful particle accelerator

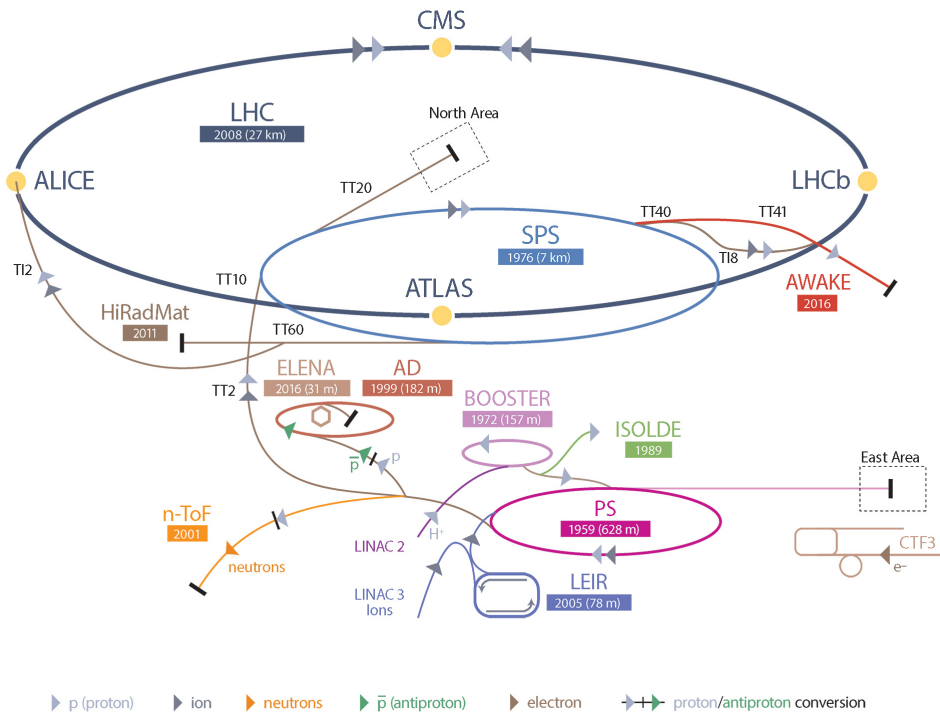


Figure 2.15: CERN accelerator complex.

1591 The different aspects of physics beyond the Standard Model of particle physics and the Standard  
 1592 Model itself can be tested through the use of very energetic and intense hadron and ion colliders.  
 1593 Powerful hadron colliders are suited for searching for strongly interacting particles. The LHC at

1594 CERN is a perfect tool to seek answers to these open questions and the experiments build along its  
 1595 beam lines already started investigating further into the SM and BSM physics.

1596 The LHC has always been considered as an  
 1597 option for the future of CERN. At the moment  
 1598 of the construction of the LEP beneath the border  
 1599 between France and Switzerland, the tunnel was  
 1600 built in order to accommodate what would be a  
 1601 Large Hadron Collider with a dipole field of 10 T  
 1602 and a beam energy in between 8 and 9 TeV [160].  
 1603 In 1985, the creation of a 'Working Group on the  
 1604 Scientific and Technological Future of CERN'  
 1605 took place to investigate such a collider [161].  
 1606 The decision was finally taken almost ten years  
 1607 later, in 1994, to construct the LHC in the LEP  
 1608 tunnel [162] and the approval of the 4 main ex-  
 1609 periments that would take place at the four inter-  
 1610 action points came in 1997 [163] and 1998 [164]:

- 1611 • ALICE [165] has been designed for the  
 1612 purpose of studying the confinement of  
 1613 quarks through exploration of the quark-  
 1614 gluon plasma that is believed to have been  
 1615 a state of matter that existed in the very first  
 1616 moment of the universe.
- 1617 • ATLAS [166] and CMS [167] are general  
 1618 purpose experiments that have been de-  
 1619 signed with the goal of continuing the ex-  
 1620 ploration of the Standard Model and the in-  
 1621 vestigation of new physics.
- 1622 • LHCb [168] has been designed to investi-  
 1623 gate the preference of matter over antimat-  
 1624 ter in the universe through CP violation.

1625 These large-scale experiments, as well as the  
 1626 full CERN accelerator complex, are displayed in  
 1627 Figure 2.15. The LHC is a 27 km long hadron  
 1628 collider and the most powerful accelerator used  
 1629 for particle physics since 2008 [169]. The LHC  
 1630 is designed to collide protons at a center-of-  
 1631 mass energy of 14 TeV and luminosity of  $10^{34}$   
 1632  $\text{cm}^{-2}\text{s}^{-1}$ , as well as  $Pb$  ions at a center-of-mass  
 1633 energy of 2.8 TeV/A with a peak luminosity of  
 1634  $10^{27} \text{ cm}^{-2}\text{s}^{-1}$ . The collider is the last of a long  
 1635 series of accelerating devices. Indeed, before be-  
 1636 ing accelerated by the LHC, the particles need to pass through different acceleration stages. All

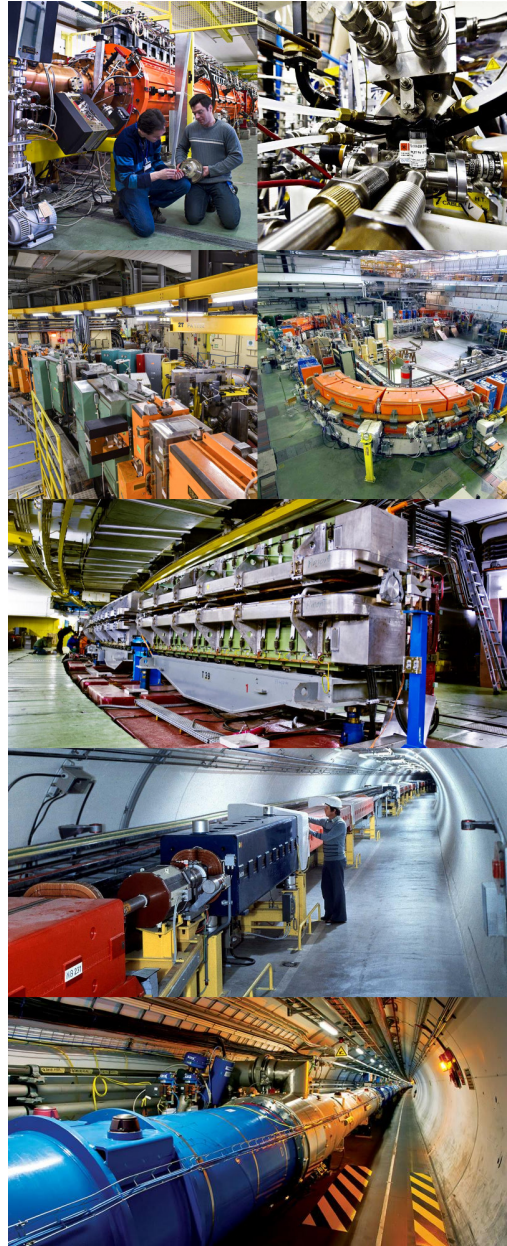


Figure 2.16: Pictures of the different accelerators. From top to bottom: first the LINAC 2 and the Pb source of LINAC 3. Then the Booster and the LEIR. Finally, the PS, the SPS and the LHC.

these acceleration stages are visible on Figure 2.15 and pictures of the accelerators are shown in Figure 2.16.

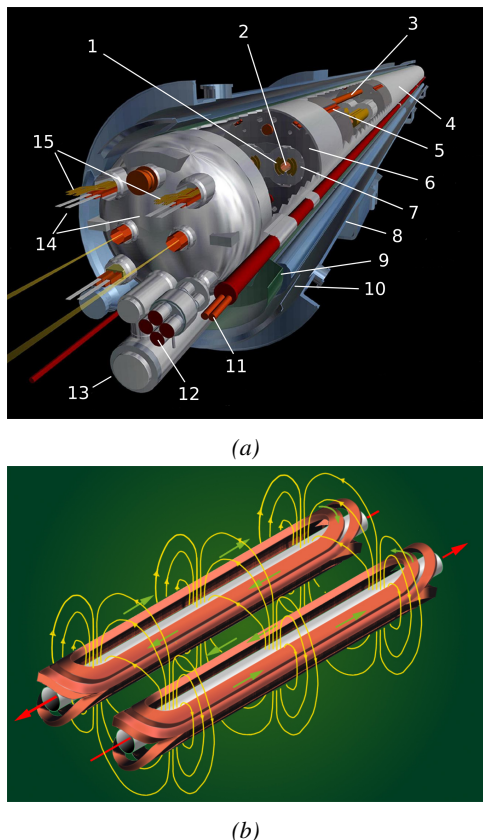


Figure 2.17: (a): schematics of the LHC cryo-dipoles. 1: Superconducting Coils, 2: Beam pipe, 3: Heat exchanger Pipe, 4: Helium-II Vessel, 5: Superconducting Bus-bar, 6: Iron Yoke, 7: Non-Magnetic Collars, 8: Vacuum Vessel, 9: Radiation Screen, 10: Thermal Shield, 11: Auxiliary Bus-bar Tube, 12: Instrumentation Feed Throughs, 13: Protection Diode, 14: Quadrupole Bus-bars, 15: Spool Piece Bus-bars. (b): magnetic field and resulting motion force applied on the beam particles.

The story of accelerated protons at CERN starts with a bottle of hydrogen gas injected into the source chamber of the linear particle accelerator *LINAC 2* in which a strong electric field strips the electron off the hydrogen molecules only to keep their nuclei, the protons. The cylindrical conductors then accelerate the protons to an energy of 50 MeV. When exiting the *LINAC 2*, the protons are divided into four bunches and injected into the four superimposed synchrotron rings of the *Booster* where they are then accelerated to reach an energy of 1.4 GeV before being injected into the *PS*. The four proton bunches are hence sent as one to the *PS* where their energy eventually reaches 26 GeV. The *PS* not only accelerates protons. It also accelerates heavy ions from the *Low Energy Ion Ring (LEIR)*. Lead is first injected into the dedicated linear collider *LINAC 3*, that accelerates the ions. Electrons are stripped off the lead ions all along the acceleration process and eventually, only bare nuclei are injected in the *LEIR* whose goal is to transform the long ion pulses received into short dense bunches for *LHC*. Ions injected and stored in the *PS* were accelerated by the *LEIR* from 4.2 MeV to 72 MeV. Directly following the *PS*, is finally the last acceleration stage before the *LHC*, the 7 km long *SPS*. The *SPS* accelerates the protons to 450 GeV and inject them in both *LHC* accelerator rings that will increase their energy up to 7 TeV. When the *LHC* runs with heavy lead ions for *ALICE* and *LHCb*, ions are injected and accelerated to reach the energy of 2.8 TeV/A.

The *LHC* beams are not continuous but are rather organised in bunches of particles. When in *pp*-collision mode, the beams are composed of 2808 bunches of  $1.15 \times 10^{11}$  protons separated by 25 ns. When in *Pb*-collision mode, the 592 *Pb* bunches are on the contrary composed of  $2.2 \times 10^8$  ions separated by 100 ns. The two parallel proton beams of the *LHC* are contained in a single twin-bore magnet due to the space restriction in the *LEP* tunnel. Indeed, building two completely separate accelerator rings next to each other was impossible. The dipoles of the 1232 twin-bore magnets are shown in Figure 2.17 alongside the magnetic field generated along the dipole section to accelerate the particles. The dipoles generate a nominal field of 8.33 T, needed to give protons and lead nucleons their nominal energy. Some 392 quadrupoles, presented in Figure 2.18, are also used to focus to the beams, as well as other multipoles to correct smaller imperfections.

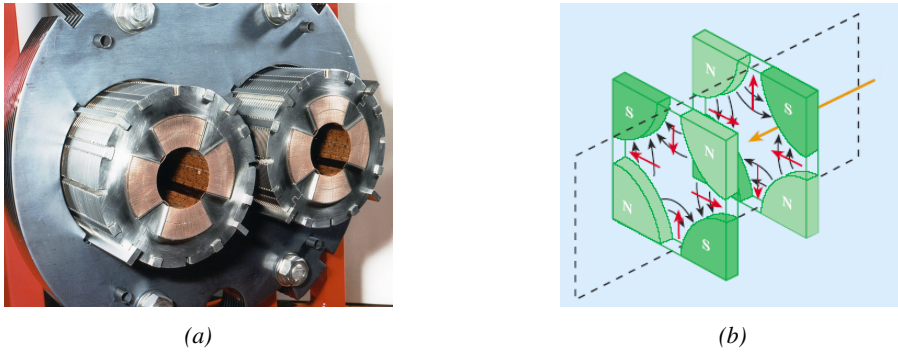


Figure 2.18: The LHC quadrupoles (a) showed together with the magnetic fields and resulting focussing force applied on the beam by two consecutive quadrupoles (b).

## 2.2.2 Timeline of operation

LHC accelerated its first proton in September 2008 but the first collisions only started one year later in November 2009. At this moment the LHC machine officially became the world's most powerful particle accelerator and entered its Physics Run 1 that lasted until February 2013. During Run 1 of the LHC program, the center-of-mass energy was only half of the nominal LHC energy. Nevertheless, the energy and luminosity displayed during Run 1 were enough for both CMS and ATLAS to discover the Higgs boson [112, 113] as showed in Figure 2.19 and for LHCb to discover pentaquarks [170] and confirm the existence of tetraquarks [171]. During this period, ALICE also reported a successful observation of the quark-gluon plasma aimed at studying the early universe [172], ATLAS reported the observation of a new particle before the discovery of the Higgs [173] and a first test of super-symmetric models was performed [174].

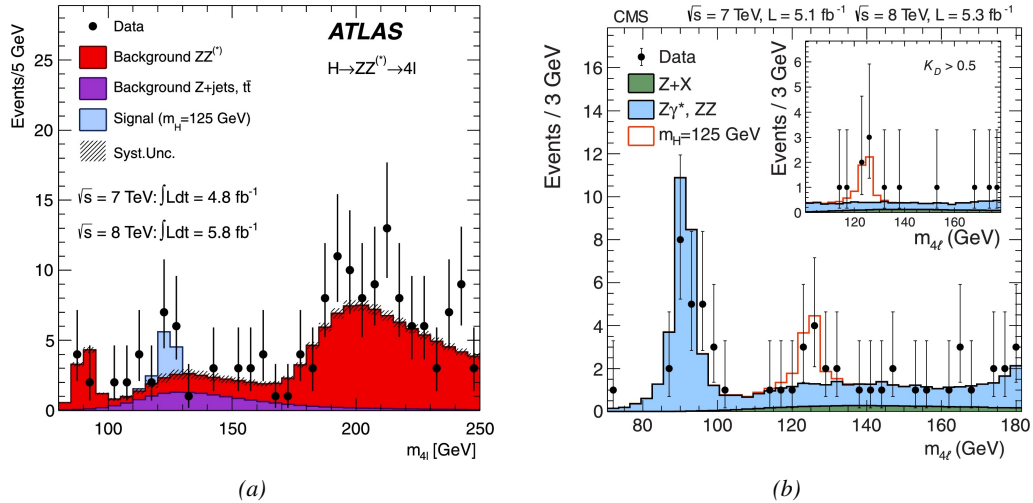


Figure 2.19: Distribution of the four-lepton invariant mass for the  $ZZ \rightarrow 4l$  analysis as presented by both (a) ATLAS [112] and (b) CMS [113] in 2012.

Run 1 was brought to an end with the start of the First Long Shutdown, an almost two years technical stop aimed at increasing the energy of the center-of-mass collisions to  $\sqrt{s} = 13 \text{ TeV}$

as well as the instantaneous luminosity. This maintenance stop was also effectively used by the experiments which upgraded part of their detection systems. Run 2 then started in 2015 and lasted until end of 2018 where the activities ended with a last heavy ion run. During the operation, the instantaneous was successfully brought to a value of  $1.7 \times 10^{34} \text{ cm}^{-2} \text{ s}^{-1}$  exceeding the design value. Run 2 has been the occasion to acquire more data to study the properties of the Higgs boson with more precision. The boson discovered in the first physics run seems to be consistent with the SM Higgs boson [114].

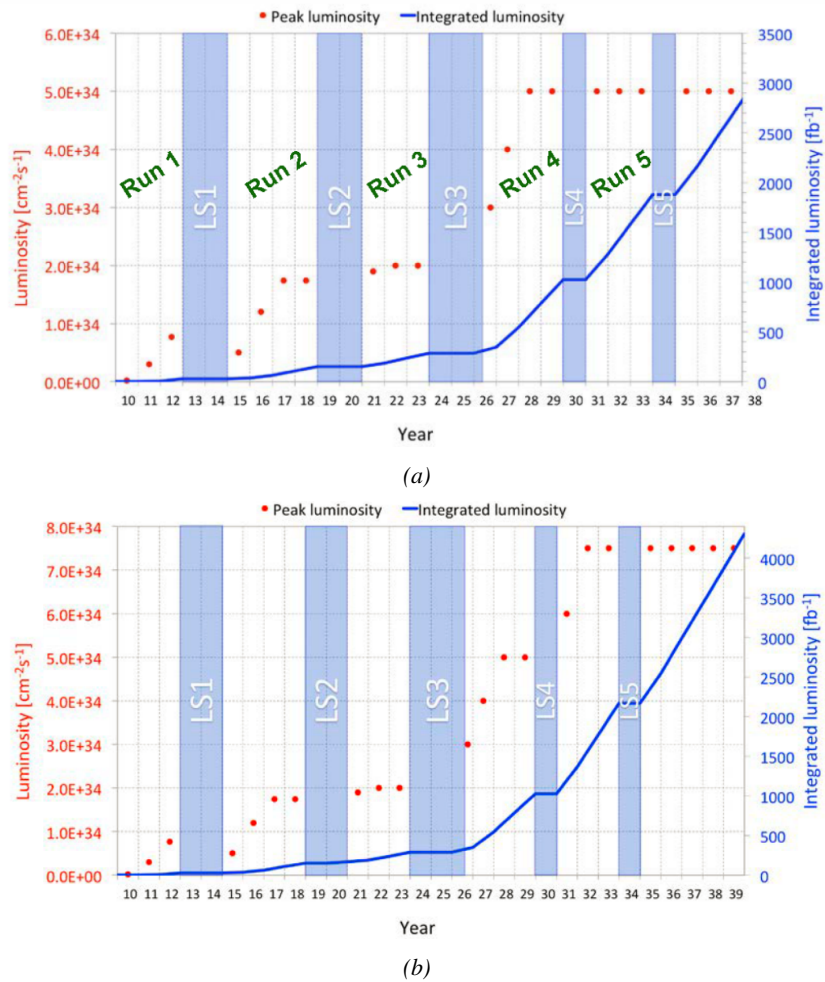


Figure 2.20: Detailed timeline projection of LHC and HL-LHC operation until 2039 showing the evolution of the instantaneous and integrated luminosity as designed (a) and in the ultimate case where the instantaneous luminosity is increased to  $7.5 \times 10^{34} \text{ cm}^{-2} \text{ s}^{-1}$  thanks to a new increase of instantaneous luminosity during Run 5 (b) [175–177].

From the end of 2018 to early 2021 the Second Long Shutdown will take place. This second maintenance stop will be the occasion to boost once again the beam energy to finally reach the design energy of LHC, 14 TeV. On the side of the maintenance work, preliminary work for the High Luminosity LHC will be performed. The preparations will consist of detector, on the side of the

1707 experiments, and beam machine upgrades, on the side of LHC. In 2021, the physics program will  
 1708 be resumed with an instantaneous luminosity fixed at  $2 \times 10^{34} \text{ cm}^{-2} \text{ s}^{-1}$ . During these 3 years of  
 1709 run, the LHC will deliver as much integrated luminosity as what was brought during the almost 7  
 1710 years of both Run 1 and 2 of data taking. Phase-1 will end with an overall  $300 \text{ fb}^{-1}$  delivered. The  
 1711 timeline so far described is summarized through the evolution of the instantaneous luminosity and  
 1712 of the corresponding integrated luminosity provided in Figure 2.20.

1713 After the Third Long Shutdown (2024-2026) that will close the activities of Run 3, the accel-  
 1714 erator will enter the HL-LHC configuration [175], increasing the instantaneous luminosity to an  
 1715 unprecedented level of  $5 \times 10^{34} \text{ cm}^{-2} \text{ s}^{-1}$  for  $pp$ -collisions ( $4.5 \times 10^{27} \text{ cm}^{-2} \text{ s}^{-1}$  for  $Pb$ -collisions),  
 1716 boosting the discovery potential of the LHC. The HL-LHC phase should last at least another 10 years  
 1717 depending on the breakthrough this machine would lead to. Already a new accelerating device, the  
 1718 FCC, as been proposed and is being investigated to prepare the future of high-energy physics after  
 1719 the LHC.

### 1720 2.2.3 High Luminosity LHC

1721 After approximately fifteen years of operation, the LHC will undergo a new series of upgrades during  
 1722 the LS3 in order to boost its discovery potential as previously discussed. The period after LS3 is  
 1723 what is referred to HL-LHC or Phase-2. The goal is to aim for a luminosity 5 to 7 times stronger  
 1724 than the nominal one trying to reach even 10 times this value if possible [175, 176]. Increasing  
 1725 the luminosity means that the beam size at the collision points needs to be reduced to boost the  
 1726 number of collisions per bunch crossing. For this purpose, new focusing and bending magnets and  
 1727 collimators will be installed at the collision points as well as newly developed "crab cavities" that  
 1728 will tilt the particle bunches just prior to the collisions by giving them transverse momentum and  
 1729 thus increasing their meeting area. In addition, the full proton injection line will be upgraded.

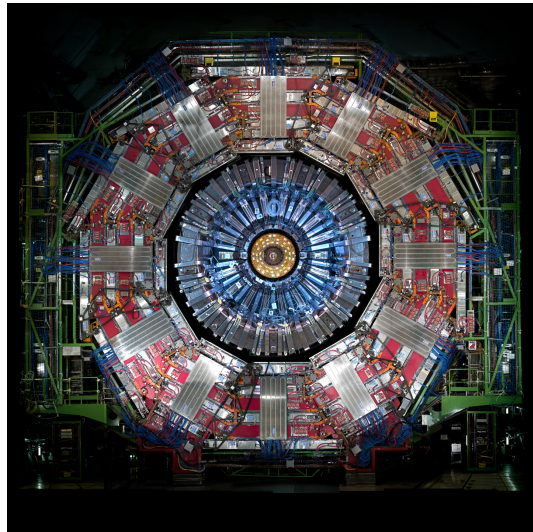
1730 On the experiments side, the pile-up (PU) will be increased up to 150 to 200 interactions per  
 1731 bunch crossing in ATLAS and CMS, making necessary a strong upgrade of the trigger system and  
 1732 of the inner trackers and of the calorimeters. Both ATLAS and CMS will also need to upgrade the  
 1733 muon trigger at the level of their endcaps mainly focusing on the coverage near the beam line in  
 1734 order to increase the detection acceptance and event selection. Moreover, the increased luminosity  
 1735 will also lead to an increased background rate and a faster ageing of the detectors.

1736 The end of 2018 marked the beginning of LS2 and the start of Phase-2 upgrade activities. From  
 1737 the HL-LHC period onwards, i.e. past LS3, the performance degradation due to integrated radiation  
 1738 as well as the average number of inelastic collisions per bunch crossing will rise substantially. This  
 1739 has become a major challenge for all of the LHC experiments, like CMS, that were forced to address  
 1740 an upgrade program for Phase-2 [177]. Dealing with the data from the muon detectors will force to  
 1741 upgrade the detectors and electronics towards the most recent technologies.

### 1742 2.2.4 The Compact Muon Solenoid experiment

1743 Among the four main LHC experiments is the Compact Muon Solenoid used as a multipurpose  
 1744 tool to investigate the SM and the physics beyond its scope. The CMS apparatus in itself is the  
 1745 heaviest detector ever built starring a 15 m diameter and a 29 m length for a total weight of 14 kT.  
 1746 A thick 4 T solenoid magnet located at the beam interaction point hosts trackers and calorimeters.  
 1747 Extending in all directions around the magnet, heavy iron return yokes are installed to extend the  
 1748 magnetic field and support a muon system. The apparatus consists of a barrel, referring to the magnet

1749 and the detectors contained in it and the part of the muon system built directly in the cylinder around  
 1750 the magnet, and of two endcaps in the forward and backward region of the detector that closes the  
 1751 apparatus and complete the detection coverage along the beam line. A front view on the barrel is  
 1752 provided in Figure 2.21 while a detailed view of the apparatus is given in Figure 2.22.



1769 *Figure 2.21: Picture of the CMS barrel. The red outer  
 1770 layer is the muon system hosted into the red iron return  
 1771 yokes. The calorimeters are the blue cylinder inside  
 1772 in magnet solenoid and the tracker is the inner yellow  
 1773 cylinder built around the beam pipe.*

1774 neutral hadrons are differentiated from electrons and charged hadrons in the calorimeters by the fact  
 1775 that they don't interact with the silicon tracker and are not influenced by the magnetic field, as can  
 1776 be seen in Figure 2.23.  
 1777

In order to efficiently detect all long living particles and measure their properties with good precision, the CMS detector uses an onion like layout around of the interaction point in order to maximize the covered solid angle. As detailed in Figure 2.23, in the innermost region of the detector, closest to the interaction point, the silicon tracker records the trajectory of charged particles. Around it, the electromagnetic calorimeter (ECAL) stops and measures the energy deposition of electrons and photons. In the next layer, the hadron calorimeter (HCAL), hadrons are stopped and their energy measured. These layers are contained inside of the magnet of CMS, the superconducting solenoid. Outside of the magnet are the muon chambers embedded into iron return yokes used to control the magnetic field and gives muons, the only particles traveling completely through the whole detector, a double bending helping in reconstructing their energy and trajectory. Note that photons and

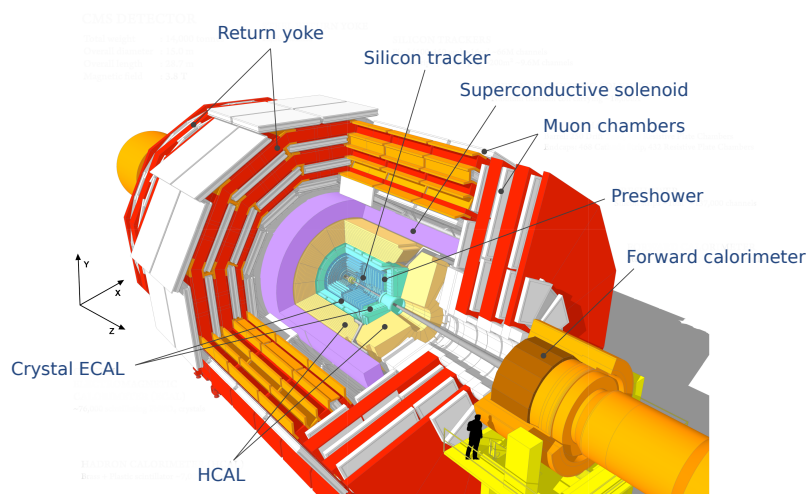


*Figure 2.22: View of the CMS apparatus and of its different components.*

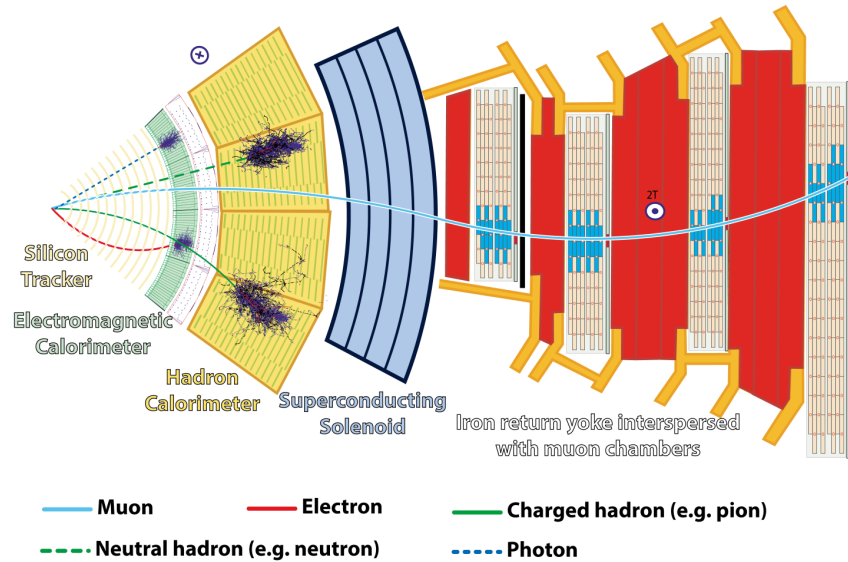


Figure 2.23: Slice showing CMS sub-detectors and how particles interact with them.

#### 1778 2.2.4.1 The silicon tracker

1779 The silicon tracker visible in  
 1780 Figure 2.24 is divided into two  
 1781 different sub-systems: the *pixel*  
 1782 *detector* at the very core and  
 1783 the *microstrip detector* around it.  
 1784 This system is composed  
 1785 of 75 million individual read-  
 1786 out channels with up to 6000  
 1787 channels per squared centime-  
 1788 ter for the pixels making it the  
 1789 world's biggest silicon detec-  
 1790 tor. This density allows for  
 1791 measurements of the particle  
 1792 tracks with a precision of the  
 1793 order of  $10\ \mu\text{m}$ . This is neces-  
 1794 sary to reconstruct all the dif-  
 1795 ferent interaction vertices with precision and have a precise measure of the curvature of the charged  
 1796 particles traveling through the magnetic field to estimate their charge and momentum.

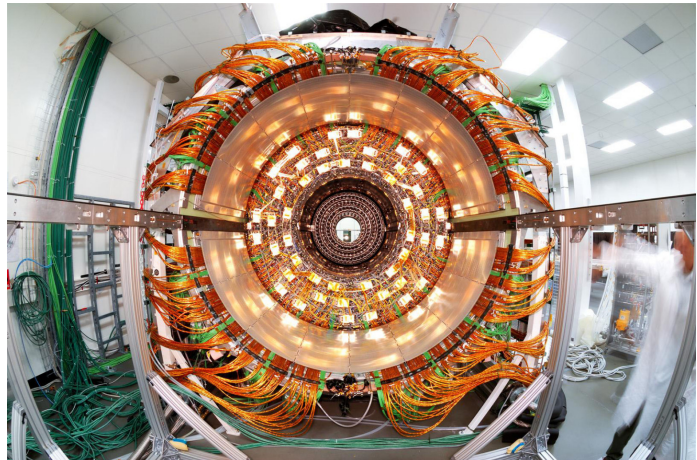
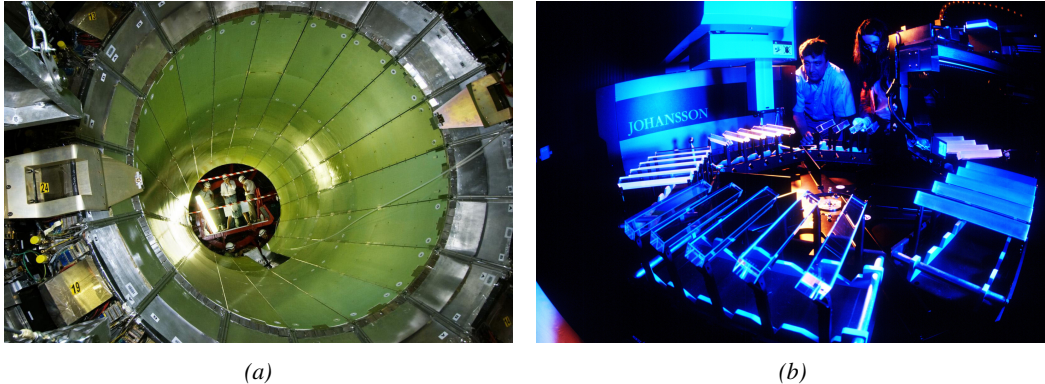


Figure 2.24: The CMS tracker.

#### 1797 2.2.4.2 The calorimeters

1798 The ECAL directly surrounding the tracker is composed of crystals of lead tungstate,  $\text{PbWO}_4$ , a  
 1799 very dense but optically transparent material used to stop high-energy electrons and photons. These  
 1800 crystal blocks basically are extremely dense scintillators which scintillate in fast, short light bursts  
 1801 proportionally to the energy deposition. The light is contained at 80% in the corresponding 25 ns

1802 lasting bunch crossing. Each crystal is isolated from the other by the carbon fiber matrix they are  
 1803 embedded in.



*Figure 2.25: (a): The electromagnetic calorimeter. (b): The lead tungstate crystals composing the ECAL.*

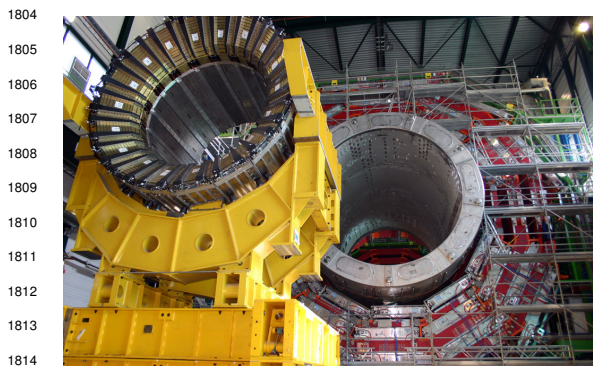


*Figure 2.26: The CMS hadron calorimeter barrel.*

1804  
 1805  
 1806  
 1807  
 1808  
 1809  
 1810  
 1811  
 1812  
 1813  
 1814  
 1815  
 1816  
 1817  
 1818  
 1819  
 1820  
 1821  
 and quartz fibers, is to precisely measure the momentum very energetic hadrons. Several layers  
 of brass or steel are interleaved with plastic scintillators readout by photodiodes using wavelength-  
 shifting fibers. The HCAL is also composed of a barrel, shown in Figure 2.26 and of endcaps. It  
 also features forward calorimeters on both sides of CMS in the region very close to the beam line at  
 high pseudorapidity ( $3.0 < |\eta| < 5.0$ ).

The ECAL is composed of a barrel containing more than 60,000 crystals and of closing endcaps containing another 15,000 crystals. In front of the ECAL endcap is installed a preshower detector made out of two layers of lead and silicon strip detectors to increase the spatial resolution close to the beam line for pion-photon and single-double photon discrimination purposes. Figure 2.25 shows the calorimeter inside of the magnet and the crystals.

The next layer is the HCAL. The role of these forward calorimeters, made using steel

#### 1822 **2.2.4.3 The muon system**

1823 Finally, in the outer region of the apparatus, a muon system is used to trigger on potentially interesting  
 1824 event by identifying muons. Three different subsystems compose the muon system as shown in  
 1825 Figure 2.27 in which a quadrant of the CMS detector focuses on muon system. Drift Tubes (DTs)  
 1826 are found in the barrel region covering the low pseudorapidity region where particles transverse  
 1827 momentum is lower and Cathode Strip Chambers (CSCs) are found in the endcap region covering  
 1828 higher pseudorapidity region closer to beam line where particles have a stronger momentum. The  
 1829 redundancy of the system is insured by Resistive Plate Chambers (RPCs) in both the barrel and end-  
 1830 cap. Nevertheless, the region closest to the beam line ( $|\eta| > 1.8$ ) was not equipped with RPCs. This  
 1831 lack of redundancy in the high pseudo rapidity region will be solved during LS2, the following Year

<sup>1832</sup> End Technical Stop (YETS) in 2021 and 2022, and LS3 where the necessary services, detectors and  
<sup>1833</sup> Link System, that collects the data and synchronizes them, will be installed.

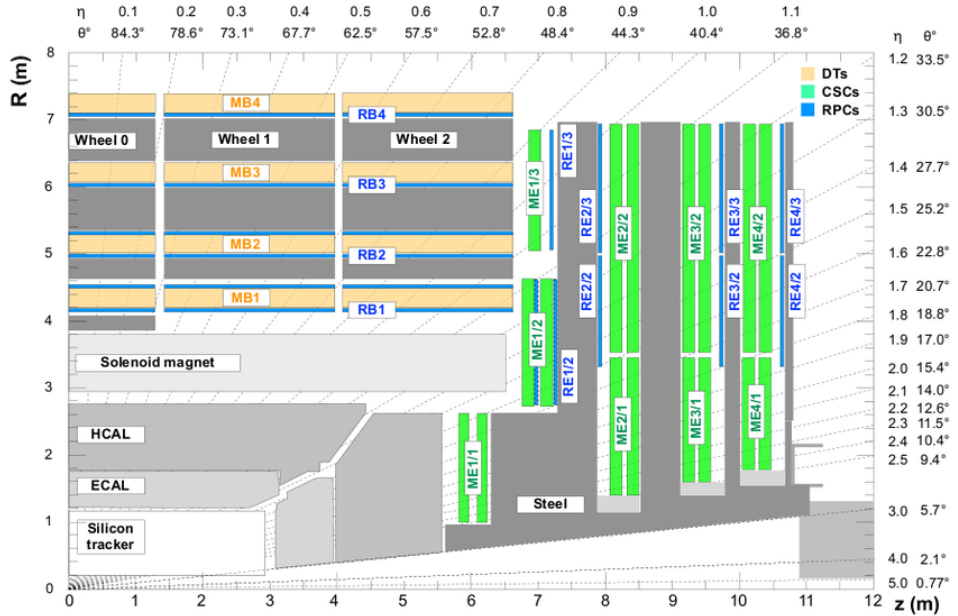


Figure 2.27: A quadrant of the muon system, showing DTs (yellow), RPCs (blue), and CSCs (green).

### <sup>1834</sup> 2.2.5 Description of the muon system

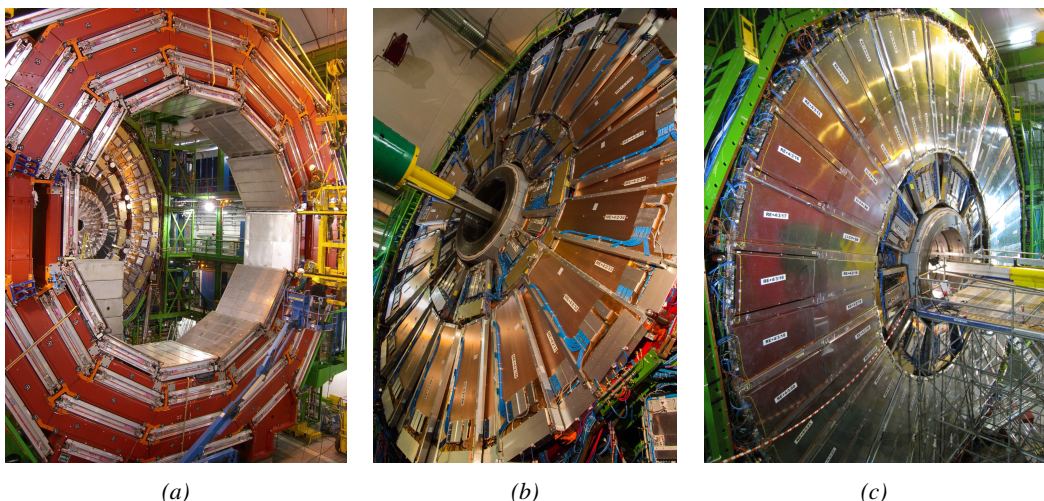


Figure 2.28: (a): Barrel wheel with its detector rings and return yokes. (b): CSC endcap disk with the two CSC stations. The outer station is made of 10 deg detectors while the inner station is made of 20 deg detectors. (c): RPC endcap disk. The inner station is not equipped, leaving the inner CSC station visible.

1835 The barrel region is divided into five *wheels* made out of four *rings* of detectors with iron return yokes  
 1836 between them. The endcaps are made out of four disks, each divided into pseudorapidity stations,  
 1837 two for CSCs (except for the first disk where three stations are equipped) and three for RPCs. Only  
 1838 two RPCs stations are equipped at present. The wheels and disks are shown in Figure 2.28. So far,  
 1839 each subsystem was dedicated to a particular task. DTs, in the barrel, and CSCs, in the endcaps, are  
 1840 used mainly for their spatial resolution. Indeed, DTs' resolution is of the order of 100  $\mu\text{m}$  along both  
 1841 the  $(r - \phi)$  and  $(r - z)$  components while the resolution of CSCs is similar but varies in a range  
 1842 from 50  $\mu\text{m}$  to 140  $\mu\text{m}$  depending on the distance to the beamline. On the other hand, RPCs are used  
 1843 as redundant detection system in the whole muon system. They display a very good intrinsic time  
 1844 resolution of 1.5 ns although the electronics only provide bunch crossing information with a time  
 1845 resolution of 25 ns.

### 1846 2.2.5.1 The Drift Tubes

1847 The 250 CMS DTs, found in the barrel covering the pseudorapidity region  $0 < |\eta| < 1.2$  and  
 1848 whose structure is shown in Figure 2.29, are composed of three *superlayers* of DT cells. Two of  
 1849 these superlayers are dedicated to measuring the  $\phi$  coordinate of the muons and while the last one  
 1850 measures the  $\eta$  (or  $z$ ) coordinate. Each superlayer consists on four layers of 60 to 70 DT cells  
 1851 arranged in quincunx to allow for a precise reconstruction of the muon path through the DT layers.  
 1852 Each DT cell is a rectangular aluminium gas volume with a central anode wire. Cathode strips are  
 1853 placed on the narrow surface of the cells and electrode strips are placed on the wide surface to help  
 1854 shaping the electric field to ensure a consistent drift velocity of electrons in the drift volume. These  
 1855 detectors are operated using a 85/15 mixture of Ar and  $\text{CO}_2$ . Outside the gas volume of each DT  
 1856 chamber is attached a Minicrate electronics (MiC) that hosts both read-out and trigger electronics.

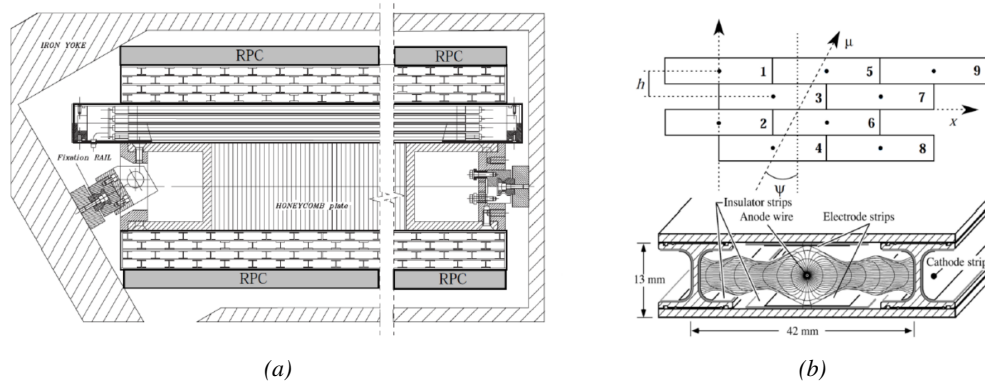


Figure 2.29: (a): Cross section of a DT module showing the two superlayers measuring the  $\phi$  coordinate, perpendicular to the cross section plane, and the superlayer measuring the  $\eta$  coordinate, placed in between the two others with a honeycomb plate and parallel to the cross section plane. The DT detector is sandwiched in between 2 RPCs whose readout strips are perpendicular to the cross section plane, measuring the  $\phi$  coordinate. (b): A DT cell is shown together with its electric field. The path of a muon through a superlayer is shown.

1857 **2.2.5.2 The Cathode Strip Chambers**

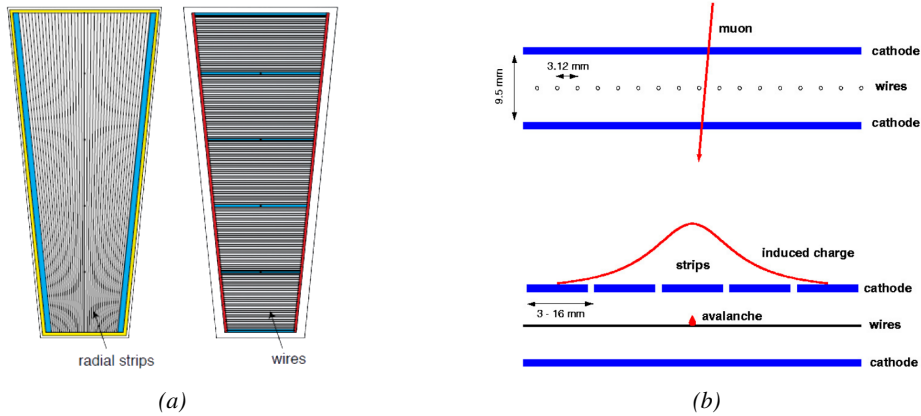


Figure 2.30: (a): Cathode strips and anode wire layout of a CSC panel. (b): Avalanche development and charge collection by anode wires and induction on cathode strips inside a CSC panel.

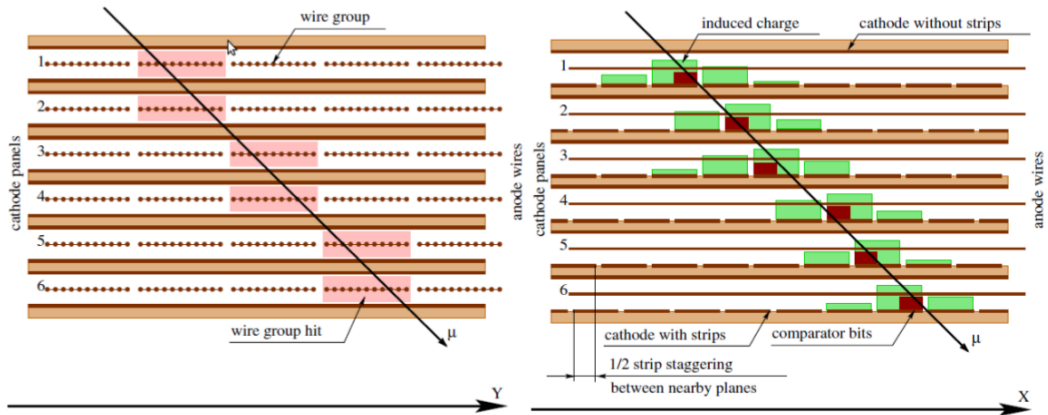


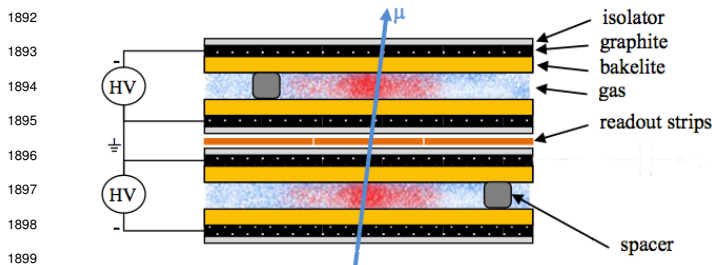
Figure 2.31: Muon track reconstruction through the six panels of a CMS CSC using the information of anode wire groups and cathode strip charge distribution combined with comparator bits to decide on which half strip the muon is more likely to have passed.

1858 The 540 CMS CSCs are found in the endcaps covering the pseudorapidity region  $0.9 < |\eta| < 2.5$   
 1859 and described through Figures 2.30 and 2.31. Each module is composed of six panels of CSC, each  
 1860 panel consisting in a wide gas volume of 9.5 mm (7 mm in the case of ME1/1 station) containing  
 1861 anode wires and whose surfaces are cathodes. The top cathode is a wide copper plane of the size of  
 1862 the gas volume. The bottom cathode is divided into thin trapezoidal copper strips radially arranged  
 1863 to measure the azimuthal coordinate  $\phi$  with a pitch ranging from 8 to 16 mm. The  $0.50 \mu\text{m}$  anode  
 1864 wires are placed perpendicularly to the strips to measure radial coordinate  $r$  and are grouped by  
 1865 ten to fifteen with a wire to wire space of 3.2 mm. In the specific case of ME1/1 placed against  
 1866 the HCAL endcap, the  $0.30 \mu\text{m}$  anode wires have a wire to wire distance of 2.5 mm and are not  
 1867 disposed perpendicularly to the strips but slightly tilted by an angle of 29 deg to compensate for the

1868 lorentz force due to the very strong local magnetic field of 4 T. These detectors are operated with a  
 1869 40/50/10 mixture of Ar, CO<sub>2</sub> and CF<sub>4</sub>. Combining the information of the multiple CSC panels, the  
 1870 detectors achieve a very precise measurement of the muon track. The read-out of the cathode strip  
 1871 signals is performed by cathode front-end boards (CFEBs) mounted on the detectors. The boards  
 1872 are used to collect and digitize the charge of the signals and transfer it to off-chamber electronics  
 1873 called Data acquisition mother boards (DMBs). In parallel, the data from the CFEBs together with  
 1874 the data from the anode wires, after treatment by on-chamber electronics called Anode local charged  
 1875 track boards (ALCTs), is used to build a fast trigger information which is sent other off-chamber  
 1876 electronics called Trigger mother boards (TMBs).

### 1877 2.2.5.3 The Resistive Plate Chambers

1878 Despite their excellent spatial resolution, the wire chambers (DTs and CSCs) are limited in terms  
 1879 of time resolution by the fact that the charge needs to drift towards the anode wire and be collected  
 1880 before having the confirmation that a particle was detected as the drift volume is not used to develop  
 1881 avalanches. Indeed, the stronger electric field close to the anode wire triggers the avalanche and the  
 1882 gain of the detector. Due to the drift, the time resolution is thus limited at best to approximately 2 to  
 1883 3 ns. In addition, even though the intrinsic time resolution of the tracking chambers is rather good  
 1884 compared to the 25 ns in between successive collisions, the processing time of the trigger system  
 1885 doesn't allow for very fast triggering as it provides a time precision of only 12.5 ns. Thus, detectors  
 1886 fully dedicated to timing measurement have been installed as a redundant system. These detectors  
 1887 are RPCs, also gaseous detectors but that use current induction instead of charge collection allowing  
 1888 for a time resolution of the order of 1 ns only. Theoretically, depending on the design used, RPCs  
 1889 could reach a time resolution of the order of 10 ps but in the context of LHC where bunch crossing  
 1890 happen every 25 ns, a time resolution of 1 ns is sufficient to accurately assign the right bunch crossing  
 1891 to each detected muon.



1900 *Figure 2.32: Double-gap layout of CMS RPCs. Muons passing through*  
 1901 *the gas volumes will create electron-ions pairs by ionising the gas. This*  
 1902 *ionisation will immediately translate into a developing avalanche.*

1903 mixture of C<sub>2</sub>H<sub>2</sub>F<sub>4</sub>, i – C<sub>4</sub>H<sub>10</sub> and SF<sub>6</sub>. Due to this geometry, the electric field inside of a  
 1904 gap is homogeneous and linear at every point in the gas translating into a uniform development of  
 1905 avalanches in the gas volume as soon as a passing muon ionises the gas. The two gaps sandwich a  
 1906 readout copper strip plane. A negative voltage is applied on the outer electrodes, used as cathodes,  
 1907 and the inner electrodes, the anodes, are simply connected to the ground as well as the readout panel  
 1908 that picks up the current induced by the accumulated charge of the growing avalanches in one or  
 1909 both of the gas gaps. This OR system allows for a lower gain (i.e. a lower electric field) on both  
 1910 gaps to reach the maximal efficiency of such a detector.

The 1056 RPCs equip the CMS muon system both in the barrel and endcap regions and cover the pseudorapidity region  $0 < |\eta| < 1.6$ . They are composed of two layers of RPC gaps as described in Figure 2.32. Each gap consists in two resistive electrodes made out of 2 mm thick Bakelite enclosing a 2 mm thick gas volume containing a 95.2/4.5/0.3

In the barrel, each layer of RPCs is made out of twelve *sectors* for a full  $2\pi$  coverage. A wheel consists in four detector *stations* corresponding to a same radius  $R$  around the beam line as can be seen in Figure 2.33. Both the two first stations are equiped with two RPC layers, one on each side of a DT module. On the other stations, further away to the beam line, a single layer of two RPCs placed side by side is installed along each DT chamber with some exceptions for the fourth station. The barrel RPCs are labeled "RB $n \pm w$ ", where  $n$  is the station number increasing with  $R$  and  $\pm w$  is the wheel number ( $w = 0$  corresponds to the central wheel). On each layers, the RPCs are distinguished thanks to extra "in" and "out" (stations 1 and 2) or "-" and "+" (stations 3 and 4). In the endcap, the detectors are mounted on the disks on three *rings*, two of which are equiped with RPCs, that can also be referred to as *stations*. A view of an RPC endcap disk can be seen in Figure 2.34. Contrary to the barrel stations, the endcap stations correspond to detectors mounted at a similar  $z$  value. Indeed, in this case the detectors are orthogonal to the beam line. Each ring covers a different  $R$  range and is composed of 36 trapezoidal detectors. The endcap RPCs are labeled "RE $\pm n/r$ ", where  $n$  is the station number, i.e. the endcap disk, and  $r$  is the ring number increasing with  $R$ . Finally, the RPC read-out is segmented along the  $z$ -coordinate in the barrel and along the  $R$ -coordinate in the endcap. This segmentation aims at dividing the read-out into several pseudo-rapidity ranges for particle assignment. At the level of a single chamber, the pseudo-rapidity segmentation is referred to as *partition*. At the level of the full system, the read-out segments corresponding to the same pseudo-rapidity range are called *rolls*. In the barrel, the read-out is divided along  $z$  into two partitions except for some RB2 detectors that have three partitions. In the endcap, all the current detectors feature three partitions along  $R$ .

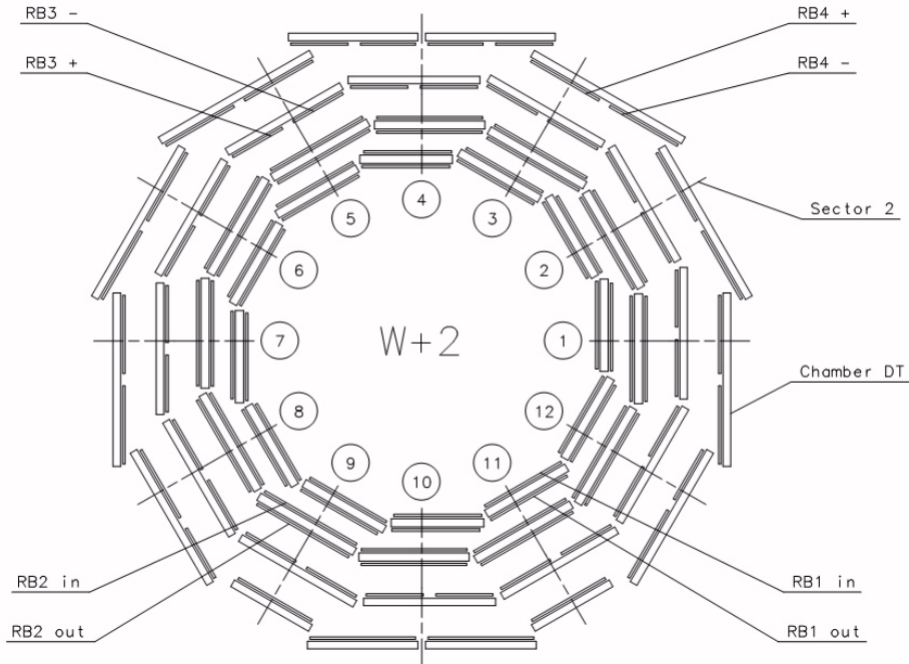


Figure 2.33: View of the positions of DT and RPC detectors in barrel Wheel W+2.

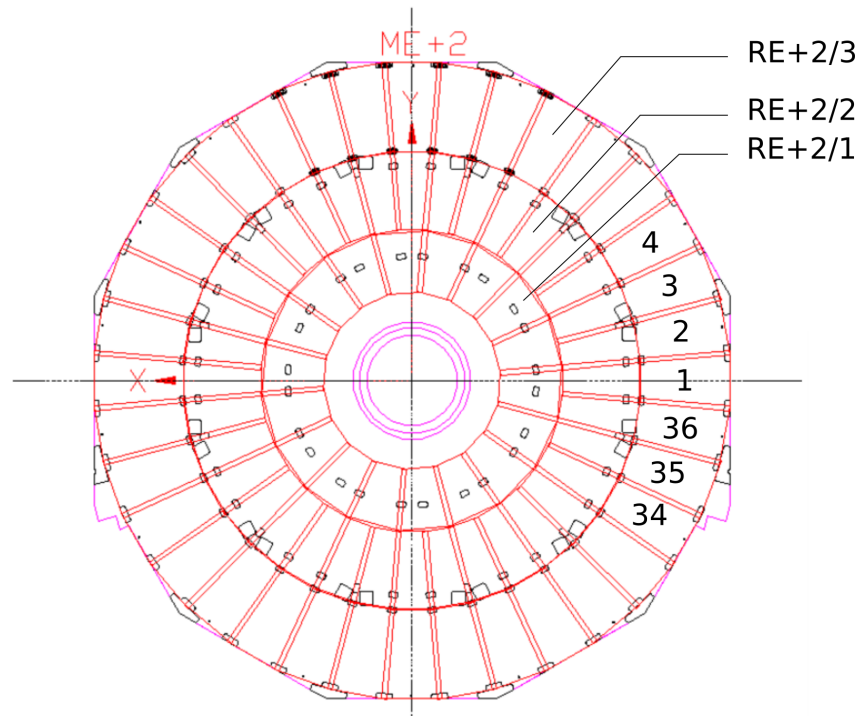


Figure 2.34: View of the positions of RPC detectors in endcap Disk +2. The first ring corresponding to RE+2/1 is not equipped with RPC detectors.

# 3

1934

1935

## Physics of Resistive plate chambers

1936 The Resistive Plate Chamber (RPC) has been developed in 1981 by Santonico and Cardarelli [178],  
1937 under the name of *Resistive Plate Counter*, as an alternative to the local-discharge spark counters  
1938 proposed in 1978 by Pestov and Fedotovich [179, 180]. Working with spark chambers implied using  
1939 high-pressure gas and high mechanical precision which the RPC simplified by formerly using a gas  
1940 mixture of argon and butane at atmospheric pressure and a constant and uniform electric field gener-  
1941 ated in between two parallel electrode plates. Moreover, a significant increase in rate capability was  
1942 introduced by the use of electrode plate material with high bulk resistivity, preventing the discharge  
1943 from growing throughout the whole gas gap. Indeed, the effect of using resistive electrodes is that  
1944 the constant electric field is locally canceled out by the development of the discharge, limiting its  
1945 growth.

1946 Through its development history, different operating modes [181–183], gas mixtures [178, 183–  
1947 188] and new detector designs [189–191] have been discovered, leading to further improvement  
1948 of the rate capability of such a detector. The low construction costs and easily achievable large  
1949 detection areas offered by RPCs, as well as the wide range of possible designs, made them a natural  
1950 choice as muon chambers and/or trigger detectors in multipurpose experiments such as CMS [192]  
1951 or ATLAS [193], time-of-flight detectors in ALICE [194], calorimeters with CALICE [195] or even  
1952 detectors for volcanic muography with ToMuVol [196].

1953 In this chapter, the general operating principles of RPCs will be introduced leading to a deeper  
1954 description of the parameters having an influence on the rate capability and the time resolution such  
1955 detectors. Even though the principle behind the operation of RPCs might seem straight forward,  
1956 attempts at proposing a model of the signal formation inside of the gas volume have so far failed at  
1957 fully explain what can be observed from the data. A detailed summary of the understanding of RPC  
1958 physics will be provided. Finally, more practical information will be given on the influence of the  
1959 environment on the operation of a real detector. The changing conditions might alter the collected  
1960 data and needs to be addressed in order to limit the systematics on the final results.

1961 **3.1 Principle**

1962 RPCs are proportional counters composed of two parallel resistive plate electrodes in between which  
1963 a constant electric field is set. The space in between the electrodes, referred to as *gap*, is filled with  
1964 a gas that is used to generate primary ionization into the gas volume. The free charge carriers (elec-  
1965 trons and cations) created by the ionization of the gas molecules are then accelerated towards the  
1966 electrodes by the electric field, as shown in Figure 3.1 [197]. Since RPCs are passive detectors, a  
1967 current on copper pick-up strips or pads placed outside of the gas volume is induced by the charge  
1968 accumulation during the growth of the avalanche resulting from the acceleration of the charge car-  
1969 riers. As a consequence, the time resolution of the detector is substantially increased compared to  
1970 detectors using charge collection at the level of the electrode as the output signal is generated by  
1971 the movement of the electrons in the electric field. The advantage of a constant electric field, over  
1972 multi-wire proportional chambers, is that the electrons are being fully accelerated from the moment  
1973 charge carriers are freed. They feel the full strength of the electric field that doesn't depend on the  
1974 distance to the readout.

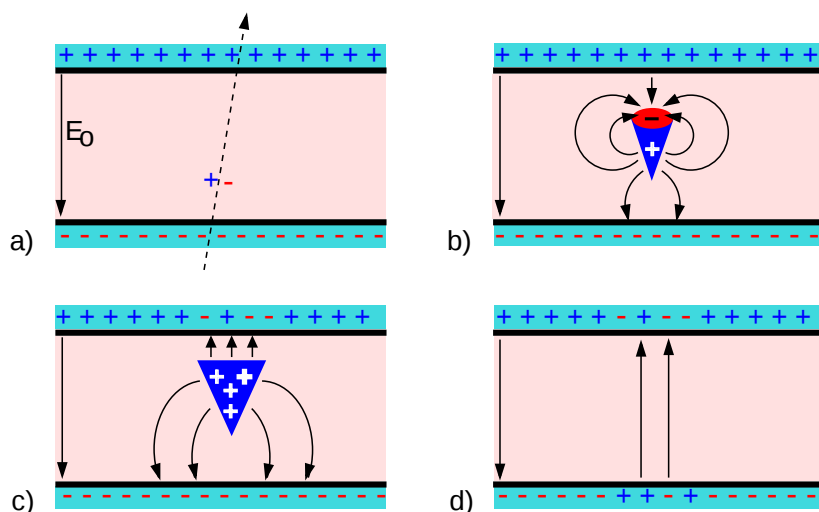


*Figure 3.1: Different phases of the avalanche development in the RPC gas volume subjected to a constant electric field  $E_0$ . a) An avalanche is initiated by the primary ionisation caused by the passage of a charged particle through the gas volume. b) Due to its growing size, the avalanche starts to locally influence the electric field. c) The electrons, lighter than the cations reach the anode first. d) The ions reach the cathode. While the charges have not recombined, the electric field in the small region around the avalanche stays affected and locally blinds the detector.*

1975 After an avalanche developed in the gas, a time long compared to the development of a discharge  
1976 is needed to recombine the charge carriers in the electrode material due to its resistivity. This prop-  
1977 erty has the advantage of affecting the local electric field only, and avoiding sparks in the detector  
1978 but, on the other hand, the rate capability is intrinsically limited by the time constant  $\tau_{RPC}$  of the  
1979 detector. Using a quasi-static approximation of Maxwell's equations for weakly conducting media,  
1980 it can be shown that the time constant  $\tau_{RPC}$  related to the charge recombination at the interface in

<sup>1981</sup> between the electrode and the gas volume is given by Equation 3.1 [198].

$$(3.1) \quad \tau_{RPC} = \frac{\epsilon_{electrode} + \epsilon_{gas}}{\sigma_{electrode} + \sigma_{gas}}$$

<sup>1982</sup> A gas can be assimilated to vacuum, leading to  $\epsilon_{gas} = \epsilon_0$  and  $\sigma_{gas} = 0$ , and the electrodes  
<sup>1983</sup> permittivity and conductivity can be written as  $\epsilon_{electrode} = \epsilon_r \epsilon_0$  and  $\sigma_{electrode} = 1/\rho_{electrode}$ ,  
<sup>1984</sup> showing the strong dependence of the time constant on the electrodes resistivity in Formula 3.2.

$$(3.2) \quad \tau_{RPC} = (\epsilon_r + 1)\epsilon_0 \times \rho_{electrode}$$

<sup>1985</sup> The resistivity targeted to build RPCs ranges from  $10^9$  to  $10^{12} \Omega \cdot \text{cm}$ . Very few materials with  
<sup>1986</sup> a low enough resistivity exist in nature. The most common RPC electrode materials are displayed in  
<sup>1987</sup> Table 3.1. When the doped glass and ceramics can offer short time constants of the order of 1 ms,  
<sup>1988</sup> the developing cost of such materials is quite high due to the very low demand. Thus, High-Pressure  
<sup>1989</sup> Laminate (HPL) is often the choice for high-rate experiments using very large RPC detection areas.  
<sup>1990</sup> To be effectively used, the surface of HPL electrodes requires a linseed oil treatment which allows  
<sup>1991</sup> for a lower intrinsic noise rate and dark current of the detectors by improving the smoothness of the  
<sup>1992</sup> electrodes surface [199]. Other experiments working at cosmic muon fluxes can safely operate with  
<sup>1993</sup> ordinary float glass.

Material	$\rho_{electrode} (\Omega \cdot \text{cm})$	$\epsilon_r$	$\tau_{RPC} (\text{ms})$
Float glass	$10^{12}$	~7	~700
High-Pressure Laminate	$10^{10}$ to $10^{12}$	~6	~6 to 600
Doped glass (LR S)	$10^9$ to $10^{11}$	~10	~1 to 100
Doped ceramics (SiN/SiC)	$10^9$	~8.5	~1
Doped ceramics (Ferrite)	$10^8$ to $10^{12}$	~20	~0.2 to 2000

*Table 3.1: Properties of the most used electrode materials for RPCs.*

## <sup>1994</sup> 3.2 Rate capability and time resolution of Resistive Plate Chambers

<sup>1996</sup> The electrode material plays a key role in the maximum intrinsic rate capability of RPCs. R&D is  
<sup>1997</sup> continuously being done to develop at always cheaper costs material with lower resistivity. Never-  
<sup>1998</sup> theless, the amount of charge released, i.e. the size of the discharge, if reduced leads to a smaller  
<sup>1999</sup> blind area in the detector, increasing the rate capability of the detector. On the other hand, the drift  
<sup>2000</sup> velocity of electrons in the gas volume being quite stable with the applied electric field, the design of  
<sup>2001</sup> a detector and the associated read-out and pulse-processing electronics will be a major component  
<sup>2002</sup> of the time resolution of RPCs. Moreover, the sensitivity of the electronics will also help increasing  
<sup>2003</sup> the rate capability. An improved sensitivity will allow for a lower gain to operate the detector. This  
<sup>2004</sup> will result in a more spatially contained signal development.

### <sup>2005</sup> 3.2.1 Operation modes

<sup>2006</sup> Being a gaseous detector using an accelerating electric field to amplify the signal of primary charge  
<sup>2007</sup> carriers, the RPC can be operated in different modes depending on the electric field intensity. Each

mode offers different performances for such a detector, and it will be showed that the operating mode corresponding to the lowest electric field possible is best suited for high-rate detectors working in collider experiments.

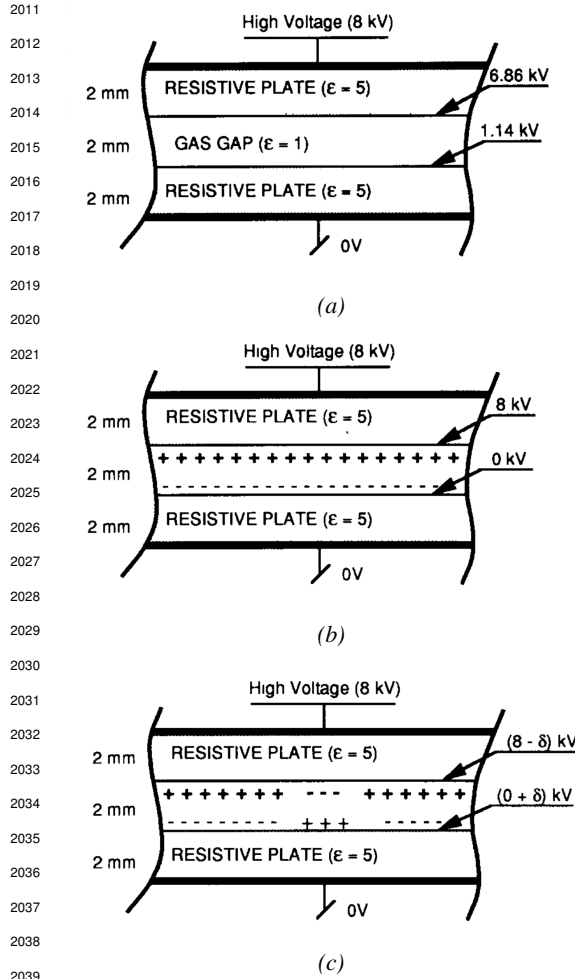


Figure 3.2: Movement of the charge carriers in an RPC. (a): Voltage across an RPC whose electrodes have a relative permittivity of 5 at the moment the tension is applied. (b): After the charge carriers moved, the electrodes are charged and there is no voltage drop over the electrodes anymore. The full potential is applied over the gas gap only. (c): The streamer discharge initiated by a charged particle transports electrons and cations towards the anode and cathode respectively.

ode and the positive ion cloud remains much smaller. The field emission of electrons on the cathode is possible. The resulting signal is weaker, of the order of a few mV as shown on Figure 3.3, and requires amplification. This is the *avalanche mode* of RPC operation. This mode offers a higher rate capability by providing smaller discharges that don't affect the electrodes charge and are more locally contained in the gas volume as was demonstrated by Crotty with Figure 3.4 [181]. The detector only stays locally blind the time the charge carriers

RPCs were developed early 1980s. At that time they were used in an operating mode now referred to as *streamer mode*. Streamers are large discharges that develop in between the two electrodes far enough to locally discharge the electrodes. If the electric field inside of the gas volume is strong enough, a large and dense cloud of positive ions will develop near the anode and extend toward the cathode. Indeed, the electrons traveling faster will be collected leaving the gas region near the anode filled with positively charged ions. The field is then strong enough so that electrons are pulled out of the cathode leading to a streamer discharge. Electrodes, though they are a unique volume of resistive material, can be assimilated to capacitors. At the moment an electric field is applied between their outer surfaces, the charge carriers inside of the volume will start moving leading to a situation where there is no potential difference across the electrodes and a higher density of negative charges, i.e. electrons, on the inner surface of the cathode. Finally, when a streamer discharge occurs, these electrons are partially released in the gas volume contributing to increase the discharge strength until the formation of a conductive plasma, the streamer. This can be understood through Figure 3.2 [181]. Streamer signals are very convenient in terms of read-out as no further amplification is required with output pulses amplitudes of the order of a few tens to few hundreds of mV as can be seen on Figure 3.3.

In contrast to the above, when the electric field is lowered, the electronic gain is reduced until the electrons get close enough to the anode. The electric field doesn't reach the point where a field emission of electrons on the cathode is possible. The resulting signal is weaker, of the order of a few mV as shown on Figure 3.3, and requires amplification. This is the *avalanche mode* of RPC operation. This mode offers a higher rate capability by providing smaller discharges that don't affect the electrodes charge and are more locally contained in the gas volume as was demonstrated by Crotty with Figure 3.4 [181]. The detector only stays locally blind the time the charge carriers

are recombined and there is no need for electrode recharge which is a long process affecting a large portion of the detector. Another advantage of avalanche signals over streamers is the better time consistency. Figure 3.3 shows very clearly that avalanche signals have a very small time jitter. Using such a mode is a natural choice for experiments in which the detectors are required to have a high detection rate.

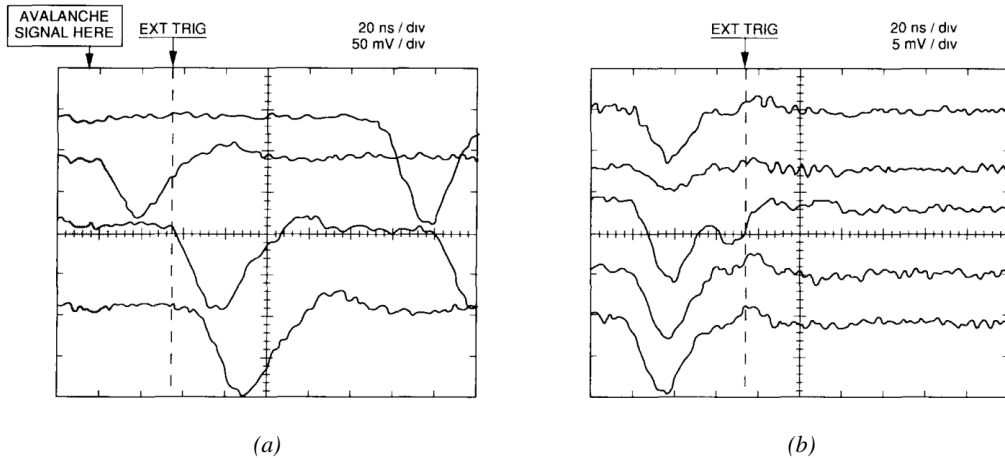


Figure 3.3: Typical oscilloscope pulses in streamer mode (a) and avalanche mode (b). In the case of streamer mode, the very small avalanche signal is visible.

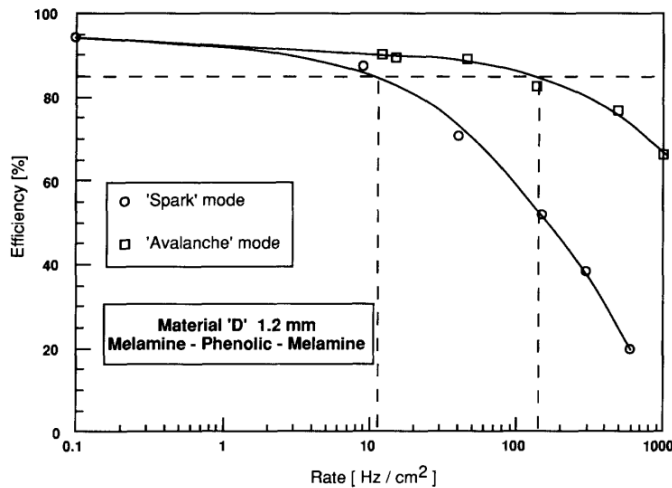
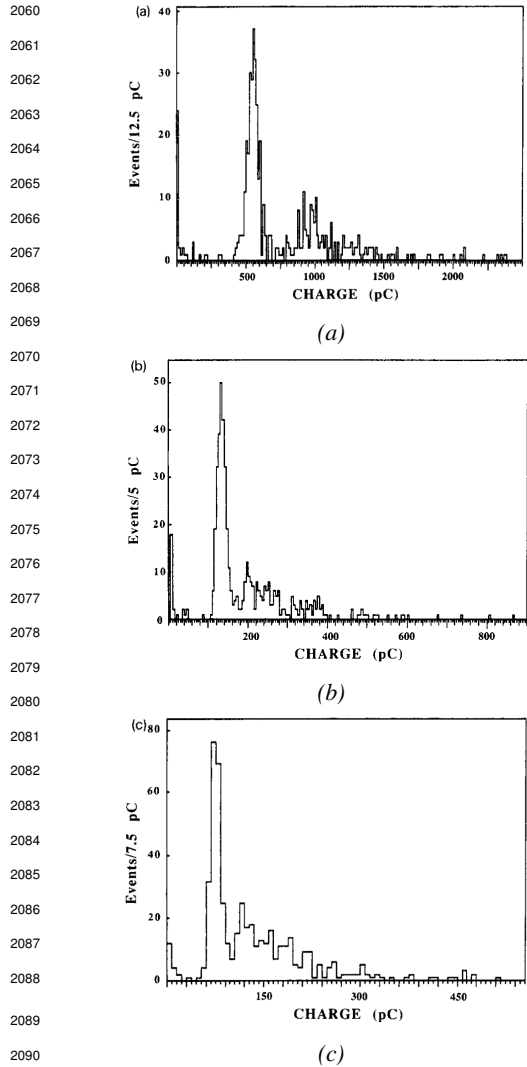


Figure 3.4: Rate capability comparison for the streamer and avalanche mode of operation. An order of magnitude in rate capability for a maximal efficiency drop of 10% is gained by using the avalanche mode over the streamer mode.

### 2059 3.2.2 Standard gas mixture for RPCs operated in collider experiments



2091 *Figure 3.5: Comparison of the charge distribution of  
2092 signals induced by cosmic muons in an RPC operated  
2093 with a gas mixture of argon, butane and bromotrifluo-  
2094 romethane ( $CF_3Br$ ). The  $Ar/C_4H_{10}$  is kept constant  
2095 at 60/40 in volume while the total amount of  $CF_3Br$  in  
2096 the mixture is varied: 0% (a), 4% (b) and 8% (c) [184].  
2097 The differences between narrow and wide gaps will be later discussed in Section 3.2.3. With  $CF_3Br$  having  
2098 a high GWP,  $C_2H_2F_4$  was preferred over it as it was considered a more suitable ecofriendly gas in  
2099 the middle of the 90s. An advantage of this new Freon component is that it features a high primary  
2100 ionization and a low operating voltage, as reported by Cardarelli et al. [183]. Thus, the new gas  
2101 mixtures used were mainly composed of  $C_2H_2F_4$  alone with lower content of i- $C_4H_{10}$  in order  
2102 to reduce the flammability of the mixtures for safety reasons. Performance and models about such  
2103 mixtures were discussed in papers of Abbrescia et al. [185, 186] and showed a better suitability of*

The first RPC working in streamer mode was operated with a 50/50 mixture of argon and butane [178], a standard mixture used at that time in multi-wire proportional chambers. This mixture takes profit of the good effective Townsend coefficient of argon to maximize the number of primary charge carriers freed in the gas by ionizing particles and of the quenching properties of butane. The Townsend coefficient of a gas tells about the multiplication and attachment of primary ionization electrons and will be discussed in Section 3.3.3. Before the discovery of the avalanche mode of RPC operation, the rate capability of RPCs operated in streamer mode was a concern. A possible performance improvement of the detectors could be achieved through the increase of fast charge ratio in the signal development, decreasing the charge induced per avalanche. As it can be seen through Figure 3.5, this effect was studied by adding fractions of Freon-based quenchers, such as  $CF_3Br$ , into the typical  $Ar/C_4H_{10}$  gas mixture and showed that a lower induced charge could lead to an improvement the rate capability [184]. This consideration led to the discovery of the avalanche mode which confirmed that the smaller the induced charge, the better the rate capability of the RPCs [181].

From this moment onward, more and more studies were conducted in order to find a gas mixture that would allow for the best suppression of streamers for the benefit of low charge avalanches. Most R&D groups working with narrow gaps started using Freon-based gas mixtures while users of wide gap RPCs kept using  $Ar/CO_2$  based mixtures. The differences between narrow and wide gaps will be later discussed in Section 3.2.3. With  $CF_3Br$  having a high GWP,  $C_2H_2F_4$  was preferred over it as it was considered a more suitable ecofriendly gas in the middle of the 90s. An advantage of this new Freon component is that it features a high primary ionization and a low operating voltage, as reported by Cardarelli et al. [183]. Thus, the new gas mixtures used were mainly composed of  $C_2H_2F_4$  alone with lower content of i- $C_4H_{10}$  in order to reduce the flammability of the mixtures for safety reasons. Performance and models about such mixtures were discussed in papers of Abbrescia et al. [185, 186] and showed a better suitability of

such a gas mixture with respect to Argon-based ones for operations with high radiation backgrounds requiring high-rate capable detectors, as can be seen from Figures 3.6 and 3.7. Indeed, although the operating voltage of a Freon-based mixture is higher than that of an Argon-based mixture, the efficiency under irradiation is more stable, the voltage range with negligible streamer probability is much wider, and the fast charge ratio available is much greater, providing with more stable operation of the detector.

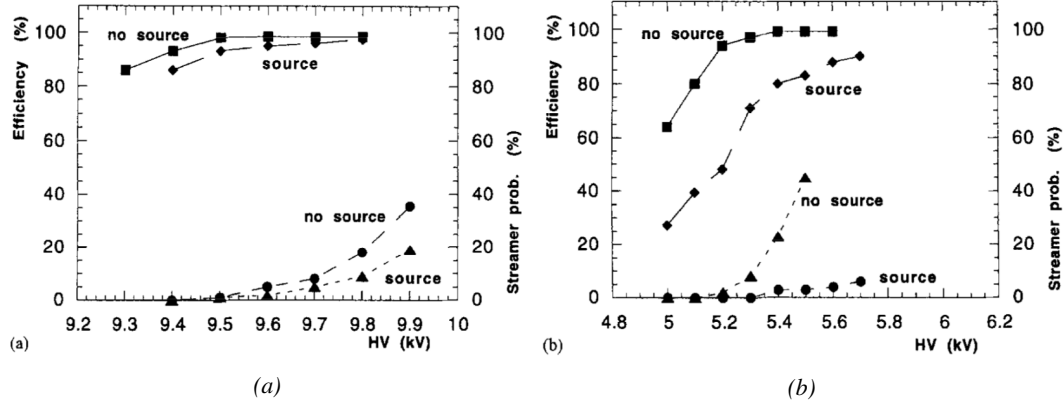


Figure 3.6: Comparison of the efficiency and streamer probability, defined as the fraction of events with an induced charge 10 times larger than that of the average avalanche, with and without irradiation by a 24 GBq  $^{137}\text{Cs}$  source of an RPC successively operated with a 90/10 mixture  $\text{C}_2\text{H}_2\text{F}_4/\text{i-C}_4\text{H}_{10}$  (a) and a 70/5/10/15 mixture of  $\text{Ar}/\text{i-C}_4\text{H}_{10}/\text{CO}_2/\text{C}_2\text{H}_2\text{F}_4$  (b) [185].

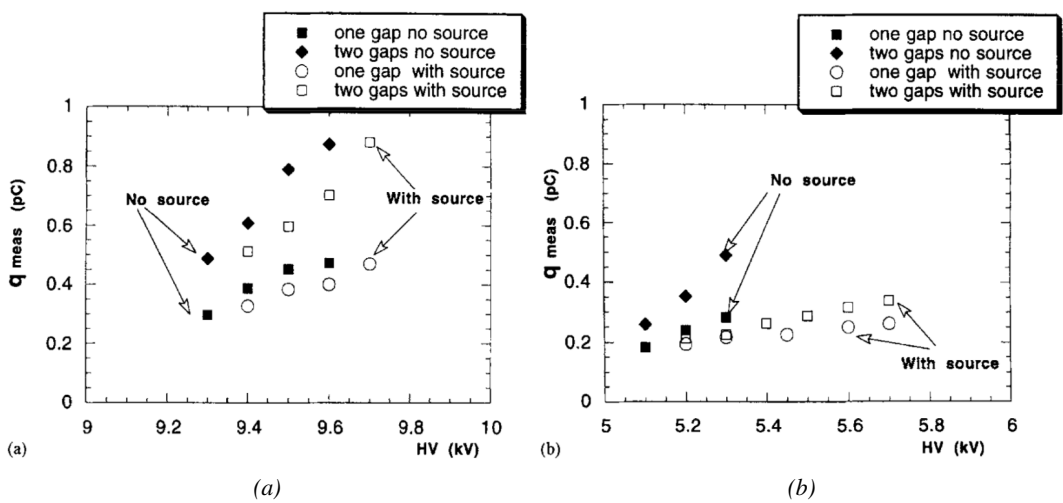


Figure 3.7: Comparison of the fast charge ratio with and without irradiation by a 24 GBq  $^{137}\text{Cs}$  source of an RPC successively operated with a 90/10 mixture  $\text{C}_2\text{H}_2\text{F}_4/\text{i-C}_4\text{H}_{10}$  (a) and a 70/5/10/15 mixture of  $\text{Ar}/\text{i-C}_4\text{H}_{10}/\text{CO}_2/\text{C}_2\text{H}_2\text{F}_4$  (b). The results are provided for both single-gap and double-gap operation [185].

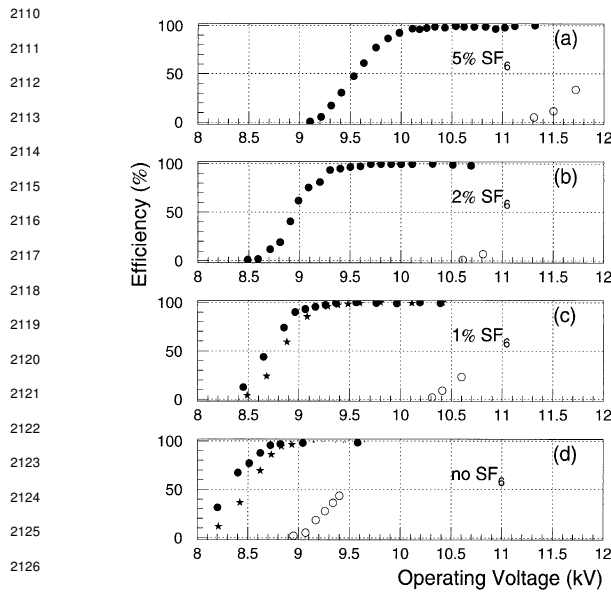


Figure 3.8: Efficiency (circles and stars with 30 mV and 100 mV thresholds respectively) and streamer probability (opened circles) as function of the operating voltage of a 2 mm single-gap HPL RPC flushed with a gas mixture containing (a) 5%, (b) 2%, (c) 1% and (d) no SF<sub>6</sub> [187].

It was later found that the streamers could be further suppressed by adding an electronegative compound into the gas mixture. The benefits of adding SF<sub>6</sub> in order to push the transitions from avalanche to streamers towards high voltages has been discussed in 1998 [187, 188]. Eventually, the high-rate RPC destined to be used in accelerator-based experiments would unanimously start using this compound into their gas mixtures. Being able to control the creation of streamers allows for slower ageing of the detector and lower power consumption as the currents going through the electrodes following the induced charges are smaller. Research is being conducted into new more ecofriendly gas mixture using gases with a much lower Global Warming

Potential. Nonetheless, the typical gas mixture with which RPCs are operated is generally composed of the following 3 gas compounds:

- Tetrafluoroethane (C<sub>2</sub>F<sub>4</sub>H<sub>2</sub>), also referred to as *Freon* or R134a, is the principal compound of the RPC gas mixtures, with a typical fraction above 90%. It is used for its high effective Townsend coefficient and the large average fast charge that allows to operate the detector with a high threshold compared to Argon, for example, that has a similar effective Townsend coefficient but suffers from a lower fast charge. To operate with similar conditions, argon would require a higher electric field leading to a higher fraction of streamers, thus limiting the rate capability of the detector [185, 186].
- Isobutane (i-C<sub>4</sub>H<sub>10</sub>), only present in a few percent in the gas mixtures, is used for its UV quenching properties [200] helping to prevent streamers due to UV photon emission during the avalanche growth.
- Sulfur hexafluoride (SF<sub>6</sub>), is used in very little quantities for its high electronegativity. Any excess of electrons is absorbed by the compound, and streamers are suppressed [187, 188]. Nevertheless, a fraction of SF<sub>6</sub> higher than 1% will not bring any extra benefice in terms of streamer cancelation power but will lead to higher operating voltage [187], as can be understood from Figure 3.8.

Nevertheless, the European Commission adopted a new "F-gas regulation" in 2014 [201] with the goal to strongly control and reduce the use of fluorinated gases with high Global Warming Potential (GWP). As potential replacement for tetrafluoroethane was proposed the trifluoriodomethane

( $CF_3I$ ), a molecule with similar properties than  $CF_3Br$  which was replaced by the tetrafluoroethane, and the 1,3,3,3-tetrafluoropropene ( $C_3H_2F_4$  or HFO-1234re), a molecule with similar properties than the actual tetrafluoroethane and proposed as a replacement in refrigerating and air conditioning systems [202]. These two gases have stronger quenching properties than  $C_2H_2F_4$  which means a much stronger electric field needs to be applied on the parallel electrodes of the RPCs in order to reach full efficiency. But the power supply system of most experiments involving RPCs would not be adapted to such high voltages. But a reduction of the working voltage can be achieved by mixing the potential replacements together with  $CO_2$  [177, 203]. Introducing carbon dioxide into the mixture while keeping similar levels of isobutane and  $SF_6$  increases the streamer probability and the best candidate identified for a compromise in between low enough working voltage and acceptable levels of streamers corresponds to a mixture containing 50% of HFO, 4.5% of  $iC_4H_{10}$ , 0.3% of  $SF_6$  and 45.2% of  $CO_2$  but is not yet considered satisfactory. On the other hand, no good replacement for  $SF_6$  has yet been identified. With its very high Global Warming Potential (23900), even small fractions of this gas in the mixture substantially increase the danger for the environment. Although finding a replacement for this gas is less critical than for the tetrafluoroethane composing more than 90% of usual RPC standard mixtures, the problem will need to be addressed.

### 3.2.3 Detector designs and performance

Different RPC designs have been used, each of them presenting its own advantages. Historically, the first type of RPC that was developed is what is now referred to as *narrow gap* RPC [178, 204].

After the avalanche mode was discovered [181], it has been shown that increasing the width of the gas gap leads to higher rate capability, due to lower charge deposition per avalanche, and lower power dissipation [204], as is shown in Figures 3.9 and 3.10. With the distance in between the electrode being larger, a weaker electric field can be applied, and a lower gain is used as a longer gas volume will contribute to the signal induction on the read-out circuit. Nevertheless, by increasing the gas gap width, the time resolution of the detector decreases. This is a natural result if the increase of active gas volume in the detector is taken into account. Indeed, for a given detection threshold on the induced charge per signal, only the small fraction of gas closest to the cathode will provide enough gain to have a detectable signal. In the case of a wider gas volume, the active region is then larger and a larger time jitter is introduced with the variation of starting position of the avalanche, as discussed in [189] and shown in Figure 3.11.

To improve both the time resolution and the rate capability, different methods were used starting from the middle of the 90s, trying to take advantage of both narrow and wide gap RPCs into a single design. Double-gap RPCs combine two narrow gaps into a single detector to increase the effective sensitive volume. Multigap RPCs in which the large volume a wide gap RPC is divided into thinner

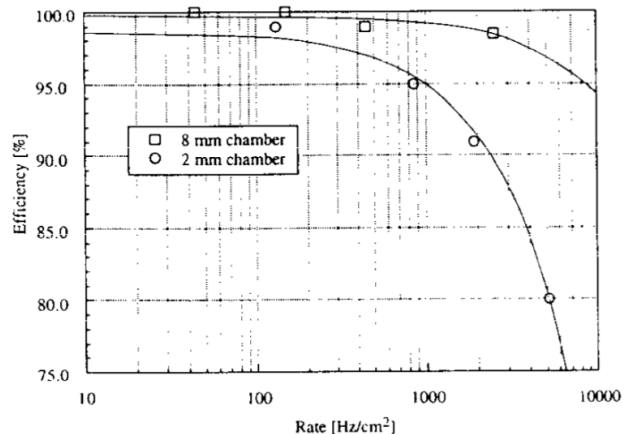
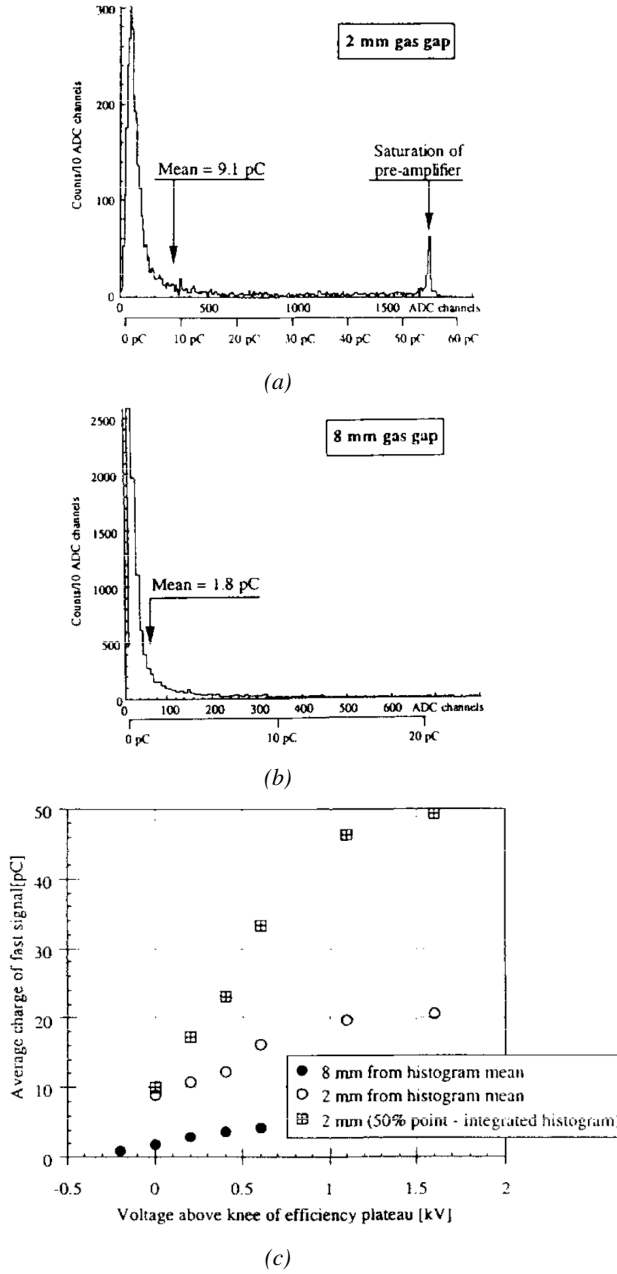
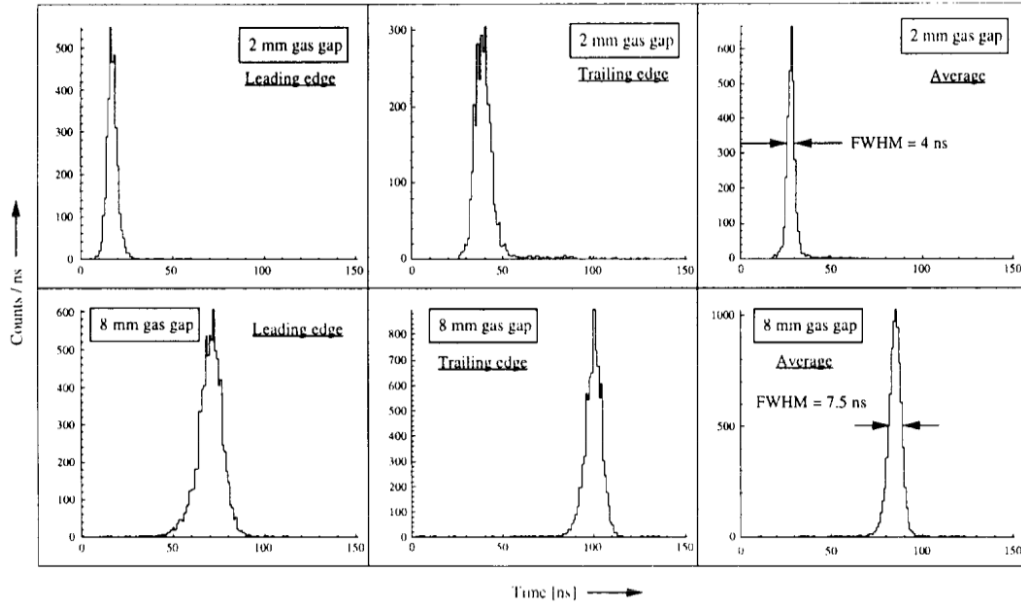


Figure 3.9: Comparison of the rate capability of 8 mm and 2 mm wide RPCs. The lines are linear fits on the data [204].

2197 sub-gaps by adding intermediate electrodes in between the cathode and anode, were developed to  
2198 improve the time resolution by mimicking narrow gap RPCs.



*Figure 3.10: Distributions of the induced charge of fast signals on 2 mm (a) and 8 mm (b) RPCs exposed to a radiation rate of  $100 \text{ Hz/cm}^2$ . Average induced charge of fast signals as a function of the high voltage applied on 2 mm and 8 mm RPCs (c). In the case of the 2 mm RPC, a saturation of the pre-amplifier was observed. The average of the distribution is underestimated, and the median is shown together with the average to account for this bias [204].*



*Figure 3.11: Time distributions of the leading, trailing, and average of both leading and trailing edges for 2 mm (top row) and 8 mm (bottom row) RPCs exposed to a 100 Hz/cm<sup>2</sup> radiation rate. The data were collected with RPCs operated at the voltage corresponding to the knee of the efficiency distribution, defined as the point where 95% of the maximum efficiency is obtained [204].*

### 2199 3.2.3.1 Double-gap RPC

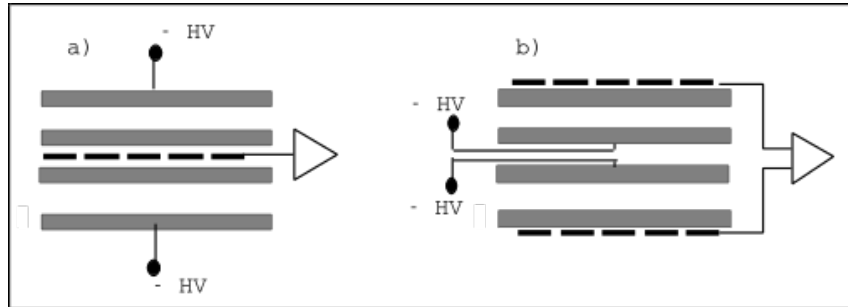


*Figure 3.12: Possible double-gap RPC layouts: a) "standard" 1D double-gap RPC, as used in the CMS experiment, where the anodes are facing each other and a 1D read-out plane is sandwiched in between them, b) double read-out double-gap RPC as used in ATLAS experiment, where the cathodes are facing each other and 2 read-out planes are used on the outer surfaces. This last layout can offer the possibility to use a 2D reconstruction by using orthogonal read-out planes.*

2200 Made out of two narrow RPC detectors stacked on top of each other as shown in Figure 3.12, this  
 2201 detector layout, popularized by the CMS [192] and ATLAS [193] LHC experiments, can be used  
 2202 as an OR system in which each individual chamber participates in the output signal and increases  
 2203 the overall sensitive volume of the detector apparatus. Keeping the copper strip read-out system at  
 2204 ground potential, CMS and ATLAS, with different goals in mind, have chosen different designs as

2205 CMS RPCs possess a 1D read-out while ATLAS RPCs offer a 2D read-out. The difference comes  
 2206 from either placing the read-out in between the gaps with the anodes facing each other, or both RPC  
 2207 gaps in between two layers of read-out panels, one along the X-axis and one along the Y-axis with  
 2208 the cathodes facing each other.

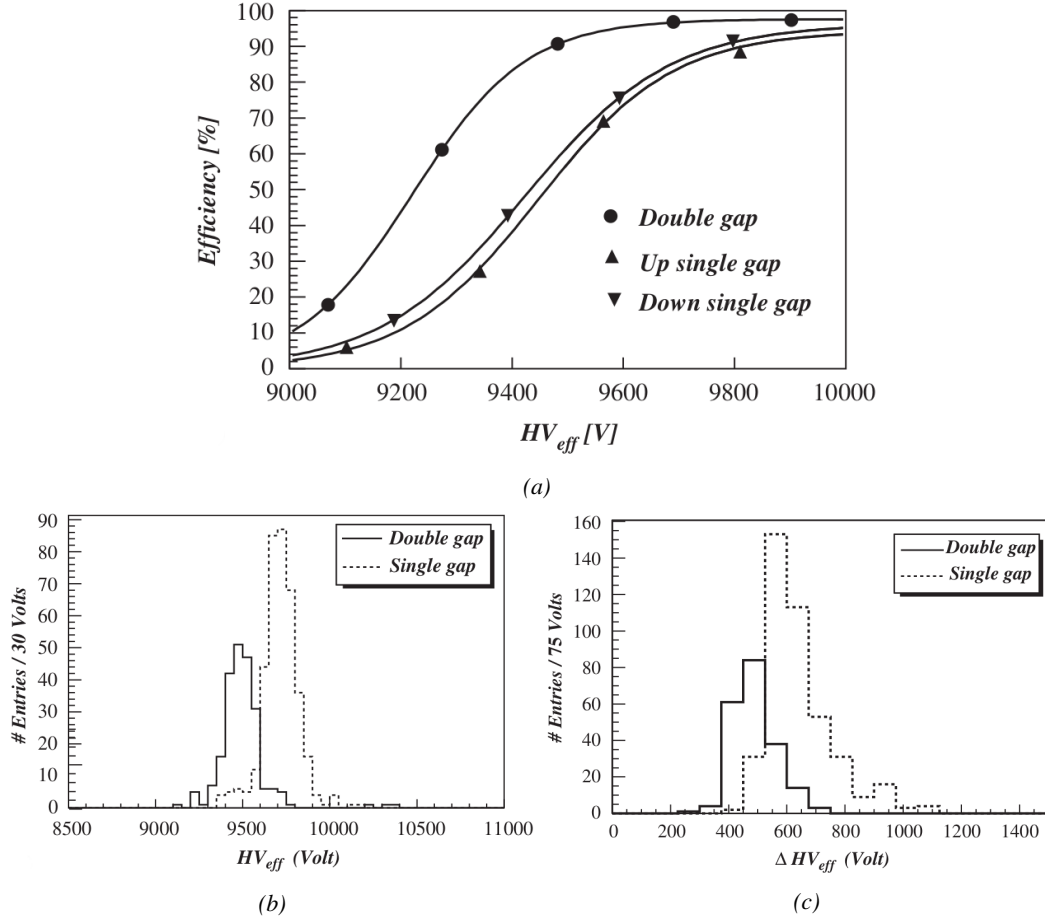


Figure 3.13: Comparison of performance of CMS double and single-gap RPCs using cosmic muons [205].  
 (a): Comparison of efficiency curves. (b): Voltage distribution at 95% of maximum efficiency. (c): Distribution of the voltage difference between the point at 90% and 10% efficiency  $\Delta_{10\%}^{90\%}$ .

2209 The gain of such a detector is reduced by a factor 2 with respect to single-gap RPCs with an effi-  
 2210 ciency plateau reached at lower voltage, as visible on Figure 3.13, due to the two gas gaps contribut-  
 2211 ing to the signal formation and offering a dynamic range, the voltage range between the reaching of  
 2212 the efficiency plateau and the start of streamers, closer to that of a wide gap RPC. A double-gap is  
 2213 then fully efficient while the individual RPC gaps composing it are only 70 to 80% efficient. Nat-  
 2214 urally, by operating the double-gap at a lower voltage, the rate capability increases as the induced  
 2215 charge per gap is decreased with respect to a single-gap detector also leading to a reduction of the  
 2216 streamer probability and a better extraction of the fast charge of the total signal as was shown already  
 2217 in Figure 3.7.

2218 **3.2.3.2 Multigap RPC (MRPC)**

2219 MRPCs have a design in which floating sub  
 2220 electrode plates are placed into a wide gap  
 2221 RPC to divide the gas volume and create a sum  
 2222 of narrow gaps [189, 190]. Similarly to the  
 2223 double-gap RPC for which the gain could be  
 2224 reduced by increasing the dynamic range, the  
 2225 multigap reduces the gain while keeping a total  
 2226 dynamic range similar to that of a wide gap  
 2227 RPC by reducing the size of each individual  
 2228 sub-gap composing the detector. The dynamic  
 2229 range, associated to the sensitive volume, and  
 2230 the comparison of each detector layout to the  
 2231 wide gap RPC is shown in Figure 3.14.

2232 By operating the detector with thinner gaps,  
 2233 its time resolution is improved. Similarly to the time resolution presented in Figure  
 2234 3.11 for the wide gap RPC of 8 mm,  
 2235 a complementary study was conducted on  
 2236 multi-gap RPCs using two 4 mm and four  
 2237 2 mm subgaps. As shown in Figure 3.15,  
 2238 an improvement of the time resolution with  
 2239 the reduced gap width and increased number  
 2240 of gaps, keeping the same total sensitive volume  
 2241 [190].

2242 After the problem of streamers was solved  
 2243 by adding  $SF_6$  into the gas mixture, the size of  
 2244 the MRPCs decreased as the research groups  
 2245 started applying the concept to the narrow gap  
 2246 RPCs leading to the now widely used micro-  
 2247 gap MRPCs. The time resolution of such a  
 2248 detector can reach of few tens of ps, with  
 2249 gas gaps of the order of a few hundred  $\mu m$   
 2250 as shown in Figure 3.16 representing a single  
 2251 cell of ALICE Time-of-flight (ToF) system consisting of double MRPCs, as studied in the early  
 2252 2000s [206].

2253 The MRPC is mainly used as ToF detector [206–210] due to its excellent timing properties that  
 2254 allows performing particle identification as explained by Williams in [211]. The principle of particle  
 2255 identification using ToF consists in the measurement of the velocity of a particle. Indeed, particles  
 2256 are defined by their mass (which is the parameter of interest here, assuming e.g. that their electric  
 2257 charge being measured using the bending angle of the particles traveling through a magnetic field)  
 2258 and this mass can be calculated by measuring the velocity  $\beta$  and momentum  $p$  of the particle:

$$(3.3) \quad \beta = \frac{p}{\sqrt{p^2 + m^2}}$$

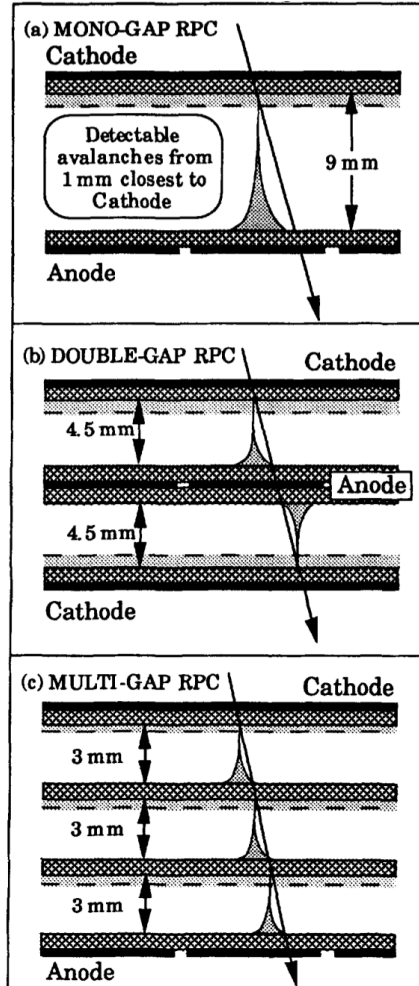
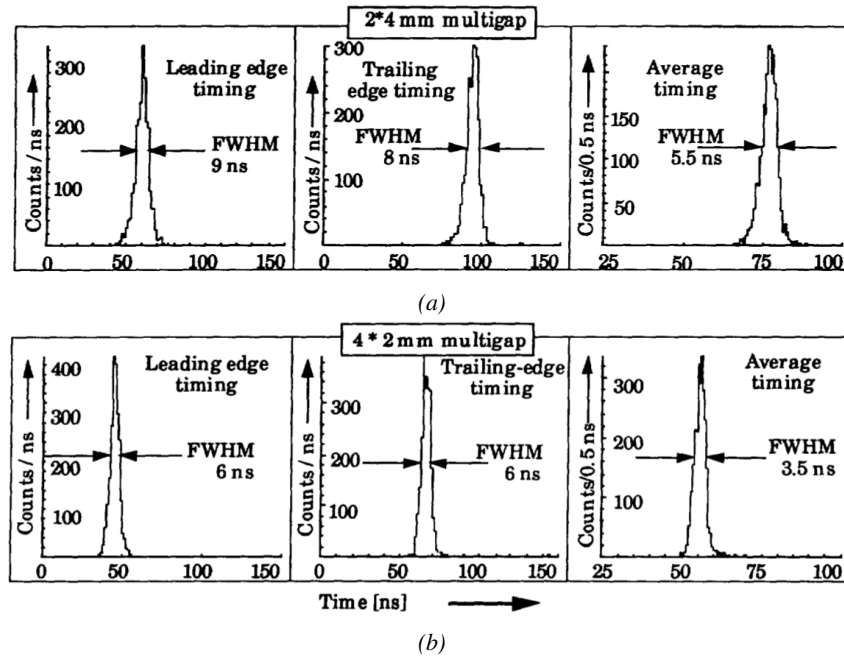
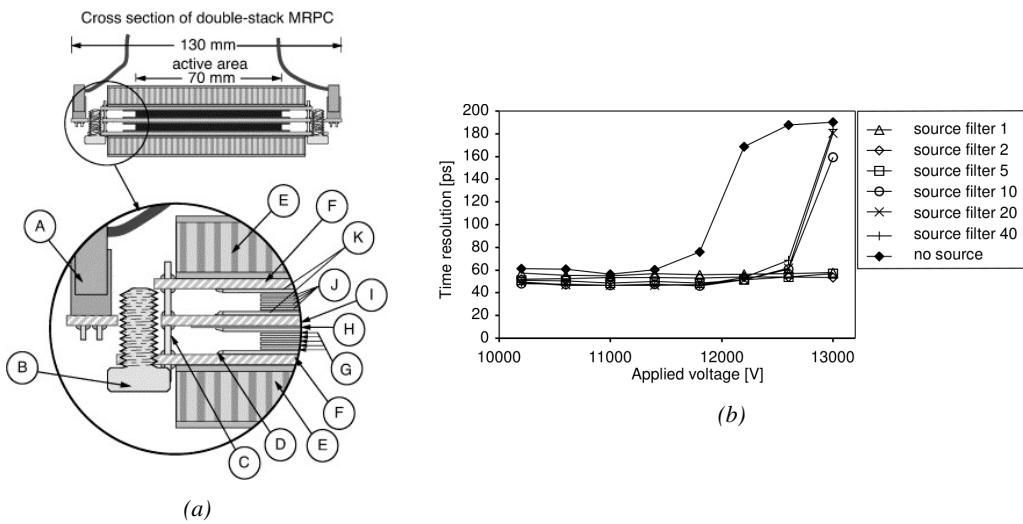


Figure 3.14: Representation of different RPC layouts (wide gap (a), double-gap (b) and multigap (c)), of the corresponding sensitive volume in gray, and of the associated avalanche size [190].



*Figure 3.15:* Time distributions of the leading, trailing, and average of both leading and trailing edges for multigap RPCs consisting in two 4 mm (a) and four 2 mm (b) exposed to a  $100 \text{ Hz/cm}^2$  radiation rate. The data were collected with RPCs operated at the voltage corresponding to the knee of the efficiency distribution, defined as the point where 95% of the maximum efficiency is obtained [190].



*Figure 3.16:* Presentation of a study for an ALICE MRPC cell prototype using  $250 \mu\text{m}$  gas gaps,  $620 \mu\text{m}$  outer glass electrodes, and  $550 \mu\text{m}$  inner floating electrodes (a), and of its time resolution performance as a function of the applied high voltage for different radiation levels corresponding to different filter settings of the  $740 \text{ GBq}$   $^{137}\text{Cs}$  source at the former CERN GIF facility (b) [206].

Intuitively, it is trivial to understand that two different particles having the same momentum will have a different velocity due to the mass difference and thus a different flight time  $T_1$  and  $T_2$  through the detector and this is used to separate and identify particles. The better the time resolution of the ToF system used, the stronger the separation will be:

(3.4)

$$T = \frac{L}{v} = \frac{L}{c \cdot \beta}$$

$$\Delta T = T_1 - T_2$$

$$\begin{aligned} &= \frac{L}{c} \left( \sqrt{1 + m_1^2/p^2} - \sqrt{1 + m_2^2/p^2} \right) \\ &\cong (m_1^2 - m_2^2) \frac{L}{2cp^2} \end{aligned}$$

Taking into account the distortion effect on the electric field inside of an MRPC built using micro gaps due to the exposition to irradiation, distortion that can be understood by monitoring the current drawn by the detector which should stay constant at a constant electric field, another benefit of using such small gas gaps is the strong reduction of the average avalanche volume and thus of the blind spot on MRPCs leading to an improved rate capability. Multigaps can sustain backgrounds of several kHz/cm<sup>2</sup> as demonstrated in Figure 3.17.

### 3.2.3.3 Charge distribution and performance limitations

A direct consequence of the different RPC layouts is a variation of intrinsic time resolution of the RPC depending on the gap size, and of its rate capability when the deposited charge per event is spread over a larger number of amplification volumes. This allows reducing of the overall gain of the detectors which is compensated by a pre-amplification of the signals at the level of the electronics. In this sense, an advantage is given to multi-gap RPCs with their sub-millimeter gas volumes providing very consistent signals.

From the charge spectrum point of view, each layout has its own advantages. While the double-gap has the highest ratio between the total charge it induces on the read-out and the charge that effectively drifts through its volume, as seen in Figure 3.18, the multigap has a charge spectrum with a maximum significantly above zero, as visible in Figure 3.19. A high induced-over-drifting charge ratio means that the double-gap can be safely operated at a high threshold or that at a similar threshold

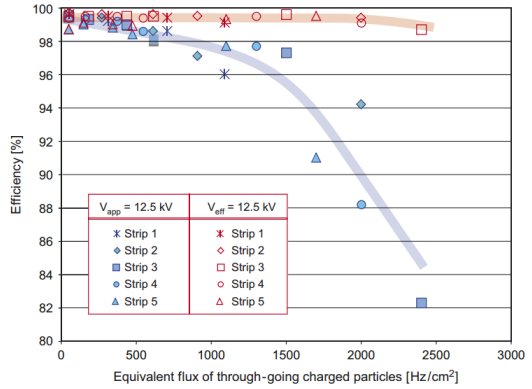


Figure 3.17: Comparison of the detector performance of ALICE ToF MRPC [212] at fixed applied voltage (in blue) and at fixed effective voltage (in red). The effective voltage is kept fixed by increasing the applied voltage according to the current drawn by the detector.

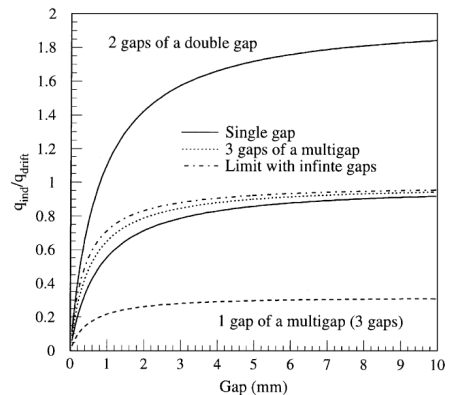
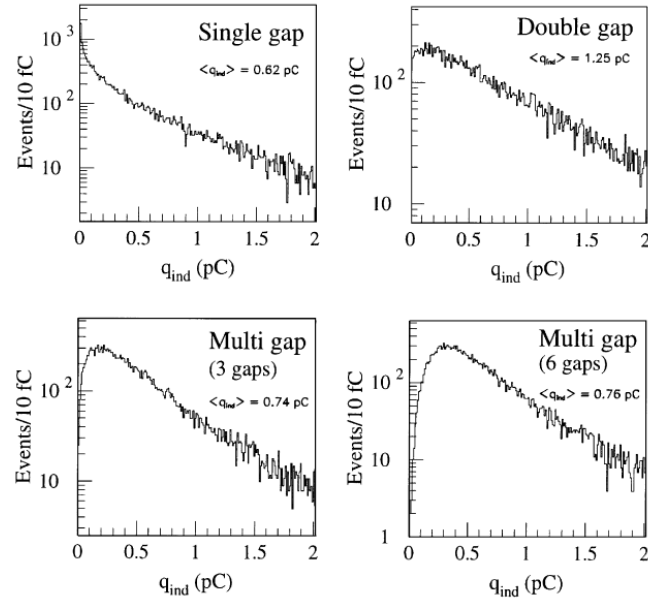
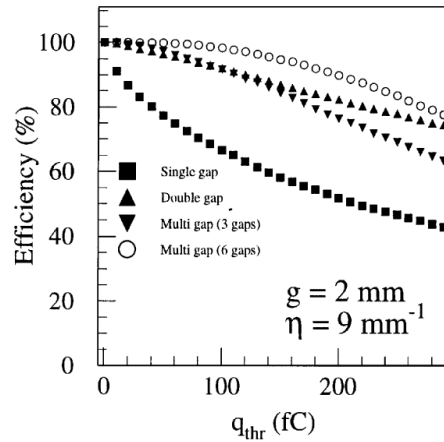


Figure 3.18: Ratio between total induced charge and drifting charge have been simulated for single-gap, double-gap and multigap layouts [213]. The total induced charge for a double-gap RPC is a factor 2 higher than for a multigap.

it can be operated with a twice smaller drifting charge, leading to a higher rate capability if operated with sensitive enough electronics. On the other hand, the strong detachment of the charge spectrum from the origin in the MRPC case allows reaching a higher efficiency with increasing threshold as most of the signals have a higher charge content due to the convolution of several single-gap spectra. The range of stable efficiency increases with the number of gaps, as presented in Figure 3.20.



*Figure 3.19:* Charge spectra have been simulated for single-gap, double-gap and multigap layouts [213]. It appears that while single-gaps show a decreasing spectrum, double and multigap layouts exhibit a spectrum whose maximum is significantly above zero. The shift of maximum value in the spectrum increases along with the number of gaps.



*Figure 3.20:* The maximal efficiency theoretical is simulated for single-gap, double-gap and multigap layouts [213] at a constant gap thickness of 2 mm and using an effective Townsend coefficient of  $9 \text{ mm}^{-1}$ .

<sub>2299</sub> **3.3 Signal formation**

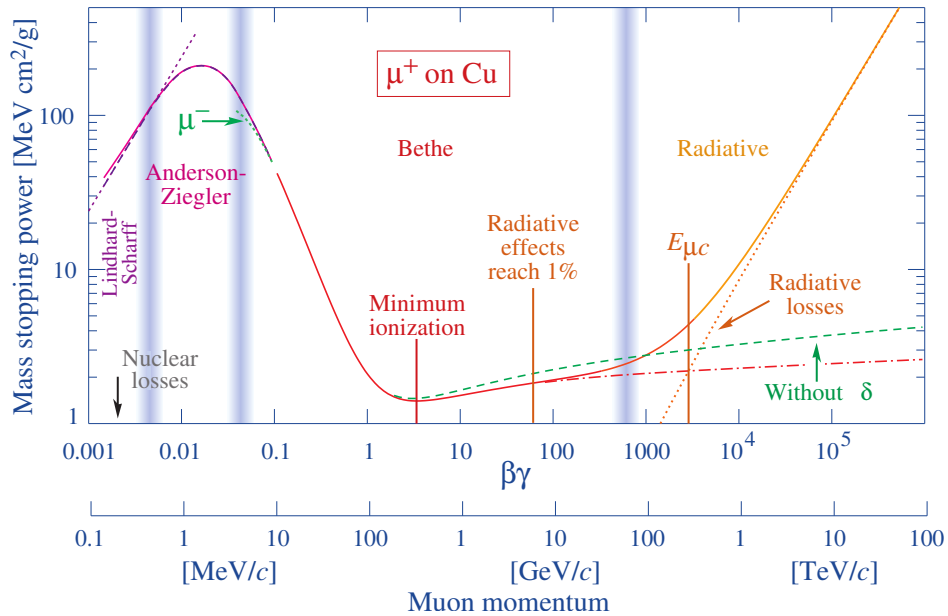


*Figure 3.21: Mass stopping power as a function of  $\beta\gamma = p/Mc$  for positive muons in copper [115]. The total stopping power is indicated with a solid line and local components with dashed lines. The vertical bands are used to indicate boundaries between different approximations used at different energy range.*

The physics of Resistive Plate Chambers still is far from fully understood and many attempts are made to describe these detectors using phenomenological models [197, 214, 215]. These theoretical works have led to a better understanding of the key principles that account for RPCs signal formation. As previously discussed, the typical mixture of such a detector is to a large extent composed by a gas with some quenching properties and a low ionization potential to easily produce electrons, with the addition of UV quencher and electronegative compounds. The electronic avalanche formation will be triggered by a charged particle passing through the gas, typically a muon in the case of most applications involving RPCs. The production of electrons in the gas of a detector is related to the energy lost by the incoming particle traveling through a material medium. The example of the mass stopping power of copper on muons is given in Figure 3.21 on which the different energy loss mechanisms at different energy ranges are visible. Once primary ionization electrons have been freed in the gas volume, the electric field applied in between the electrodes of the RPC will make the charges move and there will be a competition in the gas in between the Townsend and attachment coefficient which describe the evolution of the number of electrons in an avalanche. While drifting through the gas, the electrons are also subjected to diffusion that will affect the evolution of the avalanches. Finally, when the avalanche is big enough, the accumulation of negative (electrons) and positive (ions) charges in the gas volume will start affecting the local electric field. This effect is known as the *space charge effect*.

### 3.3.1 Energy loss at intermediate energies

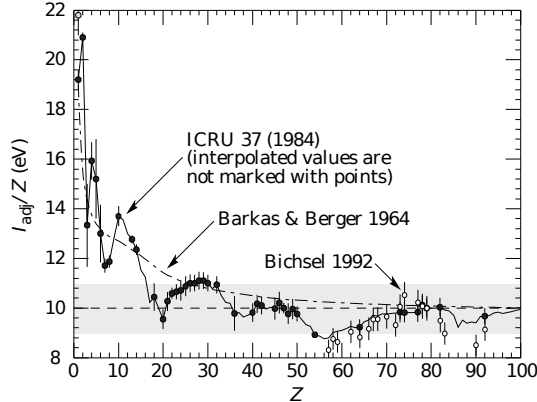


Figure 3.22: Mean excitation energies normalized to the atomic number as adopted by the ICRU [115, 216, 217].

A particle traveling through a medium will interact with its components, losing energy. When a muon travels through the gas of a gaseous detector, at the energy range usually observed, typically of the order of a few GeV for cosmic muons[115] to a few hundreds of GeV in accelerators such as the LHC, it interacts with the molecules of the gas leading to dissipation of the transferred energy in the form of inelastic scattering or ionization. The photons and electron-ion pairs resulting from these interactions can trigger avalanches in the gas which will contribute to feed the avalanche growth thanks to the strong electric field applied in between the two electrodes of an RPC.

At higher energies, the energy loss through

photon radiation can't be neglected anymore as can be seen in Figure 3.21.

The mass stopping power of moderately relativistic ( $0.1 \lesssim \beta\gamma \lesssim 1000$ ) heavy particles ( $M \gg m_e$ ) traveling through a medium via excitation and ionization processes was studied by Bethe in 1930 [218] and is well described by the so called the Bethe Formula given in Equation 3.5.

$$(3.5) \quad \left\langle -\frac{dE}{dx} \right\rangle = K z^2 \frac{Z}{A} \frac{1}{\beta^2} \left( \frac{1}{2} \ln \frac{2m_e c^2 \beta^2 \gamma^2 W_{max}}{I^2} - \beta^2 - \delta(\beta\gamma) \right)$$

The different parameters used in this equation are

$E$	- incident particle energy $\gamma Mc^2$	MeV
$x$	- mass per unit area	$\text{g cm}^{-2}$
$N_A$	- Avogadro's number	$6.022\ 140\ 857(74) \times 10^{23} \text{ mol}^{-1}$
$c$	- speed of light in vacuum	$299\ 792\ 458 \text{ m s}^{-1}$
$\mu_0$	- permeability of free space	$4\pi \times 10^{-7} \text{ N A}^{-2}$
$\epsilon_0$	- permittivity of free space $\epsilon_0 = 1/\mu_0 c^2$	$8.854\ 187\ 817 \dots \times 10^{-12} \text{ F m}^{-1}$
$\alpha$	- fine structure constant $\alpha = e^2/4\pi\epsilon_0\hbar c$	$1/137.035\ 999\ 139(31)$
$r_e$	- classical electron radius $r_e = e^2/4\pi\epsilon_0 m_e c^2$	$2.817\ 940\ 3227(19) \text{ fm}$
$e$	- elementary charge of the electron	$-1.6021766208(98) \times 10^{-19} \text{ C}$
$m_e c^2$	- electron mass $\times c^2$	$0.510\ 998\ 9461(31) \text{ MeV}$
$K$	- constant defined as $K = 4\pi N_A r_e^2 m_e c^2$	$0.307\ 075 \text{ MeV mol}^{-1} \text{ cm}^2$
$z$	- charge number of incident particle	
$Z$	- atomic number of absorbing medium	
$A$	- atomic mass of absorbing medium	$\text{g mol}^{-1}$
$\beta$	- velocity of particle $\beta = v/c$	
$\gamma$	- Lorentz factor $\gamma = (1 - \beta^2)^{-1/2}$	
$W_{max}$	- maximum energy transfer through a single collision	MeV
$I$	- mean excitation energy of absorbing medium	eV
$\delta(\beta\gamma)$	- density effect correction to ionization energy loss	

In this equation, the maximum energy transfer  $W_{max}$  is defined as function of the incident particle mass  $M$  expressed in MeV/c<sup>2</sup>:

$$(3.6) \quad W_{max} = \frac{2m_e c^2 \beta^2 \gamma^2}{1 + 2\gamma m_e/M + (m_e/M)^2}$$

and the mean excitation energy  $I$  depends on the absorber. Its determination is non-trivial, but recommendations are given by the International Commission on Radiation Units & Measurements (ICRU) based on experimental measurements and interpolations as shown in Figure 3.22.

For the case of copper, the mean stopping power is visible in Figure 3.21. The mean stopping power corresponding only to the Bethe range for other materials is given in Figure 3.23 and shows that  $\langle -dE/dx \rangle$  is similar for each material with a slow decrease with  $Z$ .

The factor affecting the equation the most is  $\beta$ . Indeed, the dependence on  $M$  is introduced at higher energies in the logarithm via the max transfer energy per single collision. In most practical cases, only the dependence on  $\beta$  is considered as most of the relativistic particles are closed to the lowest mean energy loss rate and are referred to as minimum ionizing particles (mip's). The almost logarithmic relation between the mean energy loss rate for minimum ionizing particles and  $Z$  is shown in Figure 3.24.

Finally, the term  $\delta(\beta\gamma)/2$  in Equation 3.5 corresponds to the density effect correction introduced to account for the polarization of a real media that limits the spatial extension of the electric field of relativistic particles. As the energy of a particle increases, the associated electric field will flatten and extend. Due to this effect, the distant collision contribution to Equation 3.5 will increase as  $\ln(\beta\gamma)$  but the polarization of the media truncates this rise.

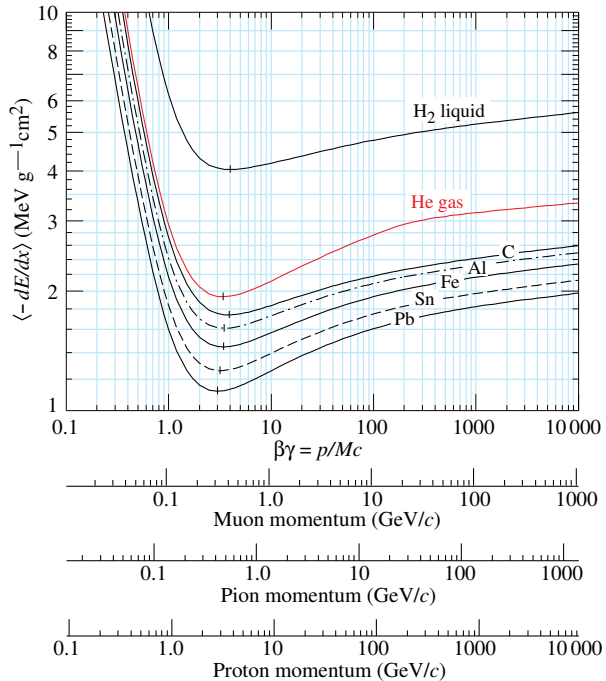


Figure 3.23: Mean mass stopping power for liquid hydrogen, as used in bubble chambers, gaseous helium, carbon, aluminum, iron, tin, and lead without the inclusion of radiative effect at higher  $\beta\gamma$  necessary for pions and muons in denser materials [115].

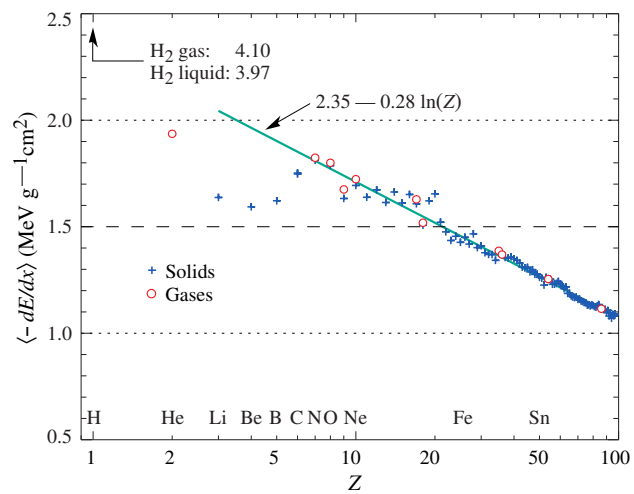


Figure 3.24: Mean mass stopping power at minimum ionization as a function of the atomic number [115].

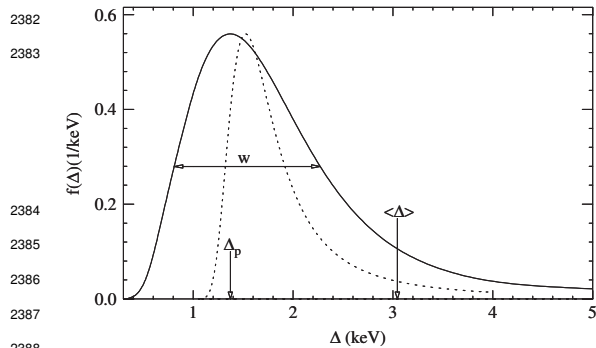


Figure 3.25: Example of straggling function (solid)  $f(\Delta)$  of particles passing through 1.2 cm of Argon gas with a  $\beta\gamma$  of 3.6. The original Landau distribution is shown with a dashed line [219].

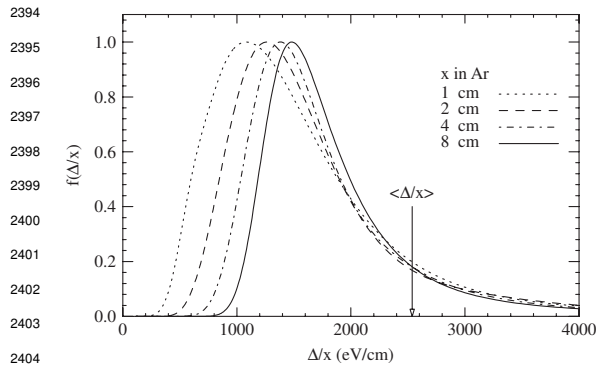


Figure 3.26: Evolution of straggling functions  $f(\Delta)$  of particles passing through a volume of Argon gas with a  $\beta\gamma$  of 3.6 with increasing thickness  $x$  [219].

Thus, the energy loss distribution is better represented by its most probable energy loss  $\Delta_p$  and its full-width-at-half-maximum (FWHM)  $w$ . As showed by Figure 3.26, the distribution is affected by the thickness of the gas volume with the most probable energy loss normalized to the thickness increasing and the width decreasing for increasing thickness, converging towards the Landau distribution, whereas the mean energy loss is unchanged. Corrections to include the electron binding energy and the atomic shell structure are brought to the original Landau equation in order to account better for the number of collisions leading to an increased width of the energy loss distribution [219]. The corrected energy loss distribution is usually referred to as *straggling function*.

In the case of gas mixtures, composed of several elements, using Bragg additivity it can be understood that the mean energy loss of the mixture is the sum of the mean energy losses in each layer of individual element  $j$  of weight fraction in the mixture  $w_j$  [115].

$$(3.8) \quad \left\langle \frac{dE}{dx} \right\rangle = \sum w_j \left\langle \frac{dE}{dx} \right\rangle_j$$

At high energies, the correction is given by Equation 3.7:

$$(3.7) \quad \delta/2 \longrightarrow \ln(\hbar\omega_p/I) + \ln(\beta\gamma) - 1/2$$

where  $\hbar\omega_p$  represents the plasma energy that depends on the electron density of the media and the electron mass and can be calculated as  $\sqrt{\rho(Z/A)} \times 28.816$  eV. The introduction of this correction term reduces the increase of the mean stopping power at higher energies as can be seen in Figure 3.21. Moreover, due to lower electron density, the effect is less visible for gases than for liquids and solids as can be seen in Figure 3.23.

The mean energy loss per collision can be difficult to measure for data samples with low statistics but is not always representative of the energy loss distribution for a given incident particle energy. Hence, it is easier to access the most probable energy loss which is a lower value than the average loss due to the distribution of the energy transfer. This value is well described by a highly skewed Landau distribution for detectors with "moderate" thickness  $x$ , expressed in g mol<sup>-1</sup>. But for gas volumes, a Landau distribution greatly underestimates the width  $w$  of the distribution and only succeeds to provide with a correct value for the most probable energy loss, as shown in Figure 3.25.

2420 **3.3.2 Primary ionization**

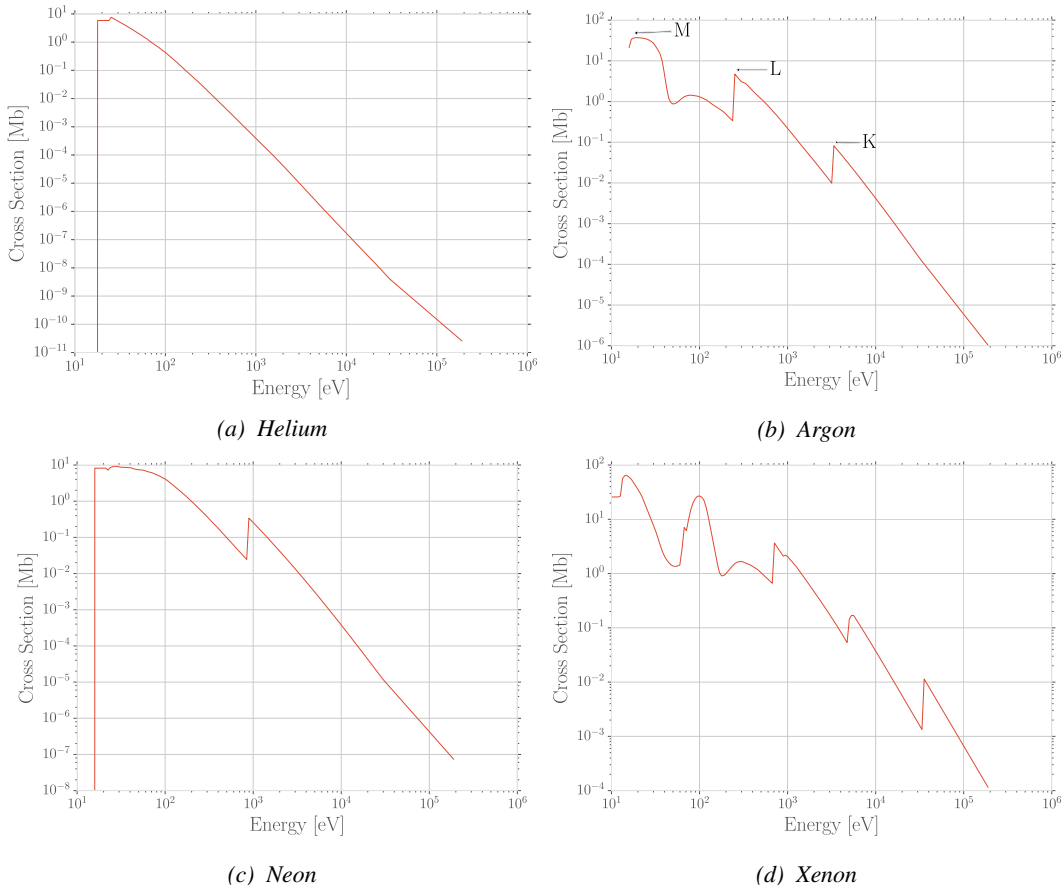


*Figure 3.27: Photoabsorption cross section as computed by HEED for noble gases with different electron shell numbers [215].*

2421 Using the Bethe formula to compute the mean energy transfer of charged particles when traveling  
2422 through a gas volume may give some feeling on the physics that affect the particle but doesn't provide  
2423 detailed enough information about the individual ionizations along its tracks at a microscopic level.  
2424 In order to simulate efficiently an RPC and hence understand the processes governing avalanche  
2425 creation and growth, knowledge on the ionization process is necessary.

2426 To convert the energy loss rate into a number of primary ionizations, the Photo-Absorption Ionisation  
2427 (PAI) model [220] was developed in 1980. It is based on the cross section of photoionization of  
2428 gas atoms and the dielectric constant of the medium through which the charged particles are going.  
2429 Indeed, the interaction of charged particles with the gas molecules, being of electromagnetic  
2430 nature, is mediated by photons and, hence, the cross section for photoionization is important to under-  
2431 stand. This approach is nevertheless semi-classical as it relies on classical electrodynamics. It only gives access to the energy transfer to the gas atoms, and no information on the energy dissipa-  
2432 tion and secondary emissions is available. The energy transferred to the medium is not all used for  
2433 ionization.  
2434

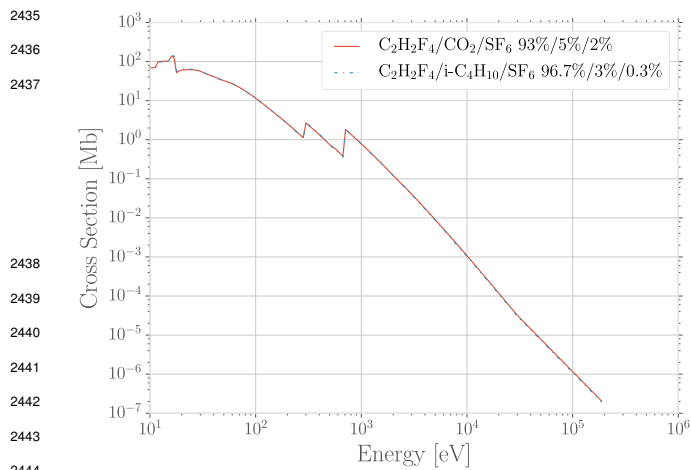


Figure 3.28: Photoabsorption cross section as computed by HEED for typical RPC gas mixtures [215]. The RPC mixture with CO<sub>2</sub> corresponds to the mixture used by CALICE SDHCAL [221] while the other one was foreseen for the experiment ATLAS [222] but has been changed since then. Both mixtures being largely composed of C<sub>2</sub>H<sub>2</sub>F<sub>4</sub>, the curves are nearly identical.

full atom rather than with a single electron. With the incoming particle interacting with a single electron, the atom is left in an excited state once the photo-electron has been emitted with an energy corresponding to the transferred energy minus the binding energy of the electron shell. The resulting vacancies in the electronic shell will be filled through emission of photons or Auger electrons and can contribute to further ionization or excitation in the gas volume. Fluorescence photons are usually not considered as they only constitute a very small fraction of secondary emissions [224].

Assuming that the transferred energy is absorbed in its totality by a single electronic shell, the PAI model was extended to the new Photo-Absorption Ionisation with Relaxation (PAIR) model [224] to include relaxations. In this model, the cross section corresponding to the whole atom is re-expressed using a sum of partial cross sections corresponding to the different electronic shells. When one or more electrons are knocked out of the atom, the vacancies are filled by electrons of the shell above with relaxation by Auger electron emission. These processes happen in cascade from the inner shell to the outer one until all the vacancies are filled and the energy has been released. This model is included in the program HEED developed at CERN [225] and gets called by Garfield [226], a program developed for the simulation of gaseous detectors. The results for the cross section for a few noble gases are given in Figure 3.27. It can be seen that for each shell, the cross section exhibits an absorption peak. More complex patterns are seen with larger atoms such as Xenon on Figure 3.27d. For gas mixtures, like the typical RPC mixtures, the cross section is shown in Figure 3.28. Both mixtures being mainly composed of C<sub>2</sub>H<sub>2</sub>F<sub>4</sub>, the variations in between the two cross section profiles are very subtle and depends on the concentration of the other compounds.

Once the interaction cross section is known, it is possible to determine the distribution of energy loss and the number of produced electrons, as shown in Figure 3.29 for Helium, Argon, which is used in gaseous detectors, and for a typical RPC mixture [215]. The distributions are computed using HEED and show typical straggling function profiles with some complex structures that can be related to interaction of the incoming particle with the different electron shells. Helium does not have a large photoabsorption cross-section according to Figure 3.27a and a muon will not likely lose

For an energy deposition  $\Delta$ , the number of electron-ion pairs produced is:

$$(3.9) \quad \Delta = n_i W$$

$W$  corresponds to the average energy per pair production that depends on the medium and is greater than the ionization potential leading to the conclusion that part of the transferred energy is dissipated through other processes [215, 223]. In order to understand the energy dissipation and the secondary emissions, the fine structure of each atom is taken into account. Through the PAI model, the incident charged particle is assumed to interact with the

2477 a lot of energy and create a lot of electrons. In a more complex atom like Argon, the cross-section is  
 2478 larger and will lead to a larger energy loss of muons and more electron produced. Finally, a complex  
 2479 gas mixture used in RPCs will offer an even larger cross-section, a wider energy loss distribution  
 2480 and will be able to produce more electrons. The same information is confirmed by looking at the  
 2481 evolution of the mean number of electron clusters produced along a muon track as a function of  
 2482 the lorentz factor associated to muons shown in Figure 3.30a. The size of these clusters is studied  
 2483 through Figure 3.30b which shows that in most of the cases ( $\approx 80\%$ ) the clusters are only composed  
 2484 of a single electron which is consistent with minimum ionizing particles.

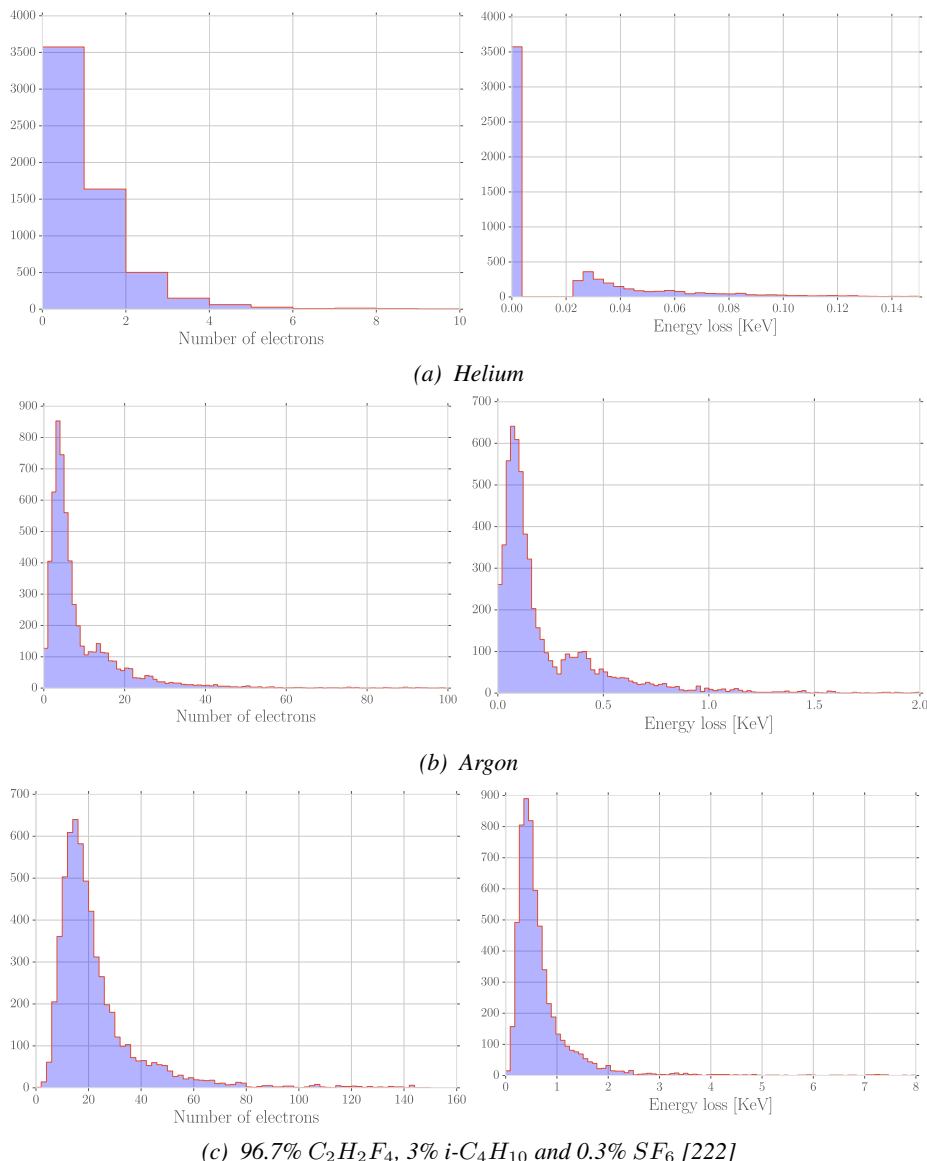


Figure 3.29: Distributions of number of electrons (left) and energy loss (right) for a 5 GeV/c muon passing through 1.2 mm of Helium (a), Argon (b) or a typical RPC gas mixture (c) [215].

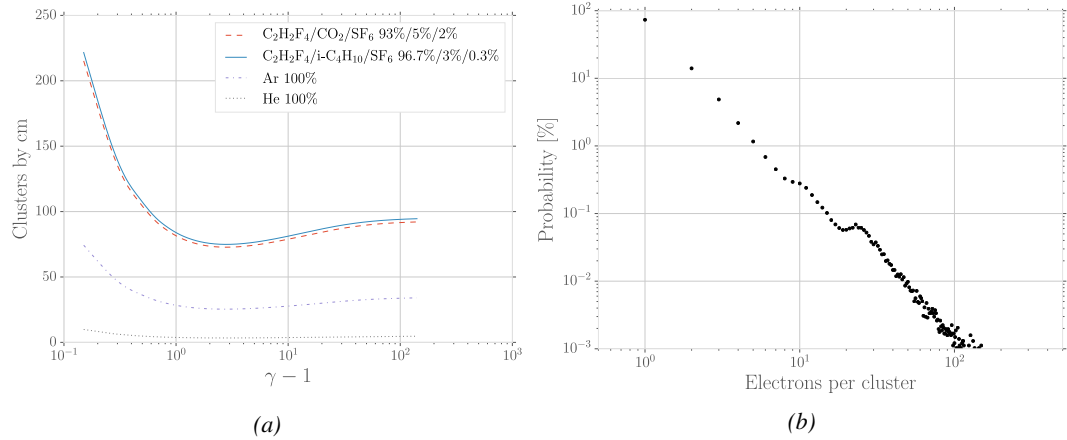


Figure 3.30: (a): Mean cluster density for muons through different gas volumes [215]. (b): Distribution of the number of electrons per cluster for a 5 GeV/c muon traveling through a mixture of 96.7%  $C_2H_2F_4$ , 3%  $i-C_4H_{10}$  and 0.3%  $SF_6$  [215, 222].

### 3.3.3 Development and propagation of avalanches

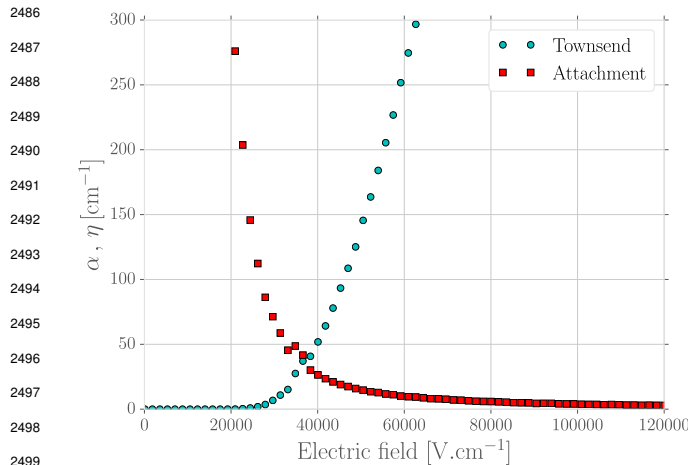


Figure 3.31: Townsend and attachment coefficient for a typical 96.7/3/0.3 mixture of  $C_2H_2F_4/i-C_4H_{10}/SF_6$ , at a temperature  $T = 296.15$  K and a pressure  $P = 1013$  hPa [215, 222].

is reached, the electrons can get attached to a gas molecule instead. These two effects can be described using a simple model in which the multiplication and attachment processes are given by the Townsend coefficient  $\alpha$  and the attachment coefficient  $\eta$ , assuming that the history of previous interactions in the gas does not influence new interactions. This model simply takes into account probabilities to have at the gas depth  $z$ , for a given number  $n$  of free electrons in the gas,  $n + 1$  or  $n - 1$  electrons at the depth  $z + dz$  (respectively  $n\alpha dz$  and  $n\eta dz$ ).

From the clusters released in the gas volume by the charged particles, free electrons will start drifting due to the electric applied in between the electrodes of the RPC. Gaining velocity and energy, these electrons in their turn will be able to ionize the gas. This process being repeated by all the produced electrons will trigger an avalanche to develop.

The growth of the avalanche can be intuitively understood as a competition between two effects. Due to their increasing energy, electrons have a probability to trigger new ionizations by interacting with gas molecules. On the other hand, before the minimal amount of energy

2510 The mean number of electrons  $\bar{n}$  and  
 2511 cations  $\bar{p}$  can be written for single compound  
 2512 gases as

$$(3.10) \quad \frac{d\bar{n}}{dz} = (\alpha - \eta)\bar{n}, \quad \frac{d\bar{p}}{dz} = \alpha\bar{n}$$

2513 which, assuming the initial conditions  
 2514  $\bar{n}(0) = 1$  and  $\bar{p}(0) = 0$ , leads to the mean  
 2515 number of electrons and cations at a depth  $z$

$$(3.11) \quad \begin{aligned} \bar{n}(z) &= e^{(\alpha-\eta)z} \\ \bar{p}(z) &= \frac{\alpha}{\alpha-\eta} \left( e^{(\alpha-\eta)z} - 1 \right) \end{aligned}$$

2516 The Townsend and attachment coefficient as a function of the applied electric field are given in  
 2517 Figure 3.31 for a standard RPC gas mixture using Magboltz [228].

2518 Nevertheless, there is more to the avalanche growth than simply these two factors. Throughout  
 2519 the 20<sup>th</sup> century, models have been developed to better understand the physics of discharges in gas.  
 2520 In 1937, Furry developed a model to describe electromagnetic cascades [227] that would be used for  
 2521 electron avalanches in gas during the 1950s. Furry realized that the use of a Poisson law to describe  
 2522 the distribution of shower sizes could not be accurate as he understood that the events occurring in  
 2523 the development of a cascade are not independent from each other, as a Poisson law would suggest.  
 2524 Indeed, part of the particles produce others and this process depends on both their original energy  
 2525 and energy lost. Compared to a Poissonian distribution, experimental results showed an excess of  
 2526 small showers and an underestimate of very large ones. To solve this problem, Furry proposed a  
 2527 distribution of sizes according to the likelihood described in Equation 3.12, in which  $\bar{n} = e^{\alpha z}$ . The  
 2528 Fury distribution is compared with a Poisson law in Figure 3.32.

$$(3.12) \quad P(n, \bar{n}) = \bar{n}^{-1} (1 - \bar{n}^{-1})^{n-1}$$

2529 In this model, no extra energy is brought to the electrons in the showers, contrary to the case  
 2530 of a gaseous detector such as an RPC where an electric field accelerates them. Using the Furry  
 2531 model, Genz studied the fluctuations in electron avalanches in gaseous detectors [229]. Collisions  
 2532 leading to ionizations leave electrons with an energy much smaller than the ionization energy  $eU_i$ ,  
 2533 where  $U_i$  is the ionization potential of a gas molecule. Hence, the electrons need to travel a distance  
 2534  $s = U_i/E$  along the electric field  $E$  to acquire a high enough energy to trigger a new ionization. For  
 2535 the probability of a new ionization to be independent from the path followed by the electrons since  
 2536 the previous ionization, the mean free path  $1/\alpha$  of electrons in the gas has to be large compared to  
 2537  $s$  and thus  $E/\alpha \gg U_i$ . The Townsend coefficient is related to the gas pressure  $p$ . Keeping  $E/\alpha$   
 2538 large compared to  $U_i$  implies that the value of  $E/p$  needs to stay lower than 100 V/cm/torr. In  
 2539 the case of proportional counters such as RPCs, avalanches are large compared to the showers Furry  
 2540 has studied in his original paper. For very large avalanche sizes, Equation 3.12 can be written as an  
 2541 exponential, as shown in Equation 3.13.

$$(3.13) \quad P(n, \bar{n}) = \bar{n}^{-1} e^{-n/\bar{n}}$$

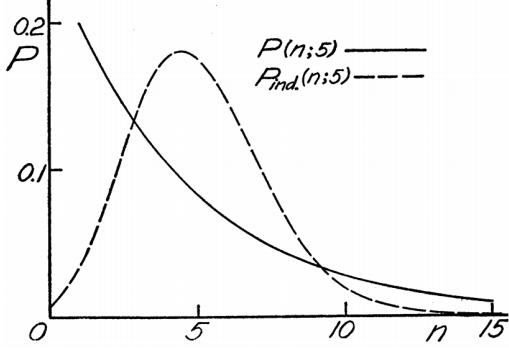


Figure 3.32: Comparison of the distribution law of Furry and the Poisson law for  $\bar{n} = 5$  [227].

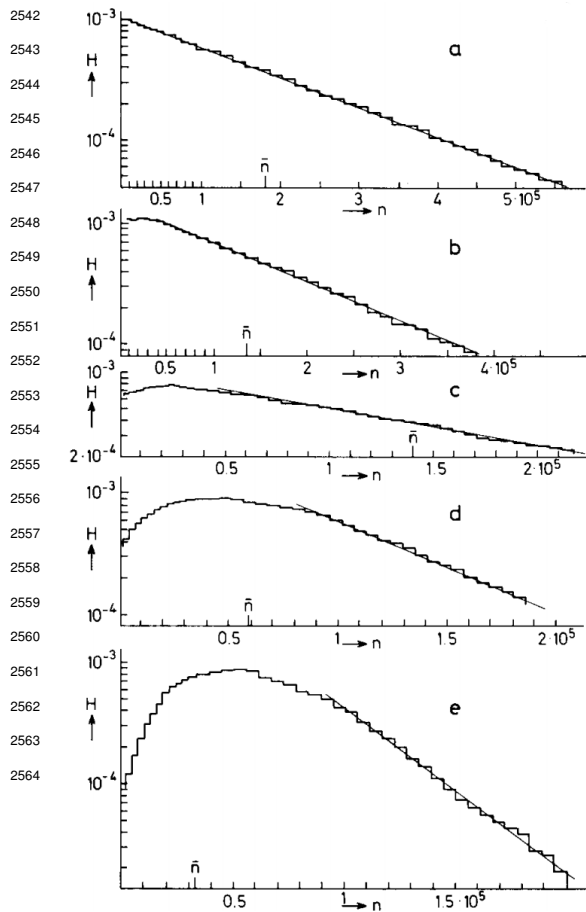


Figure 3.33: Single-electron avalanche size distribution in a proportional counter filled with methylal at different  $E/p$  values. (a) 70, (b) 76.5, (c) 105, (d) 186.5, (e) 426V/cm torr [229]. The straight lines correspond to an exponential fit.

ability better, the introduction of the attachment into the model is an important step. Despite its limitations, the Furry model had the advantage to well describe avalanches occurring when the attachment could be ignored. An extension of this model was provided by Riegler, Lippmann and Veenhof [222] who showed that it was important was to consider both the Townsend coefficient describing the multiplication *and* the attachment coefficient, and not only the effective multiplication coefficient  $\bar{\alpha} = \alpha - \eta$ . The probability to see an avalanche started by a single electron grow to a size  $n$  after having traveled a distance  $z$  through the gas is given by Equation 3.16.

$$\begin{aligned}
 P(n, z) &= P(n-1, z) (n-1)\alpha dz (1 - (n-1)\eta dz) \\
 (3.16) \quad &+ P(n, z) (1 - n\alpha dz) (1 - n\eta dz) \\
 &+ P(n, z) n\alpha dz n\eta dz \\
 &+ P(n+1, z) (1 - (n+1)\alpha dz) (n+1)\eta dz
 \end{aligned}$$

This exponential behaviour is illustrated in Figure 3.33. In practice, to fully understand the avalanche growth, taking into account the path followed by the electrons from one ionization to another is necessary. In the same paper, Genz then discusses models using Polya distributions to estimate the charge multiplication by looking at the size of the avalanche itself. Indeed, the number of charge carriers in the avalanche might become important enough to have an effect on the multiplication process. To account for this, it was proposed to use a varying Townsend coefficient such as described by Equation 3.14 depending on the depth  $x$  in the gas volume in which  $\theta$  is an empirical parameter leading to the probability distribution of Equation 3.15. In the limit where  $\theta$  goes to 0, the formula describes again the Furry model. But the data deviates from this model as well at large  $n$  values. Moreover, the introduction of an empirical parameter makes the model hard to interpret physically.

$$(3.14) \quad \alpha(n, x) = \alpha(x) \left( 1 + \frac{\theta}{n} \right), \quad n > 0$$

$$\begin{aligned}
 (3.15) \quad P(n, x) &= \frac{1 + \theta}{\bar{n}(x)} \frac{1}{\theta!} \left( \frac{n(1 + \theta)}{\bar{n}(x)} \right)^{\theta} e^{-\frac{n(1 + \theta)}{\bar{n}(x)}}
 \end{aligned}$$

In order to have a model that describes re-

The first term of this probability describes that from a state with  $n - 1$  electrons, only 1 multiplies while the others don't get attached. Both the second and third terms describes the probability that from a state with already  $n$  electrons the total number of electrons stay the same. With the second term, no electron gets attached nor multiplies while with the third term, 1 electron gets multiplied and 1 gets attached to compensate. Finally, the fourth term describes the probability to fall from a state with  $n + 1$  to a state with  $n$  electrons due to the attachment of a single electron. At the first order, the evaluation of the previous expression leads to Equation 3.17 whose general solution is given in Equation 3.18. The variables  $\bar{n}(z)$ , defined as in Equation 3.11, and  $k = \eta/\alpha$  making explicit the fact that the distribution does not depend on the effective Townsend coefficient only are introduced in the equation.

$$(3.17) \quad \frac{dP(n, z)}{dz} = -P(n, z)n(\alpha + \eta) + P(n - 1, z)(n - 1)\alpha + P(n + 1, z)(n + 1)\eta$$

$$(3.18) \quad P(n, z) = \begin{cases} k \frac{\bar{n}(z)-1}{\bar{n}(z)-k}, & n = 0 \\ \bar{n}(z) \left( \frac{1-k}{\bar{n}(z)-k} \right)^2 \left( \frac{\bar{n}(z)-1}{\bar{n}(z)-k} \right)^{n-1}, & n > 0 \end{cases}$$

The example given in Figure 3.34 shows the importance of each individual process in the growth of avalanches and the fluctuation of their size. The values of  $\alpha$  and  $\eta$  will influence the probability distribution, as can be seen from Figure 3.34a. Then, Figure 3.34b shows that the fluctuation really takes place within the very first interactions. Indeed, when the avalanche contains a large enough number of charge carriers (a few hundred), its size increases like  $e^{z(\alpha-\eta)}$ .

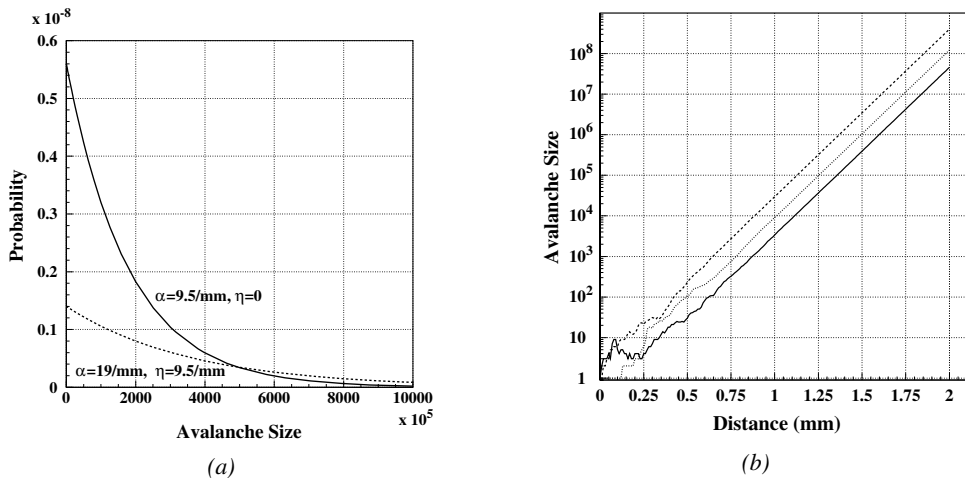
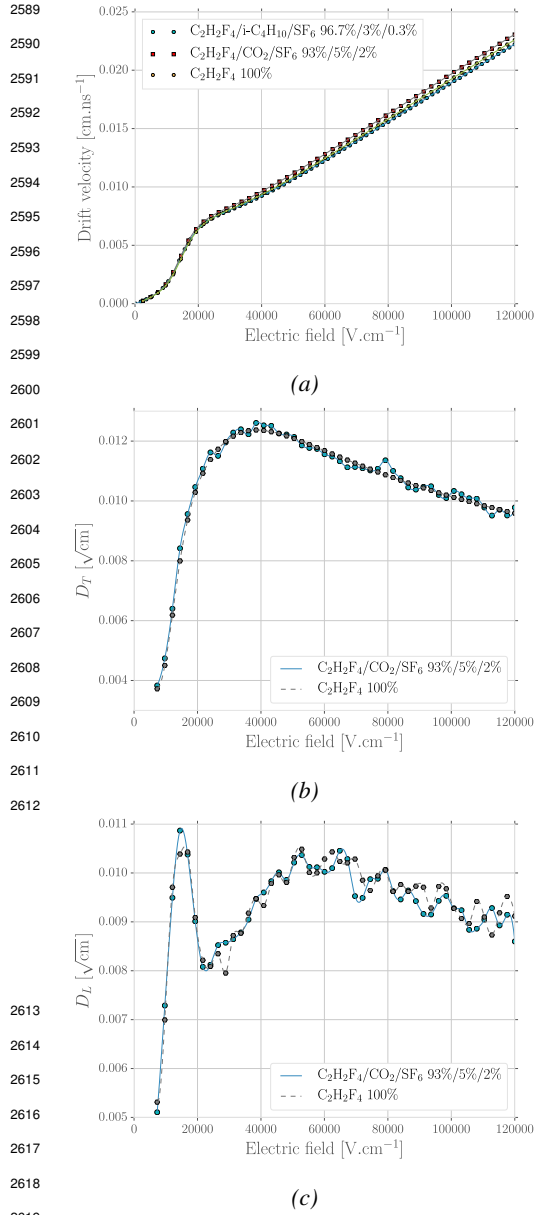


Figure 3.34: (a): Comparison of avalanche size distributions for different values of Townsend and attachment coefficients. The effective Townsend coefficient is the same for both distributions. (b): Fluctuation in avalanche sizes for avalanches started by a single electron with  $\alpha = 13 \text{ mm}^{-1}$  and  $\eta = 3.5 \text{ mm}^{-1}$  [222].

### 2588 3.3.4 Drift and diffusion of the electron cloud



2620 *Figure 3.35:* (a): Electrons mean drift velocity  
 2621 *v<sub>D</sub>* in pure C<sub>2</sub>H<sub>2</sub>F<sub>4</sub> and typical RPC gas mixtures.  
 2622 (b): Transverse diffusion coefficient in pure  
 2623 C<sub>2</sub>H<sub>2</sub>F<sub>4</sub> and a typical RPC gas mixture.  
 2624 (c): Longitudinal diffusion coefficient in pure C<sub>2</sub>H<sub>2</sub>F<sub>4</sub>  
 2625 and a typical RPC gas mixture. All results are  
 2626 given for a pressure P = 760 Torr and a tem-  
 2627 perature T = 296.15 K [215].

$$(3.20) \quad \varphi_T(r, t) = \frac{1}{D_T^2 l} \exp\left(-\frac{(r - r_0)^2}{2D_T^2 l}\right)$$

During the growth of avalanches, an electron cloud drifting along the electric field through the gas will undergo thermal diffusion due to random collisions with the gas molecules. This phenomenon can be studied using the Maxwell-Boltzmann distribution whose mean is defined by the thermal energy of the cloud  $\langle E \rangle = 3/2kT$  with an extra component coming from the constant drift motion. The drift of electrons along the field lines is usually observed on a macroscopic scale through which the speed can be assimilated to a constant  $v_D$  which corresponds to the mean drift speed over a large number of collisions in the gas.

At the microscopic scale, the electrons are drifting over a distance  $\delta z$  while acquiring the corresponding kinetic energy  $T = e_0 |\vec{E}| \delta z$  until they are slowed down by a collision in which they lose part of their energy. This process is repeated as long as electrons are free carriers. Starting at time  $t = 0$  from a point-like electron cloud at a position  $\vec{r}_0$ , the Gaussian density distribution at a time  $t$  will be described by Equation 3.19 in which the width of the isotropic distribution is  $\sigma = 2\bar{D}t$ , with  $\bar{D}$  being a diffusion coefficient expressed in m<sup>2</sup>/s [197].

$$(3.19) \quad \varphi(\vec{r}, t) = \frac{1}{(\sqrt{2\pi}\sigma(t))^3} \exp\left(-\frac{(\vec{r} - \vec{r}_0)^2}{2\sigma^2(t)}\right)$$

Now, if the constant drifting motion is added, the distribution is anisotropic and can be divided onto transversal (Equation 3.20) and longitudinal (Equation 3.21) terms,  $\varphi(r, z, t) = \varphi_T(r, t)\varphi_L(z, t)$ , with a cylindrical symmetry around the field axis [197]. The dependence on  $t$  and  $\sigma_{T,L}(t)$  can be absorbed into the diffusion coefficients by using the relations  $v_D = l/t$  and  $\sigma_{T,L}^2(t) = 2\bar{D}_{T,L}l/v_D$  and introducing new diffusion coefficients  $D_{T,L} = \sqrt{2\bar{D}_{T,L}/v_D}$  in order to explicitly show the dependence of the Gaussian width in drifted distance  $l$ .

$$(3.21) \quad \varphi_L(z, t) = \frac{1}{\sqrt{2\pi l D_L}} \exp\left(-\frac{(z - z_0)^2}{2D_L^2 l}\right)$$

These coefficients, as well as the drift velocity of the electrons, can be calculated thanks to Magboltz as shown in Figure 3.35. The influence of the diffusion on the distribution of charge carriers throughout the gas volume is depicted in Figure 3.36. From very localised electron clusters in the gas in Figure 3.36a, a Gaussian diffusion is then visible in Figure 3.36b. Due to the interactions with gas molecules during the drift, diffusions can occur in the forward and backward direction. Electrons diffused backward will effectively drift over a longer distance and multiply more than electrons diffused forward that will see a shorter drift length. As an effect, the avalanche develops over a longer time and extends over a larger gas volume than in the case the electron cloud is considered as point like and without diffusion. Moreover, as a side effect to the longer growth of the avalanche due to backward longitudinal diffusion, the total production of electrons is increased.

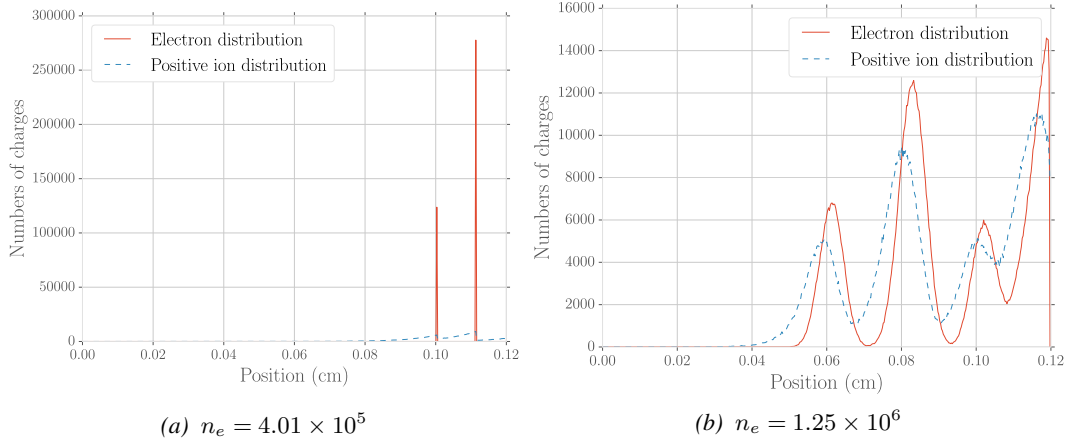


Figure 3.36: Comparison of the free charge carriers in the gas after a time  $t = 7.90$  ns in the case where no diffusion is taken into account to simulate the avalanche (a) and in the case where the diffusion is implemented (b) [215].

### 3.3.5 Space charge effect & streamers

In addition to the basic processes that influence the development of avalanches in a gaseous detector, it is important to consider also the influence of the charge carriers present in the avalanche on the electric field seen by the avalanche. Indeed, each charged particle induces an electric field and it is only natural that the increasing density of electrons and ions in the detector volume will affect the electric field. Thus, parameters such as the Townsend and attachment coefficients, drift velocity or diffusion coefficients will find themselves to be modified along the gas gap length due to this effect referred to as *space charge effect*. Figure 3.37 is a more detailed version of Figure 3.1b in which three electric field regions are distinguished [197]. When compared to the linear electric field of strength  $E_0$  that is developed in between the detector's electrodes, the accumulation of negative charges (electrons) on the front of the avalanche will reinforce the effective electric field in between the anode and the avalanche front. Deeper in the gas volume, the positive charges (cations) slowly drift towards the cathode and can induce together with the avalanche front opposite electric field

loops. Finally, due to the density of positive charges, the electric field seen in between the ions tails and the cathode charged with negative charges is on average stronger than  $E_0$  and compensate for the locally reversed field  $E_2$ . By considering that  $10^6$  charges were contained in a sphere of radius  $r_d = 0.1$  mm Lippmann roughly estimated that the space charge effect could change the electric field by 3% and the Townsend and attachment coefficient up to 14% [197, 215].

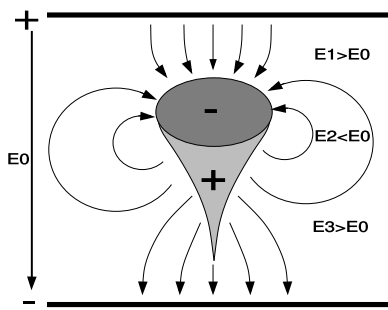


Figure 3.37: Schematic representation of an avalanche and of the electric field deformation it causes due to the local concentration of charge carriers [197].

To account for the space charge effect, the electric potential and field of free charges are solved and applied to each charge in the avalanche [197, 215]. The computation of these equations for each individual charge carrier to dynamically know the space charge field at every stage of an avalanche development is a difficult task and would require far too much computation time. A solution is to pre-compute an interpolation table keeping an adequately large number of values of the space charge field for each position in space. The values stored in the interpolation table then become very close to the analytic solution and allow for a much faster simulation.

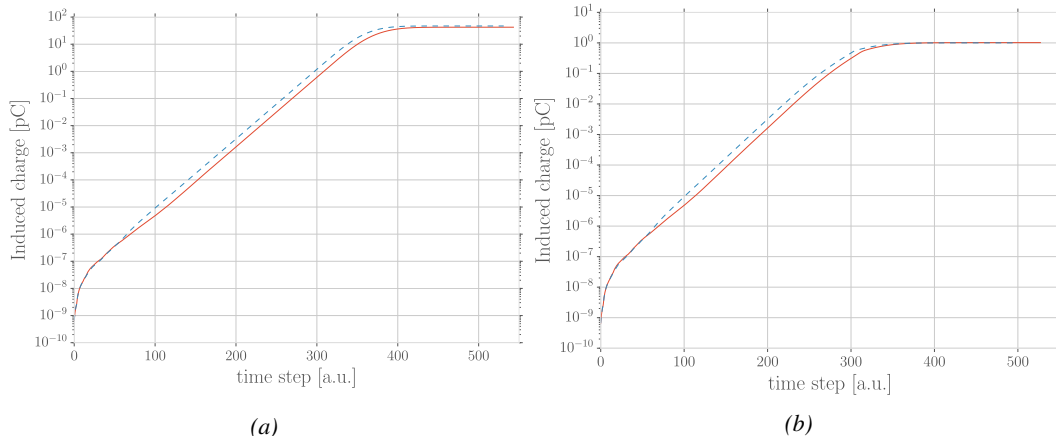


Figure 3.38: Evolution of the charge induced by an avalanche started by a single electron in a 1.2 mm thick RPC with an applied electric field of 54 kV/cm in the case space charge is not taken into account (a) and in the case it is implemented into the simulation (b). The total induced charge is correlated to the size of the avalanche [215].

The study of the space charge effect through simulation shows that it can lead to a saturation of the avalanche growth due to the deformation of the electric field, as showed through Figure 3.38. Additionally, a more precise understanding of the space charge effect is given through Figure 3.39 which looks at the distribution of charges and the distortion of the electric field at different steps of the evolution of an avalanche in a RPC. At the moment a 5 GeV muon ionizes the gas, electron-ion pairs are created in the gas in different clusters (Figure 3.39a). Later, the first clusters have reached the anode while the clusters that were created closest to the cathode are now big enough to start influencing the electric field in the gap (Figure 3.39b). When a cluster is big enough, the electric field

in front of it locally increases a lot and contributes to a stronger but very localised multiplication. At the same moment, the positive ions right behind the cluster avalanche front decrease the electric field, saturating the electron multiplication on the tail of the electron cloud (Figure 3.39c). Finally, when all the electrons have reached the anode and are recombining, the electric field still is very deformed by the distribution of both positive and negative ions in the gas volume closest to the anode (Figure 3.39d).

The electric field following the development of an avalanche can stay perturbed for a long time with respect to the avalanche development due to the slow drift of the much heavier ions. This can result in powerful secondary avalanches triggered by the fluctuation of the electric field together with the emission of UV-photons. This is a slow phenomenon compared to the development of avalanches. Experimentally, it is observed that the stronger the electric field applied over the gap, the sooner after the primary avalanche, referred to as *precursor signal* in this context, and the stronger the secondary avalanche will be. This could be due to the amount of UV-photons emitted by the growing precursor. These photons will be able to trigger new avalanches in a radius of a few mm around the precursor by knocking electrons from the cathode by photoelectric effect. The strong distortions of the electric field due to a large avalanche will be more likely to emit UV-photons as the electric field at the front of the precursor avalanche will be large, providing the electrons with a larger energy. Eventually, the new avalanches can grow to form streamers.

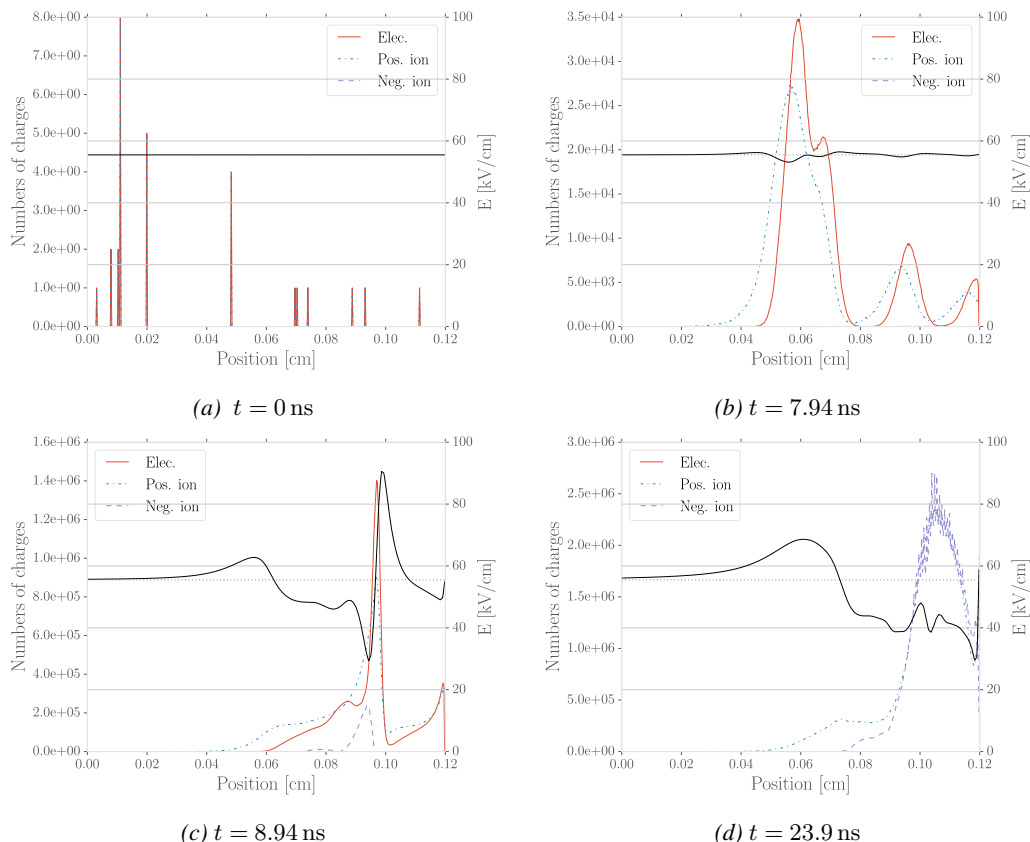


Figure 3.39: Distributions of charge carriers within the gas volume of a 1.2 mm thick RPC and the corresponding deformation of the electric field at different time steps with an applied electric field of 55.5 kV/cm [215].

### 3.4 Effect of atmospherical conditions

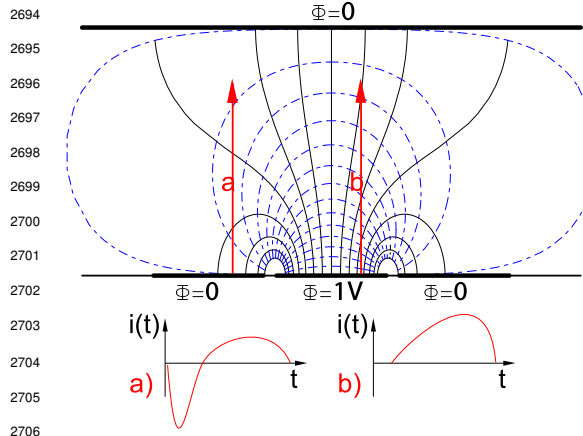


Figure 3.40: Representation of the weighting field in the volume of an RPC and the resulting induced current in the strip placed at 1 V and its neighbour connected to the ground. The induced current corresponds, as can be understood from Formula 3.22 [197].

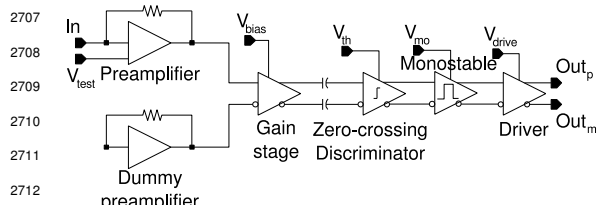


Figure 3.41: Schematics of CMS RPC FEE logic.

Formula 3.23.

$$(3.23) \quad Q(t) = \int_0^T \sum_{j=1}^{n_{Cl}} \vec{E}_{wj}(\vec{x}_j(t)) \cdot \vec{v}_{Dj}(t) e_0 N_j(t)$$

The signal induced in the readout of RPCs operated in avalanche mode is then sent into Front-End Electronics in which they will be pre-amplified and discriminated. The discrimination and digitization of signals in CMS FEE are described through Figure 3.41. On a first stage, analog signals are amplified, following the curve given on Figure 3.42, and then sent to a Constant Fraction Discriminator (CFD). At the end of the chain, 100 ns long pulses are sent to the LVDS output. The digital signals are both used as trigger for CMS and to evaluate the performance of the detectors. The performance will depend on the applied HV, i.e. on the electric field inside of the gas volume, but also on the threshold applied on the CFDs. Indeed, in order to reduce the probability to measure noise, the threshold is set to a level where the noise is strongly suppressed while the signals are not too affected. Typically, CMS FEEs are set to a threshold of 215 mV after pre-amplification, corresponding to an input charge of about 140 fC.

Accordingly to the Shockley-Ramo theorem, the movement of charge carriers, and in particular, the movement of a dense electron cloud toward the anode induces a current signal on one or more of the readout electrodes (strips or pads) [230, 231]. The ions, on the other hand, induce only a very small current as their movement is much slower than which of the electrons. The current induced by  $n_{Cl}$  clusters of  $N_j(t)$  charge carriers drifting at velocities  $\vec{v}_{Dj}(t) = \vec{x}_j(t)$  at a time  $t$  is given by Formula 3.22 in which  $e_0$  is the unit charge and  $\vec{E}_w$  is the weighting field.

(3.22)

$$i(t) = \sum_{j=1}^{n_{Cl}} \vec{E}_{wj}(\vec{x}_j(t)) \cdot \vec{v}_{Dj}(t) e_0 N_j(t)$$

The weighting field, depicted in Figure 3.40, corresponds to the electric field that would be observed in the gas gap if a readout electrode is placed at a potential of 1 V while keeping all the other electrodes grounded. Then the induced charge in the readout can be simply obtained by integrating Formula 3.22 over the duration  $T$  of the signal, as given by

The efficiency of a detector can be measured using a reference detector used as trigger as the ratio between the number of events recorded in coincidence in the detector and the reference and the total number of trigger events,  $\epsilon = n_{events}/n_{triggers}$ . An example of an efficiency measurement as a function of the effective voltage  $HV_{eff}$  is given in Figure 3.43. The data can be fitted with a sigmoidal function described as in Equation 3.24, where  $\epsilon_{max}$  is the maximal efficiency of the detector,  $\lambda$  is proportional to the slope at half maximum and  $HV_{50}$  is the value of the voltage when the efficiency reaches half of the maximum.

$$(3.24) \quad \epsilon(HV_{eff}) = \frac{\epsilon_{max}}{1 + e^{-\lambda(HV_{eff} - HV_{50})}}$$

CMS RPC also define two points on this sigmoid that called *knee* and *working point*.  $HV_{knee}$  is defined as the voltage at 95% of the maximum efficiency, and  $HV_{WP}$  is defined as in Formula 3.25.

$$(3.25) \quad HV_{WP} = HV_{knee} + \begin{cases} 100V & (\text{barrel}) \\ 150V & (\text{endcap}) \end{cases}$$

Nevertheless, the voltage applied on a detector may vary due to a change in environmental conditions. Indeed, the variation of temperature and/or pressure will have effect on the gas density and the electrode resistivity. This can be compensated by changing the electric field accordingly. The influence of variation in temperature and pressure are depicted respectively in Figure 3.44 and Figure 3.45. A standard procedure to correct for temperature and pressure variations is to keep the factor  $HV \cdot T/P$  constant using Formula 3.26 [232, 233] with reference values for  $T_0$  and  $P_0$ . For example, CMS uses  $T_0 = 293.15$  K and  $P_0 = 965$  hPa.

$$(3.26) \quad HV_{app} = HV_{eff} \frac{P_0}{P} \frac{T}{T_0}$$

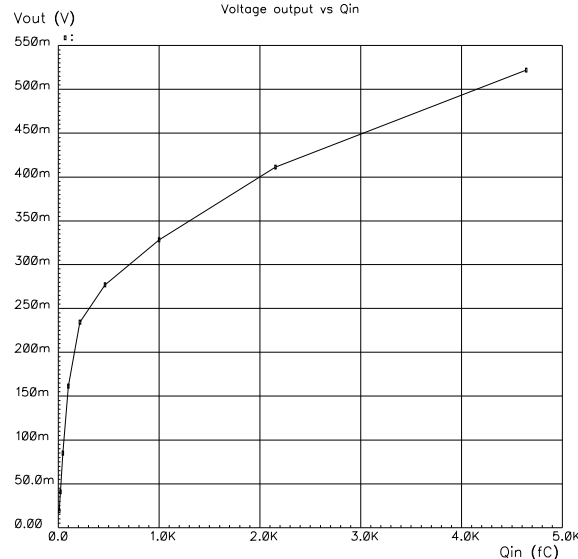


Figure 3.42: Equivalence in between the charge of the induced signal in input of the CMS FEE and the signal strength on the output of the pre-amplifier.

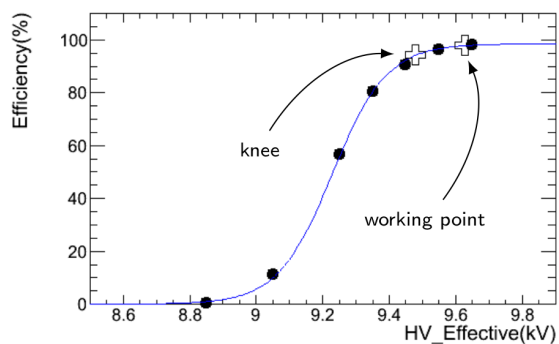
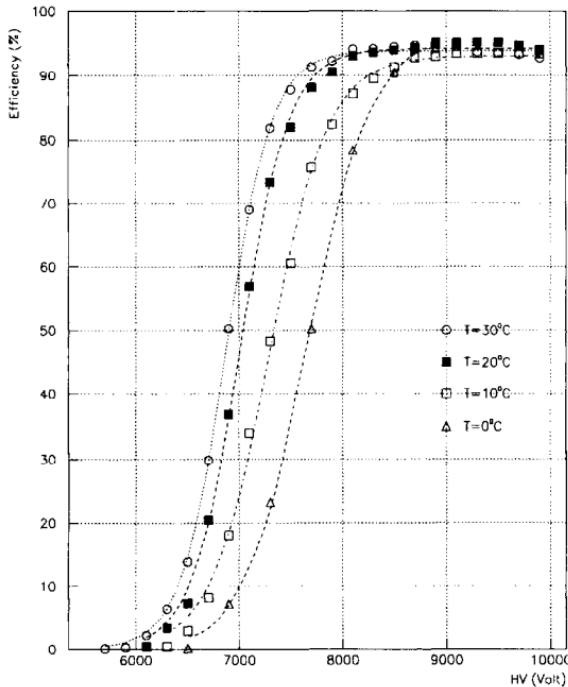
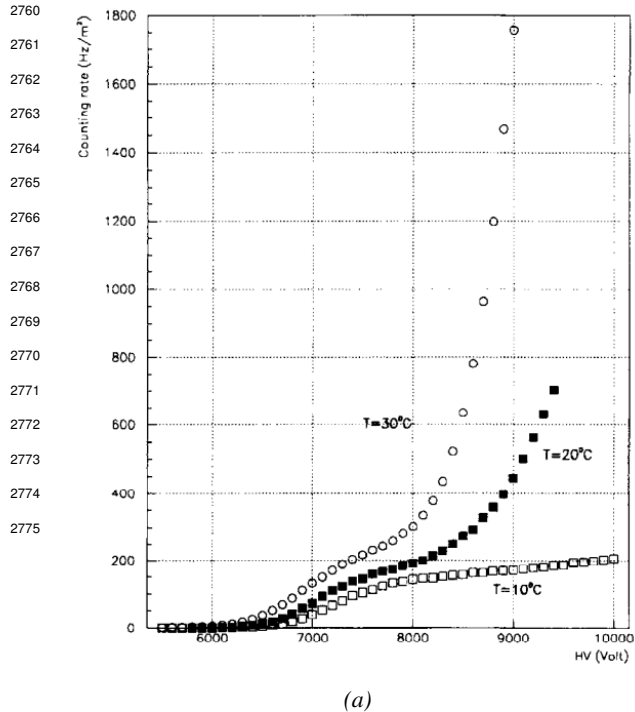


Figure 3.43: Typical efficiency sigmoid of a CMS RPC detector. The black dots correspond to the data, the blue line to the sigmoid fit and the open cross to the knee and working point extracted from the fit.



*Figure 3.44: Effect of the temperature variation on the rate (a) and the efficiency (b) of an RPC [232].*

It was actually found that such a simple procedure overcorrects the applied voltage in case the variations of temperature or pressure become significant [234–237]. CMS, considering that the temperature variations in the detector cavern were very small, decided only to improve the pressure correction, giving rise to Formula 3.27 [234] while on the other hand, ATLAS decided to have a more robust correction for both parameters and uses Formula 3.28 instead [237]. The coefficients  $\alpha$ , in the case of CMS, and  $\alpha, \beta$ , in the case of ATLAS, are extracted from a fit to data obtained during the operation of the detectors.

$$(3.27) \quad HV_{app} = HV_{eff} \left( 1 - \alpha + \alpha \frac{P_0}{P} \right) \frac{T}{T_0}$$

$$\alpha = 0.8$$

$$(3.28) \quad HV_{eff} = HV_{app} \left( 1 + \alpha \frac{\Delta T}{T_0} \right) \left( 1 - \beta \frac{\Delta P}{P_0} \right)$$

$$\alpha = 0.5, \beta = 0.71$$

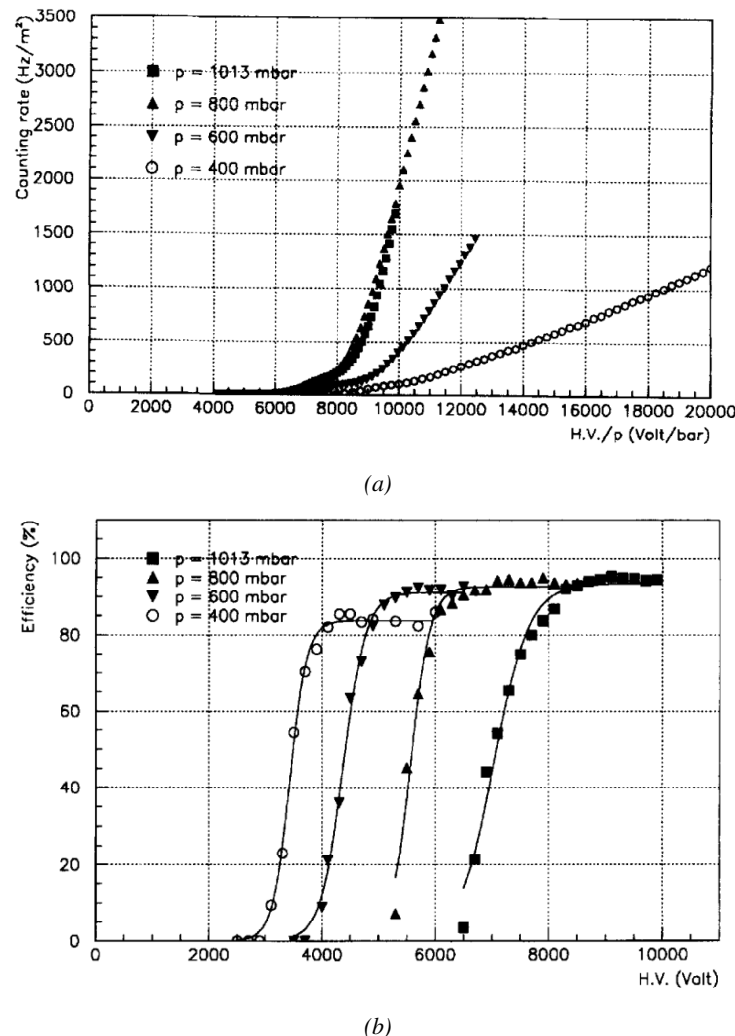


Figure 3.45: Effect of the pressure variation on the rate (a) and the efficiency (b) of an RPC [233].



# 4

2776

2777

## Muon Phase-2 Upgrade

2778 In Chapter 2, the timeline of the LHC has been described and the upcoming High Luminosity LHC  
2779 was introduced. LS3 has now started and the first HL-LHC related upgrade of CMS will take place.  
2780 In order to understand the context in which the work of this thesis was performed as well as its  
2781 motivations, it is necessary to give more insight into the reasons behind the increased instantaneous  
2782 luminosity of LHC. In a first section of the chapter, these motivations will be discussed.

2783 The muon system of CMS will then be presented in greater details than what was done in Chapter  
2784 ?? in order to have a better understanding of the need for upgrades of its different sub-systems in  
2785 the perspective of HL-LHC. Most of the detectors will require new electronics to adapt to the new  
2786 data flow and be integrated into a more robust trigger. Moreover, the redundancy of the muon system  
2787 in the endcaps will need to be improved. This will be achieved by the addition of new detectors.

2788 Finally, some insight will be given on ecofriendly gas studies for the specific case of Resistive  
2789 Plate Chambers. These studies don't fall into the scope of the HL-LHC upgrades but the necessity  
2790 of operating the detectors with gas mixtures that are more respectful of the environment is real. The  
2791 European union is starting to press the scientific community for solutions and the research institutes  
2792 are investing time into finding replacements to the gases used while maintaining similar working  
2793 performances.

### 2794 **4.1 Motivations for HL-LHC and the upgrade of CMS**

2795 As detailed in Section 2.2.2, the first data taking period, during which the LHC was only operated  
2796 at a center-of-mass energy of 7 TeV, took place until the start of LS1. It has been sufficient to  
2797 claim the discovery of a new  $125 \text{ GeV}/c^2$  particle compatible with the Higgs boson by both CMS  
2798 and ATLAS in July 2012 and hence achieve a major milestone in the history of science towards the  
2799 understanding of the fundamental nature of the universe. Nevertheless, the LHC machine holds the  
2800 potential to go further and help unravel the remaining mysteries the High-Energy Physics (HEP)  
2801 community is facing.

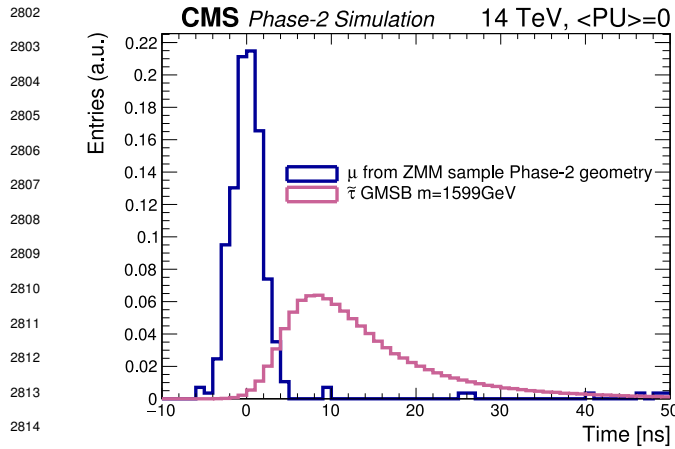


Figure 4.1: The measured transit time of an HSCP in CMS is compared to the transit time of a particle traveling at near the speed of light [177].

heavy gauge boson studies would also see their mass range limits pushed away by at least 1 TeV and could lead to a new breakthrough. Many of the Standard Model extensions discussed in Section 2.1.3 yield Heavy Stable Charged Particles (HSCPs), i.e. heavy long-lived particles. These particles would be produced at the LHC with a high momentum but a velocity significantly lower than the speed of light ( $\beta < 0.9$ ) [238–242] and/or a charge that differs from the elementary charge ( $|Q| = e$ ,  $|Q| < e$  or  $|Q| > e$ ) [241–246]. Depending on the model considered, HSCPs could be lepton-like heavy particles or on the contrary R-hadron, i.e. particles composed of a supersymmetric particle and at least one quark [241].

Over its full lifetime, the HL-LHC is expected to deliver an outstanding integrated luminosity of  $3000 \text{ fb}^{-1}$ , nearly an order of magnitude higher than what will be delivered by LHC until LS3 starts, as shown in Figure 2.20. In the case of Higgs studies, this will lead to measuring the couplings of the boson to a precision of 2 to 5%. Thanks to the estimated 15 millions of Higgs bosons created every year, a more precise measurement of potential deviations from the theoretical predictions is expected. The properties of the boson will hence be tested and compared to the SM Higgs neutral boson.

SUSY and

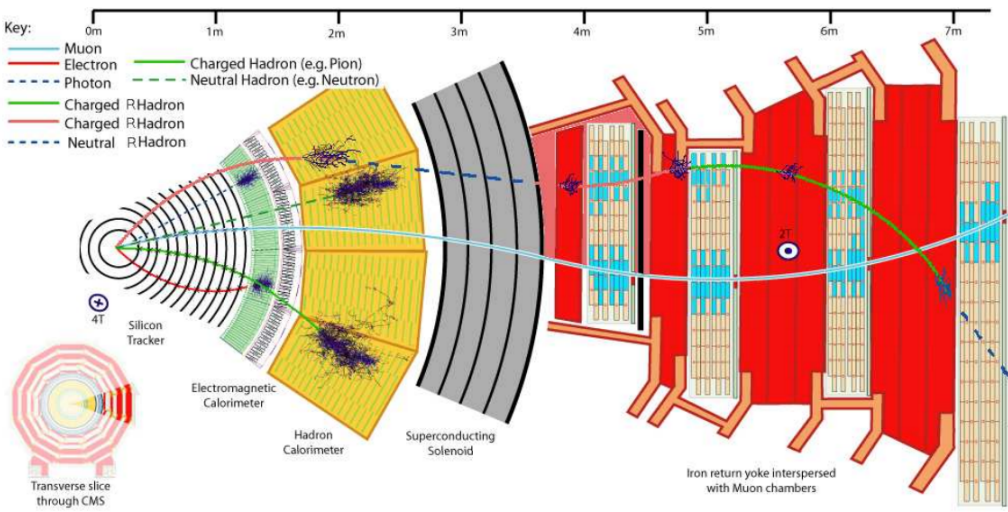


Figure 4.2: Slice of the CMS detector showing examples of passage of SM particles and R-hadrons. On the one hand, lepton-like HSCPs will appear to behave like slow and heavy muons. On the other hand, R-hadrons are likely to convert into other kind of charged or neutral R-hadrons due to interactions inside the detector volume.

2828 Due to lifetimes of the order of a few ns,  
 2829 HSCPs would travel for long enough distances  
 2830 to cross through entire typical collider detec-  
 2831 tors while appearing almost stable. Because  
 2832 of their low velocity, they can be reconstructed  
 2833 and assigned to bunch crossings different to  
 2834 the ones they effectively have been produced,  
 2835 as shown in Figure 4.1, if reconstructed at  
 2836 all. Indeed, the trigger algorithms in use at  
 2837 CMS were not designed for such slow parti-  
 2838 cles, and they assume most particles of inter-  
 2839 est will have a velocity close to the speed of  
 2840 light [242, 247].

2841 As HSCPs are long-lived particles, their  
 2842 identification would be possible thanks to the  
 2843 muon system. The main background will con-  
 2844 sist of wrongly measured muons which should  
 2845 have a lower transverse momentum, a near to  
 2846 speed-of-light velocity and a low ionisation  
 2847 energy loss. An example of passage of HSCPs  
 2848 through a slice of the CMS detector is showed  
 2849 in Figure 4.2. The tracks associated to the  
 2850 HSCPs would then have to be reconstructed in  
 2851 both the silicon detectors, for precise  $dE/dx$   
 2852 measurement, and the muon system detectors. In this case, the muon system will be used to perform  
 2853 Time-of-flight (ToF) measurements to discriminate between near speed-of-light particles and slower  
 2854 ones. The full reconstruction will then look for useful signatures such as the large transverse mo-  
 2855 mentum of the candidates, or their large ionisation energy loss alongside the low velocity accurately  
 2856 measured thanks to the muon system as depicted in Figure 4.3. The ToF measurement to identify  
 2857 beyond the Standard Model particles will mostly rely on the time information provided by the Drift  
 2858 Tubes, in the barrel region of the detector, and Cathode Strip Chambers, in the endcaps. From CMS  
 2859 point of view, it will then become necessary to increase the acceptance and redundancy of the end-  
 2860 caps toward higher pseudo-rapidity as the pseudo-rapidity region  $1.6 < |\eta| < 2.5$  is only covered  
 2861 by CSCs.

2862  
 2863 A natural consequence of the higher instantaneous luminosity will be the increase of collisions  
 2864 per bunch crossing. It is estimated that the pile-up will rise from the approximate average of 40  
 2865 collisions per bunch crossing in 2017 and 2018, presented in Figure 4.4, to 140 to 200 depending on  
 2866 the scenario considered [248]. The trigger rate will then be affected in the same way putting a lot  
 2867 of stress on the trigger algorithms. Upgrading the electronics of some of the detectors and working  
 2868 on the data flow within the experiment would help going through HL-LHC with keeping similar  
 2869 performance than during Phase-1. On the other hand, the impact of the increased background will  
 2870 become problematic in many ways and will force for upgrades or many sub-systems of CMS. The  
 2871 main effects will be a large increase of the irradiation of the detectors, mainly close to the beam  
 2872 line. Both the detectors already installed and the new detectors that will extend the coverage of the

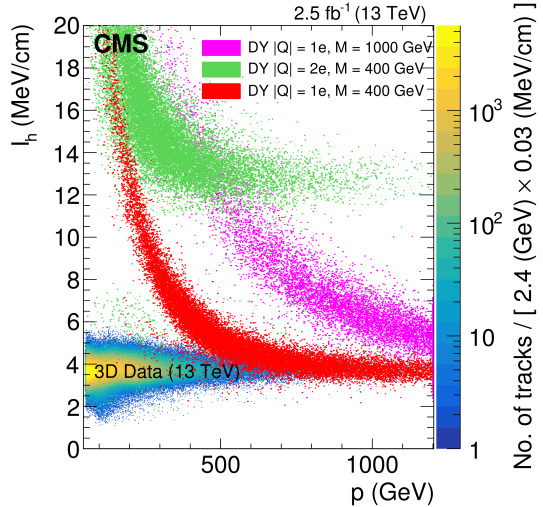


Figure 4.3: Distribution of the energy-loss  $dE/dx$  as described by Bethe-Bloch formula through the estimator  $I_h$  with increasing particle momentum for tracks in the 13 TeV data. The estimator depends on the charge deposition of the particles per unit length in the silicon detectors of CMS which is related to their energy loss as explained in a publication by the CMS Collaboration [241]. The simulated HSCPs are singly or multiply charged particles with masses of 400 and 1000 GeV.

muon system toward higher pseudo-rapidity need to be certified for the irradiation levels they will be subjected to until the end of HL-LHC. Simulations of the expected distribution of absorbed dose in the CMS detector under HL-LHC conditions show, in Figure 4.5, that detectors placed close to the beam line will have to withstand high irradiation, the radiation dose being of the order of a few tens of Gy.

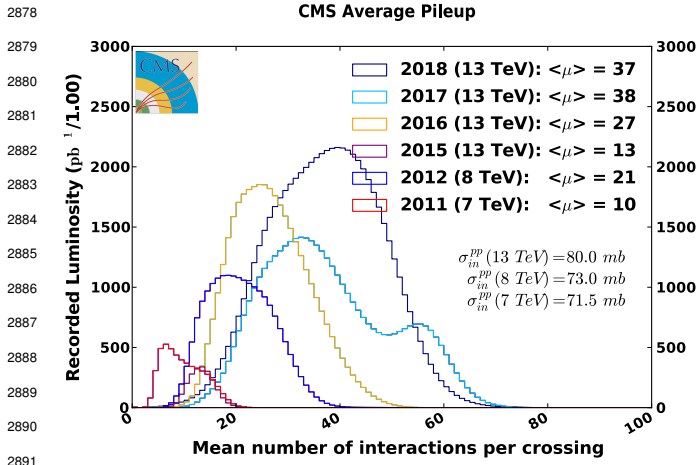


Figure 4.4: Distribution of the average number of interactions per crossing (pileup) for pp-collisions in 2011 (red), 2012 (blue), 2015 (purple), 2016 (orange), 2017 (light blue), and 2018 (navy blue). The overall mean values and the minimum bias cross sections are also shown [249].

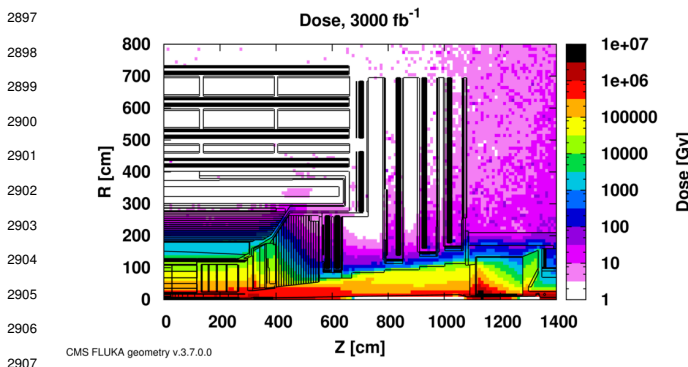


Figure 4.5: Absorbed dose in the CMS Cavern after an integrated luminosity of  $3000 \text{ fb}^{-1}$ . Using the interaction point as reference,  $R$  is the transverse distance from the beamline and  $Z$  is the distance along the beamline [177].

4.0 but the identification of muons and measurement of their energy with reasonable precision only using the tracker is nearly impossible. Thus, this increased tracker coverage range needs to be put in parallel with a matching muon detector and will open doors to multi-lepton final states in which leptons are likely to have a low transverse momentum and to be found near the beam line.

Finally, as the muon system is composed only of gaseous detectors, strong environmental concerns have risen over the last years as the European directives will restrict the use of fluorine based gas mixtures. Both the CSC and RPC subsystems, using  $CF_4$ ,  $C_2H_2F_4$ , or  $SF_6$ , will need to adapt

Improving this situation will come with the increase of hit numbers recorded along the particle track to reduce the ambiguity on muon versus background detection. Moreover, the measurement of small production cross-section and/or decay branching ratio processes, such as the Higgs boson coupling to charge leptons, and in particular to muons, or the  $B_s \rightarrow \mu^+ \mu^-$  decay, is of major interest. Such considerations give more weight to the upgrade of the forward regions to maximize the physics acceptance to the largest possible solid angle.

To ensure proper trigger performance within the present coverage, the muon system will be completed with new chambers, and the electronics of the present system will need to be upgraded. A first step into this direction will be taken by installing new gaseous detectors in each endcap layer and extend the coverage up to  $|\eta| = 2.8$ . Nevertheless, the region beyond  $|\eta| > 2.8$  and extending to  $|\eta| = 5.0$  only is covered by the forward HCAL detectors and lack redundant muon detector coverage. Extensions of the tracker in the context of HL-LHC will increase its coverage up to  $|\eta| =$

their working gas in order to strongly reduce the greenhouse potential of the mixtures released into the atmosphere due to gas leaks.

## 4.2 Necessity for improved electronics

Drift Tubes and Cathode Strip Chambers are important components used to identify and measure muons, especially thanks to their spatial resolution of the order of 100  $\mu\text{m}$ . Nevertheless, the luminosity and irradiation during HL-LHC will cause serious event loss and ageing on the electronics of these subsystems that will comprise the triggering and data transferring needs of CMS. Thus, electronics upgrade is foreseen to address these expected problems. While only the RPCs' electronic system is able to operate under Phase-2 requirements [250], DTs and CSCs will need to improve their trigger acceptance rate and latency to ensure that the Level-1 trigger threshold can stay at the same level [251]. The Level-1 trigger consists of custom hardware processors receiving data from the calorimeters and the muon system. In return, they generate a trigger signal within 3  $\mu\text{s}$ , with a maximum rate of 100 kHz. In the perspective of HL-LHC, each subsystem needs to achieve a minimum rate of 500 kHz with a latency not greater than 12.5  $\mu\text{s}$ . DTs and CSCs will also need to improve their Data Acquisition (DAQ) transfer rate to reach a minimum near 1 Tbit/s. The foreseen upgrades are expected to exceed the requirements.

The first version of Minicrate electronics (MiC1) used by DTs don't allow for high enough trigger rate. In addition to this problem, it was shown that these electronics contain components that are not radiation hard enough to sustain HL-LHC conditions and hence, a too large number of channels may fail due to radiations as showed in Figure 4.6. The MiC1 will be replaced on each detector by an improved version referred to as MiC2 while Front-End Electronics (FEE) and High Voltage (HV) modules will not need any replacement. On the other hand, CSCs showed that their electronics would be

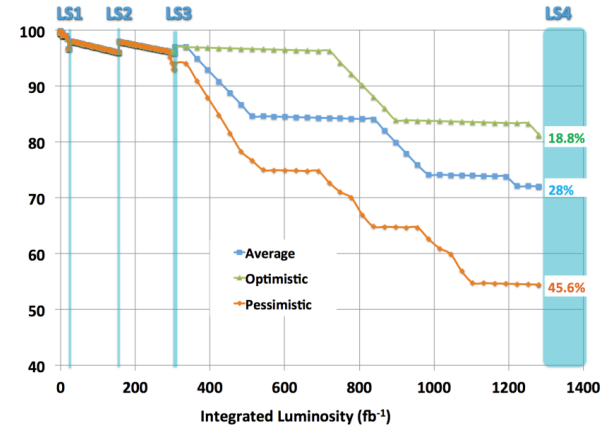


Figure 4.6: Extrapolated fraction of failing channels of the present DT MiC1 electronics as a function of the integrated luminosity for different scenarios until LS4 [177].

The first version of Minicrate electronics (MiC1) used by DTs don't allow for high enough trigger rate. In addition to this problem, it was shown that these electronics contain components that are not radiation hard enough to sustain HL-LHC conditions and hence, a too large number of channels may fail due to radiations as showed in Figure 4.6. The MiC1 will be replaced on each detector by an improved version referred to as MiC2 while Front-End Electronics (FEE) and High Voltage (HV) modules will not need any replacement. On the other hand, CSCs showed that their electronics would be

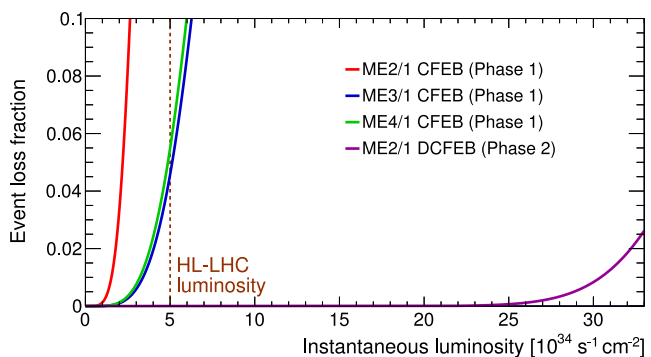


Figure 4.7: The event loss fractions as a function of the instantaneous luminosity is compared for CFEBs (Phase-1) and DCFEBs (Phase-2) at different CSC locations. HL-LHC luminosity is marked with the dashed brown line [177].

able to live through the 10 years of Phase-2, but the limited buffer depth might cause memory overflows and read-out inefficiencies with a fraction of event loss ranging from 5 to more than 10% at an instantaneous luminosity similar to which of HL-LHC depending on the expected background. The replacement of CSCs' CFEBs by digital ones, DCFEBs, with a deeper buffer would permit to make event loss negligible and satisfy HL-LHC requirements as can be seen in Figure 4.7. All these new DT and CSC electronics will be connected to the trigger electronics via optical links to ensure a faster communication [177].

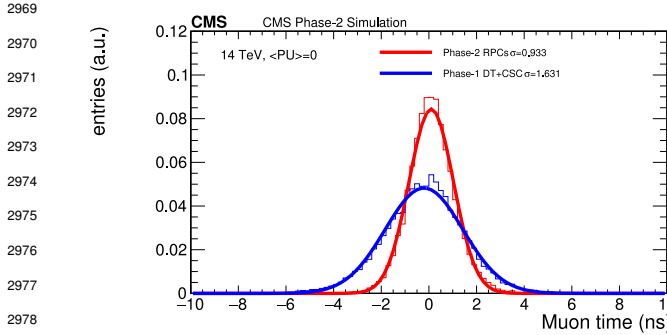


Figure 4.8: Comparison of the simulated time residuals in between reconstructed and true muon times without (blue) and with (red) the upgraded RPC link system [177].

components may become the source of failing channels throughout Phase-2. Moreover, these link boards were originally designed only to match RPC digitized signals with the corresponding bunch crossing. Due to this feature, the time resolution of the full RPC chain is hence limited to 25 ns and does not make use of the full time resolution of the detectors. The time resolution foreseen after the upgrade can be seen through Figure 4.8 and is of the order of 1 ns.

The upgrade on the side of Resistive Plate Chambers will not be done at the level of the electronics but rather that of the Link System located in the service cavern of CMS. RPC Link System connects the front-end electronics data of RPCs into CMS trigger processors. The main motivation for such an upgrade is that the electronic board composing the link system are built using obsolete and/or weak components that can easily suffer from the electromagnetic noise. These components

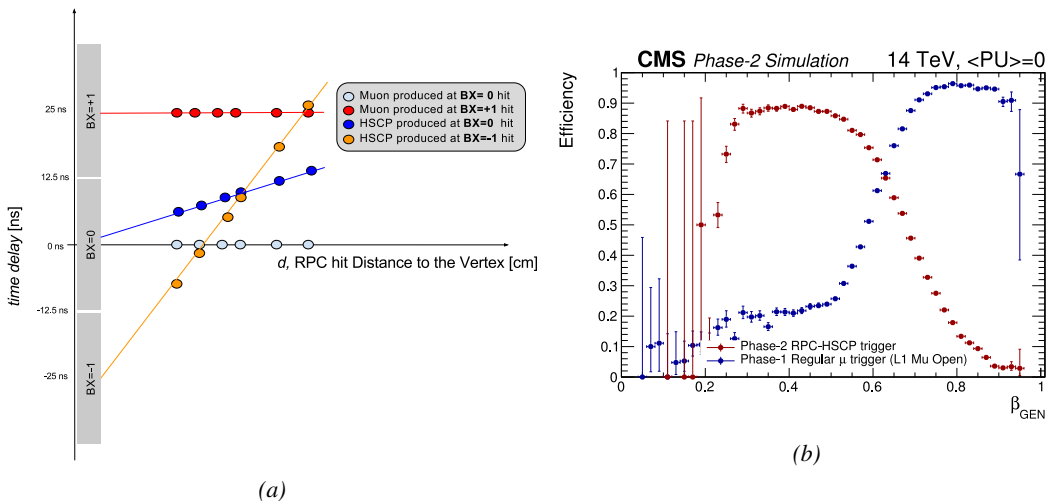


Figure 4.9: (a): Time delay with respect to a particle traveling at the speed of light measured at consecutive RPC stations for particles originating at different bunch crossings and traveling at different velocities [177]. (b): In blue is showed the standard Level-1 muon trigger efficiency as a function of  $\beta$  and in blue is showed the RPC-HSCP trigger efficiency after upgrade of the RPC Link System [177].

The exploitation of the full time resolution would make the synchronization of the RPC system easier and allow to have a finer offline out-of-time background removal within the 25 ns between consecutive bunch crossings. Moreover, this would greatly improve the trigger and reconstruction on HSCPs. Using the TOF information in between consecutive RPC stations, the minimal particle velocity than could be probed will drop from approximately 0.6 to 0.25 times the speed of light as showed in Figure 4.9. Upgrading RPC link system will require the installation of 1376 new link boards and 216 control boards. The new boards will make use of the recent progress made with fast FPGAs and will be a great improvement to the ASICs formerly used as they will be able to process signals from several detectors in parallel.

### 4.3 New detectors and increased acceptance

In the present muon system, the redundancy is assured by RPCs used for their robust bunch crossing assignments. The extension of the muon system towards higher pseudo-rapidity in an effort to complete the redundancy and to contribute to the precision of muon momentum measurements will require muon chambers with a spatial resolution less or comparable to the multiple scattering muons are subjected to while traveling through the detector volume [192].

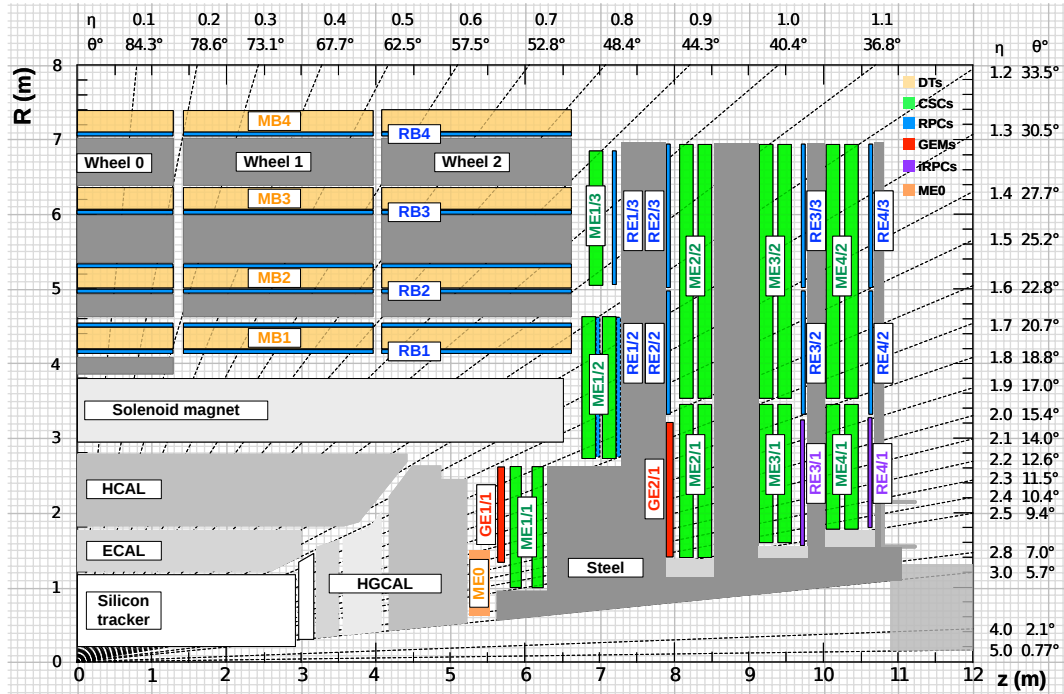


Figure 4.10: A quadrant of the muon system, showing DTs (yellow), RPCs (blue), and CSCs (green). The locations of new forward muon detectors for Phase-2 are contained within the dashed box and indicated in red for GEM stations (ME0, GE1/1, and GE2/1) and dark blue for improved RPC (iRPC) stations (RE3/1 and RE4/1).

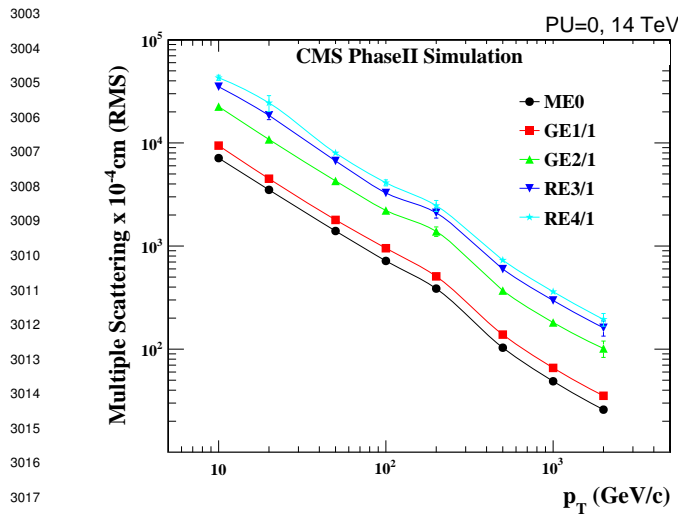


Figure 4.11: RMS of the multiple scattering displacement as a function of muon  $p_T$  for the proposed forward muon stations. All of the electromagnetic processes such as bremsstrahlung and magnetic field effect are included in the simulation.

showed by the simulation in Figure 4.11. Indeed, most of the plausible physics will be covered only considering muons with  $p_T < 100$  GeV.

### 3025 4.3.1 Gas electron multipliers

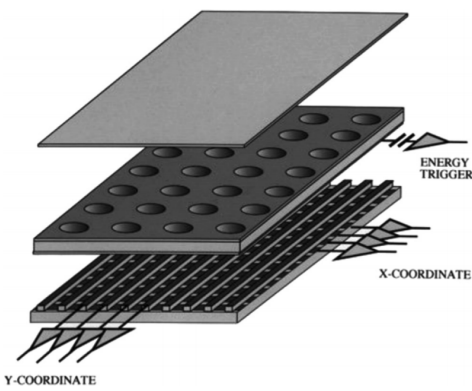


Figure 4.12: Schematics of a GEM. On top is the cathode and on the bottom, the anode on which a 2D readout is installed. Finally, the GEM foil separates the gas volume into the drift region, in between the cathode and the foil, and the induction region, in between the foil and the anode. A negative voltage is applied on the cathode. The anode is connected to the ground.

volume is confined between two planar electrodes, the anode serving as read-out panel. The gas vol-

Figure 4.10 shows a similar quadrant of CMS than the one presented in Figure 2.27 with the addition of Gas Electron Multiplier (GEM) (ME0, GE1/1 and GE2/1) and improved RPC (iRPC) (RE3/1 and RE4/1) in the pseudo-rapidity region  $1.6 < |\eta| < 2.4$ . The completion of the redundancy was already scheduled in the original CMS Technical Proposal [252] but never addressed. The coming Phase-2I is then the occasion to equip the region with the newest GEM and RPC technology. In order to match CMS requirements, a spatial resolution of  $\mathcal{O}(\text{few mm})$  will be necessary for the proposed new RPC stations while the GEMs will need a resolution better than 1 mm, as

In the region closer to the interaction point where the spatial resolution is requested for the new detectors to be better than 1 mm (at least for ME0 and GE1/1 according to Figure 4.11) and where the background rate will be the highest for muon detectors, the choice has been made to use triple GEMs, micro pattern gaseous detectors, instead of the originally planned RPCs. The GE1/1 project has been the first to be approved and demonstrators have been installed in CMS already during LS1. The rest of the detectors will be installed during LS2 while the GE2/1 and ME0 projects are still under development. ME0, GE1/1 and GE2/1 will be installed respectively close to the HCAL endcap, on the first and on the second muon endcap disks as can be seen from Figure 4.10. Gas Electron Multipliers are gaseous detectors [253] whose gas

3046 ume is divided in two or more regions by a single or multiple *GEM foils* as showed in Figure 4.12.

3047 These foils are very thin, of the order of a  
 3048 few tens of  $\mu\text{m}$ , and are pierced with holes as  
 3049 can be seen in Figure 4.13. Both surfaces of  
 3050 the GEM foils are clad with copper in order  
 3051 to apply a strong electric field in between each  
 3052 side that will generate very strong potentials  
 3053 in the holes. The gas region contained in be-  
 3054 tween the cathode and the GEM foil is called  
 3055 the drift region as the electric field is not strong  
 3056 enough to cause avalanches and thus start an  
 3057 amplification. The primary electrons drift to-  
 3058 ward the foil and are accelerated and amplified  
 3059 by the very high potential within the holes,  
 3060 as showed in Figure 4.13. Then the electrons  
 3061 reach the second drift region where they will  
 3062 induce a signal on the read-out located on the  
 3063 anode. By restraining the amplification pro-  
 3064 cess at the level of the holes, the electrons  
 3065 can stay confined in a very little space and  
 3066 thus induce a very localized current, provid-  
 3067 ing the GEMs with a very good spatial res-  
 3068 olution. The process can be repeated several  
 3069 times in a row, in order to achieve a stronger  
 3070 amplification. The GEMs that will be used in  
 3071 CMS are triple-GEM detectors operated with  
 3072 a 70/30 gas mixture of  $\text{Ar}/\text{CO}_2$ . They con-  
 3073 tain three GEM foils and hence three electron  
 3074 amplifications, as can be seen in Figure 4.14.

3075 The GEM foils used in CMS are  
 3076 50  $\mu\text{m}$  foils clad with 5  $\mu\text{m}$  of copper  
 3077 on each side. The foils are pierced  
 3078 with double-canonical holes which  
 3079 inner and outer diameters are re-  
 3080 spectively 50 and 70  $\mu\text{m}$  which are  
 3081 placed 140  $\mu\text{m}$  from each other in  
 3082 a hexagonal pattern, as showed in  
 3083 Figure 4.13. These detectors have a  
 3084 time resolution better than 10 ns and  
 3085 reach very good spatial resolutions  
 3086 of less than 200  $\mu\text{rad}$  as indeed the  
 3087 position of the hits is not measured  
 3088 along the strips but following the az-  
 3089 imuthal angle granularity of the ra-  
 3090 dially organized trapezoidal strips.

3091 The GEM Upgrade project started with GE1/1 [254]. GE1/1 detectors will already be installed

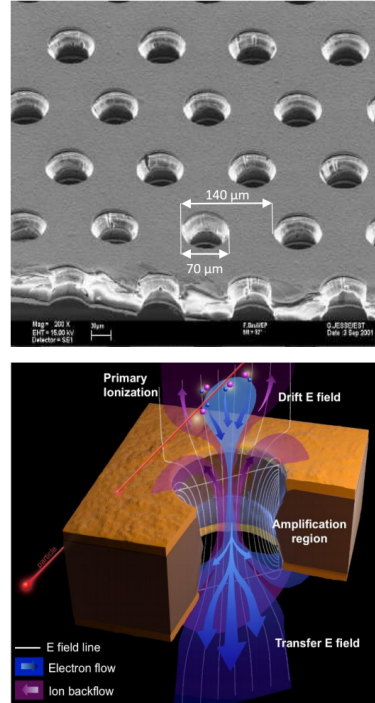


Figure 4.13: Top: Picture of a CMS GEM foil provided by a scanning electron microscope. Bottom: Representation of the electric field in a GEM hole and of the amplification electrons and ions undergo due to the very intense electric field.

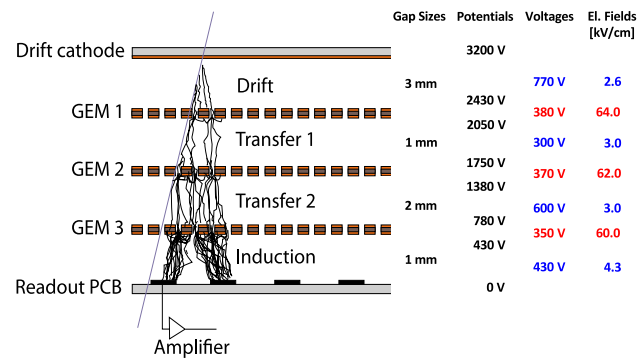


Figure 4.14: The gas volume of CMS triple-GEMs is divided into four areas. Primary electrons are created in the Drift area and amplified by three GEM-foils while drifting through Transfer areas. Reaching the Induction area, the avalanche induces current in the read-out. The typical dimensions and potentials are provided.

3092 during LS2. GE2/1 and ME0, on the other hand, will profit of the R&D knowledge and skills  
 3093 developed for GE1/1 while the requirements for each subsystem are different as they are not placed  
 3094 at the same distance from the interaction point. In this very forward region, a different position with  
 3095 respect to the center of the detector can dramatically change the conditions in which the detectors  
 3096 will have to be operated. In terms of rate capability, GE2/1, which is the furthest, is required to  
 3097 withstand  $2.1 \text{ kHz/cm}^2$  while GE1/1 needs to be better than  $10 \text{ kHz/cm}^2$  and ME0, better than  
 3098  $150 \text{ kHz/cm}^2$ . In terms of ageing with respect to charge deposition, ME0 needs to be certified to  
 3099  $840 \text{ mC/cm}^2$ , GE1/1 to  $200 \text{ mC/cm}^2$  and GE2/1 only to  $9 \text{ mC/cm}^2$ . All 3 detectors need to have a  
 3100 time resolution better than 10 ns and an angular resolution better than  $500 \mu\text{rad}$ .

3101 On each GE1/1 ring, 36 super chambers, consisting of two single GEM layers and spanning  $10^\circ$ ,  
 3102 will be installed covering the pseudo-rapidity region  $1.6 < |\eta| < 2.2$  together with ME1/1 CSCs.  
 3103 The reach of the muon system will be improved thanks to the GE2/1 that will overlap with the GE1/1  
 3104 and cover a region from  $|\eta| > 1.6$  to  $|\eta| < 2.4$  and complete the redundancy of ME2/1. The super  
 3105 chambers, built with two triple-GEM layers each consisting of four single GEM modules due to  
 3106 the rather large surface of the GE2/1 chambers, that will be installed on the first ring of the second  
 3107 endcap will span  $20^\circ$  each. Hence, a total of 72 chambers will be assembled to equip the muon  
 3108 system. Finally, the ME0 installed near the HCAL endcap will cover the region  $2.0 < |\eta| < 2.8$ .  
 3109 This subsystem will consist in super modules of six layers of triple-GEM detectors covering an  
 3110 azimuthal angle of  $20^\circ$  leading to the construction of 216 single detectors.

3111 Adding the GEMs into the forward region of the muon system will allow to strongly enhance  
 3112 the Level-1 Trigger performance as shown in Figure 4.15. In the region  $1.6 < |\eta| < 2.4$ , the trigger  
 3113 efficiency of the current system would lie between 80 and 90% under HL-LHC conditions. The  
 3114 installation of GEMs would bring the efficiency to a consistent 92 to 94% on the entire region. At  
 3115 the same time, the trigger rate is expected to fluctuate from 3 to 10 kHz with the current system  
 3116 alone. The addition of detectors to complete the redundancy would allow keeping the rate mostly  
 3117 under 2 kHz. Moreover, benefiting from the good spatial and angular resolution of the GEMs, the  
 3118 precision into the muon measurement will also be improved by an order of magnitude thanks to the  
 3119 addition of GEMs as can be seen from the simulation presented in Figure 4.16.

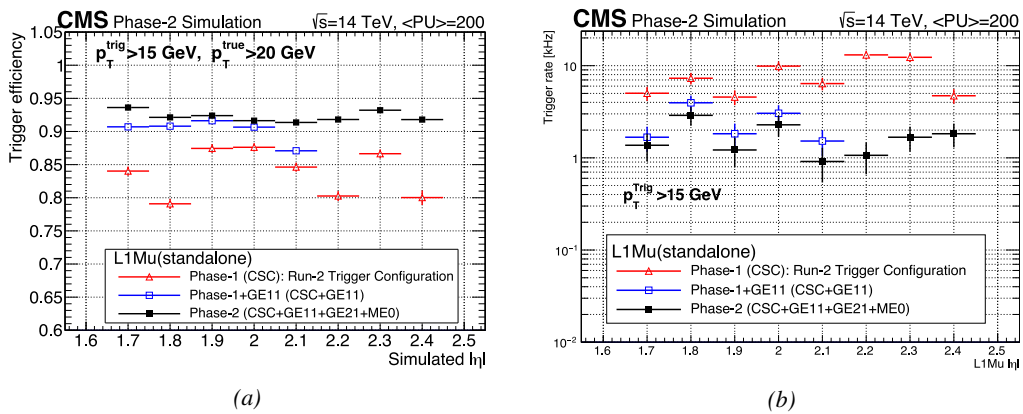


Figure 4.15: Simulated (a) efficiency and (b) rate of the standalone Level-1 muon trigger using tracks reconstructed in CSCs and all GEM stations compared with Phase-I values in the case where only CSCs are used or CSCs+GE1/1. The zones of inefficiency of the CSC subsystem are compensated by the addition of GEMs during Phase-2 and the trigger rates is kept from increasing due to the high luminosity [177].

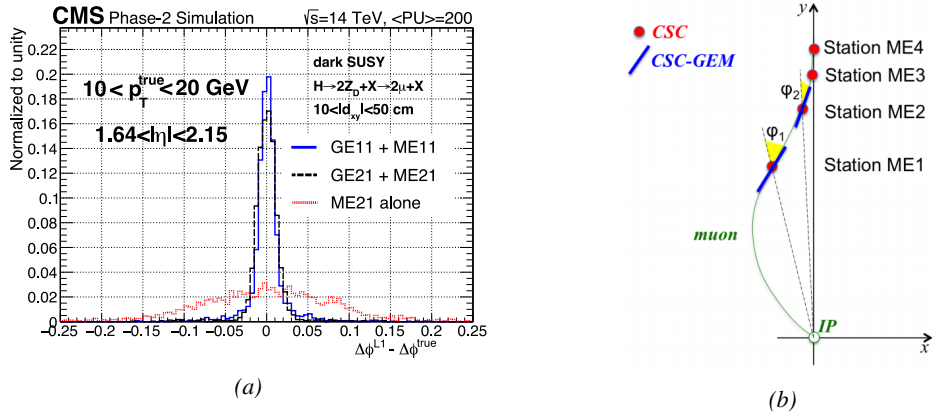


Figure 4.16: (a): Simulated resolution of the muon direction measurement  $\Delta\phi$  with Phase-2 conditions. In the second endcap station, the resolution is compared in the case of CSCs (ME2/1) alone and CSCs+GEMs (GE2/1+ME2/1) while a similar resolution measurement is given in the case of the first station (GE1/1+ME1/1) [177]. (b): The addition of GEM detectors on stations 1 and 2 (ME0 is considered to contribute to station 1) as redundant system to CSCs allows improving the muon momentum improvement through a more accurate measurement of the local bending angles  $\phi_1$  and  $\phi_2$  [177].

### 3120 4.3.2 Improved forward resistive plate chambers

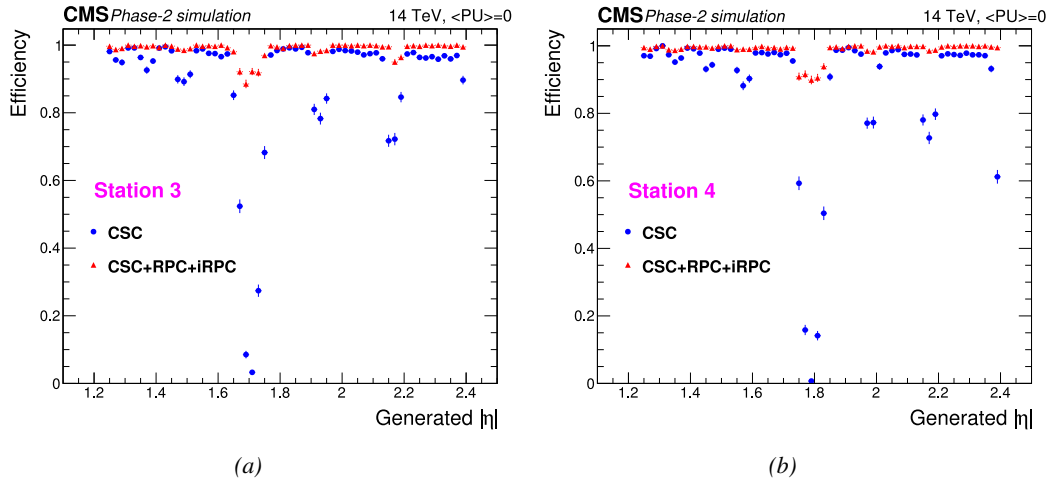


Figure 4.17: Simulation of the impact of RPC hit inclusion onto the local trigger primitive efficiency in station 3 (a) and station 4 (b) [177]. The contribution of iRPC starts above  $|\eta| = 1.8$ .

3121 Figure 4.10 shows that the iRPCs that will equip the third and fourth endcap disks in position RE3/1  
 3122 and RE4/1 will finally be the partners of the CSCs in position ME3/1 and ME4/1. They will complete  
 3123 Phase-1 plans by bringing the needed upgrades in the perspective of Phase-2 as the older chambers  
 3124 are not suitable to equip the forward region of CMS due to HL-LHC rates and charge deposition.  
 3125 By completing the redundancy, more hits along the muon track will be available and the lever arm  
 3126 will be improved. The benefits from extending the redundancy of the muon system with iRPCs to

3127 the forward most region is shown in Figure 4.17 in which the trigger efficiency is presented with and  
 3128 without RPCs. It is possible to see that the efficiency of the CMS muon trigger with the complete  
 3129 redundancy is consistently improved to a level above 95% in the region  $|\eta| > 1.8$  as the iRPCs help  
 3130 filling the holes in the CSC system.

3131 The detectors that will be installed in the coming years will have similarities with the already  
 3132 existing RPC system. 18 of the new chambers, each spanning  $20^\circ$  in  $\varphi$  around the beam axis with  
 3133 96 radially oriented trapezoidal read-out strips, will cover each muon endcap disk leading to the  
 3134 production of 72 iRPCs. The main difference with the old RPC detectors will be found at the level  
 3135 of the read-out panels. Indeed, the new chambers will not feature read-out strips segmented in  $\eta$   
 3136 but rather will favor a read-out on both strip ends to determine the position of the hits along the  
 3137 chamber. By using fast front-end electronics a radial spatial resolution of the order of 2 cm could  
 3138 be achieved to contribute to the better reconstruction of muons in the forward region where the  
 3139 bending due to the magnetic field is low. This technical choice is motivated by the fact that, in  
 3140 the case a  $\eta$  segmentation were to be used, at least five pseudo-rapidity partitions would have been  
 3141 necessary to reach the minimal radial spatial resolution ( $\approx 20$  cm). Having only one strip along the  
 3142 chamber read-out from both ends reduces by 60% the total number of channels and the necessary  
 3143 cabling, and allows for a better spatial resolution. The strip pitch will range from 6.0 mm (5.9 mm)  
 3144 on the high pseudo-rapidity end to 12.3 mm (10.9 mm) on the low one on position RE3/1 (RE4/1).  
 3145 The spatial resolution in the direction perpendicular to the strips should reach approximately 3 mm,  
 3146 better than the minimal needed resolution (Figure 4.11). Finally, the overall time resolution of the  
 3147 new installation will be equally 1 ns, as for the present due to the same link system being used even  
 3148 though the detector itself can achieve a time resolution of less than 100 ps, necessary for a spatial  
 3149 reconstruction of the hits with a resolution of 2 cm or less along the strip length.

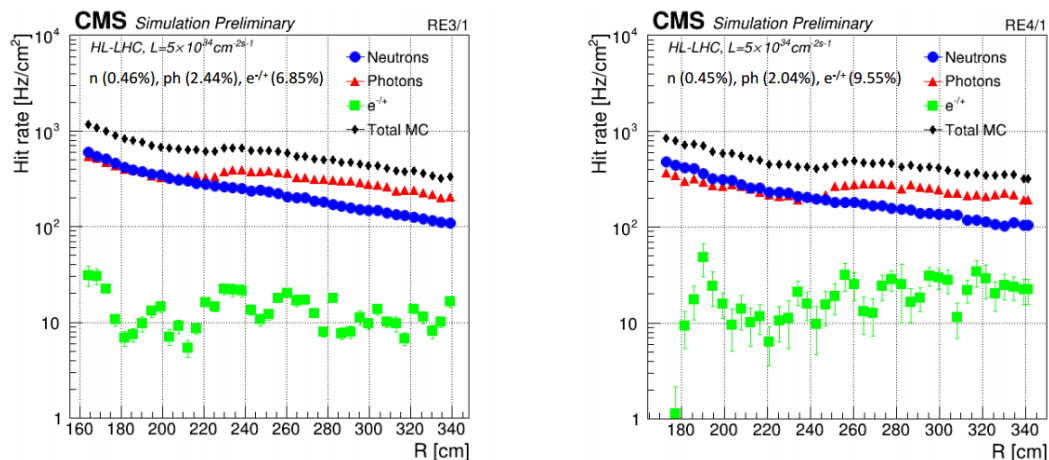


Figure 4.18: Expected hit rate due to neutrons, photons, electrons and positrons at HL-HLC instantaneous luminosity of  $5 \times 10^{34} \text{ cm}^{-2}\text{s}^{-1}$  in RE3/1 and RE4/1 chambers [255, 256]. The sensitivities of iRPCs used in the simulation for each particle are reported and differ from one endcap disk to another as the energies of the considered particles varies with the increasing distance from the interaction point.

3150 Having only a single strip instead of pseudo-rapidity segmentation will increase the probability  
 3151 of double hits in the same channel. The probability was estimated to be low enough as it shouldn't  
 3152 exceed 0.7%. This estimation was made assuming an average hit rate per unit area of  $600 \text{ Hz/cm}^2$

in the iRPCs (see Figure 4.18), a cluster size (average number of strips fired per muon) of 2, a strip active area of  $158.4 \times 0.87 \text{ cm}^2$  and a safety factor 3. The corresponding rate per strip is estimated to be 380 kHz leading to an average time interval in between two consecutive hits of 2600 ns. This is compared to the minimal time interval of 16 ns necessary to avoid ambiguities. Indeed, a maximum of 10 ns is spent by the signal traveling through the strip to reach the electronics to which can be added 1 ns of dead time and 2 Time-to-Digital Converter (TDC) clock cycles of 2.5 ns to convert the signal arrival time into a digital value in the FEEs. The probability of having ambiguous double hits in a strip is then the ratio between the minimal time interval in between two consecutive hits and the average time interval estimated from the rate the detectors would be subjected to.

The instantaneous luminosity at HL-LHC being very high, the rates at the position of the new chambers needed to be simulated in order to understand the necessary requirements for these detectors. The simulated results for different background components (neutrons, photons, electrons and positrons) are shown in Figure 4.18 assuming known sensitivities to these particles. It is shown that on average over the iRPC areas the rates would be of the order of  $600 \text{ Hz/cm}^2$  ( $600 \text{ Hz/cm}^2$  seen in RE3/1 and  $480 \text{ Hz/cm}^2$  in RE4/1) [255, 256]. Thus, taking into account a safety factor of about 3, it was decided that improved RPCs should at least be certified for rates reaching  $2 \text{ Hz/cm}^2$  which will be achieved thanks to several improvements on the design and on the electronics. The detectors design will be based on the existing RPCs as they will also feature double RPC gaps. Similarly to the existing RPC system, the electrode material will be HPL although the thickness of the electrodes and of the gas gap will be reduced to 1.4 mm as a thinner gas gap leads to a decrease of deposited charge per avalanche as showed in Figure 4.19. The charge deposition in the case of 1.4 mm thick electrodes is reduced by a factor greater than 5 when compared to 2 mm electrodes at a similar electric field. The smaller the gas gap, the more the detector becomes sensitive to gap non-uniformities across the electrode planes, making a gap of 1.4 mm a good compromise in between these two competing factors.

A lower charge deposition inside of the detector volume means a slower ageing and a longer lifetime for detectors subjected to high irradiation. But, in order to take advantage of the lower detector gain, more sensitive electronics are required such that part of the gain that was formerly achieved in the gas volume can be moved to the electronics. Achieving this with the technology developed more than ten years ago for the present system is not possible as the signal over noise ratio of such electronics doesn't allow to detect charges as low as 10 fC. Moreover, the new front-end electronics will need to be radiation hard to survive more than ten years of HL-LHC conditions. The new technology that has been chosen is based on the PETIROC ASIC manufactured by OMEGA and is a 64-channel ASIC called CMS RPCROC[177, 257, 258]. The properties of these electronics will be discussed in Chapter 6.

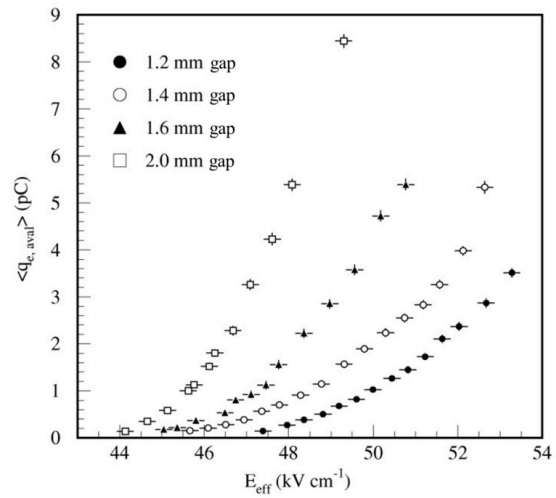
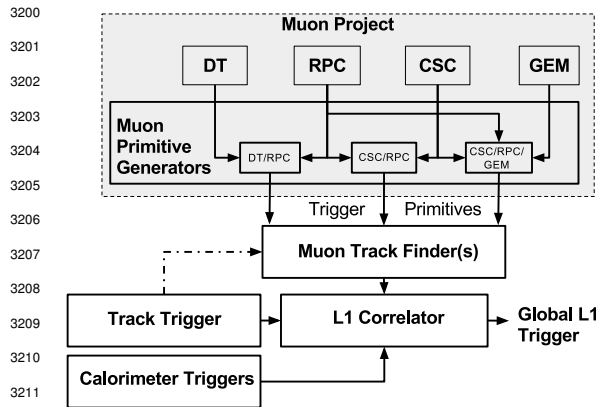


Figure 4.19: Measured average charge per avalanche as a function of the effective electric field for different gas gap thickness in double-gap RPCs using HPL electrodes [177].

## 3199 4.4 Impact on Level-1 Trigger and physics performance



3200  
 3201 *Figure 4.20: Level-1 Trigger data flow during Phase-2*  
 3202 *operations [177].*

The upgrades of the different subsystems will have a subsequent impact on the Level-1 Trigger. Indeed, although its main scheme will not be affected, the efficiency of the trigger in identifying muons and provide the DAQ with good and fast trigger that can cope with HL-LHC instantaneous luminosity is a major improvement. In addition to the upgrade of the muon system in terms of trigger accept rate and latency, the Level-1 Trigger will get extra information by including the Tracker Trigger into its Muon Track Finder logic and combine the L1 Muon Trigger with Tracker and Calorimeter Triggers to generate a Global L1 Trigger, as shown in Figure 4.20. Using the

3203  
 3204 track candidates of both the muon system and the tracker in spatial coincidence will allow for a  
 3205 much better momentum resolution thanks to better identified muons and, hence, better measured  
 3206 transverse impulsion as described in reference [177].

3207  
 3208 In terms of muon trigger, three regions are considered due to their different track finding logic:  
 3209 the Barrel Muon Track Finder (BMTF), the Endcap Muon Track Finder (EMTF) for both the barrel  
 3210 and endcap regions, and finally the Overlap Muon Track Finder (OMTF) which concerns the pseudo-  
 3211 rapidity region in which there is a common coverage by both the barrel and endcap muon systems.  
 3212 This region can be seen in Figure 4.10 for  $0.9 < |\eta| < 1.2$  and requires a specific more complex  
 3213 logic to provide an efficient reconstruction of muons due to the different orientation of the detectors  
 3214 and of the more complex magnetic field of this region. The development of a track finder specific to  
 3215 the overlap region was achieved during the Phase-1 upgrade of the L1-Trigger [259].

3216  
 3217 The upgraded RPC link system, allowing to take profit of the full 1 ns resolution of the detectors,  
 3218 will help reducing the neutron induced background, slightly improve the bunch crossing assignment,  
 3219 and help increasing the trigger efficiency in every sector. The upgrade of DT electronics is also to  
 3220 take into account as the trigger primitive generator will be renewed through the use of TDCs that  
 3221 will send the digitized signals directly to common DT/RPC back-end electronics instead of having  
 3222 an on-detector trigger logic as it will be the case until the end of Phase-1. The combination of RPC  
 3223 hits together with DT primitives will bring extra improvement in the bunch crossing assignment in  
 3224 the barrel and overlap regions and improve the efficiency of the trigger between the wheels were the  
 3225 quality of DT primitives is the poorest.

3226  
 3227 The current EMTF already uses more sophisticated algorithms by combining together RPC hits  
 3228 and CSC primitives. The GEMs, in stations 1 and 2, and the iRPCs, in stations 3 and 4, will be added  
 3229 into the EMTF algorithm. Both these contributions will help increase the efficiency of the L1 trigger  
 3230 in the endcap region in one hand, as showed by Figure 4.21, and help lowering the L1 trigger rate  
 3231 in the other hand, especially in the most forward region. Similarly to the RPC/CSC algorithms, data  
 3232 from both CSCs and GEMs are combined into the Optical TMBs (OTMBs) to build on each station,  
 3233 GEM/CSC primitives matching space and time information from both subsystems. The efficiency  
 3234 improvement and rate reduction close to the beam line will be naturally enhanced by the addition  
 3235 of more hits along the muon tracks, as can be seen from Figure 4.22 that focuses especially in the

most challenging pseudo-rapidity region. Indeed, the contribution from the GEMs to the lever arm of each track thanks to their high angular resolution will be a great asset in achieving such results, as can be seen in Figure 4.23. The rate will be partly reduced in the forward region thanks to the better spatial resolution of iRPCs, with respect to the current RPC system. The ambiguity brought by multiple local charged tracks in CSCs will be reduced, as explained through Figure 4.24. Indeed, as the rates will increase, the probability to record more than a single local charged track will greatly increase. This is due to the fact that the trigger algorithm uses information from three consecutive bunch crossings to find muon tracks. It is estimated that with iRPCs operated at 95% efficiency the resolution of ambiguous events would be of the order of 99.7%.

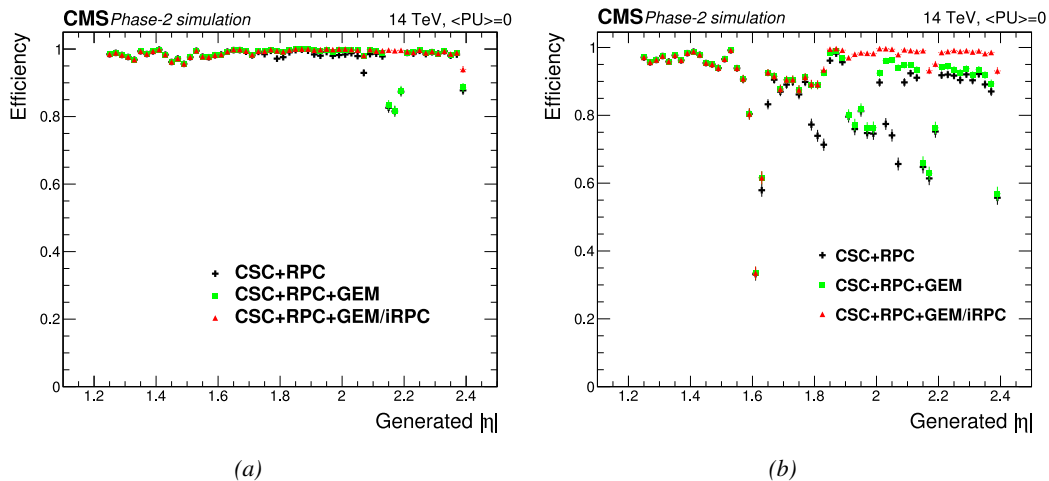


Figure 4.21: Efficiency of the L1 trigger in the endcap region after Phase-2 upgrade in the case CSC/GEM/RPC hits are requested in at least two stations out of four (a) and in all four stations (b) [177].

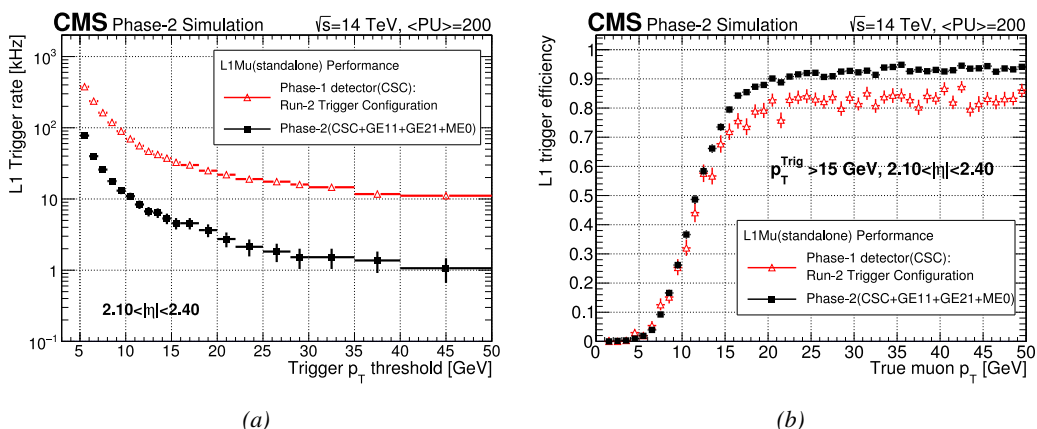


Figure 4.22: Comparison of L1 trigger performances for prompt muons with and without the addition of GEMs in the region  $2.1 < |\eta| < 2.4$  at Phase-2 conditions [177]. GEMs would allow a reduction of the trigger accept rate by an order of magnitude (a) while increasing the trigger efficiency (b).

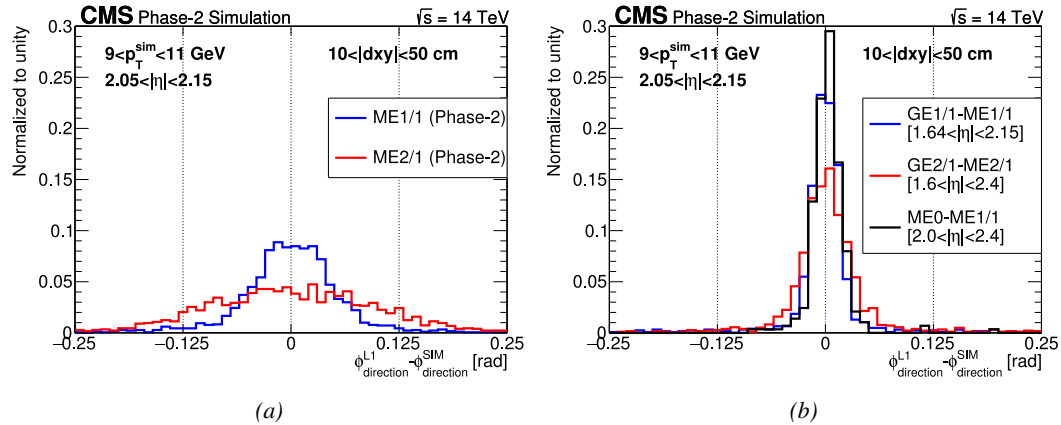


Figure 4.23: The angular resolution on reconstructed muon tracks in the GEM overlap region  $2.0 < |\eta| < 2.15$  is compared for Phase-2 conditions in the case CSC are alone (a) and in the case the GEMs' data, including ME0, is combined to which of CSCs (b) [177].

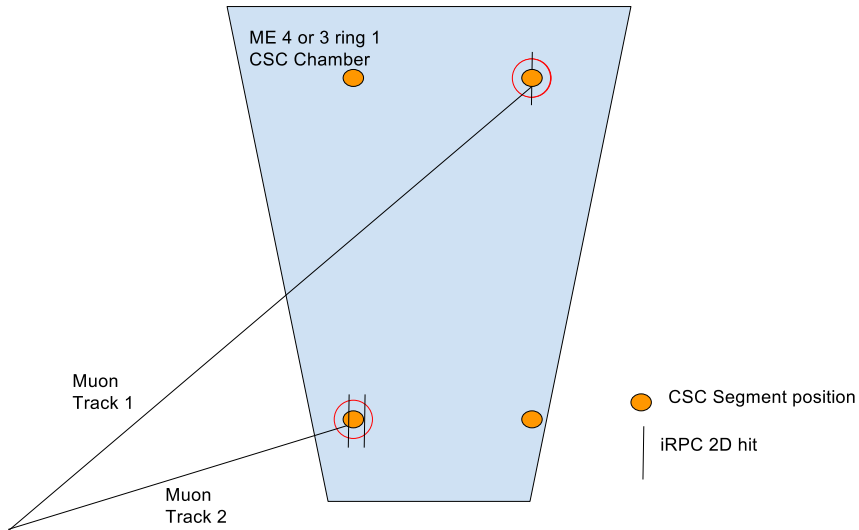
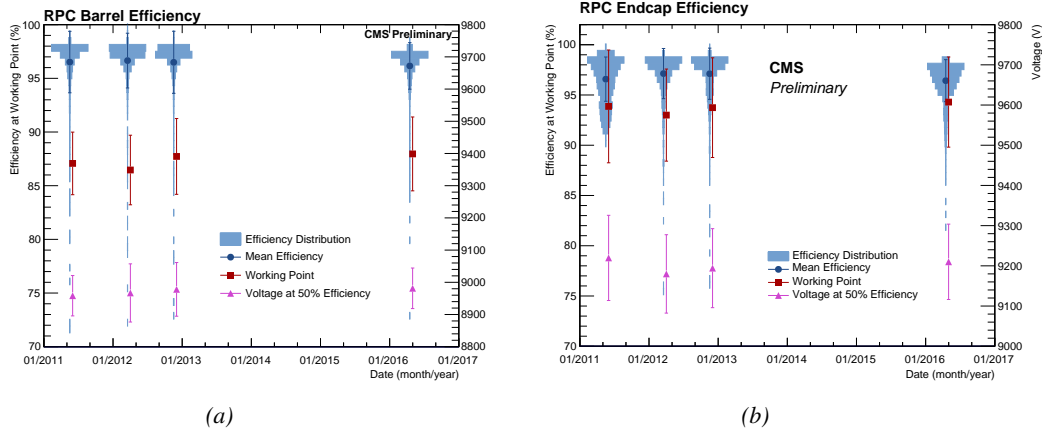


Figure 4.24: Resolution of the LCT ambiguous events thanks to the combination of CSC and iRPC readout data. Using CSCs only, two pairs of hits are possible [177].

## 4.5 Ecofriendly gas studies

In the last steps of R&D, the gas mixture of CMS RPCs was foreseen to be a 96.2/3.5/0.3 composition of  $C_2H_2F_4/i-C_4H_{10}/SF_6$  [205] but finally it was slightly changed into a 95.2/4.5/0.3 mixture of the same gases [260]. A summary of the operation performance of the RPCs since the start of LHC and of CMS data taking is given in Figure 4.25 [261]. The performance of the detectors is regularly monitored and the operating voltages updated in order to obtain a very stable performance through time. Nevertheless, the detectors will face new challenges during Phase-II during which they will be exposed to more extreme radiation conditions. Description of the longevity tests with extreme

3261 irradiation and the conclusions regarding the operation of the present RPC system will be given in  
 3262 Chapter 5.



*Figure 4.25: Evolution of the efficiency, working voltage, and voltage at 50% of maximum efficiency for CMS Barrel (a) and Endcap (b) RPCs obtained through yearly voltage scans since 2011. The working voltage of each RPC is updated after each voltage scan to ensure optimal operation [261].*

3263 It was already discussed that in the future, it is likely that the use of freon gases could be banned.  
 3264 Using  $CF_4$ ,  $C_2H_2F_4$  and  $SF_6$ , both CSC and RPC subsystems will need to address this problem  
 3265 by finding new gas mixture for the operation of their detectors. Finding a replacement for these gas  
 3266 components that were used for very specific reasons is a great challenge. Indeed, CSCs use  $CF_4$  in  
 3267 order to enhance the longevity of the detectors, increase the drift velocity of electrons and quench  
 3268 photons with a non-flammable gas mixture. RPCs use a mixture mainly composed of  $C_2H_2F_4$ , or  
 3269  $R134a$ , that features a high effective Townsend coefficient and the great average fast charge allowing  
 3270 for operations with a high threshold. The mixture also contains a small fraction of  $SF_6$  that is used  
 3271 for its electronegative properties that prevents the development of delta-rays in the gas volume that  
 3272 might trigger multiple ionization and avalanches. It only represents 0.3% of CMS standard mixture  
 3273 but more than 5% of its overall GWP.

	CSC	RPC
Greenhouse gases used	$CF_4$	$C_2H_2F_4$ and $SF_6$
Greenhouse gases fraction in the gas mixture	10%	95.2% and 0.3%
Global Warming Potential (relative to $CO_2$ )	6500	1300 and 23900
Gas mixture re-circulation	Yes, 90%	Yes, 85%
Gas mixture replenishing rate (l/hr)	700	1100
F-gas recuperation	Yes, $\approx 40\%$	No
F-gas venting rate (l/hr)	42	1047 and 3.3
$CO_2$ -equivalent rate ( $m^3/h$ )	273	1440
Relative impact (entire muon system = 100%)	16%	84%

*Table 4.1: Details of the greenhouse fluorinated gases used in CMS and of their GWP [177].*

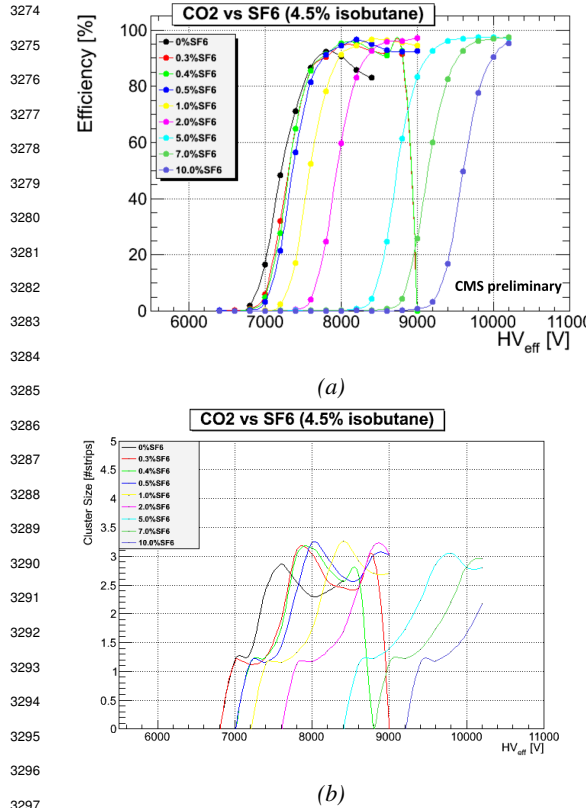


Figure 4.26: Efficiency (a) [203] and cluster size (b) of a standard double-gap RPC operated with CO<sub>2</sub> mixtures for different ratios of SF<sub>6</sub>.

needs to be conducted for both subsystems before concluding on the best alternative. Finding no good alternative to the present mixtures will require very efficient abatement system in CMS to burn and convert the greenhouse gases into less harmful ones. This way, the air pollution would be strongly reduced.

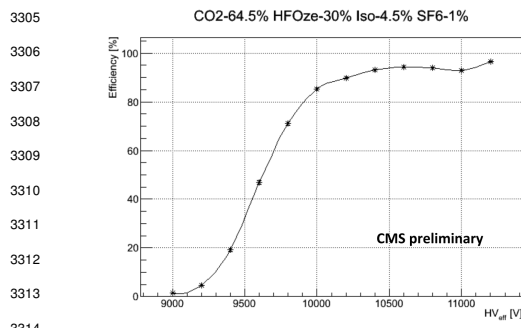


Figure 4.27: Efficiency of a CMS double-gap RPC operated with 30% of HFO, 4.5% of iC<sub>4</sub>H<sub>10</sub>, 1% of SF<sub>6</sub> and 64.5% of CO<sub>2</sub> [203].

efficiency with a plateau located at a similar high voltage than with R134a based mixtures (Fig-

All these gases have a very high GWP, as reported in Table 4.1, and only few options are left. The subsystems need to work on strongly decreasing the loss of these gases due to leaks in the gas system or need to completely change their gas mixture for more ecofriendly ones. Reducing the amount of F-gas released in the atmosphere due to leaks on the current gas system will require installation of a F-gas recuperation system on RPCs side and an upgrade of CSCs existing one in addition to the repair of existing leaks. With such measures, it is expected that the total rate of greenhouses gas vented in the atmosphere would represent only 1.6% of the current levels [177]. In the most critical case the F-gas were to be banned, it would be necessary to have replacement mixtures to operate CMS. CSC is presently investigating replacement for CF<sub>4</sub> such as CF<sub>3</sub>I, C<sub>4</sub>F<sub>6</sub>, IC<sub>3</sub>F<sub>6</sub>, C<sub>3</sub>F<sub>8</sub> or CHF<sub>3</sub>. RPCs, in collaboration with the ATLAS RPC group which uses the same gas mixture, have identified CF<sub>3</sub>I (GWP  $\leq$  1) and C<sub>3</sub>H<sub>2</sub>F<sub>4</sub> (GWP  $\sim$  6), referred to as HFO-1234ze, as potential candidates with mixtures containing CO<sub>2</sub>. CO<sub>2</sub> is already widely used by various RPC experiments in mixtures with argon. More R&D

Preliminary studies conducted in Ghent confirmed that CO<sub>2</sub> alone would require more than 1% of SF<sub>6</sub> to reach full efficiency, as presented in Figure 4.26. Even though the results obtained in Ghent don't show the streamer probability (the probability to have very large avalanches whose induced charge is greater than 20 pC), the variation of the cluster size indicates that the streamers become predominant before the efficiency plateau is reached. Then, a very first test with an HFO/CO<sub>2</sub> was performed. Only one ratio was tested as can be seen from Figure 4.27 that displays a good

ure 4.28). The status of RPC studies is presented in Figure 4.28 in which the performance (efficiency and streamer probability) of a CMS double-gap RPC operated with alternative gas mixtures is compared to the present CMS RPC mixture. Although the efficiency of detectors operated with mixtures containing  $CO_2/CF_3I$  or  $CO_2/HFO$  as a replacement for  $C_2H_2F_4$  seems to reach similar levels than which of the detectors operated with the present mixture, the new gas mixtures feature a streamer probability that far exceeds which of the present fluorinated mixture. The  $SF_6$  doesn't seem to prevent the formation of streamers as efficiently even when used at levels more than three times higher than with the standard CMS RPC mixture. Nevertheless, it is important to note that these results were obtained with a single-gap RPC while the use of a double-gap RPC reduces the operation voltage by 200 to 300 V, lowering the induced charge. A compromise in between good efficiency and acceptable level of streamer probability, and the fine-tuned composition of potential replacement gas mixtures will be kept on being studied using a standard double-gap CMS RPC.

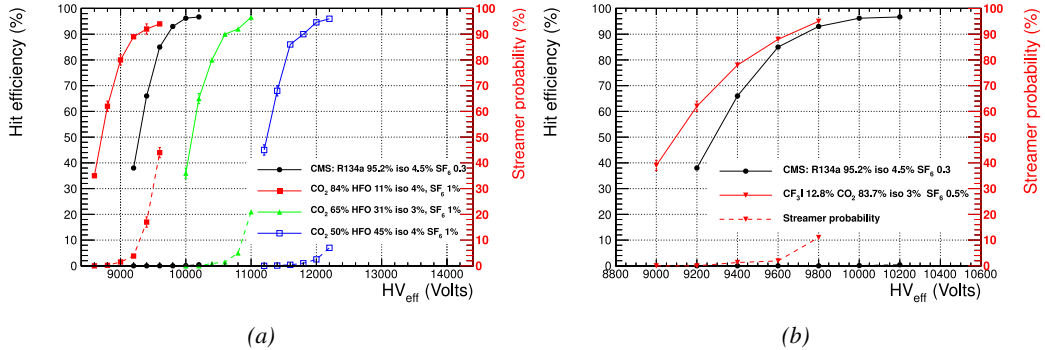


Figure 4.28: The efficiency (solid lines) and streamer probability (dashed lines) of  $HFO/CO_2$  (a) and  $CF_3I/CO_2$  (b) based gas mixtures as a function of the effective high-voltage are compared with the present CMS RPC gas mixture represented in black [177, 203]. The detector used for the study is a single-gap RPC with similar properties than CMS RPCs. The streamer probability is defined as the proportion of events with a deposited charge greater than 20 pC.

Although the technology certification was conducted with the standard CMS gas mixture which is a known reference, the iRPCs will need to be operated with new environmental-friendly gas mixtures. Studies have then been conducted with iRPCs, assuming that the  $HFO/CO_2$  mixture containing an almost equal level of both components was the most likely candidate to replace the standard mixture. In this purpose, an iRPC prototype has been built to be tested with an  $HFO/CO_2$  gas mixture. The mixture, referred to as "ecogas" in Figure 4.29, contained 50% of  $HFO$ , 4.5% of  $iC_4H_{10}$ , 0.3% of  $SF_6$  and 45.2% of  $CO_2$ . In Figure 4.29 is presented a result consistent with the blue curve obtained with 45% of  $HFO$ , 4% of  $iC_4H_{10}$ , 1% of  $SF_6$  and 50% of  $CO_2$  flushed into a standard double-gap RPC. Instead of the streamer probability, the cluster size is shown. The average number of hits generated by a muon passing through the chamber seem to have increased by 1 at the level of the knee of the sigmoid plateau using the ecogas.

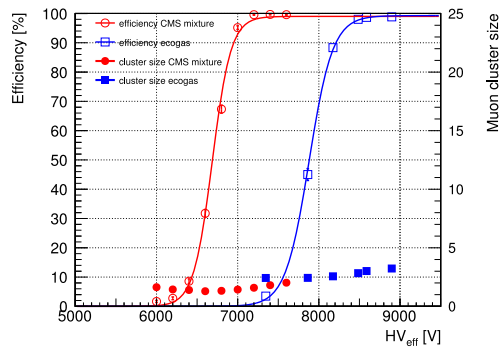


Figure 4.29: Efficiency (open symbols) and cluster size (full symbols) of an iRPC as a function of the effective voltage for the standard CMS gas mixture and an environmental-friendly gas mixture [177].

# 5

3342

3343

3344

## Longevity studies and Consolidation of the present CMS RPC system

3345 The RPC system, located in both barrel and endcap regions, provides a fast, independent muon  
3346 trigger over a large portion of the pseudo-rapidity range ( $|\eta| < 1.6$ ). During HL-LHC operations  
3347 the expected conditions in terms of background and pile-up will make the identification and correct  
3348  $p_T$  assignment a challenge for the muon system. The goal of the RPC upgrade is to provide additional  
3349 hits to the Muon System with more precise timing. All this information will be elaborated by the  
3350 Trigger System in a global way enhancing the performance of the muon trigger in terms of efficiency  
3351 and rate control. The RPC Upgrade consists of two projects: an improved Link Board System and  
3352 the extension of the RPC coverage up to  $|\eta| = 2.4$ .

3353 The Link Board System is responsible for the processing, the synchronization and the zero-  
3354 suppression of the signals coming from the RPC FEBs. The Link Board components have been  
3355 produced between 2006 and 2007 and will be subjected to ageing and failure on a long term scale.  
3356 An upgraded Link Board System will overcome the ageing problems and will allow for a more  
3357 precise timing information to the RPC hits from 25 to 1.5 ns.

3358 In order to develop an improved RPC that fulfills CMS requirements, an extensive R&D program is  
3359 being conducted. The benefits of adding two new RPC layers in the innermost ring of stations 3 and  
3360 4 will be mainly observed in the neutron-induced background reduction and efficiency improvement  
3361 for both the muon trigger and the offline reconstruction.

3362 The coverage of the RPC System up to higher pseudo-rapidity  $|\eta| = 2.1$  was part of the original  
3363 CMS TDR. Nevertheless, the expected background rates being higher than the certified rate capa-  
3364 bility of the present CMS RPCs in that region and the budget being limited, RPCs were restricted to  
3365 a smaller pseudo-rapidity range. Even though the iRPC technology that will equip the extension of  
3366 the Muon System will be different than the current CMS RPC technology, it is necessary to certify  
3367 the rate capability and longevity of the existing detectors as the radiation level will increase together  
3368 with the increase of instantaneous luminosity of the LHC. For this purpose, unused spare CMS RPC  
3369 detectors have been installed in different irradiation facilities, first of all, to certify the detectors to

3370 the new levels of irradiation they will be subjected to and, finally, to study their ageing and certify  
 3371 their good operation throughout the HL-LHC program.

3372 This chapter will discuss the longevity and consolidation studies of the present CMS RPC system  
 3373 to which I have contributed. Two different irradiation facilities have been used at CERN. In each of  
 3374 them I took a leading role in defining the experimental set-up, but also in the data collection and data  
 3375 analysis. In the first facility in which preliminary tests were conducted, I also worked on simulations  
 3376 of the experimental setup and I made predictions on the particle rate expected at the detector level.  
 3377 During the last 4 years of longevity test conducted in the second facility, I became a DAQ expert and  
 3378 built a software which is now the base for the data collection to study the longevity of CMS RPCs.  
 3379 Moreover, I also worked together with the Detector Control Software (DCS) expert to provide an  
 3380 online monitoring of the collected data. Indeed, I developed a software that automates the extractions  
 3381 of the detectors' data and produces plots at destination of the users thanks to a fast analysis. This  
 3382 software is a corner stone for the final data analysis. Documentations of both these softwares are  
 3383 given in Appendix A and Appendix B.

3384 In a first section of the chapter, the irradiation facilities will be described. The study conducted will  
 3385 then be summarized in details. A description of the set-ups as well as a comprehensive review of the  
 3386 obtained results will be provided.

## 3387 5.1 Testing detectors under extreme conditions

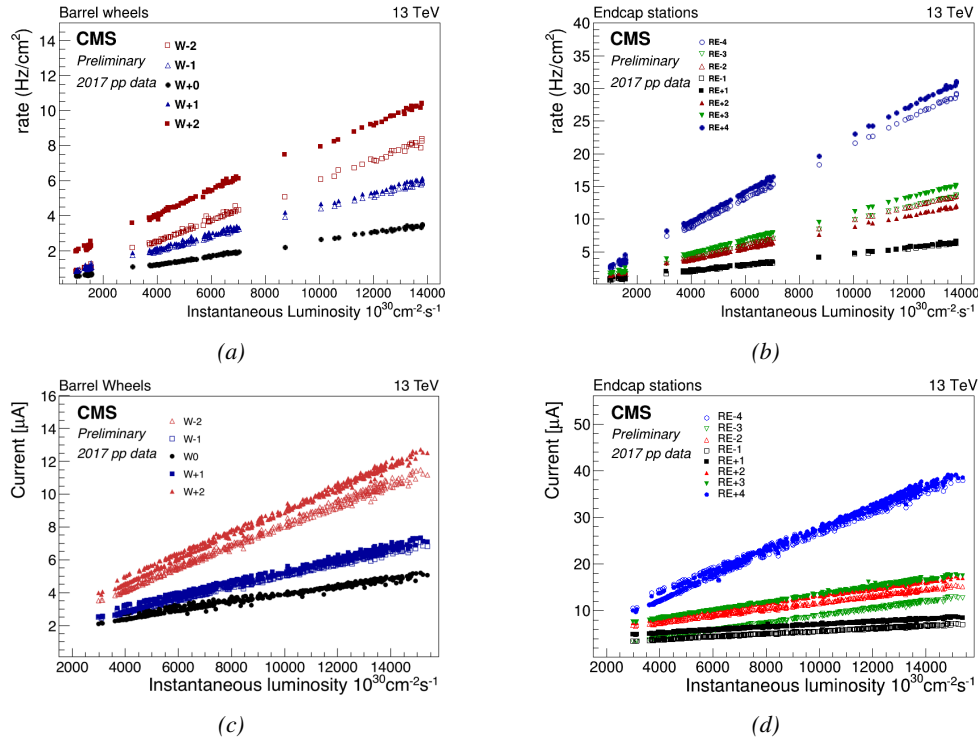


Figure 5.1: Mean RPC Barrel (left column) and Endcap (right column) rate (top row) and current (bottom row) as a function of the instantaneous luminosity as measured in 2017 p-p collision data.

The upgrade from LHC to HL-LHC will increase the peak luminosity from  $10^{34}$   $\text{cm}^{-2} \text{s}^{-1}$  to  $5 \times 10^{34}$   $\text{cm}^{-2} \text{s}^{-1}$ , increasing the total expected background to which the RPC system will be subjected. Mainly composed of low energy gammas, neutrons, and electrons and positrons from  $p$ - $p$  collisions, but also of low momentum primary and secondary muons, punch-through hadrons from calorimeters, and particles produced in the interaction of the beams with collimators, the background will mostly affect the regions of CMS that are the closest to the beam line, i.e. the RPC detectors located in the endcaps.

Data collected during 2017, presented in Figure 5.1, allows to study the values of the background rate in the entire RPC system. This was achieved thanks via the monitoring of the rates in each RPC rolls and of the current in each HV channel. A linear dependence of the mean rate or current on the instantaneous luminosity is shown in selected runs with identical LHC running parameters. It is assumed that such a linear behaviour should be observed at even higher luminosities and is therefore used to extrapolate the rates and currents that will be expected during HL-LHC. In Figure 5.2, a linear extrapolation of the distribution of the background hit rate per unit area as well as the integrated charge is shown at a HL-LHC condition. The maximum rate per unit area in the endcap detectors at HL-LHC conditions is expected to be of the order of 600 Hz/cm<sup>2</sup> while the charge deposition should exceed 800 mC/cm<sup>2</sup>. The detectors will thus have to be certified up to an irradiation of 840 mC/cm<sup>2</sup>. These extrapolations are provided with a required safety factor 3 for the certification study.

In the past, extensive long-term tests were carried out at several gamma and neutron facilities certifying the detector performance. Both full size and small prototype RPCs have been irradiated with photons up to an integrated charge of  $\sim 0.05$  C/cm<sup>2</sup> and  $\sim 0.4$  C/cm<sup>2</sup> respectively and were certified for rates reaching 200 Hz/cm<sup>2</sup> [262, 263]. Since the beginning of Run-I until December 2017, the RPC system provided stable operation and excellent performance. The average integrated charge is of about 1.66 mC/cm<sup>2</sup> in the Barrel and 4.58 mC/cm<sup>2</sup> in the Endcap, closer to the beam line, as can be seen in Figure 5.3). The detectors did not show any ageing effects for a maximum integrated charge in a detector of the order of 0.01 C/cm<sup>2</sup> and a peak luminosity reaching  $1.4 \times 10^{34}$   $\text{cm}^{-2} \text{s}^{-1}$  during the 2017 data taking period.

To perform the necessary studies on the present CMS RPC detectors, facilities offering the possibility to irradiate the chambers are necessary in order to recreate HL-LHC conditions or stronger and study the detector performance through time. A first series of such studies was conducted in the for-

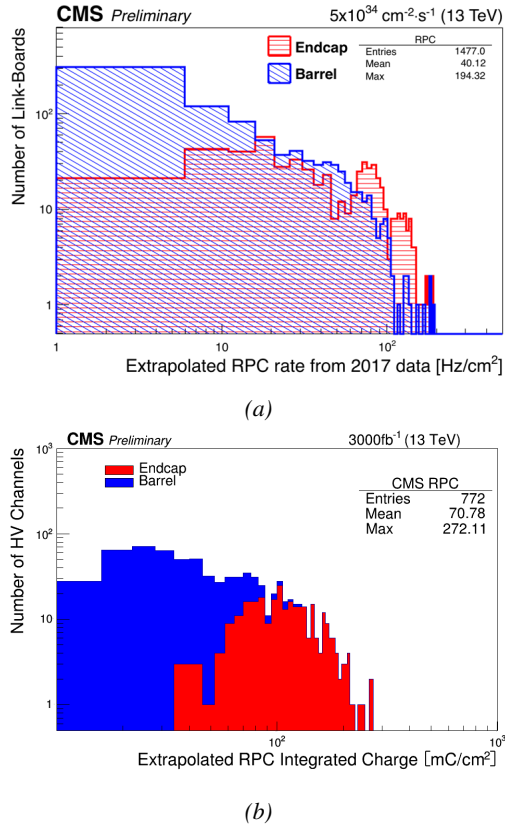


Figure 5.2: Linear extrapolation of the hit rate (a) and of the integrated charge (b) per region (Barrel, Endcap) respectively to HL-LHC instantaneous luminosity ( $5 \times 10^{34}$   $\text{cm}^{-2} \text{s}^{-1}$ ) and HL-LHC integrated luminosity (3000  $\text{fb}^{-1}$ ).

3434 former Gamma Irradiation Facility (GIF) of CERN before its dismantlement starting from September  
 3435 2014. This preliminary study was used as a stepping stone towards the building of a more powerful  
 3436 irradiation fully dedicated to longevity studies of CMS and ATLAS subsystems in the perspective  
 3437 of HL-LHC. The period of preliminary work has also been a key moment in the elaboration and  
 3438 improvement of data acquisition, offline analysis and online monitoring tools that are extensively  
 3439 used in the new gamma irradiation facility.

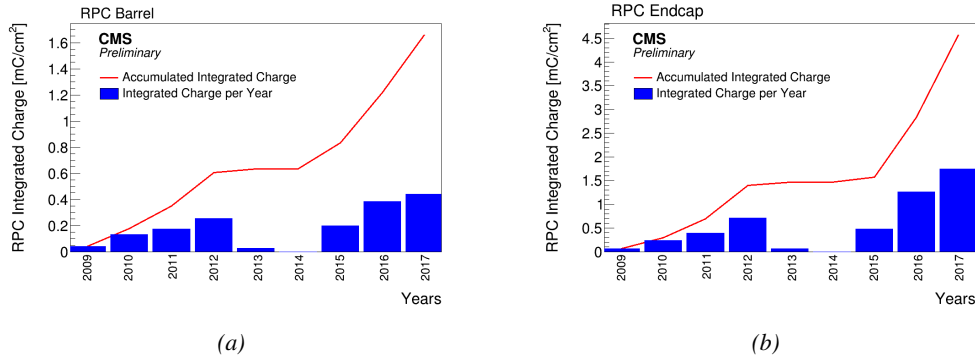


Figure 5.3: CMS RPC mean integrated charge in the Barrel region (a) and the Endcap region (b). The integrated charge per year is shown in blue. The red curve shows the evolution of the accumulated integrated charge through time. The blank period in 2013 and 2014 corresponds to LS1.

### 3440 5.1.1 The Gamma Irradiation Facility

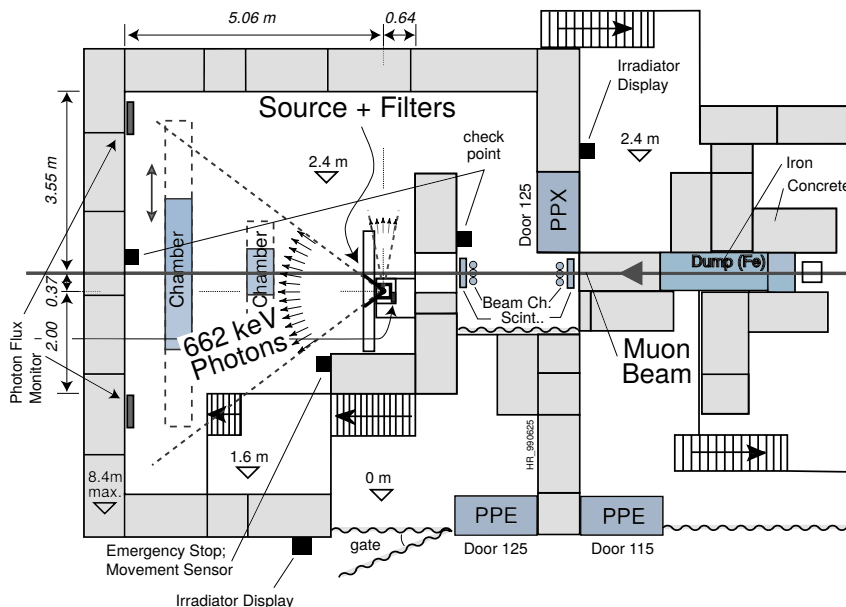


Figure 5.4: Layout of the test beam zone of GIF at CERN.

3441 Located in the SPS West Area at  
 3442 the downstream end of the X5 test beam, the GIF was a test area in  
 3443 which particle detectors were exposed to a particle beam in presence of an adjustable gamma background [264]. Its goal was to reproduce background conditions these  
 3444 detectors would endure in their operating environment at LHC. The layout of the GIF is shown in Figure  
 3445 5.4. Gamma photons are produced by a strong  $^{137}\text{Cs}$  source installed in the upstream part of the zone inside

3446 a lead container. The source container includes a collimator, designed to irradiate a  $6 \times 6 \text{ m}^2$  area at  
 3447 5 m maximum distance to the source. A thin lens-shaped lead filter helps providing with a uniform  
 3448 out-coming flux in a vertical plane, orthogonal to the beam direction. The photon rate is controlled  
 3449 by further lead filters allowing the maximum rate to be limited and to vary within a range of four  
 3450 orders of magnitude. Particle detectors under test are then placed within the pyramidal volume in  
 3451 front of the source, perpendicularly to the beam line in order to profit from the homogeneous photon  
 3452 flux. Adjusting the background flux of photons can then be done using the filters and choosing the  
 3453 position of the detectors with respect to the source. The zone is surrounded by 8 m high and 80 cm  
 3454 thick concrete walls. Access is possible through three entry points. Two access doors for personnel  
 3455 and one large gate for material. A crane allows installation of heavy equipment in the area.

3456 As described on Figure 5.5, the  $^{137}\text{Cs}$  source emits a 662 keV photon in 85% of the decays. An  
 3457 activity of 740 GBq was measured on the 5<sup>th</sup> of March 1997. The half-life of Cesium is well known  
 3458 ( $t_{1/2} = (30.05 \pm 0.08) \text{ y}$ ) and can be used to compute the activity of the source at the time of the  
 3459 study. The GIF tests were done in between the 20<sup>th</sup> and the 31<sup>st</sup> of August 2014, i.e. at a time  $t =$   
 3460  $(17.47 \pm 0.02) \text{ y}$  resulting in an attenuation of the activity from 740 GBq in 1997 to 494 GBq in  
 3461 2014.

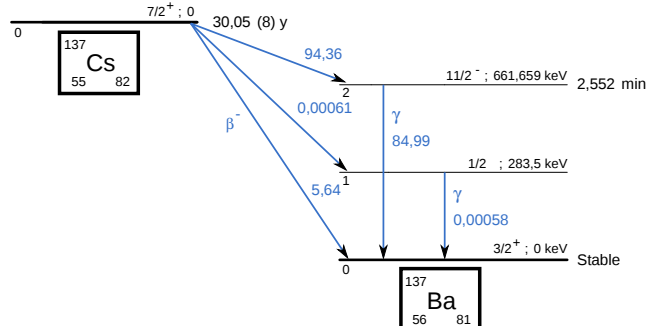


Figure 5.5:  $^{137}\text{Cs}$  decays by  $\beta^-$  emission to the ground state of  $^{137}\text{Ba}$  ( $BR = 5.64\%$ ) and via the 662 keV isomeric level of  $^{137}\text{Ba}$  ( $BR = 94.36\%$ ) whose half-life is 2.55 min.

### 3471 5.1.2 The new Gamma Irradiation Facility

3472 The GIF++, located in the SPS North Area at the downstream end of the H4 test beam, has replaced  
 3473 its predecessor during LS1 and has been operational since spring 2015 [265]. Like GIF, GIF++  
 3474 features a  $^{137}\text{Cs}$  source of 662 keV gamma photons, their fluence being controlled with a set of  
 3475 filters of various attenuation factors. The source provides two separate large irradiation areas for  
 3476 testing several full-size muon detectors with homogeneous irradiation, as presented in Figure 5.6.

3477 The source activity was measured to be about 13.5 TBq in March 2016. With the photon flux  
 3478 being far greater than HL-LHC expectations, GIF++ provides an excellent facility for accelerated  
 3479 ageing tests of muon detectors. The source is situated in a bunker designed to perform irradiation  
 3480 test along a muon beam line, which is available during selected periods throughout the year.  
 3481 The H4 beam, providing the area with muons with a maximum momentum of about 150 GeV/c,  
 3482 passes through the GIF++ zone and is used to periodically study the performance of the detectors  
 3483 placed under long term irradiation. Its flux is of 104 particles/s/cm<sup>2</sup> focused in an area of about  
 3484  $10 \times 10 \text{ cm}^2$ .

	1	2	3
A	1	10	100
B	1	1.468	100
C	1	2.154	4.642

Table 5.1: Attenuation of single filters on each filter plane of the GIF++ Cesium source.

attenuation factor (for example  $333 = 100 \times 100 \times 4.642 = 46420$ ).

Adjusting the gamma flux is possible thanks to the three planes (A, B and C) of adjustable absorbers featured on the Cesium source [266]. With properly adjusted filters, one can simulate the background expected at HL-LHC and study the performance and ageing of muon detectors in HL-LHC environment. Each plane of filters features three filters (1, 2 and 3) with different Absorption factor (ABS) listed in Table 5.1. The source absorber settings can be referred by a three digit number with a format ABC or by its

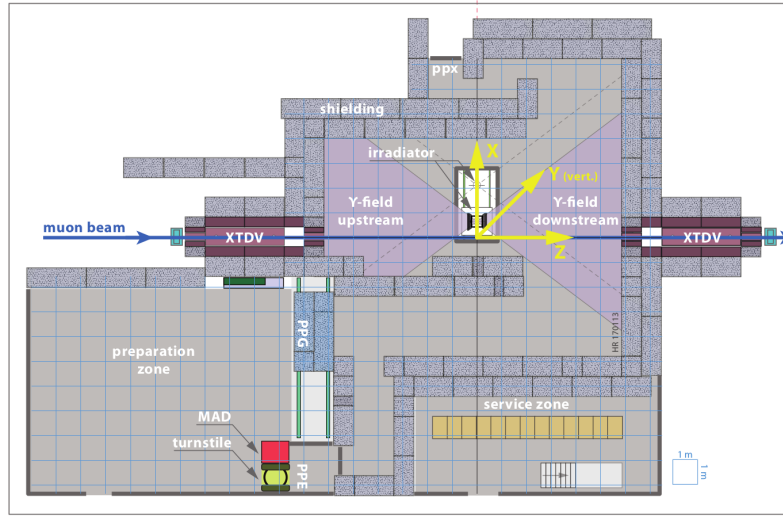


Figure 5.6: Floor plan of the GIF++ facility. When the facility downstream of the GIF++ takes electron beam, a beam pipe is installed along the beam line ( $z$ -axis). The irradiator can be displaced laterally (its center moves from  $x = 0.65$  m to 2.15 m), to increase the distance to the beam pipe.

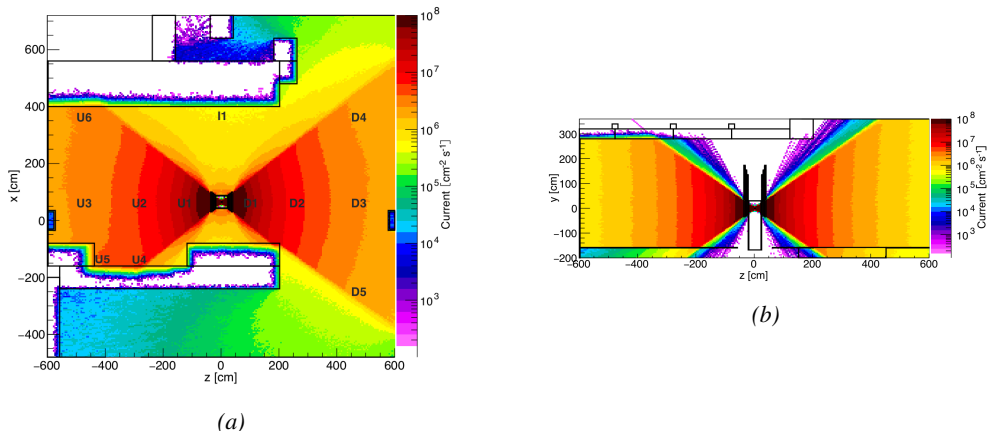


Figure 5.7: Simulated unattenuated current of photons in the xz plane (a) and yz plane (b) through the source at  $x = 0.65$  m and  $y = 0$  m [267]. With angular correction filters, the current of 662 keV photons is made uniform in xy planes.

The gamma current as simulated with GEANT4 is presented in Figure 5.7. In their simulation paper [267], Pfeiffer et al. define the particle current as "a measure of the net number of particles crossing a flat surface with a well-defined orientation. The unit of current is  $\text{m}^{-2} \text{s}^{-1}$  and thus identical to the unit of flux. Current is meaningful in cases where particles are counted without any interest in their interactions." The labels UN, DN, with  $N \in [1 : 5]$  and I1 correspond to the position of different Radiation Monitoring (RADMON) sensors measuring the irradiation in the bunker area [267]. According to the simulation results, that agree within 12% to the doses measured with the RADMONs, the RPCs that will be tested in GIF++ can expect a maximal gamma current of the order of  $2$  to  $5 \times 10^6 \text{ cm}^{-2} \text{s}^{-1}$  assuming they will always stay in a region in between sensor U5 and the back wall of the upstream area.

## 5.2 Preliminary studies at GIF

### 5.2.1 RPC test setup

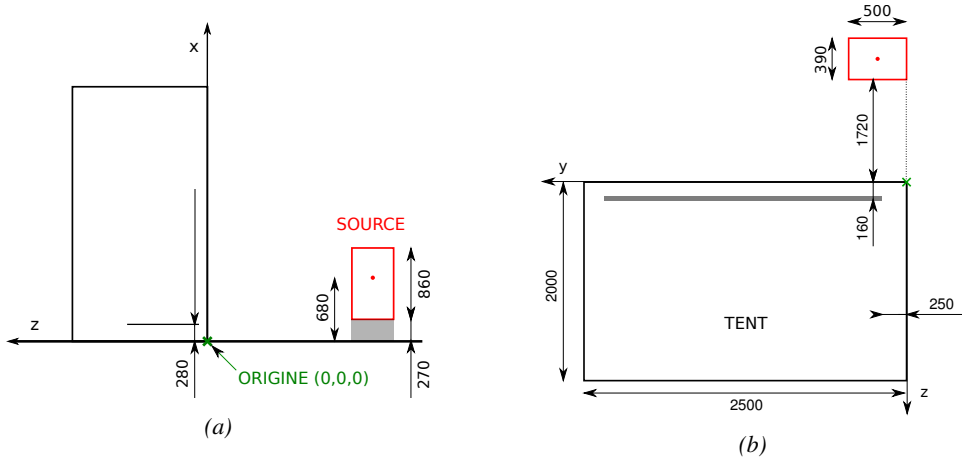


Figure 5.8: Description of the RPC setup. Dimensions are given in mm. A tent containing RPCs is placed at 1720 mm from the source container. The source is situated in the center of the container. RE-4-2-BARC-161 chamber is 160 mm inside the tent. This way, the distance between the source and the chambers plan is 2060 mm. Figure (a) provides a side view of the setup in the xz plane while Figure (b) shows a top view in the yz plane.

During Summer 2014, preliminary tests have been conducted in the GIF area on an endcap chamber of type RE4/2 and labeled RE-4-2-BARC-161 produced for the extension of the endcap with a fourth disk in 2013. This chamber has been placed into a trolley covered with a tent in order to control the temperature. The positions of the RPC inside the tent and of the tent with respect to the source in the bunker are described in Figure 5.8. The goal of the study was to have a preliminary understanding of the rate capability of the present technology used in CMS. It was decided to measure the efficiency of the RPC under irradiation for detecting cosmic muons as, at the time of the tests, the beam was not operational anymore. Three different absorber settings were used and compared to the case where the detector was not irradiated in order to study the evolution of the performance of the detector with increasing exposure to gamma radiation. First of all, measurements were done with the fully opened source. To complete this preliminary study, the gamma flux has been attenuated by

3517 a factor 2, a factor 5 and finally the source was shut down. The efficiency of the RPC at detecting  
 3518 the cosmic muons in coincidence with a cosmic trigger as well as the background rate as seen by the  
 3519 detectors were measured.

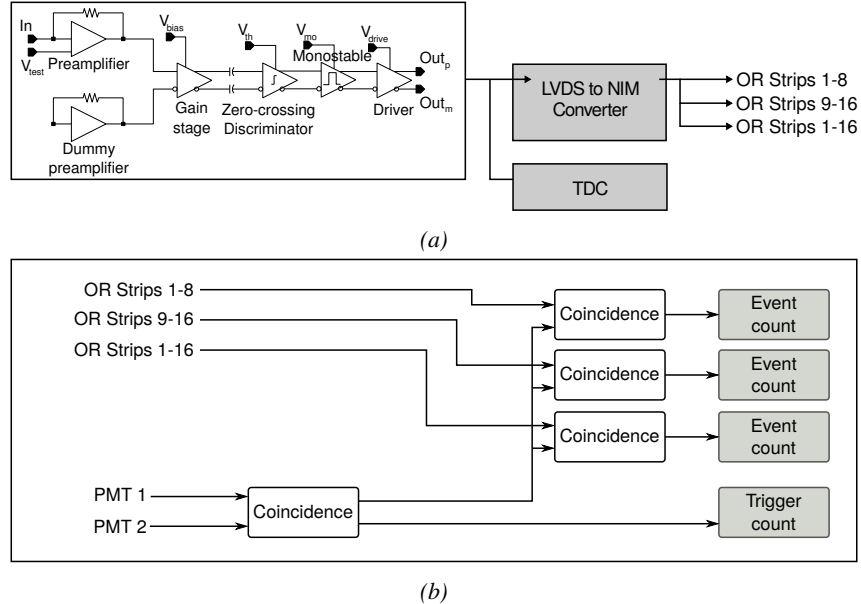


Figure 5.9: (a) Shaping of the signals from the RPC strips by the FEE. The output LVDS signals are then read-out by a TDC module connected to a computer or converted into NIM and sent to scalers. (b) Trigger logic implementation with the RPC and photomulitplier signals.

3520  
 3521  
 3522  
 3523  
 3524  
 3525  
 3526  
 3527  
 3528  
 3529  
 3530  
 3531  
 3532



3533  
 3534  
 3535  
 3536  
 3537  
 3538  
 3539

Figure 5.10: RE-4-2-BARC-161 chamber is inside the tent as described in Figure 5.8. In the top right, the two scintillators used as trigger can be seen.

The data taking was performed using a CEAN TDC module of type V1190A [268] to which the digitized output of the RPC Front-End Board is connected, as described in Figure 5.9a and the trigger signal from the telescope. The communication with the computer is performed thanks to a CAEN communication module of type V1718 [269]. In order to control the rates recorded by the detector, the digitized RPC signals are also sent to scalers as described in Figure 5.9b. The C++ DAQ software used in GIF was developed as an early attempt towards the understanding of the CAEN libraries and the data collected by the TDCs was saved into .dat files is analysed with an algorithm computing parameters such as efficiency, hit profile, cluster size, or gamma and noise rates which was developed with C++ as well. Finally, histograms and curves are produced using ROOT.

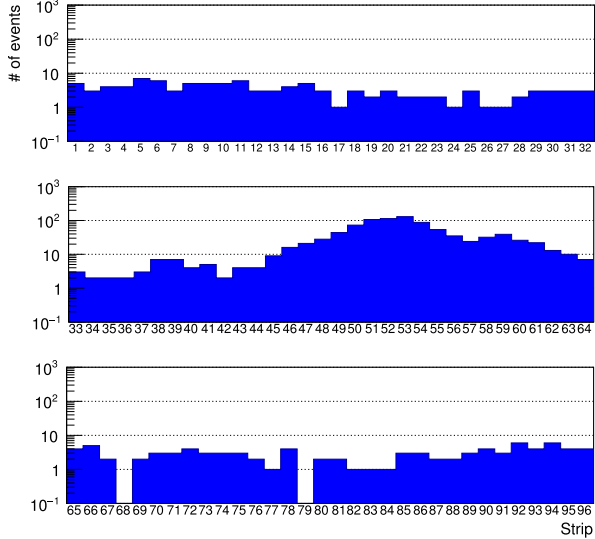
3540 The trigger system was composed of two plastic scintillators and  
 3541 was placed in front of the setup with an inclination of  $10^\circ$  with respect to  
 3542 the detector plane in order to look at cosmic muons. Using this particular  
 3543 trigger layout, shown in Figure 5.10,  
 3544 lead to a cosmic muon hit distribution into the chamber similar to the  
 3545 one of Figure 5.11. As mentioned  
 3546 in Chapter 2, the endcap RPC readout is segmented into three pseudo-  
 3547 rapidity partitions. The outer most  
 3548 partition, corresponding to the wide  
 3549 end of the chamber, is the partition  
 3550 A. The other two partitions are the  
 3551 partitions B and C. Each of them  
 3552 consists in 32 copper strips. These  
 3553 32 strips are connected to the FEEs  
 3554 by groups of 16. The trigger is  
 3555 placed in front of the half-partition  
 3556 B2 which corresponds to the last 16 strips of partition B (49 to 64).  
 3557

3558 Measured without gamma irradiation, two peaks can be seen on the profile of readout partition  
 3559 B, centered on strips 52 and 59. Some events still occur in other half-partitions than B2 contributing  
 3560 to the inefficiency of detection of cosmic muons. In the case of partitions A and C, the very low  
 3561 amount of data can be interpreted as noise. On the other hand, it is clear that a little portion of  
 3562 muons reached the half-partition B1 (strips 33 to 48). Section 5.2.2 will help us understand that  
 3563 these two peaks are due respectively to forward and backward coming cosmic particles. Forward  
 3564 coming particles are detected first by the scintillators and then the RPC while the backward going  
 3565 muons are first detected in the RPC.  
 3566

### 3567 5.2.2 Geometrical acceptance of the setup layout to cosmic muons

3568 In order to profit from a constant gamma irradiation, the detectors inside of the GIF bunker had to be  
 3569 placed in a plane orthogonal to the beam line. The muon beam that used to be available was meant to  
 3570 test the performance of detectors under test. This beam being not active anymore, another solution  
 3571 to test detector performance had to be used. Thus, it was decided to use cosmic muons detected  
 3572 through a telescope composed of two scintillators. Lead blocks were used as shielding to protect the  
 3573 photomultipliers from gammas as can be seen from Figure 5.10.  
 3574

3575 An inclination of  $\sim 10^\circ$  was given to the cosmic telescope to increase the muon trigger rate for  
 3576 this otherwise horizontal setup. A good compromise had to be found between good enough muon  
 3577 flux and narrow enough hit distribution to be sure to contain all the events into a single half-partition  
 3578 as required from the limited available readout hardware. It was then foreseen to detect muons and  
 3579 read them out only from half-partition B2. Nevertheless, a misplacement of the trigger scintillators  
 3580 resulted in an inefficiency, as can be seen in Figure 5.11 with events appearing in half-partition B1.  
 3581



3582 *Figure 5.11: Hit distributions over all three partitions of RE-4-2-BARC-161 chamber is showed. Top, middle and bottom figures respectively correspond to partitions A, B, and C.*

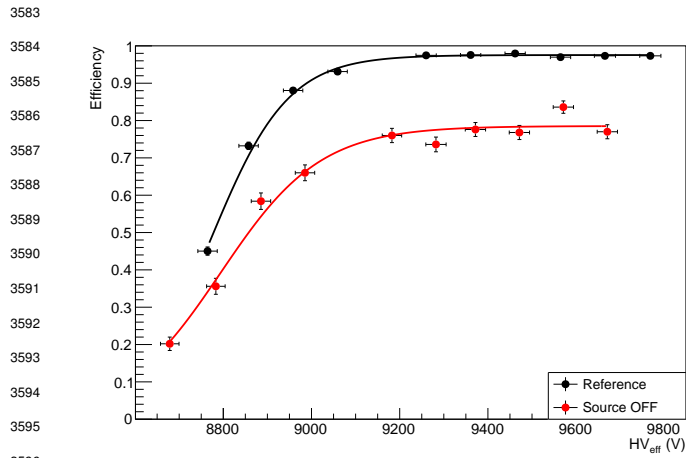


Figure 5.12: Comparison of the efficiency of chamber RE-4-2-BARC-161 with and without irradiation. Results are derived from data taken on half-partition B2 only.

by the red curve. The inefficiency too high compared to the 12.7% of data contained into the first 16 strips observed on Figure 5.11, to be explained only by the geometrical acceptance of the setup itself. Simulations have been conducted to quantify the inefficiency of the setup.

### 5.2.2.1 Geometrical acceptance simulation setup

The layout of the GIF setup has been reproduced<sup>1</sup> and incorporated into a C++ Monte Carlo (MC) simulation to study the geometrical acceptance of the telescope projected onto the readout strips [270]. A 3D view of the simulated layout is given into Figure 5.13. The RPC read-out plane is represented as a yellow trapezoid while the two scintillators as blue cuboids. The green plane corresponds to the  $4 \times 4.5 \text{ m}^2$  muon generation plane centered on the experimental setup within the simulation. The goal of the simulation is to look at muons that pass through the telescope composed of the two scintillators and define their distribution onto the RPC read-out plane. During the reconstruction, the read-out plane is then divided into its read-out strips and each muon track is assigned to a strip.

$N_\mu = 10^8$  muons are generated at a random position in the horizontal generation plane. This position corresponds to the intersection of the muon track with the generaltion plane. The plane is located at a height corresponding to the lowest point of the scintillators in order to easily simulate muons coming at very large zenith angles (i.e.  $\theta \approx \pi$ ). The position of the particle within the plane is associated with a random direction: an azimuth angle  $\phi$  chosen between 0 and  $2\pi$  and a zenith angle  $\theta$  chosen between 0 and  $\pi/2$  to follow a usual  $\cos^2\theta$  distribution for cosmic particles. Then, using the position of the muon in the generation plane and its direction, the intersection of the track with the planes of the scintillator cuboids is computed. In the case the muon wasn't found within the surface of both the scintillators, the simulation restarts and generates a new muon. On the contrary, if the track passed through the telescope, the simulation goes on. The position of the muon hit within the RPC read-out plane is computed. The hits are saved into histograms, one per read-out partition,

As can be seen in Figure 5.12, a comparison of the performance of chamber RE-4-2-BARC-161 with and without irradiation suggests an inefficiency of approximately 20%. On the 18<sup>th</sup> of June 2014, data have been taken on the chamber at CERN building 904 (Prevessin Site) with cosmic muons providing us a reference efficiency plateau of  $(97.54 \pm 0.15)\%$  represented by the black curve. A similar measurement has been done at GIF on the 21<sup>st</sup> of July with the same chamber giving a plateau of  $(78.52 \pm 0.94)\%$  represented

<sup>1</sup>Albeit only roughly using Figure 5.10 due to the lack of actual measurements of the respective positions of each parts of the experimental setup. Using reference dimensions such as the saize of the detector and the size of the photomultiplier, the positions could be deduced.

whose bins corresponds to the RPC copper strips. The strip in which the hit occured is determined by knowing precisely the geometry of the RPC. Muon hits are also filled in different histograms whether they are associated to forward coming ( $\pi \leq \phi < 2\pi$ ) or backward going ( $0 \leq \phi < \pi$ ) muons.

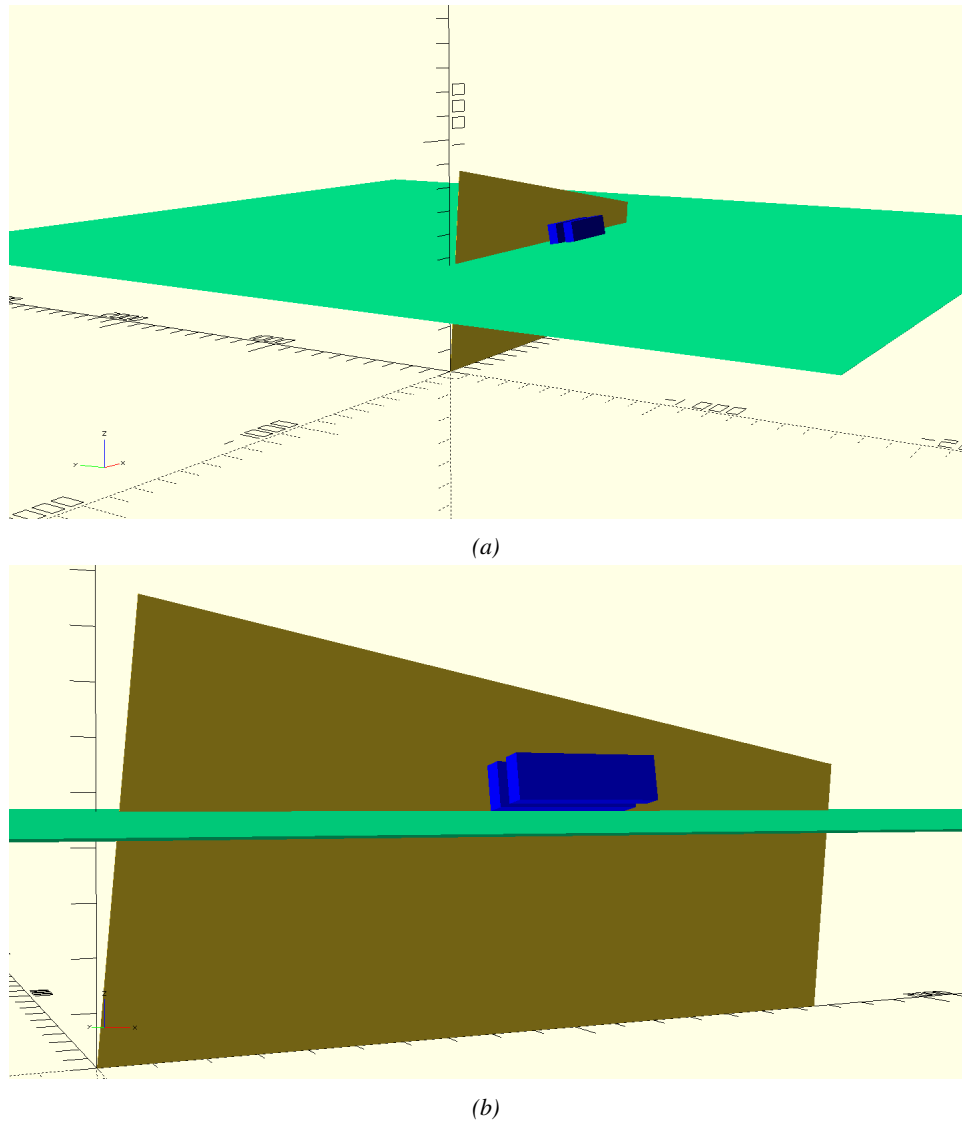


*Figure 5.13: Representation of the layout used for the simulations of the test setup. (a) Global view of the simulated setup. (b) Zoomed view on the experimental setup.*

### 5.2.2.2 Results and limitations

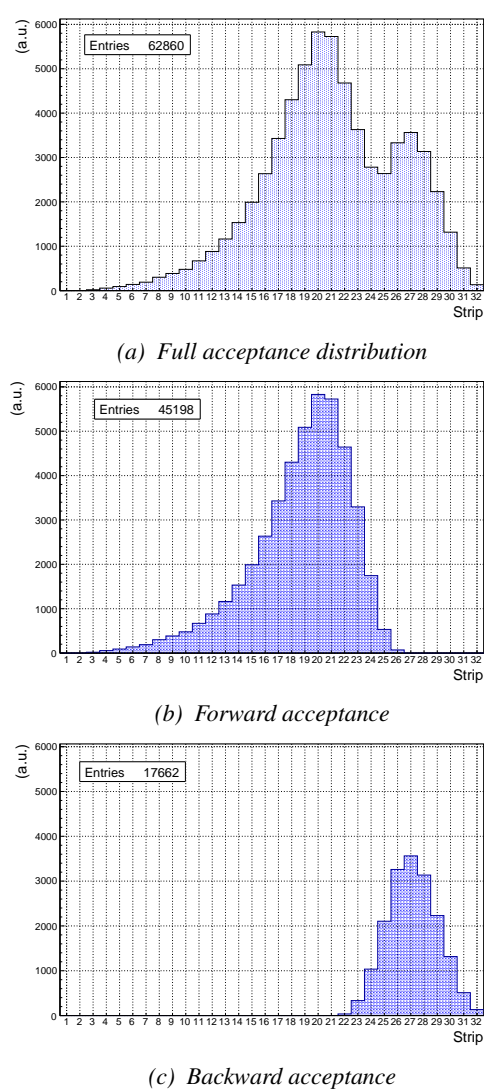


Figure 5.14: Geometrical acceptance distribution as provided by the Monte Carlo simulation.

affected by a variation of the inclination angle, as can be seen in Figure 5.16. Yet, the position of the acceptance peaks in the distribution would be in agreement with what is measured, and the contribution of farward and backward muons would never reach the observation. With an inclination of  $10^\circ$ , 28.1% of the total geometrical acceptance should contribute to detecting backward muons whereas it is measured that the hit profile contains 22.0% of backward data only. Introducing in the simulation an error of  $\pm 2^\circ$  would lead to a correction factor  $c_{geo} = 1.20^{+0.04}_{-0.03}$  allowing for a good improvement of the efficiency measured in GIF, as can be seen from Figure 5.17. GIF measurement is in agreement with the reference curve within statistical errors.

The output from the simulation is given in Figure 5.14 in which the geometrical acceptance distribution of the setup is shown. The distributions for the separate contributions of forward coming and backward going muons are all provided. The strip number is given in a range of 1 to 32 corresponding to the 32 strips contained in each RPC read-out partition even though partition B correponds, by convention, to strip numbers 33 to 64. It can be established than, out of the total amount of muons that have passed through the telescope and reached the RPC, 16.8% were hitting the 16 first strip of the read-out plane corresponding to half partition B1. This number corresponds to the inefficiency. It can be used then to correct the data by scaling up by a factor  $c_{geo} = 1/(1 - 0.168)$  the efficiency measured during data taking.

Nevertheless, the distribution showed in Figure 5.14a differs from the measured hit profile showed in Figure 5.11 as can be seen in Figure 5.15. It is difficult to evaluate a systematic uncertainty on this geometrical correction for different reasons.

First of all, even though the dimensions of the scintillators and of the RPC are well known, the position of each element of the setup with respect to one another was not measured. The extraction of the position of each part of the setup from Figure 5.10 was a first large source of error.

The inclination is also roughly measured to be  $10^\circ$  bringing more uncertainty into the simulation. The acceptance distribution would be

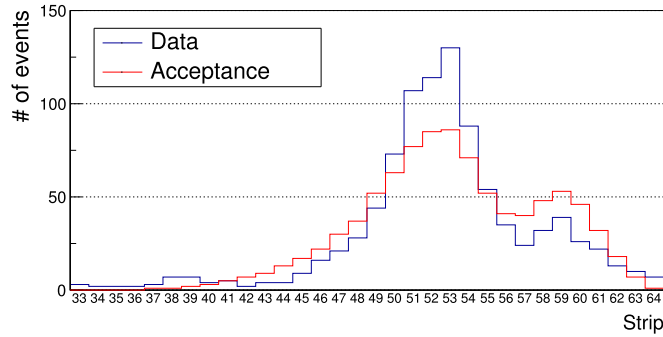


*Figure 5.15: Comparison of the hit distribution recorded in the detector and of the normalised geometrical acceptance distribution.*

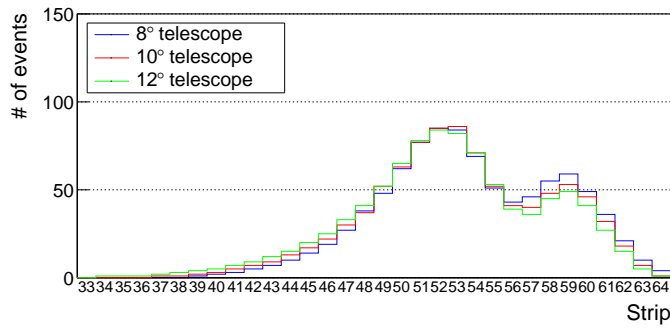


*Figure 5.16: Effect of the variation of telescope inclination on the normalised geometrical acceptance distribution.*

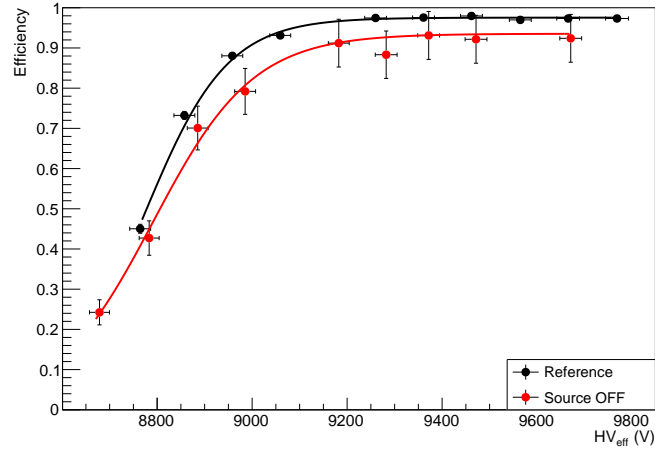


*Figure 5.17: Correction of the efficiency without source. The efficiency after correction gets much closer to the Reference measurement performed before the study in GIF by reaching a plateau of  $(93.52 \pm 2.64)\%$ .*

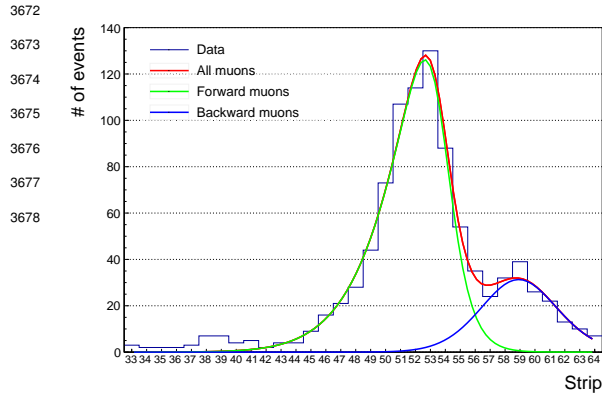


Figure 5.18: Hit distributions over read-out partition B of RE-4-2-BARC-161 chamber together with skew distribution fits corresponding to forward and backward coming muons.

Given the observed difference between the simulation and the measured data, one should realize that the geometrical acceptance and the hit profile are actually not directly comparable. The geometrical acceptance only provides with the information about what the detector can expect to see in a perfect world where all muons are detected in the exact same way. The detection would be independent from their energy or angle of incidence, and there would be no fluctuation of the detector gain due to complex avalanche development. No thresholds would be applied on the scintillators and on the RPC FEEs to reduce the noise, the cross-talk and the corresponding spread of the induced charge observed on the read-out strips. The hit profile provides the final product of all the previously mentioned contributions and can greatly differ from purely geometrical considerations. A full physics analysis involving softwares such as GEANT would be required to further refine the correction on the measured efficiency at GIF.

### 5.2.3 Photon flux at GIF

In order to understand and evaluate the  $\gamma$  flux in the GIF area, simulations have been conducted at the time GIF was opened for research purposes [264]. Table 5.2 gives the  $\gamma$  flux for different distances  $D$  to the source. The simulation was done using GEANT and a Monte Carlo N-Particle (MCNP) transport code, and the flux  $F$  is given with the estimated error from these packages expressed in %.

Nominal ABS	Photon flux $F$ [ $\text{cm}^{-2} \text{s}^{-1}$ ]			
	at $D = 50 \text{ cm}$	at $D = 155 \text{ cm}$	at $D = 300 \text{ cm}$	at $D = 400 \text{ cm}$
1	$0.12 \times 10^8 \pm 0.2\%$	$0.14 \times 10^7 \pm 0.5\%$	$0.45 \times 10^6 \pm 0.5\%$	$0.28 \times 10^6 \pm 0.5\%$
2	$0.68 \times 10^7 \pm 0.3\%$	$0.80 \times 10^6 \pm 0.8\%$	$0.25 \times 10^6 \pm 0.8\%$	$0.16 \times 10^6 \pm 0.6\%$
5	$0.31 \times 10^7 \pm 0.4\%$	$0.36 \times 10^6 \pm 1.2\%$	$0.11 \times 10^6 \pm 1.2\%$	$0.70 \times 10^5 \pm 0.9\%$

Table 5.2: Total photon flux ( $E_\gamma \leq 662 \text{ keV}$ ) with statistical error predicted considering a  $^{137}\text{Cs}$  activity of 740 GBq at different values of the distance  $D$  to the source along the  $x$ -axis of irradiation field [264].

This estimation of the backward versus forward content in the data was done through a fit using a sum of two skew distributions given in Equation 5.1. Although a skew distribution lacks physical interpretation, it allows fitting easily such kind of data, as showed in Figure 5.18.

$$(5.1) \quad \begin{aligned} g(x) &= A_g e^{\frac{-(x-\bar{x})^2}{2\sigma^2}} \\ s(x) &= \frac{A_s}{1 + e^{-\lambda(x-x_i)}} \\ sk(x) &= g(x) \times s(x) \\ &= A_{sk} \frac{e^{\frac{-(x-\bar{x})^2}{2\sigma^2}}}{1 + e^{-\lambda(x-x_i)}} \end{aligned}$$

3695 The table however does not  
 3696 provide in a direct way the flux  
 3697 at the level of the RPC under  
 3698 test. First of all, it is nec-  
 3699 essary to extract the value of  
 3700 the flux from the available data  
 3701 contained in the original paper  
 3702 and then to estimate the flux in  
 3703 2014 at the time the experimen-  
 3704 tation took place. The extraction will be performed for the case of a pointlike source emitting  
 3705 isotropic and homogeneous gamma radiations. The flux  $F_0$  is known at a given reference point sit-  
 3706 uated at  $D_0$  from the source. The gamma flux  $F$  at a distance  $D$  from the source will be expressed  
 3707 with Equation 5.2, assuming that the flux decreases as  $1/D^2$  and where  $c$  is a fitting factor that can  
 3708 be written as in Equation 5.3. Finally, using Equation 5.3 and the data of Table 5.2, with  $D_0 =$   
 3709 50 cm as reference point, Table 5.3 can be built. It is interesting to note that  $c$  for each value of  $D$   
 3710 does not depend on the absorption factor.

$$(5.2) \quad F^{ABS} = F_0^{ABS} \times \left( \frac{cD_0}{D} \right)^2$$

$$(5.3) \quad c = \frac{D}{D_0} \sqrt{\frac{F^{ABS}}{F_0^{ABS}}} \\ \Delta c = \frac{c}{2} \left( \frac{\Delta F^{ABS}}{F^{ABS}} + \frac{\Delta F_0^{ABS}}{F_0^{ABS}} \right)$$

3713 For the range of  $D/D_0$  values available, it is possible to use a simple linear fit to get the evolution  
 3714 of  $c$  that can be expressed as  $c(D/D_0) = aD/D_0 + b$ . Using Formula 5.4, but neglecting the  
 3715 uncertainty on  $D$  that will only be used when extrapolating the values for the position of the RPC  
 3716 under test whose position is not perfectly known, the results shown in Figure 5.19 is obtained.  
 3717 Figure 5.19b confirms that using only a linear fit to extract  $c$  is enough as the evolution of the rate  
 3718 that can be obtained superimposes well on the simulation points.

$$(5.4) \quad F^{ABS} = F_0^{ABS} \left( a + \frac{bD_0}{D} \right)^2, \quad \Delta F^{ABS} = F^{ABS} \left[ \frac{\Delta F_0^{ABS}}{F_0^{ABS}} + 2 \frac{\Delta a + \Delta b \frac{D_0}{D} + \Delta D \frac{bD_0}{D^2}}{a + \frac{bD_0}{D}} \right]$$

3719 During the 2014 Gif tests, the RPC read-out plane was located at a distance  $D = 206$  cm from  
 3720 the source. Moreover, to estimate the strength of the flux in 2014, it is necessary to consider the  
 3721 nuclear decay through time of the Cesium source whose half-life is well known ( $t_{1/2} = (30.05 \pm$   
 3722 0.08) y). The very first source activity measurement has been done on the 5<sup>th</sup> of March 1997 while  
 3723 the Gif tests were done in between the 20<sup>th</sup> and the 31<sup>th</sup> of August 2014, i.e. at a time  $t =$   
 3724  $(17.47 \pm 0.02)$  y resulting in an attenuation of the activity from 740 GBq in 1997 to 494 GBq in  
 3725 2014. All the needed information to extrapolate the expected flux through the detector at the moment  
 3726 of the Gif preliminary tests has now been assembled, leading to Table 5.4. By assuming an average  
 3727 sensitivity of the RPC to  $\gamma$  emitted by the  $^{137}\text{Cs}$  source of  $(2 \pm 0.2) \times 10^{-3}$  [271], the order of  
 3728 magnitude of the expected hit rate per unit area would be of the order of kHz for a fully opened  
 3729 source, as reported in the last column of the table. As photons are not charged particles, they mainly

3730 interact with the electrodes where they are converted into electrons. The HPL electrodes are not very  
 3731 sensitive to gamma photons, hence only a small fraction of the incoming flux is seen by the RPC.

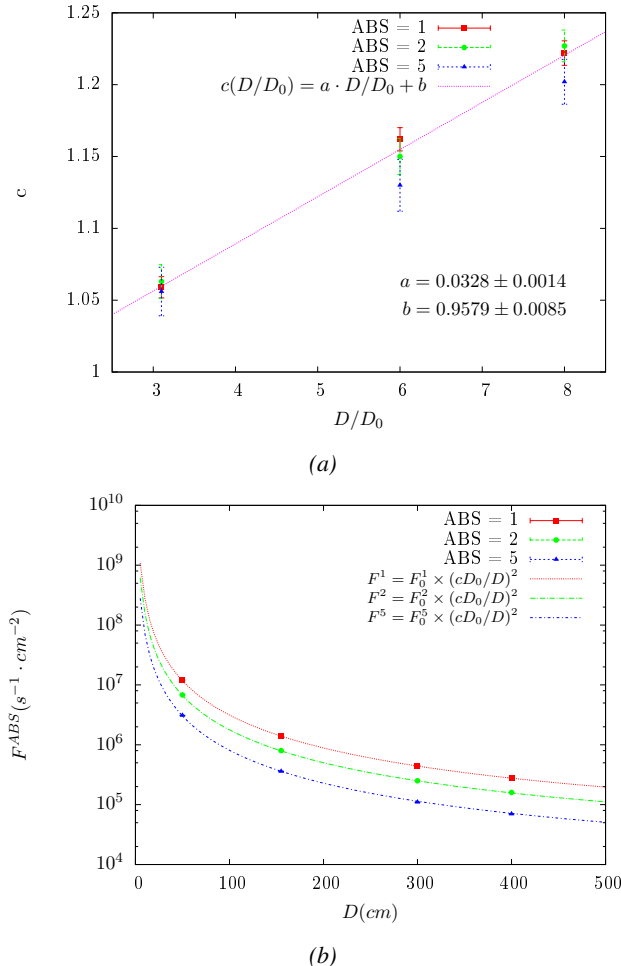


Figure 5.19: (a) Linear approximation fit performed on the data extracted from table 5.3. (b) Comparison of Equation 5.4 with the simulated flux using  $a$  and  $b$  given in figure 5.19a in Equation 5.2 and the reference  $D_0 = 50$  cm and the associated flux for each absorption factor  $F_0^{ABS}$  from table 5.2.

Nominal ABS	Photon flux $F$ [ $cm^{-2} s^{-1}$ ]			Rate [Hz/cm <sup>2</sup> ] at $D^{2014} = 206$ cm
	at $D_0^{97} = 50$ cm	at $D^{97} = 206$ cm	at $D^{2014} = 206$ cm	
1	$0.12 \times 10^8 \pm 0.2\%$	$0.84 \times 10^6 \pm 1.2\%$	$0.56 \times 10^6 \pm 1.2\%$	$1129 \pm 14$
2	$0.68 \times 10^7 \pm 0.3\%$	$0.48 \times 10^6 \pm 1.2\%$	$0.32 \times 10^6 \pm 1.2\%$	$640 \pm 8$
5	$0.31 \times 10^7 \pm 0.4\%$	$0.22 \times 10^6 \pm 1.2\%$	$0.15 \times 10^6 \pm 1.2\%$	$292 \pm 4$

Table 5.4: The data at  $D_0$  in 1997 is taken from [264]. Using Formula 5.4, the flux at  $D$ , including an error of 1 cm, can be estimated in 1997. Then, taking into account the attenuation of the source activity, the flux at  $D$  can be estimated at the time of the tests in GIF in 2014. Assuming a sensitivity of the RPC to gammas,  $s = (2 \pm 0.2) \times 10^{-3}$  [271], an estimation of the hit rate per unit area is obtained.

3732 The goal of the study was to have a good measurement of the intrinsic RPC performance without  
 3733 source irradiation. Then, taking profit of the two working absorbers, at absorption factors 5 (300 Hz)  
 3734 and 2 ( $\sim 600$  Hz) the goal was to show that the detectors fulfill the performance certification of CMS  
 3735 RPCs. Finally, a first assessment of the performance of the detectors at higher backgrounds was  
 3736 obtained with absorption factor 1 (no absorption and  $>1$  kHz)).

### 3737 5.2.4 Results and discussions

3738 The data taking at GIF has been conducted between the 21<sup>st</sup> and the 31<sup>st</sup> of August, 2014. Data  
 3739 have been collected with source both ON and OFF using three different absorber settings (ABS 5, 2  
 3740 and 1) in order to vary the irradiation on the RPC. For each source setting, two HV scans have been  
 3741 performed with two different trigger settings. During a first scan the trigger sent to the TDC module  
 3742 was the coincidence of the two scintillators composing the telescope while during a second scan  
 3743 the trigger was a pulse coming from a pulse generator in order to measure the noise or gamma rate  
 3744 seen by the chamber. Indeed, using a pulse generator allows to trigger at moments not linked to any  
 3745 physical event and, hence, to obtain a *RANDOM* trigger on noise and gamma events to measure the  
 3746 associated rates, the probability to have a pulse in coincidence with a cosmic muon being negligible.

3747 From the cosmic trigger scans, a summary of the efficiencies and corresponding cluster sizes  
 3748 is shown in Figure 5.20. The efficiency curves with Source ON show a shift with respect to the  
 3749 case without irradiation. With ABS 5, the general shape of the efficiency curve stays unchanged  
 3750 whereas a clear alteration of the performance is observed at ABS 2 and ABS 1. From the cluster  
 3751 size results, a reduction of the mean cluster size under irradiation can be observed at equivalent  
 3752 efficiency. This effect can be due to the perturbation of the electric field by the strong flux of gamma  
 3753 particles interacting with the electrodes. With the increasing number of photons being converted  
 3754 into electrons, an increasing number of charges need to be recombined all over the volume of the  
 3755 electrodes that act as capacitors. A discharge of the electrodes reduces the effective field seen in the  
 3756 gas volume by introducing a voltage drop across the electrodes thickness. The constant pressure put  
 3757 on the detector by the converting photons can become strong enough to uniformly affect the gain of  
 3758 the detector.

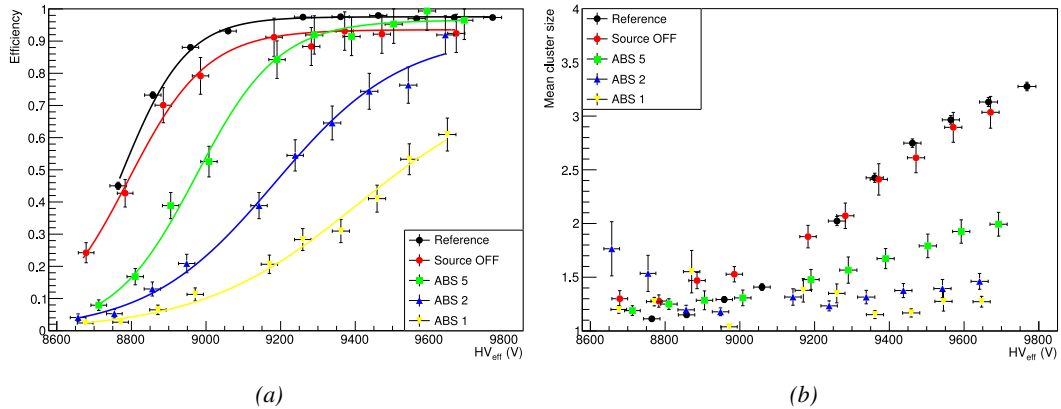
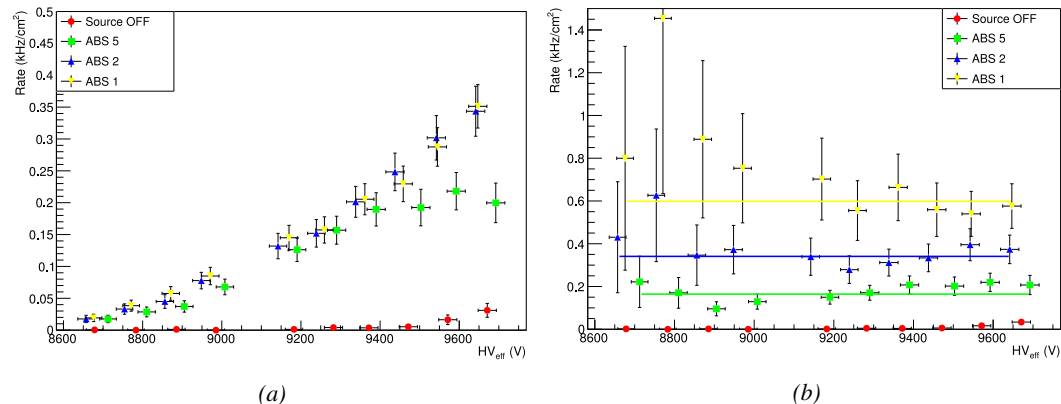


Figure 5.20: Efficiency (a) and cluster size (b) of chamber RE-4-2-BARC-161 measured at GIF with Source OFF (red) and Source ON using different absorber settings: ABS 5 (green), ABS 2 (blue) and ABS 1 (yellow). The results are compared to the Reference values obtained with cosmics.

It is necessary to study the evolution of the performance of the chamber with the increasing rate per unit area. The hit rate is measured as the number of hits detected in the RPC normalized to the surface area of the read-out and to the total integrated time. The integrated time is linked to the time window in which the TDC searches for data related to a trigger signal. Data is continuously kept in the buffer of the TDCs but not all of these data is of interest. When a trigger signal is sent to the TDC module, the TDC saves all of the data located in a certain time window set around the time stamp of the signal. The total integrated time is then the total number of trigger signals times the width of a search time window.

In Figure 5.21a, the noise rate when the source is OFF remains low but increases at voltages above 9500 V. Aside of the natural increase of the noise with increasing voltage, the rise of the noise rate in the detector can be related to the increased streamer probability observed with such a large electric field. The rates measured at GIF with source ON all show a similar behaviour until a high voltage of approximately 9400 V at which the rate of ABS 5 reaches a plateau, coinciding with the chamber reaching full efficiency. It is important to note that, even though the rates look similar independently from the gamma flux, relative to the efficiency of the chamber, the rate actually increases with increasing flux at equivalent efficiency. A rough way to measure the rate effectively observed by the detector for each source setting would be to normalize the measured rates to the efficiency of the detector. This exercise was done with Figure 5.21b from which constant fits were done on Source ON data in order to extract the rate the chamber was subjected to. This method leads to rates of  $(164 \pm 12)$  Hz/cm<sup>2</sup>,  $(340 \pm 26)$  Hz/cm<sup>2</sup> and  $(598 \pm 50)$  Hz/cm<sup>2</sup> respectively for ABS 5, 2 and 1 which is consistent with the absorber values. Also, contrary to the case of the source OFF measurement, no rise of the noise is observed at ABS 5. This difference could be explained by the efficiency shift that is related to a decrease of the electric field across the gas volume. [But, as no data were taken at higher voltage values, this assumption can't be confirmed.] Could be confirmed by a study of the streamer probability for each dataset.



*Figure 5.21: Rates in chamber RE-4-2-BARC-161 measured at GIF with Source OFF (red) and Source ON using different absorber settings: ABS 5 (green), ABS 2 (blue) and ABS 1 (yellow). On Figure (b), the rates of Figure (a) were normalized to the measured efficiency, and constant fits are performed on Source ON data showing the gamma rate in the chamber.*

The results need to be taken with care as a better estimation of the rate would have been to push the detector towards higher voltages to reach the efficiency plateau for each absorber configuration and only then extract the measured rate at working voltage, defined as in Formula 3.25. Nevertheless,

3787 using this method to estimate the rate to which the chamber is subjected, it is possible to look at the  
 3788 evolution of the  $HV_{50}$  and  $HV_{knee}$  as a function of the increasing rate as showed in Figure 5.22.  
 3789 The results from GIF suggest that at a rate of  $600 \text{ Hz/cm}^2$  the working voltage of the chamber is  
 3790 increased by a thousand V while the efficiency is reduced to approximately 80%, although the result  
 3791 still is consistent with an efficiency better than 90% due to the large error on the measurement.

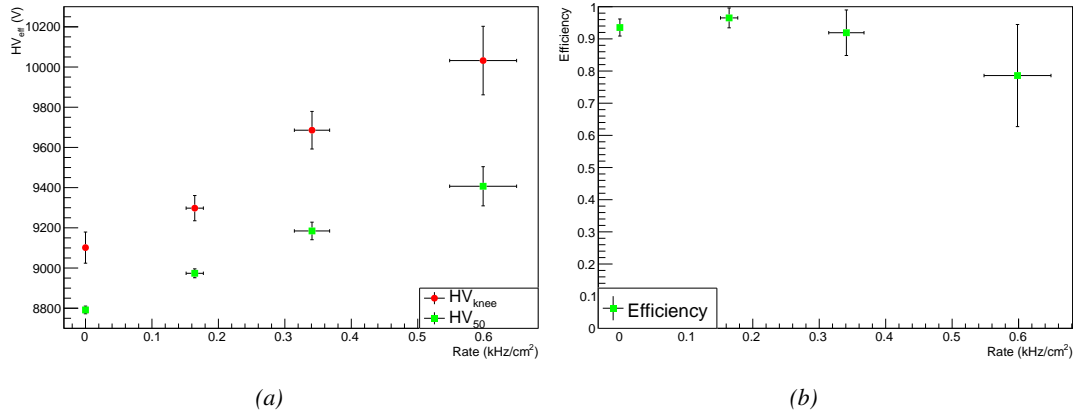


Figure 5.22: Evolution of the voltages at half maximum and at 95% of the maximum efficiency (Figure 5.22a), and of the maximum efficiency (Figure 5.22b) as a function of the rate in chamber RE-4-2-BARC-161. The data is extracted from the fits in Figures 5.20a and 5.21b.

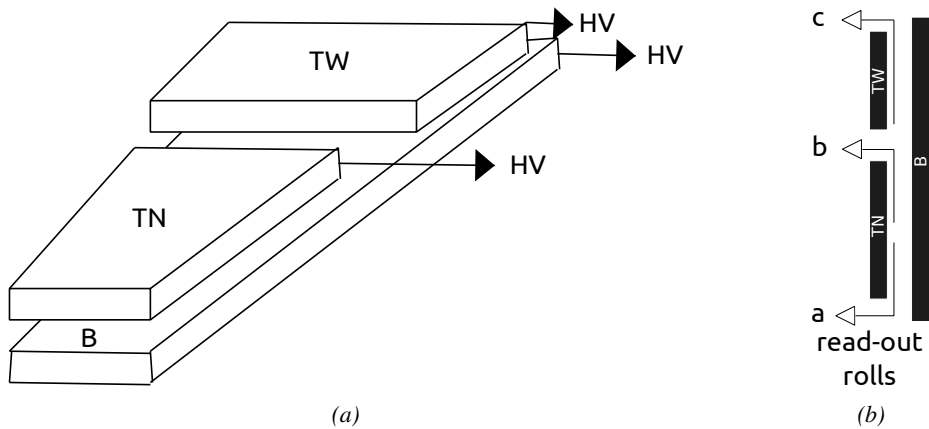
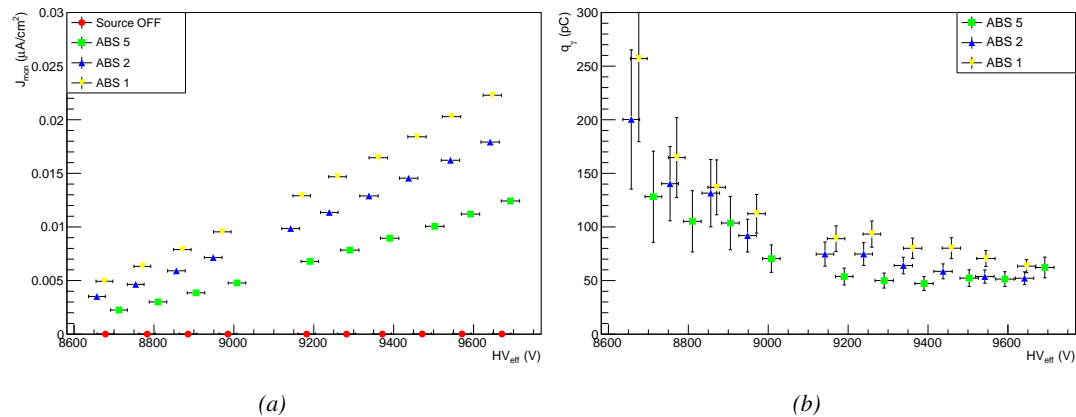


Figure 5.23: Presentation of a double-gap endcap RPC with its three RPC gaps. Due to the partitioning of the read-out strips into three rolls, the TOP layer of gap is divided into two gaps: TOP NARROW (TN) and TOP WIDE (TW). The BOTTOM (B) only consists in one gap.

3792 It is likely that the rates obtained through fitting on normalized values is underestimated. Indeed,  
 3793 monitoring the current in the three gaps composing a CMS endcap RPC (Figure 5.23) while knowing  
 3794 the rate, the charge deposition per avalanche  $q_\gamma$  can be computed. A current density, expressed in  
 3795  $\text{A/cm}^2$ , divided by a rate per unit area, expressed in  $\text{Hz/cm}^2$  yields a charge expressed in C. The  
 3796 current driven by the RPC is assumed to be due to the irradiation, hence, to the avalanches developing

in the gas volume due to the photons of the Cesium source. On the other hand, the rate is supposed to be a measure of the number of photons interacting with the detector. This way, it comes that the charge deposition per avalanche is expressed like  $q_\gamma = J_{mon}/R_\gamma$ , with  $J_{mon}$  being the monitored current density and  $R_\gamma$  the measured  $\gamma$  rate. The current density is computed as the sum of the current density measured in the top and bottom gap layers,  $J_{mon} = (I_{mon}^{TW} + I_{mon}^{TN})/(A_{TW} + A_{TN}) + I_{mon}^B/A_B$ , with  $A_{B,TN,TW}$  being the active area and  $I_{mon}^{B,TN,TW}$  the monitored currents of the gaps. According to Figure 5.24, the charge deposition per avalanche consistently converges to a value of the order of 50 pC for each absorber setting which corresponds to a value more than twice larger than what reported in literature for CMS detectors [271, 272] indicating that the rates could have been wrongly evaluated during the short study performed at GIF. An increase of the  $\gamma$  rate by a factor 2 would actually be consistent with the expected rates calculated in Table 5.4, assuming the sensitivity to  $\gamma$  to be of the order of  $(2 \pm 0.2) \times 10^{-3}$ .



*Figure 5.24: Current density (a) and charge deposition per gamma avalanche (a), defined as the current density normalized to the measured rate taken from Figure 5.21a as a function of the effective high voltage in chamber RE-4-2-BARC-161 measured at GIF with Source ON using different absorber settings: ABS 5 (green), ABS 2 (blue) and ABS 1 (yellow).*

Overall, working at GIF has been a rewarding experience as it offered CMS RPC R&D team the possibility to start developing the necessary skills and tools that would become the core of GIF++ experiment. The quality of the results can be argued both due to the little robustness of the experimental setup and the lack of available statistics to draw conclusions from, bringing large errors on the final result. The confrontation of the data to known results pointed to a failure in correctly measuring the  $\gamma$  rate at working voltage and, hence, to an overestimation of the charge per avalanche and of the drift of working voltage with increasing rate. Nevertheless, the prototypes of DAQ and offline analysis tools proved to be reliable.

### 5.3 Longevity tests at GIF++

#### 5.3.1 Selection and characterization of CMS RPCs for longevity at GIF++

In the perspective of future upgrades of LHC that would bring detectors to be operated in a high irradiation environment, the new Gamma Irradiation Facility of CERN was first proposed in 2009 [273].

3821 The Gif++ would thus provide all LHC R&D teams working on behalf of the different LHC exper-  
 3822 iment with a facility to perform longevity studies using a very intense Cesium gamma source.

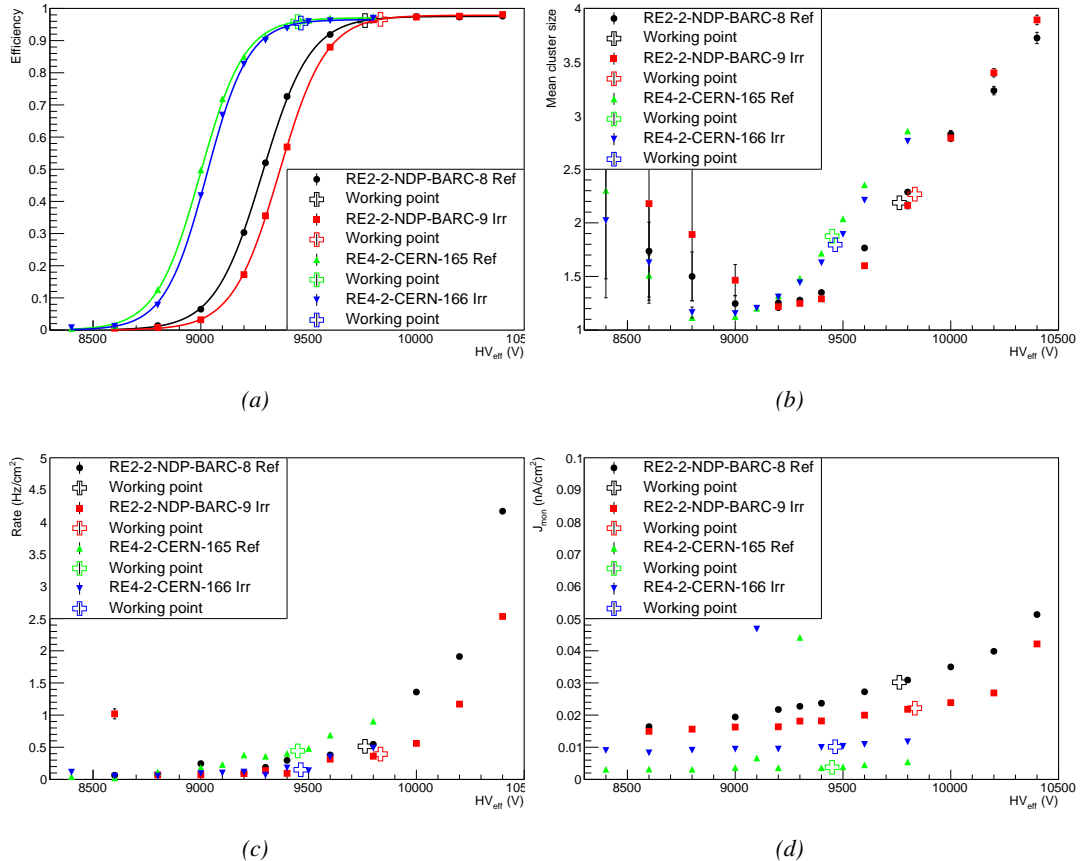


Figure 5.25: Characterization of CMS RPC detectors foreseen to be used at Gif++ for longevity studies of the present system. Using cosmic muons, efficiency (a) and cluster size (b) were measured as well as noise rate (c) and current density (d). For each detector, the working voltage, defined as in Formula 3.25, was extracted from sigmoid fits performed in Figure (a) and the values of efficiency, cluster size, noise rate and current density at this voltage are reported using open crosses.

3823 In the specific case of CMS RPC, the longevity studies imply a constant irradiation of selected  
 3824 detectors in order to accumulate a charge equivalent to what is expected during HL-LHC, i.e. a  
 3825 charge of  $0.8 \text{ C}/\text{cm}^2$  according to Figure 5.2 including a safety factor 3. Other detectors are left  
 3826 non-irradiated to be used as references. Throughout the irradiation campaign, the performance of  
 3827 the irradiated and reference detectors will be periodically probed using the high intensity H4 muon  
 3828 beam. Dedicated test beam periods will be used to measure the efficiency and  $\gamma$  rate at the level of the  
 3829 detectors. Different source absorber settings will test the rate capability of CMS RPCs, that needs to  
 3830 be certified above  $600 \text{ Hz}/\text{cm}^2$ . Using a muon beam will also help identifying signs of ageing in the  
 3831 case the performance of the irradiated detectors diverges from those of the reference detectors with  
 3832 increasing accumulated charge. Other than the performance of the detectors, signs of ageing could  
 3833 come from increasing dark current that would be related to local ageing of the electrodes triggered

3834 by the increased hydrofluoric acid ( $HF$ ) production in an irradiated environment.  $HF$  is produced  
 3835 by the decomposition of  $C_2H_2F_4$  molecules during the charge multiplication process and leads to  
 3836 increased dark current and noise in Bakelite RPCs treated with linseed oil. This effect is strongly  
 3837 reinforced by the presence of UV photons [274, 275]. A close monitoring of the current driven by the  
 3838 detectors will then be necessary as well as dedicated periodical electrode resistivity measurements  
 3839 and chromatography analyses on the gas exhaust.

3840 As the maximum background in CMS is found in the endcap disks, the choice was made to  
 3841 focus the GIF++ longevity studies on endcap chambers. Most of the RPC system was installed in  
 3842 2007. Nevertheless, the large chambers in the fourth endcap (RE4/2 and RE4/3) have been installed  
 3843 during LS1 in 2014. The HPL of these two different productions possibly having slightly different  
 3844 properties, four spare chambers of the present system were selected. From the original CMS RPC  
 3845 system, two RE2/2 spares were selected along two RE4/2 spares from the newest detectors. Having  
 3846 two chambers of each type allowed to always keep one of them non-irradiated as reference. Due  
 3847 to the limited gas flow in GIF++, the RE4 chamber remained non-irradiated until end of November  
 3848 2016 when the longevity studies could finally be started on those chambers.

3849 The performance of the chambers prior to the start of the longevity campaign was character-  
 3850 ized in Ghent before their transportation to CERN for installation in the GIF++. The results of the  
 3851 characterization are showed in Figure 5.25 and summarized in Table 5.5. A clear difference in per-  
 3852 formance for both types of chambers is observed as the working voltages of the newest chambers,  
 3853 of type RE4, are 300 to 400 V lower to the older chambers indicating that the gap thickness of RE4  
 3854 detectors could be thinner. This conclusion could as well be supported by the lower cluster size at  
 3855 working voltages that are also smaller in RE4 chambers. Even though the measured currents are  
 3856 low, RE4 detectors draw less current without irradiation than RE2 detectors pointing to a difference  
 3857 in electrode resistivity that were produced at different moments. Efficiency and noise rate levels are  
 3858 of the same order of magnitude for both type of RPCs.

RPC	RE2–2–NPD–BARC–08	RE2–2–NPD–BARC–09	RE4–2–CERN–165	RE4–2–CERN–166
Used as	Reference	Irradiation	Reference	Irradiation
$HV_{WP}$ [V]	(9762 $\pm$ 6)	(9833 $\pm$ 6)	(9449 $\pm$ 5)	(9464 $\pm$ 5)
Efficiency at WP	(96.2 $\pm$ 0.3)	(96.6 $\pm$ 0.3)	(95.9 $\pm$ 0.3)	(95.5 $\pm$ 0.3)
Cluster size at WP	(2.19 $\pm$ 0.04)	(2.27 $\pm$ 0.05)	(1.88 $\pm$ 0.04)	(1.80 $\pm$ 0.04)
Noise at WP [Hz/cm <sup>2</sup> ]	(0.51 $\pm$ 0.01)	(0.39 $\pm$ 0.01)	(0.44 $\pm$ 0.00)	(0.15 $\pm$ 0.01)
$J^{WP}$ [pA/cm <sup>2</sup> ]	(30.1 $\pm$ 0.1)	(22.2 $\pm$ 0.1)	(3.8 $\pm$ 0.0)	(10.2 $\pm$ 0.0)

Table 5.5: Summary of the characterization measurement performed in Ghent on CMS RPC detectors foreseen to be used at GIF++ for longevity studies of the present system. For each detector, the working voltage, defined as in Formula 3.25, was extracted from sigmoid fits performed in Figure 5.25a. The values of efficiency, cluster size, noise rate and current density at this voltage are reported.

### 3859 5.3.2 RPC test setup

3860 For an easy manipulation of the detectors, a trolley with a structure containing slots in which the  
 3861 RPCs can be slid vertically was used and is referred to as T1. When in position, each chamber is  
 3862 in a plane perpendicular to the beam line and the source flux as can be seen through Figure 5.26,  
 3863 and receives a uniform irradiation. Moreover the trolley allows for easy movement of the system.  
 3864 Indeed, the position of the trolley varies according to the specific measurements that are being done.

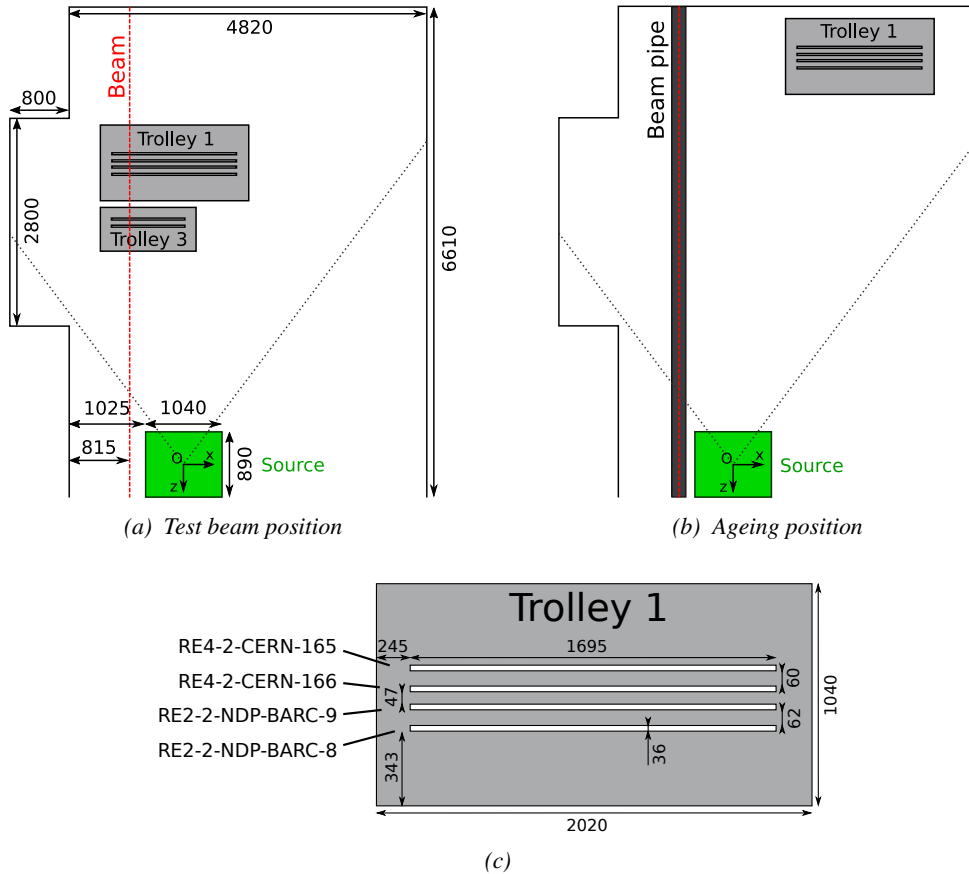


Figure 5.26: CMS RPC setup inside the GIF++ bunker during test beam (a) and ageing periods (b). The space in between the RPCs and the source is usually used by other detectors while the space in between T1 and the upstream wall is not filled. Due to the presence of the beam pipe, the trolley is moved away from the beam line during irradiation periods and placed further away from the source for less intense irradiation. The position of the trolley can vary due to the use of the space by other setups and is then not exact. Nonetheless, the position of the chambers in the trolley is fixed and given in Figure (c).

During the dedicated test beam periods, the GIF++ experiments are in control of the muon beam. The trolley is placed in the upstream region of the bunker, in the beam line, as described through Figure 5.26a. The CMS RPC detectors are the furthest away from the source as other detectors need to be certified at higher background rates. An additional trolley, referred to as T3, contains iRPCs and is placed between the source and the T1 trolley. Indeed, iRPCs need to be certified at higher rates and thus need to be placed closer to the source to receive a stronger irradiation using the same absorber settings. The space on T1 being limited, the tracking RPCs used for extra offline information during the analysis are placed on the same trolley as the iRPCs. they are kept at full efficiency at all time to reconstruct muon tracks and to correlate them with hits recorded in T1 chambers. The beam trigger system is composed of three scintillators. Two are placed outside on each side of the bunker and of the third scintillator is placed in the beam line in between T1 and the wall.

Most of the year, outside of these test beam periods, T1 is placed in the so called *ageing position* corresponding to the furthest position from the source outside of the beam line. The latter needs to

3879 stay clear during periods where GIF++ doesn't have the control of the beam so that a beam tube can  
 3880 be installed through the bunker, as can be seen in Figure 5.26b. The reason for placing the chambers  
 3881 as far as possible from the source comes from the too high irradiation delivered by the source during  
 3882 the irradiation periods where all the other groups having placed detectors in the bunker require as  
 3883 much charge integration as possible. Hence, the source is operated without any absorbers. On the  
 3884 contrary, during the test beam periods, all the groups working in GIF++ are interested in operating  
 3885 the source using various absorber settings to study the performance of their detectors under different  
 3886 irradiation conditions. T1 RPCs are kept at a stanby voltage of 6500 V when the other groups need  
 3887 to work with ABS 1 due to the proximity of the trolley to the source compared to ageing periods.

3888 From the bunker area, long cables and pipes running through the wooden floor connect the de-  
 3889 detectors to the service area, visible in Figure 5.6. The service area hosts all the high and low voltage  
 3890 power supplies, the TDCs and computers used for data acquisition and preliminary offline analysis.  
 3891 The gas system required for the gaseous detectors installed in GIF++ can also be found in the service  
 3892 area [276].

3893 The detectors read-out is, as in the case of GIF, connected to V1190A VME TDCs communicating  
 3894 with the DAQ computer via a V1718 VME bridge manufactured by CAEN. At the end of each data  
 3895 tacking, the preliminary analysis is run to fill the Detector Control Software webpage, referred to as  
 3896 WebDCS, with Data Quality Monitoring (DQM) histograms. The WebDCS is a custom made DCS  
 3897 application for the specific case of GIF++ RPCs. It provides online information about the environ-  
 3898 mental parameters in the bunker as well as the state of each detector. A constant monitoring of  
 3899 all the environmental parameters, in different points of the bunker area, gas parameters, to control its  
 3900 composition, temperature and pressure, and of the voltages and currents delivered by the power sup-  
 3901 plies is performed and displayed on the homepage of the WebDCS interface. Moreover, it contains  
 3902 the database with all the RPC data in the form of ROOT files and of summary hisograms. Hence, it  
 3903 is a useful tool for the shifters on duty in the control room located farther in the building, away from  
 3904 the beam lines.

### 3905 5.3.3 GIF++ data flow

3906 At GIF++, the CMS RPC R&D setup collects different types of data from the detector monitoring  
 3907 parameters, such as voltage and currents, the gas, source, and environmental parameters, and, of  
 3908 course, the TDC data related to the actual muon and gamma measurements. These different data  
 3909 sources correspond to three different data flows as presented in Figure 5.27.

3910 The *Data Interchange Protocol (DIP)* flow, DIP being a communication system allowing for  
 3911 exchange of real-time information between systems [277], concerns all the data coming from the  
 3912 gas composition, temperature and humidity, the environmental temperature and pressure, the source  
 3913 settings and the radiation monitoring sensors. At the experimental area, all data of interest for all of  
 3914 the users of the facility (source settings, radiation monitoring, gas composition at the exit of the gas  
 3915 mixer and general environmental information) are measured, distributed and also stored in the data  
 3916 of the experimental hall where is located the GIF++. Access to the database is done through DIP  
 3917 communication. The measurement of more specific data such as gas flow, temperature and humidity  
 3918 at the level of the detectors (upstream and downstream of the detectors) as well as environmental  
 3919 parameters has to be arranged by the users themselves. For this reason, several pressure, temper-  
 3920 ature and humidity sensors were installed on the gas distribution system of the RPC trolleys. The  
 3921 corresponding data flow, although not related to DIP itself, is saved together with the DIP data into  
 3922 the local CMS RPC database and displayed on the front page of the WebDCS. In the case any of

3923 the measured values go out of their optimal range, the WebDCS will produce corresponding alerts.  
 3924 The data are particularly important to perform the PT correction described in Section 3.4 of Chapter  
 3925 3 and to stabilize the effective voltage of the detectors. Monitoring history plots are made using  
 3926 JavaScript and are also displayed for easy access to past information, as shown in Figure 5.28.

3927 The data flow related to the monitoring of the detector high voltages and currents, referred to  
 3928 as *CAEN flow* as a reference to the manufacturer of power supplies, is handled through direct com-  
 3929 munication between the DAQ computer and the power supply main frames. Finally, the DAQ flow  
 3930 concerns all data acquired through the use of the TDCs, i.e. all the muon or gamma event data  
 3931 recorded by the detectors under test at Gif++. It was already discussed that when a trigger signal is  
 3932 sent to a TDC module, the TDC saves all of the data located in a certain time window set around the  
 3933 time stamp of the signal. The trigger signal in the case of Gif++ can be a coincidence of the trigger  
 3934 scintillators or a signal from a pulse generator. The DAQ computer extracts from the TDC buffers the  
 3935 list of fired channels and of associated time stamps for each trigger signal. The data is then used to  
 3936 reconstruct muon tracks along the CMS RPC setup at the Gif++ or to compute the noise and gamma  
 3937 rates associated to a certain source setting.

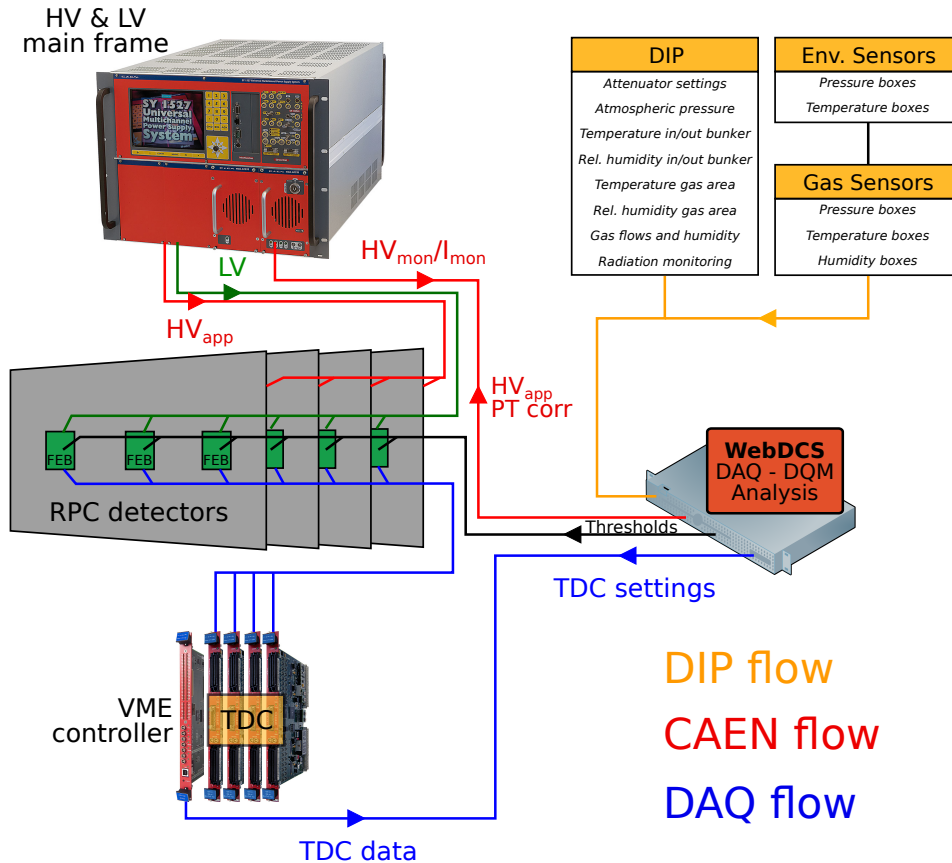


Figure 5.27: Visualisation of the main data flows in the CMS RPC setup at the Gif++. The yellow flow lines correspond to the DIP flow used for source, environmental and gas information. The red flow lines are for the CAEN flow through which the WebDCS communicates the voltages to be applied on the detectors using pressure and temperature information and retrieves the monitored voltages and currents. Finally, the blue flow lines correspond to the DAQ flow through which the RPC data is collected from the TDCs by the computer.

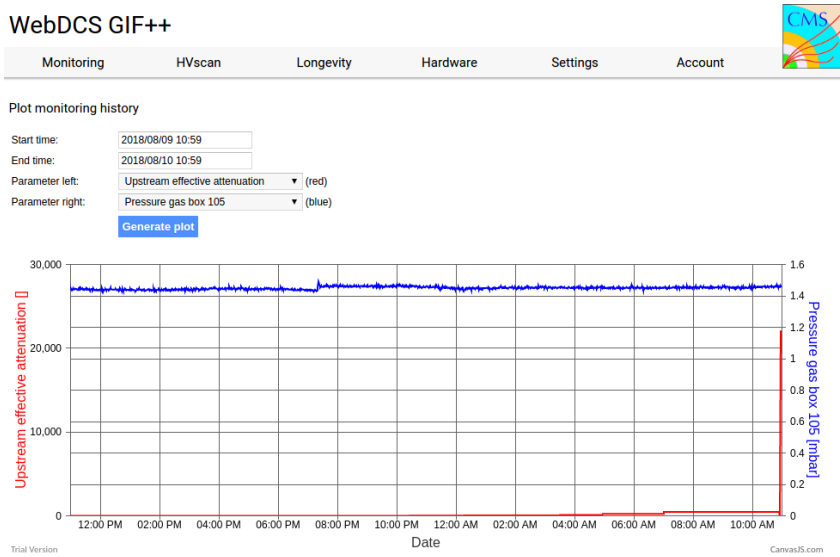


Figure 5.28: DIP monitoring history accessed through the GIF++ WebDCS interface.

### 5.3.4 Measurements performed during beam periods

As previously described, two types of measurements are performed on the chambers during beam periods. On the one hand, it is interesting to measure the efficiency of the RPCs with increasing voltage with different source absorber settings but on the other hand, it is important to correlate the efficiency information to the gamma rate seen by the chambers at the different voltages. The choice was made to separate efficiency measurements from rate measurements to better manage time and data volume. In both cases, TDC data recorded during so called *HV scans* is divided into *runs*, one for each high voltage point, whose data is stored into ROOT files. The TDC settings used during both these scans as well as the ROOT data structure are detailed in Section A.4.2 of Appendix A.

The goal of both efficiency and rate scans is to measure the rate capability of the detectors but also to monitor any degradation of the performance due to ageing. This way, during test beam periods the efficiency and corresponding gamma background are measured to correlate the evolution of rate capability at different stages of irradiation. In the absence of other signs of ageing, a reduction of the rate capability could be related to an increase of the electrodes resistivity.

#### 5.3.4.1 Efficiency scans

The HV scans performed to specifically measure the muon detection efficiency under different irradiation conditions follow a standardized procedure. Data using the DAQ is taken at the same 12 HV points for all chambers, ranging from 9 kV to 10.1 kV in steps of 100 V. For each HV run, a minimum of 5000 muon beam triggers, provided by the coincidence of the three scintillators, is required in order to accumulate enough statistics for a reliable computation of the efficiency of the detectors. In addition to the four RPCs held on T1, two tracking RPCs installed on T3 are kept at a fixed voltage of 9.7 kV to provide the analysis software [278] with beam position information to exclude off-track signals. The tracking RPCs are double gap detectors featuring 2 mm HPL electrodes and 2 mm gas gaps. They are prototypes built by the italian company *General Technica* using a different

3962 production of HPL. Finally, the monitored currents and voltages are recorded in histograms along  
 3963 with the TDC data in a different ROOT file for each run.

3964 HV scans are taken for different source settings as the goal is to irradiate all the detectors with a  
 3965 minimal rate of  $600 \text{ Hz/cm}^2$ . Usually, a full study of the performance of the detectors is performed  
 3966 with Source OFF, and then with nine absorber settings that attenuate the nominal gamma flux by  
 3967 factors from more than 200 to only 3, where settings with fully opened source are avoided with  
 3968 RPCs in test beam position. Aside of the measurement of the efficiency, it is also possible to extract  
 3969 a quantity that can be assimilated as the resistivity of the detectors by comparing the reconstructed  
 3970 sigmoids to a reference curve. This will be further detailed in a following paragraph.

### 3971 **5.3.4.2 Rate scans**

3972 The background measurements are performed using a similar HV scan procedure as for the efficiency  
 3973 measurements. The HV scan in test beam periods is taken at fewer HV points compared to the  
 3974 efficiency scans as the region of interest is located around the knee and efficiency plateau of the  
 3975 detectors, i.e. these scans are performed only on six HV points ranging from 9.5 kV to 10 kV. The  
 3976 value of the rate at the operating voltage is then deduced from the efficiency scan through linear  
 3977 interpolation. A good estimation of the rate requires a long enough integrated time of the TDC  
 3978 data. The way data is collected, detailed in Appendix A, makes the DAQ search for data stored in  
 3979 the TDC buffers prior to the trigger signal. The time window from which the data can be collected  
 3980 ranges from 25 ns to more than  $50 \mu\text{s}$ . With the Cesium source delivering a constant gamma flux, it  
 3981 was decided that a total integrated time of 0.2 s would be enough to have a reliable calculation of the  
 3982 gamma rate. This is achieved by taking 20,000 random trigger pulses delivered by a pulse generator  
 3983 at a frequency of 300 Hz while extracting  $10 \mu\text{s}$  of data from the buffers for each trigger.

3984 Separating the rate and efficiency measurements was motivated by the inconsistency of the muon  
 3985 beam provided in GIF++<sup>2</sup>. Using periods without beam to measure rates with a good statistics allows  
 3986 for faster study programs. Moreover, the number of muons per beam spill depends strongly on the  
 3987 user setups placed upstream of the GIF++ and on the specific beam optic magnet settings. Collecting  
 3988 20,000 events could then take too long for the other users at the GIF++. Hence, efficiency scans are  
 3989 performed with lower statistics, and the time window from which the TDC data are extracted is  
 3990 strongly reduced (400ns for efficiency scans versus  $10 \mu\text{s}$  for rate scans) to keep the data size to its  
 3991 bare minimum.

### 3992 **5.3.4.3 Offline analysis and Data Quality Monitoring**

3993 The data recorded during efficiency and rate scans always consists of two ROOT files per run, where  
 3994 each run corresponds to a certain HV point. One of the files contains the TDC data, a collection  
 3995 of hits and time stamps per active channel on the read-out of the RPCs, while the second is the  
 3996 CAEN main frame data, i.e. the detector currents and high voltages. The data are systematically  
 3997 analysed at the end of each scan using the Offline Analysis tool of GIF++, detailed in Appendix B,  
 3998 that produces histograms such as hit, rate and time profiles, hit multiplicities, gamma cluster sizes or  
 3999 multiplicities for the DQM display of the WebDCS, as shown in Figure 5.29. More histograms can be  
 4000 accessed through the ROOT browser included in the WebDCS, as shown in Figure 5.30. Moreover,

---

<sup>2</sup>During test beam periods, the delivery of the muon beam at the SPS North Area depends on the LHC program. As the SPS is used to feed the LHC with accelerated protons, the priority is given to the LHC. Other than the LHC, the delivery of muon beams can also be stopped due to maintenance or breakdown on the acceleration lane. This may translate into long periods with low intensity beams or even without any beam at all.

4001 the analysis performed with the Offline tool provides final results for the rate scans. On the contrary,  
 4002 the algorithm for efficiency calculation is kept simple and approximative in the tool. Including  
 4003 tracking into the analysis requires manual adjustment for each individual scan as the positions of the  
 4004 trolleys with respect to each other may vary.

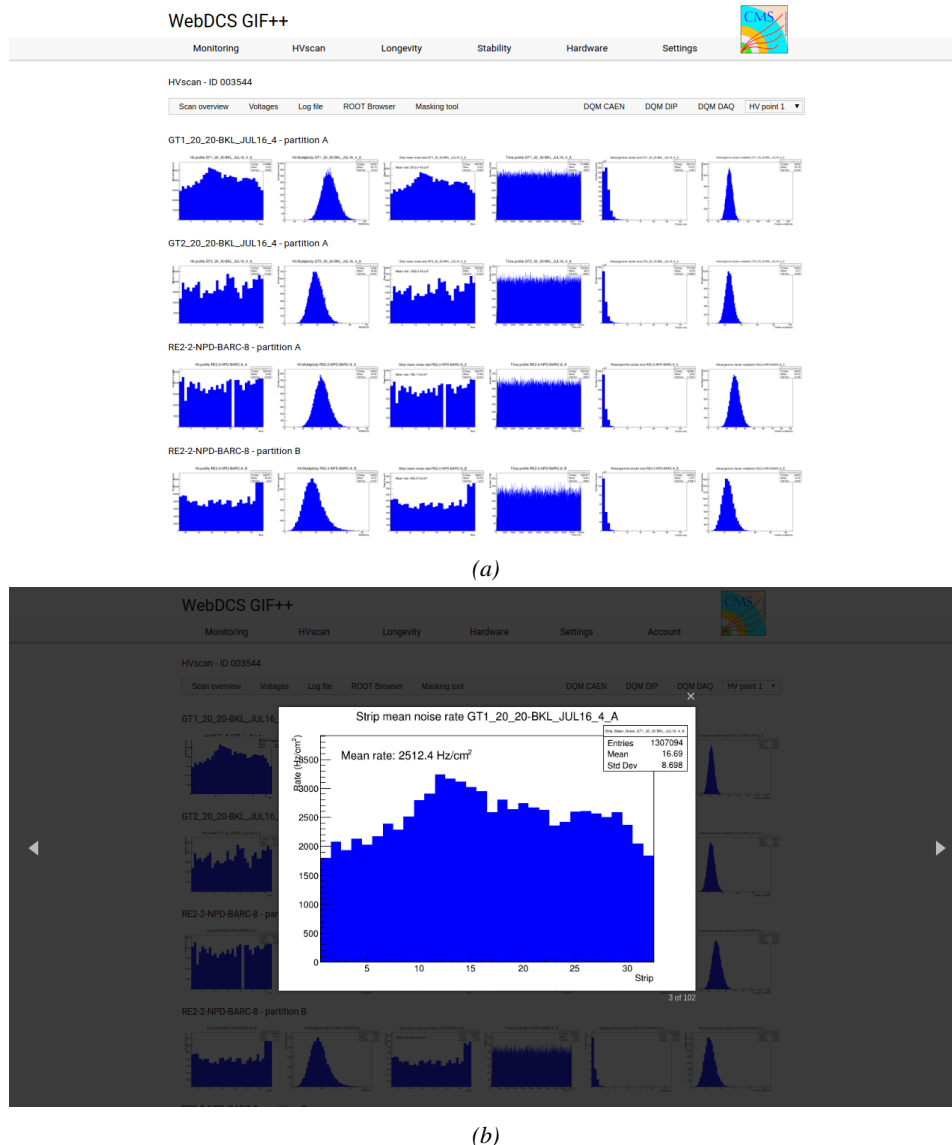


*Figure 5.29: Example of DQM page available on CMS RPC WebDCS at the Gif++: the histogram of the rate measured in one of the tracking chambers, namely GT1\_20\_20-BKL\_JUL16\_4, is selected and displayed above the page.*

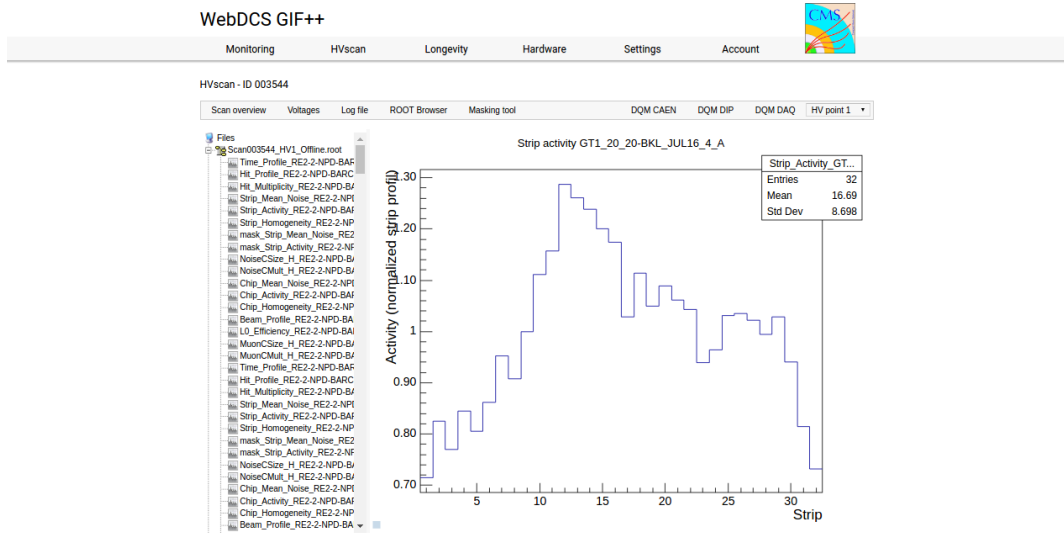


*Figure 5.30:* Example of DQM ROOT Browser page available on CMS RPC WebDCS at the GIF++: the strip activity profile, defined as the rate profile normalized to the mean rate, in one of the tracking chambers, namely GT1\_20\_20-BKL\_JUL16\_4. Available ROOT files and histograms can be browsed thanks to the left panel showing the directory and files structures.

### 4005 5.3.5 Measurements performed during irradiation periods

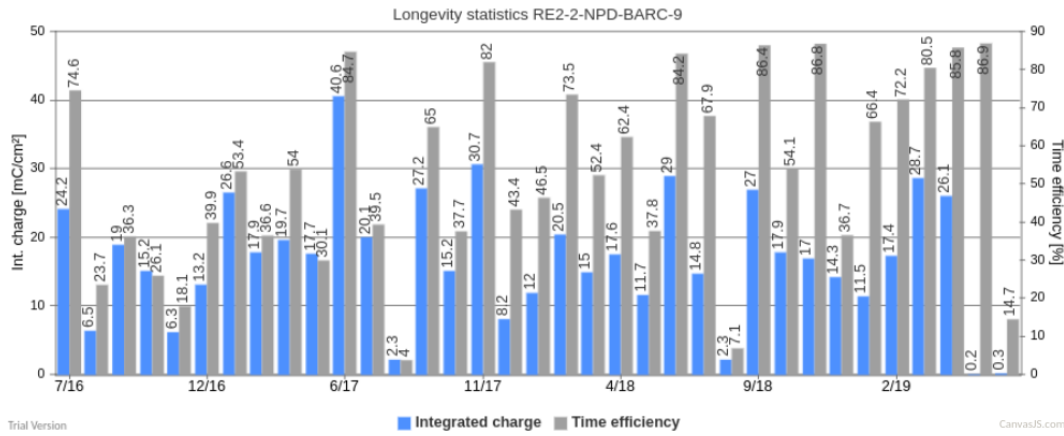


*Figure 5.31:* Longevity data for chamber RE2-2-NPD-BARC-9 in GIF++. For each month since July 2017, the integrated charge (in blue) as well as the time efficiency of irradiation (in gray) is reported.

Even though test beam periods are stressful times as an extensive data taking program needs to be finalized in a short amount of time, the biggest amount of data actually comes from irradiation periods. Indeed, when T1 is moved back to its ageing position in between each test beam periods, data is recorded at any time the source can be switched ON for irradiation. Other experiments in the area might prevent the source from staying open continuously. As an example, the time efficiency

of irradiation of CMS RPC detectors in GIF++ is presented in Figure 5.31.

Several types of measurement are performed throughout the irradiation period. As long as the detectors are being irradiated, a monitoring of the currents is performed to evaluate the corresponding integrated charge over the total irradiation time. Moreover, in order to spot any signs of ageing, the gamma rates seen by the chambers at the chosen source absorber setting as well as the noise rates and dark currents are periodically measured. During irradiation periods this is looked at every week via HV scans performed at various source settings.

Finally, the resistivity is measured periodically during the year, generally before or after test beam periods, by the use of Argon breakdown technique. The method consists in filling the detector volume with Argon instead of the CMS standard gas mixture and to increase the voltage while monitoring the current. Beyond an electric field of about  $1 \text{ kV mm}^{-1}$  at the GIF++ environmental conditions, Argon turns into a conductive plasma and does not offer electric resistance anymore. The monitoring of the currents beyond the breakdown voltage can then be used to calculate the resistivity of the electrode material.

#### 5.3.5.1 Longevity scans

The main activity of irradiation periods consists of the *longevity scans* during which the currents of the irradiated chambers are continuously monitored. The two irradiated chambers, RE2–2–NPD–BARC–09 and RE4–2–CERN–166, are both brought to a voltage of 9.8 kV while the source flux can vary depending on the needs of the groups using the facility. The currents are monitored for each active gas volume as can be seen in Figure 5.32. The integrated charge for each individual gas volume is computed by integrating through time the current density, current normalised to the surface area, flowing through each gap, as shown in Figure 5.33.

Finally, at the end of each longevity scan each gap contribution is translated into the mean chamber integrated charge. The integrated charge accumulated in each chamber is used to update the summary plots providing the collaboration with official results to be spread as can be seen from Figure 5.34. The translation from individual gap currents to total integrated charge in the chamber is done using Equation 5.5, where the equation to compute the monitored current density already mentioned in Section 5.2.4 is recalled.

$$(5.5) \quad J_{mon} = \frac{I_{mon}^{TW} + I_{mon}^{TN}}{A_{TW} + A_{TN}} + \frac{I_{mon}^B}{A_B}$$

$$Q_{int} = \int_{t_i}^{t_f} J_{mon} dt$$

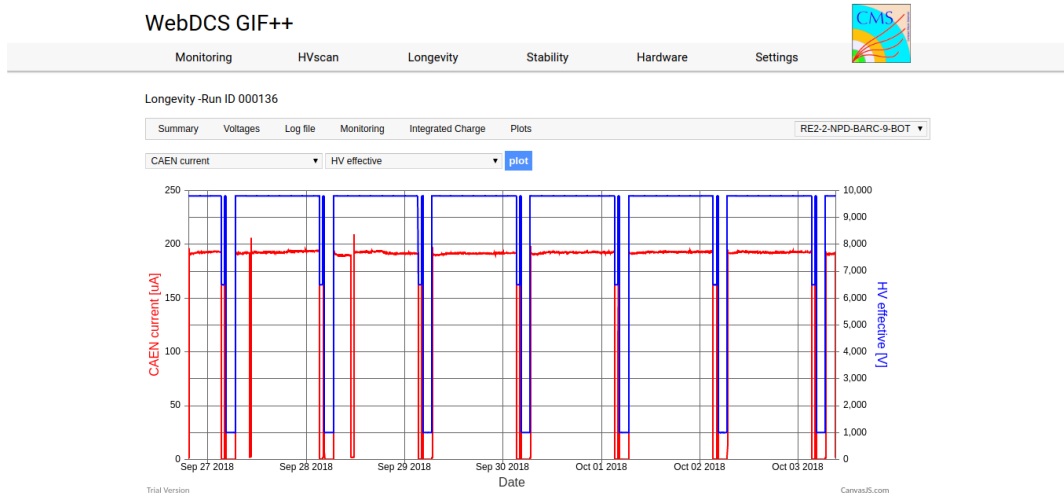


*Figure 5.32: Example of a longevity scan monitoring page available on CMS RPC WebDCS at the GIF++: the current and effective voltage, as well as environmental parameters, are monitored for the bottom gap of chamber RE2–2–NPD–BARC–9. The decrease of current is related to a decrease of the voltage due to the daily rate scan procedure or to periods during which the source was turned OFF.*

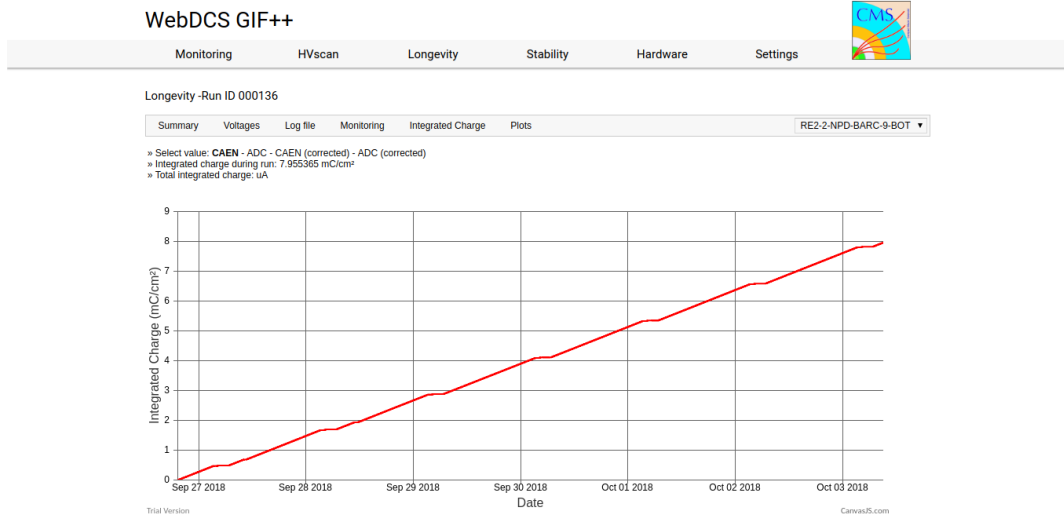


*Figure 5.33: Example of a longevity scan summary page available on CMS RPC WebDCS at the GIF++: the integrated charge is computed for the bottom gap of chamber RE2–2–NPD–BARC–9.*

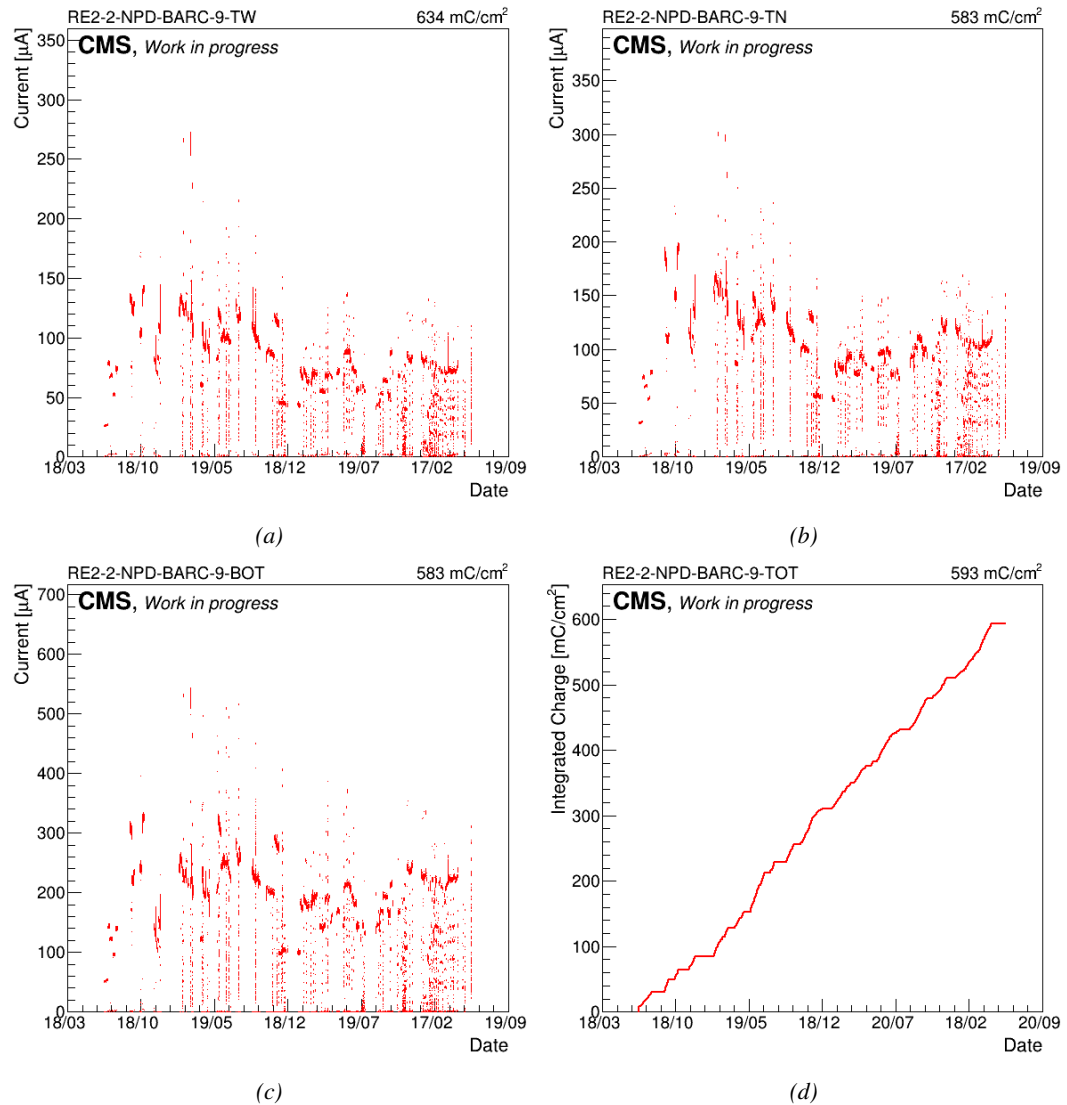


Figure 5.34: Example of current monitoring summary and of corresponding integrated charge of chamber RE2-2-NPD-BARC-09.

**4039 5.3.5.2 Daily rate monitoring scans**

4040 Every night during longevity scans, the setup performs *daily rate scans*. These scans aim at keeping  
4041 track of the gamma rate measured in the irradiated RPCs during longevity scans, but are also used  
4042 to measure the noise rate at standby voltage for each gap. The procedure for these HV scans consist  
4043 of nine runs for which 50,000 random triggers are accumulated, corresponding to 0.5 s of total  
4044 integrated time.

4045 1- All gaps are first left at the irradiation voltage of 9.8 kV to measure the gamma rate.

4046 2- Then all gaps are brought to the standby voltage of 6.5 kV to measure the noise rate of the full  
4047 detectors.

4048 3- Both top gaps (TW and TN) are brought to a voltage equivalent to an OFF status, i.e. 1 kV so  
4049 that the noise contribution of only the bottom gap at standby voltage can be measured.

4050 4- The bottom gaps are ramped up toward the working voltage of 9.8 kV to measure their contri-  
4051 bution to the gamma rate estimation.

4052 5-8 The steps 3 and 4 are repeated on TN and then on TW, keeping the bottom and the top gap  
4053 which is not of interest at a voltage of 1 kV. This way, the individual contribution to the noise  
4054 and gamma rates are known.

4055 9- Both TW and TN are brought to working voltage while the bottom gap is left at 1 kV to  
4056 measure the gamma rate for the full top layer at once.

4057 Finally, the voltages of all gaps are brought back to working voltage for the longevity program to  
4058 continue until the next daily scan. These scans are responsible for the drop of voltages and currents  
4059 observed in Figure 5.32. The procedure previously described is highlighted in Figure 5.35.

4060 Similarly to the efficiency and rate scans taken during test beam periods, the data is here stored  
4061 in two separate ROOT files for the TDC and CAEN data for each run. At the same time, the currents  
4062 are still monitored by the longevity scan and saved into the GIF++ database for an easy evaluation  
4063 of the currents to the integrated charge. The Offline Analysis tool then provides the DQM page with  
4064 histograms, and daily values can be compiled into long term monitoring plots to study the variations  
4065 of rate and current with increasing integrated charge, as presented in Figure 5.36. The variations  
4066 of the rate and current are correlated and correspond mainly to change of source irradiation, gas  
4067 flow, gas humidity, or environmental conditions. The rates on every single read-out channel are  
4068 also tracked to control their activity with increasing integrated charge and, this way, understand  
4069 the appearance of hot spots through noisy channels, as shown in Figure 5.37. The activity of a  
4070 strip is defined as the rate of the individual channel normalized to the mean rate measured in the  
4071 corresponding read-out partition.

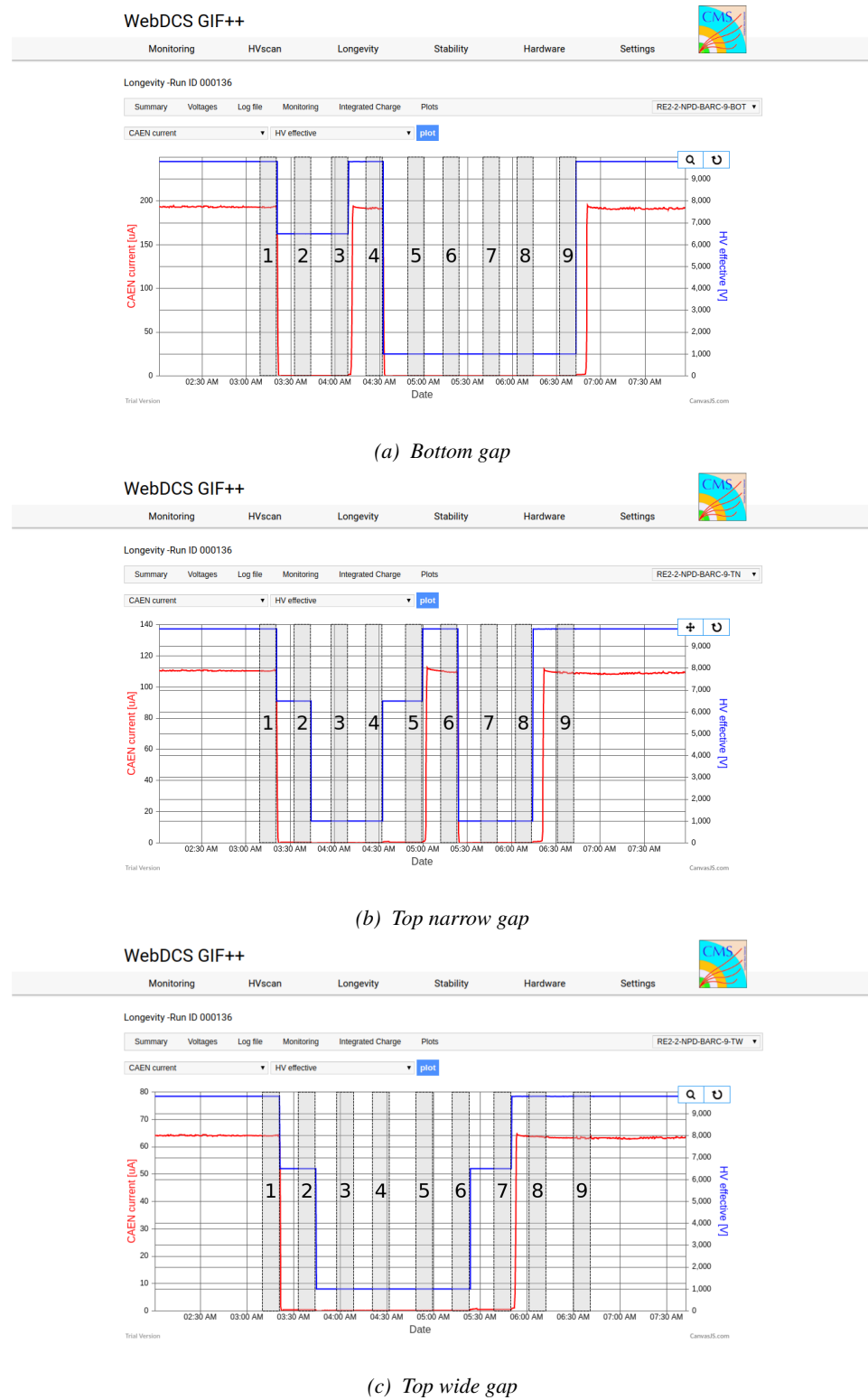


Figure 5.35: Example of daily scan procedure of chamber RE2-2-NPD-BARC-09 with highlighted runs on the CMS RPC WebDCS at the Gif++.

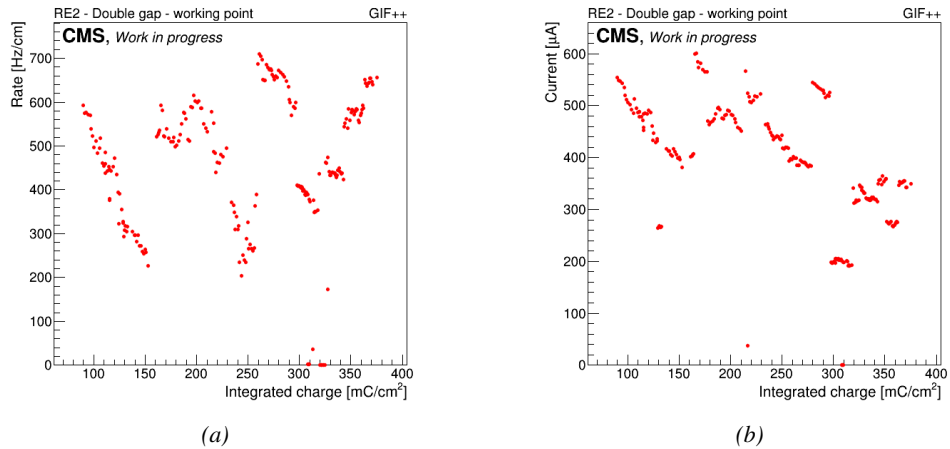


Figure 5.36: Example of rate (Figure 5.36a) and current (Figure 5.36b) monitoring of chamber RE2-2-NPD-BARC-09 with increasing integrated charge.

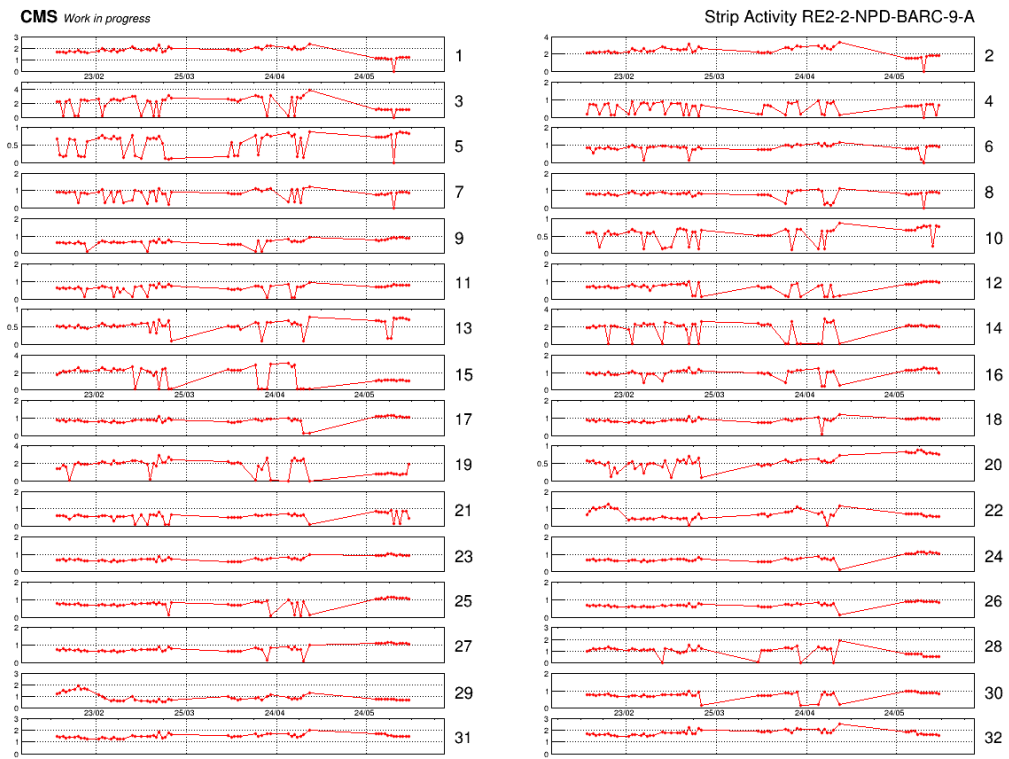


Figure 5.37: Example of strip activity of chamber RE2-2-NPD-BARC-09 monitored over time.

#### 4072 5.3.5.3 Weekly noise monitoring scans

4073 Once a week, the source is turned OFF to make a noise scan for the CMS RPC. This scan consist of a  
 4074 HV scan composed of seven runs and involving both the irradiated but also the reference chambers,

4075 providing with a weekly monitoring of the evolution of the irradiated chambers noise and dark  
 4076 current. The first run is taken at standby voltage for all chambers while the next six runs are taken  
 4077 at voltages ranging from 9.4 to 9.9 kV in order to access for both type of chambers, RE2 and RE4,  
 4078 in the voltage region where the efficiency rises and reaches its plateau. On the occasion of this scan,  
 4079 the ongoing longevity scan is stopped. A new one will be started once the weekly scans are over.

#### 4080 **5.3.5.4 Weekly source scans**

4081 Directly following the weekly noise scans, HV rate scans are organised at different source settings  
 4082 (usually ABS 6.8, 4.6 and 3.3). The procedure of these HV scans consists of 9 runs at voltages  
 4083 ranging from 9.3 to 10.1 kV, involving the four RPCs in order to have a weekly comparison of the  
 4084 values recorded in every chamber. Measuring with all detectors at the same time allows getting rid  
 4085 of potential systematics that might make the rates (noise or gamma) vary from one measurement to  
 4086 another. If such systematic effect occurs, they will be observed in all detectors.

#### 4087 **5.3.5.5 Weekly current scans**

4088 The previously detailed daily rate scans, but also the weekly noise and source scans are interesting  
 4089 tools to look at an increase of noise rates and dark currents or at a loss of rate capability. They could  
 4090 point to an increase of surface resistivity of the electrodes through the absorption of hydrofluoric  
 4091 acid. Nevertheless, periodically measuring the currents on wider high voltage ranges allows to have  
 4092 access to the ohmic part of the current driven by the detectors related to the electrodes resistance.  
 4093 This is why precise current scans, consisting only in measuring the current driven through the four  
 4094 detectors, are performed each week. The scan procedure includes measurements at 131 high voltage  
 4095 points in between 500 V and 10 kV, in steps of 100 V until the standby voltage of 6.5 kV is reached  
 4096 and then in steps of 50 V. The current increase in between 500 V and the voltage where charge  
 4097 multiplication starts to occur is only driven by the resistance of the detector electrode and thus  
 4098 increases linearly. Hence, a fit on the current in this voltage range gives access to the resistance of  
 4099 the system electrodes/gas. If any variation of the electrode resistance occurs, the global resistance  
 4100 will increase and so will the current. Technically, these scans will record a ROOT file per HV step  
 4101 that will have the same format as the CAEN ROOT file saved during other HV scans. The data is also  
 4102 analysed using the Offline Analysis tool to provide with DQM histograms as well as standardized  
 4103  $I/V$  tables.

#### 4104 **5.3.6 Extraction and monitoring of the resistivity**

4105 A critical parameter to monitor is the resistivity of the electrodes. Its variation would impact the rate  
 4106 capability of the RPC. An increase of the resistivity with increased irradiation is expected. In the first  
 4107 place, the measurement of the resistivity of the electrodes is done using the so called *Argon scans*.  
 4108 Such tests are performed regularly before or after test beam periods through high voltage scans of  
 4109 the detectors operated with pure Argon. The electric field strength at which Argon breaks down  
 4110 being well known, the current beyond the breakdown voltage is monitored and gives an information  
 4111 about the resistance of the couple of electrodes. The resistivity is then deduced by using Formula 5.6  
 4112 where  $S$  is the surface area of the gas gap and  $l$  the thickness of a single electrode.

$$(5.6) \quad \rho = R \times \frac{S}{2 \times l}$$

Unfortunately, the Argon scans are not performed often enough. The reason for this resides in the fact that the gas lines providing with Argon at the Gif++ are not humidified. Operating too often the detectors with dry gas could lead to the rise of the resistivity due to a loss of humidity of the electrodes. There exist other ways to access a quantity directly related to the resistivity. During the testbeam periods, the efficiency of the detectors is measured with both source OFF and source ON with high irradiation. The shift of voltage introduced by an irradiation is directly linked to the rate capability of the detector and hence to the resistivity of the electrodes. By comparing the efficiency curves observed with source ON and OFF, it is possible to access the resistance of the detector as in Formula 5.7.

$$(5.7) \quad R = \frac{\Delta HV_{eff}}{\Delta I_{mon}} = \frac{HV_{eff}^{ON} - HV_{eff}^{OFF}}{I_{mon}^{ON} - I_{mon}^{OFF}}$$

It is important to note that the result provided by using this method will only concern the resistance of the detector under the beam, including the resistance of the gas volume. The translation to the resistivity of the electrodes is not straight forward. Also, the quality of the resistance extraction depends on which voltage and current values are being used and on which level of irradiation is available in the data. The influence of the efficiency at which the voltage and current are extracted and of the minimal irradiation necessary to get an optimal result have been studied for the case of August 2018 testbeam data. During August 2018 testbeam period, HV scans were done on partition C of the RPCs (bottom and top narrow gas gaps) with source OFF and with seven different ABS values: ABS 313 (464), ABS 312 (215), ABS 311 (100), ABS 213 (46.4), ABS 212 (21.5), ABS 123 (6.8), and ABS 122 (3.2). T1 was placed at a distance of 5.6 m from the source close to the bunker upstream wall. This position corresponds to a gamma current of the order of  $5 \times 10^5 \text{ cm}^{-2} \text{ s}^{-1}$  with source fully open.

In a first step, the efficiency sigmoids were computed as a function of the effective voltage, as in Equation 3.24, but also the bottom and top narrow gaps as a function of the monitored current by using Equation 5.8, the same equation but for currents instead of voltages. The curves are given in Figure 5.38.

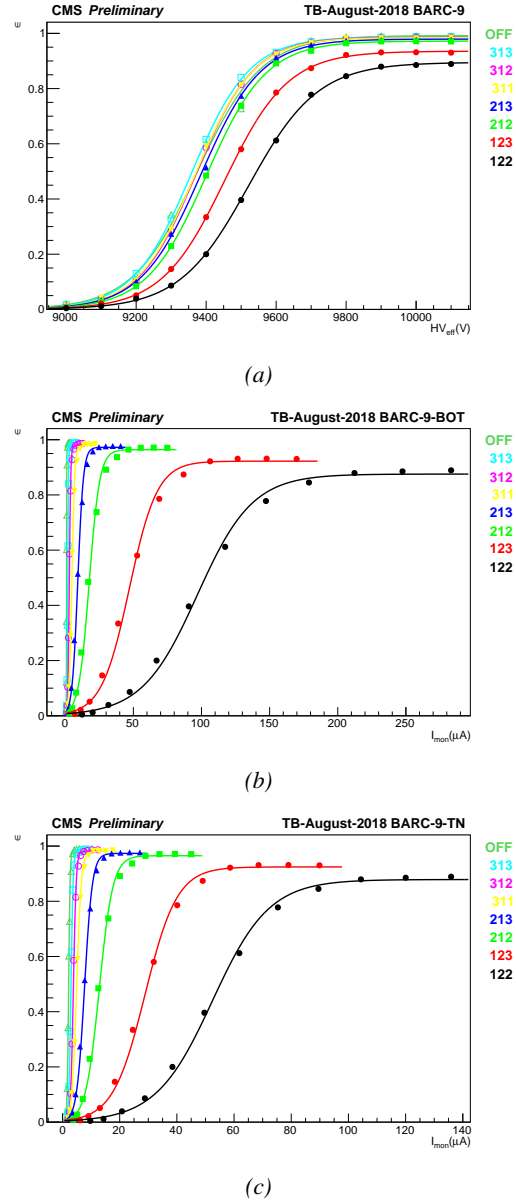
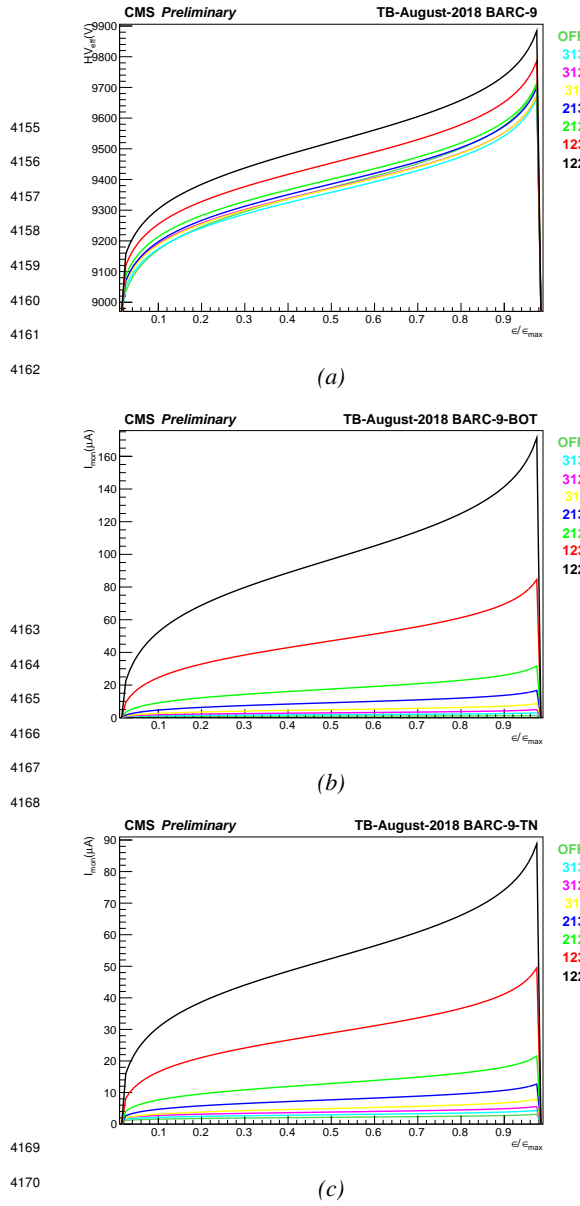


Figure 5.38: Chamber RE2-2-NPD-BARC-09.



4169  
4170  
4171  
4172  
4173  
4174  
4175  
4176  
4177  
4178  
4179  
4180  
4181

*Figure 5.39: Chamber RE2-2-NPD-BARC-09.*

$$(5.8) \quad \epsilon(I_{mon}) = \frac{\epsilon_{max}}{1 + e^{-s(I_{mon} - I_{50})}}$$

In a second step, the curves are inverted to express the effective voltage and the monitored current as functions of the efficiency of the detector as in Equation 5.9 where the maximum efficiency was set to 1 to normalize each measurement to its maximum efficiency. The resulting inverted sigmoids are shown in Figure 5.39.

$$(5.9) \quad HV_{eff}(\epsilon)|_{\epsilon_{max}=1} = HV_{50} + \frac{1}{\lambda} \ln \left( \frac{\epsilon}{1-\epsilon} \right)$$

$$I_{mon}(\epsilon)|_{\epsilon_{max}=1} = I_{50} + \frac{1}{s} \ln \left( \frac{\epsilon}{1-\epsilon} \right)$$

This step was used to directly get the difference in voltage or current between the source ON and OFF measurements that can be expressed as in Equation 5.10. The shift in effective voltage and monitored currents are shown in Figure 5.40.

$$(5.10) \quad \Delta HV_{eff}(\epsilon)|_{\epsilon_{max}=1} = \Delta HV_{50}$$

$$+ \frac{\Delta \lambda}{\lambda^{ON} \lambda^{OFF}} \ln \left( \frac{\epsilon}{1-\epsilon} \right)$$

$$\Delta I_{mon}(\epsilon)|_{\epsilon_{max}=1} = \Delta I_{50}$$

$$+ \frac{\Delta s}{s^{ON} s^{OFF}} \ln \left( \frac{\epsilon}{1-\epsilon} \right)$$

Finally, the corresponding resistivity like value is computed using Equation 5.6. The resistivity as given by this equation are given in Figure 5.41. The efficiency at the knee of the sigmoids where  $\epsilon = 0.95 \times \epsilon_{max}$  would be the best location to extract the value of this resistivity. At this value of the efficiency, the performance of the detectors is stable and a little variation of voltage does not have a large effect the efficiency. From Figure 5.41, it is important to remark that extracting a reasonable value is only possible with strong irradiation scans. For lower irradiations, the efficiency

4182  
4183  
4184  
4185

and current shifts are too small and the variations of the sigmoid curves near the knee make it hard to reach a good order of magnitude for the extracted value.

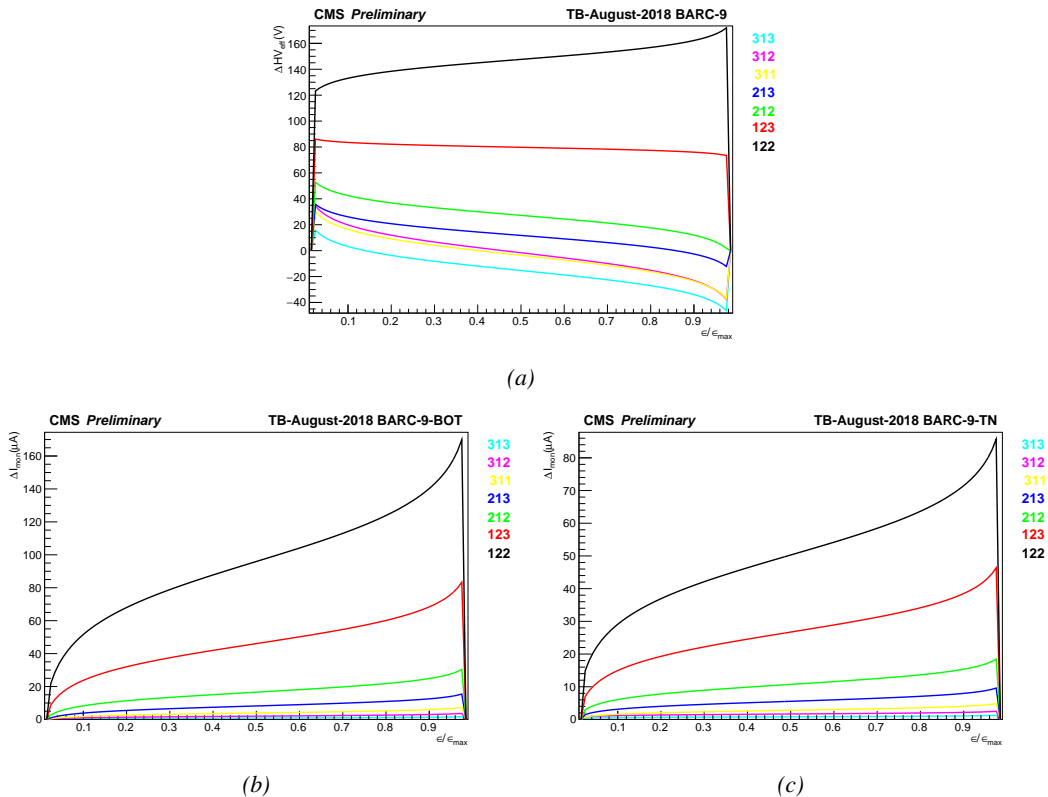


Figure 5.40: Chamber RE2-2-NPD-BARC-09.

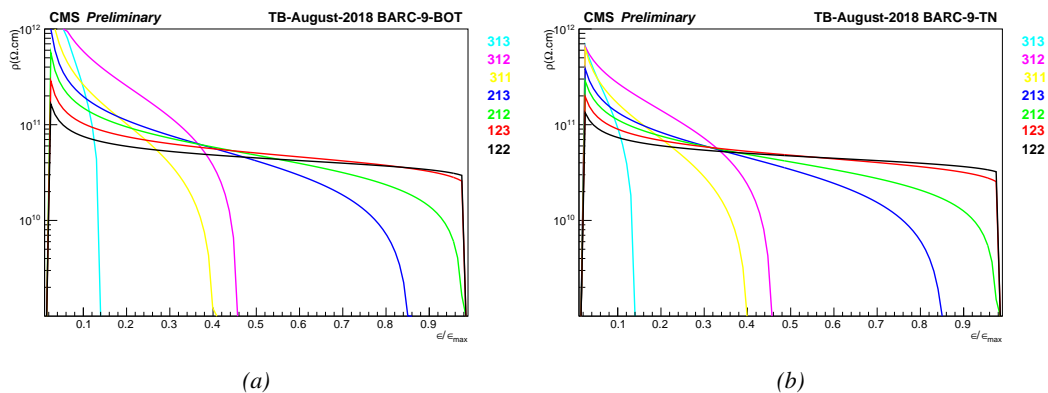


Figure 5.41: Chamber RE2-2-NPD-BARC-09.

### 5.3.7 Results and discussions

Since 2015, CMS RPCs have been irradiated in GIF++ with the goal to reach a total integrated charge per irradiated detector of  $0.84 \text{ C/cm}^2$  while certifying the detectors to a rate capability of  $600 \text{ Hz/cm}^2$ . As of today, the RE2 and RE4 chambers respectively achieved 51 and 26% of the total irradiation program. A few years of irradiation are expected before reaching the end of the longevity study and a final answer on whether the detector will be able to live through HL-LHC or not. A negative answer to this question would probably lead to solutions to replace the detectors before HL-LHC or to improve the shielding of these detectors against background radiation in the experimental cavern, which could be a more sustainable solution.

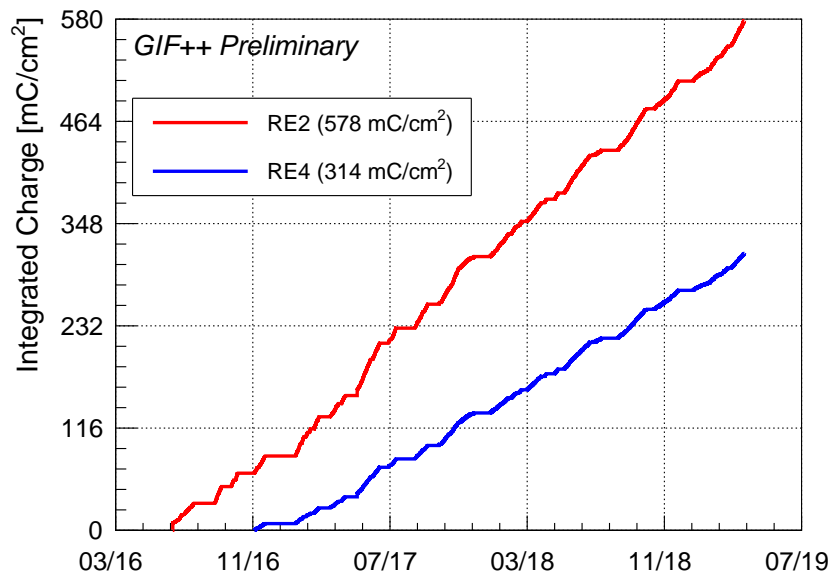


Figure 5.42: Total integrated charge in the irradiated RPCs, RE2-2-NPD-BARC-9 and RE4-2-CERN-165, in April 2019. The irradiation of the RE2 chamber started in June 2016 while the RE4 chamber couldn't be irradiated before November 2016.

# 6

4195

4196

4197

## Improved RPC investigation and preliminary electronics studies

4198 The extension in the endcap of the RPC sub-system towards higher pseudo-rapidity will bring the  
4199 new detectors to be exposed to much more intense background radiations due to the proximity of the  
4200 detectors with the beam line (Figure 4.5). The challenge will be to produce high counting rate de-  
4201 tectors with limited ageing rate to ensure a stable operation of the detector over a period longer than  
4202 ten years. In Chapter ?? was discussed the influence of the detector design (number and thickness  
4203 of gas volumes, OR system, etc...) on the charge deposition and rate capability. Nevertheless, this  
4204 question can also be addressed from the electronics point of view as a better signal-to-noise ratio  
4205 would also mean the possibility to greatly lower the charge threshold on the signals to be detected,  
4206 allowing to use the detector at lower gain, hence lowering the charge deposition per avalanche in the  
4207 gas volume. Cardarelli showed that the production of low-noise fast FEEs could help decreasing the  
4208 charge deposition per avalanche at working voltage by an order of magnitude, virtually increasing  
4209 the life expectancy of such a detector in the same way [279].

### 4210 6.1 FEE candidates for the production of iRPCs

4211 The extension of the third or fourth endcap disks with improved RPCs has been presented in  
4212 Chapter ?? together with the expected background levels (Figure 4.18). An important piece of  
4213 these iRPCs will be the Front-End Electronics that will equip the chambers. A fast, low-jitter and  
4214 low-charge sensitive electronics will help reducing further the charge deposition in the detector by  
4215 making it possible to operate at lower gain.

4216 In the context of the CMS Muon Upgrade, two FEE solutions have been considered to equip the  
4217 iRPCs. The baseline for the RPC upgrade is based on the PETIROC ASIC, initially for Time-of-  
4218 flight (ToF) applications. A back-up solution is also under study and focusses on a new low-noise  
4219 preamplifier designed in INFN laboratories in Rome to replace the preamplification stage of the  
4220 already existing CMS RPC Front-End Board.

4221 The FEEs that are foreseen to equip the new RPCs need to be able to detect charges as small as  
 4222 10 fC. Not only the new electronics need to be fast and reliable, they also should be able to sustain  
 4223 the high radiation the detectors will be subjected to in the region closest to the beam.

### 4224 6.1.1 CMS RPCROC: the RPC upgrade baseline

4225 Designed by Weeroc, a spin-off company from the french OMEGA laboratory, the PETIROC 2A  
 4226 consists in a fast and low jitter 32-channel ASIC originally developed to read-out Silicon Photomul-  
 4227 tiplier (SiPM) in ToF applications and that allows for precise time measurements [257, 258]. The  
 4228 ASIC uses an AMS 350 ns SiGe technology. The block diagram of the ASIC is showed on Fig-  
 4229 ure 6.1. A 10-bit DAC allows to adjust the trigger level in a dynamical range spanning from 0.5 to  
 4230 a few tens of photoelectrons and a 6-bit DAC to adjust the response of each individual channel to  
 4231 similar a level.

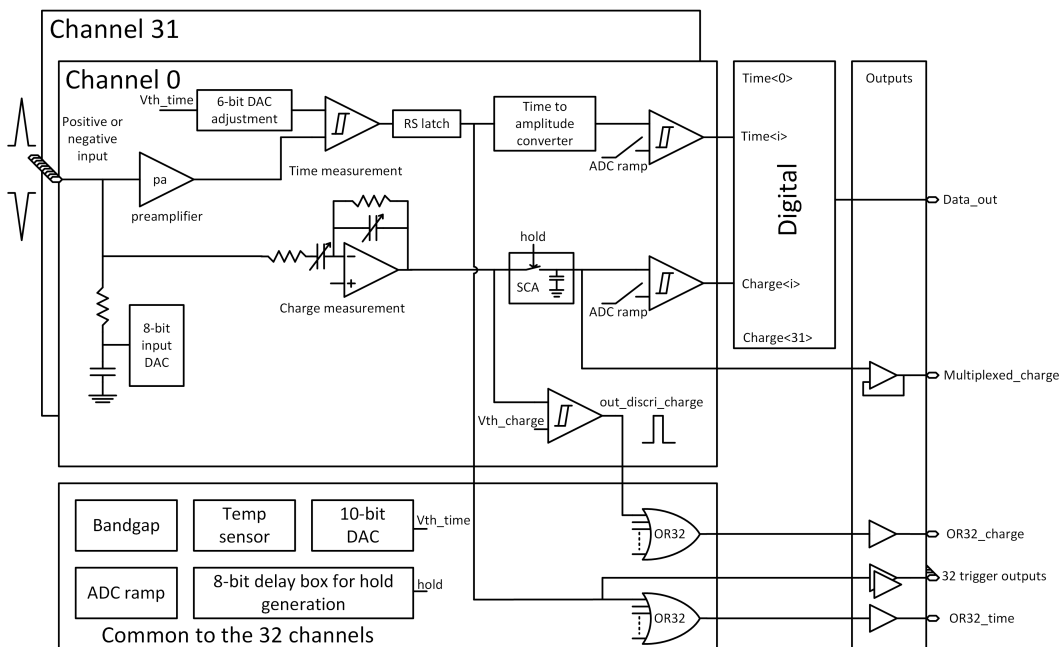


Figure 6.1: PETIROC 2A block diagram.

4232 Nevertheless, in order to adapt this ASIC to CMS, modifications were brought to the PETIROC [177]  
 4233 and not all its functions will be used [280]. In the new CMS RPCROC, showed in Figure 6.2, the  
 4234 measurement of the charge will be performed by a Time-over-Threshold (ToT) technic, taking profit  
 4235 of the capacity the ASIC has in measuring both the leading and trailing edges of the input signals.  
 4236 The dynamic range will be expanded towards lower values to allow for the detection of charges as  
 4237 low as 10 fC. Due to the radiation levels that are foreseen at the level of the iRPCs, the SiGe tech-  
 4238 nology will be replaced by the Taiwan Semiconductor Manufacturing Company (TSMC) 130 nm  
 4239 CMOS, to increase its radiation hardness while keeping fast pre-amplification and discrimination  
 4240 with a very low jitter that can reach less than 20 ps if no internal clock is used, as can be seen from  
 4241 Figure 6.3. The ASIC is associated with an FPGA which purpose is to measure time of the signals.  
 4242 The FPGA is equipped with a TDC with a time resolution of 50-100 ps developed by Tsinghua

<sup>4243</sup> University. The full system will provide a measurement of the signal position along the strip with a  
<sup>4244</sup> precision of a few cm by measuring the signal timing on both ends of the strips.



*Figure 6.2: View of the RPCROC Front-End Electronics in which the PETIROC 2A ASIC is visible as well as the FPGA on which the TDC is hosted.*

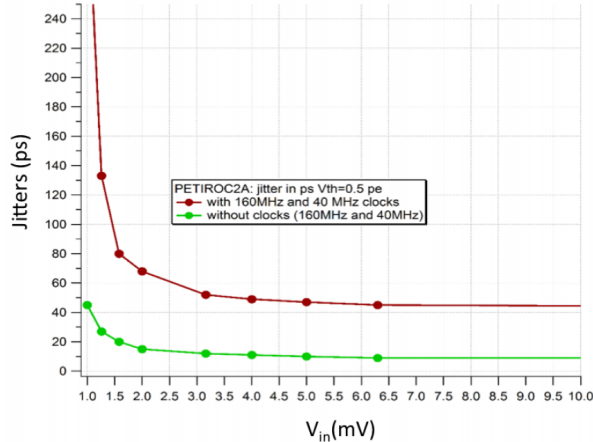


*Figure 6.3: The PETIROC time jitter as a function of the input signal amplitude, measured with and without internal clocks.*

<sup>4245</sup> In order to read-out all 96 strips, 3 ASICs and 3 TDCs, each having an increased number of 64-  
<sup>4246</sup> channels, are hosted on a FEB attached to the chamber. Two scenarios are being studied to connect  
<sup>4247</sup> the ASICs to the read-out strips [280]. The corresponding read-out panels are showed in Figure 6.4.

4248 On the one hand there is the possibility to design a standard trapezoidal strip panel and to directly  
 4249 connect the strips to the ASICs using coaxial cables of similar impedance than the strips. On the other hand,  
 4250 the return lines could be embedded directly in extra layers of the strip panel to offer the possibility to minimize  
 4251 the amount of on-detector cables by using a single connector to send the signals to the FEB's inputs. The first version of the panel is referred to as *coaxial design* while the  
 4252 second as *return design*. In the case of the return design panel, the read-out area is a little smaller  
 4253 than in the case of the coaxial panel. This was motivated by the need to shield the return strips  
 4254 beneath the copper ground plane visible on the side of the PCB.  
 4255

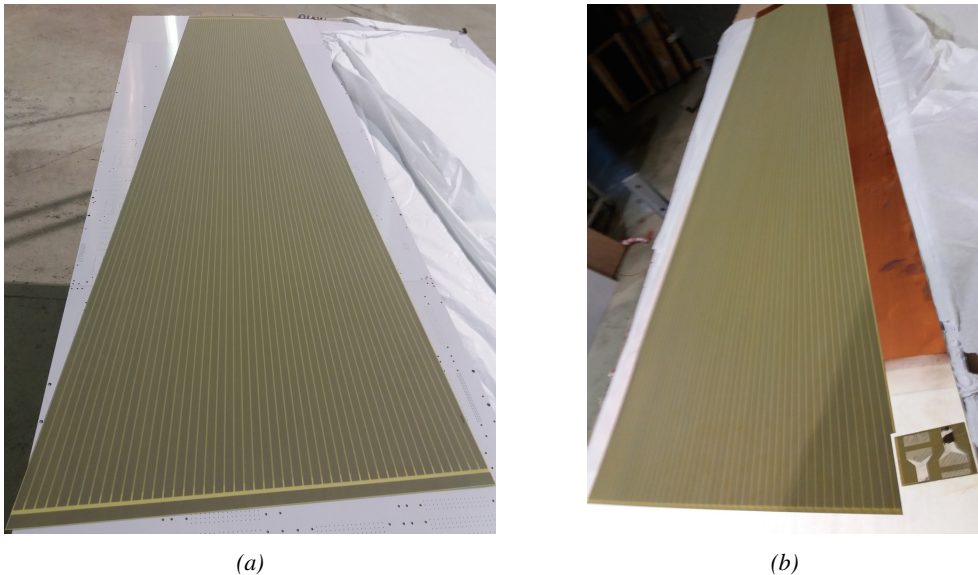


Figure 6.4: View of the coaxial design (Figure 6.4a) and of the return design (Figure 6.4b) of read-out panels used in the iRPC prototypes. Only half PCBs with 48 strips are showed.

### 4256 6.1.2 INFN Front-End Board: a robust back-up solution

4257 Even though the baseline for the electronics that will equip the iRPCs will be the CMS RPCROC, a  
 4258 back-up solution needs to be certified. The back-up has been found in a Front-End Electronics fea-  
 4259 turing a fast and low-noise ( $1000 e^-$  rms) Silicon (Si) preamplifier and a Silicon-Germanium (SiGe)  
 4260 discriminator [281] associated with an optimized read-out panel [282]. The low-noise preamplifier is  
 4261 a new version of a preliminary production of a SiGe preamplifier by the team of Cardarelli working  
 4262 with INFN Roma with the purpose of equipping the new generation of ATLAS RPCs [283].

4263 The FEB is equipped with eight channels of preamplifiers using a Bipolar Junction Transis-  
 4264 tor (BJT) technology and two discriminator ASICs of four channels using Hetero Junction bipolar  
 4265 Transistor (HJT) technology. The input signals are amplified at an amplification factor of 0.2 to  
 4266 0.4 mV/fC and are then discriminated with a threshold of 0.5 mV at minimum. For each channel,  
 4267 the LVDS output is proportional in width to the Time-over-Threshold in the discriminator of the am-  
 4268 plified signal with a minimum width of 3 ns. This method allows for an estimation of the avalanche  
 4269 charge as the width of the signals usually is consistent and proportionnal to the amount of charge  
 4270 released in the gas volume.

4271 The read-out panel features 96 trapezoidal copper strips and has a similar design to the read-out

<sup>4272</sup> panels used for the CMS RPCROC. As for now, the strips are only read-out from one end.

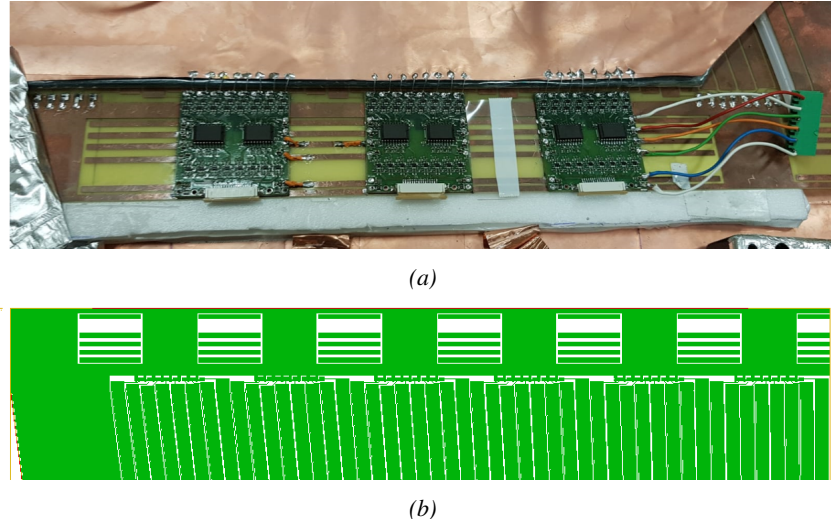


*Figure 6.5: Experimental setup used to test the INFN preamplifier with respect to the CMS FEEs.*

## <sup>4273</sup> 6.2 Preliminary electronics tests at CERN

### <sup>4274</sup> 6.2.1 INFN preamplifiers as upgrade candidates

<sup>4275</sup> INFN electronics were the first ones to be tested by CMS RPC group in collaboration with colleagues  
<sup>4276</sup> from INFN Roma working in the ATLAS RPC group. The tests with CMS RPCs were performed in  
<sup>4277</sup> February 2013 outside of the old GIF facility presented in Chapter 5.1.1. Four preamplifier channels  
<sup>4278</sup> were lended by Cardarelli to equip four CMS RPC channels as presented in Figure 6.9. They were  
<sup>4279</sup> directly connected to the strips for the signals induced by muons passing through the gas volume of  
<sup>4280</sup> the chamber to be amplified. The output was then sent to a discriminator to digitize the signals and  
<sup>4281</sup> filter out the noise by tuning the threshold level. The NIM quad discriminator 821 manufactured by  
<sup>4282</sup> LECROY used during this experiment only allows at minimum to set the threshold at a voltage of  
<sup>4283</sup> approximately 30 mV on the input signals. Thus, two values of discrimination were used ( $\sim 75$  mV  
<sup>4284</sup> and  $\sim 30$  mV).

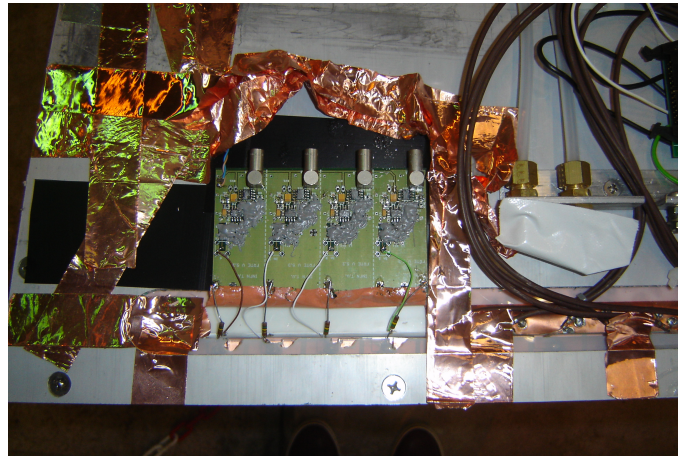
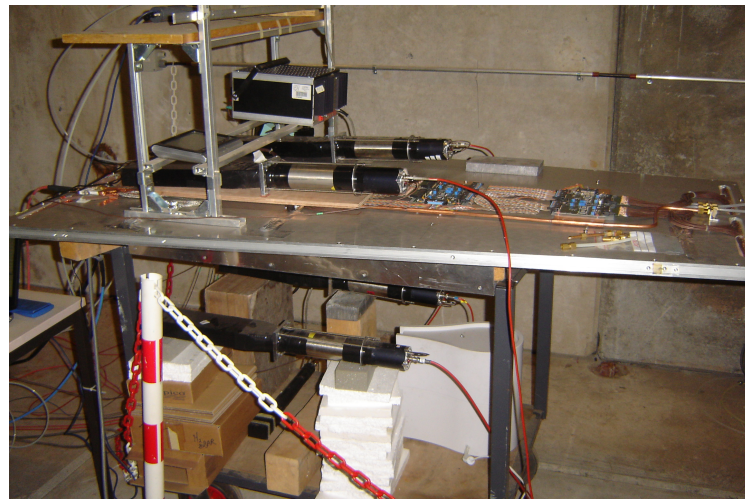


Figure 6.6: The four channels of INFN preamplifiers are mounted directly on a CMS RPC and connected to the four outermost read-out strips of the detector.

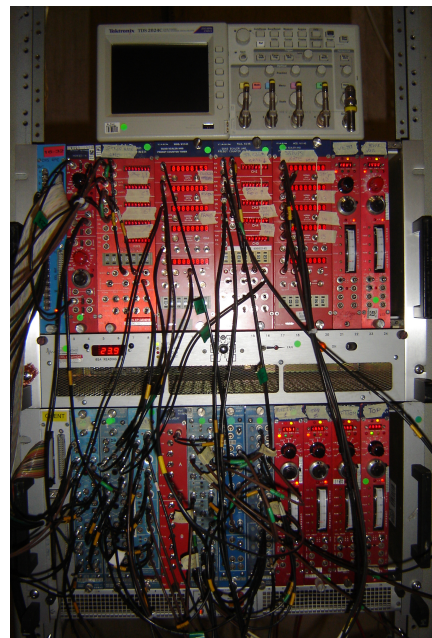
4285      The performance of the chamber equipped with these new preamplifiers was compared to the  
4286      performance of CMS FEEs. The experimental setup used is described in Figure 6.7. PMTs a little  
4287      less wide than four strips were used to trigger the data taking. Two pairs were used in coincidence  
4288      on both the strips connected to the INFN preamplifiers and to the ones connected to the CMS FEEs.  
4289      An extra PMT, placed perpendicularly to the rest of the setup at the bottom of the setup was used  
4290      to detect potential showers and send VETO signals if necessary. A last PMT was used close to the  
4291      power supplies to measure and discard signals due to electromagnetic noise and is not visible on  
4292      the pictures. Finally, after discrimination, the output of the INFN preamplifiers together with the  
4293      signals from the CMS FEEs were sent to scalers to count the detected signals versus the number of  
4294      trigger coincidences as no DAQ software was available at the time. The full pulse processing for this  
4295      experiment is shown in Figure 6.8.



(a)



(b)



(c)

Figure 6.7: Experimental setup used to test the INFN preamplifier with respect to the CMS FEEs.

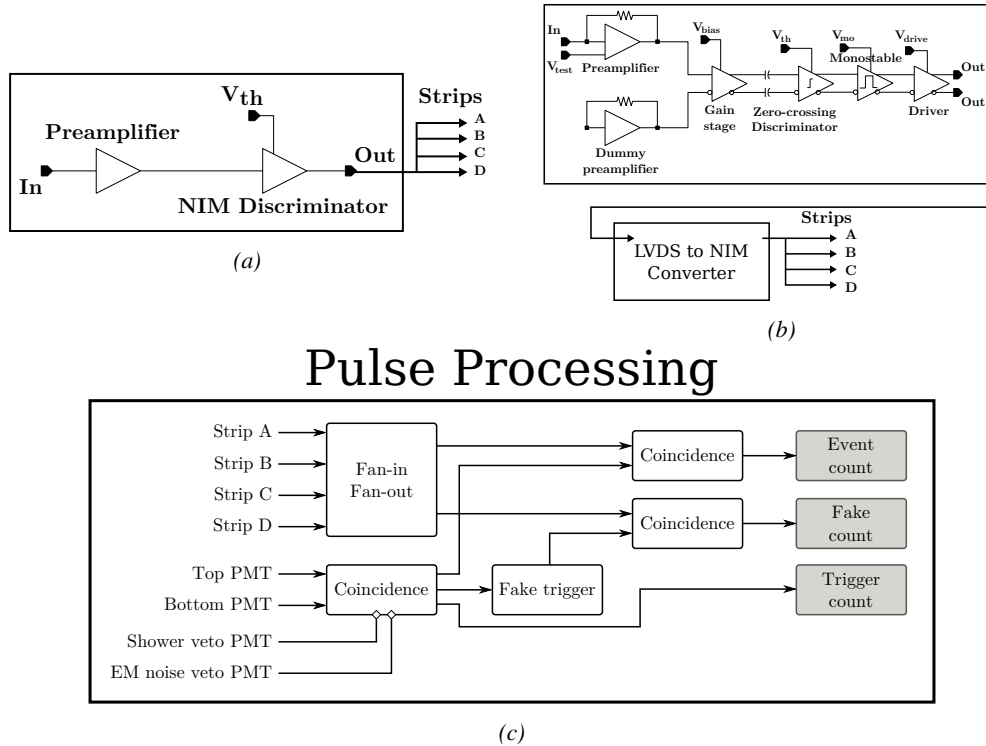


*Figure 6.8: The block diagrams corresponding to the signal treatment for both INFN preamplifier (Figure 6.8a) and CMS FEEs (Figure 6.8b) are shown. The digitized signals are then counted in coincidence with the trigger signals provided by PMTs (Figure 6.8c).*

The data taking program consisted in High Voltage scans. A first point was taken at 0 V to only measure noise. Then the HV was increased to an applied value of 7 kV. The voltage was increased in steps of 500 V until 8 kV from where it was increased in steps of 100 V until an upper limit of 10 kV. After rising the voltage over the electrodes of the RPC, a waiting period of 15 minutes was observed to leave time to the electrodes to charge and to the currents to stabilize. The currents were reported at the moment the data taking was started. At each HV step, except at 0 V, approximatively 300 triggers were taken to estimate the efficiency of the detector by counting the number of hits in the system (A or B or C or D), referring to the strips. The noise rate per unit area was measured during the first 100 s of data taking by counting the number of hits received in each read-out strip. The cluster size, the average number of adjacent strips fired during a muon event, could not be measured due to the lack of available scalers.

During the data acquisition, in addition to counting the number of signals with respect to the number of triggers, the current or the noise rate per unit area as a function of the increasing voltage, the environmental parameters were monitored. Using the information provided by a humidity and temperature sensor on the gas input line together with the environmental pressure given by a weather station, the applied voltage could be corrected following Formula 3.27. Moreover, the voltage line was filtered to prevent noise and higher currents in the RPC under test.

The results of the preliminary tests are presented in Figure 6.9. More details on the fit performed on the data are provided in Table 6.1. As can be seen, being able to use electronics with a much higher sensitivity allows for a HV shift of up to 475 V with a threshold as low as 3 fC corresponding

to the lowest threshold available on the discriminator modules. On the other hand, the higher charge sensitivity also brings a higher noise level. After a first series of measurement performed with a bad grounding leading to grounding loops and hence an artificially higher noise, it can be concluded that the noise rate per unit area of such electronics is approximately one of manitude higher than the noise rate measured with the CMS FEB. The noise reaches approximately  $2 \text{ Hz/cm}^2$  at the level of the working in the case of the INFN preamplifier while it is lower than  $0.2 \text{ Hz/cm}^2$  for the CMS FEB. It is likely that the higher sensitivity also brings a higher sensitivity to local discharges happening in the gas due to fluctuations of the electric field. The surface of the electrodes not being perfectly smooth, the local electric field may vary quickly. The gas molecules circulating in the gas could then be ionised by the fast variation of the field and trigger an avalanche that can then be detected. Reducing the noise rate per unit area would then come from an improvement of the detector itself rather than from a reduction of the electronic noise of the INFN preamplifier.

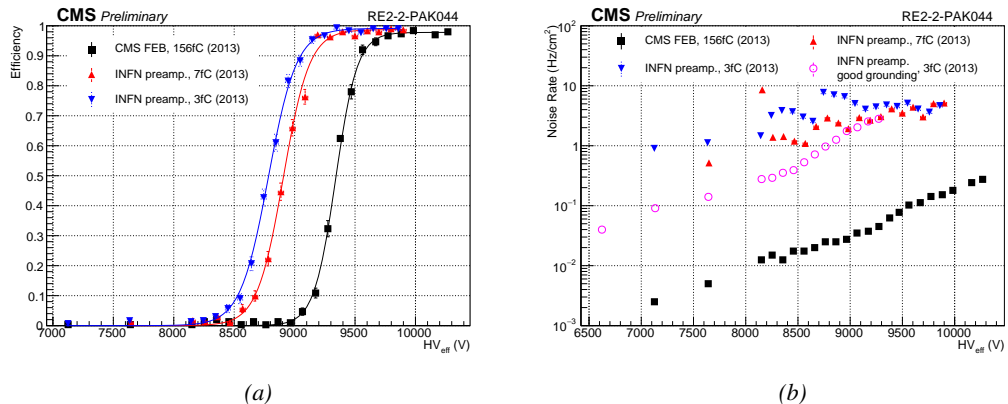


*Figure 6.9: Efficiency (Figure 6.9a) and noise rate per unit area (Figure 6.9b) of the CMS RE2-2 detector tested with the standard CMS FEBs (black) and with the INFN preamplifier at different thresholds (red and blue). An extra HV scan was performed with better conditions to measure the noise with a threshold of 3 fC on the INFN preamplifiers.*

Data	$\epsilon_{max}$	$\lambda (\times 10^{-2} \text{ V}^{-1})$	$\text{HV}_{50}$ (V)	$\epsilon_{WP}$	$\text{HV}_{WP}$ (V)
CMS FEB, 156fC (2013)	$(0.978 \pm 0.004)$	$(1.12 \pm 0.07)$	$(9339 \pm 11)$	$(0.97 \pm 0.01)$	$(9752 \pm 27)$
INFN preamp., 7fC (2013)	$(0.987 \pm 0.003)$	$(0.93 \pm 0.05)$	$(8907 \pm 11)$	$(0.97 \pm 0.01)$	$(9374 \pm 27)$
INFN preamp., 3fC (2013)	$(0.991 \pm 0.003)$	$(0.86 \pm 0.04)$	$(8783 \pm 11)$	$(0.98 \pm 0.01)$	$(9276 \pm 27)$

*Table 6.1: Results of the sigmoid fit (Formula 3.24) performed on the data presented in Figure 6.9a. The working point and its corresponding efficiency are computed using Formulas 3.24 and 3.25.*

## 6.2.2 INFN preamplifiers mounted onto CMS Front-End Board

Following the first experiment performed in the experimental hall aside of the old GIF, a new series of tests has been done in the CMS RPC assembly laboratory at CERN. For this purpose, the preamplifiers have been designed to be standalone single channels. To have a consistent comparison with the CMS FEB, a FEB prototype has been built based on the current CMS design. As shown in Figure 6.10, the preamplifiers are meant to be plugged in one of the available 16 channels of the board that produces an LVDS output with similar characteristics than the CMS FEB.

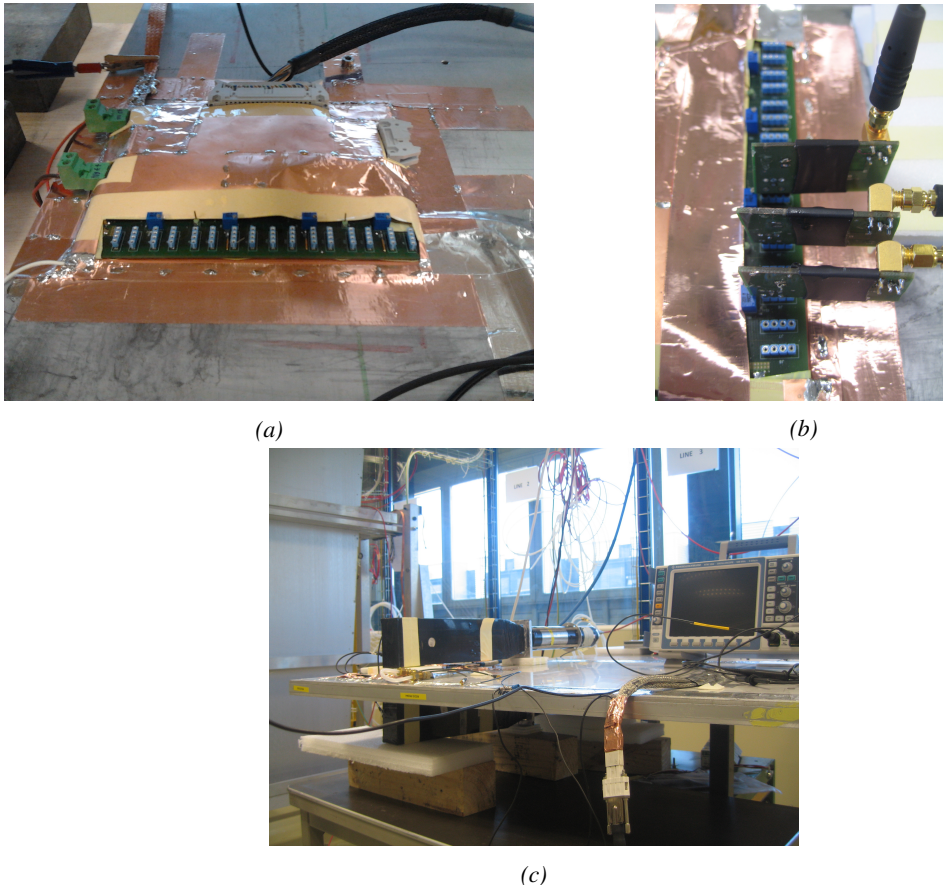


*Figure 6.10: Figure reffig:Setup-INFN-904:A: Shielded Front-End Board on which the INFN preamplifiers are to be mounted. Figure reffig:Setup-INFN-904:B: Three INFN preamplifiers connected onto the test FEB. Figure reffig:Setup-INFN-904:C: Experimental setup used to test the INFN preamplifier single mounted on a FEB similar to the CMS FEB.*

At the time of the second experiment, only three channels could be lent by the team of INFN Roma. The impedance of the preamplifiers was set to  $100\ \Omega$  at delivery. The strips are then connected to the preamplifiers using  $50\ \Omega$  coaxial cables equipped with SMC connectors, known for their good transmission. To match the impedance of the preamplifier input with the signal cable, a  $100\ \Omega$  resistor was added in parallel of the input line. In CMS endcap RPCs, the strips are left floating. For the purpose of this test, it was necessary to terminate the strips on both ends to prevent reflections in the transmission line. The impedance of the strips being approximately  $25\ \Omega$ , the strips were terminated with  $50\ \Omega$  resistors on the signal cable side, and with  $25\ \Omega$  resistors on the end side.

The threshold of the zero-crossing discriminators used on the FEB is controlled via a labview interface similar to the one used to control the threshold of the CMS FEB. Various thresholds were used in a range in between 7 and 5 fC. These values are a little higher than the minimal threshold of about 3 fC used during the first experiment due to limitations of the FEB itself.

Finally, it was decided to use the same PMTs than in the first experiment as trigger. This time, they were placed on their narrow side to only cover an area on the detector smaller than three strips. On the data acquisition side, no DAQ software was available yet at the time of experimentation

4350 and scalers were once again used. As can be seen from Figure 6.11, the pulse processing has been  
 4351 inspired by the previous scheme. Thanks to the lower number of channels to monitor, the cluster  
 4352 size could be estimated by counting the signals on single channels (A, B and C on their own) but  
 4353 also on groups of two (A and B, B and C) and three channels (A and B and C) in coincidence with  
 4354 the trigger.

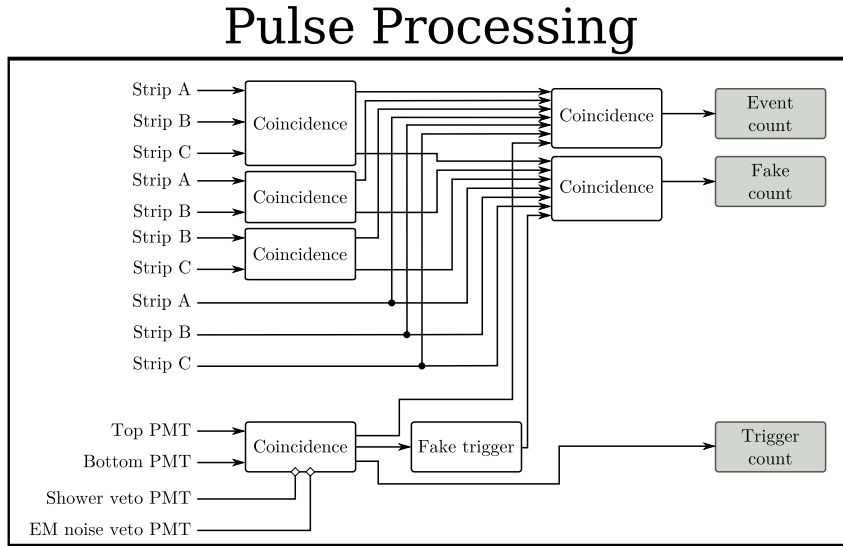
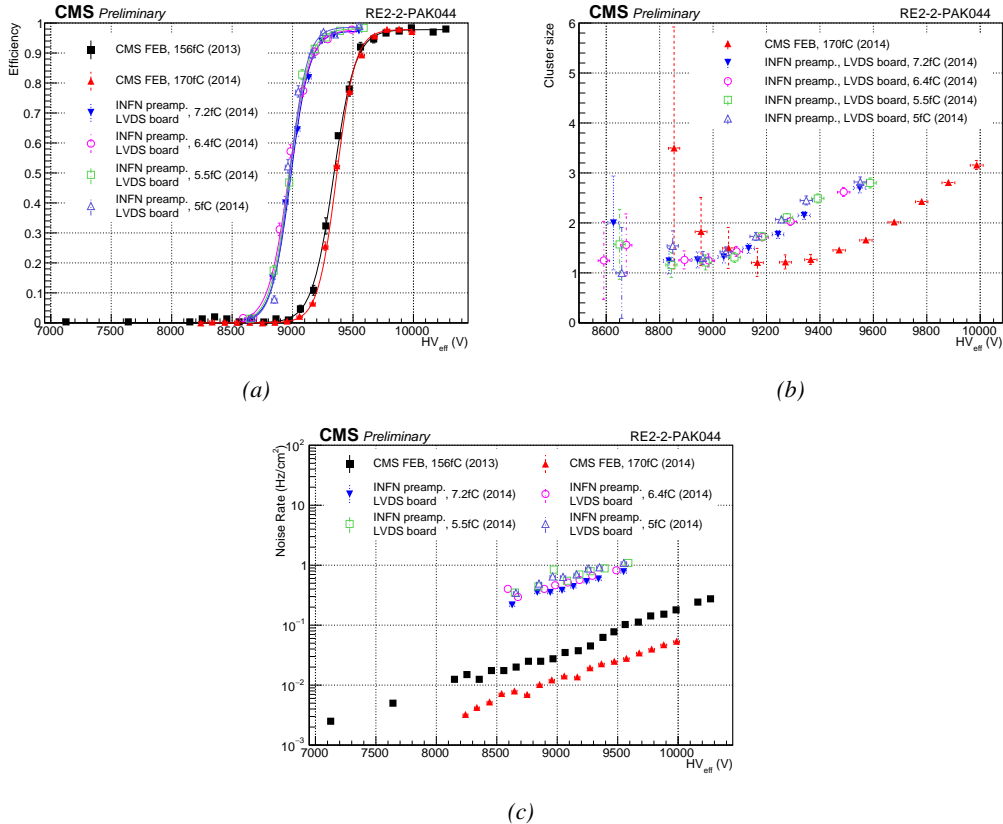


Figure 6.11: Similarly to Figure 6.8c, the signals are counted in coincidence with the trigger signals provided by PMTs. To estimate the cluster size, the channels are counted by groups of three, two but also alone.

4355 The results of the second round of tests with INFN preamplifiers are presented in Figure 6.12  
 4356 and Table 6.2. These results are consistent with what was measured with the first tested prototypes.  
 4357 The efficiency sigmoid has been measured once again with the CMS FEB, using a threshold of  
 4358 170 fC and is in agreement with the data collected in 2013. The performance of the detector with the  
 4359 preamplifiers tuned at 7.2 and 6.4 fC falls in the very same values than the setting at 7 fC according  
 4360 to the table. A maximum shift of 410 V is observed for a threshold of 5 fC.

4361 With the care placed into having a good grounding of the setup as well as a good impedance  
 4362 matching, the noise rate per unit area is this time lower than what previously measured. Nevertheless,  
 4363 it still is more than one order of magnitude higher than in the case of the CMS FEB with a threshold  
 4364 set at 170 fC. The noise rate is measured to be at lowest around 0.7 Hz/cm<sup>2</sup> when measured to be  
 4365 approximately 0.05 Hz/cm<sup>2</sup> for the CMS FEB. At such high threshold values, the noise rate per unit  
 4366 area is not expected to vary much. The data collected at the RPC assembly laboratory then displays  
 4367 much better data taking conditions with both electronics.

4368 Finally, the cluster size is measured to be similar for both electronics at the level of the working  
 4369 point and is in between 2.2 and 2.4 strips on average. The spatial resolution of both devices would  
 4370 then be the same.



*Figure 6.12: Efficiency (Figure 6.12a), cluster size (Figure 6.12b) and noise rate per unit area (Figure 6.12c) of the CMS RE2-2 detector tested with the standard CMS FEBs (black and red) and with the INFN preamplifier mounted onto the CMS FEB at different thresholds (blue, pink, green and purple).*

Data	$\epsilon_{\text{max}}$	$\lambda \cdot 10^{-2} \text{ V}^{-1}$	$HV_{50}$ (V)	$\epsilon_{WP}$	$HV_{WP}$ (V)
CMS FEB, 156fC (2013)	$(0.978 \pm 0.004)$	$(1.12 \pm 0.07)$	$(9339 \pm 11)$	$(0.97 \pm 0.01)$	$(9752 \pm 27)$
CMS FEB, 170fC (2014)	$(0.978 \pm 0.003)$	$(1.30 \pm 0.06)$	$(9364 \pm 9)$	$(0.97 \pm 0.01)$	$(9740 \pm 19)$
INFN/CMS FEB, 7.2fC (2014)	$(0.973 \pm 0.006)$	$(1.26 \pm 0.09)$	$(8985 \pm 10)$	$(0.97 \pm 0.01)$	$(9368 \pm 26)$
INFN/CMS FEB, 6.4fC (2014)	$(0.978 \pm 0.007)$	$(1.16 \pm 0.08)$	$(8969 \pm 11)$	$(0.97 \pm 0.01)$	$(9372 \pm 28)$
INFN/CMS FEB, 5.5fC (2014)	$(0.981 \pm 0.005)$	$(1.26 \pm 0.09)$	$(8973 \pm 12)$	$(0.97 \pm 0.01)$	$(9357 \pm 28)$
INFN/CMS FEB, 5fC (2014)	$(0.987 \pm 0.004)$	$(1.37 \pm 0.10)$	$(8976 \pm 12)$	$(0.98 \pm 0.01)$	$(9342 \pm 28)$

*Table 6.2: Results of the sigmoid fit (Formula 3.24) performed on the data presented in Figure 6.12a. The working point and its corresponding efficiency are computed using Formulas 3.24 and 3.25.*

In addition to the tests performed on the electronics with the CMS RPC, the electronics also have been tested on a gRPC designed in Ghent. The gRPC used for this experiment is described in Figure 6.13. The detector, showed on Figure 6.14, uses a double-gap layout with float glass electrodes of 1.1 mm and a gas gap of 1.2 mm. The electrodes themselves are made out of four pieces of glass glued together. Such a design was studied for high-rate detection purposes and aimed to serve as a proof of concept for RPCs built using small pieces assembled together to produce a larger detection area. Indeed, in the context of R&D in the field of high-rate RPCs, most low resistivity materials are custom made doped glass or ceramics plates. These materials can't be

<sup>4379</sup> produced in large areas as they are not manufactured on a large enough scale. Thus, building large  
<sup>4380</sup> detectors requires using such methods.

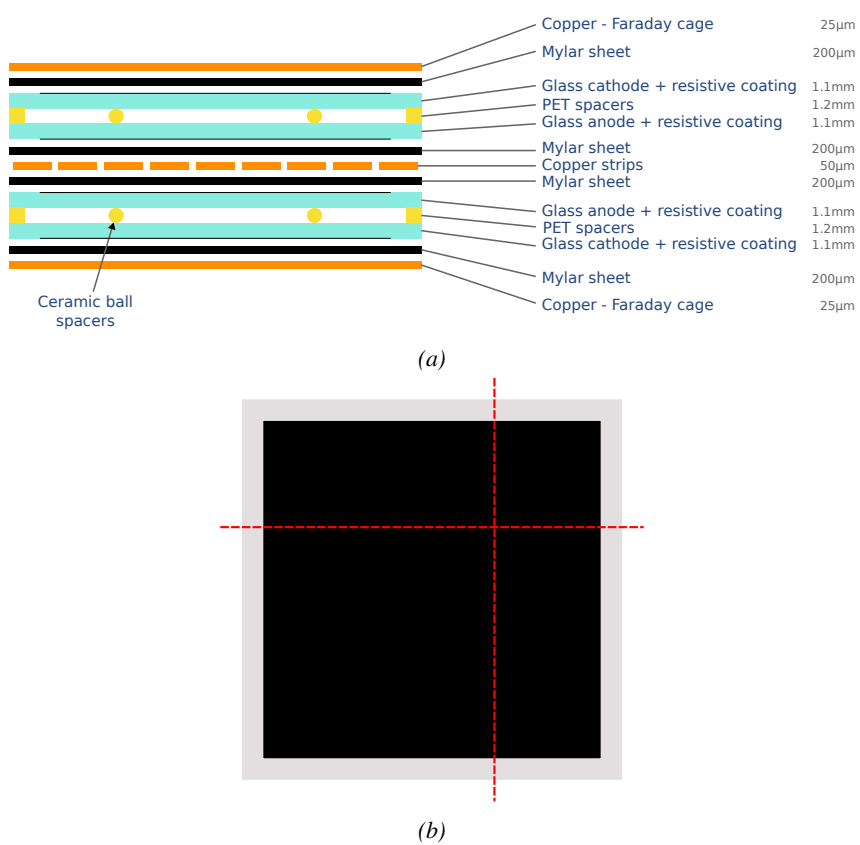


*Figure 6.13: The glass RPC developed by Ghent uses a double-gap design (Figure 6.13a). The electrodes are made of four pieces of float glass glued into a single plate (Figure 6.13b). Indeed a gluing technique has been investigated as most new low resistivity materials foreseen for RPCs of the new generation are not available in large areas.*

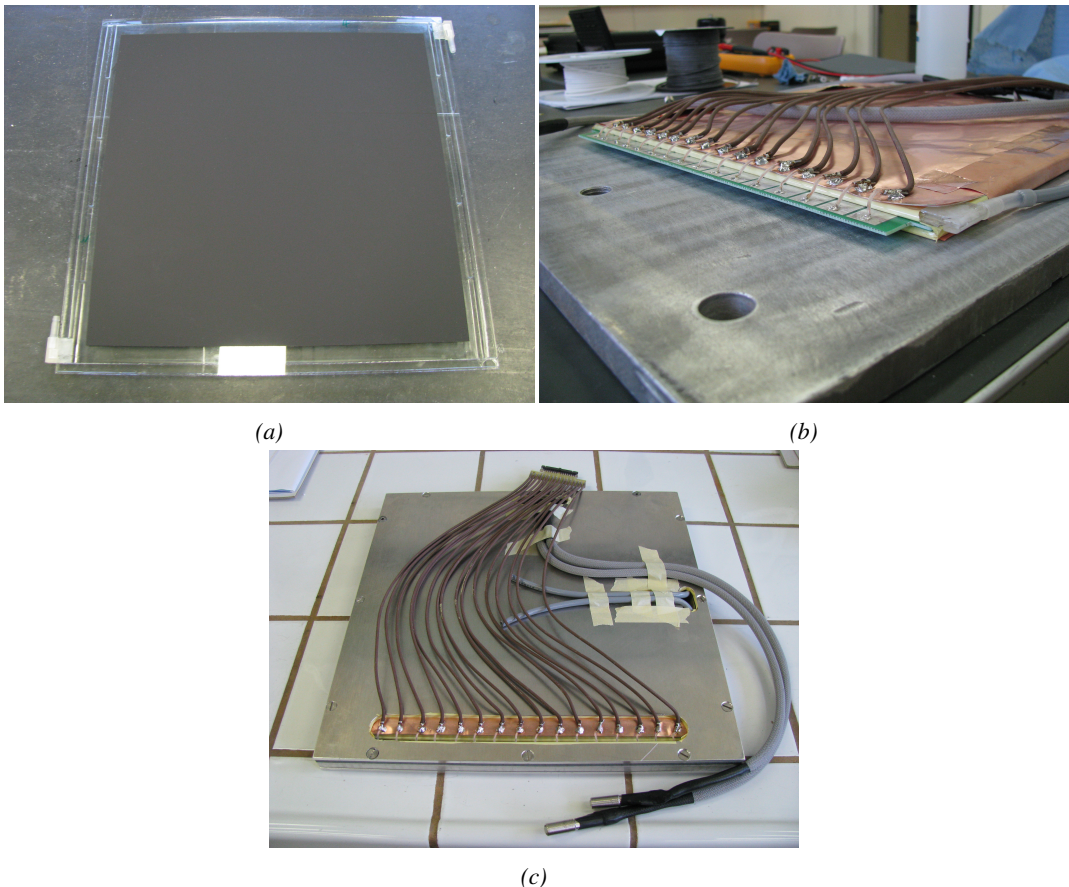


*Figure 6.14: Figure 6.14a: A gap used to conceive the gRPC tested at CERN. Figure 6.14b: Both gaps with their read-out panel are placed into a faraday made out of copper. Figure 6.14c: The faraday cage containing the double-gap gRPC is finally placed into its aluminium case.*

4381        The tests involving this detector were conducted in 2015 with the setup described by Figure 6.15.  
 4382        The photomultipliers used to trigger the data taking were a little larger than the detector and the strips  
 4383        themselves. Similarly to the case of the GIF experiment described in Section 5.2.2 of Chapter 5, it  
 4384        has been necessary to evaluate the geometrical acceptance of the setup to detect cosmic muons.  
 4385        This way, a C++ Monte Carlo simulation has been written using the dimensions of the experimental  
 4386        setup. By running 1000 simulations in which a million muons were generated in a source plane much  
 4387        larger than the experimental setup itself to reach high zenith angles, the geometrical acceptance was  
 4388        measured to be  $(0.9835 \pm 0.0014)$ . This factor has then been used to correct the measured efficiency  
 4389        of the detector.

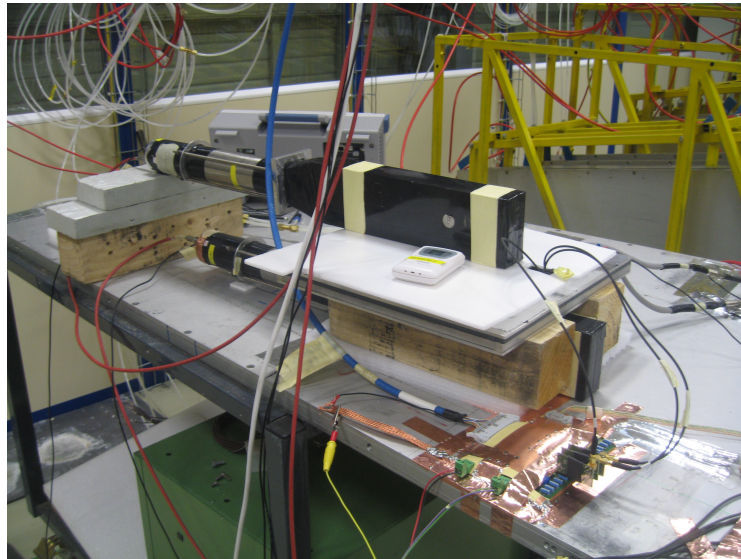


*Figure 6.15: Experimental setup used to test the INFN preamplifier mounted on the CMS like FEB with the glass RPC build by Ghent.*

4390     Thanks to the activities ongoing for the preparation of the CMS RPC experiment taking place  
 4391     at GIF++ and detailed in Chapter 5, a first prototype of DAQ software was available to automate  
 4392     the data tacking process. Thanks to this early version of the software, the pulse processing was  
 4393     made more simple. The three channels connected to the preamplifiers were sent directly into a  
 4394     V1190A TDC manufactured by CAEN. The trigger was provided by the same trigger pulse process-  
 4395     ing described in Figure 6.11. The output of the coincidence of both scintillators was sent into the  
 4396     **TRIGGER** input of the TDC. The communication with the computer was done thanks to a V1718  
 4397     module. More details on the DAQ can be found in Appendix A. Contrary to the data now collected  
 4398     at GIF++, the output of the first DAQ script consisted in a simple text file using a format described  
 4399     in Source Code 6.1. The analysis is then performed using a loop through the data file.

```

Evt0      nHits
ChHit1    THit1
ChHit2    THit2
ChHit3    THit3
ChHit4    THit4
ChHit5    THit5
4400
...
Evt1      nHits
ChHit1    THit1
ChHit2    THit2
ChHit3    THit3
...
  
```

4401 *Source Code 6.1: Description of the format used to store the data collected during the experiment aiming at  
 testing the INFN electronics with a gRPC built by Ghent. For each trigger received in the TDC module, an  
 event is created. A first line containing two columns is written in the output file with the event number EvtX  
 and the recorded number of hits nHits. This line is directly followed by the list of hits in each channel ChHitX  
 and their corresponding time stamp THitX organized into two columns.*

The results of the experiment with the gRPC are provided in Figure 6.16 and Table 6.3. The efficiency of the detector reaches 95% at working voltage, indicating that such a detector using electrodes composed of several glued pieces can be an option for the future of RPC technologies. The benefits of the preamplifiers is once again visible through the huge efficiency shift towards lower voltages. The shift reaches almost 470 V for thresholds lower than 6 fC.

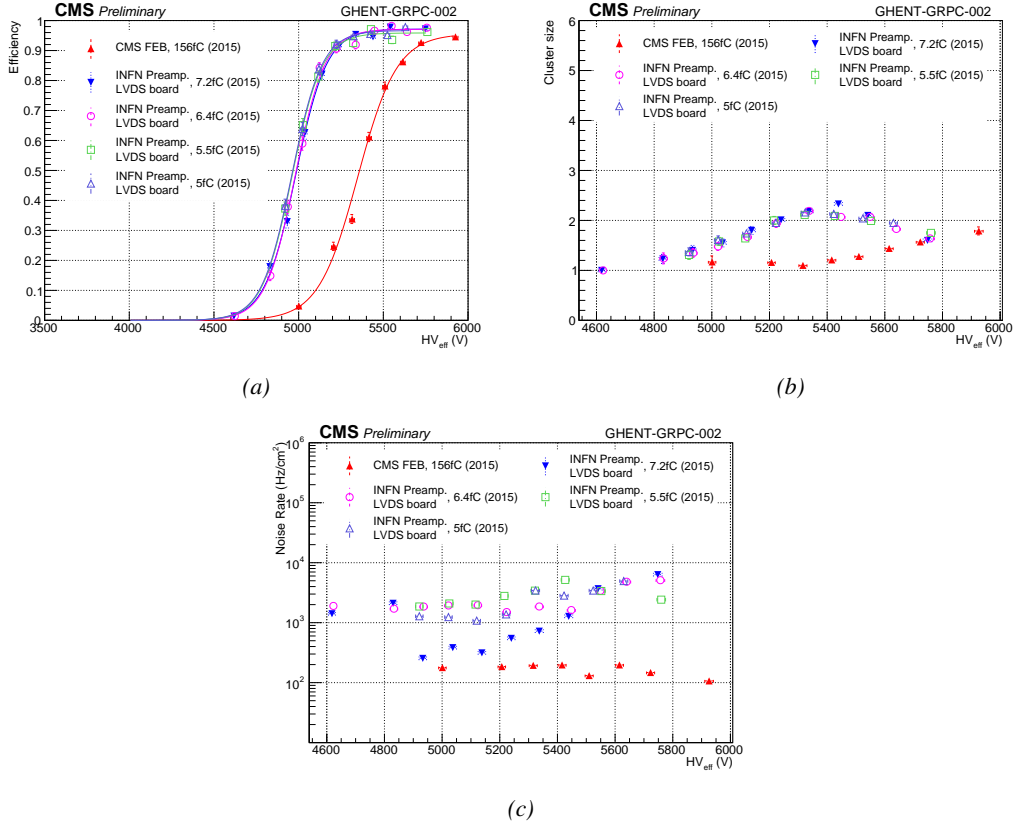


Figure 6.16: Efficiency (Figure 6.16a), cluster size (Figure 6.16b) and noise rate per unit area (Figure 6.16c) of the Ghent gRPC detector tested with the standard CMS FEBs (red) and with the INFN preamplifier mounted onto the CMS FEB at different thresholds (blue, pink, green and purple).

Data	$\epsilon_{max}$	$\lambda \cdot 10^{-2} \text{ V}^{-1}$	$HV_{50}$ (V)	$\epsilon_{WP}$	$HV_{WP}$ (V)
CMS FEB, 156fC (2015)	( $0.956 \pm 0.007$ )	( $0.86 \pm 0.04$ )	( $5349 \pm 8$ )	( $0.94 \pm 0.01$ )	( $5839 \pm 23$ )
INFN/CMS FEB, 7.2fC (2015)	( $0.972 \pm 0.006$ )	( $1.09 \pm 0.06$ )	( $4983 \pm 8$ )	( $0.96 \pm 0.01$ )	( $5403 \pm 22$ )
INFN/CMS FEB, 6.4fC (2015)	( $0.971 \pm 0.005$ )	( $1.13 \pm 0.06$ )	( $4981 \pm 8$ )	( $0.96 \pm 0.01$ )	( $5391 \pm 22$ )
INFN/CMS FEB, 5.5fC (2015)	( $0.959 \pm 0.006$ )	( $1.13 \pm 0.11$ )	( $4960 \pm 11$ )	( $0.95 \pm 0.02$ )	( $5371 \pm 37$ )
INFN/CMS FEB, 5fC (2015)	( $0.967 \pm 0.006$ )	( $1.12 \pm 0.11$ )	( $4959 \pm 11$ )	( $0.96 \pm 0.02$ )	( $5371 \pm 38$ )

Table 6.3: Results of the sigmoid fit (Formula 3.24) performed on the data presented in Figure 6.16a. The working point and its corresponding efficiency are computed using Formulas 3.24 and 3.25.

The cluster size also shows a shift but its value suddenly decreases after 5.4 kV. After a rise above 2, the cluster size drops when the detector reaches the plateau. A first idea to explain this

phenomenon would be to check the cluster algorithm to make sure that it is not biased and does not introduce a fake split of the clusters due to arbitrarily strict selection rules. Clusters are always made of neighbour strips getting a hit within a certain time window. In the algorithm written to analyse the data, it is required for the maximum time difference between the earliest hit and the latest hit in a cluster to be smaller than 10 ns. Physically, assuming of drift velocity of the electrons in the gas of the order of 0.1 mm/ns [284], the growth of an avalanche only takes a few ns. This effect is visible in Figure 6.17a in which the maximum time difference has been artificially increased to 300 ns. The peak reveals that the avalanches are not expected to grow over a time period longer than 10 ns. No peak emerges at time differences longer than 10 ns indicating that the choice of a short time development within the algorithm was justified. This conclusion is supported by Figure 6.17b in which the evolution of the reconstructed cluster size with increasing maximum time difference shows no effect.

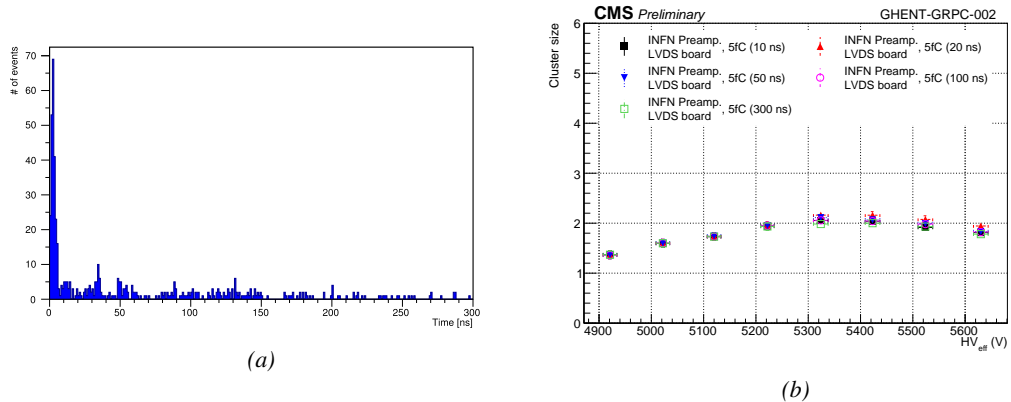


*Figure 6.17: Figure 6.17a: Time difference between the first and last hit composing a cluster in the gRPC. The maximum time difference is set to 300 ns. Figure 6.17b: Variation of the reconstructed average cluster size as a function of the time constraint used in the algorithm.*

Due to the available number of channels, the cluster size is limited to 3. It is reasonable to assume that this only is the cause of the fall of cluster size beyond 5.4 kV. Indeed looking closely at both Figure 6.18 and Figure 6.19, the link between increasing HV and decreasing cluster size can be understood. On the one hand, Figure 6.18 indicates that the cluster size features at first a maximum at 1. The maximum moves then from 1 to 3 over the points at 5120 V, 5222 V and 5324 V. Then over the last three voltage points, the bin at 2 drops to the profit of the bin at 1, the bin at 3 staying more or less stable. On the other hand, Figure 6.19 provides us more information about the localisation of the clusters among the three read-out strips. At the lowest two voltages, most of the data is contained in the central strip. At 5120 V, the highest bin is the one corresponding to the central strip with a cluster size of 1. Already at 5222 V, the balance changes towards the central strip with 3 strips in the clusters. At 5324 V, even more events happen with clusters of all 3 strips while the events with a single hit in the side strips starts to increase. The number of events with cluster made of all 3 strips will not vary much anymore while the number of events with clusters made of 2 strips will decrease and the single hits in the side strips will continue rising. This information indicates that the avalanches in the gap start to get stronger. Indeed, the increase of the events containing single hits mainly increases on the side strips points to an intensification of the avalanche gain on the strip adjacent to the three channels connected to the read-out setup. Only a single hit is read-out while

in reality this was the contribution of bigger avalanches. The events with clusters of size 2 tend to decrease due to the stronger gain that should normally be triggering wider avalanches. The cluster size distribution of Figure 6.18 gives the impression that the distribution is moving towards higher values but the geometrical limitation of the system due to the very low number of channels makes it impossible to measure.

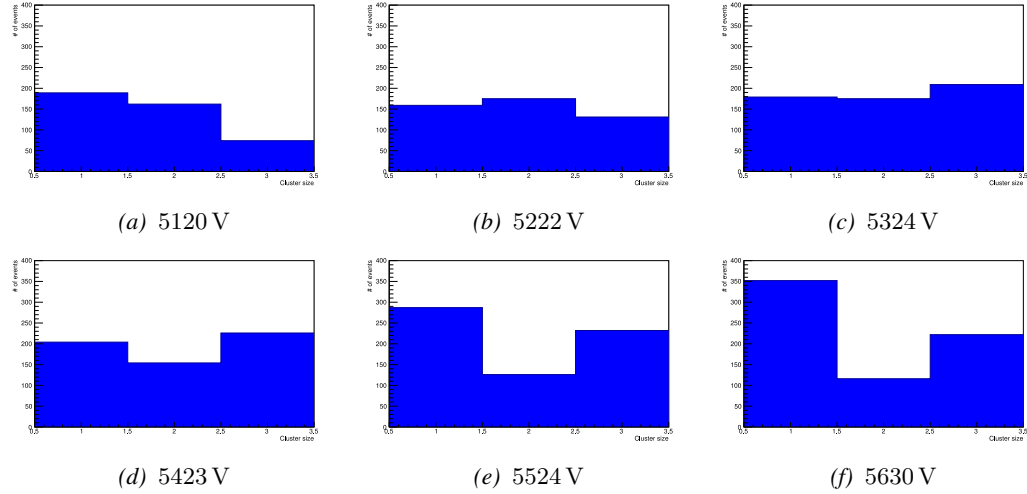


*Figure 6.18: Evolution of the cluster size distribution with increasing voltage for the gRPC tested with the INFN preamplifiers using a threshold of 5 fC.*

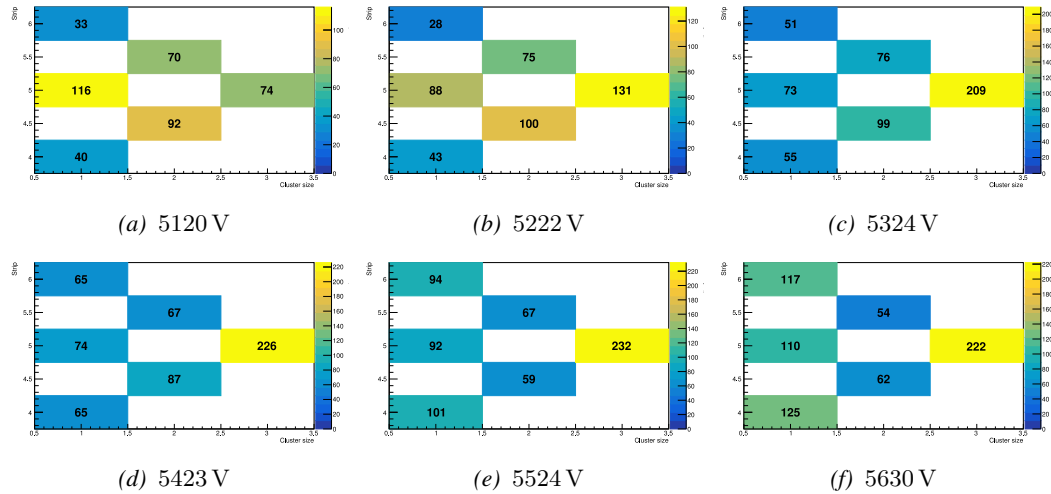


*Figure 6.19: Map of the cluster size distribution as a function of the cluster position with increasing voltage for the gRPC tested with the INFN preamplifiers using a threshold of 5 fC.*

Eventhough the performance of the detector are promising, the results concerning the noise rate per unit area seem to indicate that the detector and its combination with the electronics in the case of this experiment produces very high levels of noise, if compared to the noise measured in the RE4

4446 detector. With each type of electronics, the noise doesn't indicate a clear correlation with increasing  
 4447 voltage. The hypothesis at this stage would be that the noise is not created inside of the gas volume by  
 4448 avalanches triggered along the glueing lines, where the electric field could be abruptly perturbed.  
 4449 It would rather come from the read-out channel itself, and from its connection to the electronics.  
 4450 Indeed, looking at the noise profile measured in the detector and presented in Figure 6.20a, it is clear  
 4451 that the noise is localised in two areas corresponding to the HV connectors in the case of the HV  
 4452 scan performed with the CMS FEB. Moreover, contrary to the very careful work performed on the  
 4453 RE2 chamber to match the impedance of the strips with the read-out cables connected to the board  
 4454 on which the INFN preamplifiers are mounted, no matching was done on the gRPC due to a lack  
 4455 of time. The noise measured in the tested three channels is showed in Figure 6.20b. This region of  
 4456 the detector doesn't correspond to the HV connectors according to Figure 6.20a. Nevertheless, the  
 4457 number of hits counted in the detector is much higher than in the CMS FEB case. Looking more  
 4458 carefully to Figure 6.21 presenting the hit time profile in both cases together with the time profile of  
 4459 the CMS RE2-2 detector tested with INFN preamplifiers, it is clear that the detector is noisier. Also,  
 4460 the reflections due to the impedance mismatch is clearly visible in Figure 6.21b.

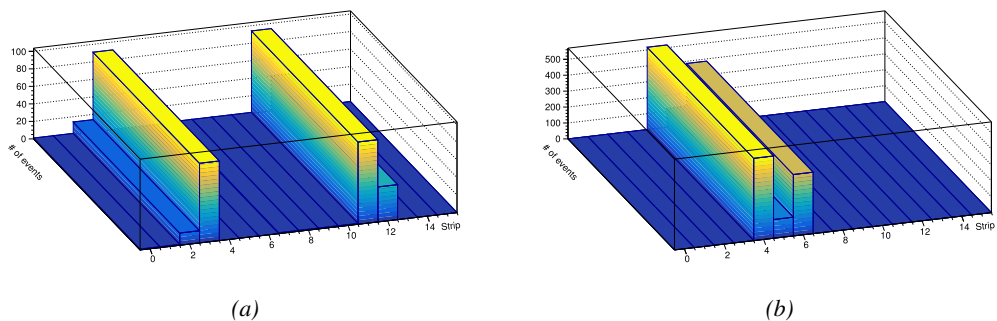
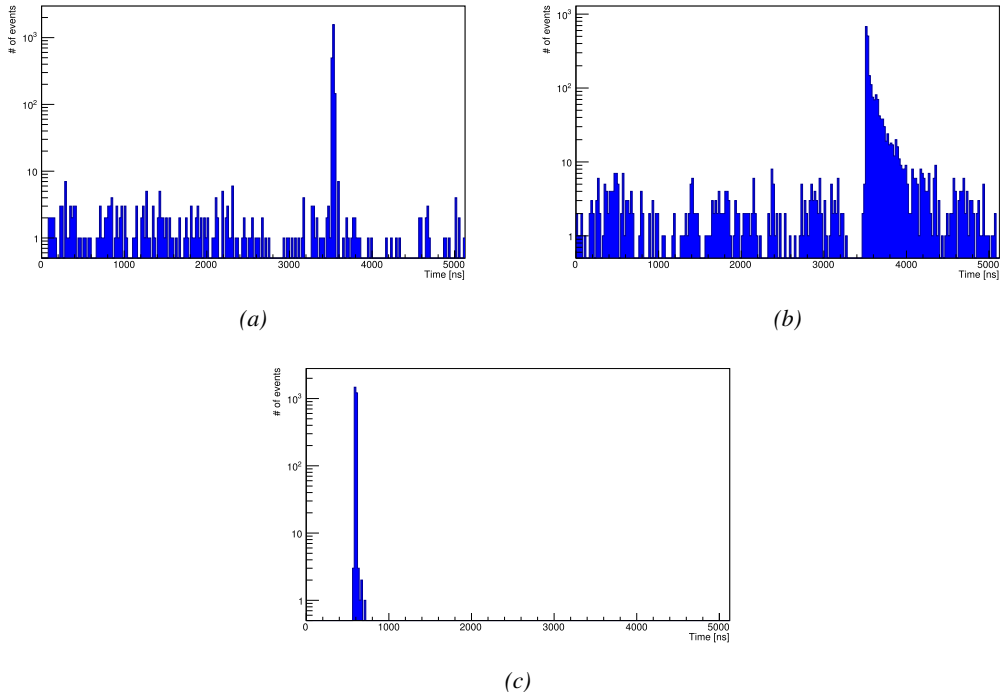


Figure 6.20: Noise profile measured in the glass RPC built by Ghent tested with the standard CMS FEB (Figure 6.20a) and the INFN preamplifiers mounted on a CMS-like FEB (Figure 6.20b).



*Figure 6.21: The arrival time of the hits recorded in the gRPC tested with the CMS FEB (Figure 6.21a) and with the INFN preamplifiers (Figure 6.21b), and recorded in the CMS RE2 RPC tested with the INFN preamplifiers (Figure 6.21c).*

### 6.2.3 HARDROC 2 based RPC read-out

The HAdronic RPC Digital Read-Out Chip (HARDROC) ASIC, as its name suggests, has been developed for RPC applications and in particular for the read-out RPCs of the Semi-Digital HCAL (SDHCAL) that is being studied in the perspective of the International Linear Collider (ILC). The SDHCAL detectors are required to have a high granularity compared to the CMS RPCs and hence, they use 1 cm<sup>2</sup> read-out pads instead of strips. This choice results in a huge number of channels. The ASIC is mounted directly on the read-out pannel for compactness as can be seen in Figure ?? and feature three thresholds to provide a semi-digital information.

The PETIROC that inspired the CMS RPCROC uses a similar technology than the one developed for the HARDROC and is manufactured by the same company. It is safe to conclude that the preliminary results obtained with the HARDROC electronics constitute a strong indication on the potential performance of a FEB developed specifically for CMS detectors. The leading institute in the development of the SDHCAL based on single-gap glass RPCs (gRPCs) is the Institut de Physique Nucléaire de Lyon (IPNL) which also played a great role in developing iRPCs for CMS.

A read-out pannel using the HARDROC 2 technology was lended by this institute and was tested onto a CMS RPC. Contrary to the tests with the INFN preamplifiers that were made using an RE2-2 CMS RPC built in 2007 for the second endcap disk of CMS, the choice was made to use an RE4-3 detector built during LS1 to equip the fourth endcap. Indeed, the pannel can't be sandwiched between two RPC gaps due to the embedded electronics and a single CMS RPC gap was used. At the time of this experiment, only RE4-3 gaps were available and the choice was made to change

4481 detector with respect to the previous series of tests conducted on the INFN preamplifiers. As for  
 4482 the INFN preamplifiers, the pannel has been tested on the gRPC built by UGent. The gRPC being  
 4483 smaller than the HARDROC read-out that was used for the experiment but thanks to the 2D read-out  
 4484 using pads, this was not a problem for the data acquisition.



(a)

(b)

*Figure 6.22: Experimental setups used to test the HARDROC2 electronics with a CMS RE4-3 gap (Figure 6.22a) and a gRPC gap built in Ghent (Figure 6.22b).*

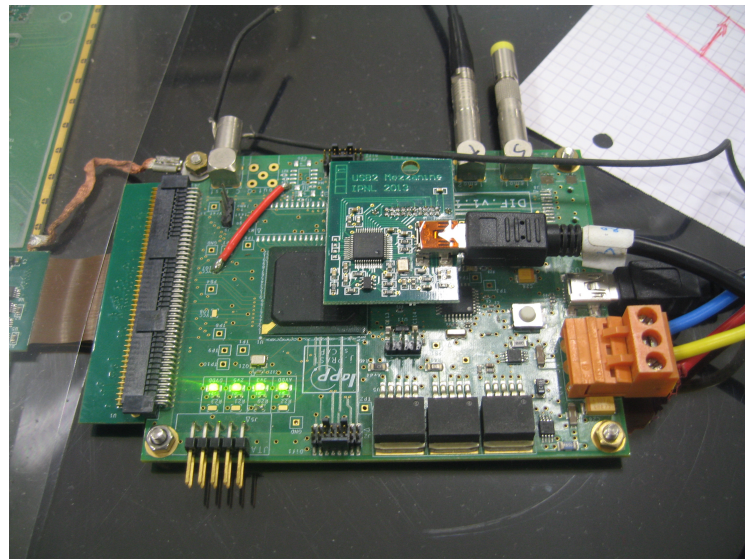


*Figure 6.23: HARDROC2 control chip with its "Mezzanine" used to collect the data from the different HARDROC ASICs and communicate with the computer. On top of the picture, the trigger is brought by a coaxial cable. The connection with the computer is assured by both the USB cables.*

4485 Once again, the experiment was conducted in the CMS RPC assembly laboratory at CERN and  
 4486 the setups are shown in Figure 6.22. The read-out panel is placed directly on top of the gaps and  
 4487 pressed against the detector surface thanks to weights. The same PMTs are used to provide a trigger

to the data acquisition. In the particular case of the HARDROC 2 electronics, the output signal does not correspond to the LVDS signals provided by the CMS FEB. Moreover, there would be more than 1500 channels to constantly monitor and unfortunately, there would not be enough VME TDC modules to use with the DAQ software designed for the experiment involving the INFN preamplifiers. Nevertheless, a custom-made DAQ software was designed by the members of IPNL's team to read-out the electronics through the chip presented in Figure 6.23. The data is stored in the buffer of the ASIC continuously and dumped into the computer when a trigger is signal is received.

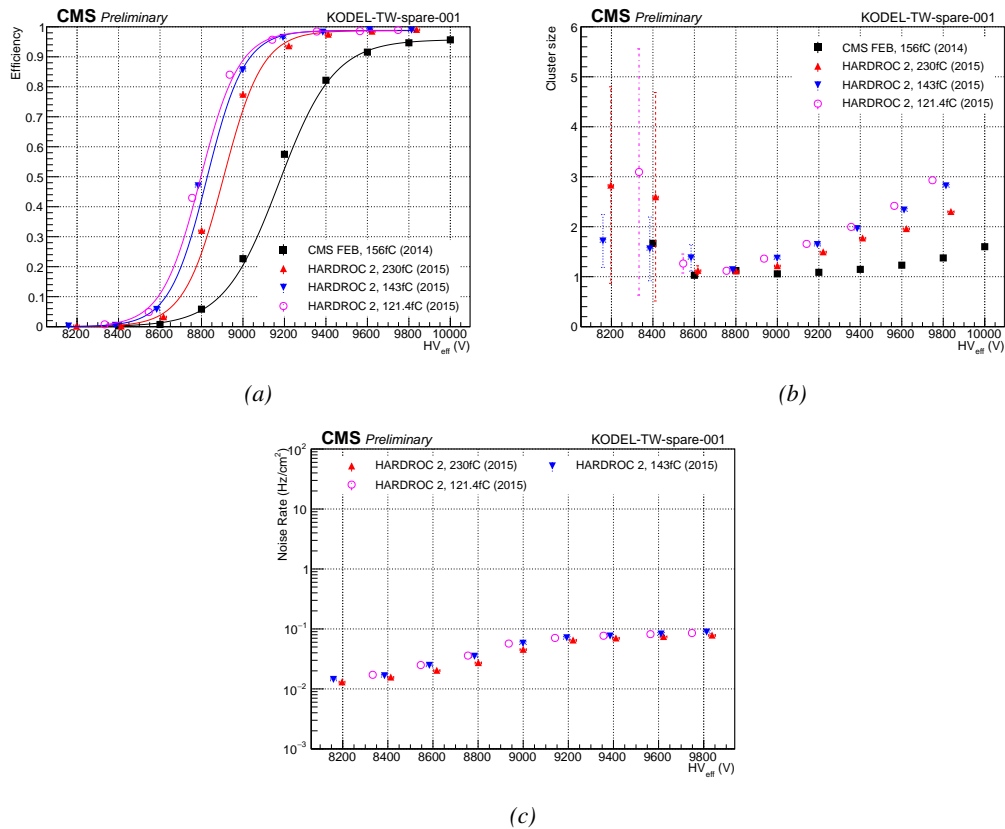


Figure 6.24: Efficiency (Figure 6.24a), cluster size (Figure 6.24b) and noise rate per unit area (Figure 6.24c) of the CMS RE4-3 detector tested in single gap mode with the standard CMS FEBs (black) and with the HARDROC 2 readout panel at different thresholds (red, blue and pink).

Data	$\epsilon_{max}$	$\lambda \cdot 10^{-2} \text{ V}^{-1}$	$HV_{50}$ (V)	$\epsilon_{WP}$	$HV_{WP}$ (V)
CMS FEB, 156fC (2014)	$(0.958 \pm 0.000)$	$(0.75 \pm 0.00)$	$(9174 \pm 1)$	$(0.94 \pm 0.00)$	$(9716 \pm 2)$
HARDROC 2, 230fC (2015)	$(0.987 \pm 0.002)$	$(1.06 \pm 0.04)$	$(8905 \pm 8)$	$(0.98 \pm 0.01)$	$(9333 \pm 17)$
HARDROC 2, 143fC (2015)	$(0.988 \pm 0.001)$	$(1.10 \pm 0.04)$	$(8826 \pm 8)$	$(0.98 \pm 0.01)$	$(9243 \pm 17)$
HARDROC 2, 121.4fC (2015)	$(0.987 \pm 0.001)$	$(1.07 \pm 0.04)$	$(8795 \pm 8)$	$(0.98 \pm 0.01)$	$(9220 \pm 17)$

Table 6.4: Results of the sigmoid fit (Formula 3.24) performed on the data presented in Figure 6.24a. The working point and its corresponding efficiency are computed using Formulas 3.24 and 3.25.

The results of the tests conducted with the HARDROC 2 on a CMS gap are presented in Fig-

ure 6.24 and Table 6.4. These results can hardly be compared to what was measured with the INFN preamplifiers as the detector was not tested using the single-gap mode. The tested thresholds are high compared to the ones displayed by the INFN preamplifiers and are of the order of magnitude of the current CMS FEB. Nevertheless, the performance of the detector equipped with this read-out pannel is measured to be better. Indeed, a shift of 400 to 500 V is observed at thresholds ranging from 230 to 121.4 fC. [Here it could be nice to bring an explanation to this observation.]

The cluster size is provided for information as a direct comparison of the cluster size measured with  $1\text{ cm}^2$  pads and long copper strips with width of a few cm is not possible. The measured cluster size at working voltage with the CMS FEB is consistent with what would be expected of a single-gap RPC. Indeed, the usage of two gaps in an OR system allows for a stronger overall gain and hence, the cluster size is greater. A more precise estimation of the charge spread inside of the gap is obtained using pads instead of strips. At working voltage, an avalanche is detected within less than two pads on average. An extra information could be used to further improve the spatial resolution of the detector. Indeed, as stated in the introduction of the Section, the HARDROC 2 is a semi-digital electronics and features three threshold levels. Tuning these thresholds would lead to an approximation of the induced charge profile over the neighbouring pads. A gaussian fit over the digitized distribution would give an estimation of the position of the avalanche center.

Finally, the noise measured in the electronics is of the same order of what had been measured in Figure 6.12c. It is safe to assume that the noise level in the case of a single-gap RPC is expected to be of the same order of magnitude than its double-gap counterpart as the noise mainly is electromagnetic. Figure 6.25 provides a clearer understanding of the position of the trigger PMTs and of the noise measured with the HARDROC. The noise of the electronics itself is very small and the read-out pannel is sensitive enough to measure the noise in the RPC gap. Indeed, except for a few visible hot spots, the observed noise profile corresponds perfectly to the spacer positions inside of the gap volume. The PET buttons used to maintain the uniformity of the gas volume cause noise at their proximity as they modify the local electric field.

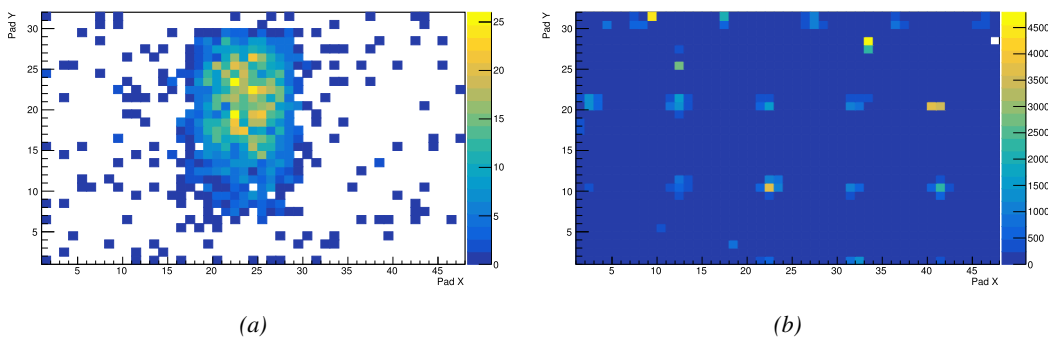


Figure 6.25: Measured muon (Figure 6.25a) and noise (Figure 6.25a) profiles in the read-out pads of the HARDROC 2 over a CMS RE4-3 gap. The inner structure of the gap and the presence of the spacers in the volume is visible.

The results of the experiment with the gRPC are provided in Figure 6.26 and Table 6.5. Unfortunately the gRPC had not been tested in single gap mode with the CMS FEB. Thus, a direct comparison is not possible as the data were not collected in similar conditions. The detector could only be tested with a single HARDROC 2 threshold setting (143 fC). As for the double-gap, the effi-

4526 efficiency of the single-gap reaches 95% at working voltage. The working voltage is consistent with the  
 4527 double-gap detector operated with the CMS FEB indicating that the HARDROC is more sensitive to  
 4528 lower charges. The difference in efficiency rising is consistent with the use of one gap versus two in  
 4529 the case of the CMS FEB.

4530 As discussed in the case of the CMS RE4-3 gap, the direct comparison of the cluster sizes is  
 4531 not possible. In this sense, the proximity of both results only is fortuitous. The cluster size of  
 4532 approximately 1.6 measured with the HARDROC 2 at working voltage is of the same order than  
 4533 what had previously been measured for the CMS gap indicating that at equivalent performance, the  
 4534 gain and hence, the induced charge could be comparable.

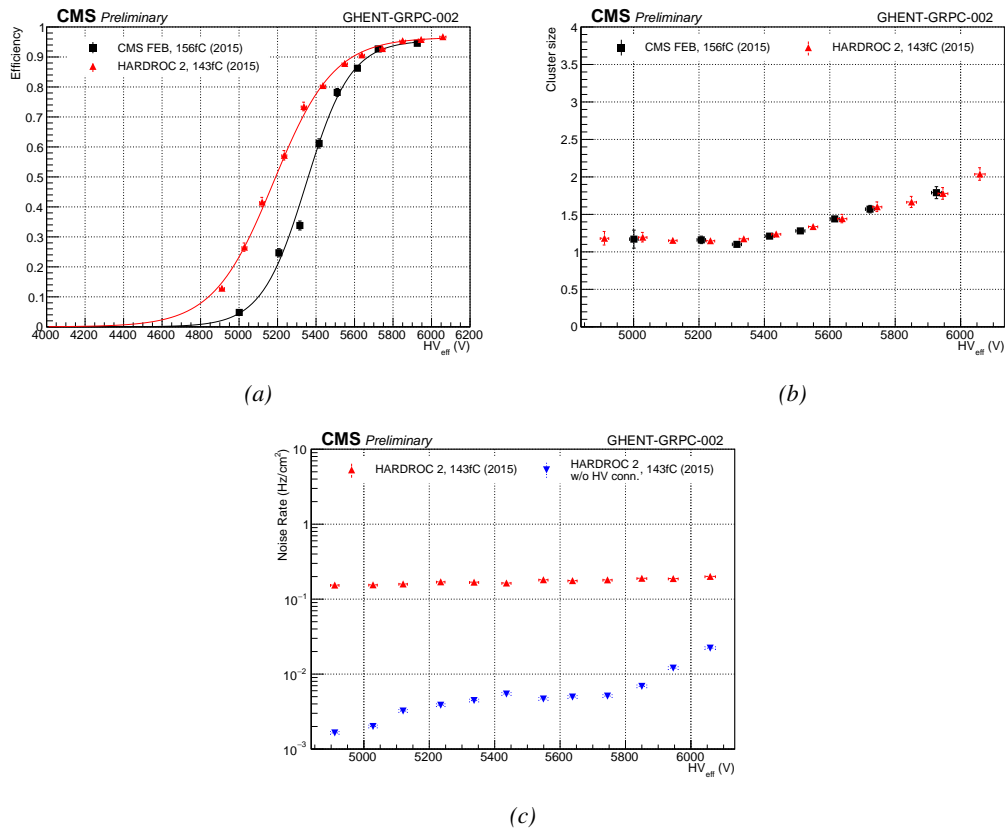


Figure 6.26: Efficiency (Figure 6.24a), cluster size (Figure 6.24b) and noise rate per unit area (Figure 6.24c) of the UGent gRPC tested in double-gap mode with the standard CMS FEBs (black) and in single-gap with the HARDROC 2 readout panel at a threshold of 143 fC (red).

Data	$\epsilon_{max}$	$\lambda \cdot 10^{-2} \text{ V}^{-1}$	$HV_{50}$ (V)	$\epsilon_{WP}$	$HV_{WP}$ (V)
CMS FEB, 156fC (2015)	$(0.956 \pm 0.007)$	$(0.86 \pm 0.04)$	$(5349 \pm 8)$	$(0.94 \pm 0.01)$	$(5839 \pm 23)$
HARDROC 2, 143fC (2015)	$(0.966 \pm 0.004)$	$(0.64 \pm 0.02)$	$(5179 \pm 7)$	$(0.95 \pm 0.01)$	$(5790 \pm 25)$

Table 6.5: Results of the sigmoid fit (Formula 3.24) performed on the data presented in Figure 6.26a. The working point and its corresponding efficiency are computed using Formulas 3.24 and 3.25.

4535 Finally, the noise measured in the electronics seemed higher than in the case of the CMS gap.

Looking closer to the noise profile provided in Figure 6.27, it can be seen that the noise measurement was affected by the HV connector. Indeed, the high noise measured in pads 41 and 42 along X and 22 to 25 along Y, corresponds exactly to the position of the HV connector on the cathode side. Contrary to the case of the CMS gap were the HV connector was far from the read-out area, the gRPC is smaller than the read-out and due to the poor grounding of the setup the electric field created by the HV connector could affect the read-out. Excluding the corresponding pads gives a much more reliable noise measurement as can be seen in Figure 6.26c. Through the noise profile, a better understanding of the gRPC uniformity can be obtained. First of all, the row corresponding to Y=16 seem consistently noisier than the neighbouring pads and could correspond to the glueing line that lies along this pad row. The noise increase along this line is not very clear though and no corresponding behaviour can be observed along the other glueing line along column X=30. But the gas volume corresponding to the largest glass plate, spreading from columns 31 to 47 along X and rows 1 to 15 clearly shows a stronger noise in its center. The detection area being small, only a few ceramic ball spacers were used to maintain the distance in between the electrodes. It is not impossible that the ball spacer located in the center of this volume popped out. Due to the absence of a spacer, the force applied by electric field onto the electrodes could have made the distance in between the electrodes smaller and artificially increased the observed electric field, also increasing the measured noise.

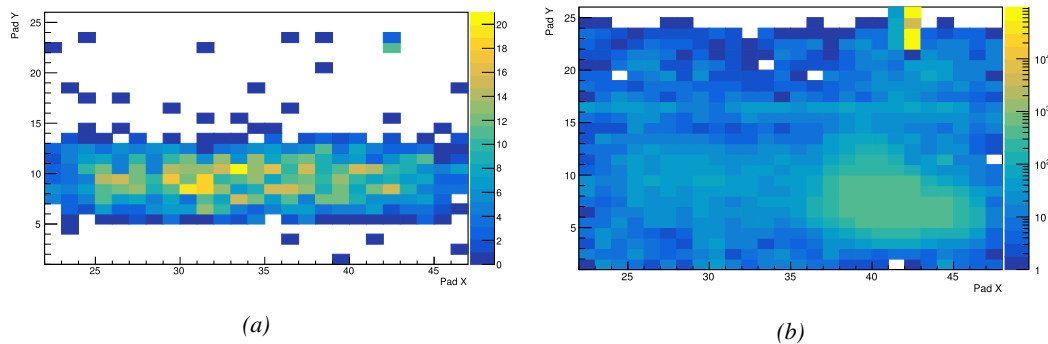


Figure 6.27: Measured muon (Figure 6.27a) and noise (Figure 6.27b) profiles in the read-out pads of the HARDROC 2 over a gRPC gap built by Ghent.

#### 6.2.4 Outlooks and current FEE certification status



# 7

4554

4555

## Conclusions and outlooks

4556 The CMS RPC upgrade has been and will keep on being an exciting scientific research. The collab-  
4557 oration converged towards the solutions that will be adopted in the perspective of HL-LHC. Even-  
4558 though the consolidation of the present CMS RPC infrastructure and the certification of the new  
4559 technologies that will complete the redundancy of the muon system are still ongoing, the future of  
4560 the experiment from the RPC point of view is now clear.

4561 To reach this point, the contribution of Ghent during the preliminary phase of tests between 2012  
4562 and 2015 has been decisive in both the consolidation of the present detectors and in the selection of  
4563 the Front-End Electronics that will equip the iRPCs. At every step, Ghent University played a  
4564 leading role in setting up the experiments but also in gathering and analysing the data. First of all,  
4565 two potential FEE technologies were selected and it was showed that both of them could be used for  
4566 new CMS detectors. On one side, the INFN amplifier provided a very interesting sensitivity to low  
4567 charge depositions. On the other hand, the FEEs developed by OMEGA (HARDROC, PETIROC)  
4568 showed that they could provide a reduction of the working voltage at similar charge deposition  
4569 ranges. Moreover, this technology had already been certified through multiple experiments using  
4570 detectors such as scintillators and RPCs. Finally, it had the advantage of proposing a 2D read-out  
4571 that would greatly improve the spatial resolution of the detectors in the radial direction. The expertise  
4572 of the Instrumentation group was demonstrated in this campaign.

4573 As a natural continuation, a door was opened to join the GIFT++ effort at key positions. A major  
4574 contribution to the development of the Data Acquisition, Data Quality Monitoring and data analysis  
4575 tools was provided and will keep helping the collaboration in conducting robust R&D research in  
4576 the future. Indeed, new young experts are emerging and taking over the tools to improve them with  
4577 fresh ideas. So far, the CMS RPC group is on the way of certifying the current RPC system for the  
4578 HL-LHC period. The Link-system will be upgraded and the present detectors should live through  
4579 the high-luminosity phase of the LHC without important change in their performance. The RPC  
4580 that will complete the redundancy of the muon system are being certified as well and show very  
4581 good performance under high-irradiation that is so far foreseen to stay stable throughout the whole  
4582 Phase-2.

4583     Nevertheless, the present thesis document only focusses on the R&D produced by the CMS RPC  
4584     on the present and new detection technologies that are and will be used at CMS. Few information  
4585     about the very important research being conducted in order to find a replacement to the standard  
4586     RPC gas mixture is provided. The outcome of this search for new gases will be of major interest as  
4587     the restriction for the standard mixture will get harder.

4588     Once the R&D will be complete, the next phase will consist in the upgrade of the RPC sub-  
4589     system. Ghent will mainly take part in manufacturing the detectors for the expension of the endcaps  
4590     as was already the case for the production of the RE4 detectors for the fourth endcap disk of CMS  
4591     between 2012 and 2013. After LS3, the LHC will finally enter its high-luminosity phase and new  
4592     breakthrough will be foreseen. The good performance of the RPCs and of all of CMS sub-systems  
4593     will be important in this reguard and the skills developed during the present R&D will become an  
4594     important asset in maintaining the performance of the detectors at their best level.

# A

4595

4596

## A data acquisition software for CAEN VME TDCs

4597

4598 Certifying detectors in the perspective of HL-LHC required to develop tools for the GIF++ experiment.  
4599 Among them was the C++ Data Acquisition (DAQ) software that allows to make the communications  
4600 in between a computer and TDC modules in order to retrieve the RPC data [285]. In this  
4601 appendix, details about this software, as of how the software was written, how it functions and how  
4602 it can be exported to another similar setup, will be given.

### 4603 A.1 GIF++ DAQ file tree

4604 GIF++ DAQ source code is fully available on github at [https://github.com/afagot/GIF\\_](https://github.com/afagot/GIF_DAQ)  
4605 DAQ. The software requires 3 non-optional dependencies:

- 4606 • CAEN USB Driver, to mount the VME hardware,
- 4607 • CAEN VME Library, to communicate with the VME hardware, and
- 4608 • ROOT, to organize the collected data into a TTree.

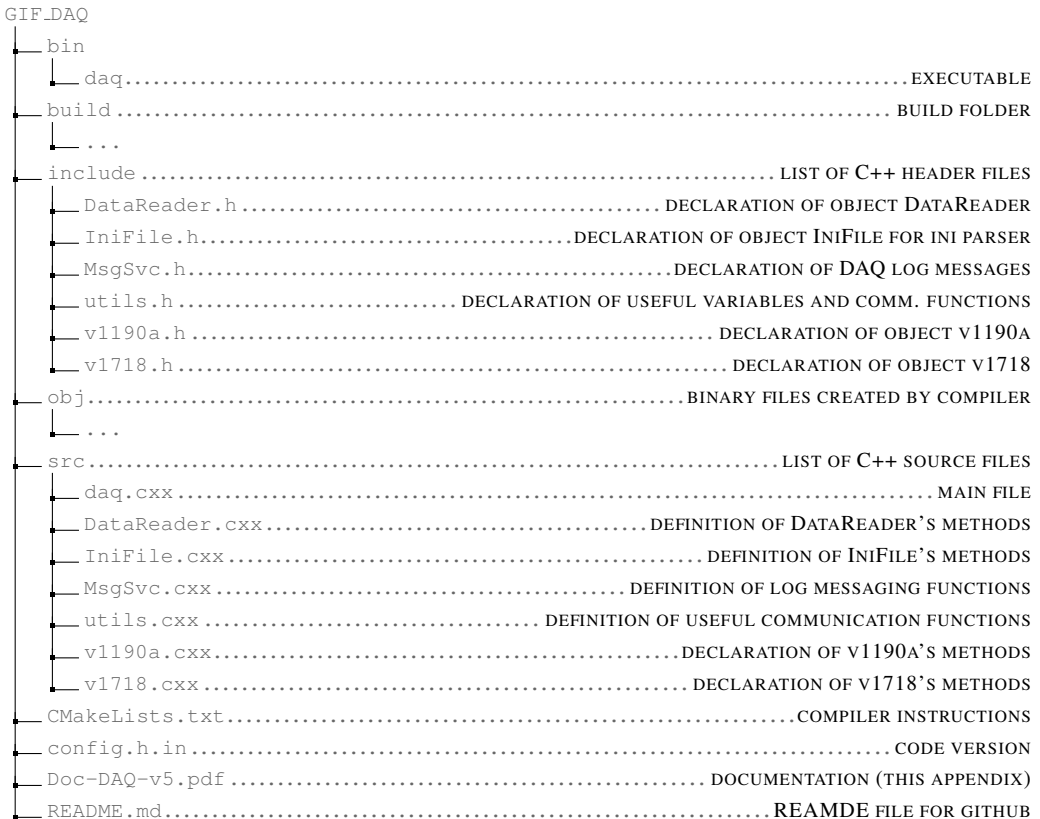
4609 The CAEN VME library will not be packaged by distributions and will need to be installed man-  
4610 ually. To compile the GIF++ DAQ project via a terminal, from the DAQ folder use the command:

```
4611 mkdir build
4612 cd build
4613 cmake ..
4614 make install
```

4613 The source code tree is provided below along with comments to give an overview of the files' con-  
4614 tent. The different objects created for this project (`v1718`, `v1190a`, `IniFile` & `DataReader`) will be

4615 described in details in the following sections.

4616



## 4617 A.2 Usage of the DAQ

4618 GIF++ DAQ, as used in GIF++, is not a standalone software. Indeed, the system being more com-  
 4619 plexe, the DAQ only is a sub-layer of the software architecture developped to control and monitor  
 4620 the RPCs that are placed into the bunker for performance study in an irradiated environment. The top  
 4621 layer of GIF++ is a Web Detector Control System (webDCS) application. The DAQ is only called  
 4622 by the webDCS when data needs to be acquired. The webDCS operates the DAQ through command  
 4623 line. To start the DAQ, the webDCS calls:

4624

4625    bin/daq /path/to/the/log/file/in/the/output/data/folder

4626 where /path/to/the/log/file/in/the/output/data/folder is the only argument required. This  
 4627 log file is important for the webDCS as this file contains all the content of the communication of the  
 4628 webDCS and the different systems monitored by the webDCS. Its content is constantly displayed  
 4629 during data taking for the users to be able to follow the operations. The communication messages  
 4630 are normally sent to the webDCS log file via the functions declared in file `MsgSvc.h`, typically  
 4631 `MSG_INFO(string message)`.

4632

### A.3 Description of the readout setup

The CMS RPC setup at GIF++ counts 5 V1190A Time-to-Digital Converter (TDC) manufactured by CAEN [268]. V1190A are VME units accepting 128 independent Multi-Hit/Multi-Event TDC channels whose signals are treated by 4 100 ps high performance TDC chips developed by CERN / ECP-MIC Division. The communication between the computer and the TDCs to transfer data is done via a V1718 VME master module also manufactured by CAEN and operated from a USB port [269]. These VME modules are all hosted into a 6U VME 6021 powered crate manufactured by W-Ie-Ne-R than can accommodate up to 21 VME bus cards [286]. These 3 components of the DAQ setup are shown in Figure A.1.

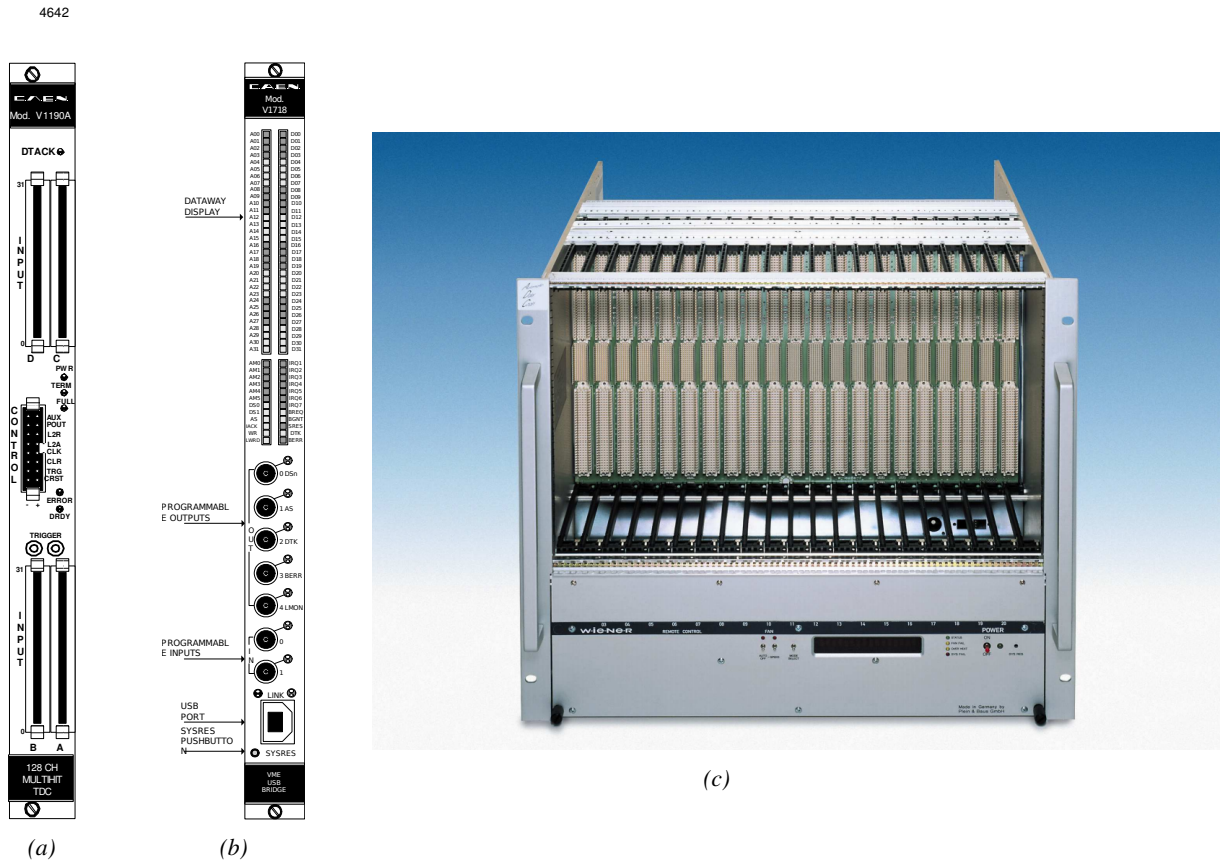


Figure A.1: (A.1a) View of the front panel of a V1190A TDC module [268]. (A.1b) View of the front panel of a V1718 Bridge module [269]. (A.1c) View of the front panel of a 6U 6021 VME crate [286].

### A.4 Data read-out

To efficiently perform a data readout algorithm, C++ objects to handle the VME modules (TDCs and VME bridge) have been created along with objects to store data and read the configuration file that comes as an input of the DAQ software.

### A.4.1 V1190A TDCs

The DAQ used at GIF takes profit of the *Trigger Matching Mode* offered by V1190A modules. This setting is enabled through the method `v1190a::SetTrigMatching (int ntdcs)` where `ntdcs` is the total number of TDCs in the setup this setting needs to be enabled for (Source Code A.1). A trigger matching is performed in between a trigger time tag, a trigger signal sent into the TRIGGER input of the TDC visible on Figure A.1a, and the channel time measurements, signals recorded from the detectors under test in our case. Control over this data acquisition mode, explained through Figure A.2, is offered via 4 programmable parameters:

- **match window:** the matching between a trigger and a hit is done within a programmable time window. This is set via the method  
`void v1190a::SetTrigWindowWidth(Uint windowHeight, int ntdcs)`
- **window offset:** temporal distance between the trigger tag and the start of the trigger matching window. This is set via the method  
`void v1190a::SetTrigWindowWidth(Uint windowHeight, int ntdcs)`
- **extra search margin:** an extended time window is used to ensure that all matching hits are found. This is set via the method  
`void v1190a::SetTrigSearchMargin(Uint searchMargin, int ntdcs)`
- **reject margin:** older hits are automatically rejected to prevent buffer overflows and to speed up the search time. This is set via the method  
`void v1190a::SetTrigRejectionMargin(Uint rejectMargin, int ntdcs)`

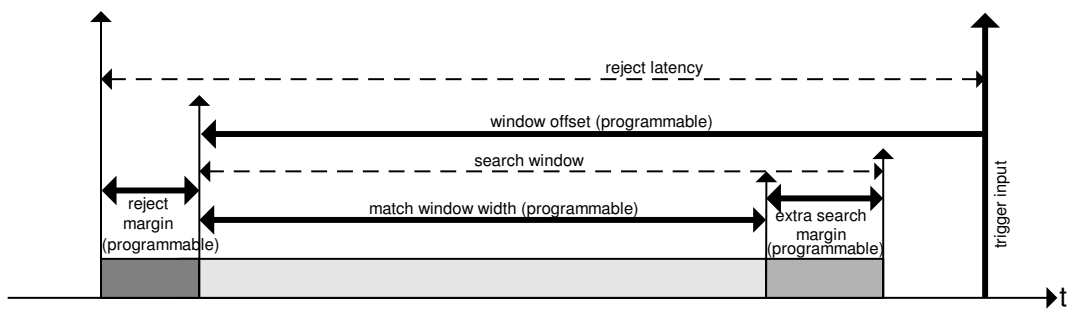


Figure A.2: Module V1190A Trigger Matching Mode timing diagram [268].

Each of these 4 parameters are given in number of clocks, 1 clock being 25 ns long. It is easy to understand at this level that there are 3 possible functioning settings:

- **1:** the match window is entirely contained after the trigger signal,
- **2:** the match window overlaps the trigger signal, or
- **3:** the match window is entirely contained before the trigger signal as displayed on Figure A.2.

In both the first and second cases, the sum of the window width and of the offset can be set to a maximum of 40 clocks, which corresponds to 1  $\mu$ s. Evidently, the offset can be negative, allowing

4675 for a longer match window, with the constraint of having the window ending at most 1  $\mu$ s after the  
4676 trigger signal. In the third case, the maximum negative offset allowed is of 2048 clocks (12 bit) cor-  
4677 responding to 51.2  $\mu$ s, the match window being strictly smaller than the offset. In the case of GIF++,  
4678 the choice has been made to use this last setting by delaying the trigger signal. During the studies  
4679 performed in GIF++, both the efficiency of the RPCs, probed using a muon beam, and the noise or  
4680 gamma background rate are monitored. The extra search and reject margins are left unused.

4681 To probe the efficiency of RPC detectors, the trigger time tag is provided by the coïncidence of  
4682 scintillators when a bunch of muons passes through GIF++ area is used to trigger the data acquisi-  
4683 tion. For this measurement, it is useful to reduce the match window width only to contain the muon  
4684 information. Indeed, the delay in between a trigger signal and the detection of the corresponding  
4685 muon in the RPC being very contant (typically a few tens of ns due to jitter and cable length), the  
4686 muon signals are very localised in time. Thus, due to a delay of approximalety 325 ns in between  
4687 the muons and the trigger, the settings were chosen to have a window width of 24 clocks (600 ns)  
4688 centered on the muon peak thanks to a negative offset of 29 clocks (725 ns).

4689 On the otherhand, monitoring the rates don't require for the DAQ to look at a specific time window.  
4690 It is important to integrate enough time to have a robust measurement of the rate as the number of  
4691 hits per time unit. The triggering signal is provided by the pulse generator integrated into the com-  
4692 munication module V1718 at a frequency of 100 Hz to ensure that the data taking occurs in a random  
4693 way, uncorrelated with beam physics, to probe only the irradiation spectrum on the detectors. The  
4694 match window is set to 400 clocks (10  $\mu$ s) and the negative offset to 401 clocks as it needs to exceed  
4695 the value of the match window.

4696

4697 The v1190a object, defined in the DAQ software as in Source Code A.1, offers the possil-  
4698 ity to store all TDCs in the readout setup into a single object containing a list of hardware ad-  
4699 dresses (addresses to access the TDCs' buffer through the VME crate) and each constructor and  
4700 method acts on the list of TDCs to set the different acquisition parameters as describe above.  
4701 The type of trigger matching is chosen with `v1190a::SetTrigMatching()` and the time substrac-  
4702 tion, used to have a time measurement referring to the beggining of the time window, is set by  
4703 `v1190a::SetTrigTimeSubtraction()`. Then, the wiwdow width and offset are respectively set  
4704 thanks to `v1190a::SetTrigWindowWidth()` and `v1190a::SetTrigWindowOffset()`. The rejection  
4705 and extra search margin, even if left unused and hence set to a default value of 0, can be set through  
4706 `v1190a::SetTrigRejectionMargin()` and `v1190a::SetTrigSearchMargin()`. These methods are  
4707 then called in `v1190a::SetTrigConfiguration()` that uses the information contained in the config-  
4708 uration file `IniFile *inifile` to set the different TDC parameters. A thorough explaination of the  
4709 content of the configuration file is provided in Section A.5.2.

4710

4711 Among the other methods of class `v1190a` can be found a set of the detection mode (`v1190a::SetTDC`  
4712 `DetectionMode()`), of the TDC time resolution (`v1190a::SetTDCResolution()`), of the dead time  
4713 in between two consecutive signals recorded into a single channel (`v1190a::SetTDCDeadTime()`) or  
4714 of the maximal number of signals that can be recorded per event (`v1190a::SetTDCEventSize()`). To  
4715 help with setting these parameters, `enum` were used (`EdgeMode`, `Resolution`, `DeadTime` and `HitMax`  
4716 are defined in `include/v1190a.h`).

```

4717
class v1190a
{
    private :
        long             Handle;
        vector<Data32>   Address;
        CVDataWidth      DataWidth;
        CVAAddressModifier AddressModifier;

    public:

        v1190a(long handle, IniFile *inifile, int ntdcs);
        ~v1190a();
        Data16 write_op_reg(Data32 address, int code, string error);
        Data16 read_op_reg(Data32 address, string error);
        void Reset(int ntdcs);
        void Clear(int ntdcs);
        void TestWR(Data16 value,int ntdcs);
        void CheckTDCStatus(int ntdcs);
        void CheckCommunication(int ntdcs);
        void SetTDCTestMode(Data16 mode,int ntdcs);
        void SetTrigMatching(int ntdcs);
        void SetTrigTimeSubtraction(Data16 mode,int ntdcs);
        void SetTrigWindowWidth(Uint windowHeight,int ntdcs);
        void SetTrigWindowOffset(Uint windowOffset,int ntdcs);
        void SetTrigSearchMargin(Uint searchMargin,int ntdcs);
        void SetTrigRejectionMargin(Uint rejectMargin,int ntdcs);
        void GetTrigConfiguration(int ntdcs);
        void SetTrigConfiguration(IniFile *inifile,int ntdcs);
        void SetTDCDetectionMode(Data16 mode,int ntdcs);
        void SetTDCResolution(Data16 lsb,int ntdcs);
        void SetTDCDeadTime(Data16 time,int ntdcs);
        void SetTDCHeadTrailer(Data16 mode,int ntdcs);
        void SetTDCEventSize(Data16 size,int ntdcs);
        void SwitchChannels(IniFile *inifile,int ntdcs);
        void SetIRQ(Data32 level, Data32 count,int ntdcs);
        void SetBlockTransferMode(Data16 mode,int ntdcs);
        void Set(IniFile *inifile,int ntdcs);
        void CheckStatus(CVErrorCodes status) const;
        int ReadBlockD32(Uint tdc, const Data16 address,
                         Data32 *data, const Uint words, bool ignore_berr);
        Uint Read(RAWData *DataList,int ntdcs);
};

4718

```

4719       *Source Code A.1: Description of C++ object v1190a.*

4720       The detection mode corresponds to the type of edge detection the TDC will be using to  
 4721 record the data. The TDCs can record the time stamp of the leading edge alone, of the trailing edge  
 4722 alone, of both or they can operate in pair mode, meaning that the leading edge is recorded together  
 4723 with the time difference in between leading and trailing edges. This last mode is not very practical  
 4724 for the case of GIF++ measurements as the information is coded into a single words in the TDC's  
 4725 buffer, putting strong constraints on the time window and duration of the input signals. Indeed,  
 4726 when recording the edges individually (single edge or both edges), a 32-bit word, of which 18 are  
 4727 used to provide the time information alone, is stored into memory for each signal edge. With the  
 4728 pair mode, instead of having one 32-bit word per edge, only a single 32-bit word is written of which  
 4729 12 are used for the leading edge time information and 6 for the width of the pulse, as described on  
 4730 p73 of reference [268]. This way, even though the pair mode is convenient to use as it automatically

4731 correlates a leading edge with the corresponding signal width in a single word, it is advised to be  
 4732 careful when using it and to be aware of the extra time constraints (for both leading time and signal  
 4733 width) that will come for choosing this setting. If it is necessary to work with large input signals,  
 4734 the mode recording both edges will be preferred to the pair mode and the association of a leading  
 4735 and trailing edges pair will then be performed offline by the user. Then, the time resolution is to be  
 4736 chosen in a range from 100 to 800 ps, the dead time in a range from 5 to 100 ns, and the maximal  
 4737 number of hits per event in a range from 0 to 128 with the possibility to choose to have no limits.

#### 4738 A.4.2 DataReader

4739 Enabled thanks to `v1190a::SetBlockTransferMode()`, the data transfer is done via Block Transfer  
 4740 (BLT). Using BLT allows to transfer a fixed number of events called a *block*. This is used together  
 4741 with an Almost Full Level (AFL) of the TDCs' output buffers, defined through `v1190a::SetIRQ()`.  
 4742 This AFL gives the maximum amount of 32735 words (16 bits, corresponding to the depth of a TDC  
 4743 output buffer) that can be written in a buffer before an Interrupt Request (IRQ) is generated and seen by  
 4744 the VME Bridge V1718, which sends a `BUSY` signal intended to stopping the data acquisition during  
 4745 the transfer of the content of each TDC buffers before resuming. For each trigger, 6 words or more  
 4746 are written into the TDC buffer:

- 4747 • **a global header** providing information of the event number since the beginning of the data  
 4748 acquisition,
- 4749 • **a TDC header** which is enabled thanks to `v1190a::SetTDCHeadTrailer()`,
- 4750 • **the TDC data (if any)**, 1 for each hit recorded during the event, providing the channel and the  
 4751 time stamp associated to the hit,
- 4752 • **a TDC error** providing error flags,
- 4753 • **a TDC trailer** which is enabled thanks to `v1190a::SetTDCHeadTrailer()`,
- 4754 • **a global trigger time tag** that provides the absolute trigger time relatively to the last reset,  
 4755 and
- 4756 • **a global trailer** providing the total word count in the event.

4757 CMS RPC FEEs provide with 100 ns long LVDS output signals that are injected into the TDCs'  
 4758 input. Any avalanche signal that gives a signal above the FEEs threshold is thus recorded by the  
 4759 TDCs as a hit within the match window. Each hit is assigned to a specific TDC channel with a time  
 4760 stamp, with a precision of 100 ps. The reference time,  $t_0 = 0$ , is provided by the beginning of the  
 4761 match window. Thus for each trigger, coming from a scintillator coincidence or the pulse generator,  
 4762 a list of hits is stored into the TDCs' buffers and will then be transferred into a ROOT Tree.  
 4763 When the BLT is used, it is easy to understand that the maximum number of words that have been set  
 4764 as AFL will not be a finite number of events or, at least, the number of events that would be recorded  
 4765 into the TDC buffers will not be a multiple of the block size. In the last BLT cycle to transfer data,  
 4766 the number of events to transfer will most probably be lower than the block size. In that case, the  
 4767 TDC can add fillers at the end of the block but this option requires to send more data to the computer  
 4768 and is thus a little slower. Another solution is to finish the transfer after the last event by sending a  
 4769 bus error that states that the BLT reached the last event in the pile. This method has been chosen in

4770   GIF++.

4771   Due to irradiation, an event in GIF++ can count up to 300 words per TDC. A limit of 4096 words  
 4772   (12 bits) has been set to generate IRQ which represent from 14 to almost 700 events depending on  
 4773   the average of hits collected per event. Then the block size has been set to 100 events with enabled  
 4774   bus errors. When an AFL is reached for one of the TDCs, the VME bridge stops the acquisition by  
 4775   sending a BUSY signal.

4776

4777   The data is then transferred one TDC at a time into a structure called `RAWData` (Source Code A.2).  
 4778   Note that the structure as presented here is used when a single edge detection is used as there is only  
 4779   one time stamp list associated to the hits. When using detection on both edges, a second time stamp  
 4780   list could be added and when using pair detection, a list with the signal width could be added instead.

4781

```
4782   struct RAWData {
    vector<int>                         *EventList;
    vector<int>                         *NHitsList;
    vector<int>                         *QFlagList;
    vector<vector<int> >         *ChannelList;
    vector<vector<float> >        *TimeStampList;
};
```

4783

*Source Code A.2: Description of data holding C++ structure `RAWData`.*

```
4784   class DataReader
{  

    private:  

        bool              StopFlag;  

        IniFile *iniFile;  

        Data32          MaxTriggers;  

        v1718            *VME;  

        int              nTDCs;  

        v1190a           *TDCs;  

        RAWData          TDCData;  

    public:  

        DataReader();  

        virtual ~DataReader();  

        void            SetIniFile(string inifilename);  

        void            SetMaxTriggers();  

        Data32           GetMaxTriggers();  

        void            SetVME();  

        void            SetTDC();  

        int             GetQFlag(Uint it);  

        void            Init(string inifilename);  

        void            FlushBuffer();  

        void            Update();  

        string          GetFileName();  

        void            WriteRunRegistry(string filename);  

        void            Run();  

};
```

4785

*Source Code A.3: Description of C++ object `DataReader`.*

4786

4787   In order to organize the data transfer and the data storage, an object called `DataReader` was  
 4788   created (Source Code A.3). On one hand, it has `v1718` and `v1190a` objects as private members for  
 communication purposes, such as VME modules settings via the configuration file `*iniFile` or data

4789 read-out through `v1190a::Read()` and on the other hand, it contains the structure `RAWData` that allows  
 4790 to organise the data in vectors reproducing the tree structure of a ROOT file.  
 4791 Each event is transferred from `TDCData` and saved into branches of a ROOT `TTree` as 3 integers  
 4792 that represent the event ID (`EventCount`), the number of hits read from the TDCs (`nHits`), and the  
 4793 quality flag that provides information for any problem in the data transfer (`qflag`), and 2 lists of  
 4794 *nHits* elements containing the fired TDC channels (`TDCCh`) and their respective time stamps (`TDCTS`),  
 4795 as presented in Source Code A.4. The ROOT file file is named using information contained into  
 4796 the configuration file, presented in section A.5.2. The needed information is extracted using method  
 4797 `DataReader::GetFileName()` and allow to build the output filename format `ScanXXXXXX_HVX_DAQ.root`  
 4798 where `ScanXXXXXX` is a 6 digit number representing the scan number into GIF++ database and `HVX`  
 4799 the HV step within the scan that can be more than a single digit. An example of ROOT data file is  
 4800 provided with Figure A.3.

```
4801
4802     RAWData TDCData;
4803     TFile *outputFile = new TFile(outputFileName.c_str(), "recreate");
4804     TTree *RAWDataTree = new TTree("RAWData", "RAWData");

4805     int          EventCount = -9;
4806     int          nHits    = -8;
4807     int          qflag    = -7;
4808     vector<int>  TDCCh;
4809     vector<float> TDCTS;

4810     RAWDataTree->Branch("EventNumber", &EventCount, "EventNumber/I");
4811     RAWDataTree->Branch("number_of_hits", &nHits, "number_of_hits/I");
4812     RAWDataTree->Branch("Quality_flag", &qflag, "Quality_flag/I");
4813     RAWDataTree->Branch("TDC_channel", &TDCCh);
4814     RAWDataTree->Branch("TDC_TimeStamp", &TDCTS);

4815     //...
4816     //Here read the TDC data using v1190a::Read() and place it into
4817     //TDCData for as long as you didn't collect the requested amount
4818     //of data.
4819     //...
4820
4821     for(Uint i=0; i<TDCData.EventList->size(); i++) {
4822         EventCount = TDCData.EventList->at(i);
4823         nHits    = TDCData.NHitsList->at(i);
4824         qflag    = TDCData.QFlagList->at(i);
4825         TDCCh   = TDCData.ChannelList->at(i);
4826         TDCTS   = TDCData.TimeStampList->at(i);
4827         RAWDataTree->Fill();
4828     }

```

4803     *Source Code A.4: Highlight of the data transfer and organisation within `DataReader::Run()` after the data  
 has been collected into `TDCData`.*

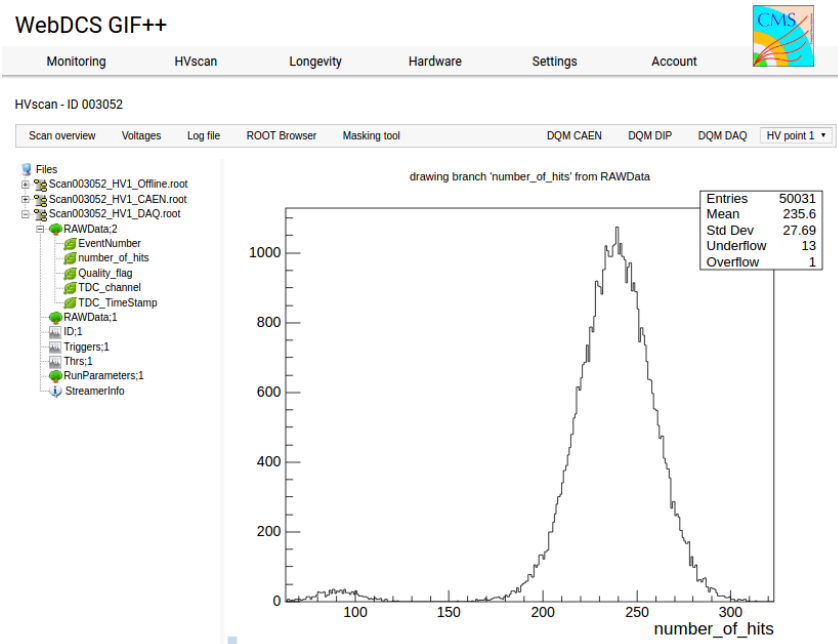


*Figure A.3: Structure of the ROOT output file generated by the DAQ. The 5 branches (EventNumber, number\_of\_hits, Quality\_flag, TDC\_channel and TDC\_TimeStamp) are visible on the left panel of the ROOT browser. On the right panel is visible the histogram corresponding to the variable nHits. In this specific example, there were approximately 50k events recorded to measure the gamma irradiation rate on the detectors. Each event is stored as a single entry in the TTree.*

#### 4804    A.4.3 Data quality flag

4805    Among the parameters that are recorded for each event, the quality flag is determined on the fly  
 4806    by checking the data recorded by every single TDC. An `enum` called `QualityFlag` was written to  
 4807    associate the key `GOOD` to the integer 1 and `CORRUPTED` to 0. From method `v1190a::Read()`, it can  
 4808    be understood that the content of each TDC buffer is readout one TDC at a time. Entries are created  
 4809    in the data list for the first TDC and then, when the second buffer is readout, events corresponding  
 4810    to entries that have already been created to store data for the previous TDC are added to the existing  
 4811    list element. On the contrary, when an event entry has not been yet created in the data list, a new  
 4812    entry is created.

4813    It is possible that each TDC buffer contains a different number of events. In cases where the first  
 4814    element in the buffer list is an event for corresponds to a new entry, the difference in between the  
 4815    entry from the buffer and the last entry in the data list is recorded and checked. If it is greater than 1,  
 4816    what should never be the case, the quality flag is set to `CORRUPTED` for this TDC and an empty entry  
 4817    is created in the place of the missing ones. Missing entries are believe to be the result of a bad hold  
 4818    on the TDC buffers at the moment of the readout. Indeed, the software hold is effective only on 1  
 4819    TDC at a time and no solution as been found yet to completely block the writting in the buffers when  
 4820    an IRQ is received.

4821    At the end of each BLT cycle, the ID of the last entry stored for each TDC buffer is not recorded.  
 4822    When starting the next cycle, if the first entry in the pile corresponds to an event already existing  
 4823    in the list, the readout will start from this list element and will not be able to check the difference

4824 in between this entry's ID and the one of the last entry that was recorded for this TDC buffer in  
 4825 the previous cycle. In the case events were missing, the flag stays at its initial value of 0, which is  
 4826 similar to CORRUPTED and it is assumed that then this TDC will not contribute to number\_of\_hits,  
 4827 TDC\_channel or TDC\_TimeStamp. Finally, since there will be 1 RAWData entry per TDC for each event  
 4828 (meaning nTDCs entries, referring to DataReader private attribute), the individual flags of each TDC  
 4829 will be added together. The final format is an integer composed nTDCs digits where each digit is the  
 4830 flag of a specific TDC. This is constructed using powers of 10 like follows:

4831        TDC 0: QFlag =  $10^0 \times \text{QualityFlag}$

4832        TDC 1: QFlag =  $10^1 \times \text{QualityFlag}$

4833        ...

4834        TDC N: QFlag =  $10^N \times \text{QualityFlag}$

4835        and the final flag to be with N digits:

4836        QFlag = n....3210

4837        each digit being 1 or 0. Below is given an example with a 4 TDCs setup.

4838        If all TDCs were good : QFlag = 1111,

4839        but if TDC 2 was corrupted : QFlag = 1011.

4840        When data taking is over and the data contained in the dynamical RAWData structure is transferred  
 4841 to the ROOT file, all the 0s are changed into 2s by calling the method DataReader::GetQFlag().  
 4842 This will help translating the flag without knowing the number of TDCs beforehand. Indeed, a flag  
 4843 111 could be due to a 3 TDC setup with 3 good individual TDC flags or to a more than 3 TDC setup  
 4844 with TDCs those ID is greater than 2 being CORRUPTED, thus giving a 0.

4845        The quality flag has been introduced quite late, in October 2017 only, to the list of GIFT++ DAQ  
 4846 parameters to be recorded into the output ROOT file. Before this addition, the missing data, corrupting  
 4847 the quality for the offline analysis, was contributing to artificially fill data with lower multiplicity.  
 4848 Looking at TBranch number\_of\_hits provides an information about the data of the full GIFT++  
 4849 setup. When a TDC is not able to transfer data for a specific event, the effect is a reduction of the  
 4850 total number of hits recorded in the full setup, this is what can be seen from Figure A.4. After offline  
 4851 reconstruction detector by detector, the effect of missing events can be seen in the artificially filled  
 4852 bin at multiplicity 0 shown in Figure A.5. Nonetheless, for data with high irradiation levels, as it is  
 4853 the case for Figure A.5a, discarding the fake multiplicity 0 data can be done easily during the offline  
 4854 analysis. At lower radiation, the missing events contribution becomes more problematic as the mul-  
 4855 tiplicity distribution overlaps the multiplicity 0 and that in the same time the proportion of missing  
 4856 events decreases. Attempts to fit the distribution with a Poisson or skew distribution function were  
 4857 not conclusive and this very problem has been at the origin of the quality flag that allows to give a  
 4858 non ambiguous information about each event quality.

4859

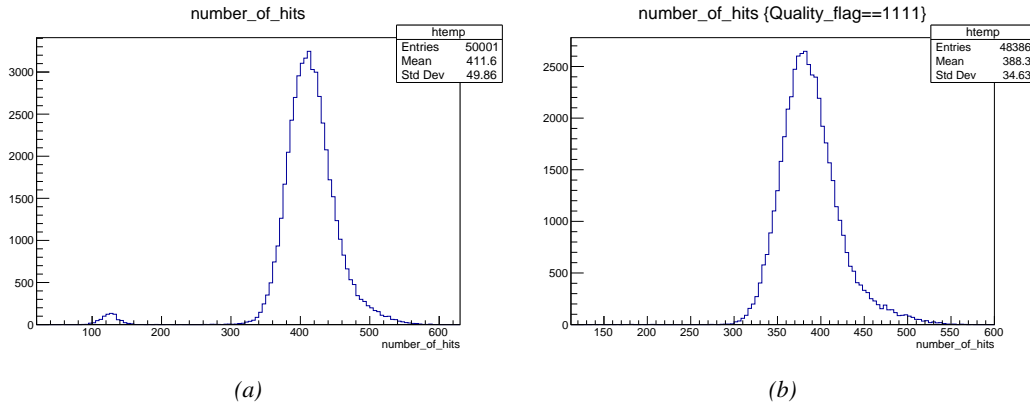


*Figure A.4: The effect of the quality flag is explained by presenting the content of TBranch `number_of_hits` of a data file without `Quality_flag` in Figure A.4a and the content of the same TBranch for data corresponding to a `Quality_flag` where all TDCs were labelled as `GOOD` in Figure A.4b taken with similar conditions. It can be noted that the number of entries in Figure A.4b is slightly lower than in Figure A.4a due to the excluded events.*

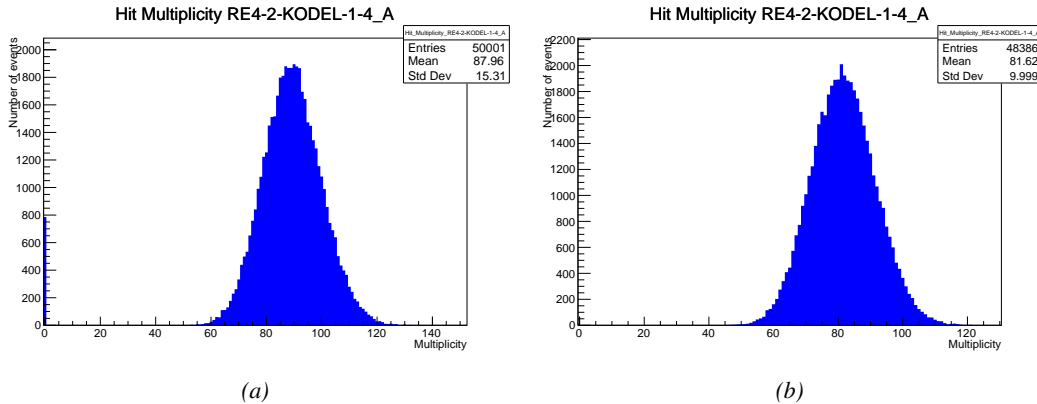


*Figure A.5: Using the same data as previously showed in Figure A.4, the effect of the quality flag is explained by presenting the reconstructed hit multiplicity of a data file without `Quality_flag` in Figure A.5a and the reconstructed content of the same RPC partition for data corresponding to a `Quality_flag` where all TDCs were labelled as `GOOD` in Figure A.5b taken with similar conditions. The artificial high content of bin 0 is completely suppressed.*

## 4860 A.5 Communications

4861 To ensure data readout and dialog in between the machine and the TDCs or in between the webDCS  
 4862 and the DAQ, different communication solutions were used. First of all, it is important to have a  
 4863 module to allow the communication in between the TDCs and the computer from which the DAQ  
 4864 operates. When this communication is effective, shifters using the webDCS to control data taking  
 4865 can thus send instructions to the DAQ.

4866

<sup>4867</sup> **A.5.1 V1718 USB Bridge**

<sup>4868</sup> In the previous section, the data transfer as been discussed. The importance of the `v1718` object  
<sup>4869</sup> (Source Code A.5), used as private member of `DataReader`, was not explicited. VME master  
<sup>4870</sup> modules are used for communication purposes as they host the USB port that connects the pow-  
<sup>4871</sup> ered crate buffer to the computer were the DAQ is installed. From the source code point of view,  
<sup>4872</sup> this object is used to control the communication status, by reading the returned error codes with  
<sup>4873</sup> `v1718::CheckStatus()`, or to check for IRQs coming from the TDCs through `v1718::CheckIRQ()`.  
<sup>4874</sup> To ensure that triggers are blocked at the hardware level, a NIM pulse is sent out of one of the two  
<sup>4875</sup> first programmable outputs of the module (`v1718::SendBUSY()`) to the VETO of the coïndidence  
<sup>4876</sup> module where the trigger signals originate. As long as this signal is ON, no trigger can reach the  
<sup>4877</sup> TDCs anymore. Finally, used in the case of noise and background measurements in which the trig-  
<sup>4878</sup> ger needs not to be provided by the muon beam but by an uncorrelated source, a pulse generator  
<sup>4879</sup> is enabled with `v1718::RDMTriggerPulse()`. The "random" pulse is sent through the third and  
<sup>4880</sup> fourth outputs of the module. Both the BUSY signal and the random pulse are shaped in the method  
<sup>4881</sup> `v1718::SetPulsers()` where the number of pulses to be generated, their width, as well as the period  
<sup>4882</sup> of the pulse generator is defined.

<sup>4883</sup>

```
class v1718{
    private:
        int Handle;
        Data32 Data;           // Data
        CVIRQLevels Level;     // Interrupt level
        CVAddressModifier AM;   // Addressing Mode
        CVDataWidth dataSize;  // Data Format
        Data32 BaseAddress;    // Base Address

    public:
        v1718(IniFile *inifile);
        ~v1718();
        long GetHandle(void) const;
        int SetData(Data16 data);
4884        Data16 GetData(void);
        int SetLevel(CVIRQLevels level);
        CVIRQLevels GetLevel(void);
        int SetAM(CVAddressModifier am);
        CVAddressModifier GetAM(void);
        int SetDataSize(CVDataWidth datasize);
        CVDataWidth GetDataSize(void);
        int SetBaseAddress(Data16 baseaddress);
        Data16 GetBaseAddress(void);
        void CheckStatus(CVErrorCodes status) const;
        bool CheckIRQ();
        void SetPulsers(UINT RDM_Frequency);
        void SendBUSY(PulserLevel level);
        void RDMTriggerPulse(PulserLevel level);
};
```

<sup>4885</sup>

*Source Code A.5: Description of C++ object v1718.*

## 4886 A.5.2 Configuration file

4887 The DAQ software takes as input a configuration file written using INI standard [287]. This file is  
 4888 partly filled with the information provided by the shifters when starting data acquisition using the  
 4889 webDCS, as shown by Figure A.6. This information is written in section **[General]** and will later  
 4890 be stored in the ROOT file that contains the DAQ data as can be seen from Figure A.3. Indeed,  
 4891 another `TTree` called `RunParameters` as well as the 2 histograms `ID`, containing the scan number,  
 4892 start and stop time stamps, and `Triggers`, containing the number of triggers requested by the shifter,  
 4893 are available in the data files. Moreover, `ScanID` and `HV` are then used to construct the file name  
 4894 thanks to the method `DataReader::GetFileName()`.

Chamber	RE2-2-NPD-BARC-8	RE4-2-CERN-105	RE2-2-NPD-BARC-9	RE4-2-CERN-105	RE4-2-KODEL-1-4	Max triggers
HV <sub>eff</sub> 1	8600	8500	8600	8500	6500	
HV <sub>eff</sub> 2	8700	8600	8700	8600	6600	
HV <sub>eff</sub> 3	8800	8700	8800	8700	6700	
HV <sub>eff</sub> 4	8900	8800	8900	8800	6800	
HV <sub>eff</sub> 5	9000	8900	9000	8900	6900	
HV <sub>eff</sub> 6	9100	9000	9100	9000	7000	
HV <sub>eff</sub> 7	9200	9100	9200	9100	7100	
HV <sub>eff</sub> 8	9300	9200	9300	9200	7200	
HV <sub>eff</sub> 9	9400	9300	9400	9300	7300	
HV <sub>eff</sub> 10	9500	9400	9500	9400	7400	

Figure A.6: WebDCS DAQ scan page. On this page, shifters need to choose the type of scan (Rate, Efficiency or Noise Reference scan), the gamma source configuration at the moment of data taking, the beam configuration, and the trigger mode. These information will be stored in the DAQ ROOT output. Are also given the minimal measurement time and waiting time after ramping up of the detectors is over before starting the data acquisition. Then, the list of HV points to scan and the number of triggers for each run of the scan are given in the table underneath.

4895 The rest of the information is written beforehand in the configuration file template, as explicated  
 4896 in Source Code A.6, and contains the hardware addresses to the different VME modules in the  
 4897 setup as well as settings for the TDCs. As the TDC settings available in the configuration file are not  
 4898 supposed to be modified, an improvement would be to remove them from the configuration file and  
 4899 to hardcode them inside of the DAQ code itself or to place them into a different INI file that would  
 4900 host only the TDC settings to lower the probability for a bad manipulation of the configuration file  
 4901 that can be modified from one of webDCS' menus.

```

4902
[General]
TdcS=4
ScanID=$scanid
HV=$HV
RunType=$runtype
MaxTriggers=$maxtriggers
Beam=$beam
[VMEInterface]
Type=V1718
BaseAddress=0xFF0000
Name=VmeInterface
int_trig_freq=100
[TDC0]
Type=V1190A
BaseAddress=0x00000000
Name=Tdc0
StatusA00-15=1
StatusA16-31=1
StatusB00-15=1
StatusB16-31=1
StatusC00-15=1
StatusC16-31=1
StatusD00-15=1
StatusD16-31=1
[TDC1]
Type=V1190A
BaseAddress=0x11110000
Name=Tdc1
StatusA00-15=1
StatusA16-31=1
StatusB00-15=1
StatusB16-31=1
StatusC00-15=1
StatusC16-31=1
StatusD00-15=1
StatusD16-31=1
4903
[TDC2]
Type=V1190A
BaseAddress=0x22220000
Name=Tdc2
StatusA00-15=1
StatusA16-31=1
StatusB00-15=1
StatusB16-31=1
StatusC00-15=1
StatusC16-31=1
StatusD00-15=1
StatusD16-31=1
[TDC3]
Type=V1190A
BaseAddress=0x44440000
Name=Tdc3
StatusA00-15=1
StatusA16-31=1
StatusB00-15=1
StatusB16-31=1
StatusC00-15=1
StatusC16-31=1
StatusD00-15=1
StatusD16-31=1
[TDCSettings]
TriggerExtraSearchMargin=0
TriggerRejectMargin=0
TriggerTimeSubtraction=0b1
TdcDetectionMode=0b01
TdcResolution=0b10
TdcDeadTime=0b00
TdcHeadTrailer=0b1
TdcEventSize=0b1001
TdcTestMode=0b0
BLTMode=1

```

*Source Code A.6: INI configuration file template for 4 TDCs. In section [General], the number of TDCs is explicitated and information about the ongoing run is given. Then, there are sections for each and every VME modules. There buffer addresses are given and for the TDCs, the list of channels to enable is given. Finally, in section [TDCSettings], a part of the TDC settings are given.*

4904

```

typedef map< const string, string > IniFileData;

class IniFile{
    private:
        bool          CheckIfComment(string line);
        bool          CheckIfGroup(string line, string& group);
        bool          CheckIfToken(string line, string& key, string& value);
        string         FileName;
        IniFileData   FileData;
        int           Error;

    public:
        IniFile();
        IniFile(string filename);
        virtual      ~IniFile();

    // Basic file operations
    void          SetFileName(string filename);
    int           Read();
    int           Write();
    IniFileData   GetFileData();

    // Data readout methods
    Data32 addressType(string groupname, string keyname, Data32 defaultvalue);
    long          intType(string groupname, string keyname, long defaultvalue);
    long long    longType(string groupname, string keyname, long long
    ↵ defaultvalue);
    string         stringType(string groupname, string keyname, string defaultvalue);
    float         floatType(string groupname, string keyname, float defaultvalue);

    // Error methods
    string         GetErrorMsg();
};

4905

```

4906

*Source Code A.7: Description of C++ object IniFile used as a parser for INI file format.*

4907

In order to retrieve the information of the configuration file, the object `IniFile` has been developed to provide an INI parser, presented in Source Code A.7. It contains private methods returning a boolean to check the type of line written in the file, whether a comment, a group header or a key line (`IniFile::CheckIfComment()`, `IniFile::CheckIfGroup()` and `IniFile::CheckIfToken()`). The key may sometimes be referred to as *token* in the source code. Moreover, the private element `FileData` is a map of `const` string to string that allows to store the data contained inside the configuration file via the public method `IniFile::GetFileData()` following the formatting (see method `IniFile::Read()`):

4908

4909

4910

4911

4912

4913

4914

4915

4916

```

    string group, token, value;
    // Get the field values for the 3 strings.
    // Then concatenate group and token together as a single string
    // with a dot separation.
    token = group + "." + token;
    FileData[token] = value;

```

4917 More methods have been written to translate the different keys into the right variable format  
 4918 when used by the DAQ. For example, to get a **float** value out of the configuration file data, knowing  
 4919 the group and the key needed, the method `IniFile::floatType()` can be used. It takes 3 arguments  
 4920 being the group name and key name (both `string`), and a default **float** value used as exception in  
 4921 the case the expected combination of group and key cannot be found in the configuration file. This  
 4922 default value is then used and the DAQ continues on working after sending an alert in the log file for  
 4923 further debugging.

4924

### 4925 A.5.3 WebDCS/DAQ intercommunication

4926 When shifters send instructions to the DAQ via the configuration file, it is the webDCS itself that  
 4927 gives the start command to the DAQ and then the 2 softwares use inter-process communication  
 4928 through file to synchronise themselves. This communication file is represented by the variable `const`  
 4929 `string __runstatuspath`.

4930 On one side, the webDCS sends commands or status that are readout by the DAQ:

- 4931 • INIT, status sent when launching a scan and read via function `CtrlRunStatus(...)`,
- 4932 • START, command to start data taking and read via function `CheckSTART()`,
- 4933 • STOP, command to stop data taking at the end of the scan and read via function `CheckSTOP()`,  
and
- 4935 • KILL, command to kill data taking sent by user and read via function `CheckKILL()`. Note that  
4936 the DAQ doesn't stop before the current ROOT file is safely written and saved.

4937 and on the other, the DAQ sends status that are controled by the webDCS:

- 4938 • DAQ\_RDY, sent with `SendDAQReady()` to signify that the DAQ is ready to receive commands  
4939 from the webDCS,
- 4940 • RUNNING, sent with `SendDAQRunning()` to signify that the DAQ is taking data,
- 4941 • DAQ\_ERR, sent with `SendDAQError()` to signify that the DAQ didn't receive the expected com-  
4942 mand from the webDCS or that the launch command didn't have the right number of argu-  
4943 ments,
- 4944 • RD\_ERR, sent when the DAQ wasn't able to read the communication file, and
- 4945 • WR\_ERR, sent when the DAQ wasn't able to write into the communication file.

### 4946 A.5.4 Example of inter-process communication cycle

4947 Under normal conditions, the webDCS and the DAQ processes exchange commands and status via  
 4948 the file hosted at the address `__runstatuspath`, as explained in subsection A.5.3. An example of  
 4949 cycle is given in Table A.1. In this example, the steps 3 to 5 are repeated as long as the webDCS tells  
 4950 the DAQ to take data. A data taking cycle is the equivalent as what is called a *Scan* in GIFT++ jargon,

4951 referring to a set a runs with several HV steps. Each repetition of steps 3 to 5 is then equivalent to a  
 4952 single *Run*.

4953 At any moment during the data taking, for any reason, the shifter can decide that the data taking  
 4954 needs to be stopped before it reached the end of the scheduled cycle. Thus at any moment on the  
 4955 cycle, the content of the inter-process communication file will be changed to `KILL` and the DAQ will  
 4956 shut down right away. The DAQ checks for `KILL` signals every 5s after the TDCs configuration is  
 4957 over. So far, the function `CheckKILL()` has been used only inside of the data taking loop of method  
 4958 `DataReader::Run()` and thus, if the shifter decides to KILL the data taking during the TDC con-  
 4959 figuration phase or the HV ramping in between 2 HV steps, the DAQ will not be stopped smoothly  
 4960 and a *force kill* command will be sent to stop the DAQ process that is still awake on the computer.  
 4961 Improvements can be brought on this part of the software to make sure that the DAQ can safely  
 4962 shutdown at any moment.

4963

step	actions of webDCS	status of DAQ	<code>__runstatuspath</code>
1	launch DAQ ramp voltages ramping over wait for currents stabilization	readout of IniFile configuration of TDCs	INIT
2		configuration done send DAQ ready wait for <code>START</code> signal	DAQ_RDY
3	waiting time over send <code>START</code>		START
4	wait for run to end monitor DAQ run status	data taking ongoing check for <code>KILL</code> signal	RUNNING
5		run over send <code>DAQ_RDY</code> wait for next DCS signal	DAQ_RDY
6	ramp voltages ramping over wait for currents stabilization		DAQ_RDY
3	waiting time over send <code>START</code>		START
4	wait for run to end monitor DAQ run status	update IniFile information data taking ongoing check for <code>KILL</code> signal	RUNNING
5		run over send <code>DAQ_RDY</code> wait for next DCS signal	DAQ_RDY
7	send command <code>STOP</code>	DAQ shuts down	STOP

Table A.1: Inter-process communication cycles in between the webDCS and the DAQ through file string signals.

## A.6 Software export

4964 In section A.2 was discussed the fact that the DAQ as written in its last version is not a standalone  
 4965 software. It is possible to make it a standalone program that could be adapted to any VME setup

4967 using V1190A and V1718 modules by creating a GUI for the software or by printing the log messages  
4968 that are normally printed in the webDCS through the log file, directly into the terminal. This  
4969 method was used by the DAQ up to version 3.0 moment where the webDCS was completed. Also, it  
4970 is possible to check branches of DAQ v2.X to have example of communication through a terminal.

4971 DAQ v2.X is nonetheless limited in its possibilities and requires a lot of offline manual interventions  
4972 from the users. Indeed, there is no communication of the software with the detectors' power  
4973 supply system that would allow for a user a predefine a list of voltages to operate the detectors at  
4974 and loop over to take data without any further manual intervention. In v2.X, the data is taken for a  
4975 single detector setting and at the end of each run, the softwares asks the user if he intends on taking  
4976 more runs. If so, the software invites the user to set the operating voltages accordingly to what is  
4977 necessary and to manual update the configuration file in consequence. This working mode can be a  
4978 very first approach before an evolution and has been successfully used by colleagues from different  
4979 collaborations.

4980 For a more robust operation, it is recommended to develop a GUI or a web application to interface  
4981 the DAQ. Moreover, to limit the amount of manual interventions, and thus the probability to make  
4982 mistakes, it is also recommended to add an extra feature into the DAQ by installing the HV Wrapper  
4983 library provided by CAEN of which an example of use in a similar DAQ software developped by a  
4984 master student of UGent, and called TinyDAQ, is provided on UGent's github. Then, this HV Wrapper  
4985 will help you communicating with and give instructions to a CAEN HV powered crate and can  
4986 be added into the DAQ at the same level where the communication with the user was made in DAQ  
4987 v2.X. In case you are using another kind of power system for your detectors, it is stringly adviced to  
4988 use HV modules or crates that can be remotely controloled via a using C++ libraries.

4989



# B

4990

4991

## Details on the offline analysis package

4992 The data collected in GIF++ thanks to the DAQ described in Appendix A is difficult to interpret by  
4993 a human user that doesn't have a clear idea of the raw data architecture of the ROOT data files. In  
4994 order to render the data human readable, a C++ offline analysis tool was designed to provide users  
4995 with detector by detector histograms that give a clear overview of the parameters monitored during  
4996 the data acquisition [278]. In this appendix, details about this software in the context of GIF++, as  
4997 of how the software was written and how it functions will be given.

### 4998 B.1 GIF++ Offline Analysis file tree

4999 GIF++ Offline Analysis source code is fully available on github at [https://github.com/aafagot/GIF\\_OfflineAnalysis](https://github.com/aafagot/GIF_OfflineAnalysis). The software requires ROOT as non-optionnal dependency  
5000 as it takes ROOT files in input and write an output ROOT file containing histograms. To compile the  
5001 GIF++ Offline Analysis project is compiled with cmake. To compile, first a build/ directory must  
5002 be created to compile from there:  
5003

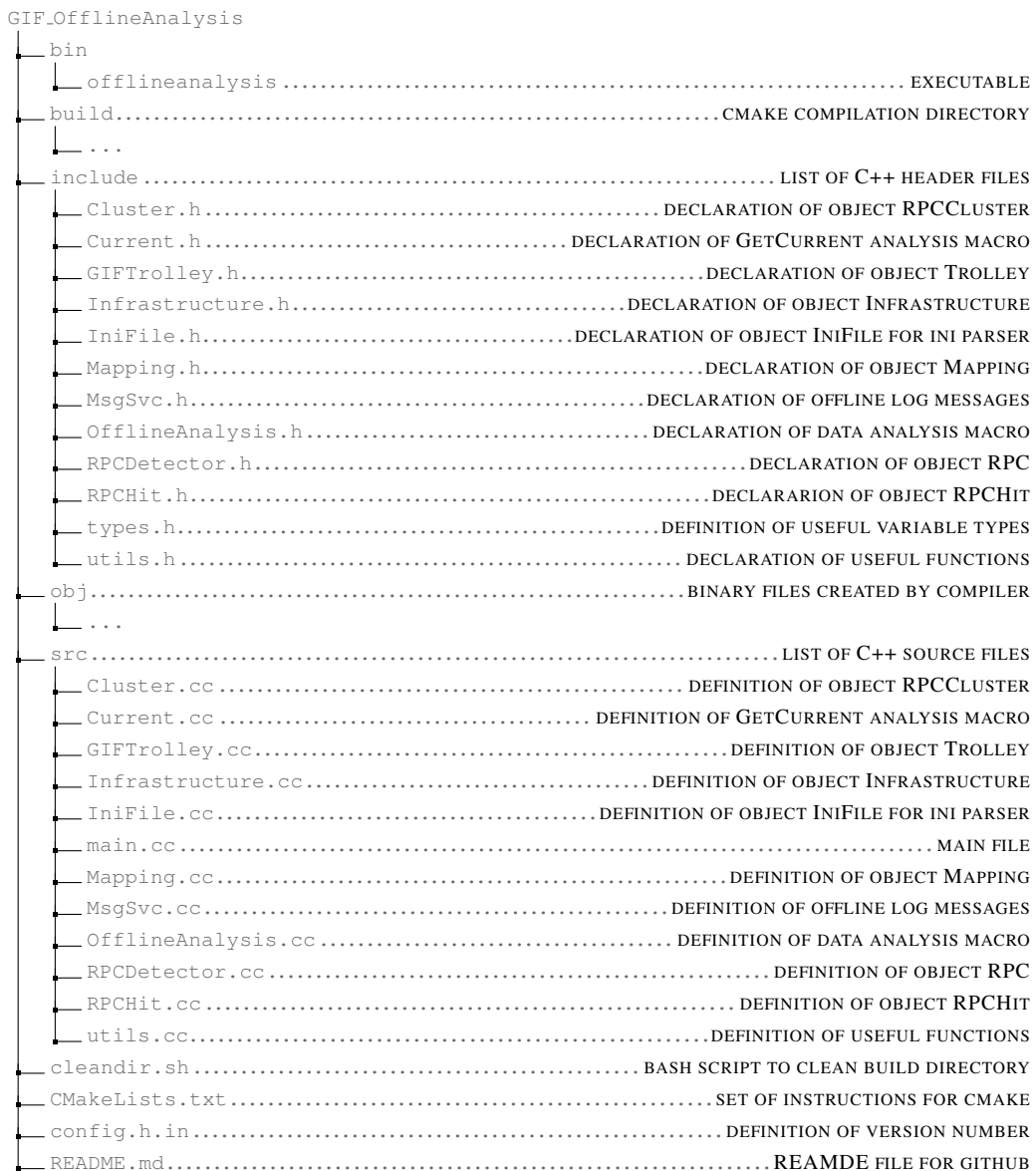
```
5004 mkdir build
5005 cd build
5006 cmake ..
5007 make
5008 make install
```

5006 To clean the directory and create a new build directory, the bash script cleandir.sh can be used:

```
5007
5008 ./cleandir.sh
```

5009 The source code tree is provided below along with comments to give an overview of the files' con-  
5010 tent. The different objects created for this project (`Infrastructure`, `Trolley`, `RPC`, `Mapping`, `RPCHit`,  
5011 `RPCCluster` and `Inifile`) will be described in details in the following sections.

5012



5013

## B.2 Usage of the Offline Analysis

5014

In order to use the Offline Analysis tool, it is necessary to know the Scan number and the HV Step of the run that needs to be analysed. This information needs to be written in the following format:

5016

5017

```
Scan00XXXX_HVY
```

5018

where XXXX is the scan ID and Y is the high voltage step (in case of a high voltage scan, data will be taken for several HV steps). This format corresponds to the base name of data files in the database

5019

5020 of the Gif++ webDCS. Usually, the offline analysis tool is automatically called by the webDCS at  
 5021 the end of data taking or by a user from the webDCS panel if an update of the tool was brought.  
 5022 Nonetheless, an expert can locally launch the analysis for tests on the Gif++ computer, or a user can  
 5023 get the code on its local machine from github and download data from the webDCS for its own anal-  
 5024 ysis. To launch the code, the following command can be used from the `GIF_OfflineAnalysis` folder:

5025

```
5026 bin/offlineanalysis /path/to/Scan00XXXX_HVY
```

5027 where, `/path/to/Scan00XXXX_HVY` refers to the local data files. Then, the offline tool will by itself  
 5028 take care of finding all available ROOT data files present in the folder, as listed below:

5029

- `Scan00XXXX_HVY_DAQ.root` containing the TDC data as described in Appendix A.4.2 (events,  
 hit and timestamp lists), and
- `Scan00XXXX_HVY_CAEN.root` containing the CAEN mainframe data recorded by the monitor-  
 ing tool webDCS during data taking (HVs and currents of every HV channels). This file is  
 created independently of the DAQ.

5034

## B.2.1 Output of the offline tool

5035

### B.2.1.1 ROOT file

5036

The analysis gives output ROOT datafiles that are saved into the data folder and called using the  
 5037 naming convention `Scan00XXXX_HVY_Offline.root`. Inside those, a list of `TH1` histograms can be  
 5038 found. Its size will vary as a function of the number of detectors in the setup as each set of histograms  
 5039 is produced detector by detector. For each partition of each chamber, can be found:

5040

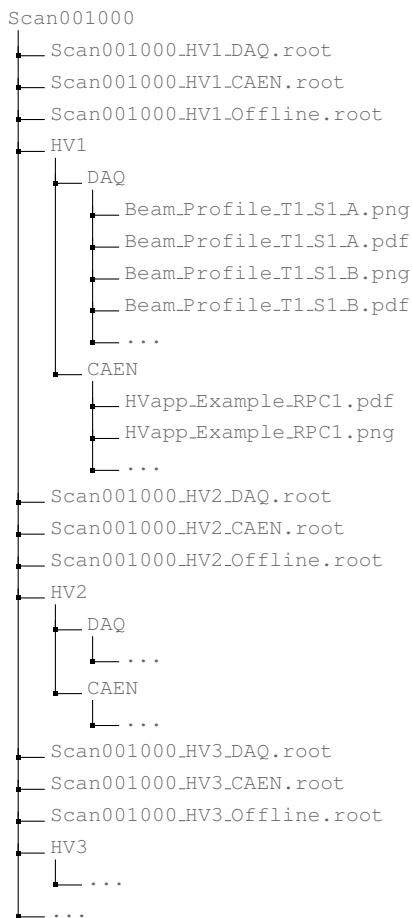
- `Time_Profile_Tt_Sc_p` shows the time profile of all recorded events (number of events per  
 time bin),
- `Hit_Profile_Tt_Sc_p` shows the hit profile of all recorded events (number of events per chan-  
 nel),
- `Hit_Multiplicity_Tt_Sc_p` shows the hit multiplicity (number of hits per event) of all recorded  
 events (number of occurrences per multiplicity bin),
- `Time_vs_Strip_Profile_Tt_Sc_p` shows the 2D time vs strip profile of all recorded events  
 (number of events per time bin per strip),
- `Strip_Mean_Noise_Tt_Sc_p` shows noise/gamma rate per unit area for each strip in a se-  
 lected time range. After filters are applied on `Time_Profile_Tt_Sc_p`, the filtered version  
 of `Hit_Profile_Tt_Sc_p` is normalised to the total integrated time and active detection area  
 of a single channel,
- `Strip_Activity_Tt_Sc_p` shows noise/gamma activity for each strip (normalised version of  
 previous histogram - strip activity = strip rate / average partition rate),
- `Strip_Homogeneity_Tt_Sc_p` shows the *homogeneity* of a given partition (homogeneity =  
 $\exp(-\text{strip rates standard deviation}(\text{strip rates in partition}/\text{average partition rate}))$ ),

- 5056     ● `mask_Strip_Mean_Noise_Tt_Sc_p` shows noise/gamma rate per unit area for each masked  
 5057       strip in a selected time range. Offline, the user can control the noise/gamma rate and decide to  
 5058       mask the strips that are judged to be noisy or dead. This is done via the *Masking Tool* provided  
 5059       by the webDCS,
- 5060     ● `mask_Strip_Activity_Tt_Sc_p` shows noise/gamma activity per unit area for each masked  
 5061       strip with respect to the average rate of active strips,
- 5062     ● `NoiseCSize_H_Tt_Sc_p` shows noise/gamma cluster size, a cluster being constructed out of  
 5063       adjacent strips giving a signal at the *same time* (hits within a time window of 25 ns),
- 5064     ● `NoiseCMult_H_Tt_Sc_p` shows noise/gamma cluster multiplicity (number of reconstructed  
 5065       clusters per event),
- 5066     ● `Chip_Mean_Noise_Tt_Sc_p` shows the same information than `Strip_Mean_Noise_Tt_Scp` us-  
 5067       ing a different binning (1 chip corresponds to 8 strips),
- 5068     ● `Chip_Activity_Tt_Sc_p` shows the same information than `strip_Activity_Tt_Scp` using  
 5069       chip binning,
- 5070     ● `Chip_Homogeneity_Tt_Sc_p` shows the homogeneity of a given partition using chip binning,
- 5071     ● `Beam_Profile_Tt_Sc_p` shows the estimated beam profile when taking efficiency scan. This  
 5072       is obtained by filtering `Time_Profile_Tt_Sc_p` to only consider the muon peak where the  
 5073       noise/gamma background has been subtracted. The resulting hit profile corresponds to the  
 5074       beam profile on the detector channels,
- 5075     ● `Efficiency_Fake_Tt_Ss_p` shows the efficiency given by fake hits by probing outside the  
 5076       peak in an uncorrelated window as wide as the peak window,
- 5077     ● `Efficiency_Peak_Tt_Ss_p` shows the efficiency given by hits contained in the peak window,
- 5078     ● `PeakCSize_H_Tt_Sc_p` shows the cluster size that was estimated using all the hits in the peak  
 5079       window,
- 5080     ● `PeakCMult_H_Tt_Sc_p` shows the cluster multiplicity that was estimated using all the hits in  
 5081       the peak window,
- 5082     ● `L0_Efficiency_Tt_Sc_p` shows the level 0 muon efficiency that was estimated **without** muon  
 5083       tracking after correction,
- 5084     ● `MuonCSize_H_Tt_Sc_p` shows the level 0 muon cluster size that was estimated **without** muon  
 5085       tracking after correction, and
- 5086     ● `MuonCMult_H_Tt_Sc_p` shows the level 0 muon cluster multiplicity that was estimated **without**  
 5087       muon tracking after correction.

5088     In the histogram labels, *t* stands for the trolley number (1 or 3), *c* for the chamber slot label in  
 5089       trolley *t* and *p* for the partition label (A, B, C or D depending on the chamber layout) as explained  
 5090       in Chapter 5.3.

5092 In the context of GIF++, an extra script called by the webDCS is called to extract the histograms  
 5093 from the ROOT files. The histograms are then stored in PNG and PDF formats into the correspond-  
 5094 ing folder (a single folder per HV step, so per ROOT file). An example of histogram organisation is  
 5095 given bellow for an hypothetical scan 001000 with at least 3 HV steps and whose chamber located in  
 5096 slot 1 of trolley 1 is called *Example\_RPC1* and has at least 2 read-out partitions A and B. The goal is  
 5097 to then display the histograms graphs on the Data Quality Monitoring (DQM) page of the webDCS,  
 5098 as presented in Figure 5.29, in order for the users to control the quality of the data taking at the end  
 5099 of data taking.

5100



5101

### B.2.1.2 CSV files

5102

Moreover, up to 4 CSV files can be created depending on which ones of the 3 input files were in the  
 5103 data folder:

5104

- `Offline-Corrupted.csv`, is used to keep track of the amount of data that was corrupted and removed from old data format files that don't contain any data quality flag.

5105

- 5106     ● `Offline-Current.csv`, contains the summary of the currents and voltages applied on each  
5107       RPC HV channel.
- 5108     ● `Offline-L0-EffCl.csv`, is used to write the efficiencies, cluster size and cluster multiplicity  
5109       of efficiency runs. Note that `L0` refers here to *Level 0* and means that the results of efficiency and  
5110       clusterization are a first approximation calculated without performing any muon tracking in  
5111       between the different detectors. This offline tool provides the user with a preliminar calcula-  
5112       tion of the efficiency and of the muon event parameters. Another analysis software especially  
5113       dedicated to muon tracking is called on selected data to retrieve the results of efficiency and  
5114       muon clusterization using a tracking algorithm to discriminate noise or gamma from muons  
5115       as muons are the only particles that pass through the full setup, leaving hits than can be used  
5116       to reconstruct their tracks.
- 5117     ● `Offline-Rate.csv`, is used to write the noise or gamma rates measured in the detector readout  
5118       partitions.

5119     Note that these 4 CSV files are created along with their *headers* (`Offline-[...]-Header.csv`  
5120       containing the names of each data columns) and are automatically merged together when the offline  
5121       analysis tool is called from the webDCS, contrary to the case where the tool is runned locally from  
5122       the terminal as the merging bash script is then not called. Thus, the resulting files, used to make  
5123       official plots, are:

- 5124     ● `Corrupted.csv`,
- 5125     ● `Current.csv`,
- 5126     ● `L0-EffCl.csv`.
- 5127     ● `Rate.csv`.

### 5128     **B.3 Analysis inputs and information handling**

5129     The usage of the Offline Analysis tool as well as its output have been presented in the previous sec-  
5130       tion. It is now important to dig further and start looking at the source code and the inputs necessary  
5131       for the tool to work. Indeed, other than the raw ROOT data files that are analysed, more information  
5132       needs to be imported inside of the program to perform the analysis such as the description of the  
5133       setup inside of GIFT++ at the time of data taking (number of trolleys, of RPCs, dimensions of the  
5134       detectors, etc...) or the mapping that links the TDC channels to the coresponding RPC channels in  
5135       order to translate the TDC information into human readable data. Two files are used to transmit all  
5136       this information:

- 5137
- 5138     ● `Dimensions.ini`, that provides the necessary setup and RPC information, and
- 5139     ● `ChannelsMapping.csv`, that gives the link between the TDC and RPC channels as well as the  
5140       *mask* for each channel (masked or not?).

### 5141 B.3.1 Dimensions file and IniFile parser

5142 GIF++ CMS RPC setup consists in detectors held into trolleys inside of the GIF++ bunker. Each of  
 5143 these detector may have a read-out segmented to cover different pseudo-rapidity range once intalled  
 5144 in CMS. The segmentation of the read-out is referred to as "partitions". This input file, present in  
 5145 every data folder, allows the analysis tool to know of the number of active trolleys, the number of  
 5146 active RPCs in those trolleys, and the details about each RPCs such as the number of RPC gaps, the  
 5147 number of pseudo-rapidity partitions, the number of strips per partion or the dimensions. To do so,  
 5148 there are 3 types of groups in the INI file architecture. Groups are sections of the INI file content  
 5149 starting with a title encapsulated in between square brackets. A first general group, appearing only  
 5150 once at the head of the document, gives information about the number of active trolleys as well  
 5151 as their IDs, as presented in Source Code B.1. For each active trolley, a group similar to Source  
 5152 Code B.2 can be found containing information about the number of active detectors in the trolley  
 5153 and their IDs. Each trolley group as a `Tt` name format, where `t` is the trolley ID. Finally, for each  
 5154 detector stored in slots of an active trolley, there is a group providing information about their names  
 5155 and dimensions, as shown in Source Code B.3. Each slot group as a `TtSs` name format, where `s` is  
 5156 the slot ID of trolley `t` where the active RPC is hosted.

```
5157 [General]
5158 nTrolleys=2
      TrolleysID=13
```

5159 *Source Code B.1: Example of `[General]` group as might be found in `Dimensions.ini`. In GIF++, only 2 trolleys are available to hold RPCs and place them inside of the bunker for irradiation. The IDs of the trolleys are written in a single string as "13" and then read character by character by the program.*

```
5160 [T1]
      nSlots=4
      SlotsID=1234
```

5161 *Source Code B.2: Example of trolley group as might be found in `Dimensions.ini`. In this example, the file tells that there are 4 detectors placed in the holding slots of the trolley T1 and that their IDs, written as a single string variable, are 1, 2, 3 and 4.*

```
5162 [T1S1]
      Name=RE2-2-NPD-BARC-8
      Partitions=3
      Gaps=3
      Gap1=BOT
      Gap2=TN
      Gap3=TW
      AreaGap1=11694.25
      AreaGap2=6432
      AreaGap3=4582.82
      Strips=32
      ActiveArea-A=157.8
      ActiveArea-B=121.69
      ActiveArea-C=93.03
```

5163 *Source Code B.3: Example of slot group as might be found in `Dimensions.ini`. In this example, the file provides information about a detector named RE2-2-NPD-BARC-8, having 3 pseudo-rapidity readout partitions and stored in slot S1 of trolley T1. This is a CMS RE2-2 type of detector. This information will then be used for example to compute the rate per unit area calculation.*

5164 This information is read-out and stored in a C++ object called `IniFile`, that parses the information  
 5165 of the INI input file and stores it into a local buffer for later use. This INI parser is the exact  
 5166 same one that was previously developed for the GIF++ DAQ and described in Appendix A.5.2.

### 5167 B.3.2 TDC to RPC link file and Mapping

5168 The same way the INI dimension file information is stored using `map`, the channel mapping and  
 5169 mask information making the link in between TDC channels and RPC strips is stored and accessed  
 5170 through `map`. First of all, the mapping CSV file is organised into 3 columns separated by tabulations:

5171 

5172    RPC_channel	5172    TDC_channel	5172    mask
---------------------	---------------------	--------------

5173       using as formatting for each field:

5174 

5175    TSCCC	5175    TCCC	5175    M
---------------	--------------	-----------

5176 `TSCCC` is a 5-digit integer where `T` is the trolley ID, `s` the slot ID in which the RPC is held inside  
 5177 the trolley `T` and `ccc` is the RPC channel number, or *strip* number, that can take values up to  
 5178 3-digits depending on the detector,

5179 `TCCC` is a 4 digit integer where `T` is the TDC ID to which the RPC is connected, `ccc` is the TDC  
 5180 channel number linked to the RPC strip that can take values in between 0 and 127, and

5181 `M` is a 1-digit integer indicating if the channel should be considered (`M = 1`) or discarded (`M = 0`)  
 5182 during analysis. Note that the absence of a third column is interpreted by the mapping file  
 5183 parser as `M = 1` by default.

5184       This mapping and masking information is readout and stored thanks to the object `Mapping`, pre-  
 5185 sented in Source Code B.4. Similarly to `IniFile` objects, this class has private methods to provide  
 5186 with parser rules. The first one, `Mapping::CheckIfNewLine()` is used to find the newline character  
 5187 '`\n`' or return character '`\r`' (depending on which kind of operating system interacted with the file).  
 5188 Finding and identifying a newline or return character is used for the simple reason that the masking  
 5189 information has been introduced only during the year 2017 but the channel mapping files exist since  
 5190 2015 and the very beginning of data taking at GIF++. This means that in the older data folders,  
 5191 before the upgrade, the channel mapping file only had 2 columns, the RPC channel and the TDC  
 5192 channel. For compatibility reasons, this method helps controlling the character following the readout  
 5193 of the 2 first fields of a line. In case any end of line character is found, no mask information is present  
 5194 in the file and the default `M = 1` is used. On the contrary, if the next character was a tabulation or a  
 5195 space, the mask information is present.

5196       Once the 3 fields have been readout, the second private method `Mapping::CheckIfTDCCh()` is  
 5197 used to control that the TDC channel is an existing TDC channel by checking its format. Finally,  
 5198 the information is stored into 3 different maps (`Link`, `ReverseLink` and `Mask`) thanks to the public  
 5199 method `Mapping::Read()`. `Link` allows to get the RPC channel by knowing the TDC channel while  
 5200 `ReverseLink` does the opposite by returning the TDC channel by knowing the RPC channel. Finally,  
 5201 `Mask` returns the mask associated to a given RPC channel.

```

5202 typedef map<Uint,Uint> MappingData;

5203 class Mapping {
5204     private:
5205         bool          CheckIfNewLine(char next);
5206         bool          CheckIfTDCCh(Uint channel);
5207         string        FileName;
5208         MappingData  Link;
5209         MappingData  ReverseLink;
5210         MappingData  Mask;
5211         int           Error;
5212
5213     public:
5214         Mapping();
5215         Mapping(string baseName);
5216         ~Mapping();
5217
5218         void SetFileName(const string filename);
5219         int  Read();
5220         Uint GetLink(Uint tdcchannel);
5221         Uint GetReverse(Uint rpcchannel);
5222         Uint GetMask(Uint rpcchannel);
5223     };

```

5204 *Source Code B.4: Description of C++ object Mapping used as a parser for the channel mapping and mask file.*

## 5205 B.4 Description of GIF++ setup within the Offline Analysis tool

5206 In the previous section, the tool input files have been discussed. The dimension file information is  
 5207 stored in a map hosted by the `IniFile` object. But this information is then used to create a series of  
 5208 new objects that helps defining the GIF++ infrastructure directly into the Offline Analysis. Indeed,  
 5209 from the `RPC`, to the more general `Infrastructure`, every element of the GIF++ infrastrucutre is  
 5210 recreated for each data analysis based on the information provided in input. All this information  
 5211 about the infrastructure will be used to assign each hit signal to a specific strip channel of a specific  
 5212 detector, and having a specific active area. This way, rate per unit area calculation is possible.  
 5213

### 5214 B.4.1 RPC objects

5215 `RPC` objects have been developped to represent physical active detectors in GIF++ at the moment  
 5216 of data taking. Thus, there are as many `RPC` objects created during the analysis than there were  
 5217 active RPCs tested during a run. Each `RPC` hosts the information present in the corresponding INI  
 5218 slot group, as showed in B.3, and organises it using a similar architecture. This can be seen from  
 5219 Source B.5.

5220 To make the object more compact, the lists of gap labels, of gap active areas and strip active  
 5221 areas are stored into `vector` dynamical containers. `RPC` objects are always contructed thanks to the  
 5222 dimension file information stored into the `IniFILE` and their ID, using the format `TtSs`. Using the  
 5223 `RPC` ID, the constructor calls the methods of `IniFILE` to initialise the `RPC`. The other constructors  
 5224 are not used but exist in case of need. Finally, some getters have been written to access the different  
 5225 private parameters storing the detector information.

5226

**5227 B.4.2 Trolley objects**

5228 Trolley objects have been developed to represent physical active trolleys in GIF++ at the moment  
5229 of data taking. Thus, there are as many trolley objects created during the analysis than there were  
5230 active trolleys hosting RPCs under test during a run. Each Trolley hosts the information present in  
5231 the corresponding INI trolley group, as shown in B.2, and organises it using a similar architecture.  
5232 In addition to the information hosted in the INI file, these objects have a dynamical container of RPC  
5233 objects, representing the active detectors the active trolley was hosting at the time of data taking.  
5234 This can be seen from Source Code B.6.

5235 Trolley objects are always constructed thanks to the dimension file information stored into the  
5236 IniFILE and their ID, using the format `Tt`. Using the Trolley ID, the constructor calls the methods  
5237 of `IniFile` to initialise the Trolley. Retrieving the information of the RPC IDs via `SlotsID`, a new  
5238 RPC is constructed and added to the container `RPCs` for each character in the ID string. The other  
5239 constructors are not used but exist in case of need. Finally, some getters have been written to access  
5240 the different private parameters storing the trolley and detectors information.

5241

**5242 B.4.3 Infrastructure object**

5243 The Infrastructure object has been developed to represent the GIF++ bunker area dedicated to  
5244 CMS RPC experiments. With this very specific object, all the information about the CMS RPC  
5245 setup within GIF++ at the moment of data taking is stored. It hosts the information present in the  
5246 corresponding INI general group, as shown in B.1, and organises it using a similar architecture. In  
5247 addition to the information hosted in the INI file, this object has a dynamical container of Trolley  
5248 objects representing the active trolleys in GIF++ area, themselves containing RPC objects. This can  
5249 be seen from Source Code B.7.

5250 The Infrastructure object is always constructed thanks to the dimension file information stored  
5251 into the `IniFILE`. Retrieving the information of the trolley IDs via `TrolleysID`, a new Trolley is  
5252 constructed and added to the container `Trolleys` for each character in the ID string. By extension,  
5253 it is easy to understand that the process described in Section B.4.2 for the construction of RPCs  
5254 takes place when a trolley is constructed. The other constructors are not used but exist in case of  
5255 need. Finally, some getters have been written to access the different private parameters storing the  
5256 infrastructure, trolleys and detectors information.

```

5257
class RPC{
    private:
        string      name;           //RPC name as in webDCS database
        UInt       nGaps;          //Number of gaps in the RPC
        UInt       nPartitions;    //Number of partitions in the RPC
        UInt       nStrips;         //Number of strips per partition
        vector<string> gaps;      //List of gap labels (BOT, TOP, etc...)
        vector<float>  gapGeo;        //List of gap active areas
        vector<float>  stripGeo;      //List of strip active areas

    public:
        RPC();
        RPC(string ID, IniFile* geofile);
        RPC(const RPC& other);
        ~RPC();
        RPC& operator=(const RPC& other);

        string GetName();
        UInt   GetNGaps();
        UInt   GetNPartitions();
        UInt   GetNStrips();
        string GetGap(UInt g);
        float  GetGapGeo(UInt g);
        float  GetStripGeo(UInt p);
};

5258

```

5259   *Source Code B.5: Description of C++ objects RPC that describe each active detectors used during data taking.*

```

5260
class Trolley{
    private:
        UInt       nSlots;        //Number of active RPCs in the considered trolley
        string     SlotsID;       //Active RPC IDs written into a string
        vector<RPC*> RPCs;       //List of active RPCs

    public:
        Trolley();
        Trolley(string ID, IniFile* geofile);
        Trolley(const Trolley& other);
        ~Trolley();
        Trolley& operator=(const Trolley& other);

        UInt   GetNSlots();
        string GetSlotsID();
        UInt   GetSlotID(UInt s);
        RPC*   GetRPC(UInt r);
        void   DeleteRPC(UInt r);

        //Methods to get members of RPC objects stored in RPCs
        string GetName(UInt r);
        UInt   GetNGaps(UInt r);
        UInt   GetNPartitions(UInt r);
        UInt   GetNStrips(UInt r);
        string GetGap(UInt r, UInt g);
        float  GetGapGeo(UInt r, UInt g);
        float  GetStripGeo(UInt r, UInt p);
};

5261

```

5261   *Source Code B.6: Description of C++ objects Trolley that describe each active trolley used during data taking.*

```

class Infrastructure {
    private:
        Uint             nTrolleys;   //Number of active Trolleys in the run
        string          TrolleysID;  //Active trolley IDs written into a string
        vector<Trolley*> Trolleys;  //List of active Trolleys (struct)

    public:
        Infrastructure();
        Infrastructure(IniFile* geofile);
        Infrastructure(const Infrastructure& other);
        ~Infrastructure();
        Infrastructure& operator=(const Infrastructure& other);

        Uint    GetNTrolleys();
        string GetTrolleysID();
        Uint    GetTrolleyID(Uint t);

5262      Trolley* GetTrolley(Uint t);
        void    DeleteTrolley(Uint t);

        //Methods to get members of GIFTrolley objects stored in Trolleys
        Uint    GetNSlots(Uint t);
        string GetSlotsID(Uint t);
        Uint    GetSlotID(Uint t, Uint s);
        RPC*   GetRPC(Uint t, Uint r);

        //Methods to get members of RPC objects stored in RPCs
        string GetName(Uint t, Uint r);
        Uint    GetNGaps(Uint t, Uint r);
        Uint    GetNPartitions(Uint t, Uint r);
        Uint    GetNStrips(Uint t, Uint r);
        string GetGap(Uint t, Uint r, Uint g);
        float  GetGapGeo(Uint t, Uint r, Uint g);
        float  GetStripGeo(Uint t, Uint r, Uint p);
    };

```

*Source Code B.7: Description of C++ object Infrastructure that contains the full information about CMS RPC experiment in GIF++.*

## **5264 B.5 Handeling of data**

*5265 As discussed in Appendix A.4.2, the raw data uses a TTree architecture where every entry is related*  
*5266 to a trigger signal provided by a muon or a random pulse, whether the goal of the data taking was to*  
*5267 measure the performance of the detector or the noise/gamma background respectively. Each of these*  
*5268 entries, referred also as events, contain a more or less full list of hits in the TDC channels to which*  
*5269 the detectors are connected. To this list of hits corresponds a list of time stamps, marking the arrival*  
*5270 of the hits within the TDC channel.*

*5271 The infrastructure of the CMS RPC experiment within GIF++ being defined, combining the raw*  
*5272 data information with the information provided by both the mapping/mask file and the dimension*  
*5273 file allows to build new physical objects that will help in computing efficiency or rates.*

### 5274 B.5.1 RPC hits

5275 The raw data stored in the ROOT file as output of the GIFT++ DAQ, is readout by the analysis tool  
 5276 using the structure `RAWData` presented in Source Code B.9 that differs from the structure presented  
 5277 in Appendix A.4.2 as it is not meant to hold all of the data contained in the ROOT file. In this sense,  
 5278 this structure is in the case of the offline analysis tool not a dynamical object and will only be storing  
 5279 a single event contained in a single entry of the `TTree`.

5280

```
class RPCHit {
    private:
        Uint Channel;      //RPC channel according to mapping (5 digits)
        Uint Trolley;     //0, 1 or 3 (1st digit of the RPC channel)
        Uint Station;     //Slot where is held the RPC in Trolley (2nd digit)
        Uint Strip;       //RPC strip where the hit occurred (last 3 digits)
        Uint Partition;   //Readout partition along eta segmentation
        float TimeStamp; //Time stamp of the arrival in TDC

    public:
        RPCHit();
        RPCHit(Uint channel, float time, Infrastructure* Infra);
        RPCHit(const RPCHit& other);
        ~RPCHit();
        RPCHit& operator=(const RPCHit& other);

        Uint GetChannel();
        Uint GetTrolley();
        Uint GetStation();
        Uint GetStrip();
        Uint GetPartition();
        float GetTime();
};

typedef vector<RPCHit> HitList;
typedef struct GIFHitList {HitList rpc[NTROLLEYS][NSLOTS][NPARTITIONS];}
    ↪ GIFHitList;

bool SortHitbyStrip(RPCHit h1, RPCHit h2);
bool SortHitbyTime(RPCHit h1, RPCHit h2);
```

5282

*Source Code B.8: Description of C++ object `RPCHit`.*

5283

```
struct RAWData{
    int iEvent;           //Event i
    int TDCHits;         //Number of hits in event i
    int QFlag;           //Quality flag list (1 flag digit per TDC)
    vector<Uint> *TDCCh; //List of channels giving hits per event
    vector<float> *TDCTS; //List of the corresponding time stamps
};
```

5284

*Source Code B.9: Description of C++ structure `RAWData`.*

5285 Each member of the structure is then linked to the corresponding branch of the ROOT data tree,  
 5286 as shown in the example of Source Code B.10, and using the method `GetEntry(int i)` of the ROOT  
 5287 class `TTree` will update the state of the members of `RAWData`.

5288 The data is then analysed entry by entry and to each element of the TDC channel list, a `RPCHit` is  
 5289 constructed by linking each TDC channel to the corresponding RPC channel thanks to the Mapping

object. The information carried by the RPC channel format allows to easily retrieve the trolley and slot from which the hit was recorded (see section B.3.2). Using these 2 values, the readout partition can be found by knowing the strip channel and comparing it with the number of partitions and strips per partition stored into the `Infrastructure` object.

```
5290   TTree* dataTree = (TTree*)dataFile.Get("RAWData");
5291   RAWData data;
5292
5293   dataTree->SetBranchAddress("EventNumber", &data.iEvent);
5294   dataTree->SetBranchAddress("number_of_hits", &data.TDCNHits);
5295   dataTree->SetBranchAddress("Quality_flag", &data.QFlag);
5296   dataTree->SetBranchAddress("TDC_channel", &data.TDCCh);
5297   dataTree->SetBranchAddress("TDC_TimeStamp", &data.TDCTS);
```

5296       *Source Code B.10: Example of link in between RAWData and TTree.*

5297       Thus `RPCHit` objects are then stored into 3D dynamical list called `GIFHitList` (Source Code B.8)  
 5298 where the 3 dimensions refer to the 3 layers of the readout in `GIF++` : in the bunker there are *trolleys*  
 5299 ( $\tau$ ) holding detectors in *slots* ( $s$ ) and each detector readout is divided into 1 or more pseudo-rapidity  
 5300 *partitions* ( $p$ ). Using these 3 information allows to assign an address to each readout partition and  
 5301 this address will point to a specific hit list.

5302

### 5303       **B.5.2 Clusters of hits**

5304       All the hits contained in the ROOT file have been sorted into the different hit lists through the  
 5305 `GIFHitList`. At this point, it is possible to start looking for clusters. A cluster is a group of adjacent  
 5306 strips getting hits within a time window of 25 ns. These strips are then assumed to be part of the same  
 5307 physical avalanche signal generated by a muon passing through the chamber or by the interaction of  
 5308 a gamma stopping into the electrodes of the RPCs.

5309       To keep the cluster information, `RPCCluster` objects have been defined as shown in Source  
 5310 Code B.11. Using the information of each individual `RPCHit` taken out of the hit list, it stores  
 5311 the cluster size (number of adjacent strips composing the cluster), the first and last hit, the center for  
 5312 spatial reconstruction and finally the start and stop time stamps as well as te time spread in between  
 5313 the first and last hit.

5314

5315       To investigate the hit list of a given detector partition, the function `Clusterization()` defined  
 5316 in `include/Cluster.h` needs the hits in the list to be time sorted. This is achieved by calling func-  
 5317 tion `sort()` of library `<algorithm>` using the comparator `SortHitbyTime(RPCHit h1, RPCHit h2)`  
 5318 defined in `include/RPCHit.h` that returns `true` if the time stamp of hit `h1` is lower than that of `h2`.  
 5319 A first isolation of strips is made only based on time information. All the hits within the 25 ns win-  
 5320 dow are taken separately from the rest. Then, this sub-list of hits is sorted this time by ascending  
 5321 strip number, using this time the comparator `SortHitbyStrip(RPCHit h1, RPCHit h2)`. Finally, the  
 5322 groups of adjacent strips are used to construct `RPCCluster` objects that are then stored in a temporary  
 5323 list of clusters that is at the end of the process used to know how many clusters were reconstructed  
 5324 and to fill their sizes into an histogram that will allows to know the mean size of muon or gamma  
 5325 clusters. This method to group hits together into clusters is limited as no systematic study of the  
 5326 average avalanche time development into TDC hits was performed and that there is no correlation

5327 of both spatial and time information to make the first selection of hits. Due to this, two clusters  
 5328 developping consecutively next to each other during a total time longer to 25 ns could be wrongly  
 5329 grouped as a cluster composed of the first developed cluster plus a part of the second cluster while  
 5330 the rest of the second cluster would be placed in a second truncated cluster. This kind of event  
 5331 is not likely but needs to be taken into account nonetheless. A possible improvement would be to  
 5332 identify clusters in a 2D space whose dimensions are time and strip. In this 2D space, the cluster  
 5333 could be geometrically identified as isolated groups of adjacent strips receiving a hit at a similar time.  
 5334

```

5334
5335   class RPCCluster{
5336     private:
5337       Uint ClusterSize; //Size of cluster #ID
5338       Uint FirstStrip; //First strip of cluster #ID
5339       Uint LastStrip; //Last strip of cluster #ID
5340       float Center; //Center of cluster #ID ((first+last)/2)
5341       float StartStamp; //Time stamp of the earliest hit of cluster #ID
5342       float StopStamp; //Time stamp of the latest hit of cluster #ID
5343       float TimeSpread; //Time difference between earliest and latest hits
5344           //of cluster #ID
5345
5346     public:
5347       RPCCluster();
5348       RPCCluster(HitList List, Uint cID, Uint cSize, Uint first, Uint firstID);
5349       RPCCluster(const RPCCluster& other);
5350       ~RPCCluster();
5351       RPCCluster& operator=(const RPCCluster& other);
5352
5353       Uint GetID();
5354       Uint GetSize();
5355       Uint GetFirstStrip();
5356       Uint GetLastStrip();
5357       float GetCenter();
5358       float GetStart();
5359       float GetStop();
5360       float GetSpread();
5361   };
5362
5363   typedef vector<RPCCluster> ClusterList;
5364
5365   //Other functions to build cluster lists out of hit lists
5366   void BuildClusters(HitList &cluster, ClusterList &clusterList);
5367   void Clusterization(HitList &hits, TH1 *hcSize, TH1 *hcMult);
  
```

5336

*Source Code B.11: Description of C++ object Cluster.*

## 5337 B.6 DAQ data Analysis

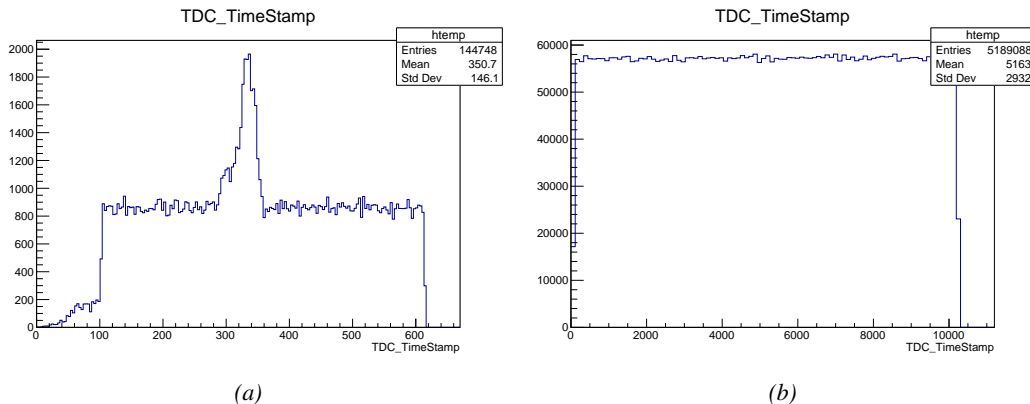
5338 All the ingredients to analyse GIFT++ data have been introduced. This section will focus on the  
 5339 different part of the analysis performed on the data, from determining the type of data the tool is  
 5340 dealing with to calculate the hit and cluster rate per unit area in each detector or reconstructing  
 5341 muon or gamma clusters.

### 5342 B.6.1 Determination of the run type

5343 In GIF++, both the performance of the detectors in detecting muons in an irradiated environment  
 5344 and the gamma or noise background can be independantly measured. These correspond to different  
 5345 run types and hence, to different TDC settings giving different data to look at.

5346 In the case of performance measurements, the trigger for data taking is provided by the coin-  
 5347 cidence of several scintillators when muons from the beam passing through the area are detected.  
 5348 Data is collected in a 600 ns wide window centered around the arrival of muons in the RPCs. The  
 5349 expected time distribution of hits is shown in Figure B.1a. The muon peak is clearly visible in the  
 5350 center of the distribution and is to be extracted from the gamma background that composes the flat  
 5351 part of the distribution.

5352 On the other hand, gamma background or noise measurements are focussed on the non muon  
 5353 related physics and the trigger needs to be independant from the muons to give a good measurement  
 5354 of the gamma/noise distribution as seen by the detectors. The trigger is then provided by a pulse  
 5355 generated by the DAQ at a frequency of 100 Hz whose pulse is not likely to be on time with a muon.  
 5356 In order to increase the integrated time without increasing proportionnaly the acquisition time, the  
 5357 width of the acquisition windows are increased to 10  $\mu$ s. The time distribution of the hits is expected  
 5358 to be flat, as shown by Figure B.1b.



5359 *Figure B.1: Example of expected hit time distributions in the cases of efficiency (Figure B.1a) and noise/gamma  
 5360 rate per unit area (Figure B.1b) measurements as extracted from the raw ROOT files. The unit along the x-axis  
 5361 corresponds to ns. The fact that "the" muon peak is not well defined in Figure B.1a is due to the contribution  
 5362 of all the RPCs being tested at the same time that don't necessarily have the same signal arrival time. Each  
 5363 individual peak can have an offset with the ones of other detectors. The inconsistancy in the first 100 ns of both  
 5364 time distributions is an artefact of the TDCs and are systematically rejected during the analysis.*

5365 The ROOT files include a `TTree` called `RunParameters` containing, among other things, the infor-  
 5366 mation related to the run type. The run type can then be accessed as described by Source Code B.12  
 5367 and the function `IsEfficiencyRun()` is then used to determine if the run file is an efficiency run or,  
 5368 on the contrary, another type of run (noise or gamma measurement).

5369 Finally, the data files will have a slightly different content whether it was collected before or after  
 5370 October 2017 and the upgrade of the DAQ software that brought a new information into the ROOT  
 5371 output. This is discussed in Appendix A.4.3 and implies that the analysis will differ a little depending  
 5372 on the data format. Indeed, as no information on the data quality is stored, in older data files, the cor-  
 5373 rections for missing events has to be done at the end of the analysis. The information about the type

5368 of data format is stored in the variable `bool isNewFormat` by checking the list of branches contained  
 5369 in the data tree via the methods `TTree::GetListOfBranches()` and `TCollection::Contains()`.

```
5370
5371     TTree* RunParameters = (TTree*)dataFile.Get("RunParameters");
5372     TString* RunType = new TString();
5373     RunParameters->SetBranchAddress("RunType", &RunType);
5374     RunParameters->GetEntry(0);
```

5372       *Source Code B.12: Access to the run type contained in `TTree* RunParameters`.*

## 5373       **B.6.2 Beam time window calculation for efficiency runs**

5374 Knowing the run type is important first of all to know the width of the acquisition window to be used  
 5375 for the rate calculation and finally to be able to seek for muons. Indeed, the peak that appears in the  
 5376 time distribution for each detectors is then fitted to extract the most probable time window in which  
 5377 the tool should look for muon hits. The data outside of this time window is then used to evaluate the  
 5378 noise or gamma background the detector was subjected to during the data taking. Computing the  
 5379 position of the peak is done calling the function `SetBeamWindow()` defined in file `src/RPCHit.cc` that  
 5380 loops a first time on the data. The data is first sorted in a 3D array of 1D histograms (`GIFH1Array`, see  
 5381 `include/types.h`). Then the location of the highest bin is determined using `TH1::GetMaximumBin()`  
 5382 and is used to define a window in which a gaussian fit will be applied to compute the peak width.  
 5383 This window is a 80 ns defined by Formula B.1 around the central bin.

$$(B.1a) \quad t_{center}(ns) = bin \times width_{bin}(ns)$$

$$(B.1b) \quad [t_{low}; t_{high}] = [t_{center} - 40; t_{center} + 40]$$

5384 Before the fit is performed, the average number of noise/gamma hits per bin is evaluated using  
 5385 the data outside of the fit window. Excluding the first 100 ns, the average number of hits per bin  
 5386 due to the noise or gamma is defined by Formula B.2 after extracting the amount of hits in the time  
 5387 windows  $[100; t_{low}]$  and  $[t_{high}; 600]$  thanks to the method `TH1::Integral()`. This average number  
 5388 of hits is then subtracted to every bin of the 1D histogram, in order to *clean* it from the noise or  
 5389 gamma contribution as much as possible to improve the fit quality. Bins where  $\langle n_{hits} \rangle$  is greater  
 5390 than the actual bin content are set to 0.

$$(B.2a) \quad \Delta t_{noise}(ns) = 600 \overbrace{-t_{high} + t_{low}}^{-80ns} - 100 = 420ns$$

$$(B.2b) \quad \langle n_{hits} \rangle = width_{bin}(ns) \times \frac{\sum_{t=100}^{t_{low}} + \sum_{t=t_{high}}^{600}}{\Delta t_{noise}(ns)}$$

5391 Finally, the fit parameters are extracted and saved for each detector in 3D arrays of `float`  
 5392 (`muonPeak`, see `include/types.h`), a first one for the mean arrival time of the muons, `PeakTime`,  
 5393 a second for the height or strength of the peak, `PeakHeight`, and a third one for the width of the  
 5394 peak, `PeakWidth`. The width is on purpose chosen to be wider than the peak and defined as  $6\sigma$  of the  
 5395 gaussian fit, for a peak range being as given by Formula B.3.

$$(B.3) \quad [t_{low}^{peak}; t_{high}^{peak}] = [t_{center}^{peak} - 3\sigma; t_{center}^{peak} + 3\sigma]$$

5396 For a finer analysis, it is advised to determine more precisely the width of the peak to exclude  
 5397 as much noise or background hits as possible. The same settings are applied to every partitions of  
 5398 the same detector. To determine which one of the detector's partitions is directly illuminated by the  
 5399 beam, the peak height of each partition is compared and the highest one is then used to define the  
 5400 peak settings.

5401 It is not possible to identify the particles causing the hits, hence muons, background gamma  
 5402 particles or even noise could be responsible of hits within the time window. To be able to account  
 5403 for this effect, the peak width extracted from the fit on the peak will also be used to define a fake  
 5404 time window, uncorrelated to the muon peak and in which a fake efficiency, contribution from both  
 5405 background and noise, will be measured. This window corresponds to the time range described in  
 5406 Formula B.4.

$$(B.4) \quad [t_{low}^{fake}; t_{high}^{fake}] = [600 - 6\sigma; 600]$$

### 5407 B.6.3 Data loop and histogram filling

5408 3D arrays of histogram are created to store the data and display it on the DQM of GIF++ webDCS  
 5409 for the use of shifters. The dimensions correspond to the different layers held into the GIF++ infras-  
 5410 tructure (trolleys `T` containing RPCs or *slots* `s` each being divided into read-out partitions `p`). These  
 5411 histograms, presented in section B.2.1.1, are filled while looping on the data. Before starting the  
 5412 analysis loop, it is necessary to control the entry quality for the new file formats featuring `QFlag`. If  
 5413 the `QFlag` value for this entry shows that 1 TDC or more have a `CORRUPTED` flag, then this event is  
 5414 discarded. The loss of statistics is low enough to be neglected. `QFlag` is controlled using the func-  
 5415 tion `IsCorruptedEvent()` defined in `src/utils.cc`. As explained in Appendix A.4.3, each digit of  
 5416 this integer represent a TDC flag that can be either 1 or 2. Each 2 is the sign of a `CORRUPTED` state.  
 5417 Then, the data is accessed entry by entry in the ROOT `TTree` using `RAWData` and each hit in the hit  
 5418 list is assigned to a detector channel and saved in the corresponding histograms. As described in  
 5419 Source Code B.13, in the first part of the analysis, in which the loop over the ROOT file's content is  
 5420 performed, the different steps are:

5421 **1- RPC channel assignment and control:** a check is done on the RPC channel extracted thanks  
 5422 to the mapping via the method `Mapping::GetLink()`. If the channel is not initialised and is 0, or if  
 5423 the TDC channel is not contained in a range in between X000 and X127, X being the TDC ID, the  
 5424 hit is discarded. This means there was a problem in the mapping. Often a mapping problem leads to  
 5425 the failure of the offline tool.

5426 **2- Creation of a `RPCHit` object:** to easily get the trolley, slot and partition in which the hit has  
 5427 been assigned, this object is particularly helpful.

5428 **3- General histograms are filled:** the hit is filled into the time distribution, global hit distribution  
 5429 and time versus strip histograms, and if the arrival time is within the first 100 ns, it is discarded and  
 5430 nothing else happens and the loop proceeds with the next hit in the list, going back to step 1.

5431

```

for(int h = 0; h < data.TDCCh->size(); h++) {
    Uint tdcchannel = data.TDCCh->at(h);
    UInt rpcchannel = RPCChMap->GetLink(tdcchannel);
    float timestamp = data.TDCTS->at(h);
    //Get rid of the hits in channels not considered in the mapping
    if(rpcchannel != NOCHANNELLINK) {
        RPCHit hit(rpcchannel, timestamp, GIFInfra);
        UInt T = hit.GetTrolley();
        UInt S = hit.GetStation()-1;
        UInt P = hit.GetPartition()-1;
        //Fill the time and hit profiles
        TimeProfile_H.rpc[T][S][P]->Fill(hit.GetTime());
        HitProfile_H.rpc[T][S][P]->Fill(hit.GetStrip());
        TimeVSChanProfile_H.rpc[T][S][P]->Fill(hit.GetStrip(),hit.GetTime());
        //Reject the 100 first ns due to inhomogeneity of data
        if(hit.GetTime() >= TIMEREJECT) {
            Multiplicity.rpc[T][S][P]++;
            if(IsEfficiencyRun(RunType)) {
                //Define peak time range for efficiency calculation
                float lowlimit_eff = PeakTime.rpc[T][S][P]
                    - PeakWidth.rpc[T][S][P];
                float highlimit_eff = PeakTime.rpc[T][S][P]
                    + PeakWidth.rpc[T][S][P];
                bool peakrange = (hit.GetTime() >= lowlimit_eff
                    && hit.GetTime() < highlimit_eff);
                //Fill hits inside of the defined peak and noise range
                if(peakrange) {
                    BeamProfile_H.rpc[T][S][P]->Fill(hit.GetStrip());
                    PeakHitList.rpc[T][S][P].push_back(hit);
                } else {
                    StripNoiseProfile_H.rpc[T][S][P]->Fill(hit.GetStrip());
                    NoiseHitList.rpc[T][S][P].push_back(hit);
                }
                //Then define time range for fake efficiency
                float highlimit_fake = BMTDCWINDOW;
                float lowlimit_fake = highlimit_fake
                    - (highlimit_eff-lowlimit_eff);
                bool fakerange = (hit.GetTime() >= lowlimit_fake
                    && hit.GetTime() < highlimit_fake);
                //Fill the hits inside of the fake window
                if(fakerange) {
                    FakeHitList.rpc[T][S][P].push_back(hit);
                }
            } else {
                //Fill the hits inside of the defined noise range
                StripNoiseProfile_H.rpc[T][S][P]->Fill(hit.GetStrip());
                NoiseHitList.rpc[T][S][P].push_back(hit);
            }
        }
    }
}

```

5432

*Source Code B.13: For each entry of the raw ROOT data file, the code loops over the list of channels and corresponding time stamps contained in branches `TDC_channel` and `TDC_TimeStamp` and constructs `RPCHit` objects that are filled in the peak, noise and fake hit lists and also fills the time, hit, beam and noise profiles.*

5433

**5434 4- Multiplicity counter:** the hit multiplicity counter of the corresponding detectors is incremented.

5435 **5-a-1 Efficiency runs - Is the hit within the peak window? :** if the hit is contained in the peak  
 5436 window previously defined by Formula B.3, it is filled into the beam hit profile histogram of the  
 5437 corresponding chamber, added into the list of peak hits and increments the counter of *in time* hits.  
 5438 The term *in time* here refers to the hits that are likely to be muons by arriving in the expected time  
 5439 window. If the hit is outside of the peak window, it is filled into the noise profile histogram of  
 5440 the corresponding detector, added into the list of noise/gamma hits and increments the counter of  
 5441 noise/gamma hits.

5442 **5-a-2 Efficiency runs - Is the hit within the fake window? :** if the hit is contained in the fake  
 5443 window previously defined by Formula B.4, it is added into the list of fake hits. Counting the fake  
 5444 hits outside the peak window allows to estimate the probability to detect in time background or noise.

5445 **5-b- Noise/gamma rate runs - Noise histograms are filled:** the hit is filled into the noise profile  
 5446 histogram of the corresponding detector, added into the list of noise/gamma hits and increments the  
 5447 counter of noise/gamma hits.

```
5448
  for(UInt tr = 0; tr < GIFInfra->GetNTrolleys(); tr++) {
    UInt T = GIFInfra->GetTrolleyID(tr);
    for(UInt sl = 0; sl < GIFInfra->GetNSlots(tr); sl++) {
      UInt S = GIFInfra->GetSlotID(tr,sl) - 1;
      UInt nStripsPart = GIFInfra->GetNStrips(tr,sl);
      string rpcID = GIFInfra->GetName(tr,sl);
      for (UInt p = 0; p < GIFInfra->GetNPartitions(tr,sl); p++) {
        //Clusterize noise/gamma data
        sort(NoiseHitList.rpc[T][S][p].begin(),
              NoiseHitList.rpc[T][S][p].end(),SortHitbyTime);
        Clusterization(NoiseHitList.rpc[T][S][p],
                       NoiseCSize_H.rpc[T][S][p],NoiseCMult_H.rpc[T][S][p]);
        //Clusterize muon data and fill efficiency histograms based on
        //the content of peak and fake hit vectors if efficiency run
        if(IsEfficiencyRun(RunType)){
          //Peak data
          sort(PeakHitList.rpc[T][S][p].begin(),
                PeakHitList.rpc[T][S][p].end(),SortHitbyTime);
          Clusterization(PeakHitList.rpc[T][S][p],
                         PeakCSize_H.rpc[T][S][p],PeakCMult_H.rpc[T][S][p]);
          if(PeakHitList.rpc[T][S][p].size() > 0)
            EfficiencyPeak_H.rpc[T][S][p]->Fill(DETECTED);
          else EfficiencyPeak_H.rpc[T][S][p]->Fill(MISSED);

          //Fake data
          if(FakeHitList.rpc[T][S][p].size() > 0)
            EfficiencyFake_H.rpc[T][S][p]->Fill(DETECTED);
          else EfficiencyFake_H.rpc[T][S][p]->Fill(MISSED);
        }
        //Save and reinitialise the hit multiplicity
        HitMultiplicity_H.rpc[T][S][p]->Fill(Multiplicity.rpc[T][S][p]);
        Multiplicity.rpc[T][S][p] = 0;
      }
    }
  }
```

5450 *Source Code B.14: Loops to clusterize the hit lists and fill efficiency and multiplicity histograms.*

5451 After the loop on the hit list of the entry is over, the next step is to clusterize the 3D lists filled

5452 in the previous steps, as displayed in Source Code B.14. A 3D loop is then started over the active  
 5453 trolley, slot and RPC partitions to access these objects. Each `NoiseHitList` and `PeakHitList`, in  
 5454 case of efficiency run, are clusterized as described in section B.5.2. There corresponding cluster size  
 5455 and multiplicity histograms are filled at the end of the clustering process.

5456 Then, the peak and fake efficiency histograms are filled in case of efficiency run. The selection is  
 5457 simply made by checking whether the RPC detected signals in the peak window or/and fake window  
 5458 during this event. In the case a hit is recorded in either of both time windows, the histogram is  
 5459 filled with 1. On the contrary, the histogram is filled with 0. Finally, it is useful to remind that  
 5460 at this level, it is not possible yet to discriminate in between a muon hit and noise or gamma hit.  
 5461 the histograms `PeakCSize_H`, `PeakCMult_H` and `EfficiencyPeak_H` are then subjected to noise and  
 5462 background contamination. This contamination is estimated thanks to the fake efficiency histogram  
 5463 `EfficiencyFake_H` and corrected at the moment the results will be written into output CSV files and  
 5464 the histograms `MuonCSize_H`, `MuonCMult_H` and `Efficiency0_H` will be filled. The correction will be  
 5465 explained in Section B.6.4.3.

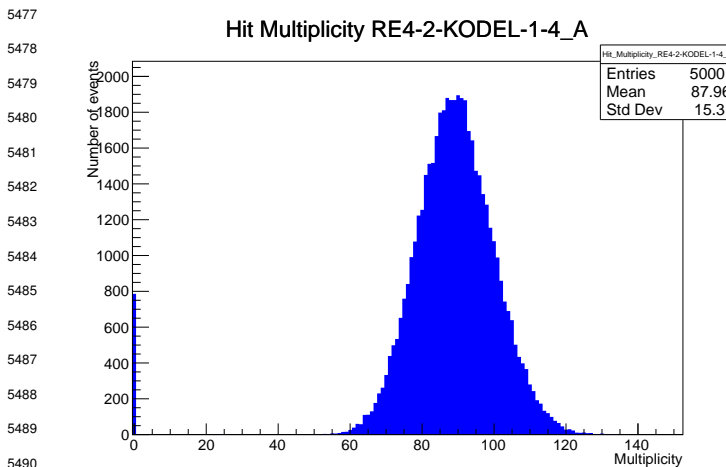
5466 Finally, the loop ends on the filling of the general hit multiplicity histogram of each detector  
 5467 partitions.

## 5468 B.6.4 Results calculation

5469 As mentioned in section B.2.1, the analysis of DAQ data provides the user with 3 CSV files and  
 5470 a ROOT file associated to each and every ROOT data file. The fourth CSV file is provided by the  
 5471 extraction of the CEAN main frame data monitored during data taking and will be discussed later.  
 5472 After looping on the data in the previous part of the analysis macro, the output files are created and a  
 5473 3D loop on each RPC readout partitions is started to extract the histograms parameters and compute  
 5474 the final results.

5475

### 5476 B.6.4.1 Rate normalisation



5491 *Figure B.2: The effect of the quality flag is explained by presenting the*  
 5492 *reconstructed hit multiplicity of a data file without `Quality_flag`. The*  
 5493 *artificial high content of bin 0 is the effect of corrupted data.*

The hit rate normalization corresponds to translating a number of hits recorded during the full duration of data taking into a rate per unit area value. In order to achieve such result, it is first needed to know the total integrated time and the active area of the read-out partition on which the hits are counted. The total integrated is simply the noise window used for each event multiplied by the total number of events stored in the data file.

Nevertheless, to analyse old data format files, not containing any quality flag, it is

needed to estimate the amount of corrupted data via a fit as the corrupted data will always fill events with a fake "0 multiplicity". Indeed, as no hits were stored in the DAQ ROOT files, these events artificially contribute to fill the bin corresponding to a null multiplicity, as shown in Figure B.2. In the case the mean of the hit multiplicity distribution is high, the contribution of the corrupted data can easily be evaluated for later correction by comparing the level of the bin at multiplicity 0 and of a skew fit curve that should indicate a value consistent with 0. A skew fit has been chosen over a Poisson fit as it was giving better results for lower mean multiplicity values. Nevertheless, for low irradiation cases, as explained in Appendix A.4.3, the hit multiplicity distribution mean is, on the contrary, rather small and the probability to record events without hits can't be considered small anymore, leading to a difficult and non-reliable estimation of the corruption.

```

5495
5496     needed to estimate the amount of corrupted data via a fit as the corrupted data will always fill events
5497     with a fake "0 multiplicity". Indeed, as no hits were stored in the DAQ ROOT files, these events
5498     artificially contribute to fill the bin corresponding to a null multiplicity, as shown in Figure B.2. In
5499     the case the mean of the hit multiplicity distribution is high, the contribution of the corrupted data
5500     can easily be evaluated for later correction by comparing the level of the bin at multiplicity 0 and
5501     of a skew fit curve that should indicate a value consistent with 0. A skew fit has been chosen over
5502     a Poisson fit as it was giving better results for lower mean multiplicity values. Nevertheless, for
5503     low irradiation cases, as explained in Appendix A.4.3, the hit multiplicity distribution mean is, on
5504     the contrary, rather small and the probability to record events without hits can't be considered small
5505     anymore, leading to a difficult and non-reliable estimation of the corruption.

5505
5506     if(!isNewFormat) {
5507         TF1* GaussFit = new TF1("gaussfit","[0]*exp(-0.5*((x-[1])/[2])**2)",0,Xmax);
5508         GaussFit->SetParameter(0,100);
5509         GaussFit->SetParameter(1,10);
5510         GaussFit->SetParameter(2,1);
5511         HitMultiplicity_H.rpc[T][S][p]->Fit(GaussFit,"LIQR","","",0.5,Xmax);

5512         TF1* SkewFit = new TF1("skewfit","[0]*exp(-0.5*((x-[1])/[2])**2) / (1 +
5513         <- exp(-[3]*(x-[4])))",0,Xmax);
5514         SkewFit->SetParameter(0,GaussFit->GetParameter(0));
5515         SkewFit->SetParameter(1,GaussFit->GetParameter(1));
5516         SkewFit->SetParameter(2,GaussFit->GetParameter(2));
5517         SkewFit->SetParameter(3,1);
5518         SkewFit->SetParameter(4,1);
5519         HitMultiplicity_H.rpc[T][S][p]->Fit(SkewFit,"LIQR","","",0.5,Xmax);

5520         double fitValue = SkewFit->Eval(1,0,0,0);
5521         double dataValue = (double)HitMultiplicity_H.rpc[T][S][p]->GetBinContent(2);
5522         double difference = TMath::Abs(dataValue - fitValue);
5523         double fitTOdataVSentries_ratio = difference / (double)nEntries;
5524         bool isFitGOOD = fitTOdataVSentries_ratio < 0.01;
5525         double nSinglehit = (double)HitMultiplicity_H.rpc[T][S][p]->GetBinContent(1);
5526         double lowMultRatio = nSinglehit / (double)nEntries;
5527         bool isMultLOW = lowMultRatio > 0.4;
5528         if(isFitGOOD && !isMultLOW){
5529             nEmptyEvent = HitMultiplicity_H.rpc[T][S][p]->GetBinContent(1);
5530             nPhysics = (int)SkewFit->Eval(0,0,0,0);
5531             if(nPhysics < nEmptyEvent)
5532                 nEmptyEvent = nEmptyEvent-nPhysics;
5533         }
5534     }
5535     double corrupt_ratio = 100.*(double)nEmptyEvent / (double)nEntries;
5536     outputCorrCSV << corrupt_ratio << '\t';
5537     float rate_norm = 0.;
5538     float stripArea = GIFInfra->GetStripGeo(tr,sl,p);

5539     if(IsEfficiencyRun(RunType)){
5540         float noiseWindow = BMTDCWINDOW - TIMEREJECT - 2*PeakWidth.rpc[T][S][p];
5541         rate_norm = (nEntries-nEmptyEvent)*noiseWindow*1e-9*stripArea;
5542     } else
5543         rate_norm = (nEntries-nEmptyEvent)*RDMNOISEWDW*1e-9*stripArea;

```

*Source Code B.15: Definition of the rate normalisation variable. It takes into account the number of non corrupted entries and the time window used for noise and background calculation, to estimate the total integrated time, and the strip active area to express the result as rate per unit area.*

5508 As can be seen in Source Code B.15, conditions have been applied to prevent bad fits and wrong  
 5509 corruption estimation in cases where :

- 5510 • The difference in between the data for multiplicity 1 and the corresponding fit value should be  
 5511 lower than 1% of the total amount of data :  $\frac{|n_{m=1} - sk(1)|}{N_{tot}} < 0.01$  where  $n_{m=1}$  is the number  
 5512 of entries with multiplicity 1,  $sk(1)$  the value of the skew fit, as defined by Formula 5.1, for  
 5513 multiplicity 1 and  $N_{tot}$  the total number of entries.
- 5514 • The amount of data contained in the multiplicity 0 bin should not exceed 40% of the total  
 5515 data content:  $\frac{n_{m=0}}{N_{tot}} \leq 0.4$  where  $n_{m=0}$  is the number of entries with multiplicity 0. This  
 5516 number has been determined to be the maximum to be able to separate the excess of data due  
 5517 to corruption from the hit multiplicity distribution.

5518 Those 2 conditions need to be fulfilled to estimate the corruption of old data format files. If the  
 5519 fit was successful, the level of corruption is written in `Offline-Corrupted.csv` and the number of  
 5520 corrupted entries, refered as the integer `nEmptyEvent`, is subtracted from the total number of entries  
 5521 when the rate normalisation factor is computed as explicitated in Source Code B.15. Note that for new  
 5522 data format files, the number of corrupted entries being set to 0, the definition of `rate_norm` stays  
 5523 valid.

#### 5524 B.6.4.2 Rate and activity

```
int nNoise = StripNoiseProfile_H.rpc[T][S][p]->GetEntries();
float averageNhit = (nNoise>0) ? (float)(nNoise/nStripsPart) : 1.;

for(Uint st = 1; st <= nStripsPart; st++){
    float stripRate =
        StripNoiseProfile_H.rpc[T][S][p]->GetBinContent(st)/rate_norm;
    float stripAct =
        StripNoiseProfile_H.rpc[T][S][p]->GetBinContent(st)/averageNhit;

    StripNoiseProfile_H.rpc[T][S][p]->SetBinContent(st,stripRate);
    StripActivity_H.rpc[T][S][p]->SetBinContent(st,stripAct);
}
```

5526 *Source Code B.16: Description of the loop that allows to set the content of each strip rate and strip activity  
 channel for each detector partition.*

5527 At this point, the strip rate histograms, `StripNoiseProfile_H.rpc[T][S][p]`, only contain an  
 5528 information about the total number of noise or background rate hits each channel received during the  
 5529 data taking. As described in Source Code B.16, a loop on the strip channels will be used to normalise  
 5530 the content of the rate distribution histogram for each detector partitions. The initial number of hits  
 5531 recorded for a given bin will be extracted and 2 values are computed.

- 5532 • The strip hit rate, defined as the number of hits recorded in the bin normalised like described  
 5533 in the previous section, using the variable `rate_norm` and the corresponding bin in histogram  
 5534 `StripNoiseProfile_H.rpc[T][S][p]` is updated, and
- 5535 • the strip activity, defined as the number of hits recorded in the bin normalised to the average  
 5536 number of hits per bin contained in the partition histogram, using the variable `averageNhit`.  
 5537 This value provides an information on the homogeneity of the detector response to the gamma

5538 background or of the detector noise. An activity of 1 corresponds to an average response.  
 5539 Above 1, the channel is more active than the average and bellow 1, the channel is less active.  
 5540 This value is filled in the histograms `StripActivity_H.rpc[T][S][p]`.

5541 On each detector partitions, which are read-out by a single FEE, all the channels are not pro-  
 5542 cessed by the same chip. Each chip can give a different noise response and hence, histograms using  
 5543 a chip binning are used to investigate chip related noise behaviours. The average values of the strip  
 5544 rate or activity grouped into a given chip are extracted using the using the function `GetChipBin()`  
 5545 and stored in dedicated histograms as described in Source Codes B.17 and B.18 respectively.

```
5546 float GetChipBin(TH1* H, Uint chip){  

  5547   Uint start = 1 + chip*NSTRIPSCHIP;  

   int nActive = NSTRIPSCHIP;  

   float mean = 0.;  

   for(Uint b = start; b <= (chip+1)*NSTRIPSCHIP; b++) {  

     float value = H->GetBinContent(b);  

     mean += value;  

     if(value == 0.) nActive--;  

   }  

   if(nActive != 0) mean /= (float)nActive;  

   else mean = 0.;  

   return mean;  

}
```

5548 *Source Code B.17: Function used to compute the content of a bin for an histogram using chip binning.*

```
5549 for(Uint ch = 0; ch < (nStripsPart/NSTRIPSCHIP); ch++) {  

  5550   ChipMeanNoiseProf_H.rpc[T][S][p]->  

    SetBinContent(ch+1,GetChipBin(StripNoiseProfile_H.rpc[T][S][p],ch));  

   ChipActivity_H.rpc[T][S][p]->  

    SetBinContent(ch+1,GetChipBin(StripActivity_H.rpc[T][S][p],ch));  

}
```

5550 *Source Code B.18: Description of the loop that allows to set the content of each chip rate and chip activi-  
 5551 ty bins for each detector partition knowing the information contained in the corresponding strip distribution  
 5552 histograms.*

5551 The activity variable is then used to evaluate the homogeneity of the detector response to back-  
 5552 ground or of the detector noise. The homogeneity  $h_p$  of each detector partition can be evaluated  
 5553 using the formula  $h_p = \exp(-\sigma_p^R / \langle R \rangle_p)$ , where  $\langle R \rangle_p$  is the partition mean rate and  $\sigma_p^R$  is the  
 5554 rate standard deviation calculated over the partition channels. The more homogeneously the rates  
 5555 are distributed and the smaller will  $\sigma_p^R$  be, and the closer to 1 will  $h_p$  get. On the contrary, if the  
 5556 standard deviation of the channel's rates is large,  $h_p$  will rapidly get to 0. This value is saved into  
 5557 histograms as shown in Source Code B.19 and could in the future be used to monitor through time,  
 5558 once extracted, the evolution of every partition homogeneity. This could be of great help to under-  
 5559 stand the apparition of eventual hot spots due to ageing of the chambers subjected to high radiation  
 5560 levels. The monitored homogeneity information could then be combined with a monitoring of the  
 5561 activity of each individual channel in order to have a finer information. Monitoring tools have been  
 5562 suggested and need to be developed for this purpose.

```

5563
float MeanPartSDev = GetTH1StdDev(StripNoiseProfile_H.rpc[T][S][p]);
float strip_homog = (MeanPartRate==0)
    ? 0.
    : exp(-MeanPartSDev/MeanPartRate);
StripHomogeneity_H.rpc[T][S][p]->Fill("exp -#left(#frac{\#sigma_{Strip
    \rightarrow Rate}}{\#mu_{(Strip Rate)}}\#right)",strip_homog);
StripHomogeneity_H.rpc[T][S][p]->GetYaxis()->SetRangeUser(0.,1.);

5564
float ChipStDevMean = GetTH1StdDev(ChipMeanNoiseProf_H.rpc[T][S][p]);
float chip_homog = (MeanPartRate==0)
    ? 0.
    : exp(-ChipStDevMean/MeanPartRate);
ChipHomogeneity_H.rpc[T][S][p]->Fill("exp -#left(#frac{\#sigma_{(Chip
    \rightarrow Rate}}{\#mu_{(Chip Rate)}}\#right)",chip_homog);
ChipHomogeneity_H.rpc[T][S][p]->GetYaxis()->SetRangeUser(0.,1.);
```

5565       *Source Code B.19: Storage of the homogeneity into dedicated histograms.*

#### 5566     B.6.4.3 Correction of muon performance parameters

5567 By previously filling the peak and fake efficiency histograms as well as the peak and noise cluster  
 5568 size and cluster multiplicity it is possible to compute the efficiency of muon detection, the muon  
 5569 cluster size, as well as the muon cluster multiplicity. This calculation is based on independant  
 5570 event probabilities. The independant events that can be measured in the data are, " $\mu$ : A muon was  
 5571 detected" and " $\gamma$ : noise or background was detected". It is trivial to realize that the data in the peak  
 5572 window corresponds to the intersection of both events, " $\mu \cup \gamma$ : a muon or noise or background was  
 5573 detected". This way, the efficiency measured in the peak window is actually the probability of the  
 5574 event  $\mu \cup \gamma$  while the efficiency in the fake window is then the probability of the event  $\gamma$  alone.  
 5575 Assuming that  $\mu$  and  $\gamma$  are independant, the probability of their intersection can be written as in  
 5576 Formula B.5.

$$(B.5) \quad P(\mu \cup \gamma) = P(\mu) + P(\gamma) - P(\mu)P(\gamma)$$

5577 Isolating the probability of the event  $\mu$  alone, actually corresponding to the muon detection  
 5578 efficiency, can be then calculated with the quantities that are contained in the peak and fake histogram  
 5579 as in Formula B.6.

$$(B.6) \quad P(\mu) = \frac{P(\mu \cup \gamma) - P(\gamma)}{1 - P(\gamma)} \quad \Leftrightarrow \quad \epsilon_\mu = \frac{\epsilon_{peak} - \epsilon_{fake}}{1 - \epsilon_{fake}}$$

5580 When it comes to the computation of the muon cluster size, a similar reasoning than for the muon  
 5581 detection efficiency computation can be used. Indeed, using Formula B.5, out of the total number of  
 5582 events where a muon or noise or background can be expressed as a sum of fractions of events  $\mu$ ,  $\gamma$   
 5583 and  $\mu \cap \gamma$ , the latter being the event corresponding to the detection of both events simultaneously, as  
 5584 showed in Formula B.7. The fractions can be expressed as a ratio of the probabilities already known,  
 5585 using this time the notation  $P(\mu \cap \gamma)$  instead of  $P(\mu)P(\gamma)$ . This choice was made to make the code  
 5586 a little clearer.

$$(B.7) \quad 1 = F_\mu + F_\gamma + F_{\mu \cap \gamma} = \frac{P(\mu) - P(\mu \cap \gamma)}{P(\mu \cup \gamma)} + \frac{P(\gamma) - P(\mu \cap \gamma)}{P(\mu \cup \gamma)} + \frac{P(\mu \cap \gamma)}{P(\mu \cup \gamma)}$$

```

if(IsEfficiencyRun(RunType)){  

    //Evaluate the probabilities for each detection case with errors  

    float P_peak = EfficiencyPeak_H.rpc[T][S][p]->GetMean();  

    float P_fake = EfficiencyFake_H.rpc[T][S][p]->GetMean();  

    float P_muon = (P_peak-P_fake)/(1-P_fake);  

    float P_both = P_muon*P_fake;  

    float P_peak_err = sqrt(P_peak*(1.-P_peak)/nEntries);  

    float P_fake_err = sqrt(P_fake*(1.-P_fake)/nEntries);  

    float P_muon_err = sqrt(P_muon*(1.-P_muon)/nEntries);  

    float P_both_err = sqrt(P_both*(1.-P_both)/nEntries);  

    Efficiency0_H.rpc[T][S][p]->Fill("muon efficiency",P_muon);  

    Efficiency0_H.rpc[T][S][p]->Fill("muon efficiency error",P_muon_err);  

    //For each case get the fraction of events it represents  

    float F_both = P_both/P_peak;  

    float F_muon = (P_muon-P_both)/P_peak;  

    float F_fake = (P_fake-P_both)/P_peak;  

    float F_both_err = F_both*(P_both_err/P_both+P_peak_err/P_peak);  

    float F_muon_err = (P_muon_err+F_both_err+F_muon*P_peak_err)/P_peak;  

    float F_fake_err = (P_fake_err+F_both_err+F_fake*P_peak_err)/P_peak;  

    //Get the measured cluster sizes correcting using the fractions  

    float CS_peak = PeakCSIZE_H.rpc[T][S][p]->GetMean();  

    float CS_fake = NoiseCSIZE_H.rpc[T][S][p]->GetMean();  

    float CS_peak_err = 2*PeakCSIZE_H.rpc[T][S][p]->GetStdDev()  

        /sqrt(PeakCSIZE_H.rpc[T][S][p]->GetEntries());  

    float CS_fake_err = 2*NoiseCSIZE_H.rpc[T][S][p]->GetStdDev()  

        /sqrt(NoiseCSIZE_H.rpc[T][S][p]->GetEntries());  

    float CS_muon = (CS_peak-CS_fake*(F_fake+F_both/2.))/(F_muon+F_both/2.);  

    float CS_muon_err = (CS_peak_err  

        +(F_fake+F_both/2.)*CS_fake_err  

        +CS_muon*F_muon_err  

        +CS_fake*(F_fake_err+F_both_err/2.))  

        /(F_muon+F_both/2.);  

    MuonCSIZE_H.rpc[T][S][p]->Fill("muon cluster size",CS_muon);  

    MuonCSIZE_H.rpc[T][S][p]->Fill("muon cluster size error",CS_muon_err);  

    //Finally get the muon cluster multiplicity as peak-fake  

    float noiseWindow = BMTDCWINDOW - TIMEREJECT - 2*PeakWidth.rpc[T][S][p];  

    float peakWindow = 2*PeakWidth.rpc[T][S][p];  

    float CM_peak = PeakCMult_H.rpc[T][S][p]->GetMean();  

    float CM_fake = NoiseCMult_H.rpc[T][S][p]->GetMean()*peakWindow/noiseWindow;  

    float CM_muon = CM_peak-CM_fake;  

    float CM_peak_err = 2*PeakCMult_H.rpc[T][S][p]->GetStdDev()  

        /sqrt(PeakCMult_H.rpc[T][S][p]->GetEntries());  

    float CM_fake_err = 2*NoiseCMult_H.rpc[T][S][p]->GetStdDev()  

        /sqrt(NoiseCMult_H.rpc[T][S][p]->GetEntries())  

        * peakWindow/noiseWindow;  

    float CM_muon_err = CM_peak_err + CM_fake_err;  

    MuonCMult_H.rpc[T][S][p]->Fill("muon cluster multiplicity",CM_muon);  

    MuonCMult_H.rpc[T][S][p]->Fill("muon cluster multiplicity  

    ↳ error",CM_muon_err);  

    //Write in the output CSV file  

    outputEffCSV << P_muon << '\t' << P_muon_err << '\t'  

        << CS_muon << '\t' << CS_muon_err << '\t'  

        << CM_peak << '\t' << CM_peak_err << '\t';
}

```

Source Code B.20: Analysis algorithm to compute muon efficiency, cluster size and multiplicity knowing the peak and fake efficiency, cluster size and multiplicity.

5589    Each ones of these events have an associated cluster size. The cluster size of the noise or back-  
 5590    ground already is measured thanks to the clusterization of the noise hit list. In the same way, the  
 5591    peak cluster size corresponds to the cluster measured for the event  $\mu \cup \gamma$ . Nevertheless, the cluster  
 5592    of the event  $\mu \cap \gamma$  is not known but it can be assumed that the probability of having more than 1  
 5593    noise or background cluster contained in the peak window is very low if the peak wondow duration  
 5594    is compared to the background rate that rarely seen to go beyond 2000 Hz/cm<sup>2</sup> [to be confirmed].  
 5595    Hence, the cluster size that is likely to be measured in such kind of event where both a muon and a  
 5596    background or noise cluster was recorded is the average of the muon cluster size and the background  
 5597    cluster size. The cluster size  $C_{\mu \cup \gamma}$  probed in the peak can then be written as in Formula B.8 and  
 5598    leads to the expression for the muon cluster size  $C_\mu$  written in Formula B.9.

$$(B.8) \quad C_{\mu \cup \gamma} = C_\mu F_\mu + C_\gamma F_\gamma + \frac{C_\mu + C_\gamma}{2} \times F_{\mu \cap \gamma}$$

$$(B.9) \quad C_\mu = \frac{C_{\mu \cup \gamma} - C_\gamma \times (F_\gamma + F_{\mu \cap \gamma}/2)}{F_\mu + F_{\mu \cap \gamma}/2}$$

5599    Finally, the computation of the muon cluster multiplicity comes quite naturally as the cluster  
 5600    multiplicity measured in the peak to which is subtracted the background cluster multiplpicity taken  
 5601    in a window of similar width. These calculations, as well as the error propagation that was not  
 5602    explicited here, can be seen going through Source Code B.20.

#### 5603    B.6.4.4 Strip masking tool

5604    The offline tool is automatically called at the end of each data taking to analyse the data and offer  
 5605    the shifter DQM histograms to control the data quality. After the histograms have been published  
 5606    online in the DQM page, the shifter can decide to mask noisy or dead channels that will contribute  
 5607    to bias the final rate calculation by editing the mask column of `ChannelsMapping.csv` as can be seen  
 5608    in Figure B.3.

5609    From the code point of view, the function `GetTH1Mean()` is used to retrieve the mean rate par-  
 5610    tition by partition after the rates have been calculated strip by strip and filled into the histograms  
 5611    `StripNoiseProfile_H.rpc[T][S][p]`, as described through Source Code B.21.

5612    Once the mask for each rejected channel has been updated, the shifter can manually run the  
 5613    offline tool again to update the DQM plots, now including the masked strips, as well the rate results  
 5614    written in the output CSV file `Offline-Rate.csv`. If not done during the shifts, the strip masking  
 5615    procedure needs to be carefully done by the person in charge of data analysis on the scans that were  
 5616    selected to produce the final results.

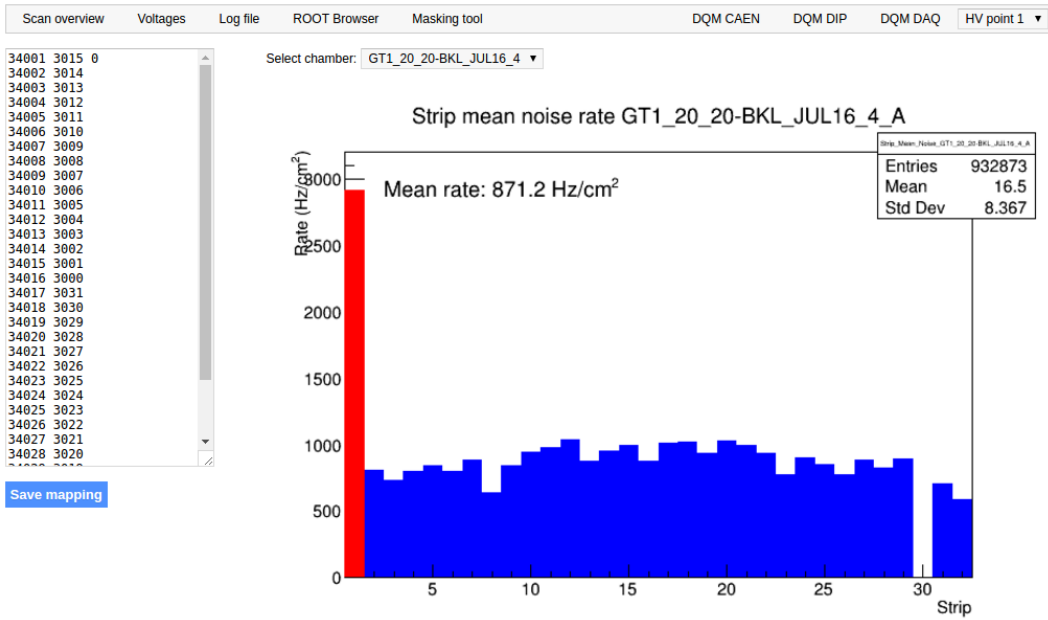


*Figure B.3: Display of the masking tool page on the webDCS. The window on the left allows the shifter to edit ChannelsMapping.csv. To mask a channel, it only is needed to set the 3rd field corresponding to the strip to mask to 0. It is not necessary for older mapping file formats to add a 1 for each strip that is not masked as the code is versatile and the default behaviour is to consider missing mask fields as active strips. The effect of the mask is directly visible for noisy channels as the corresponding bin turns red. The global effect of masking strips will be an update of the rate value showed on the histogram that will take into consideration the rejected channels.*

```

float GetTH1Mean (TH1* H){
    int nBins = H->GetNbinsX();
    int nActive = nBins;
    float mean = 0.;

    for(int b = 1; b <= nBins; b++){
        float value = H->GetBinContent (b);
        mean += value;
        if(value == 0.) nActive--;
    }

    if(nActive != 0) mean /= (float)nActive;
    else mean = 0.;

    return mean;
}

```

*Source Code B.21: The function GetTH1Mean() is used to return the mean along the y-axis of TH1 histograms containing rate information. In order to take into account masked strips whose rate is set to 0, the function looks for masked channels and decrement the number of active channels for each null value found.*

5619 **B.6.4.5 Output CSV files filling**

```

for (UInt tr = 0; tr < GIFInfra->GetNTrolleys(); tr++) {
    UInt T = GIFInfra->GetTrolleyID(tr);
    for (UInt sl = 0; sl < GIFInfra->GetNSlots(tr); sl++) {
        UInt S = GIFInfra->GetSlotID(tr,sl) - 1;
        float MeanNoiseRate = 0.;
        float ClusterRate = 0.;
        float ClusterSDev = 0.;

        for (UInt p = 0; p < GIFInfra->GetNPartitions(tr,sl); p++) {
            float MeanPartRate = GetTH1Mean(StripNoiseProfile_H.rpc[T][S][p]);
            float cSizePart = NoiseCSize_H.rpc[T][S][p]->GetMean();
            float cSizePartErr = (NoiseCSize_H.rpc[T][S][p]->GetEntries()==0)
                ? 0.
                : 2*NoiseCSize_H.rpc[T][S][p]->GetStdDev() /
                    sqrt(NoiseCSize_H.rpc[T][S][p]->GetEntries());
            float cMultPart = NoiseCMult_H.rpc[T][S][p]->GetMean();
            float cMultPartErr = (NoiseCMult_H.rpc[T][S][p]->GetEntries()==0)
                ? 0.
                : 2*NoiseCMult_H.rpc[T][S][p]->GetStdDev() /
                    sqrt(NoiseCMult_H.rpc[T][S][p]->GetEntries());
            float ClustPartRate = (cSizePart==0) ? 0.
                : MeanPartRate/cSizePart;
            float ClustPartRateErr = (cSizePart==0) ? 0.
                : ClustPartRate * cSizePartErr/cSizePart;

            outputRateCSV << MeanPartRate << '\t'
                << cSizePart << '\t' << cSizePartErr << '\t'
                << cMultPart << '\t' << cMultPartErr << '\t'
                << ClustPartRate << '\t' << ClustPartRateErr << '\t';

            RPCArea += stripArea * nStripsPart;
            MeanNoiseRate += MeanPartRate * stripArea * nStripsPart;
            ClusterRate += ClustPartRate * stripArea * nStripsPart;
            ClusterSDev += (cSizePart==0)
                ? 0.
                : ClusterRate*cSizePartErr/cSizePart;
        }
        MeanNoiseRate /= RPCArea;
        ClusterRate /= RPCArea;
        ClusterSDev /= RPCArea;
        outputRateCSV << MeanNoiseRate << '\t' << ClusterRate << '\t'
            << ClusterSDev << '\t';
    }
}

```

5621 *Source Code B.22: Description of rate result calculation and writing into the CSV output Offline-Rate.csv. Are saved into the file for each detector, the mean partition rate, cluster size and cluster mutiplicity, along with their errors, for each partition and as well as a detector average.*

5622 All the histograms have been filled. Parameters will then be extracted from them to compute the  
 5623 final results that will later be used to produce plots. Once the results have been computed, the very  
 5624 last step of the offline macro is to write these values into the corresponding CSV outputs. Aside of  
 5625 the file Offline-Corrupted.csv, 2 CSV files are being written by the macro OfflineAnalysis(),  
 5626 Offline-Rates.csv and Offline-L0-EffCl.csv that respectively contain information about noise  
 5627 or gamma rates, cluster size and multiplicity, and about level 0 reconstruction of the detector effi-  
 5628 ciency, muon cluster size and multiplicity. Details on the computation and file writing are respec-

5629 tively given in Sources Codes B.22 and B.20.

5630 **Noise/gamma background variables** are computed and written in the output file for each detector  
 5631 partitions. A detector average of the hit and cluster rate is also provided, as shown through Sources  
 5632 Code B.22. The variables that are written for each partition are:

- 5633 • The mean partition hit rate per unit area, `MeanPartRate`, that is extracted from the histogram  
`StripNoiseProfile_H` as the mean value along the y-axis, as described in section B.6.4.4. No  
 5634 error is recorded for the hit rate as this is considered a single measurement. No statistical error  
 5635 can be associated to it and the systematics are unknown.
- 5636 • The mean cluster size, `cSizePart`, is extracted from the histogram `NoiseCSize_H` and it's  
 5637 statistical error, `cSizePartErr`, is taken to be  $2\sigma$  of the total distribution.
- 5638 • The mean cluster multiplicity per trigger, `cMultPart`, is extracted from the histogram `NoiseCMult_H`  
 5639 and it's statistical error, `cMultPartErr`, is taken to be  $2\sigma$  of the total distribution. It is impor-  
 5640 tant to point to the fact that this variable gives an information that is dependent on the buffer  
 5641 window width used for each trigger for the calculation.
- 5642 • The mean cluster rate per unit area, `ClustPartRate`, is defined as the mean hit rate normalised  
 5643 to the mean cluster size and it's statistical error, `ClustPartRateErr`, is then obtained using the  
 5644 relative statistical error on the mean cluster size.

5645 **Muon performance variables** are computed as discussed in the Section B.6.4.3 and written in  
 5646 the output file for each detector partitions as shown through Sources Code B.20. It is reminded that  
 5647 this offline tool doesn't include any tracking algorithm to identify muons from the beam and only  
 5648 relies on the hits arriving in the time window corresponding to the beam time and is corrected thanks  
 5649 to the estimation of the contribution of the background and noise to the efficiency of the detector.  
 5650 Assuming that the detection of background and muons were independent events, a probabilistic  
 5651 approach was then used to correct efficiency, muon cluster size and muon cluster multiplicity. The  
 5652 variables that are written for each partition are:

- 5653 • The muon efficiency, referred to as the probability to detect a muon in the peak window  
`P_muon`, also filled in histogram `Efficiency0_H`. The statistical error related to the efficiency,  
 5654 `P_muon_err`, is computed using a binomial distribution, as the efficiency measures the proba-  
 5655 bility of "success" and "failure" to detect muons.
- 5656 • The mean muon cluster size, `CS_muon`, and its related statistical error, `CS_muon_err`, also filled  
 5657 in the histogram `MuonCSize_H`.
- 5658 • The mean muon cluster multiplicity, `CM_muon`, and its related statistical error, `CM_muon_err`,  
 5659 also filled in the histogram `MuonCMult_H`.

5660 In addition to these 2 CSV files, the histograms are saved in ROOT file `Scan00XXXX_HVY_Offline.root`  
 5661 as explained in section B.2.1.1.

## 5664 B.7 Current information extraction

5665 Detectors under test at GIF++ are connected both to a CAEN HV power supply and to a CAEN  
5666 ADC that reads the currents inside of the RPC gaps bypassing the supply cable. During data tak-  
5667 ing, the webDCS records into a ROOT file called `Scan00XXXX_HVY_CAEN.root` histograms with the  
5668 monitored parameters of both CAEN devices. Are recorded for each RPC channels (in most cases,  
5669 a channel corresponds to an RPC gap):

- 5670 • the effective voltage,  $HV_{eff}$ , set by the webDCS using the PT correction on the CAEN power  
5671 supply,
- 5672 • the applied voltage,  $HV_{app}$ , monitored by the CAEN power supply, and the statistical error  
5673 related to the variations of this value through time to follow the variation of the environmental  
5674 parameters defined as the RMS of the histogram divided by the square root of the number of  
5675 recorded points,
- 5676 • the monitored current,  $I_{mon}$ , monitored by the CAEN power supply, and the statistical error  
5677 related to the variations of this value through time to follow the variation of the environmental  
5678 parameters defined as the RMS of the histogram divided by the square root of the number of  
5679 recorded points,
- 5680 • the corresponding current density,  $J_{mon}$ , defined as the monitored current per unit area,  
5681  $J_{mon} = I_{mon}/A$ , where  $A$  is the active area of the corresponding gap,
- 5682 • the ADC current,  $I_{ADC}$ , recorded through the CAEN ADC module that monitors the dark  
5683 current in the gap itself. First of all, the resolution of such a module is better than that of  
5684 CAEN power supplies and moreover, the current is not read-out through the HV supply line  
5685 but directly at the chamber level giving the real current inside of the detector. The statistical  
5686 error is defined as the RMS of the histogram distribution divided by the square root of the  
5687 number of recorded points.

5688 Once extracted through a loop over the element of GIF++ infrastructure via the C++ macro  
5689 `GetCurrent()`, these parameters, organised in 9 columns per detector HV supply line, are written in  
5690 the output CSV file `Offline-Current.csv`. The macro can be found in the file `Current.cc`.

## References

- 5692 [1] K. Ruedenberg and W.H.E. Schwarz. “Three Millennia of Atoms and Molecules”. In: *Pio-*  
5693 *neers of Quantum Chemistry*. Ed. by E. Thomas Strom and Angela K. Wilson. Vol. 1122.  
5694 ACS Symposium Series, 2013, pp. 1–45.
- 5695 [2] A. Lavoisier. *Traité élémentaire de chimie*. Éditions la Bibliothèque Digitale, 2014 (first  
5696 published 1789).
- 5697 [3] J. Dalton. *A New System of Chemical Philosophy*. William Dawson and Sons, 1808.
- 5698 [4] J. von Fraunhofer. “Bestimmung des Brechungs- und des Farben-Zerstreuungs - Vermögens  
5699 verschiedener Glasarten, in Bezug auf die Vervollkommnung achromatischer Fernröhre”. In:  
5700 *Denkschriften der Königlichen Akademie der Wissenschaften zu München*. Die Akademie,  
5701 1817, pp. 193–226.
- 5702 [5] J.J. Thomson. “XL. Cathode Rays”. In: *The London, Edinburgh, and Dublin Philosophical  
5703 Magazine and Journal of Science* 44:269 (1897), pp. 293–316.
- 5704 [6] J.B. Perrin. “Nouvelles propriétés des rayons cathodiques”. In: *Comptes Rendus Hebdo-*  
5705 *madiques des Séances de L'Académie des Sciences*. Vol. 121. Académie des Sciences, 1895,  
5706 pp. 1130–1134.
- 5707 [7] H. Becquerel. “Déviation du rayonnement du radium dans un champ électrique”. In: *Comptes  
5708 Rendus Hebdomadaires des Séances de L'Académie des Sciences*. Vol. 130. Académie des  
5709 Sciences, 1900, p. 809.
- 5710 [8] J.J. Thomson. “XXIV. On the structure of the atom: an investigation of the stability and  
5711 periods of oscillation of a number of corpuscles arranged at equal intervals around the cir-  
5712 cumference of a circle; with application of the results to the theory of atomic structure”. In:  
5713 *The London, Edinburgh, and Dublin Philosophical Magazine and Journal of Science* 7:39  
5714 (1904), pp. 237–265.
- 5715 [9] E. Rutherford and T. Royds. “XXIV. Spectrum of the radium emanation”. In: *The Lon-*  
5716 *don, Edinburgh, and Dublin Philosophical Magazine and Journal of Science* 16:92 (1904),  
5717 pp. 313–317.
- 5718 [10] H. Geiger. “On the scattering of the  $\alpha$ -particles by matter”. In: *Proceedings of the Royal  
5719 Society A* 81 (1908), pp. 174–177.
- 5720 [11] H. Geiger and E. Marsden. “On a diffuse reflection of the  $\alpha$ -particles”. In: *Proceedings of  
5721 the Royal Society A* 82 (1909), pp. 495–500.
- 5722 [12] H. Geiger. “The scattering of  $\alpha$ -particles by matter”. In: *Proceedings of the Royal Society A*  
5723 83 (1910), pp. 492–504.
- 5724 [13] H. Geiger and E. Marsden. “LXI. The laws of deflexion of a particles through large angles”.  
5725 In: *The London, Edinburgh, and Dublin Philosophical Magazine and Journal of Science*  
5726 25:148 (1913), pp. 604–623.

- 5727 [14] E. Rutherford. "LXXIX. The Scattering of  $\alpha$  and  $\beta$  Particles by Matter and the Structure of  
5728 the Atom". In: *The London, Edinburgh, and Dublin Philosophical Magazine and Journal of*  
5729 *Science* 21:125 (1911), pp. 669–688.
- 5730 [15] E. Rutherford. "LIV. Collision of  $\alpha$  particles with light atoms. IV. An anomalous effect in  
5731 nitrogen". In: *The London, Edinburgh, and Dublin Philosophical Magazine and Journal of*  
5732 *Science* 37:222 (1919), pp. 581–587.
- 5733 [16] O. Masson. "XXIV. The constitution of atoms". In: *The London, Edinburgh, and Dublin*  
5734 *Philosophical Magazine and Journal of Science* 41:242 (1921), pp. 281–285.
- 5735 [17] W. Prout. "On the Relation between the Specific Gravities of Bodies in their Gaseous State  
5736 and the Weights of their Atoms." In: *Annals of Philosophy* 6 (1815), pp. 321–330.
- 5737 [18] W. Prout. "Correction of a Mistake in the Essay on the Relation between the Specific Gravities  
5738 of Bodies in their Gaseous State and the Weights of their Atoms". In: *Annals of Philoso-*  
5739 *phy* 7 (1816), pp. 111–113.
- 5740 [19] E. Rutherford. "Bakerian Lecture: Nuclear constitution of atoms". In: *Proceedings of the*  
5741 *Royal Society A* 97 (1920), pp. 374–400.
- 5742 [20] W. Bothe and H. Becker. "Künstliche Erregung von Kern- $\gamma$ -Strahlen". In: *Zeitschrift für*  
5743 *Physik* 66 (1930), pp. 289–306.
- 5744 [21] H. Becker and W. Bothe. "Die in Bor und Beryllium erregten  $\gamma$ -Strahlen". In: *Zeitschrift für*  
5745 *Physik* 76 (1932), pp. 421–438.
- 5746 [22] I. Curie and F. Joliot. "Émission de protons de grande vitesse par les substances hydro-  
5747 génées sous l'influence de rayons  $\gamma$  très pénétrants". In: *Comptes Rendus Hebdomadaires*  
5748 *des Séances de L'Académie des Sciences*. Vol. 194. Académie des Sciences, 1932, pp. 273–  
5749 275.
- 5750 [23] J. Chadwick. "Possible Existence of a Neutron". In: *Nature* 129 (1932), p. 312.
- 5751 [24] J. Chadwick. "Bakerian lecture. The neutron". In: *Proceedings of the Royal Society A* 142  
5752 (1933), pp. 1–25.
- 5753 [25] Max Plank. "Ueber das Gesetz der Energieverteilung im Normalspectrum". In: *Annalen Der*  
5754 *Physik* 309 (1901), pp. 553–563.
- 5755 [26] A. Einstein. "Über einen die Erzeugung und Verwandlung des Lichtes betreffenden heuris-  
5756 tischen Gesichtspunkt". In: *Annalen Der Physik* 322 (1905), pp. 132–148.
- 5757 [27] N. Bohr. "I. On the constitution of atoms and molecules". In: *The London, Edinburgh, and*  
5758 *Dublin Philosophical Magazine and Journal of Science* 26:151 (1913), pp. 1–25.
- 5759 [28] H.G.J. Moseley. "XCIII. The high-frequency spectra of the elements". In: *The London, Edin-  
5760 burgh, and Dublin Philosophical Magazine and Journal of Science* 26:156 (1913), pp. 1024–  
5761 1034.
- 5762 [29] A. Sommerfeld. "Zur Quantentheorie der Spektrallinien". In: *Annalen Der Physik* 356 (1916),  
5763 pp. 1–94.
- 5764 [30] P. Zeeman. "XXXII. On the influence of magnetism on the nature of the light emitted by a  
5765 substance". In: *The London, Edinburgh, and Dublin Philosophical Magazine and Journal of*  
5766 *Science* 43:262 (1897), pp. 226–239.
- 5767 [31] P. Zeeman. "VII. Doublets and triplets in the spectrum produced by external magnetic forces".  
5768 In: *The London, Edinburgh, and Dublin Philosophical Magazine and Journal of Science*  
5769 44:266 (1897), pp. 55–60.

## BIBLIOGRAPHY

---

- 5770 [32] P. Zeeman. "VII. Doublets and triplets in the spectrum produced by external magnetic forces.—(II.)" In: *The London, Edinburgh, and Dublin Philosophical Magazine and Journal of Science* 44:268 (1897), pp. 255–259.
- 5773 [33] P. Zeeman. "XXI. Measurements concerning radiation-phenomena in the magnetic field.—(I.)" In: *The London, Edinburgh, and Dublin Philosophical Magazine and Journal of Science* 45:273 (1898), pp. 197–201.
- 5776 [34] W. Gerlach and O. Stern. "Der experimentelle Nachweis der Richtungsquantelung im Magnetfeld". In: *Zeitschrift für Physik* 9 (1922), pp. 349–352.
- 5778 [35] W. Pauli. "Über den Einfluß der Geschwindigkeitsabhängigkeit der Elektronenmasse auf den Zeeman-Effekt". In: *Zeitschrift für Physik* 31 (1925), 373–385.
- 5780 [36] W. Pauli. "Über den Zusammenhang des Abschlusses der Elektronengruppen im Atom mit der Komplexstruktur der Spektren". In: *Zeitschrift für Physik* 31 (1925), 765–783.
- 5782 [37] G.E. Uhlenbeck and S. Goudsmit. "Spinning Electrons and the Structure of Spectra". In: *Nature* 117 (1926), pp. 264–265.
- 5784 [38] W. Pauli. "Zur Quantenmechanik des magnetischen Elektrons". In: *Zeitschrift für Physik* 43 (1927), 601–623.
- 5786 [39] L. De Broglie. "Recherches sur la théorie des Quanta". PhD thesis. University of Paris, 1924.
- 5787 [40] E. Schrödinger. "An Undulatory Theory of the Mechanics of Atoms and Molecules". In: *Phys. Rev.* 28 (1927), pp. 1049–1070.
- 5789 [41] P. Dirac. "The quantum theory of the emission and absorption of radiation". In: *Proceedings of the Royal Society A* 114 (1928), pp. 243–265.
- 5791 [42] P. Dirac. "The quantum theory of the electron". In: *Proceedings of the Royal Society A* 117 (1928), pp. 610–624.
- 5793 [43] J. R. Oppenheimer. "On the Theory of Electrons and Protons". In: *Phys. Rev.* 35 (1930), pp. 562–563.
- 5795 [44] P. Dirac. "Quantised singularities in the electromagnetic field". In: *Proceedings of the Royal Society A* 133 (1931), pp. 60–72.
- 5797 [45] J. R. Oppenheimer. "Note on the Theory of the Interaction of Field and Matter". In: *Phys. Rev.* 35 (1930), pp. 461–477.
- 5799 [46] H.A. Bethe. "The Electromagnetic Shift of Energy Levels". In: *Phys. Rev.* 72 (1947), pp. 339–341.
- 5801 [47] H.F.J. Dyson. "The Radiation Theories of Tomonaga, Schwinger, and Feynman". In: *Phys. Rev.* 75 (1949), pp. 486–502.
- 5803 [48] H. Yukawa. "On the Interaction of Elementary Particles. I". In: *Proc. Phys. Math. Soc. Jap.* 17 (1935), pp. 48–57.
- 5805 [49] C.D. Anderson and S.H. Neddermeyer. "Cloud Chamber Observations of Cosmic Rays at 4300 Meters Elevation and Near Sea-Level". In: *Phys. Rev.* 50 (1936), pp. 263–271.
- 5807 [50] S.H. Neddermeyer and C.D. Anderson. "Note on the Nature of Cosmic-Ray Particles". In: *Phys. Rev.* 51 (1937), pp. 884–886.
- 5809 [51] J.C. Street and E.C. Stevenson. "New Evidence for the Existence of a Particle of Mass Intermediate Between the Proton and Electron". In: *Phys. Rev.* 52 (1937), pp. 1003–1004.
- 5811 [52] C.M.G. Lattes et al. "Processes involving charged mesons". In: *Nature* 159 (1947), pp. 694–697.

- 5813 [53] C.M.G. Lattes et al. “Observations on the Tracks of Slow Mesons in Photographic Emulsions  
5814 (Part 1)”. In: *Nature* 160 (1947), pp. 453–456.
- 5815 [54] C.M.G. Lattes et al. “Observations on the Tracks of Slow Mesons in Photographic Emulsions  
5816 (Part 2)”. In: *Nature* 160 (1947), 486–492.
- 5817 [55] R. Blorklund et al. “High Energy Photons from Proton-Nucleon Collisions”. In: *Phys. Rev.*  
5818 77 (1950), pp. 213–218.
- 5819 [56] G.D. Rochester and C.C. Butler. “Evidence for the Existence of New Unstable Elementary  
5820 Particles”. In: *Nature* 160 (1947), 855–857.
- 5821 [57] A. Pais. “Some Remarks on the  $V$ -Particles”. In: *Phys. Rev.* 86 (1952), pp. 663–672.
- 5822 [58] M. Gell-Mann. “Symmetries of Baryons and Mesons”. In: *Phys. Rev.* 125 (1962), pp. 1067–  
5823 1084.
- 5824 [59] K. Nishijima and T. Nakano. “Charge Independence for  $V$ -particles”. In: *Progress of Theoretical  
5825 Physics* 10 (1953), 581–582.
- 5826 [60] K. Nishijima. “Charge Independence Theory of  $V$ -Particles”. In: *Progress of Theoretical  
5827 Physics* 13 (1955), pp. 285–304.
- 5828 [61] M. Gell-Mann. “The interpretation of the new particles as displaced charge multiplets”. In:  
5829 *Il Nuovo Cimento* 4 (1956), 848–866.
- 5830 [62] W. Heisenberg. “Über den Bau der Atomkerne. I”. In: *Zeitschrift für Physik* 77 (1932), 1–11.
- 5831 [63] V.E. Barnes et al. “Observation of a Hyperon with Strangeness Minus Three”. In: *Phys. Rev.  
5832 Lett.* 12 (1964), pp. 204–206.
- 5833 [64] M. Gell-Mann. “A schematic model of baryons and mesons”. In: *Physics Letters* 8 (1964),  
5834 pp. 214–215.
- 5835 [65] G. Zweig. *An SU(3) Model for Strong Interaction Symmetry and its Breaking*. Tech. rep.  
5836 CERN-TH-401. CERN, 1964.
- 5837 [66] G. Zweig. *An SU(3) Model for Strong Interaction Symmetry and its Breaking (II)*. Tech. rep.  
5838 CERN-TH-412. CERN, 1964.
- 5839 [67] E.D. Bloom et al. “High-Energy Inelastic  $e - p$  Scattering at  $6^\circ$  and  $10^\circ$ ”. In: *Phys. Rev. Lett.*  
5840 23 (1969), pp. 930–934.
- 5841 [68] M. Breidenbach et al. “Observed Behavior of Highly Inelastic Electron-Proton Scattering”.  
5842 In: *Phys. Rev. Lett.* 23 (1969), pp. 935–939.
- 5843 [69] B.J. Bjørken and S.L. Glashow. “Elementary particles and SU(4)”. In: *Physics Letters* 11  
5844 (1964), pp. 255–257.
- 5845 [70] S. Glashow et al. “Weak Interactions with Lepton-Hadron Symmetry”. In: *Phys. Rev. D* 2  
5846 (1970), pp. 1285–1292.
- 5847 [71] J.H. Christenson et al. “Evidence for the  $2\pi$  Decay of the  $K_2^0$  Meson”. In: *Phys. Rev. Lett.* 13  
5848 (1964), pp. 138–140.
- 5849 [72] M. Kobayashi and T. Maskawa. “ $CP$ -Violation in the Renormalizable Theory of Weak Interac-  
5850 tion”. In: *Progress of Theoretical Physics* 49 (1973), pp. 652–657.
- 5851 [73] H. Harari. “A new quark model for hadrons”. In: *Physics Letters B* 57 (1975), pp. 265–269.
- 5852 [74] B. Richter et al. “Discovery of a Narrow Resonance in  $e^+e^-$  Annihilation”. In: *Phys. Rev.  
5853 Lett.* 33 (1974), pp. 1406–1408.
- 5854 [75] S. Ting et al. “Experimental Observation of a Heavy Particle  $J$ ”. In: *Phys. Rev. Lett.* 33  
5855 (1974), pp. 1404–1405.

## BIBLIOGRAPHY

---

- 5856 [76] S.W. Herb et al. “Observation of a Dimuon Resonance at 9.5 GeV in 400 GeV Proton-  
5857 Nucleus Collisions”. In: *Phys. Rev. Lett.* 39 (1977), pp. 252–255.
- 5858 [77] S. Abashi et al. “Search for High Mass Top Quark Production in  $\bar{p}p$  Collisions at  $\sqrt{s} =$   
5859 1.8 TeV”. In: *Phys. Rev. Lett.* 74 (1995), pp. 2422–2426.
- 5860 [78] F. Abe et al. “Observation of Top Quark Production in  $\bar{p}p$  Collisions with the Collider De-  
5861 tector at Fermilab”. In: *Phys. Rev. Lett.* 74 (1995), pp. 2626–2631.
- 5862 [79] F. Tkachov. “A contribution to the history of quarks: Boris Struminsky’s 1965 JINR publi-  
5863 cation”. In: (2009).
- 5864 [80] O.W. Greenberg. “Spin and Unitary-Spin Independence in a Paraquark Model of Baryons  
5865 and Mesons”. In: *Phys. Rev. Lett.* 13 (1964), pp. 598–602.
- 5866 [81] M.Y. Han and Y. Nambu. “Three-Triplet Model with Double  $SU(3)$  Symmetry”. In: *Phys.*  
5867 *Rev.* 139 (1965), B1006–B1010.
- 5868 [82] R.P. Feynman. “The behavior of hadron collisions at extreme energies”. In: *Conf. Proc.*  
5869 *C690905* (1969), pp. 237–258.
- 5870 [83] J.D. Bjorken and E.A. Paschos. “Inelastic Electron-Proton and  $\gamma$ -Proton Scattering and the  
5871 Structure of the Nucleon”. In: *Phys. Rev.* 185 (1969), pp. 1975–1982.
- 5872 [84] H. Fritzsch et al. “Advantages of the color octet gluon picture”. In: *Physics Letters B* 47  
5873 (1973), pp. 365–368.
- 5874 [85] D.J. Gross and F. Wilczek. “Ultraviolet Behavior of Non-Abelian Gauge Theories”. In: *Phys.*  
5875 *Rev. Lett.* 30 (1973), pp. 1343–1346.
- 5876 [86] H.D. Politzer. “Reliable Perturbative Results for Strong Interactions?” In: *Phys. Rev. Lett.* 30  
5877 (1973), pp. 1346–1349.
- 5878 [87] S. Bethke. “ $\alpha_s$  2002”. In: *Nuclear Physics B* 121 (2003), pp. 74–81.
- 5879 [88] E. Fermi. “Versuch einer Theorie der  $\beta$ -Strahlen. I”. In: *Zeitschrift für Physik* 88 (1934),  
5880 pp. 161–177.
- 5881 [89] W. Pauli. “Dear radioactive ladies and gentlemen”. In: *Phys. Today* 31N9 (1978), p. 27.
- 5882 [90] C.L. Cowan Jr. et al. “Detection of the Free Neutrino: a Confirmation”. In: *Science* 20 (1956),  
5883 pp. 103–104.
- 5884 [91] E.J. Konopinski and H.M. Mahmoud. “The Universal Fermi Interaction”. In: *Phys. Rev.* 92  
5885 (1953), pp. 1045–1049.
- 5886 [92] L.M. Lederman et al. “Observation of High-Energy Neutrino Reactions and the Existence of  
5887 Two Kinds of Neutrinos”. In: *Phys. Rev. Lett.* 9 (1962), pp. 36–44.
- 5888 [93] T.D. Lee and C.N. Yang. “Question of Parity Conservation in Weak Interactions”. In: *Phys.*  
5889 *Rev.* 104 (1956), pp. 254–258.
- 5890 [94] G. Gamow and E. Teller. “Selection Rules for the  $\beta$ -Disintegration”. In: *Phys. Rev.* 49 (1936),  
5891 pp. 895–899.
- 5892 [95] C.S. Wu et al. “Experimental Test of Parity Conservation in Beta Decay”. In: *Phys. Rev.* 105  
5893 (1957), pp. 1413–1415.
- 5894 [96] S. Weinberg. “A Model of Leptons”. In: *Phys. Rev. Lett.* 19 (1967), pp. 1264–1266.
- 5895 [97] Y. Nambu and G. Jona-Lasinio. “Dynamical Model of Elementary Particles Based on an  
5896 Analogy with Superconductivity. I”. In: *Phys. Rev.* 122 (1961), pp. 345–358.
- 5897 [98] Y. Nambu and G. Jona-Lasinio. “Dynamical Model of Elementary Particles Based on an  
5898 Analogy with Superconductivity. II”. In: *Phys. Rev.* 124 (1961), pp. 246–254.

- 5899 [99] J. Bardeen et al. “Microscopic Theory of Superconductivity”. In: *Phys. Rev.* 106 (1957),  
 5900 pp. 162–164.
- 5901 [100] Y. Nambu. “Quasi-Particles and Gauge Invariance in the Theory of Superconductivity”. In:  
 5902 *Phys. Rev.* 117 (1960), pp. 648–663.
- 5903 [101] J. Goldstone. “Quasi-Particles and Gauge Invariance in the Theory of Superconductivity”.  
 5904 In: *Il Nuovo Cimento* 19 (1961), pp. 154–164.
- 5905 [102] P.W. Anderson. “Plasmons, Gauge Invariance, and Mass”. In: *Phys. Rev.* 130 (1963), pp. 439–  
 5906 442.
- 5907 [103] J. Schwinger. “Gauge Invariance and Mass”. In: *Phys. Rev.* 125 (1962), pp. 397–398.
- 5908 [104] F. Englert and R. Brout. “Broken Symmetry and the Mass of Gauge Vector Mesons”. In:  
 5909 *Phys. Rev. Lett.* 13 (1964), pp. 321–323.
- 5910 [105] P.W. Higgs. “Broken Symmetries and the Masses of Gauge Bosons”. In: *Phys. Rev. Lett.* 13  
 5911 (1964), pp. 508–509.
- 5912 [106] G.S. Guralnik et al. “Global Conservation Laws and Massless Particles”. In: *Phys. Rev. Lett.*  
 5913 13 (1964), pp. 585–587.
- 5914 [107] Wikipedia. *Standard Model*. 2018. URL: [https://en.wikipedia.org/wiki/Standard\\_Model](https://en.wikipedia.org/wiki/Standard_Model).
- 5916 [108] UA1 Collaboration. “Experimental observation of isolated large transverse energy electrons  
 5917 with associated missing energy at  $s = 540 \text{ GeV}$ ”. In: *Physics Letters B* 122 (1983), pp. 103–  
 5918 116.
- 5919 [109] UA2 Collaboration. “Observation of single isolated electrons of high transverse momentum  
 5920 in events with missing transverse energy at the CERN pp collider”. In: *Physics Letters B* 122  
 5921 (1983), pp. 476–485.
- 5922 [110] UA1 Collaboration. “Experimental observation of lepton pairs of invariant mass around  
 5923  $95 \text{ GeV}/c^2$  at the CERN SPS collider”. In: *Physics Letters B* 126 (1983), pp. 398–410.
- 5924 [111] UA2 Collaboration. “Evidence for  $Z_0 \rightarrow e^+e^-$  at the CERN pp collider”. In: *Physics  
 5925 Letters B* 129 (1983), pp. 130–140.
- 5926 [112] ATLAS Collaboration. “Observation of a new particle in the search for the Standard Model  
 5927 Higgs boson with the ATLAS detector at the LHC”. In: *Physics Letters B* 716 (2012), pp. 1–  
 5928 29.
- 5929 [113] CMS Collaboration. “Observation of a new boson at a mass of 125 GeV with the CMS  
 5930 experiment at the LHC”. In: *Physics Letters B* 716 (2012), pp. 30–61.
- 5931 [114] ATLAS Collaboration and CMS Collaboration. “Combined Measurement of the Higgs Bo-  
 5932 son Mass in  $pp$  Collisions at  $\sqrt{s} = 7$  and 8 TeV with the ATLAS and CMS Experiments”.  
 5933 In: *Physical Review Letters* 114 (2015). 191803.
- 5934 [115] M. Tanabashi et al. (Particle Data Group). “Review of Particle Physics”. In: *Phys. Rev. D* 98  
 5935 (2018), p. 030001.
- 5936 [116] A.A. Arkhipov. “Proton proton total cross-sections from the window of cosmic ray experi-  
 5937 ments”. In: *Elastic and diffractive scattering. Proceedings, 9th Blois Workshop, Pruhonice,  
 5938 Czech Republic*. 2001, pp. 293–304.
- 5939 [117] H. Pointcaré. “The Milky Way and the Theory of Gases”. In: *Popular Astronomy* 14 (1906),  
 5940 pp. 475–488.
- 5941 [118] J.C. Kapteyn. “First Attempt at a Theory of the Arrangement and Motion of the Sidereal  
 5942 System”. In: *Astrophysical Journal* 55 (1922), p. 302.

## BIBLIOGRAPHY

---

- 5943 [119] F. Zwicky. “Republication of: The redshift of extragalactic nebulae (First published in  
5944 1933)”. In: *General Relativity and Gravitation* 41 (2009), pp. 207–224.
- 5945 [120] F. Zwicky. “On the Masses of Nebulae and of Clusters of Nebulae”. In: *Astrophysical Journal* 86 (1937), p. 217.
- 5947 [121] H.W. Babcock. “The rotation of the Andromeda Nebula”. In: *Lick Observatory bulletin* 498  
5948 (1939), pp. 41–51.
- 5949 [122] V.C. Rubin and W.K. Ford Jr. “Rotation of the Andromeda Nebula from a Spectroscopic  
5950 Survey of Emission Regions”. In: *Astrophysical Journal* 159 (1970), p. 379.
- 5951 [123] D.H. Rogstad and G.S. Shostak. “Gross Properties of Five Scd Galaxies as Determined from  
5952 21-CENTIMETER Observations”. In: *Astrophysical Journal* 176 (1972), p. 315.
- 5953 [124] Planck Collaboration. “Planck 2015 results. XIII. Cosmological parameters”. In: *A&A* 594.A13  
5954 (2016).
- 5955 [125] N. Jarosik et al. “Seven-year Wilkinson Microwave Anisotropy Probe (WMAP\*) observa-  
5956 tions: Sky maps, Systematic errors, and Basic Results”. In: *ApJS* 192.14 (2011).
- 5957 [126] E. Verlinde. “Emergent Gravity and the Dark Universe”. In: *SciPost Phys.* 2 (2017), p. 016.
- 5958 [127] A. Maeder. “An alternative to the  $\Lambda$ CDM model: the case of scale invariance”. In: *ApJ*  
5959 834.194 (2017).
- 5960 [128] E. Corbelli and P. Salucci. “The extended rotation curve and the dark matter halo of M33”.  
5961 In: *Monthly Notices of the Royal Astronomical Society* 311 (2000), pp. 441–447.
- 5962 [129] S. Dimopoulos and H. Georgi. “Softly broken supersymmetry and SU(5)”. In: *Nuclear  
5963 Physics B* 193 (1981), pp. 150–162.
- 5964 [130] F. Tanedo. *The Hierarchy Problem: why the Higgs has a snowball’s chance in hell*. 2012.  
5965 URL: [https://www.quantumdiaries.org/2012/07/01/the-hierarchy-  
5966 problem-why-the-higgs-has-a-snowballs-chance-in-hell/](https://www.quantumdiaries.org/2012/07/01/the-hierarchy-problem-why-the-higgs-has-a-snowballs-chance-in-hell/).
- 5967 [131] G. Jungman et al. “Supersymmetric dark matter”. In: *Physics Reports* 267 (1996), pp. 10–  
5968 14.
- 5969 [132] A.H. Chamseddine et al. “Locally Supersymmetric Grand Unification”. In: *Phys. Rev. Lett.*  
5970 49 (1982), pp. 970–974.
- 5971 [133] A. Askew et al. “Searching for dark matter at hadron colliders”. In: *International Journal  
5972 of Modern Physics A* 29 (2014), p. 1430041.
- 5973 [134] N. Arkani-Hamed et al. “The hierarchy problem and new dimensions at a millimeter”. In:  
5974 *Physics Letters B* 429 (1998), pp. 263–272.
- 5975 [135] N. Arkani-Hamed et al. “Phenomenology, astrophysics, and cosmology of theories with  
5976 submillimeter dimensions and TeV scale quantum gravity”. In: *Phys. Rev. D* 59 (1999),  
5977 p. 086004.
- 5978 [136] T. Kaluza. “Zum Unitätsproblem der Physik”. In: *Sitzungsber. Preuss. Akad. Wiss. Berlin  
5979 (Math. Phys.)* 1921 (1921), pp. 966–972.
- 5980 [137] O. Klein. “The Atomicity of Electricity as a Quantum Theory Law”. In: *Nature* 118 (1926),  
5981 p. 516.
- 5982 [138] L. Randall and R. Sundrum. “Large Mass Hierarchy from a Small Extra Dimension”. In:  
5983 *Phys. Rev. Lett.* 83 (1999), pp. 3370–3373.
- 5984 [139] L. Randall and R. Sundrum. “An Alternative to Compactification”. In: *Phys. Rev. Lett.* 83  
5985 (1999), pp. 4690–4693.

- 5986 [140] M. Strassler and K. Zurek. “Echoes of a hidden valley at hadron colliders”. In: *Phys. Let. B*  
 5987 651 (2007), pp. 374–379.
- 5988 [141] A. Sakharov. “Violation of CP i variance, C asymmetry, and baryon asymmetry of the uni-  
 5989 verse”. In: *JETP Letters* 5 (1967), pp. 24–27.
- 5990 [142] M.E. Shaposhnikov and G. Farrar. “Baryon asymmetry of the Universe in the minimal stan-  
 5991 dard model”. In: *Phys. Rev. Lett.* 70 (1993), pp. 2833–2836.
- 5992 [143] V.A. Kuzmin et al. “On anomalous electroweak baryon-number non-conservation in the  
 5993 early universe”. In: *Physics Letters B* 155 (1985), pp. 36–42.
- 5994 [144] L. Canetti et al. “Matter and antimatter in the universe”. In: *New J. Phys.* 14.095012 (2012).
- 5995 [145] CMS Collaboration. “Search for black holes and sphalerons in high-multiplicity final states  
 5996 in proton-proton collisions at  $\sqrt{s} = 13$  TeV”. In: *Journal of High Energy Physics* 11 (2018).
- 5997 [146] B. Shuve and Y. Cui. “Probing baryogenesis with displaced vertices at the LHC”. In: *Journal  
 5998 of High Energy Physics* 2 (2015).
- 5999 [147] The ACME Collaboration. “Order of Magnitude Smaller Limit on the Electric Dipole Mo-  
 6000 ment of the Electron”. In: *Science* 343 (2014), pp. 269–272.
- 6001 [148] N. Neri et al. “On the search for the electric dipole moment of strange and charm baryons  
 6002 at LHC”. In: *The European Physical Journal C* 77 (2017), p. 181.
- 6003 [149] J. Stevens and M. Sher. “Detecting a heavy neutrino electric dipole moment at the LHC”.  
 6004 In: *Physics Letters B* 777 (2018), pp. 246–249.
- 6005 [150] R. Davis Jr. et al. “Search for Neutrinos from the Sun”. In: *Physical Review Letters* 20  
 6006 (1968), pp. 1205–1209.
- 6007 [151] B. Pontecorvo. “Neutrino Experiments and the Problem of Conservation of Leptonic Charge”.  
 6008 In: *Sov. Phys. JETP* 26 (1968), pp. 984–988.
- 6009 [152] SNO Collaboration. “Direct Evidence for Neutrino Flavor Transformation from Neutral-  
 6010 Current Interactions in the Sudbury Neutrino Observatory”. In: *Physical Review Letters*  
 6011 89.011301 (2002).
- 6012 [153] Z. Maki et al. “Remarks on the Unified Model of Elementary Particles”. In: *Progress of  
 6013 Theoretical Physics* 28 (1962), pp. 870–880.
- 6014 [154] P. Minkowski. “ $\mu \rightarrow e\gamma$  at a rate of one out of  $10^9$  muon decays?” In: *Physics Letters B*  
 6015 67 (1977), pp. 421–428.
- 6016 [155] R.N. Mohapatra and G. Senjanović. “Neutrino Mass and Spontaneous Parity Nonconserva-  
 6017 tion”. In: *Phys. Rev. Lett.* 44 (1980), pp. 912–915.
- 6018 [156] CERN. Geneva. LHC Experiments Committee. *CMS Physics Technical Design Report Vol-  
 6019 ume II: Physics Performance*. Tech. rep. CERN-LHCC-2006-021 ; CMS-TDR-8-2. CMS  
 6020 Collaboration, 2006.
- 6021 [157] P.W.F. Valle. “Neutrino physics overview”. In: *J. Phys.: Conf. Ser.* 53 (2006), pp. 473–505.
- 6022 [158] T. Massam et al. “Experimental observation of antideuteron production”. In: *Il Nuovo Ci-  
 6023 mento A* 63 (1965), pp. 10–14.
- 6024 [159] ALEPH Collaboration. “Determination of the number of light neutrino species”. In: *Physics  
 6025 Letters B* 231 (1989), pp. 519–529.
- 6026 [160] CERN, ed. (1985).
- 6027 [161] CERN, ed. (1986).
- 6028 [162] CERN, ed. (1994).

---

## BIBLIOGRAPHY

---

- 6029 [163] CERN, ed. (1998).
- 6030 [164] CERN, ed. (1999).
- 6031 [165] CERN. Geneva. LHC Experiments Committee. *Letter of Intent for A Large Ion Collider*  
6032 *Experiment [ALICE]*. Tech. rep. CERN-LHCC-93-016. ALICE Collaboration, 1993.
- 6033 [166] CERN. Geneva. LHC Experiments Committee. *ATLAS : technical proposal for a general-*  
6034 *purpose pp experiment at the Large Hadron Collider at CERN*. Tech. rep. CERN-LHCC-94-  
6035 43. ATLAS Collaboration, 1994.
- 6036 [167] CERN. Geneva. LHC Experiments Committee. *CMS : letter of intent by the CMS Col-*  
6037 *laboration for a general purpose detector at LHC*. Tech. rep. CERN-LHCC-92-003. CMS  
6038 Collaboration, 1992.
- 6039 [168] CERN. Geneva. LHC Experiments Committee. *LHCb : letter of intent*. Tech. rep. CERN-  
6040 LHCC-95-5. LHCb Collaboration, 1995.
- 6041 [169] L. Evans and P. Bryant. “LHC Machine”. In: *JINST* 3 (2008). S08001.
- 6042 [170] LHCb Collaboration. “Observation of  $J/\psi p$  Resonances Consistent with Pentaquark States  
6043 in  $\Lambda_b^0 \rightarrow J/\psi K^- p$  Decays”. In: *Physical Review Letters* 115 (2015). 072001.
- 6044 [171] LHCb Collaboration. “Observation of  $J/\psi\phi$  Structures Consistent with Exotic States from  
6045 Amplitude Analysis of  $B^+ \rightarrow J/\psi\phi K^+$  Decays”. In: *Physical Review Letters* 118 (2017).  
6046 022003.
- 6047 [172] ALICE Collaboration. *First results from proton-lead collisions*. URL: <http://aliceinfo.cern.ch/Public/en/Chapter1/results-pPb.html>.
- 6048
- 6049 [173] ATLAS Collaboration. “Observation of a New  $\chi_b$  State in Radiative Transitions to  $\Upsilon(1S)$   
6050 and  $\Upsilon(2S)$  at ATLAS”. In: *Physical Review Letters* 108 (2012). 152001.
- 6051 [174] LHCb Collaboration. “First Evidence for the Decay  $B_s^0 \rightarrow \mu^+\mu^-$ ”. In: *Physical Review*  
6052 *Letters* 110 (2013). 021801.
- 6053 [175] CERN. Geneva. *High-Luminosity Large Hadron Collider (HL-LHC) Technical Design Re-*  
6054 *port V. 0.1*. Tech. rep. CERN-2017-007-M. 2017.
- 6055 [176] CERN. Geneva. LHC Experiments Committee. *CMS, the Compact Muon Solenoid : tech-*  
6056 *nical proposal*. Tech. rep. CERN-2015-005. 2015.
- 6057 [177] CERN. Geneva. LHC Experiments Committee. *The Phase-2 Upgrade of the CMS Muon*  
6058 *Detectors*. Tech. rep. CERN-LHCC-2017-012, CMS-TDR-016. CMS Collaboration, 2017.
- 6059 [178] R. Santonico and R. Cardarelli. “Development of resistive plate counters”. In: *Nucl. Instr.*  
6060 *Meth. Phys. Res.* 187 (1981), pp. 377–380.
- 6061 [179] Yu.N. Pestov and G.V. Fedotovich. *A picosecond time-of-flight spectrometer fot eh VEPP-*  
6062 *2M based on local-discharge spark counter*. Tech. rep. SLAC-TRANS-0184. SLAC, 1978.
- 6063 [180] W.W. Ash, ed. *Spark Counter With A Localized Discharge*. Vol. SLAC-R-250. 1982, pp. 127–  
6064 131.
- 6065 [181] I. Crotty et al. “The non-spark mode and high rate operation of resistive parallel plate cham-  
6066 bers”. In: *NIMA* 337 (1993), pp. 370–381.
- 6067 [182] I. Crotty et al. “Further studies of avalanche mode operation of resistive parallel plate cham-  
6068 bers”. In: *NIMA* 346 (1994), pp. 107–113.
- 6069 [183] R. Cardarelli et al. “Avalanche and streamer mode operation of resistive plate chambers”.  
6070 In: *NIMA* 382 (1996), pp. 470–474.

- 6071 [184] R. Cardarelli et al. “Performance of a resistive plate chamber operating with pure  $CF_3Br$ ”.  
 6072 In: *NIMA* 333 (1993), pp. 399–403.
- 6073 [185] M. Abbrescia et al. “Performance of a Resistive Plate Chamber operated in avalanche mode  
 6074 under  $^{137}Cs$  irradiation”. In: *NIMA* 392 (1997), pp. 155–160.
- 6075 [186] M. Abbrescia et al. “Properties of C2H2F4-based gas mixture for avalanche mode operation  
 6076 of resistive plate chambers”. In: *NIMA* 398 (1997), pp. 173–179.
- 6077 [187] P. Camarri et al. “Streamer suppression with SF6 in RPCs operated in avalanche mode”. In:  
 6078 *NIMA* 414 (1998), pp. 317–324.
- 6079 [188] E. Cerron Zeballos et al. “Effect of adding SF6 to the gas mixture in a multigap resistive  
 6080 plate chamber”. In: *NIMA* 419 (1998), pp. 475–478.
- 6081 [189] E. Cerron Zeballos et al. “A new type of resistive plate chamber: The multigap RPC”. In:  
 6082 *NIMA* 374 (1996), pp. 132–135.
- 6083 [190] M.C.S. Williams. “The development of the multigap resistive plate chamber”. In: *Nucl.  
 6084 Phys. B* 61 (1998), pp. 250–257.
- 6085 [191] H. Czyrkowski et al. “New developments on resistive plate chambers for high rate opera-  
 6086 tion”. In: *NIMA* 419 (1998), pp. 490–496.
- 6087 [192] CERN. Geneva. LHC Experiments Committee. *The CMS muon project : Technical Design  
 6088 Report*. Tech. rep. CERN-LHCC-97-032. CMS Collaboration, 1997.
- 6089 [193] CERN. Geneva. LHC Experiments Committee. *ATLAS muon spectrometer: Technical de-  
 6090 sign report*. Tech. rep. CERN-LHCC-97-22. ATLAS Collaboration, 1997.
- 6091 [194] CERN. Geneva. LHC Experiments Committee. *ALICE Time-Of-Flight system (TOF) : Tech-  
 6092 nical Design Report*. Tech. rep. CERN-LHCC-2000-012. ALICE Collaboration, 2000.
- 6093 [195] The CALICE collaboration. “First results of the CALICE SDHCAL technological proto-  
 6094 type”. In: *JINST* 11 (2016).
- 6095 [196] PoS, ed. *Density Imaging of Volcanoes with Atmospheric Muons using GRPCs*. International  
 6096 Europhysics Conference on High Energy Physics - HEP 2011. 2011.
- 6097 [197] C. Lippmann. “Detector Physics of Resistive Plate Chambers”. PhD thesis. Johann Wolf-  
 6098 gang Goethe-Universität, 2003.
- 6099 [198] W. Riegler. “Induced signals in resistive plate chambers”. In: *NIMA* 491 (2002), pp. 258–  
 6100 271.
- 6101 [199] M. Abbrescia et al. “Effect of the linseed oil surface treatment on the performance of resis-  
 6102 tive plate chambers”. In: *NIMA* 394 (1997), pp. 13–20.
- 6103 [200] G.Battistoni et al. “Sensitivity of streamer mode to single ionization electrons”. In: *NIMA*  
 6104 235 (1985), pp. 91–97.
- 6105 [201] The European Parliament and the Council of the European Union. “Regulation (EU) No  
 6106 517/2014 of 16 April 2014 on fluorinated greenhouse gases and repealing Regulation (EC)  
 6107 No 842/2006”. In: *Official Journal of the European Union* 150 (2014), pp. 195–230.
- 6108 [202] Honeywell International Inc. *Solstice(R) ze Refrigerant (HFO-1234ze): The Environmental  
 6109 Alternative to Traditional Refrigerants*. Tech. rep. FPR-003/2015-01. 2015.
- 6110 [203] D. Piccolo. *Preliminary results of Resistive Plate Chambers operated with eco-friendly gas  
 6111 mixtures for application in the CMS experiment*. 2016. URL: <https://indico.ugent.be/event/0/session/18/contribution/28/material/slides/0.pdf>.
- 6113 [204] E. Cerron Zeballos et al. “A comparison of the wide gap and narrow gap resistive plate  
 6114 chamber”. In: *NIMA* 373 (1996), pp. 35–42.

## BIBLIOGRAPHY

---

- 6115 [205] M. Abbrescia et al. “Cosmic ray tests of double-gap resistive plate chambers for the CMS  
6116 experiment”. In: *NIMA* 550 (2005), pp. 116–126.
- 6117 [206] ALICE Collaboration. “A study of the multigap RPC at the gamma irradiation facility at  
6118 CERN”. In: *NIMA* 490 (2002), pp. 58–70.
- 6119 [207] B. Bonner et al. “A multigap resistive plate chamber prototype for time-of-flight for the  
6120 STAR experiment at RHIC”. In: *NIMA* 478 (2002), pp. 176–179.
- 6121 [208] S. Yang et al. “Test of high time resolution MRPC with different readout modes for the  
6122 BESIII upgrade”. In: *NIMA* 763 (2014), pp. 190–196.
- 6123 [209] A. Akindinovg et al. “RPC with low-resistive phosphate glass electrodes as a candidate for  
6124 the CBM TOF”. In: *NIMA* 572 (2007), pp. 676–681.
- 6125 [210] JINST, ed. *Development of the MRPC for the TOF system of the MultiPurpose Detector.*  
6126 RPC2016: XII Workshop on Resistive Plate Chambers and Related Detectors. 2016.
- 6127 [211] M.C.S. Williams. “Particle identification using time of flight”. In: *Journal of Physics G* 39  
6128 (2012).
- 6129 [212] A. Alici et al. “Aging and rate effects of the Multigap RPC studied at the Gamma Irradiation  
6130 Facility at CERN”. In: *NIMA* 579 (2007), pp. 979–988.
- 6131 [213] M. Abbrescia et al. “The simulation of resistive plate chambers in avalanche mode: charge  
6132 spectra and efficiency”. In: *NIMA* 431 (1999), pp. 413–427.
- 6133 [214] JINST, ed. *Description and simulation of physics of Resistive Plate Chambers.* RPC2016:  
6134 XII Workshop on Resistive Plate Chambers and Related Detectors. 2016.
- 6135 [215] V. François. “Description and simulation of the physics of Resistive Plate Chambers”. PhD  
6136 thesis. LPC - Laboratoire de Physique Corpusculaire - Clermont-Ferrand, 2017.
- 6137 [216] International Commission on Radiation Units and Measurements. *Stopping Powers for Elec-*  
6138 *trons and Positions.* Tech. rep. Report 37. 1984.
- 6139 [217] International Commission on Radiation Units and Measurements. *Stopping Power and Ranges*  
6140 *for Protons and Alpha Particles.* Tech. rep. Report 49. 1994.
- 6141 [218] H. Bethe. “Zur Theorie des Durchgangs schneller Korpuskularstrahlen durch Materie”. In:  
6142 *Annalen der Physik* 397 (1930), pp. 325–400.
- 6143 [219] H. Bichsel. “A method to improve tracking and particle identification in TPCs and silicon  
6144 detectors”. In: *NIMA* 562 (2006), pp. 154–197.
- 6145 [220] W. W. M. Allison and J. H. Cobb. “Relativistic charged particle identification by energy  
6146 loss”. In: *Annual Review of Nuclear and Particle Science* 30 (1980), 253–298.
- 6147 [221] J. Phys.: Conf. Ser., ed. *Results of the CALICE SDHCAL technological prototype.* 16th  
6148 International Conference on Calorimetry in High Energy Physics (CALOR 2014). 2015.
- 6149 [222] W. Riegler et al. “Detector physics and simulation of resistive plate chambers”. In: *NIMA*  
6150 500 (2003), pp. 144–162.
- 6151 [223] International Commission on Radiation Units and Measurements. *Average energy to pro-*  
6152 *duce an ion pair.* Tech. rep. Report 31. 1994.
- 6153 [224] I.B. Smirnov. “Modeling of ionization produced by fast charged particles in gases”. In:  
6154 *NIMA* 554 (2005), pp. 474–493.
- 6155 [225] I.B. Smirnov. *HEED++ simulation program.* 2010. URL: <http://ismirnov.web.cern.ch/ismirnov/heed>.

- [226] R. Veenhof et al. *Garfield++ - simulation of tracking detectors*. 2015. URL: <http://garfieldpp.web.cern.ch/garfieldpp/>.
- [227] W. H. Furry. “On Fluctuation Phenomena in the Passage of High Energy Electrons through Lead”. In: *Phys. Rev.* 52 (1937), pp. 569–581.
- [228] S.F. Biagi. “Monte Carlo simulation of electron drift and diffusion in counting gases under the influence of electric and magnetic fields”. In: *NIMA* 421 (1999), pp. 234–240.
- [229] H. Genz. “Single electron detection in proportional gas counters”. In: *Nucl. Instr. and Meth.* 112 (1973), pp. 83–90.
- [230] W. Shockley. “Currents to Conductors Induced by a Moving Point Charge”. In: *Journal of Applied Physics* 9 (1938), p. 635.
- [231] S. Ramo. “Currents Induced by Electron Motion”. In: *Proceedings of the IRE* 27 (1939), pp. 584–585.
- [232] M. Abbrescia et al. “Resistive plate chambers performances at cosmic rays fluxes”. In: *NIMA* 359 (1995), pp. 603–609.
- [233] M. Abbrescia et al. “Resistive plate chambers performances at low pressure”. In: *NIMA* 394 (1997), pp. 341–348.
- [234] M. Abbrescia. “Operation, performance and upgrade of the CMS Resistive Plate Chamber system at LHC”. In: *NIMA* 732 (2013), pp. 195–198.
- [235] F. Thyssen. “Commissioning, Operation and Performance of the CMS Resistive Plate Chamber System”. PhD thesis. Universiteit Gent, 2014.
- [236] M. Bianco. “ATLAS RPC certification and commissioning with cosmic rays”. PhD thesis. Università del Salento, 2007.
- [237] M. Bianco. “ATLAS RPC certification with cosmic rays”. In: *NIMA* 602 (2009), pp. 700–704.
- [238] M. Drees and X. Tata. “Signals for heavy exotics at hadron colliders and supercolliders”. In: *Physics Letters B* 252 (1990), pp. 695–702.
- [239] D.A. Milstead et al. “Stable massive particles at colliders”. In: *Physics Reports* 438 (2007), pp. 1–63.
- [240] Z. Ligeti et al. “Supermodels for early LHC”. In: *Physics Letters B* 690 (2010), pp. 280–288.
- [241] CMS Collaboration. “Search for long-lived charged particles in proton-proton collisions at  $\sqrt{s} = 13 \text{ TeV}$ ”. In: *Phys. Rev. D* 94 (2016), p. 112004.
- [242] V. Khachatryan et al. “Search for long-lived charged particles in proton-proton collisions at  $\sqrt{s} = 13 \text{ TeV}$ ”. In: *Phys. Rev. D* 94 (2017), 112004.
- [243] A. Kusenko and M. Shaposhnikov. “Supersymmetric Q-balls as dark matter”. In: *Physics Letters B* 418 (1998), pp. 46–54.
- [244] B. Koch et al. “Black holes at LHC?” In: *J. Phys. G: Nucl. Part. Phys.* 34 (2007). S535.
- [245] J. Schwinger. “Magnetic Charge and Quantum Field Theory”. In: *Phys. Rev.* 144 (1966). 1087.
- [246] M Yu Khlopov et al. “Dark matter with invisible light from heavy double charged leptons of almost-commutative geometry?” In: *Class. Quantum Grav.* 23 (2006). 7305.
- [247] PoS, ed. *Search for Heavy Stable Charged Particles in CMS*. Vol. 084-EPS-HEP2009. 2009, p. 438.

## BIBLIOGRAPHY

---

- 6200 [248] L.E. Medina Medrano et al. “Studies on Luminous Region, Pile-up and Performance for  
6201 HL-LHC Scenarios”. In: *Proc. of International Particle Accelerator Conference (IPAC’17),  
6202 Copenhagen, Denmark, 14-19 May, 2017*. JACoW, 2017, pp. 1908–1911.
- 6203 [249] CMS Collaboration. *CMS Luminosity - Public Results*. Version 158. 2019. URL: <https://twiki.cern.ch/twiki/bin/view/CMSPublic/LumiPublicResults>.
- 6205 [250] CERN. Geneva. LHC Experiments Committee. *Technical Proposal for the Phase-II Up-  
6206 grade of the CMS Detector*. Tech. rep. CERN-LHCC-2015-010, CMS-TDR-15-02. CMS  
6207 Collaboration, 2015.
- 6208 [251] CERN. Geneva. LHC Experiments Committee. *The Phase-2 Upgrade of the CMS Level-1  
6209 Trigger - Interim Report to the LHCC*. Tech. rep. CERN-LHCC-2017-013, CMS-TDR-017.  
6210 CMS Collaboration, 2017.
- 6211 [252] CERN. Geneva. LHC Experiments Committee. *High-Luminosity Large Hadron Collider  
6212 (HL-LHC) Preliminary Design Report*. Tech. rep. CERN-LHCC-94-38. CMS Collaboration,  
6213 1994.
- 6214 [253] F. Sauli. “GEM: A new concept for electron amplification in gas detectors”. In: *Nucl. Instr.  
6215 Meth. Phys. Res.* 386 (1997), pp. 531–534.
- 6216 [254] CERN. Geneva. LHC Experiments Committee. *CMS Technical Design Report for the Muon  
6217 Endcap GEM Upgrade*. Tech. rep. CERN-LHCC-2015-012, CMS-TDR-013. CMS Collabora-  
6218 tion, 2015.
- 6219 [255] A. Gelmi. *CMS iRPC at HL-LHC: background study*. 2018. URL: [https://indico.cern.ch/event/732794/contributions/3021836/attachments/1657792/2654574/iRPC\\_bkg\\_study\\_Upgrade29\\_05\\_18.pdf](https://indico.cern.ch/event/732794/contributions/3021836/attachments/1657792/2654574/iRPC_bkg_study_Upgrade29_05_18.pdf).
- 6222 [256] A. Gelmi and E. Voevodina. “Background rate study for the CMS improved-RPC at HL-  
6223 LHC using GEANT4”. In: *Nucl. Instr. Meth. Phys. Res. A* (2018).
- 6224 [257] IEEE, ed. *Petiroc, a new front-end ASIC for time of flight application*. Vol. 2013 IEEE  
6225 Nuclear Science Symposium and Medical Imaging Conference (2013 NSS/MIC). 2014.
- 6226 [258] JINST, ed. *Petiroc and Citiroc: front-end ASICs for SiPM read-out and ToF applications*.  
6227 Vol. Topical Workshop on Electronics for Particle Physics 2013 (TWEPP-13). 2014.
- 6228 [259] P.Bortignon. “Design and performance of the upgrade of the CMS L1 muon trigger”. In:  
6229 *Nucl. Instr. Meth. Phys. Res.* 824 (2016), pp. 256–257.
- 6230 [260] JINST, ed. *Performance of the Resistive Plate Chambers in the CMS experiment*. The 9<sup>th</sup>  
6231 International Conference on Positioin Sensitive Detectors. 2012.
- 6232 [261] PoS, ed. *The CMS RPC detector performance during Run-II data taking*. The European  
6233 Physical Society Conference on High Energy Physics (EPS-HEP2017). 2018.
- 6234 [262] M. Abbrescia et al. “Study of long-term performance of CMS RPC under irradiation at the  
6235 CERN GIF”. In: *NIMA* 533 (2004), pp. 102–106.
- 6236 [263] H.C. Kim et al. “Quantitative aging study with intense irradiation tests for the CMS forward  
6237 RPCs”. In: *NIMA* 602 (2009), pp. 771–774.
- 6238 [264] S. Agosteo et al. “A facility for the test of large-area muon chambers at high rates”. In:  
6239 *NIMA* 452 (2000), pp. 94–104.
- 6240 [265] PoS, ed. *CERN GIF ++ : A new irradiation facility to test large-area particle detectors for  
6241 the high-luminosity LHC program*. Vol. TIPP2014. 2014, pp. 102–109.
- 6242 [266] H. Reithler. *Filters for GIF++*. RWTH Aachen University, CMS-CERN. 2013. URL: <https://edms.cern.ch/document/1324028/1>.

- 6244 [267] D. Pfeiffer et al. “The radiation field in the Gamma Irradiation Facility GIF++ at CERN”.  
 6245 In: *NIMA* 866 (2017), pp. 91–103.
- 6246 [268] CAEN. *Mod. V1190-VX1190 A/B, 128/64 Ch Multihit TDC*. 14th ed. 2016.
- 6247 [269] CAEN. *Mod. V1718 VME USB Bridge*. 9th ed. 2009.
- 6248 [270] A. Fagot. *GIF Cosmic Muon Monte Carlo Simulation*. 2017. URL: <https://github.com/afagot/Cosmics-Simulation>.
- 6249 [271] G. Pugliese et al. “Aging study for resistive plate chambers of the CMS muon trigger detector”. In: *NIMA* 515 (2003), pp. 342–347.
- 6250 [272] G. Pugliese et al. “Long-term performance of double gap resistive plate chambers under  
 6253 gamma irradiation”. In: *NIMA* 477 (2002), pp. 293–298.
- 6254 [273] M. Capeans et al. on behalf of the GIF and GIF++ User Communities. “A GIF++ Gamma  
 6255 Irradiation Facility at the SPS H4 Beam Line”. CERN-SPSC-2009-029 / SPSC-P-339. 2009.
- 6256 [274] R. Guida et al. “Results about HF production and bakelite analysis for the CMS Resistive  
 6257 Plate Chambers”. In: *NIMA* 594 (2008), pp. 140–147.
- 6258 [275] F. Bellini et al. “Study of HF production in BaBar Resistive Plate Chambers”. In: *NIMA* 594  
 6259 (2008), pp. 33–38.
- 6260 [276] J. Eysermans. *WebDCS GIF++*. CERN. 2016. URL: <https://www.webdcs.cern.ch>.
- 6261 [277] JACoW, ed. *Monitoring of CERN’s Data Interchange Protocol (DIP) System*. Vol. ICALEPCS2017-THPHA162. 2018, pp. 1797–1800.
- 6264 [278] A. Fagot and S. Carrillo. *GIF++ Offline Analysis v6*. 2017. URL: [https://github.com/afagot/GIF\\_OfflineAnalysis](https://github.com/afagot/GIF_OfflineAnalysis).
- 6266 [279] R. Cardarelli et al. “RPC performance vs. front-end electronics”. In: *NIMA* 661 (2012),  
 6267 S198–S200.
- 6268 [280] C. Combaret et al. “Fast timing measurement for CMS RPC Phase-II upgrade”. In: *JINST*  
 6269 13 (2018), p. C09001.
- 6270 [281] L. Pizzimento et al. “Development of a new Front End electronics in Silicon and Silicon-  
 6271 Germanium technology for the Resistive Plate Chamber detector for high rate experiments”.  
 XIV RPC 2018 - Workshop on resistive plate chambers and related detectors. 2018.
- 6273 [282] E. Alunno Camelia et al. “Optimization of RPCs read-out panel with electromagnetic simu-  
 6274 lation”. XIV RPC 2018 - Workshop on resistive plate chambers and related detectors. 2018.
- 6275 [283] R. Cardarelli et al. “Performance of RPCs and diamond detectors using a new very fast low  
 6276 noise preamplifier”. In: *JINST* 8 (2013), P01003.
- 6277 [284] J. de Urquijo et al. “Electron swarm coefficients in 1,1,1,2 tetrafluoroethane (R134a) and its  
 6278 mixtures with Ar”. In: *The European Physical Journal D* 51 (2009), pp. 241–246.
- 6279 [285] A. Fagot. *GIF++ Data Acquisition Software for CMS RPC*. 2016. URL: [https://github.com/afagot/GIF\\_DAQ](https://github.com/afagot/GIF_DAQ).
- 6281 [286] W-Ie-Ne-R. *VME 6021-23 VXI*. 5th ed. 2016.
- 6282 [287] Wikipedia. *INI file*. 2017. URL: [https://en.wikipedia.org/wiki/INI\\_file](https://en.wikipedia.org/wiki/INI_file).